University of Vermont
ScholarWorks @ UVM

Graduate College Dissertations and Theses | Dissertations and Theses

2017

4d Strain Path Recorded In The Lower Crust During The Transition From Convergence To Continental Rifting, Doubtful Sound, Fiordland, New Zealand

Michael Ingram
University of Vermont

Follow this and additional works at: https://scholarworks.uvm.edu/graddis

 Part of the Geology Commons

Recommended Citation

Ingram, Michael, "4d Strain Path Recorded In The Lower Crust During The Transition From Convergence To Continental Rifting, Doubtful Sound, Fiordland, New Zealand" (2017). *Graduate College Dissertations and Theses*. 683.
https://scholarworks.uvm.edu/graddis/683

This Thesis is brought to you for free and open access by the Dissertations and Theses at ScholarWorks @ UVM. It has been accepted for inclusion in Graduate College Dissertations and Theses by an authorized administrator of ScholarWorks @ UVM. For more information, please contact donna.omalley@uvm.edu.

4D STRAIN PATH RECORDED IN THE LOWER CRUST DURING THE TRANSITION FROM CONVERGENCE TO CONTINENTAL RIFTING, DOUBTFUL SOUND, FIORDLAND, NEW ZEALAND

A Thesis Presented

by

Michael Ingram

to

The Faculty of the Graduate College

of

The University of Vermont

In Partial Fulfillment of the Requirements
for the Degree of Master of Science
Specializing in Geology

January, 2017

Defense Date: November 16, 2016
Thesis Examination Committee:

Keith A. Klepeis, Ph.D., Advisor
Mandar M. DeWoolkar, Ph.D., Chairperson
Laura E. Webb, Ph.D.
Cynthia J. Forehand, Dean of the Graduate College

ABSTRACT

Doubtful Sound, in SW New Zealand, exposes an exhumed section of lower crust that represents the root of an Early Cretaceous magmatic arc. Here, the lower crust underwent a change from contraction to extension and these tectonic cycles are fundamental to the growth of continental crust. Mafic-intermediate granulite gneisses occur below the extensional Doubtful Sound shear zone (DSSZ) which records the retrogression and transposition of granulite fabrics at the upper amphibolite facies. I compared 3D rock fabrics, microstructures and textures within and below the DSSZ to determine the processes involved in the shift from contraction to extension and to infer the sequential processes of transforming L>S granulites to L=S amphibolites.

Below the DSSZ, dehydration zones around felsic veins and leucosome in migmatitic orthogneiss record granulite facies metamorphism. Aggregates of clinopyroxene (cpx) and orthopyroxene (opx) that are rimmed by garnet (grt) and interstitial melt are set in a plagioclase (pl) matrix. Peritectic grt, pl-grt symplectites, beads of pl along grain boundaries, and elongate, inclusion-free pl reflect the anatexis. Pl exhibits a crystal preferred orientation (CPO) and evidence of subgrain rotational recrystallization and grain boundary migration, indicating subsolidus deformation outlasted melting. Mafic aggregates are boudinaged and opx developed subgrains. During peak metamorphism high strain was partitioned to locations enriched in melt, producing L>S fabrics and an upward trajectory in the strain path. A comparison of mineral grain shapes indicates that pl accommodated most of the strain. Granulite-amphibolite transitional rocks inside the DSSZ record a heterogeneous retrogression of the granulites to a polyphase metamorphic assemblage of hornblende (hbl), biotite (bt), and fine pl. Also preserved is the resetting of high strain L>S granulite to low strain, L=S amphibolite. Folia of porphyroblastic hbl + bt progressively penetrate the pl matrix via solution mass transfer. Porphyroblastic pl in the rock matrix becomes increasingly transposed to gneissic layering. A path of decreasing gradient from high strain L>S granulite to low strain L=S amphibolite reflects the development of the DSSZ fabric, growth of new minerals and onset to deformation at the amphibolite facies. Inside the DSSZ, amphibolites show an increasing strain gradient from low strain L=S amphibolite to high strain L=S amphibolite. Pl aggregates lack a CPO and are mostly annealed but preserve grain boundary migration microstructures. Hbl is recrystallized and forms asymmetric fish. Evidence of high fluid activity and reaction softening within the DSSZ include increased hbl + bt and bt beards on pl relative to rocks outside the DSSZ.

My observations suggest that magma, heat, and melting initially weakened the lower crust, facilitating the development of high strain zones with L>S fabrics. Partially molten regions deformed by suprasolidus flow and solid portions deformed mostly by dislocation creep in pl and boudinage of cpx + opx. Later, the lower crust was weakened and high strain fabrics were reset from overprinting and transposition as retrogression progressed and low strain L=S fabrics formed. During extension there was an upward trajectory in the strain path to high strain L=S fabrics within the DSSZ, where hbl and bt accommodated more strain. My results illustrate the importance of 1) melting, cooling, and hydration in controlling strain partitioning and the rheological evolution of lower crustal shear zones, and 2) the importance of integrating microstructural and fabric analysis to determine strain paths.

ACKNOWLEDGEMENTS

I owe the success of this project to my advisor Keith Klepeis. Your generous gifts of patience and support as I hurdled into growing a family and starting a career will never be forgotten. I admire the passion and knowledge you have for teaching and research. On top of many memorable moments in the lab and teaching field geology I will forever cherish the moments when the squalls blew in, the plug in our boat came out, drifting in the fiords while eating chocolate (and sardines), possum infested living quarters, clinging to precarious outcrops, making laughter for being afraid of Kias, endless hours behind the rock saws, but most importantly I will remember how you were always interested in the wellbeing of myself and my family before we discussed work. Thank you for your mentorship and the experience of a lifetime.

I cannot thank my beloved wife enough for the sacrifices she made so that I could finish this project. You have always been in my corner cheering me on and while there never seemed to be an ideal time to sneak away and write, you let me work without even flinching. The good news is we have new bedtime reading material for the kiddos that will surely put them right to sleep!

I would like to thank Jeff Webber for his valuable field work and creating FABRIC. Jeff leant countless hours of assistance and provided indispensable insight. Many thanks also to Laura Webb for always having an open door, and thank you to the rest of the Geology department.

TABLE OF CONTENTS

Page

ACKNOWLEDGEMENTS ii

LIST OF FIGURES vi

CHAPTER 1: INTRODUCTION 1

CHAPTER 2: LITERATURE REVIEW 4

2.1. Composition of the Malaspina Orthogneiss 4

2.2 Structure of the Malaspina Orthogneiss 8

Deformation events and fabrics 8

Structure of Hall Arm and Crooked Arm 9

Structure of the Doubtful Sound Shear Zone (DSSZ) 10

2.3 Cretaceous Tectonic History of Fiordland, New Zealand 11

2.8 Strain and Fabric Analyses 13

Chapter 3: STRUCTURES AND MICROSTRUCTURES OF DOUBTFUL SOUND, CROOKED ARM, AND HALL ARM 15

3.1 Mapping Units 16

Metadiorites 16

Hornblendites 17

Granulites and garnet granulites 17

Retrogressed granulites 17

Amphibolites 18

3.2 Overview and Relative Chronology of Structures 18

D_1 18

D_2 19

D_3 20

3.3 Doubtful Sound 21

Domain 1 (Doubtful Sound) 25

Synthesis of Domain 1 28

Domain 2 (Doubtful Sound) 35

Synthesis of Domain 2 41

Domain 3 (Doubtful Sound) 42

Synthesis of Domain 3 43

3.4 Crooked Arm 46

Domain 1 (Crooked Arm) 51

Synthesis of domain 1 52

Domain 2 (Crooked Arm) 59

Synthesis of domain 2 64

3.5 Hall Arm 82

Domain 1 (Hall Arm) 86

Domain 2 (Hall Arm) 86

Domain 3 (Hall Arm) 91

Synthesis of Hall Arm 93

Estimated Temperatures of Deformation 94

Mechanisms of Deformation 95

Chapter 4: FABRIC ANALYSIS 96

4.1 Introduction 96

4.2 Methods 97

Orienting cut faces 98

Digitizing 99

R_f/Φ technique 100

4.3 Fabric Results 101
Metadiorites and D_1 101
Granulites, weakly retrogressed granulites, and D_2 103
Granulite-amphibolite and D_2-D_3 transition 104
Amphibolites and D_3 105
Summary of results 105

4.4 Discussion 106
Step 1 108
Step 2 108
Step 3 109
Step 4 109
Step 5 110
Conclusion 111

BIBLIOGRAPHY 126

APPENDIX A 132

LIST OF FIGURES

Figure Page

Figure 1. An overview geologic map of Fiordland (blue box on inset map) showing the distribution of plutonic rocks that comprise the Median Batholith and extensional structures such as the Doubtful Sound Shear Zone (this study). 3

Figure 2. A geographic map of the Doubtful Sound region in Fiordland, New Zealand. The base map is a digital elevation model, the lighter the color the higher the elevation. The white space within the map are fiords.....5

Figure 3. A Cretaceous reconstruction of Gondwana at ~120 Ma after Mortimer (2008) that shows the tectonic regime in which the Malaspina Pluton was emplaced. The reconstruction shows oceanic subduction beneath the paleo-Gondwana continent and arc magmatism (in red). 12

Figure 4. A site map showing the locations of field site and structural domains. All of the circles and "x's" also represent field locations. Domain 1 consists of mostly metadiorite rocks, Domain 2 contains granulite and garnet granulite rocks, and Domain 3 is composed of mostly amphibolite rocks and structures that define the Doubtful Sound Shear Zone. 22

Figure 5. A structural map of Doubtful Sound and a lower hemisphere equal-area stereographic projection showing. The foliation trajectories define domes within the metadiorite and granulite domains. Note that in the grey (Domain 1) L_1 trends northwest-southeast, in the orange (Domain 2) L_2 trends mostly east, and in the green area to the north (Domain 3), L_3 trends mostly northeast. 23

Figure 6. A cross section of Doubtful Sound, from Crooked Arm to Hall Arm. This section shows the structure and locations of Domains 1, 2 and 3. A dome of mostly metadiorite and a dome of mostly granulite lie below the Doubtful Sound Shear Zone (DSSZ). The DSSZ penetrates the granulites and has a top-down-to-the-northeast sense of shear. Lozenges of granulite have transposed S_2 foliations in the region of Crooked Arm. Above the topographic profile are the site names and features. The line of section is shown in Figure 5. 24

Figure 7. Photomicrographs of sample 12DC16A. The rock type is a metadiorite that shows S_1 foliation defined by the alignment of hornblende. These images are evidence of crystallization textures during magmatic flow that was accommodated by dislocation creep in plagioclase. A) Plane light photomicrograph showing coarse hornblende aggregates and a plagioclase matrix. B) Cross polarized photomicrograph of "A". C) Plane light photomicrograph showing coarse hornblende grains. D) Cross polarized photomicrograph of "C" that also shows plagioclase grain boundary migration and subgrains. E) Cross polarized photomicrograph showing radial biotite overgrowing hornblende. F) Cross polarized photomicrograph that shows the interlocking plagioclase grain boundaries. 29

Figure 8. All photomicrographs are of sample 12DC16B and are cross polarized. The rock type is a garnet granulite. These images show evidence of dislocation creep in plagioclase and textures of biotite that represent hydration. A) Grain boundary migration and subgrains in plagioclase. B) Biotite tail on garnet. C) Simple twinning of an orthopyroxene grain in the plagioclase matrix. Note the lack of recrystallization in the plagioclase matrix, indicating deformation was not pervasive. D) Clinopyroxene moat around orthopyroxene. 30

Figure 9. All photomicrographs are of sample 12DC10A. The rock type is a metadiorite that has a spaced and non-continuous S_1 foliation. These images show the plagioclase matrix, aggregates of hornblende that define S_1, and evidence of dislocation creep in plagioclase. A) Plane polarized photomicrograph showing an overview of the sample, hornblende aggregates and the plagioclase matrix. B) Cross polarized photomicrograph of "A". C) A plane polarized photomicrograph and blow up of a hornblende aggregate showing sub-millimeter hornblende grains. D) Cross polarized photomicrograph of "C". E) Cross polarized photomicrograph showing amoeboid grain boundaries on plagioclase and evidence of grain boundary migration in the same mineral. 31

Figure 10. A site photo from 12DC09 in Domain 1 of Doubtful Sound that provides evidence of magma mingling between a mafic, hornblendite dike and its host while the Malaspina pluton was still partially molten. The mafic dike shows gradational and undulose contacts with the host rock. The pod is approximately three meters long. 32

Figure 11. A) Site photos from 12DC33 in Domain 1 of Doubtful Sound that shows a swarm or hornblende rich dikes that intrude the host metadiorite and are evidence of magma mingling. B) A close up of the mingling between mafic and intermediate magmas at site 12DC33. 32

Figure 12. All photomicrographs are of sample 12DC35B from Domain 1 in Doubtful Sound. The rock type is a garnet granulite. These images show evidence of dislocation creep in plagioclase and symplectite textures. A) Cross polarized photomicrograph of an elongate garnet surrounded by potassium feldspar (suggesting the presence of melt) and subgrains of plagioclase in the matrix. B) Cross polarized photomicrograph of an aggregate of garnet and clinopyroxene. C) Plane light photomicrograph of an orthopyroxene. D) Cross polarized photomicrograph of "C". E) Plane light photomicrograph of a symplectite with vermicular texture. F) Cross polarized photomicrograph of "E".....33

Figure 13. All photomicrographs are of sample 12DC35C from Domain 1 in Doubtful Sound and are cross polarized. The rock type is a garnet granulite. The images show microstructures of a centimeter scale shear zone and evidence of melt. A) An overview of the shear zone (top right of image). Note the millimeter scale plagioclase and hornblende aggregates in the walls and the grain size reduction in the shear zone. B) Garnet and fine plagioclase in the shear zone. C) A close up of garnet that has rims of biotite in the shear zone. D) Plagioclase outside of the shear zone that has bent twins and beads of rounded plagioclase that are interpreted to represent melt. E) An image outside of the shear showing fine plagioclase beads, garnet and hornblende. F) Myrmekite textures in plagioclase outside of the shear zone.....34

Figure 14. A) Site photo of 12DC36 in Domain 2 of Doubtful Sound showing boudinaged hornblendite sheets. B) A close up from "A" showing the S_2 foliation of the metadiorite host and leucosome in the boudin neck which indicates melt was mobile during deformation. 37

Figure 15. Both images are cross polarized photomicrographs of sample 12DC59A in Domain 2 of Doubtful Sound. The rock type is a granulite that preserves the S_2 foliation. These images show evidence of high temperature deformation and anatexis (see section 3.3 for discussion). A) An overview of a granulite showing elongate pyroxene aggregates set in a plagioclase matrix. The pyroxene aggregates define S_2. B) A close up of plagioclase grain boundaries and a melt bead. 37

Figure 16. All photomicrographs are of sample 12DC57A from Domain 2 in Doubtful Sound. The rock type is a garnet granulite. The images show microstructures of high temperature metamorphism, deformation, anatexis, and dislocation creep in clinopyroxene. A) A plane light overview photomicrograph showing trains of pyroxene and a clinopyroxene moat on orthopyroxene. B) A cross polarized photomicrograph of "A". C) A plane light photomicrograph showing elongate clinopyroxene grains set in the plagioclase matrix. D) A cross polarized photomicrograph of "C". The box outlines the extent of "E". E) A cross polarized photomicrograph of clinopyroxene showing grain boundaries and

subgrains. F) A cross polarized photomicrograph showing elongate and inclusion free plagioclase grains, as well as elongate orthopyroxene grains. 38

Figure 17. All photos are site photos from 12DC55 in Domain 2 of Doubtful Sound. The rock types are granulites and garnet granulites with a weakly developed S_2 foliation. These images show the patchwork of garnet granulite metamorphism. A) An outcrop of granulite and a local garnet granulite reaction zone. B) A close up of the garnet granulite zone from "A" showing peritectic garnet. C) Peritectic garnets surrounded by leucosome. D) Peritectic garnet on the edge of a garnet granulite reaction zone. Note the plagioclase matrix and wispy alignment of pyroxene. E) Leucosome vein studded with peritectic garnets that cross cuts the garnet granulite. F) Small fold in a leucosome vein. 39

Figure 18. All photomicrographs are cross polarized light. The sample is denoted in the upper right corner. The rock types are granulites and garnet granulites that preserve the S_2 foliation. A) An overview photomicrograph showing elongate trains of pyroxene that define S_2. B) Grain boundary migration in plagioclase. C) A fractured garnet in the center of the image and garnet with inclusions in the upper right. D) The blue clinopyroxene has a thin reaction rim and the arrow points to grain boundary migration and deformation twins in plagioclase. 40

Figure 19. Site photographs from 12DC53. The host rock is a metadiorite. Photos A and B show the lack of aligned hornblende any pyroxene into a foliation plane, and euhedral peritectic garnet with reaction rims. 41

Figure 20. All images are from the Doubtful Sound Shear Zone at site 12DC51 in Domain 3 of Doubtful Sound. The rock type is an amphibolite that has a S_3 foliation. The foliation is identified by the alignment of hornblende and feldspar porphyroclasts. A) A cluster of asymmetric feldspar porphyroclasts. B) An elongate potassium feldspar porphyroclast in the center of the photo, and porphyroblastic hornblende in the foliation below. C) A photo showing a potassium feldspar porphyroclast and the hbl+pl foliation. D) A potassium feldspar porphyroclast in the center of the photo with tails of plagioclase and beards of hornblende. 44

Figure 21. All photomicrographs are from sample 12DC51.A from the Doubful Sound Shear Zone (DSSZ) in Domain 3 of Doubtful Sound. The rock type is an amphibolite and the images show the microstructures associated with the DSSZ. A) The field of view is 12 mm. This is a plane light overview photomicrograph showing the semicontinous foliation of aligned hornblende. B) The field of view is 12 mm. A cross polarized photomicrograph of "A". C) A cross polarized photomicrograph showing the formation of a tripple junction in the center of the

image and grain boundary migration in plagioclase. D) A cross polarized photomicrograph showing a simple twinned hornblende in the center of the image that has a tail of finer grained hornblende to the right. 45

Figure 22. A site location and geologic map showing the penetrative nature of the DSSZ into regions of granulite. Cross sections B-B' and C-C' can be seen in Figure 24. 48

Figure 23. A structural map of Crooked Arm and a lower hemisphere equal-area stereographic projection showing the NE-SW trending L_2 and L_3 lineations. While both lineations trend NE-SW, L_3's in proximity to L_2s consistently trend more northerly. 49

Figure 24. Cross section of Crooked Arm from Figure 23 showing mostly granulite in Domain 1, the penetrative DSSZ with transitional and amphibolite rocks that enclose lozenges of granulite in Domain 2, and the thickest zone of the DSSZ at the cover rock contact. 50

Figure 25. All photomicrographs are from sample 12DC39.A and the rock is a metadiorite with D_2 deformation. These images show the heterogeneous compositoin of the folation and evidence of dislocation creep in plagioclase. A) An overview plane light photomicrograph showing clots of hornblende and biotite that are semiconnected yet set in the plagioclase matrix. B) A cross polarized photomicrograph showing grain boundary migration and subgrains in plagioclase, as well as biotite that has grown along plagioclase grain boundaries. C) A plane light photomicrograph of a hornblende, plagioclase and biotite layer that shows the fine inclusions of plagioclase. D) A cross polarized photomicrograph of "C". E) A plane light photomicrograph showing a large plagioclase grain on the left that is surrounded by a mixture of fine plagioclase, hornblende and biottie. F) A cross polarized photomicrograph of "E" that shows grain boundary migration and subgrains in plagioclase. 55

Figure 26. All photos are from site 12DC41. These images show the interaction of the dioritic orthogneiss with the hornblendites. A) A site photo showing bands of metadiorite that iintruded hornblendite. B) A photo showing the contact between the orthogneiss and hornblendite. C) A photo showing the orthogneiss and hornblendite. Just above the sharpie marker you can see a small enclave that is nearly dismembered from the mafic rock. D) A close up of the enclave from "C". E) A folded pegmatite dike that cross cuts the orthogneiss. F) A close up of the pegmatite dike from "E" showing a weak fabric and garnets 56

Figure 27. Both photomicrographs are cross polarized light and from sample 12DC41.A. The rock is a hornblendite that was in contact with a dioritic orthogneiss. A) An overview showing that the hornblendite is mainly composed of hornblende and biotite, but that it contains fine plagioclase along grain boundaries. B) This images shows the shape perferred orintation of hornblende. The foliation traces from the bottom left to the top right of the image. 57

Figure 28. All photomicrographs are from sample 12DC42.A, a metadiorite that preserves D_2 deformation. The field of view for "A" and "B" is 12 mm. A) A plane light overview photomicrograph that shows aggregates of hornblende and a matrix of plagioclase with fine grained hornblende and biotite along the grain boundaries. B) A cross polarized photomicrograph of "A" that also shows a porphyroblastic plagioclase on the left of the image. C) A plane light photomicrograph of a hornblende aggregate showing subhedral to anhedral grain shapes and inclusions of plagioclase. D) A cross polarized photomicrograph of "C". E) A cross polarized photomicrograph of a plagioclase domain that shows fine hornblende and biotite along plagioclase grain boundaries. F) A cross polarized photomicrograph of a plagioclase domain showing grain boundary migration and subgrains. 58

Figure 29. All photos are from site 12DC38 where garnet granulites with a S_2 and L_2 fabric are exposed. A) This image shows a relict domain of the $L_1 \geq S_1$ garnet granulite fabric with a leucosome vein that is transposed into a shearzone of the $L_2 > S_2$ garnet granulite rocks. B) A view of elongate pyroxene and plagioclase form an $L_2 > S_2$ domain of garnet granulite. Towards the top of the image is a train of peritectic garnets in a thin leucosome vein. C) $L_2 > S_2$ garnet granulites with peritectic garnet. D) $L_2 > S_2$ garnet granulites with pyroxenes rimmed by garnet. 65

Figure 30. All photos are from site 12DC38 where garnet granulites with $L_2 > S_2$ fabrics are exposed. A) An overview showing domains of $L_1 \geq S_1$ garnet granulite with leucosome veins and domains of $L_2 > S_2$ garnet granulite. The $L_1 \geq S_1$ domains are identified by the coarser grained pyroxenes and the foliation being transposed into the streaky $L_2 > S_2$. B) Mostly $L_2 > S_2$ rocks with zones of garnet granulite. C) A relict domain of $L_1 \geq S_1$ garnet granulite in the center of the photo with the foliation being transposed into into the $L_2 > S_2$ garnet granulites at the top and bottom. D) A boudinaged mafic dike surrounded by garnet granulite. E) The pencil points to a boudinaged mafic layer overprinted by garnet. F) Peritectic garnet surrounded by leucosome. 66

Figure 31. All photomicrographs are from site 12DC38. The sample is denoted in the top right corner. These images show evidence of anatexis and deformation at temperatures greater than 750° C (Schwartz et al., 2016) in garnet granulites that have a $L_2 > S_2$ fabric. A) A plane light photomicrograph showing clinopyroxene moats on orthphyroxene. The large grain of orthopyroxene towards the center of

the image has a moat of clinopyroxene that is surrounded by a film/moat of potassium feldspar. B) A cross polarized photomicrograph of “A”. C) A plane light photomicrograph of a garnet granulite showing a boudinaged aggregate of pyroxene with a moat of potassium feldspar. D) A cross polarized photomicrograph of “C”. E) A plane light photomicrograph of a garnet surrounded by a film of potassium feldspar. F) A cross polarized photomicrograph of “F”. 67

Figure 32. All photomicrographs are from sample 12DC38B which is a garnet granulite with L_2 and S_2 fabrics. These images show evidence of dislocation creep in orthopyroxene. A) A plane light photomicrograph of an asymmetric orthopyroxene aggregate with subgrains that is isolated in the plagioclase matrix. B) A cross polarized photomicrograph of “A”. C) A plane light photomicrograph of a orthopyroxene grains with subgrains. Also shown are garnets with interstitial quarts and a film of potassium feldspar. D) A cross polarized photomicrograph of “C”. 68

Figure 33. All photomicrographs are from site 12DC38. The samples are garnet granulites with L_2 and S_2 fabrics. The sample name is denoted in the upper right corner. These images show that garnet rims pyroxene grains and also occurs as large aggregates with tails of pyroxene. A) An overview plane light photomicrograph showing garnet rimming elongate pyroxene grains. B) A cross polarized photomicrograph of “B”. C) A plane light photomicrograph showing rims of garnet on pyroxene. D) A cross polarized photomicrograph of “C”. E) A plane light photomicrograph of a garnet aggregate with a tail of clinopyroxene. F) A cross polarized photomicrograph of “E”.....69

Figure 34. All images are from site 12DC44 and show an amphibolite shear zone (D_3) croscutting granulite fabrics (D_2). A) An overview of the site. The two persons are standing on the retrogressed granulite pod and the two boxes show the locations of images “B” and “C”. B) This image shows the amphibolite shear zone in the top right quadrant transposing retrogressed granulites in the rest of the image. Note the transposition of the retrogressed granulite S_2 foliation into the shear zone just right of the hammer. C) An alternative view showing the shear zone in the center of the image and the transposition of the older fabric in the bottom of the image. 70

Figure 35. A outcrop sketch and photo of site 12DC44. This sketch shows domains of retrogressed granulites in orange (S_2/L_2) and amphibolite shear zones in green (S_3/L_3). The top of the exposure is a thick zone of foliated (S_3) amphibolites. Note the transposition of the retrogressed granulite fabrics into the shear zone and the two opposing senses of shear.....71

Figure 36. All photomicrograhs are from a pod of retrogressed granulite with a $L_2>S_2$ fabric at site 12DC44. These images show microstructures associated with D_2 deformation and the retrogression of granulites. Images A, B, C and E are plane polarized light and images D and E are cross polarized light. A) A overview photomicrograph showing elongate mafic aggregates and the plagioclase matrix. The field of view is 12 mm. B) This image shows radial clots of biotite growing along the margins of a mafic aggregate. C) This image shows the heterogeneous replacemnent of pyroxene by hornblende, plagioclase, and biotite. D) A cross polarized photomicrograph of "C". E) A fan of radial biotite. F) This image is from the plagioclase matrix and shows grain boundary migration and the formation of subgrains. 72

Figure 37. All images are photomicrographs taken from a amphibolite shear zone with $L_3=S_3$ fabrics that cross cuts retrogressed granulite rocks with $L_2>S_2$ fabrics. Images A, B, and C are plane light and images D, E and F are cross polarized light. These photomicrographs show the microstructures associated with D_3 deformation. A) An overview image that shows the gneissic layering. B) A cross polarized image of "A". C) This image is of a mafic foliation layer and shows subedral hornblende and biotite grains with the inclusions of fine grained plagioclase. D) A image of a plagioclase foliation layer that shows evidence of grain boudary migration and recovery via the formation of tripple junctions. E) An asymmetric porphyroblastic plagioclase grain with biotite beards. F) This image shows the biotite shear bands cross cutting plagioclase aggregates. The foliation is from left to right and the shear bands are from bottom left to upper right, giving a top-down to the northeast sense of shear.....73

Figure 38. All photomicrographs are from sample 12DC45.A, a retrogressed granulite with a D_2 fabric that shows the early stages of S_3 overprinting S_2. The field of view for A and B is 12 mm. A) An overview plane light photomicrograph showing gneissic layering of hbl + bt layers and plagioclase layers. B) A cross polarized photomicrograph of "A". C) A plane light photomicrograph showing biotite shear bands cross cutting the hornblende aggregates. Foliation is from left to right and shear bands are from bottom left to upper right. D) A cross polarized photomicrograph of "C". 74

Figure 39. This is a outcrop sketch and photo of site 13DC63. The sketch shows amphibolite rocks penetrating retrogressed granulite which creates a lozenge of retrogressed granulite.....75

Figure 40. All images are from sample 13DC63.B, a retrogressed granulite from the center of a lozenge of D_2 deformation that is cross cut by a amphibolite shear zones (D_3). These images show the microstructures of plagioclase deformation during D_2 and the early stages of granulite retrogression. A) An overview plane

light photomicrograph of a mafic aggregate. This image shows a mostly green core and brown rim of biotite on a aggregate of retrogressed pyroxene. B) A cross polarized phtomicrograph of “A” showing ameboid grain boudaries in the plagioclase matrix and heterogeneous phase mixture of the mafic aggregate. C) A cross polarized photomicrograph of a mafic aggregate that shows subhedral hornblende and symplectite in the core, with a rim of myrmekite. D) A plane light photomicrograph of a mafic aggregate show radial biotite on the rim of the aggregate and fine plagioclase inclusions in the core. E) A cross polarized photomicrograph of retrogressed mafic aggregate that has a heterogeneous core and a rim of symplectite. F) A cross polarized photomicrograph of a retrogressed mafic aggregate that shows a core of hornblende and symplectite, and grain boundary migration and subgrains in the plagioclase matrix. 76

Figure 41. All photomicrographs are from sample 13DC63.A, an amphibolite from a D_3 shear zone that cross cuts retrogressed granulite rocks with D_2 deformation. A) A plane light overview photomicrograph showing the disjunctive and anastomosing S3 foliation from left to right. The box indicates the location of image “C”. B) A cross polarized photomicrograph of “A”. The box indicates the location of image “D”. C) A plane light photomicrograph showing a rounded porphyroblastic plagioclase grain with a hornblende beard. D) A cross polarized photomicrograph of “C” that shows plagioclase subgrain mantles on the porphyroblast. E) A cross polarized photomicrograph that show subgrains in plagioclase and a simple twinned euhedral hornblende in the lower right. F) A cross polarized photomicrograph from a foliation domain. This image shows the shape preferred orientation of hornblende, plagioclase subgrains, and grain boundary migration in plagioclase.....77

Figure 42. Diagram of a vertical face showing an outcrop sketch of site 13DC64 that exposes pods of hornblendite and coarse granulite that are cross cut by amphibolite shear zones. Domains in yellow preserve D_2 deformation and domains in green preserve D_3 deformation. The hornblendite pod in the bottom center of the image has dismembered pieces that have been included into the shear zones. In the shadows of the granulite pods the shear zone fabric is folded. Capping the outcrop is a horizon of extensional shear bands (S_3). Asymmetry of the pods and orientation of the shear bands give a top-down–to-the-northeast sense of shear.....78

Figure 43. All photomicrographs are from sample 13DC64.A, a amphibolite rock from a D_3 shear zone that cross cuts retrogressed granulite rocks with D_2 deformation. These images show the microstructures associated with D_3 shearing. A) A plane light overview photomicrograph that shows the discontinuous and anastamosing foliation from left to right. B) A cross polarized photomicrograph of “A”. C) A cross polarized photomicrograph that shows an isolated aggregate of plagioclase in the center of the image. The plagioclase aggregate is bound by

hornblende and biotite and shows grain boundary migration. The development of subgrains is seen in the top left corner of the image. D) A cross polarized photomicrograph showing euhedral hornblende and laths of biotite.....79

Figure 44. A) An outcrop sketch of site 12DC46. This outcrop exposes a lozenge of retrogressed granulites with D_2 deformation that is crosscut by D_3 shear zones of amphibolite rocks. Transposition of the older S_2 foliation gives a top-down-to-the-northeast sense of shear. The box in the lower left indicates where photo "C" was taken. B) An overview photo of the site. C) A photo of the D_3 amphibolite shear zone that shows a folded pegmatite dike and porphyroblastic plagioclase. 80

Figure 45. All photomicrographs are from a retrogressed granulite at site 12DC46 that preserves D_2 deformation. The sample was taken on the margin of a D_3 amphibolite shear zone. The lack of symplectites, lack of radial biotite, and the presence of lathe shaped biotite indicates a progression in the retrogression and transition from D_2 to D_3 fabrics. A) An overview plane light photomicrograph that shows heterogeneous foliation (from left to right) of hornblende, biotite, and fine grained plagioclase. Also shown are finer grained hornblende and biotite that are penetrating plagioclase domains. B) A cross polarized photomicrograph of "A". C) A cross polarized photomicrograph of a S_2 foliation layer that shows fine grained plagioclase inclusions in the foliation and hornblende grains. D) A cross polarized photomicrograph from a plagioclase domain that shows grain boundary migration and the development of subgrains. 81

Figure 46. Geologic map of Hall Arm showing metadiorite rock along the northern shore, granulite rock at the end of Hall Arm and mostly granulite-amphibolite transitional and amphibolite rocks along the southern shore.....83

Figure 47. A structural map and equal area lower hemisphere stereographic projection showing SE trending lineations in the metadiorites (L_1), E-W trending lineations in the granulite (L_2), and NE-SW trending lineations in the amphibolite (L_3). Foliation trajectories show the metadiorite dome. 84

Figure 48. Cross sections of Hall Arm from Figure 46 showing a thick zone of the DSSZ along the east coast that has shear bands. Along the west coast are exposures of metadiorite with patchy granulite metamorphism and penetrative splays of amphibolite. 85

Figure 49. All photomicrographs are from sample 12DC30.B, a retrogressed granulite with a $L_2>S_2$ fabric from Domain 2 in Hall Arm that shows the plagioclase matrix and retrogression of pyroxene. A) An overview, plane polarized photomicrograph that shows a plagioclase matrix and aggregates of mafic

minerals. B) A cross polarized photomicrograph of “A”. C) A cross polarized photomicrograph that shows an orthopyroxene surrounded by hornblende and biotite. D) A cross polarized photomicrograph of two orthopyroxene grains. The arrow points to the grain boundary. E) A cross polarized photomicrograph of a retrogressed clinopyroxene aggregate. The center of the aggregate has a relict pyroxene surrounded by a heterogeneous mixture of plagioclase, hornblende, and opaque minerals. Rimming the aggregate is radial biotite. F) A cross polarized photomicrograph that shows myrmekite textures in plagioclase. 88

Figure 50. All photomicrographs are from sample 12DC29.A, a retrogressed granulite with a D_2 fabric from Domain 2 in Hall Arm. A) An overview, plane light photomicrograph that shows mafic aggregates set in a plagioclase matrix. B) A cross polarized photomicrograph of “A”. C) A cross polarized photomicrograph of a plagioclase domain showing grain boundary migration. D) A cross polarized photomicrograph that shows the early stages of retrogression resulting in blebby plagioclase between anhedral grains of hornblende and biotite. 89

Figure 51. All photomicrographs are from sample 12DC26.B, a retrogressed granulite with a transitional fabric between D_2 and D_3 deformation. A) A plane light photomicrograph that shows the hbl + bt + pl foliation layers. B) A cross polarized photomicrograph of “A”. C) A cross polarized photomicrograph of a broken hornblende grain that is in filled with biotite. D) A cross polarized photomicrograph of a porphyroblastic plagioclase grain that has recrystallized tails of plagioclase. 90

Figure 52. All photomicrographs are from sample 12DC22.A, an amphibolite rock with a D_3 fabric from domain 3 in Hall Arm. A) An overview, plane light photomicrograph that shows the anastomosing foliation layers of hornblende and biotite. B) A cross polarized photomicrograph of “A”. C) A plane light photomicrograph of a foliation layer that shows euhedral hornblende and biotite. D) A cross polarized photomicrograph of “C”. E) A cross polarized photomicrograph of fractured hornblende with incipient biotite. F) A cross polarized photomicrograph of a porphyroblastic plagioclase grain on the left with a recrystallized tail. 92

Figure 53. Examples of S-tectonites (top) and L-tectonites (bottom). Scanned images of cut rock sample faces were superimposed onto cubes to show the rock fabric. The three dimensional ellipsoids show how L-tectonites have a much more rodded shape than the more flattened S-tectonites. The ellipsoids are actual data from the fabric analysis with the X,Y, and Z axis showing the maximum stretching, intermediate, and maximum shortening directions, respectively. 114

Figure 54. Scanned images and digitization of plagioclase on a high strain garnet granulite (D_2) sample.The left column shows the three faces that were cut for digitizing plagioclase aggregates. Digitizing is shown in the center column where the colors were inverted so that plagioclase appears black, which helped to identify boundaries. The right column shows the two dimensional ellipses that were fit to each digitized shape. 115

Figure 55. R_f/Φ plots (top of the figure) from the high strain garnet granulite (D_2) showing the calculation of strain for the three analyzed faces (XY, XZ, and YZ). A normalized ellipse is fit to each face which are then used to create the three dimensional ellipsoid (bottom right). Data generated from the ellipsoids include lineation trend and plunge (T/P), and the strike and dip of the foliation (S/D). These data were plotted on an equal-area lower hemisphere stereographic projection (bottom left) and compared to actual field measurements. This comparison (shown below the ellipsoid) shows that the calculated lineations and foliations closely match the field measurements, indicating that the fabric results can be used for further analysis such as comparing flow directions with deformation style among different rock types. 116

Figure 56. Scanned images and digitization of plagioclase on a low strain amphibolite sample (D_3).The left column shows the three faces that were cut for digitizing plagioclase aggregates. Digitizing is shown in the center column where the colors were inverted so that plagioclase appears black, which helped to identify boundaries. The right column shows the two dimensional ellipses that were fit to each digitized shape. 117

Figure 57. R_f/Φ plots (top of the figure) from the low strain amphibolite (D_3) showing the calculation of strain for the three analyzed faces (XY, XZ, and YZ). A normalized ellipse is fit to each face which are then used to create the three dimensional ellipsoid (bottom right). Data generated from the ellipsoids include lineation trend and plunge (T/P), and the strike and dip of the foliation (S/D). These data were plotted on an equal-area lower hemisphere stereographic projection (bottom left) and compared to actual field measurements. This comparison (shown below the ellipsoid) shows that the calculated lineations and foliations closely match the field measurements, indicating that the fabric results can be used for further analysis such as comparing flow directions with deformation style among different rock types. 118

Figure 58. Nadai plots of plagioclase (left) and hornblende/pyroxene (right). Samples that plot in the upper part of the diagram are more strongly distorted (shape change) than those closer to the apex (bottom of diagram). The data show that the metadiorites are low strained, mostly an L=S fabric and that the garnet granulite samples were the highest strained and most prolate. The transitional and

amphibolite rocks show a range in strain intensity but girdle the centerline indicating a mostly L=S fabric. Hornblende and pyroxene appear to accommodate less strain than plagioclase but when these minerals are compared for the same sample there is not a remarkable difference. 119

Figure 59. Clouds drawn around the point data (removed) from figure 58 to help visualize the range of fabrics for each rock type. The clouds are a means for assessing error and distinguishing deformation styles.....120

Figure 60. Fabric data from the undeformed Misty Pluton samples that were used as a baseline to compare the Malaspina Orthogneiss samples to. The Misty samples are dioritic without a foliation or lineation. 120

Figure 61. A strain and flow map showing lineation trajectories and the XY strain ellipses. This map shows the SE/NW flow in the domain of metadiorite, high strain and mostly E/W flow in domains of granulite and weakly retrogressed granulite, and low to moderate strain as well as NE/SW flow in domains of amphibolite. 121

Figure 62. Steps 1 and 2 of fabric transformation from the high strain $L_2>S_2$ (step 0) garnet granulites to high strain $L_3=S_3$ amphibolites. Scanned faces of the XY plane were digitized to show how the inclusion free plagioclase matrix in the garnet granulites is eventually penetrated by porphyroblastic hornblende and biotite, which becomes apparent in step 2. The ellipoids show the three dimensional shape of plagioclase aggregates and how these shapes change from stretched to flattened (see figure 63 for steps 3 through 5) 123

Figure 63. Steps 3 through 5 of reconstructing high strain $L_2>S_2$ garnet granulites (steps 1 and 2 in figure 62) to high strain $L_3=S_3$ amphibolites (step 5). Scanned faces of the XY plane were digitized to show the growth of new hornblende and biotite that eventually connects into a continuous S_3 foliation (step 5). The fabric ellipsoids show a resetting of the plagioclasee strain markers (step 4) as plagioclase becomes porphyroblastic. 124

Figure 64. A Nadai Plot showing the strain path from D_1 (grey) to D_2 (orange) to D_3 (yellow and green). PTt data is included to show the conditions during each deformation event (Gibson and Ireland, 1995; Tulloch and Kimbrough, 2003; Hollis et al., 2004; Klepeis et al., 2007; King et al., 2008; Stowell et al., 2014; Klepeis et al., 2016; Schwartz et al., 2016). 125

CHAPTER 1: INTRODUCTION

Within convergent margins, the physical properties of the lower crust repeatedly are thermally and mechanically altered during cycles of magmatism, thickening and orogenesis. These cycles are recorded in the rock record as change in pressure and temperature, mineralogy, deformation, melt and fluids. They also result in changes in lower crustal rheology (Afonso and Ranalli, 2004; Brown and Solar, 2000; Bürgmann and Dresen, 2008; Culshaw et al., 2011; Gerbi et al., 2010) which influences the styles and extent that deformation may be pervasive or localized. Answering where, how, and when deformation in the lower crust is accommodated may help us understand the relative strength of the lower crust, how mountains are built, how continental crust is thinned, and why we see different distributions of rock types throughout the lithosphere. While many studies decipher the interplay of mineral assemblages, identify metamorphic and microstructural processes, and study deformation in the lower crust, we lack information on how the three dimensional rock fabrics change throughout these processes. I contribute to this problem by merging 3D fabric data with pressure, temperature, and time (PTt), as well as structural and microstructural observations to create a comprehensive and four dimensional history of deformation in the lower crust.

My study is focused on answering the process of how lower crust rock fabrics developed, and the process of fabric transformation in Fiordland, New Zealand, during the transition from a convergent to an extensional tectonic regime. I present results from a field and laboratory based investigation from Doubtful Sound, Fiordland, which exposes domes of the lower crust. Within these exposures are records of magmatism,

metamorphism and deformation during pluton emplacement and at the granulite and amphibolite facies. The extents of these exposures are unusually large (Fig. 1) and they offer a supreme opportunity to research progressive deformation that occurred in the lower crust at a variety of pressure, temperature, metamorphic, and structural conditions. I have applied field techniques, 3D fabric analysis, and microstructural analysis to document the styles and processes of deformation. From these analyses I have characterized three deformation events, mapped their extent, defined their associated processes, and created a strain path that links fabric transformation across each deformation vent. The three events are: 1) the development of a weak L=S fabric, NW-SE mineral lineations, patchy metamorphism, and metastability during crustal thickening, 2) prograde granulite facies metamorphism, melting, and the formation of L≥S tectonites during ≈ E-W stretching and flow at peak metamorphic conditions, and 3) hydration and retrogression of granulites to amphibolite facies, the transformation of L≥S tectonites to S=L tectonites, and NE-SW extensional shearing.

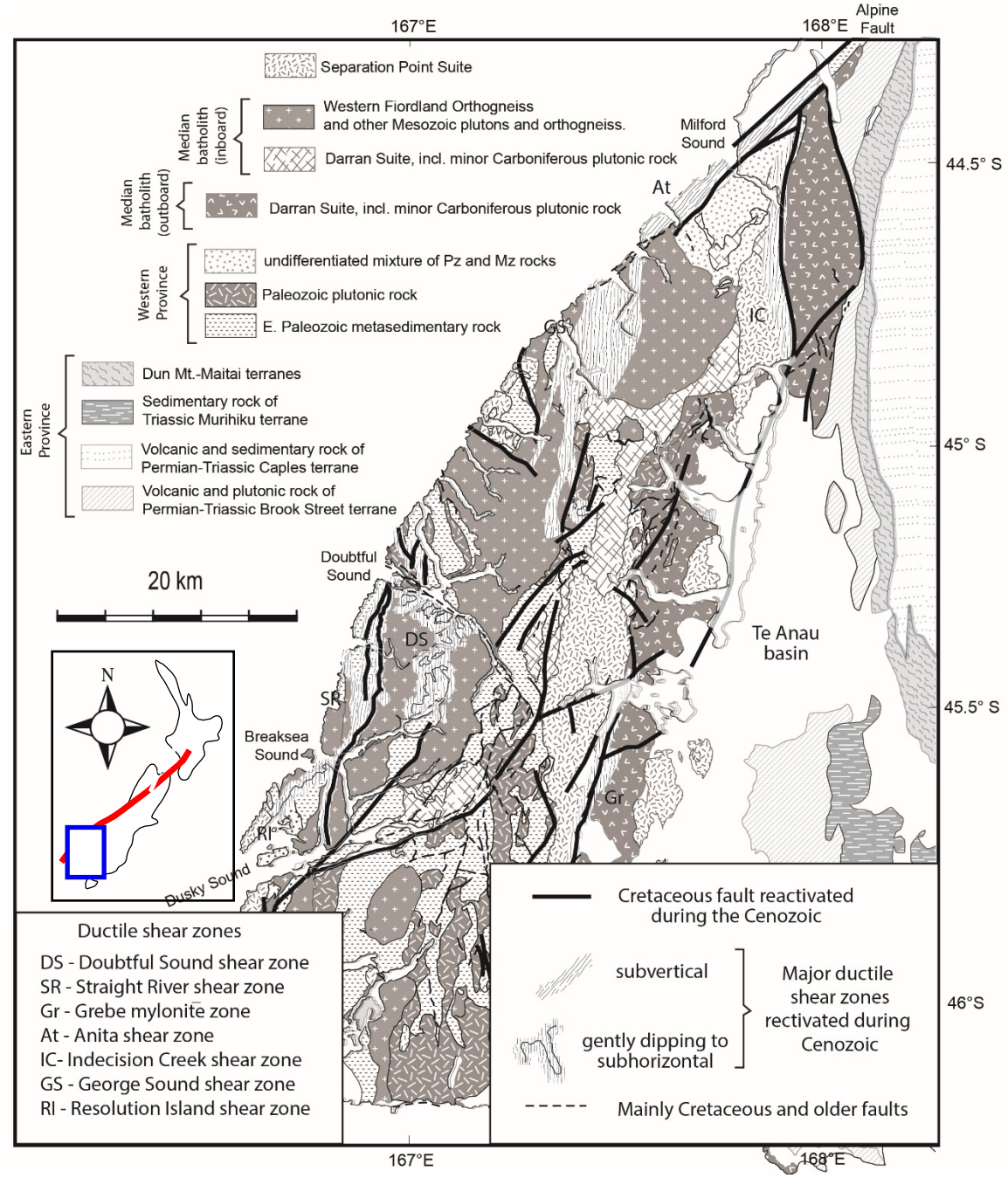

Figure 1. An overview geologic map of Fiordland (blue box on inset map) showing the distribution of plutonic rocks that comprise the Median Batholith and extensional structures such as the Doubtful Sound Shear Zone (this study).

CHAPTER 2: LITERATURE REVIEW

2.1. Composition of the Malaspina Orthogneiss

Pioneering work in the Doubtful Sound region began with Turner in 1939. The reader is referred to Figure 2 for a geographic map of the Doubtful Sound region. Relevant to this study are Turner's (1939) observations along the shore lines of Hall Arm, Elizabeth Island, and the west coast of Doubtful Sound. In these regions Turner identified four primary rock types that were distinguished by mineral assemblage. They are: (1) hbl + pl gneiss with minor biotite (abbreviations after Whitney, 2010): (2) hbl + pl + bt gneisses; (3) hbl + pl + ep gneiss with minor biotite; (4) non-feldspathic hbl + bt gneisses. Turner (1939) noted that there are transitional rocks between each of the above rock types and that garnet and pyroxene appear along the northern entrance to Hall Arm and the west coast of Doubtful Sound.

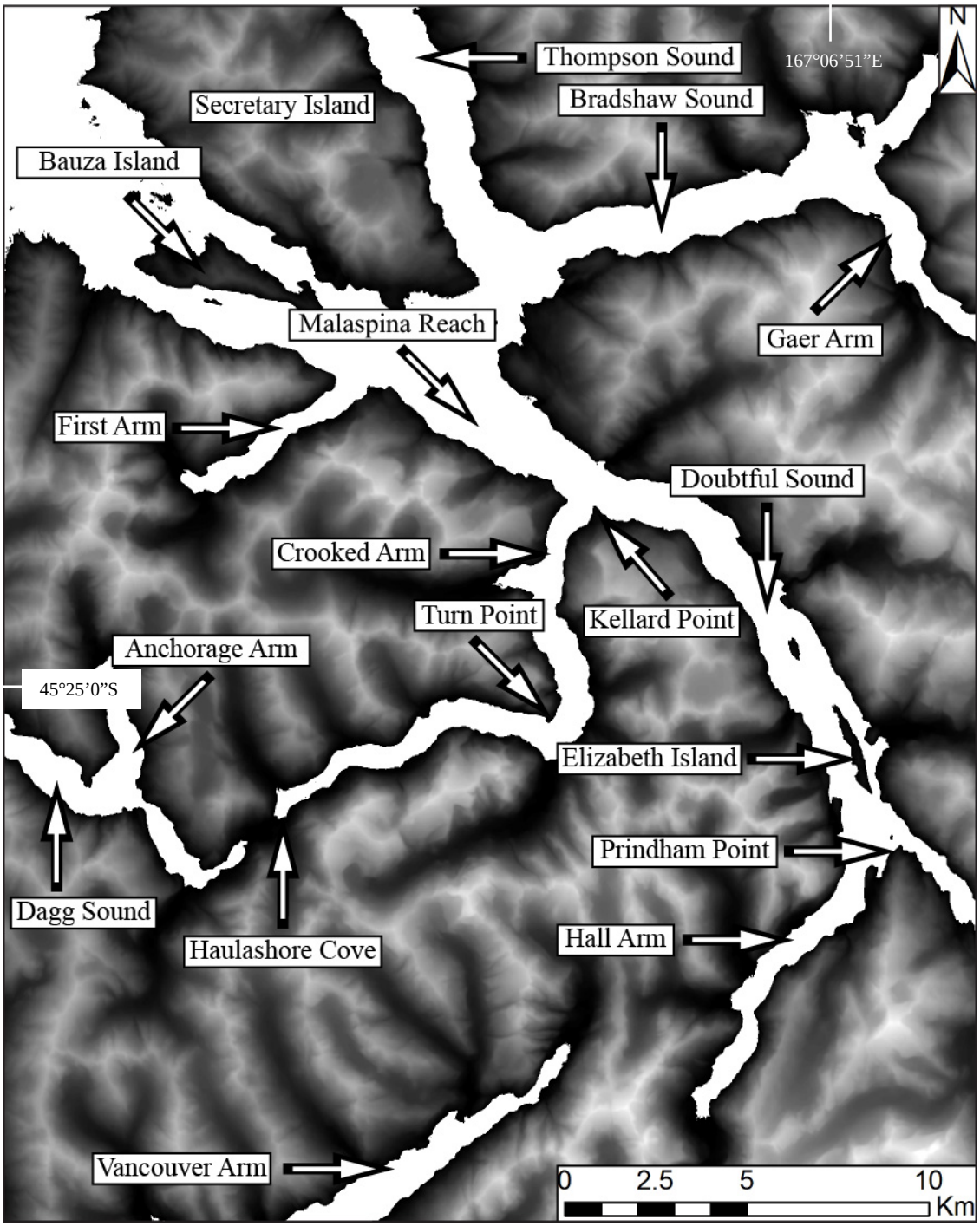

Figure 2. A geographic map of the Doubtful Sound region in Fiordland, New Zealand. The base map is a digital elevation model, the lighter the color the higher the elevation. The white space within the map are fiords.

On the north side of Hall Arm, Turner (1939) documented leucocratic grt + pl granulites, the presence of orthopyroxene, and garnet coronas with interstitial quartz around pyroxene. North of Hall Arm and west of Elizabeth Island Turner (1939) describes coarse, equant plagioclase grains that are 1 mm to 2 mm in diameter, and often studded with garnet. Approximately 1.5 km south of Kellard Point, on the west coast of Doubtful Sound, Turner (1939) describes plagioclase augen that are wrapped by biotite, and the presence of garnet with vermicular quartz inclusions. Ultimately, Turner (1939) recognized the presence of high metamorphic grade rocks along the west coast of Doubtful Sound.

Building off of Turner's (1939) recognition of garnet granulites in Doubtful Sound, and the mapping of a large positive Bouguer gravity anomaly (Reily, 1965; Woodward, 1972) Oliver (1976, 1980) conducted a thorough geologic investigation from Doubtful Sound to Breaksea Sound. Oliver (1976, 1980) defined three units within the Malaspina Pluton: (1) Malaspina Gneisses; (2) Turn Point Gneisses; and (3) Waipero Cove Gneisses. Oliver (1976, 1980) interpolated the Malaspina Gneisses to be the structurally lowest unit, and interpreted it to constitute a basement granulite zone. Above the Malaspina Gneisses Oliver (1976, 1980) projected the Turn Point Gneiss, which was described as partly retrogressed Malaspina Gneisses and as a transition zone to the Waipero Cove Gneiss. The Waipero Cove Gneiss was projected by Oliver (1976, 1980) to be the structurally highest unit in the Malaspina Pluton, which constituted an amphibolite zone in contact with the Deep Cove Gneiss cover rock. Here-after the

Malaspina Gneiss, Turn Point Gneiss, and Waipero Cove Gneiss will be referred to as granulite, retrogressed or transition granulites, and amphibolite gneisses, respectively.

Oliver (1976, 1980) appointed the granulite gneisses as hornblende granulites that can be distinguished by the presence of orthopyroxene and described them as “medium grained, equigranular, granoblastic, with elongate micro-structures defined by lenticular-shaped aggregates of mafic grains, with embayed or gently curving boundaries”. In the field Oliver (1976, 1980) observed that the granulite gneisses are often cross cut by anorthositic veins which are studded with garnet. Near the anorthositic veins Oliver (1976, 1980) observed a reaction zone in the granulite gneiss that has the mineral assemblage pl + grt + cpx + qtz + rt + ap. Under thin section Oliver (1976, 1980) noted that in the reaction zones garnet forms coronas around clinopyroxene.

Oliver’s (1976, 1980) evidence that the transition gneisses are partly retrogressed granulite gneisses was the presence of relict cpx + ilm + mag intergrowths, and the presence of biotite. The transition gneisses were described as feldspathic with two assemblages: (1) pl + hbl + relict cpx + ilm and mag intergrowths + bt + spn + ep + qtz + ap; and (2) pl + grt + relict cpx + qtz + bt + hbl + rt + spn + ep + ap. Oliver (1976, 1980) also describes the transition gneisses as “streaky and sometimes coarsely rodded but generally having a medium to coarse-grained inequigranular granoblastic elongate microstructure defined by lenticles of xenoblastic hornblende and clinopyroxene whose grain boundaries are commonly sutured”. In Turn Point (Figure 2), the transition gneisses were described with biotite radiating around mafic minerals. Oliver (1976, 1980)

distinguished the amphibolite gneisses from the transition gneisses when all of the clinopyroxene had been replaced by hornblende.

2.2 Structure of the Malaspina Orthogneiss

Deformation events and fabrics

Oliver (1976) provided the first detailed descriptions of deformation in the Doubtful Sound region. He defined six deformation events, (D_1-D_6) in the Malaspina Orthogneiss. D_1 deformed the igneous layering (S_0) and resulted in F_1 folds in the Malaspina pluton. D_2 resulted in F_2 folds that deformed hornblendite veins and formed a new S_2 foliation and L_2 lineation. Oliver (1976, 1980) defines L_2 by the alignment of prismatic pyroxene or hornblende and notes that "S_2 is the most common foliation found in the granulites". It is during D_2 that Oliver (1976, 1980) suggests most of the hornblendite sheets were intruded. D_3 deformed D_2 structures and occurred at amphibolite facies. During the event "A penetrative foliation surface, S_3, was not formed although a strong lineation, L_3, formed along the F_3, fold hinges". Oliver (1976) states that L_3 "is the most common lineation found in the granulites". D_4 deformation sheared the granulites, forming S_4 and L_4. Oliver (1976) interpreted this deformation to be heterogeneous and to be focused along areas of fluid transfer in the granulites, and also pointed out there is variability in the orientations of the shear zones. D_5 deformation folded the D_4 shear zones and D_6 domed the Malaspina Orthogneiss during regional uplift.

Klepeis et al. (2007) simplified the fabrics within the Malaspina orthogneiss into three types based on cross cutting relationships and mineral assemblage. The first fabric is a magmatic fabric coincidental with the emplacement of the Western Fiordland Orthogneiss (WFO). These fabrics were described as “heterogeneous but widespread” and “composed of hydrous, two-pyroxene igneous assemblages”. Penetrating the magmatic fabric is a prograde garnet granulite fabric. The third fabric is associated with the Doubtful Sound Shear Zone and was described by the authors as a “retrogressive upper amphibolite facies mylonite”.

Structure of Hall Arm and Crooked Arm

In Hall Arm Turner (1939) documented a prominent northeast dipping foliation, whereas along the west coast of Doubtful Sound Turner (1939) documented an east dipping foliation. On the south side of Hall Arm, approximately one kilometer from the entrance, Turner (1939) describes a streaky and well foliated hbl + pl + ep + bt gneiss.

At the entrance of Crooked Arm and at Kellard Point, Oliver (1976) observed mylonitized marbles, and along the north-south stretch of Crooked Arm the foliation was generally observed dipping moderately to the north. Immediately south of Kellard Point gneisses with “flattened, spindle shaped aggregates of mafic minerals” were characterized with an L=S fabric. Further south (~ 1.8 km) along the west coast of Crooked Arm Oliver (1976) observed the transition gneisses with relict clinopyroxene. Oliver (1976) observed that the well-developed foliation dissipates ~ 2.3 km south of Kellard Point, where the rocks are L≥S granulite gneisses with well-developed lineations

defined by the alignment of mafic minerals. At the turn in Crooked Arm, Oliver (1980) describes the presence of coarse grained and streaky gneisses that are coarsely rodded.

From Oliver's (1976) structural contour map, two anticlines and one syncline, all of which have fold axis that trend NNE, are shown. The axis of the western-most anticline trends from Anchorage Arm to the end of First Arm, and the eastern most anticline has an axis that trends between Crooked Arm and Hall Arm. Oliver (1976) also mapped a syncline that trends NNE through the middle of Vancouver Arm.

Structure of the Doubtful Sound Shear Zone (DSSZ)

Oliver (1976) initially hypothesized that the contact between the Deep Cove Gneiss and Malaspina Orthogneiss was a thrust fault. He observed mylonitic marbles or thick zones of deformed rock at the contact. One line of evidence the author used for the thrust fault hypothesis was that both the Deep Cove Gneiss and the Malaspina Orthogneiss near the contact were metamorphosed at amphibolite facies conditions, indicating that both units deformed at similar conditions. Gibson et al. (1988) subsequently re-interpreted the DSSZ as an extensional shear zone. The authors' lines of evidence were kinematic indicators in the Malaspina Orthogneiss and the cover rock. Asymmetric porphyroclast tails, S-C bands in the Malaspina Orthogneiss, and fold asymmetry in the cover rock pointed Gibson et. al. (1988) to an easterly sense of extensional shearing, resulting in L-S tectonites in the DSSZ.

Klepeis et al. (2007) furthered our understanding of the DSSZ, finding it to be focused along the cover rock contact but also to contain splays of upper amphibolite facies mylonite that range from 10-100m in thickness. The authors' observations of

asymmetric lozenges and clasts, as well as C'-S fabrics in the shear zone pointed to a top-down-to-the-northeast and top-down-to-the-southwest sense of shear. Klepeis et al. (2007) were the first to discuss the behavior of minerals in the DSSZ. By using the R_f/Φ technique on mineral clasts they found an increase in feldspar strain from outside to inside the DSSZ and were able to infer other minerals such as hornblende and biotite accommodated some strain. Their three dimensional analysis showed a rotation of the clasts towards the maximum finite extension direction.

2.3 Cretaceous Tectonic History of Fiordland, New Zealand

In the Late Cretaceous Fiordland was situated along the paleo-Gondwana margin above an active subduction zone (Figure 3). During this event a suit of plutons were emplaced throughout the middle to lower crust (Allibone et al., 2009; Bradshaw, 1989; Hollis et al., 2004; Mattinson et al., 1986; McCulloch et al., 1987), and subsequently buried and metamorphosed at the granulite facies (Bradshaw, 1989; Daczko et al., 2002; Gibson and Ireland, 1995; Hollis et al., 2004; Oliver, 1976). In Doubtful Sound, the magmatism and subduction emplaced, buried, and metamorphosed the Malaspina Pluton at garnet granulite facies ca. 116-114 Ma (Flowers et al., 2005; Hollis et al., 2004). Gibson and Ireland (1995) estimated peak P-T conditions of 10-12 kbar at 800-830°C, and in Hollis et al. (2004) estimated peak P-T conditions of 10-13 kbar at 750-850°C. Circa 114 Ma the tectonic regime switched from convergence to extension (Klepeis et al., 2007). This led to retrogression at the amphibolite facies, the development of extensional shear zones (Gibson et al., 1988; Klepeis et al., 2007; Oliver, 1990; Spell et al., 2000), and cooling from $T \geq 700°C$ to $550° \leq T \leq 650°C$ ca. 113.5 Ma. Subsequent

extensional deformation at the amphibolite facies (Oliver, 1980; Gibson and Ireland, 1995; Hollis et al., 2004), accommodated by the Doubtful Sound Shear Zone (DSSZ), occurred through ca. 102 Ma (Klepeis et al., 2007).

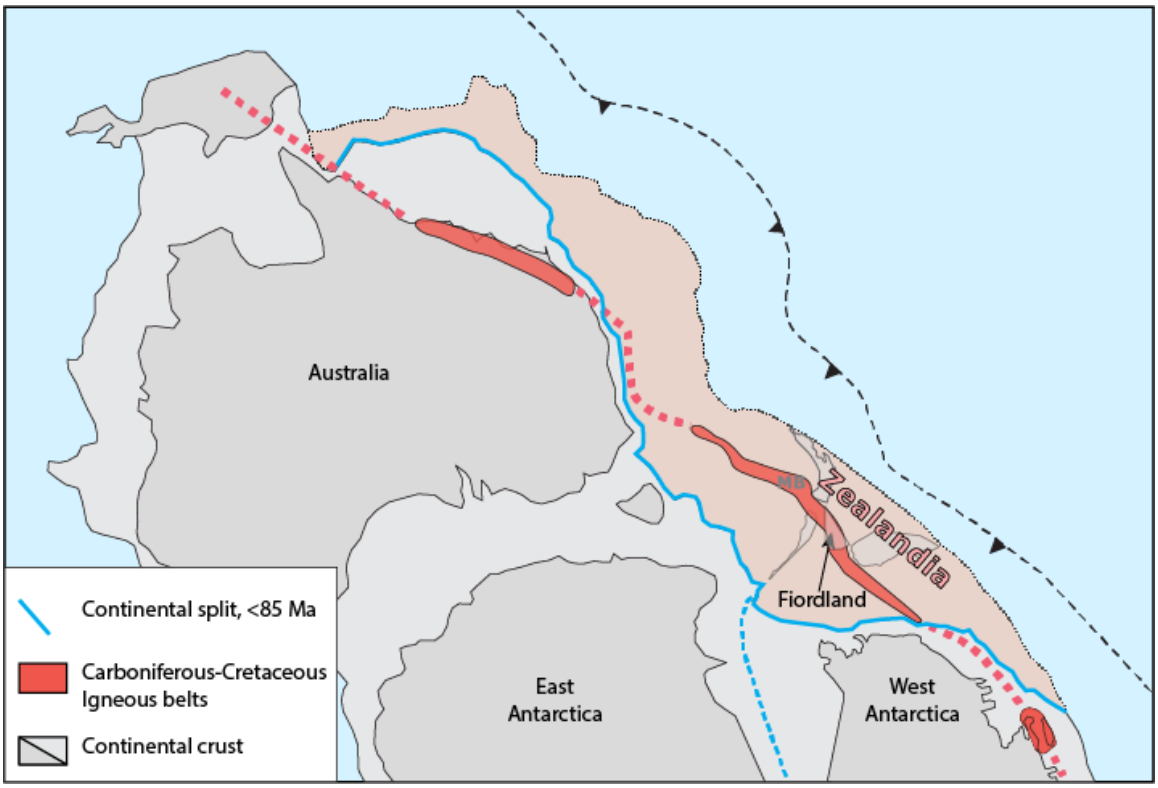

Figure 3. A Cretaceous reconstruction of Gondwana at ~120 Ma after Mortimer (2008) that shows the tectonic regime in which the Malaspina Pluton was emplaced. The reconstruction shows oceanic subduction beneath the paleo-Gondwana continent and arc magmatism (in red).

2.8 Strain and Fabric Analyses

A common goal in structural geology and studies of the middle to lower crust is to identify where and why ductile deformation was concentrated and/or absent during tectonic events. The R_f/Φ technique (Ramsay, 1967, Dunnet, 1969, Lisle, 1985) has been used in a number of applications to document strain gradients, such as gradients across a fold-thrust belt (Alsleben et al., 2008), to show non-linear increases in strain as a thrust is approached (Xypolias et al., 2007), and to show that rocks of different compositions will record different strains (Czeck et al., 2009). Webber et al. (2015) recently showed a difference in strain accommodation based on grain size.

Since 3D fabric analysis requires special programs a lot of effort is spent on understanding rheology and strain partitioning. Gerbi et al. (2010) used numerical modeling to determine that the bulk strength of amphibolite rocks can decrease by orders of magnitude inside shear zones from the influx of fluid. In deeper crustal terrains, it has been found that deformation following the strain hardening from cooling and crystallization of magmas often results in discrete shear zones within the lower crust (Dumond et al., 2010). Also at depth, deformation during partial melting has been found responsible for the initiation of exhumation (Labrousse et al., 2011). Lozenges (gently curved rhombus shapes of rock) are becoming increasingly documented in mid to lower crustal terrains and Ponce et al., (2012) has shown that the orientation of pre-existing foliation relative to bulk kinematics can influence the partitioning of strain and penetrative structure of younger shear zones.

Other methods of identifying strain gradients include the mapping of rock fabrics. Waters-Tormey and Tikoff (2007) mapped the relative intensity of foliation development to infer strain localization at lithologic boundaries. Alternatively, lineation intensity has been used to show flow in fold hinges (Bonamici et al., 2011 and Sullivan, 2006) and flow around gneiss domes (Betka and Klepeis 2013). Stokes et al., (2012) found that deformation creating strong linear fabrics was partially accommodated by dissolution-precipitation creep in amphibolites.

A key factor in all of the studies mentioned above is understanding the relative strength of different minerals during deformation. Plagioclase tends to be one of the weaker minerals in the lower crust, often develops a crystal preferred orientation (CPO) (Ji and Minprice, 1990; Mehl and Hirth, 2008), and at high temperatures deforms via dislocation creep, diffusion-controlled creep (Rybacki and Dresen, 2004) and by diffusion-accommodated grain boundary sliding (Rosenberg and Stunitz, 2003). In contrast, amphiboles have been found to be load bearing (Kenkmann and Dressen, 2001) and to accommodate strain via chemically induced grain boundary migration (Kruse and Stunitz, 1999). Laboratory methods have shown that the strength of clinopyroxene is among the highest of minerals common in the lower crust (Bystricky and Mackwell, 2001).

Chapter 3: STRUCTURES AND MICROSTRUCTURES OF DOUBTFUL SOUND, CROOKED ARM, AND HALL ARM

My project explores how Cretaceous exposures of lower crust in Doubtful Sound, Hall Arm, and Crooked Arm, located in central Fiordland, New Zealand (Figure 1), accommodated extension after subduction-related crustal thickening in the middle to Late Cretaceous. Doubtful Sound offers phenomenal exposures of the otherwise rare lower crust, and the Malaspina Orthogneiss hosts a variety of rock types and fabrics. The metamorphic grade of rock types in the Malaspina Orthogneiss range from garnet granulite to upper amphibolite, and the fabric types range from L>S tectonites to S>L tectonites. I address the following questions about deformation in the Malaspina Pluton: (1) where and when was deformation concentrated within the Malaspina Pluton? (2) what were the 3D geometries of mineral aggregates? And (3) how did the rock fabrics evolve as the tectonic regime switched from convergent to extensional?

Crosscutting relationships of foliations with different mineral assemblages unveiled three deformation events (D_1, D_2 and D_3) and set the framework for identifying structural domains in my field area. Microstructure analysis unveiled how different minerals accommodated deformation during each event and record evidence for processes such as anatexis, dislocation creep, and solution mass transfer. My 3D fabric analysis on hand specimens computed the geometries of rock fabrics and the relative degree of stretching versus flattening associated with each deformation event. These three methods of analysis were used in conjunction with one another to delineate structural domains and to understand the 4D process of transitioning from a convergent

to extensional tectonic regime. The following sections will characterize the rock types, structure and microstructure, and processes of deformation in domains of D_1, D_2, and D_3 deformation.

3.1 Mapping Units

My work in mapping the Malaspina Pluton in Doubtful Sound, Crooked Arm, and Hall Arm has fine-tuned where the locations of six rock types (Oliver, 1979) are exposed. The rock types are: 1) metadiorites, 2) hornblendites, 3) granulite orthogneiss, 4) garnet granulite orthogneiss, 5) retrogressed granulite orthogneiss, and 6) amphibolite orthogneiss. The delineation of these six rock types is based on cross-cutting relationships, mineral assemblage and metamorphic grade. Below each mapped unit is described and for simplicity the term “orthogneiss” will be dropped from all units.

Metadiorites

Metadiorites along Doubtful sound are composed of pl + hbl + bt. In these rocks hornblende and plagioclase is assumed to be primary and associated with the emplacement of the pluton. Hornblende occurs as large euhedral grains and as aggregates of finer euhedral grains. Plagioclase grains are equally large and euhedral. Radial biotite that overprints hornblende is interpreted to be a secondary mineral. At the end of Crooked Arm and near Kellard Point the metadiorites are primarily composed of pl + hbl + bt secondary growth of hbl + bt. Hornblende is generally fine grained and clumped into aggregates. Plagioclase forms the matrix of the rock and isolated grains of biotite are generally found along the boundaries of other minerals. These rocks are different than the retrogressed

granulites discussed below because there is little evidence that these rocks reached the granulite facies.

Hornblendites

Hornblendite rocks occur as mafic pods and intrusions into metadiorite. They are primarily composed of hornblende but also contain small amounts of fine grained plagioclase and biotite. The hornblende grains are euhedral. Biotite is also euhedral and found along hornblende grain boundaries and in hornblende pressure shadows. Plagioclase occurs as subhedral blebs along hornblende grain boundaries.

Granulites and garnet granulites

Granulite and garnet granulite rocks are a pro-grade metamorphic rock derived from diorites. They are primarily composed of pl + cpx + opx ± grt ± bt. These rocks can be identified by their mineral composition and the plagioclase matrix. If the rocks contain garnet I will refer to them as garnet granulites, if they do not contain garnet I will refer to them as granulites.

Retrogressed granulites

The retrogressed granulites are derived from the granulites and possibly garnet granulites. They have a primary mineral assemblage of pl + hbl + bt ± cpx ± opx. All minerals overprinting and rimming cpx are secondary. In outcrop these rocks are identified by pyroxene in the cores of mafic aggregates and an earthy gold rim of biotite around the mafic aggregates. Lenticular, subhedral grains of hornblende and biotite are often penetrating the plagioclase matrix. In thin section the distinction between the retrogressed granulites and both types of granulites is very clear. The mafic aggregates may have

pyroxene cores and are generally composed of anhedral hornblende, symplectite pseudomorphs of pyroxene, and radial clots of biotite. In more fully retrogressed granulite rocks the mafic aggregates have developed subhedral hornblende.

Amphibolites

Amphibolite facies rocks within my study area are primarily composed of pl + hbl + bt ± ep. In coarser grained amphibolite the minerals are mostly primary and associated with emplacement. In finer grained amphibolite the minerals overprinting hbl and pl are secondary. Evidence of secondary mineral growth stems from porphyroblastic plagioclase and subhedral to euhedral hornblende and biotite. These rocks do not have a plagioclase matrix and may or may not have foliation.

3.2 Overview and Relative Chronology of Structures

I have identified three primary deformation events that affected my study area. These events were identified by cross-cutting relationships, metamorphic grade, microstructures, and correlation these to my 3D fabric results. Below is a description of the foliations and lineations that formed during D_1, D_2, and D_3. I used the features of the foliations and lineations to correlate field sites and to define structural domains within my field area. I also provide a general description of where these events are exposed.

D_1

D_1 coincides with the emplacement of the Malaspina Orthogneiss and produced S_1 and L_1. A weak, non-continuous, gneissic foliation identified by the compositional layering of hbl±cpx±opx+bt+pl and plagioclase in granulite and metadiorite defines S_1. The orientation of S_1 is variable and defines kilometer scale domes. Aligned hornblende

and plagioclase that gently/moderately plunge NW-SE define L_1. Typical outcrops that contain S_1/L_1 along the west coast of Elizabeth Island and along the neighboring west coast of Doubtful Sound. These localities are often intruded by hornblendite bodies of various shapes. Rocks within domains of D_1 deformation are often coarse grained with euhedral to subhedral plagioclase and hornblende.

D_2

D_2 resulted in S_2 and L_2 structures that are found in the granulites, garnet granulites, and retrogressed granulites. While S_2, defined by the alignment of mafic minerals is weak, L_2 lineations are robust. Elongate mafic minerals and rodded plagioclase define the L_2 stretching lineations. These lineations typically trend east-west and northeast-southwest. Outcrops that preserve these structures are exposed at the end of Hall Arm, north of Elizabeth Island along the west coast of Doubtful Sound, and throughout Crooked Arm.

In Crooked Arm, L_2 stretching lineations trend E-W to NE-SW in both types of granulites and in the retrogressed granulites. At the end of Hall Arm retrogressed granulites record the same stretching directions. These outcrops often have a streaky appearance due to the intensity of the lineation and lack of foliation. In Crooked Arm the garnet granulites may have elongate pyroxenes rimmed with garnet, all of which are set in a plagioclase matrix. Along the west coast of Doubtful Sound the intensity of the L_2 stretching lineations vary, but consistently trend E-W.

D_3

Rocks affected by D_3 are generally amphibolites with secondary hbl, bt, and pl. This event is associated with the Doubtful Sound Shear Zone, and produced S_3/L_3. Well-developed S_3 is a gneissic foliation with aligned hornblende, biotite and plagioclase. In contrast to L_2, L_3 lineations are not as rodded or stretched, rather they are identified by the alignment of hornblende, biotite, and plagioclase. L_3 trends NE-SE and when in proximity to rocks with L_2 structures L_3 is observed to be more northerly. Outcrops containing these structures are exposed along the entrance of Hall Arm, throughout Crooked Arm and along the west coast of Doubtful Sound. In Crooked Arm and near Kellard Point are the thickest zones of D_3 deformation. Thinner splays of S_3 cross cut S_2 farther inside Crooked Arm and along the west coast of Doubtful Sound. Due to the varied development of S_3/L_3, as it overprints S_2/L_2, it is often difficult to recognize.

D_3 deformation has penetrated the plagioclase matrix found in the granulite and retrogressed granulite rocks with S_3 folia of hbl+bt, and also recrystallized plagioclase. When looking closely at domains of plagioclase at the hand sample scale, fine hornblende and biotite is found between plagioclase grains. The nature of hornblende and biotite varies from euhedral to anhedral, and foliation layers of hornblende and biotite often have fine plagioclase inclusions. Sense of shear indicators are given by asymmetric plagioclase porphyroclasts and the transposition of S_2 fabrics into zones of S_3 fabrics.

3.3 Doubtful Sound

The region of Doubtful Sound described below includes Elizabeth Island and the west coast between Crooked Arm and Hall Arm. Figure 4 and Figure 5 show site locations and observations, as well as structures. Field observations, structures, and microstructures from this region will be described from the southeast to the northwest. Through examination, I found structures and deformational processes associated with magmatism, granulite facies deformation, and amphibolite facies shearing. I define three distinct domains along this stretch of Doubtful Sound that have been identified by rock type and preservation of structures. Domains with S_1/L_1 and S_2/L_2 structures will be described first, followed be a description of S_3/L_3 structures.

A cross section along Doubtful Sound from Crooked Arm to Hall Arm (Figure 6) shows a dome of mostly metadiorite and traces of S_1 to the southeast. A dome of mostly granulite in the center of the section is cross cut by the amphibolite facies DSSZ. This cross section provides a good representation of how the granulite facies metamorphism was both pervasive and patchy, and how the DSSZ penetrated the Malaspina Orthogneiss.

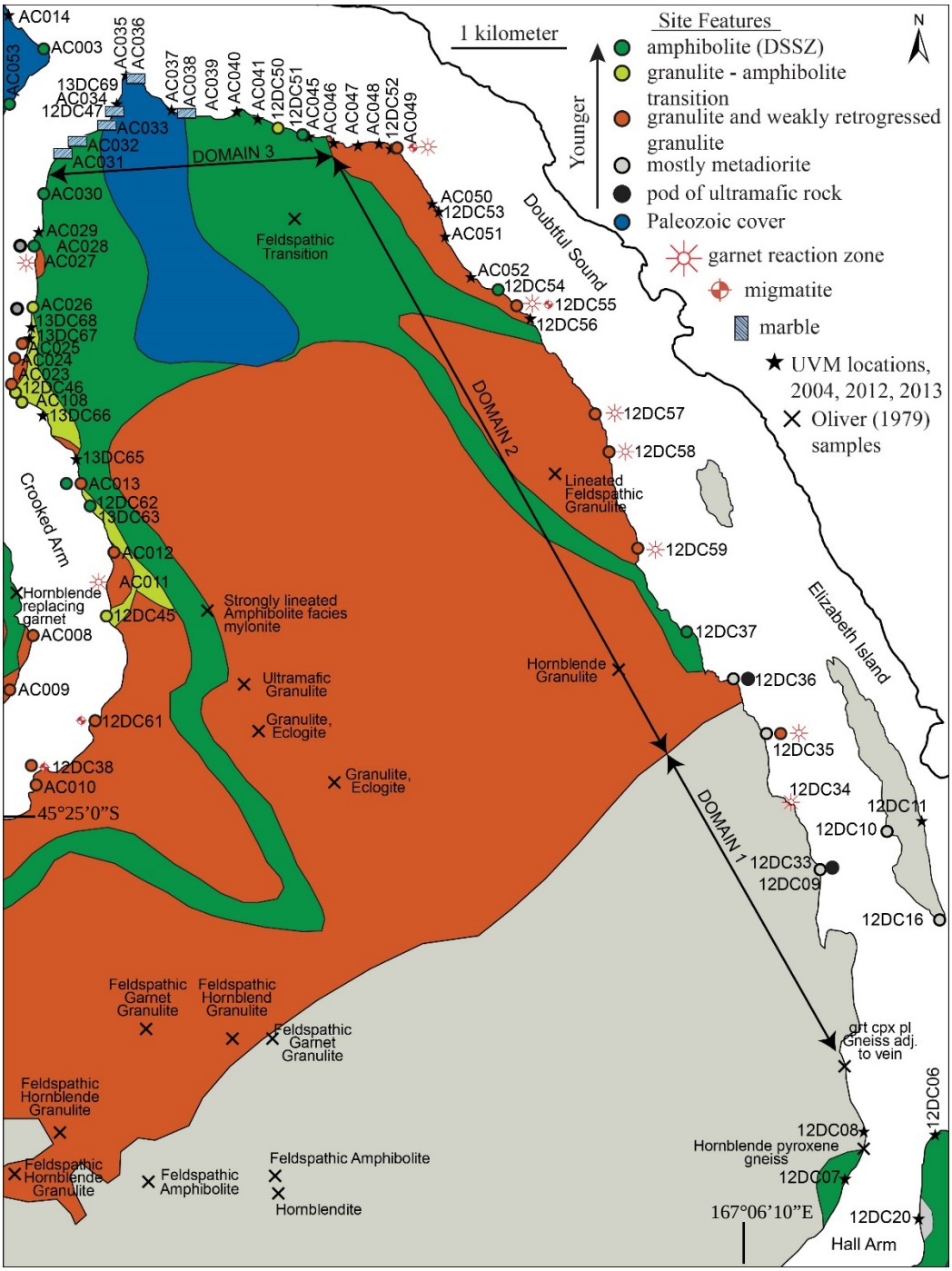

Figure 4. A site map showing the locations of field site and structural domains. All of the circles and "x's" also represent field locations. Domain 1 consists of mostly metadiorite rocks, Domain 2 contains granulite and garnet granulite rocks, and Domain 3 is composed of mostly amphibolite rocks and structures that define the Doubtful Sound Shear Zone.

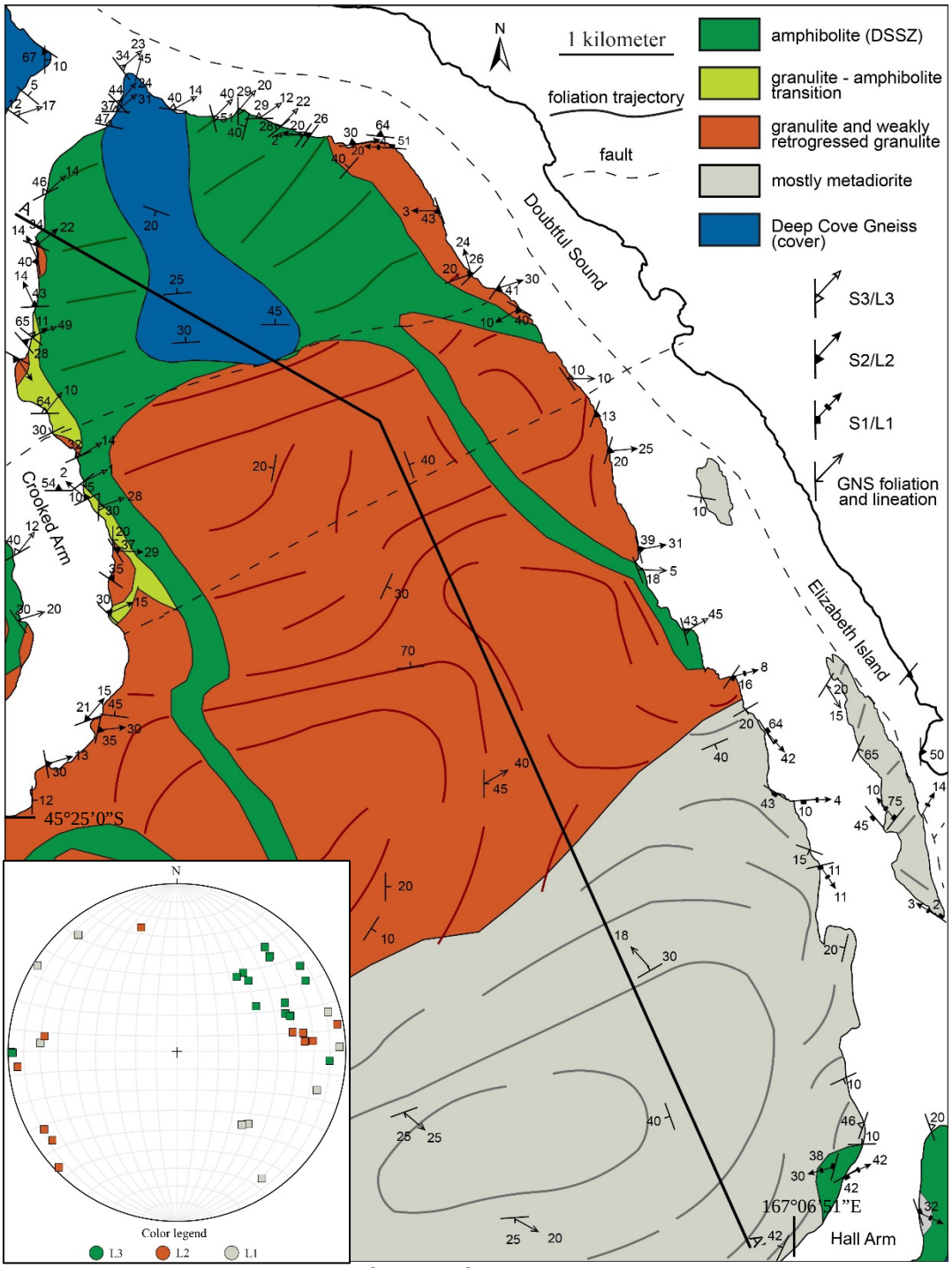

Figure 5. A structural map of Doubtful Sound and a lower hemisphere equal-area stereographic projection showing. The foliation trajectories define domes within the metadiorite and granulite domains. Note that in the grey (Domain 1) L_1 trends northwest-southeast, in the orange (Domain 2) L_2 trends mostly east, and in the green area to the north (Domain 3), L_3 trends mostly northeast.

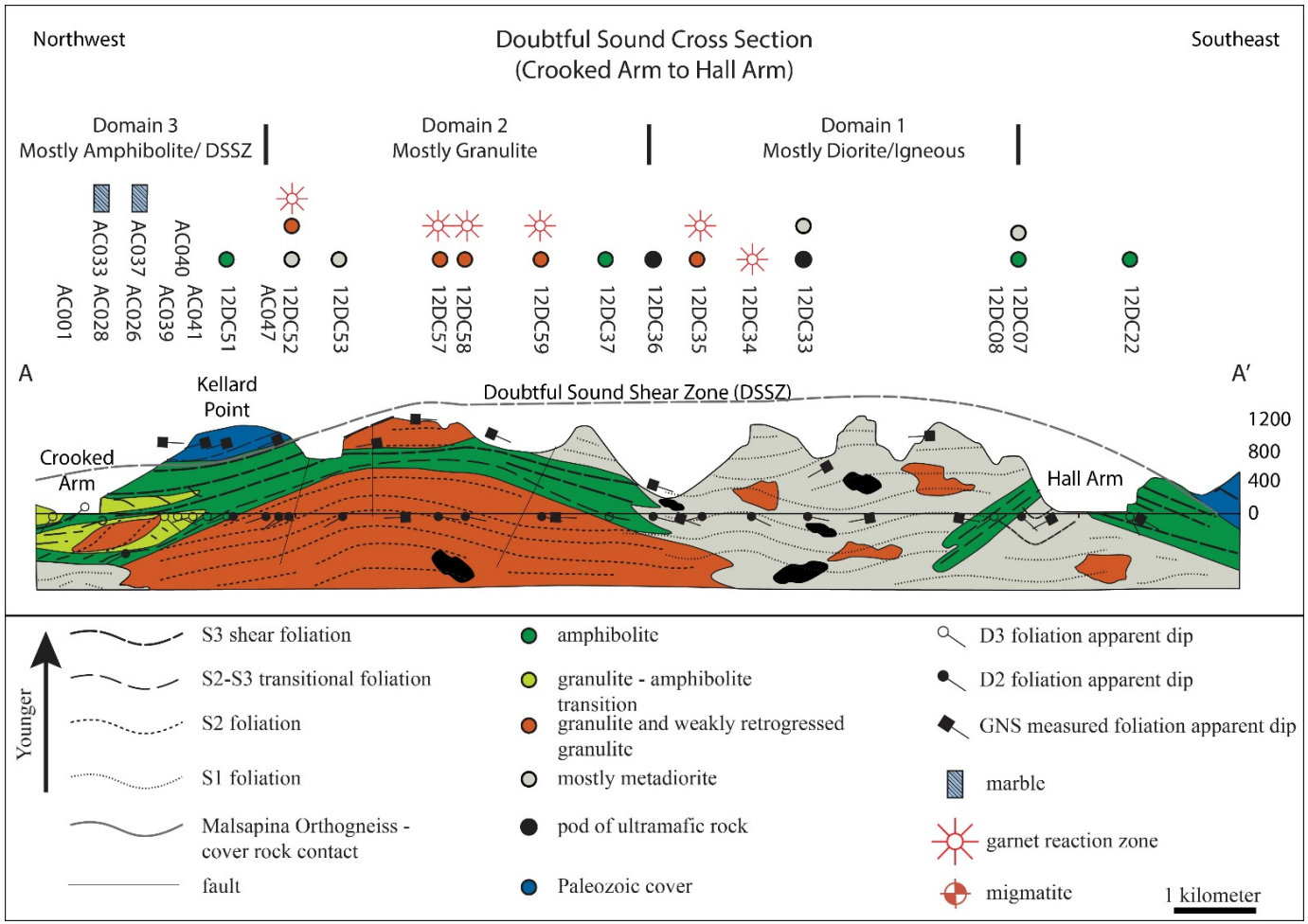

Figure 6. A cross section of Doubtful Sound, from Crooked Arm to Hall Arm. This section shows the structure and locations of Domains 1, 2 and 3. A dome of mostly metadiorite and a dome of mostly granulite lie below the Doubtful Sound Shear Zone (DSSZ). The DSSZ penetrates the granulites and has a top-down-to-the-northeast sense of shear. Lozenges of granulite have transposed S_2 foliations in the region of Crooked Arm. Above the topographic profile are the site names and features. The line of section is shown in Figure 5.

Domain 1 (Doubtful Sound)

Domain 1 is located on the west coast of Doubtful Sound, from the entrance of Hall Arm to the northern tip of Elizabeth Island, and continues westward into the mountainous region between Crooked Arm and Hall Arm. The rock types exposed along the coasts are mainly metadiorites and garnet granulites that preserve S_1 and L_1. Mingling with the host rock are irregular shaped masses of hornblendite and thick hornblendite dikes. Most outcrops have a weak to moderately developed gneissic foliation (S_1) and a northwest-southeast trending aligned mineral lineation (L_1).

Site 12DC16 is at the southern tip of Elizabeth Island and exposes metadiorites with local garnet coronas around hornblende, and patches garnet granulites. Here the S_1 foliation that is identified by compositional layering of mafic and felsic minerals dips gently to the northeast. Hornblende mineral lineations define L_1 and plunge gently to the northwest. The rocks here have an L_1=S_1 fabric. Large equant grains of hornblende and plagioclase are indicative of igneous textures. When looking on the S_1 foliation plane hornblende often has one tapered end and one blunt, square end. On this surface plagioclase grains are equally large and euhedral with square corners. In thin section (Figure 7) large, inclusion free plagioclase are interlocked with smooth grain boundaries forming the rock matrix. Millimeter scale subhedral hornblende are set in the matrix and are often over printed by radial biotite. Plagioclase also occurs as small inclusions within the masses of hornblende.

A sample of garnet granulite (Figure 8) shows simple twinned orthopyroxene rimmed by small and rounded grains of clinopyroxene, as well as orthopyroxene with a

moat of clinopyroxene. Plagioclase has cuspate-lobate grain boundaries and garnets are fractured. The space between the garnets is often filled with quartz. One zone of garnets has a conspicuous tail of densely aligned biotite. Both the metadiorites and garnet granulites show evidence of dislocation creep through grain boundary migration in plagioclase.

Farther north, along the west coast of Elizabeth Island at Site 12DC10, S_1 is broadly folded. The mineral aligned L_1 lineations gently plunge to the northwest. Under thin section (Figure 9) hornblende is set in a plagioclase matrix. Clots of fine hornblende form the larger aggregates that are apparent at the hand sample scale. Plagioclase grains in the matrix are on the millimeter scale, and fine grained plagioclase is included in the aggregates of hornblende. The plagioclase grain boundaries are slightly cuspate-lobate and appear to be annealed.

Across the fiord from Elizabeth Island, on the west coast of Doubtful Sound, at site 12DC09 and 12DC33 are phenomenal exposures of hornblendite bodies intruding the metadiorites (Figure 10 and Figure 11). The hornblendite body at site 12DC09 can be seen when the tide is low, and it has an amorphous oval shape. The top contact of the intrusion is gradational into the host rock with gentle curves, whereas the bottom contact is swirly and even more gradational into the host rock. Within the middle of the hornblendite pod are streaks of plagioclase. At site 12DC33 the hornblendite intrusion is more massive and branching. The boundary between the intrusion and the host metadiorite is also gradational.

Approximately 1.3 km north from the hornblende intrusions, at site 12DC35, both metadiorites and garnet granulites are exposed. This locality is on the margin of Domain 1 and the fabrics here resemble the Domain 2 fabrics that will be discussed below. Since the lineations are defined by aligned hornblende and trend northwest I am classifying them as L_1, and this site remains in Domain 1. Foliations (S_1) are identified by the alignment of mafic minerals and dip to the north. At this site centimeter scale garnets are surrounded by leucosome, and garnet granulite reaction zones overprint the host metadiorites. In thin section, (Figure 12) plagioclase is inclusion free, has cuspate-lobate grain boundaries and subgrains have developed. Garnet is elongate and fractured, and surrounded by a film of potassium-feldspar and grains of clinopyroxene. Hornblende is still present but much of it has been altered and now forms a symplectite.

Also found at site 12DC35 is a shear zone in the garnet granulites. The shear zone is a few centimeters wide and transposes the S_1 granulite foliation. In thin section, (Figure 13) the shear zone is identified by the grain size reduction of plagioclase. Inside the shear zone are grains of hornblende, fine grained plagioclase, and garnets surrounded by biotite. The shear zone walls contain elongate plagioclase, garnet, and ratty hornblende. Fine beads of plagioclase and myrmekite can be found along plagioclase grain boundaries.

Synthesis of Domain 1

Domain 1 in Doubtful Sound is significant because it preserves the structures and textures of the Malaspina during emplacement. My supporting evidence is the following:

1. The compositional layering and large grain size of mafic and felsic minerals.
2. The presence of hornblendite pods and dikes that have gradational contacts with the host rock.
3. The lack of recrystallization and lack of a well formed foliation or lineation suggests minimal deformation.

I interpret the consistently NW-SE trending L_1 lineation to record magmatic flow and that the arrangement of the S_1 foliations show a dome-like structure for this domain (Figure 5). The formation of the S_1 and L_1 structures was accommodated by dislocation creep in plagioclase through grain boundary migration and subgrain development. Melt beads, and garnet reaction zones attest to partial melting and granulite facies metamorphism after and possibly during final crystallization of the Malaspina pluton. Secondary features such as the radial biotite suggests retrogression during exhumation.

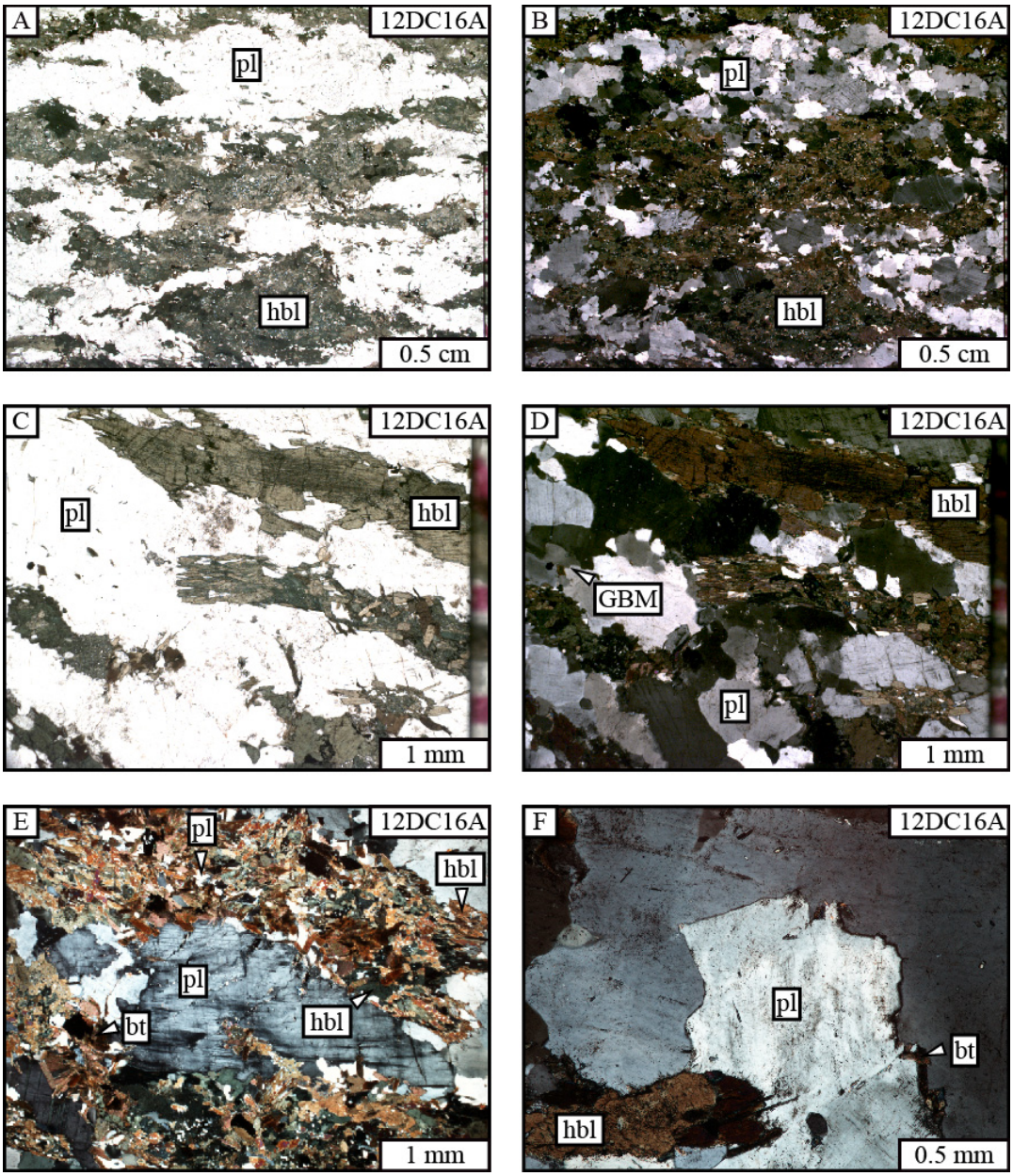

Figure 7. Photomicrographs of sample 12DC16A. The rock type is a metadiorite that shows S_1 foliation defined by the alignment of hornblende. These images are evidence of crystallization textures during magmatic flow that was accommodated by dislocation creep in plagioclase. A) Plane light photomicrograph showing coarse hornblende aggregates and a plagioclase matrix. B) Cross polarized photomicrograph of "A". C) Plane light photomicrograph showing coarse hornblende grains. D) Cross polarized photomicrograph of "C" that also shows plagioclase grain boundary migration and subgrains. E) Cross polarized photomicrograph showing radial biotite overgrowing hornblende. F) Cross polarized photomicrograph that shows the interlocking plagioclase grain boundaries.

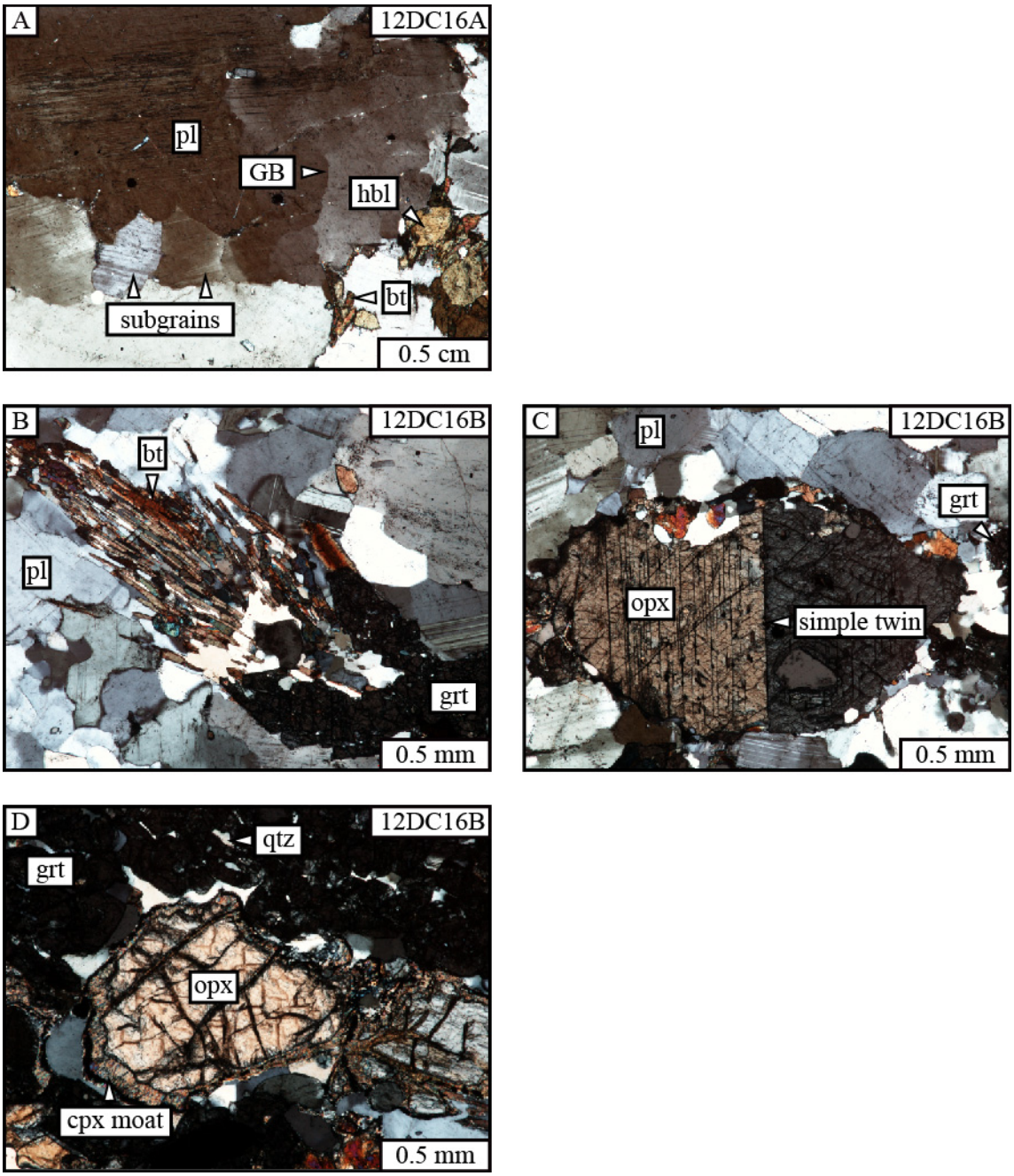

Figure 8. All photomicrographs are of sample 12DC16B and are cross polarized. The rock type is a garnet granulite. These images show evidence of dislocation creep in plagioclase and textures of biotite that represent hydration. A) Grain boundary migration and subgrains in plagioclase. B) Biotite tail on garnet. C) Simple twinning of an orthopyroxene grain in the plagioclase matrix. Note the lack of recrystallization in the plagioclase matrix, indicating deformation was not pervasive. D) Clinopyroxene moat around orthopyroxene.

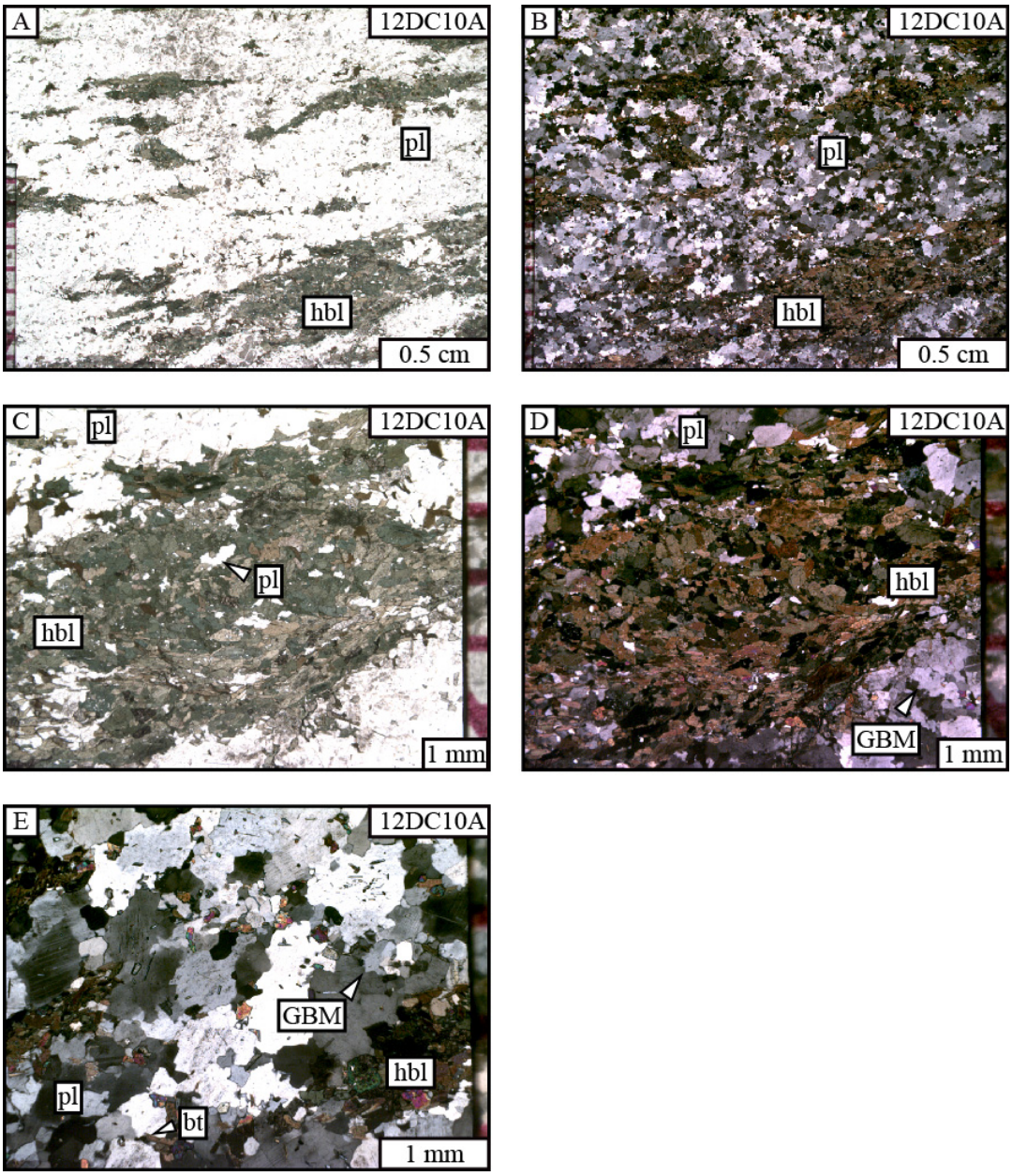

Figure 9. All photomicrographs are of sample 12DC10A. The rock type is a metadiorite that has a spaced and non-continuous S_1 foliation. These images show the plagioclase matrix, aggregates of hornblende that define S_1, and evidence of dislocation creep in plagioclase. A) Plane polarized photomicrograph showing an overview of the sample, hornblende aggregates and the plagioclase matrix. B) Cross polarized photomicrograph of "A". C) A plane polarized photomicrograph and blow up of a hornblende aggregate showing sub-millimeter hornblende grains. D) Cross polarized photomicrograph of "C". E) Cross polarized photomicrograph showing amoeboid grain boundaries on plagioclase and evidence of grain boundary migration in the same mineral.

Figure 10. A site photo from 12DC09 in Domain 1 of Doubtful Sound that provides evidence of magma mingling between a mafic, hornblendite dike and its host while the Malaspina pluton was still partially molten. The mafic dike shows gradational and undulose contacts with the host rock. The pod is approximately three meters long.

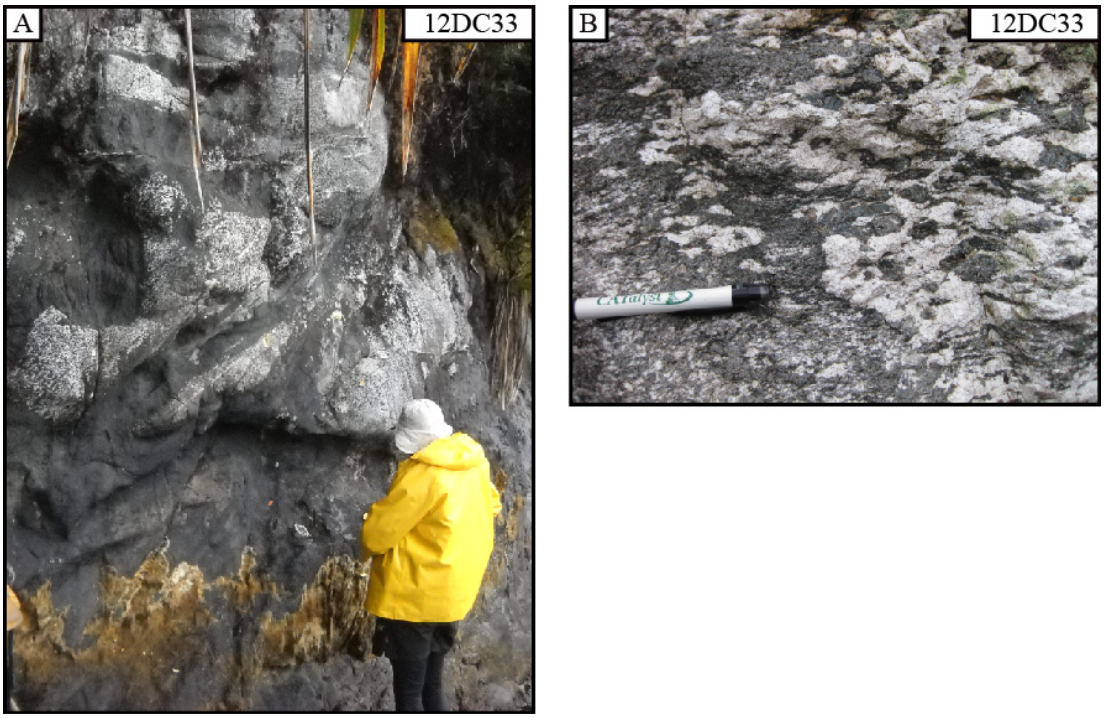

Figure 11. A) Site photos from 12DC33 in Domain 1 of Doubtful Sound that shows a swarm or hornblende rich dikes that intrude the host metadiorite and are evidence of magma mingling. B) A close up of the mingling between mafic and intermediate magmas at site 12DC33.

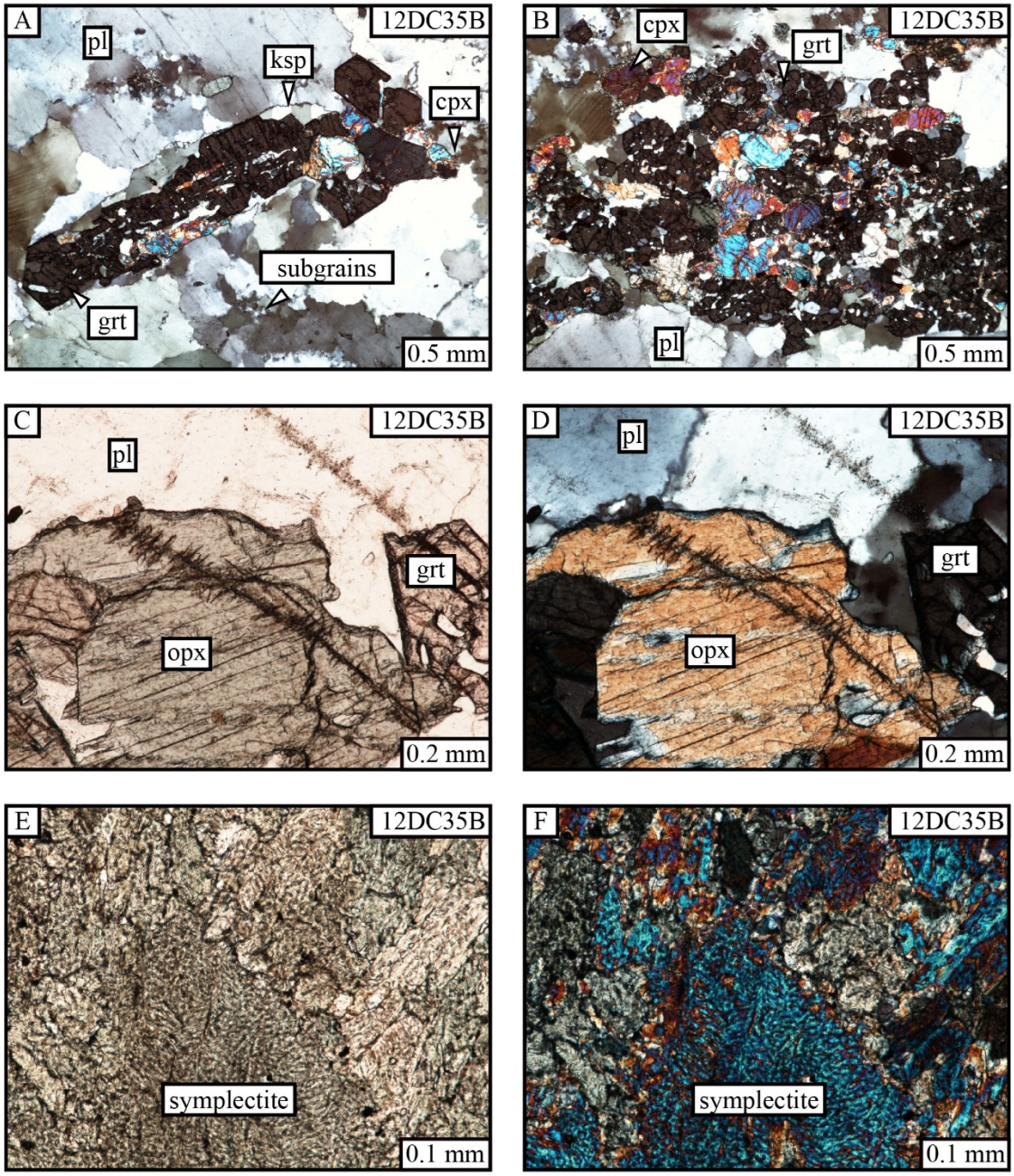

Figure 12. All photomicrographs are of sample 12DC35B from Domain 1 in Doubtful Sound. The rock type is a garnet granulite. These images show evidence of dislocation creep in plagioclase and symplectite textures. A) Cross polarized photomicrograph of an elongate garnet surrounded by potassium feldspar (suggesting the presence of melt) and subgrains of plagioclase in the matrix. B) Cross polarized photomicrograph of an aggregate of garnet and clinopyroxene. C) Plane light photomicrograph of an orthopyroxene. D) Cross polarized photomicrograph of "C". E) Plane light photomicrograph of a symplectite with vermicular texture. F) Cross polarized photomicrograph of "E".

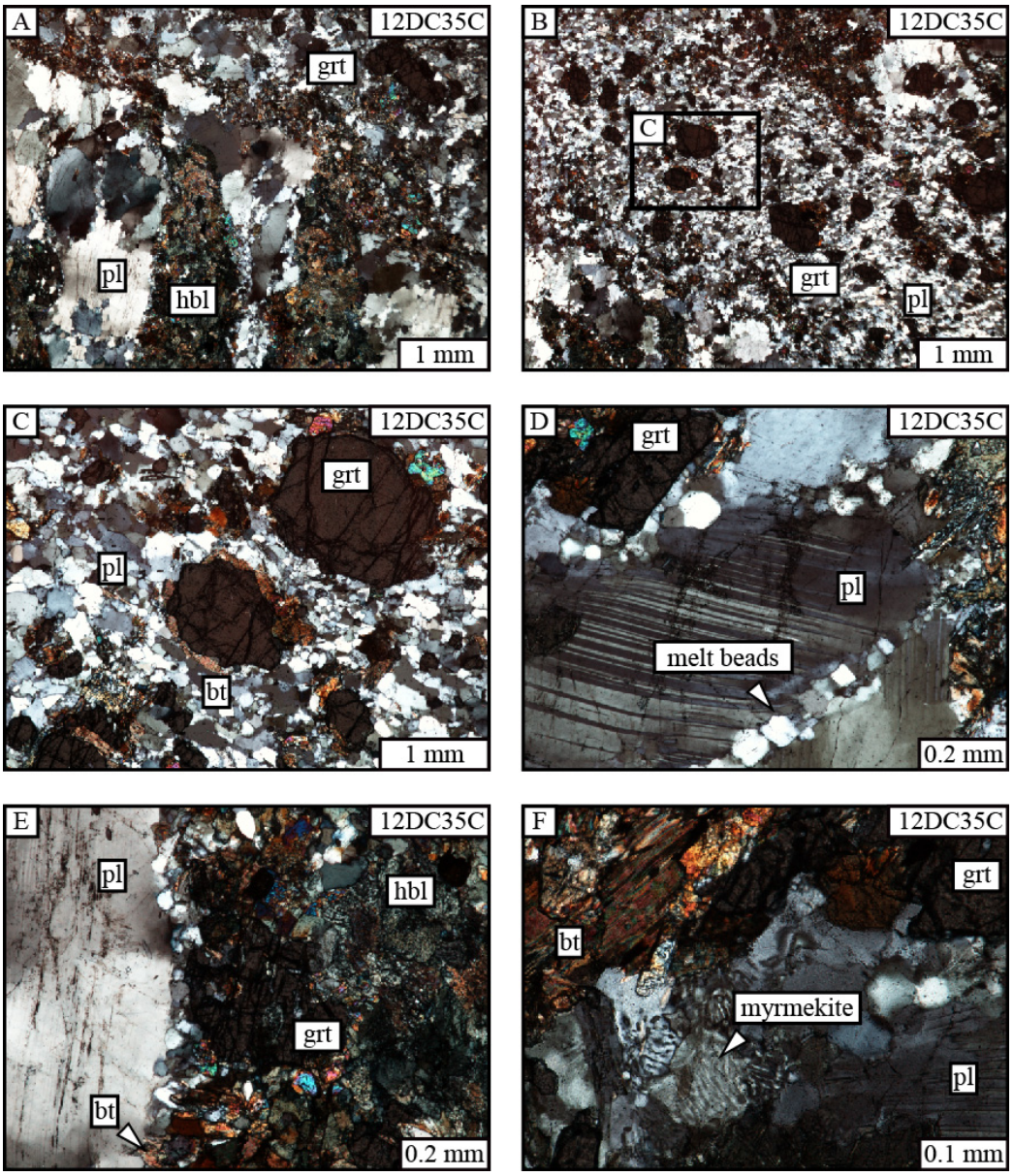

Figure 13. All photomicrographs are of sample 12DC35C from Domain 1 in Doubtful Sound and are cross polarized. The rock type is a garnet granulite. The images show microstructures of a centimeter scale shear zone and evidence of melt. A) An overview of the shear zone (top right of image). Note the millimeter scale plagioclase and hornblende aggregates in the walls and the grain size reduction in the shear zone. B) Garnet and fine plagioclase in the shear zone. C) A close up of garnet that has rims of biotite in the shear zone. D) Plagioclase outside of the shear zone that has bent twins and beads of rounded plagioclase that are interpreted to represent melt. E) An image outside of the shear showing fine plagioclase beads, garnet and hornblende. F) Myrmekite textures in plagioclase outside of the shear zone.

Domain 2 (Doubtful Sound)

Domain 2 extends from the northern boundary of Domain 1, northwest along the coast of Doubtful Sound, and ends approximately two kilometers east from Kellard point (see Figure 2 for landmark locations). This domain is characterized by mostly $L_2 \geq S_2$ tectonites that formed during granulite facies deformation. The degree of S_2 and L_2 development in this domain varies from sparsely developed to pervasive. Gneisses in the center of this domain have a plagioclase matrix, weak S_2 foliation, and E-W trending L_2 lineations. The northwestern quarter of this domain is characterized by dioritic orthogneisses that have weakly developed S_2 foliations and L_2 lineations. Two splays of amphibolites cross cut the granulites, and the northern end of this domain transitions into a zone of amphibolites with S_3 and L_3 fabrics.

Site 12DC36 (Figure 14) marks the transition from Domain 1 to Domain 2. Contained here are boudinaged mafic sheets with necks in-filled with leucosome. The host rock is a metadiorite and garnet granulite with an east trending L_2 mineral lineation. This site is cross cut by numerous faults and dikes of leucosome.

Along the shore from sites 12DC59-12DC55 are outcrops of granulite and garnet granulite with a moderately developed S_2 foliation. The foliation is identified by the alignment of pyroxene. Lineations (L_2) consistently trend down dip to the east, and are well defined by the alignment and stretching of both mafic minerals and plagioclase. Dehydration reaction zones form a patchwork of garnet granulites. At site 12DC59 trains of pyroxene taper at their ends and the plagioclase matrix contains beads of fine plagioclase along grain boundaries (Figure 15). At site 12DC57 orthopyroxene has moats

of clinopyroxene and garnets with interstitial quartz. Clinopyroxene grains appear to be developing subgrains and plagioclase grains in the matrix are elongate and inclusion free (Figure 16). Similar garnet granulite reaction zones (Figure 17) and microstructures (Figure 18) are observed at site 12DC55. At this site peritectic garnets have over grown the S_2 foliation of aligned pyroxene.

Sites 12DC53 and 12DC52 are located in the northwest quarter of Domain 2 where the garnet granulite reaction zones are less prevalent but peritectic garnets are still present (Figure 19). This section of Domain 2 mostly exposes metadiorites with weakly developed west trending lineations (L_2) that are defined by the alignment of hornblende. S_2 foliations dip to the west and north and are identified by the alignment of hornblende into semi-continuous layers.

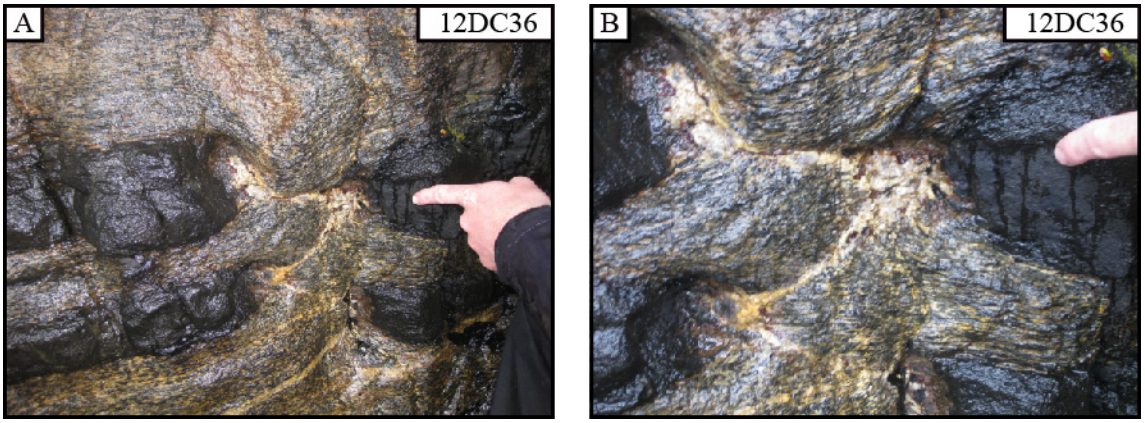

Figure 14. A) Site photo of 12DC36 in Domain 2 of Doubtful Sound showing boudinaged hornblendite sheets. B) A close up from "A" showing the S_2 foliation of the metadiorite host and leucosome in the boudin neck which indicates melt was mobile during deformation.

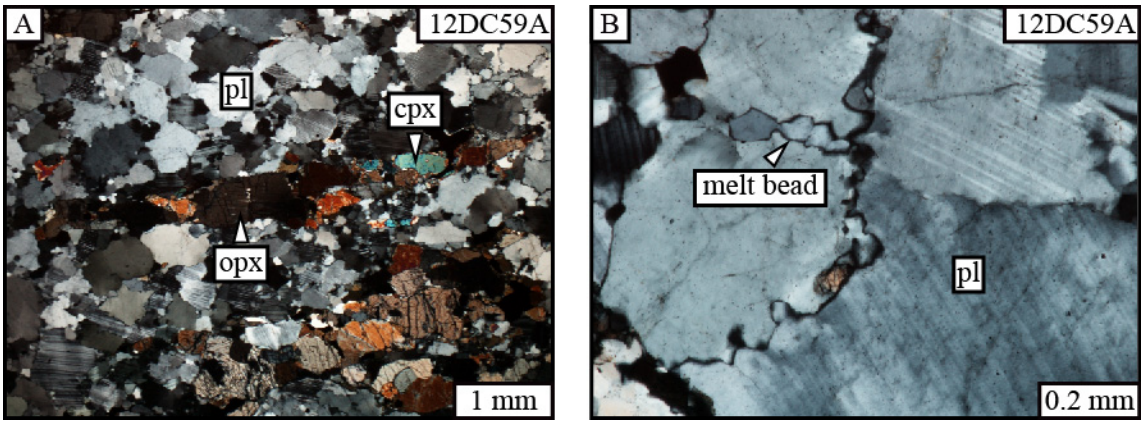

Figure 15. Both images are cross polarized photomicrographs of sample 12DC59A in Domain 2 of Doubtful Sound. The rock type is a granulite that preserves the S_2 foliation. These images show evidence of high temperature deformation and anatexis (see section 3.3 for discussion). A) An overview of a granulite showing elongate pyroxene aggregates set in a plagioclase matrix. The pyroxene aggregates define S_2. B) A close up of plagioclase grain boundaries and a melt bead.

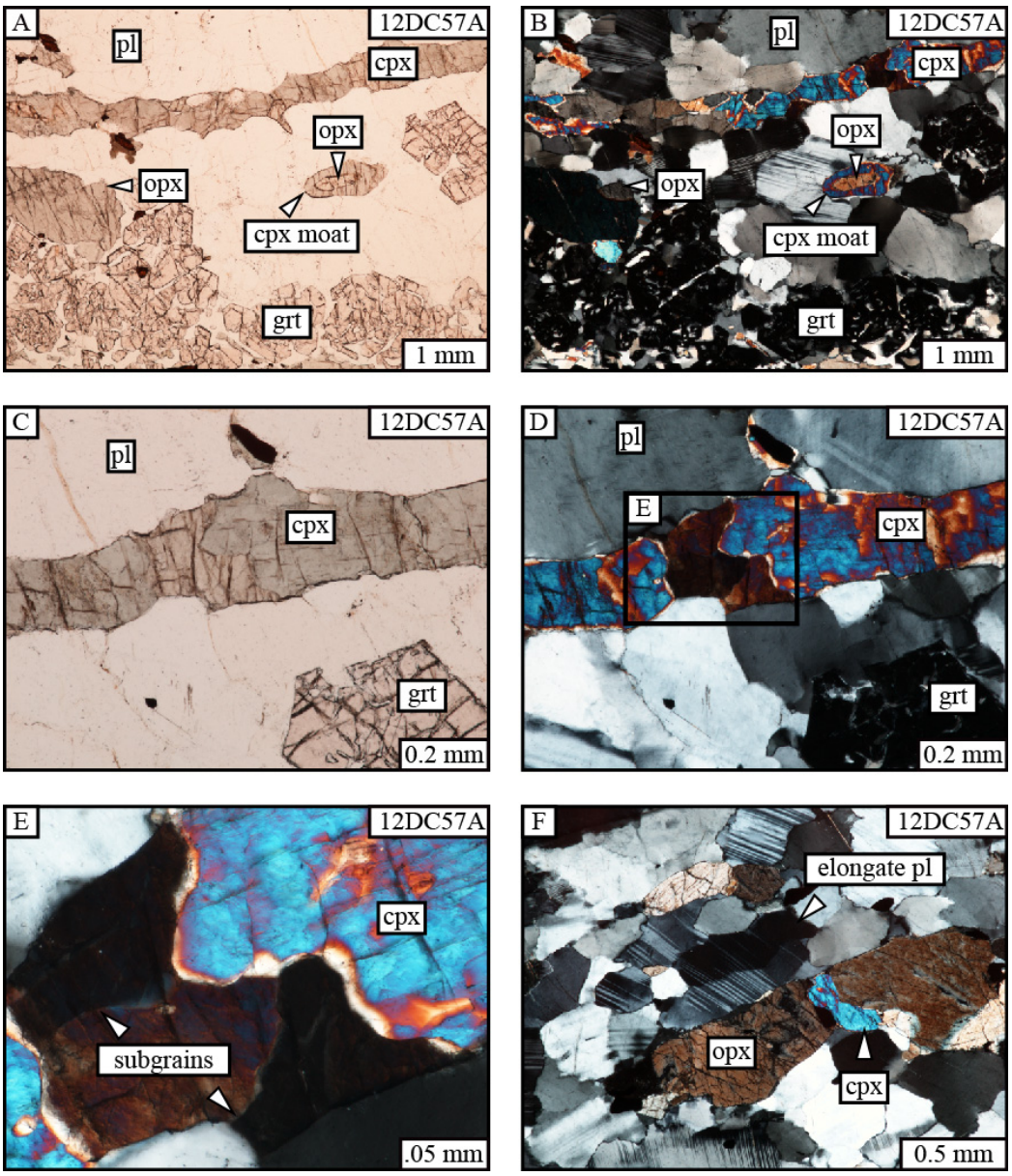

Figure 16. All photomicrographs are of sample 12DC57A from Domain 2 in Doubtful Sound. The rock type is a garnet granulite. The images show microstructures of high temperature metamorphism, deformation, anatexis, and dislocation creep in clinopyroxene. A) A plane light overview photomicrograph showing trains of pyroxene and a clinopyroxene moat on orthopyroxene. B) A cross polarized photomicrograph of "A". C) A plane light photomicrograph showing elongate clinopyroxene grains set in the plagioclase matrix. D) A cross polarized photomicrograph of "C". The box outlines the extent of "E". E) A cross polarized photomicrograph of clinopyroxene showing grain boundaries and subgrains. F) A cross polarized photomicrograph showing elongate and inclusion free plagioclase grains, as well as elongate orthopyroxene grains.

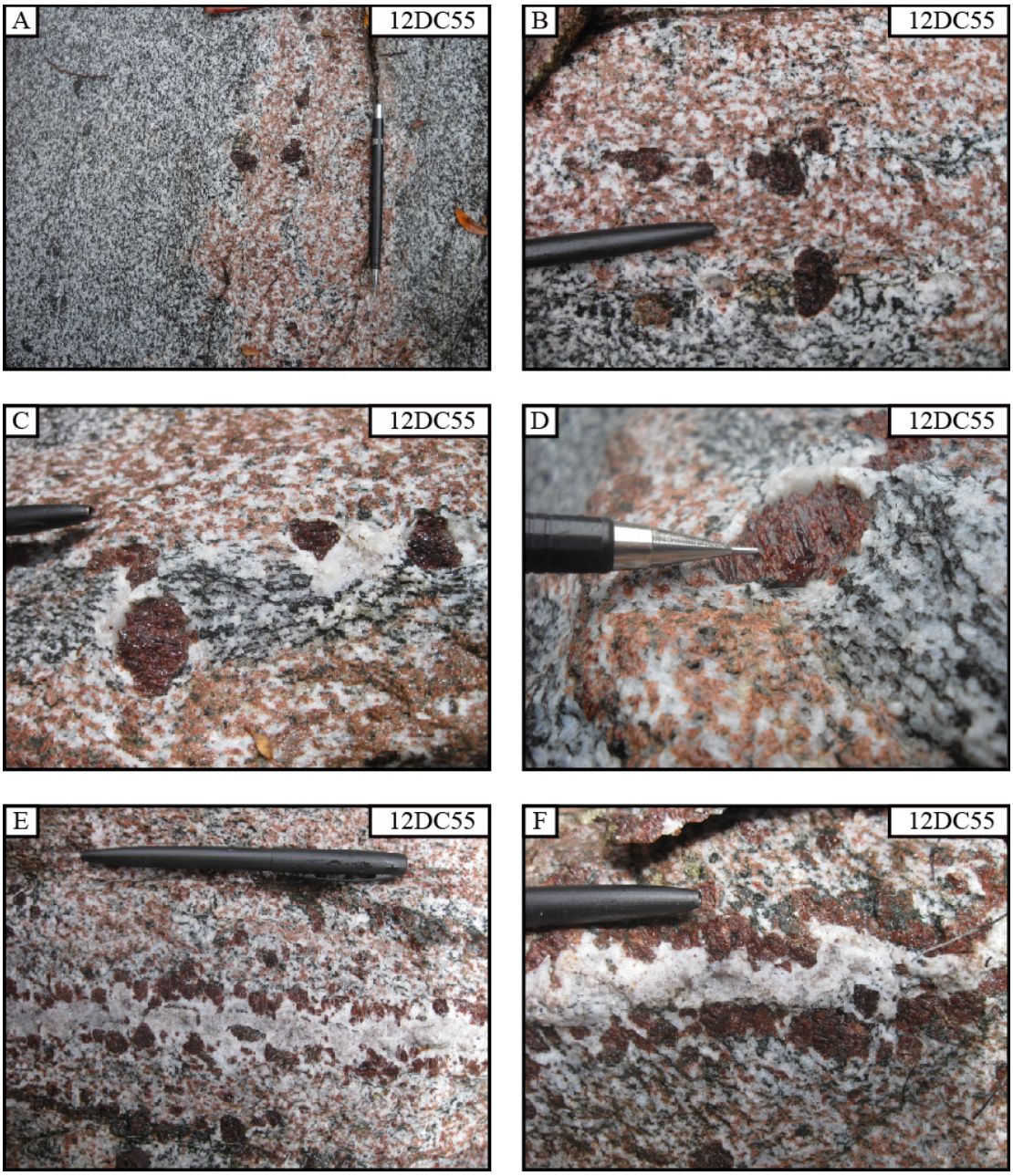

Figure 17. All photos are site photos from 12DC55 in Domain 2 of Doubtful Sound. The rock types are granulites and garnet granulites with a weakly developed S_2 foliation. These images show the patchwork of garnet granulite metamorphism. A) An outcrop of granulite and a local garnet granulite reaction zone. B) A close up of the garnet granulite zone from "A" showing peritectic garnet. C) Peritectic garnets surrounded by leucosome. D) Peritectic garnet on the edge of a garnet granulite reaction zone. Note the plagioclase matrix and wispy alignment of pyroxene. E) Leucosome vein studded with peritectic garnets that cross cuts the garnet granulite. F) Small fold in a leucosome vein.

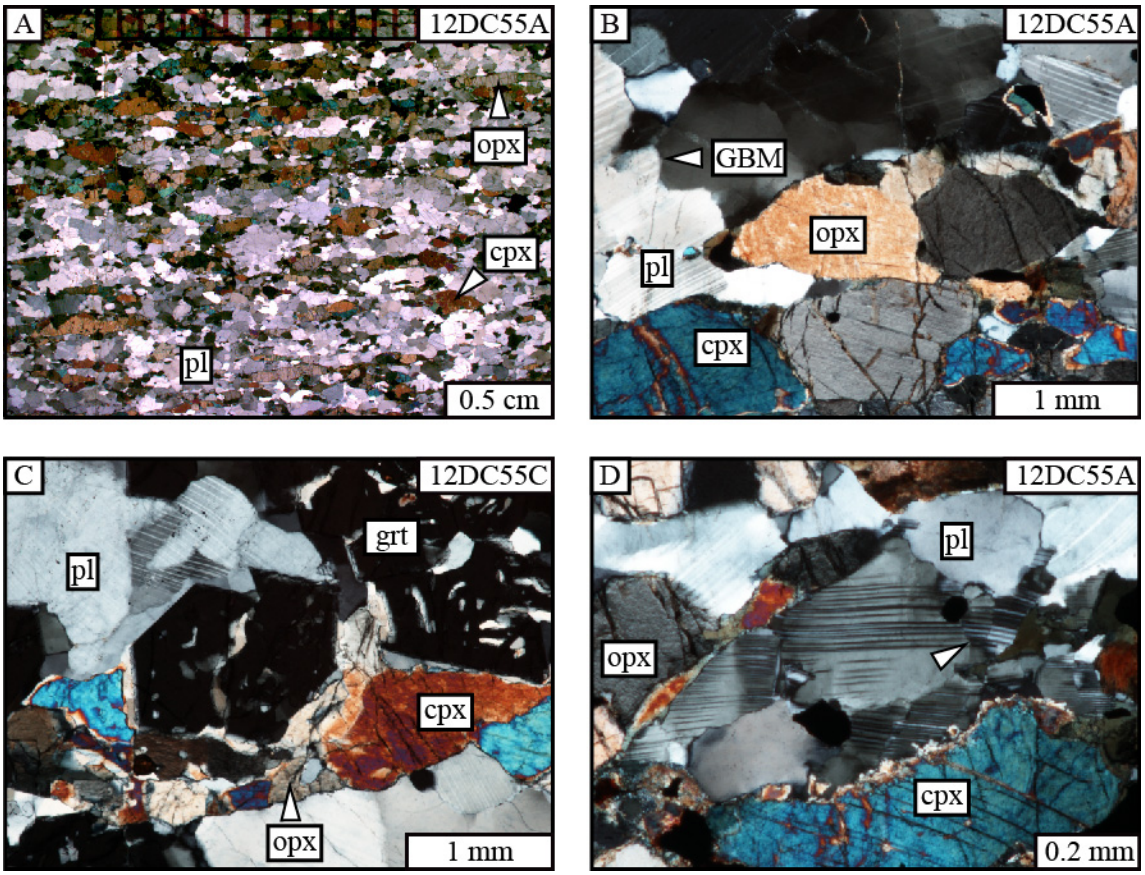

Figure 18. All photomicrographs are cross polarized light. The sample is denoted in the upper right corner. The rock types are granulites and garnet granulites that preserve the S_2 foliation. A) An overview photomicrograph showing elongate trains of pyroxene that define S_2. B) Grain boundary migration in plagioclase. C) A fractured garnet in the center of the image and garnet with inclusions in the upper right. D) The blue clinopyroxene has a thin reaction rim and the arrow points to grain boundary migration and deformation twins in plagioclase.

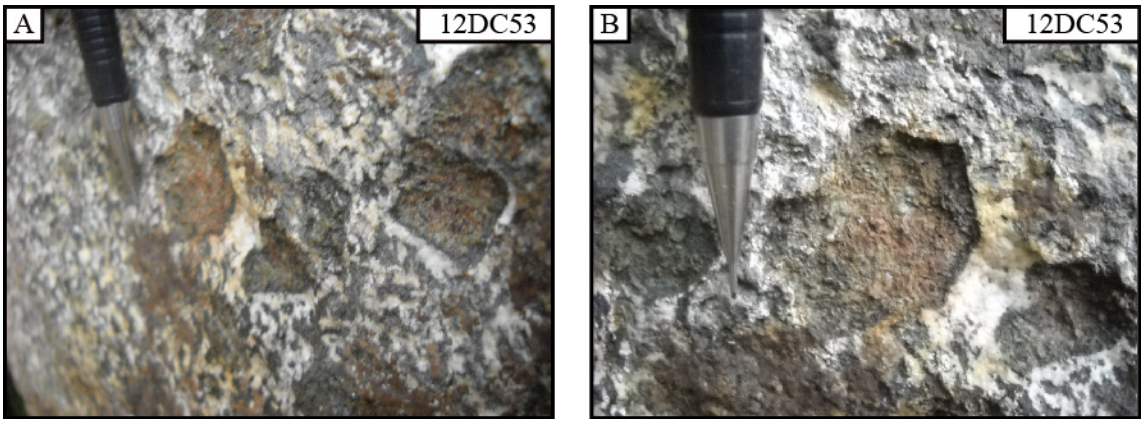

Figure 19. Site photographs from 12DC53. The host rock is a metadiorite. Photos A and B show the lack of aligned hornblende any pyroxene into a foliation plane, and euhedral peritectic garnet with reaction rims.

Synthesis of Domain 2

Domain 2 in Doubtful sound records structures and processes associated with garnet granulite facies metamorphism. The boudinaged mafic dike with infilled leucosome at site 12DC36 indicates that extension occurred while melt from granulite facies metamorphism was still present. The variable alignment of mafic minerals into a S_2 foliation suggests that deformation was distributed across this domain. From the consistent trend of L_2 lineation I infer that the dominant direction of flow was E-W.

Due to the temperatures associated with the deformation, suprasolidus flow and dislocation creep in plagioclase were the primary mechanisms of deformation. I propose that deformation outlasted anatexis, and that the subgrain development in pyroxene attests to granulite facies temperatures during deformation. Records of how pyroxene deformed are rare in Domain 2, but from the preserved subgrains at site 12DC57 I infer that pyroxene also deformed through dislocation creep.

Domain 3 (Doubtful Sound)

Domain 3, a locality known as the Doubtful Sound Shear Zone, extends approximately 1.5 kilometers east and west from Kellard Point. The center of this domain is composed of an approximately 1 kilometer wide swath of Paleozoic cover rock, Kellard Point Gneiss (KPG), which dips to the north and rises into the mountains to the south. Below the KPG are well foliated (S_3) amphibolites. The S_3 foliations are composed of aligned hornblende and pyroxene. Trains of elongate feldspar porphyroclasts also define L_3.

Site 12DC51 marks the boundary between Domain 2 and Domain 3. Outcropping here are pl + hbl + bt + ksp amphibolites. The S_3 foliation of aligned hornblende and plagioclase dips to the west, and the L_3 hornblende mineral lineation is down dip. Asymmetric potassium feldspar grains have tails of ksp + hbl and give a top-down-to-the-west sense of shear. Intruded dikes of a granitic composition have been dismembered into asymmetric clasts that also give a top-down-to-the-west sense of shear (Figure 20). In thin section trains of millimeter sized hornblende define the foliation. The hornblende grains show simple twinning and some are asymmetric with tails of fine grained hornblende. In general the hornblende grains have a ratty shape with jagged grain boundaries. Plagioclase grain sizes vary from millimeter to sub millimeter scale, and they show evidence of recovery by the formation of 120° triple junctions (Figure 21).

A coarser grained equivalent of the above outcrop is found at site 12DC50. The foliation here is less continuous than at site 12DC51, and large porphyroblastic plagioclase are set in a hornblende matrix. A L_3 lineation of aligned hornblende and

plagioclase moderately plunges to the northeast. Biotite is found as clots in the hornblende matrix and as laths between plagioclase grains.

Around the corner of Kellard Point, just inside the entrance to Crooked Arm at site 12DC47 and 13DC69 are sheared marbles. The marbles have a mylonitic texture and Kellard Point is composed of a mixture of marble, amphibolite gneiss, schist and orthogneiss. The rocks are highly deformed and show a penetrative foliation that approximately parallels S_3 in the Malaspina. The mylonite textures indicate that some deformation associated with the DSSZ was partitioned into the host rock. Penetrative L_3 lineations at Kellard Point, like L_3 in the Malaspina mostly trend NNE, slightly oblique to the trend of the older L_2. This relationships is observed best near Kellard Point and suggests that stretching directions recorded by L_1, L_2 and L_3 are all slightly different and can be distinguished on the basis of mineral assemblage, cross cutting relationships and orientation.

Synthesis of Domain 3

Domain 3 along Doubtful Sound shows that extensional deformation associated with the DSSZ was also accommodated by the Paleozoic cover rock. Weak marble layers and quartz rich amphibolites allowed deformation to penetrate the cover rock. While annealing has erased many microstructures from plagioclase in the amphibolitic footwall to the DSSZ, the microstructural evidence of grain boundary migration is still preserved, and core mantle structures indicated plagioclase deformed through dislocation creep. The amphibolites also show that hornblende and biotite begin to accommodate more of the strain.

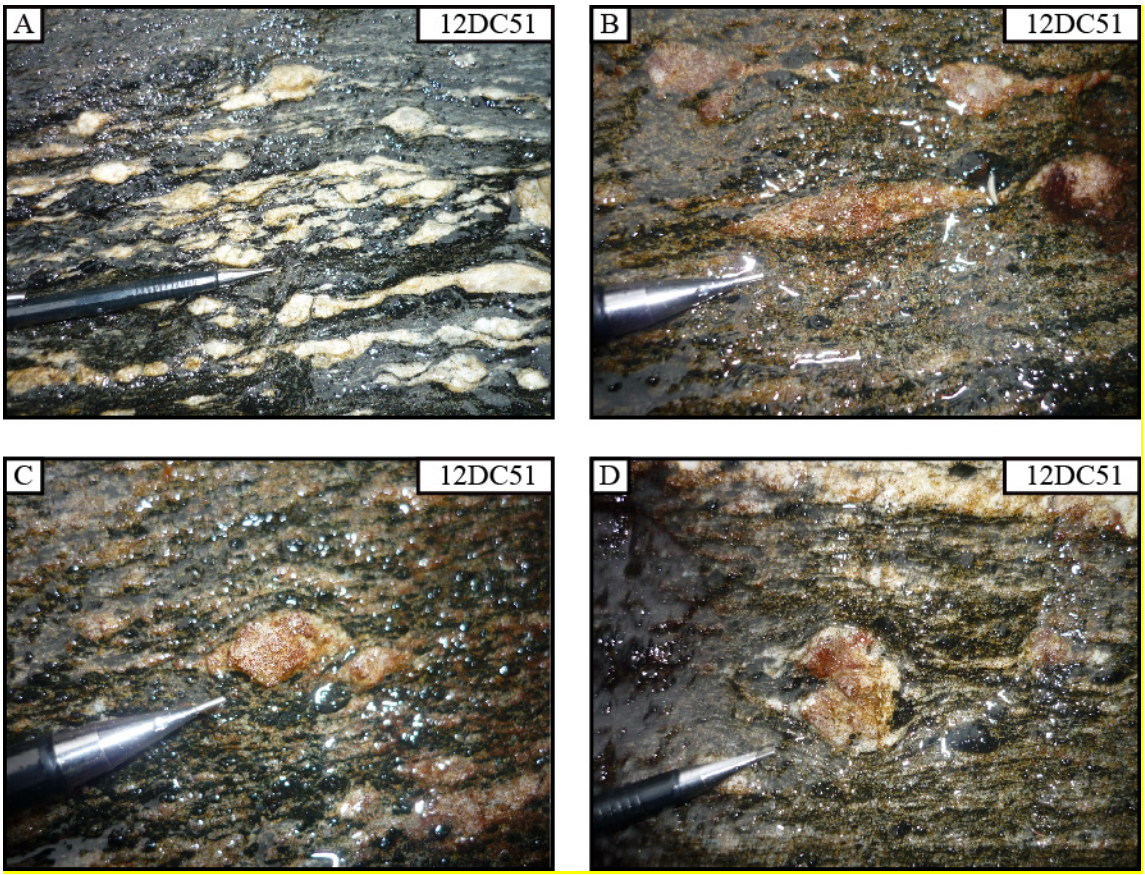

Figure 20. All images are from the Doubtful Sound Shear Zone at site 12DC51 in Domain 3 of Doubtful Sound. The rock type is an amphibolite that has a S_3 foliation. The foliation is identified by the alignment of hornblende and feldspar porphyroclasts. A) A cluster of asymmetric feldspar porphyroclasts. B) An elongate potassium feldspar porphyroclast in the center of the photo, and porphyroblastic hornblende in the foliation below. C) A photo showing a potassium feldspar porphyroclast and the hbl+pl foliation. D) A potassium feldspar porphyroclast in the center of the photo with tails of plagioclase and beards of hornblende.

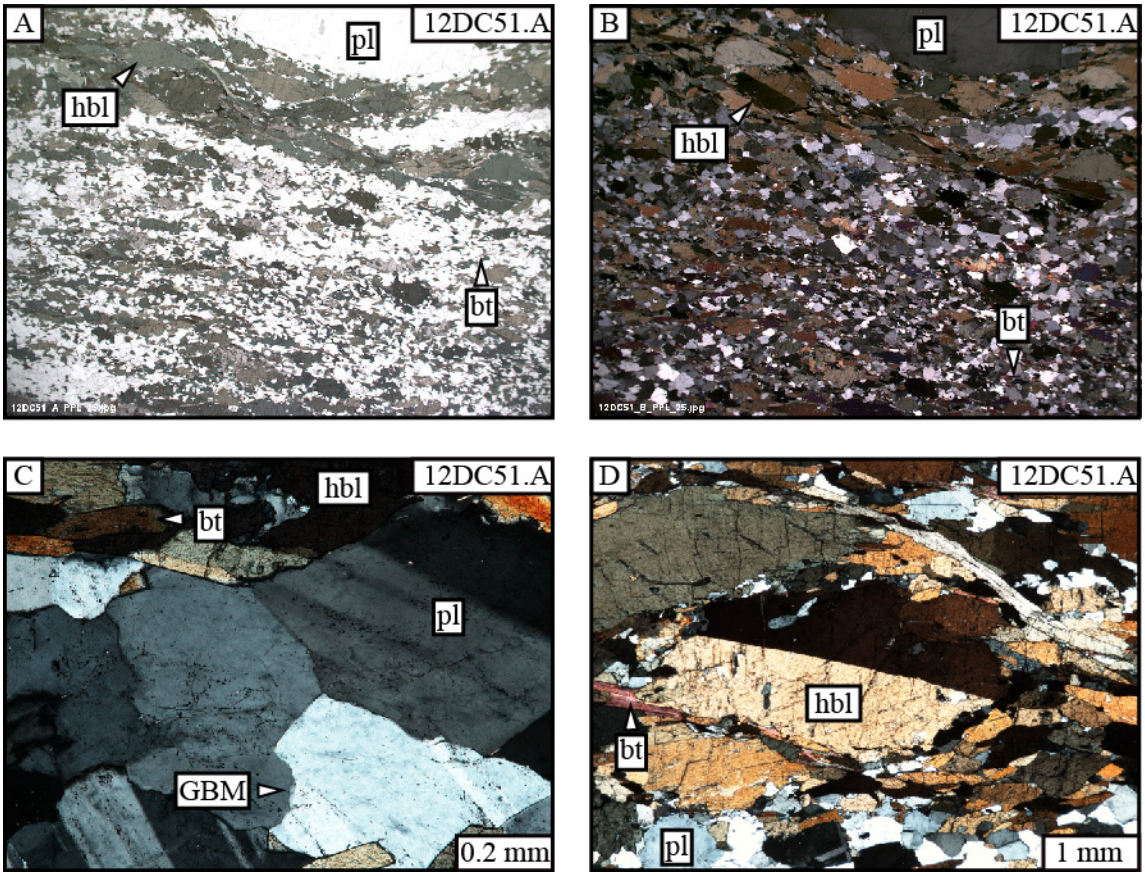

Figure 21. All photomicrographs are from sample 12DC51.A from the Doubful Sound Shear Zone (DSSZ) in Domain 3 of Doubtful Sound. The rock type is an amphibolite and the images show the microstructures associated with the DSSZ. A) The field of view is 12 mm. This is a plane light overview photomicrograph showing the semicontinous foliation of aligned hornblende. B) The field of view is 12 mm. A cross polarized photomicrograph of "A". C) A cross polarized photomicrograph showing the formation of a tripple junction in the center of the image and grain boundary migration in plagioclase. D) A cross polarized photomicrograph showing a simple twinned hornblende in the center of the image that has a tail of finer grained hornblende to the right.

3.4 Crooked Arm

Crooked Arm records the metamorphic and structural transformation from L-tectonite granulites (S_2/L_2) to S-tectonite amphibolites (S_3/L_3). Granulite and garnet granulite L-tectonites that preserve S_2/L_2 often remain as lozenges cross cut by a network of amphibolite shear zones (S_3/L_3). Early development of S_2'/L_2 is recorded in metadiorite orthogneisses at the end of Crooked Arm, a region where hornblendite intrusions remain and evidence of granulite facies metamorphism is minimal. Near the "Crook" of Crooked Arm outcrops of garnet granulite have mature S_2/L_2 fabrics and show evidence of melt. The network of amphibolite shear zones are anastomosing throughout Crooked Arm, give top down-to-the-northeast/southwest senses of shear, and vary in thickness from one kilometer to meters thick. A site location map, structural map, and cross section can be seen in Figure 22, Figure 23, and Figure 24.

I took samples of, metadiorite, garnet granulite and retrogressed granulite from the centers/margins of the lozenges, and I sampled amphibolites from the shear zones. From these samples I determined the changes in mineral assemblage/development, deformation mechanisms, and fabric type (L vs. S tectonites). The two end members I found are rodded and strongly lineated (L_2) garnet granulites and mylonitic amphibolites (L_3/S_3).

I used my field data and samples to define three domains in Crooked Arm. Domain 1 extends from the end of Crooked Arm to approximately two kilometers from Turn Point (see Figure 2 for landmark locations). Domain 2 extends from the eastern boundary of Domain 1 to approximately one and a half kilometers from Kellard Point.

Domain 3 is located on the west shore of Crooked arm and extends from the entrance south approximately one kilometer, merging into Domain 3 of Doubtful Sound. For a representative description of Domain 3 I refer you to the descriptions from Doubtful Sound.

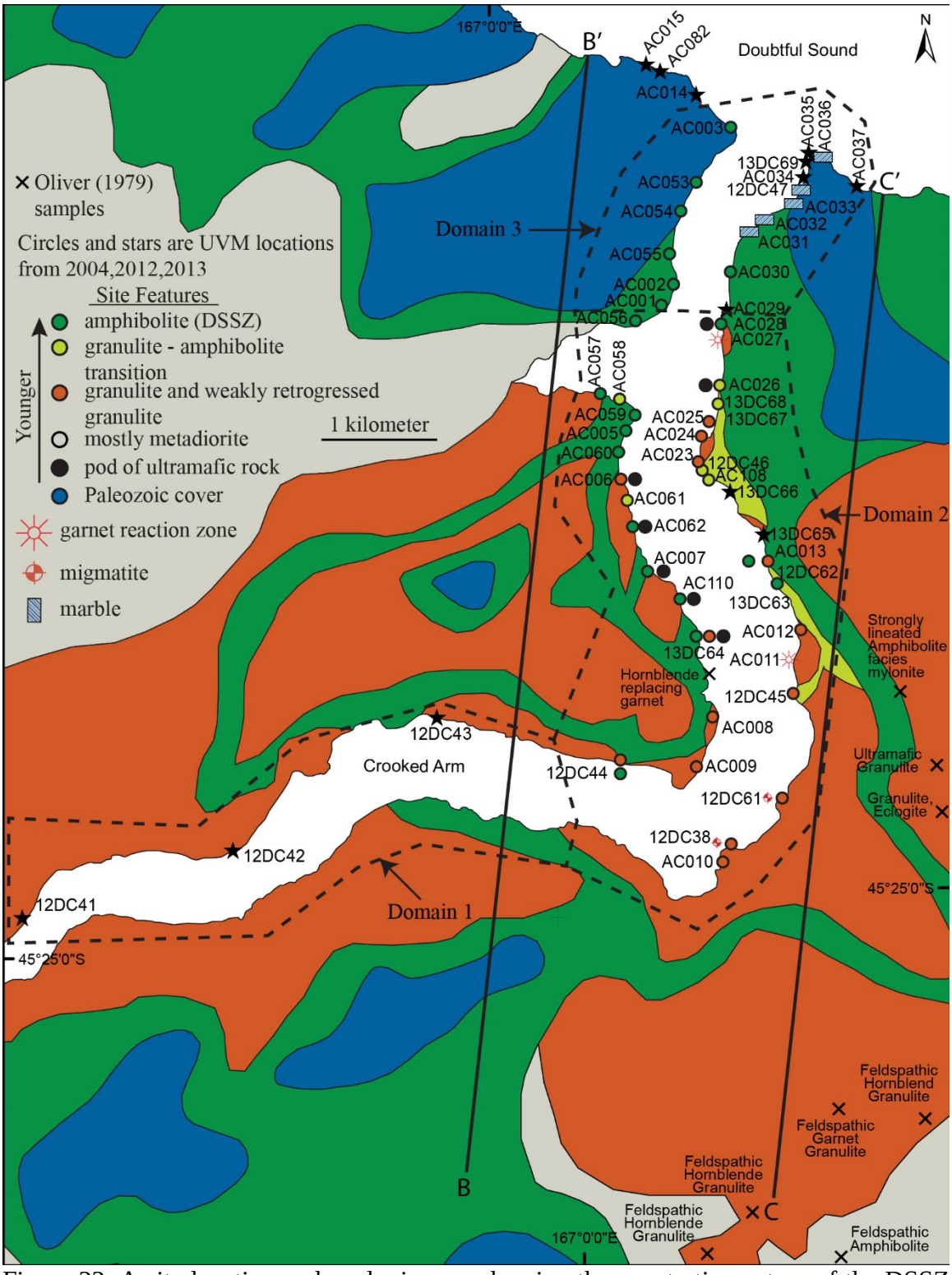

Figure 22. A site location and geologic map showing the penetrative nature of the DSSZ into regions of granulite. Cross sections B-B' and C-C' can be seen in Figure 24.

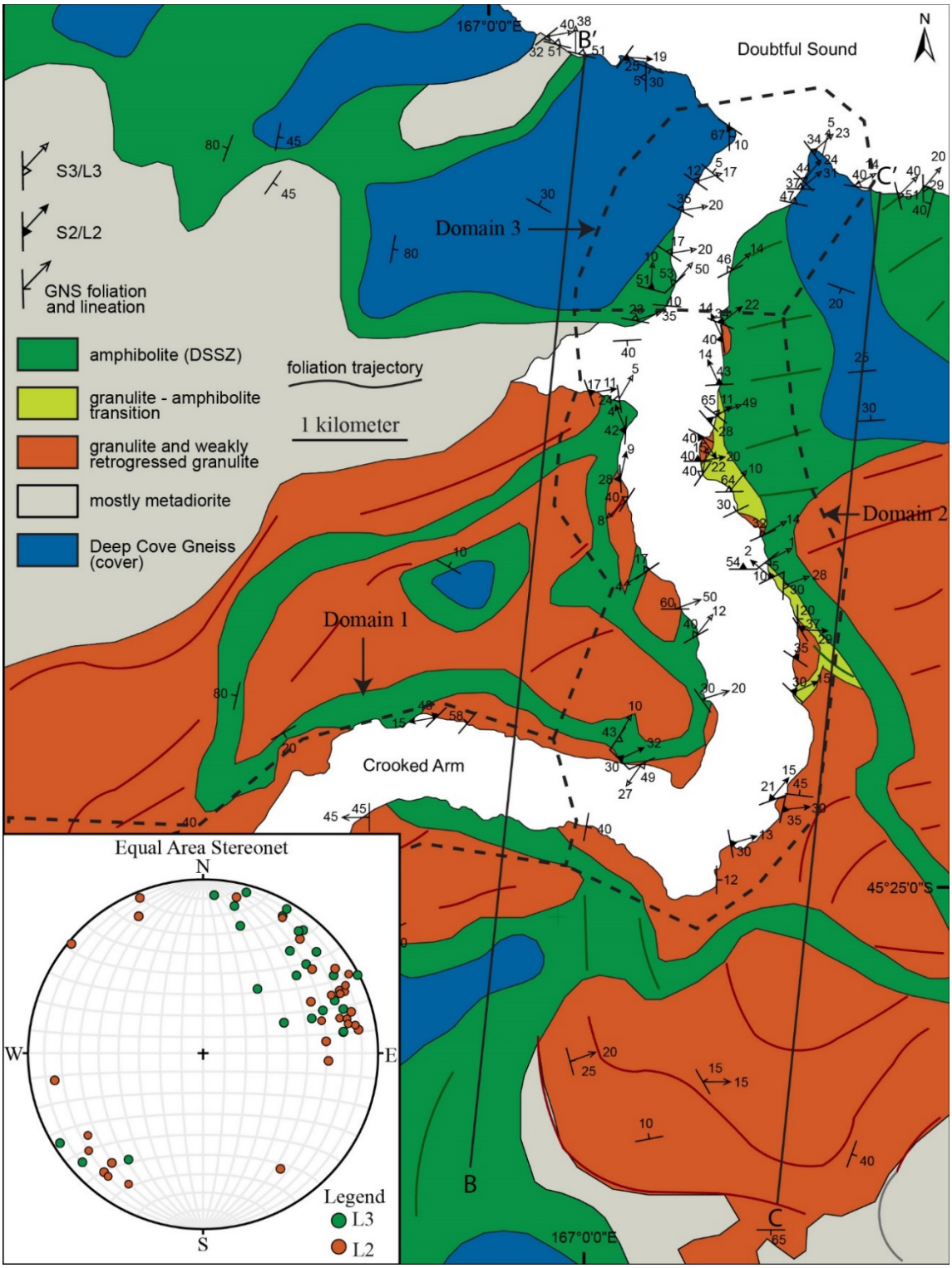

Figure 23. A structural map of Crooked Arm and a lower hemisphere equal-area stereographic projection showing the NE-SW trending L_2 and L_3 lineations. While both lineations trend NE-SW, L_3's in proximity to L_2s consistently trend more northerly.

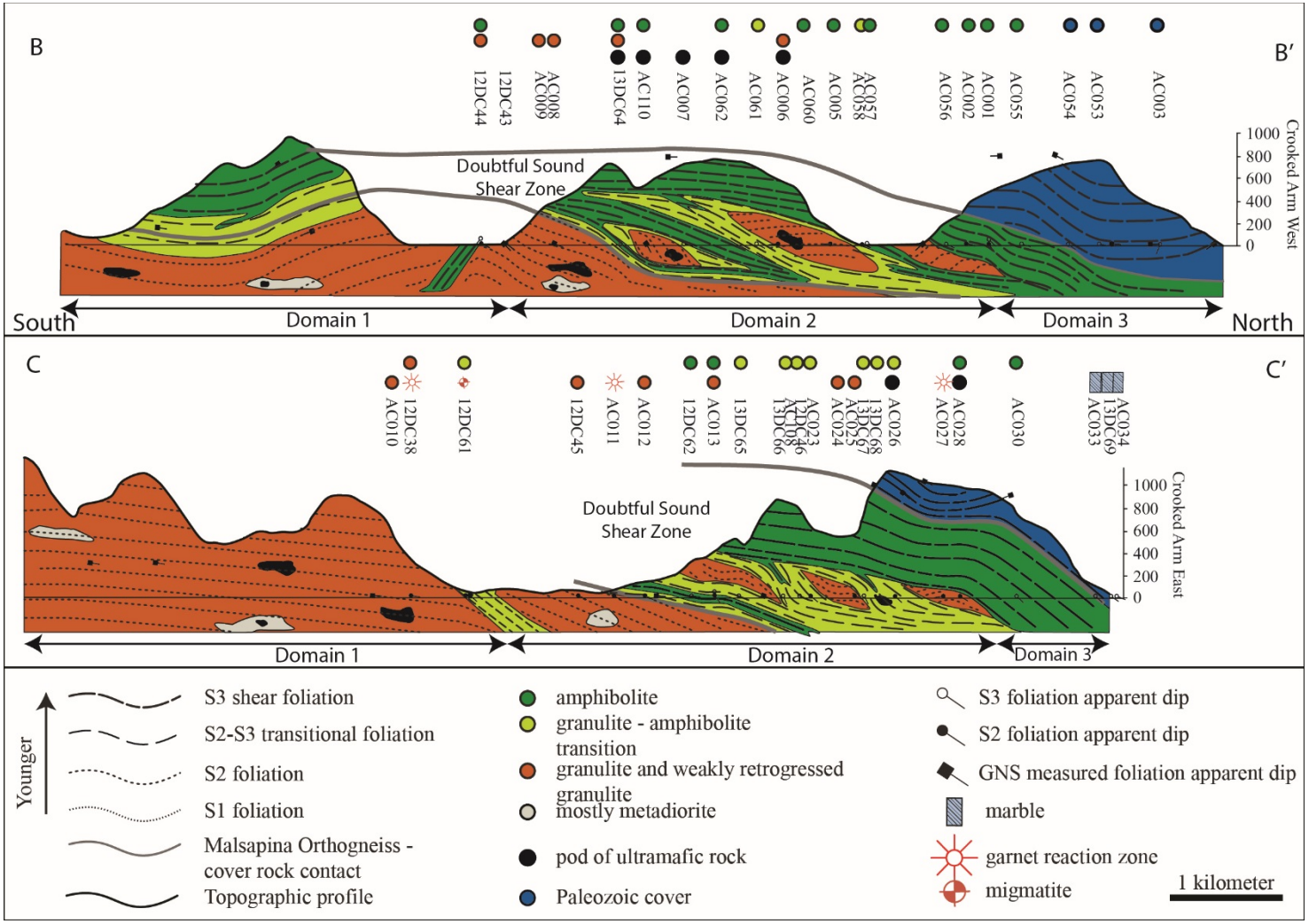

Figure 24. Cross section of Crooked Arm from Figure 23 showing mostly granulite in Domain 1, the penetrative DSSZ with transitional and amphibolite rocks that enclose lozenges of granulite in Domain 2, and the thickest zone of the DSSZ at the cover rock contact.

Domain 1 (Crooked Arm)

This domain is mostly characterized by granulite orthogneisses with an $L_2 \geq S_2$ fabric. Mineral stretching lineations (L_2) plunge NE-SE and to the west. Rocks in this domain have a moderate S_2 foliation with a range of dip directions. Also located in this domain are hornblendite intrusions. The following is a description of outcrops and microstructures.

Cropping out at site 12DC39 are dioritic orthogneisses and a pod of biotite rich orthogneiss. The pod of biotite rich orthogneiss has a dome structure and is weakly deformed. The host metadiorites at this site are well foliated (S_2) and lineated (L_2). Aligned hornblende with inclusions of fine plagioclase define the foliation which dips moderately to the south and northwest. In thin section (Figure 25) plagioclase grains show dynamic recrystallization and the formation of sub grains through grain boundary migration. Some larger plagioclase porphyroclasts are almost completely recrystallized to subgrains. Biotite is aligned and has grown along plagioclase grain boundaries.

Sites 12DC41, 12DC42, and 12DC43 expose metadiorites that are strongly lineated and rodded in appearance. At site 12DC41 the metadiorite is in contact with weakly foliated hornblendite rocks (Figure 26). Bands of the orthogneiss intrude the hornblendite rocks and finger size enclaves are nearly dismembered from the mafic host. A folded pegmatite dike cross cuts the orthogneiss, has developed a minor fabric and includes garnet. A thin section of the hornblendite (Figure 27) shows a uniform grain size of hornblende and fine, irregular shaped plagioclase along hornblende grain boundaries. Hornblende and biotite show a shape preferred orientation and define the foliation.

A representative thin section of the metadiorites from 12DC42 (Figure 28) shows that aggregates of hornblende are elongate and contain fine inclusions of plagioclase. The terminus of hornblende aggregates are acicular and often overlap with neighboring aggregates. The grain boundaries of the hornblende aggregates often are matted with the plagioclase matrix. Individual grains of hornblende protrude into the plagioclase matrix, forming small "cups" of plagioclase that line the hornblende aggregate boundary. Biotite is mostly aligned with hornblende but is also found as small needles along grain boundaries in the plagioclase matrix. Plagioclase forms the matrix of the rock and shows evidence of dynamic recrystallization through grain boundary migration.

Synthesis of domain 1

Domain 1 in Crooked Arm represents a region where D_2 deformation occurred without pervasive granulite facies metamorphism. The inclusion-free plagioclase matrix that shows grain boundary migration and the development of subgrains is consistent with observations of D_2 deformation in Domain 2 along Doubtful sound. Unique to this domain is the retrogression of granulites to amphibolites without D_3 structures, which resulted into nearly monomineralic aggregates of hornblende. This is significant because most areas where retrogressed D_2 fabrics are observed show phase mixtures of relic pyroxene, hornblende symplectite, biotite, and fine grained plagioclase in the mafic aggregates (see Domain 2 descriptions below). I make the following interpretations for this domain:

1) Retrogression occurred in a low strain environment where minerals were able to equilibrate with the environment, and that this area did not feel the effects of D_3.
2) Remnants of hornblendite bodies show that magma mingling during pluton emplacement was widespread.

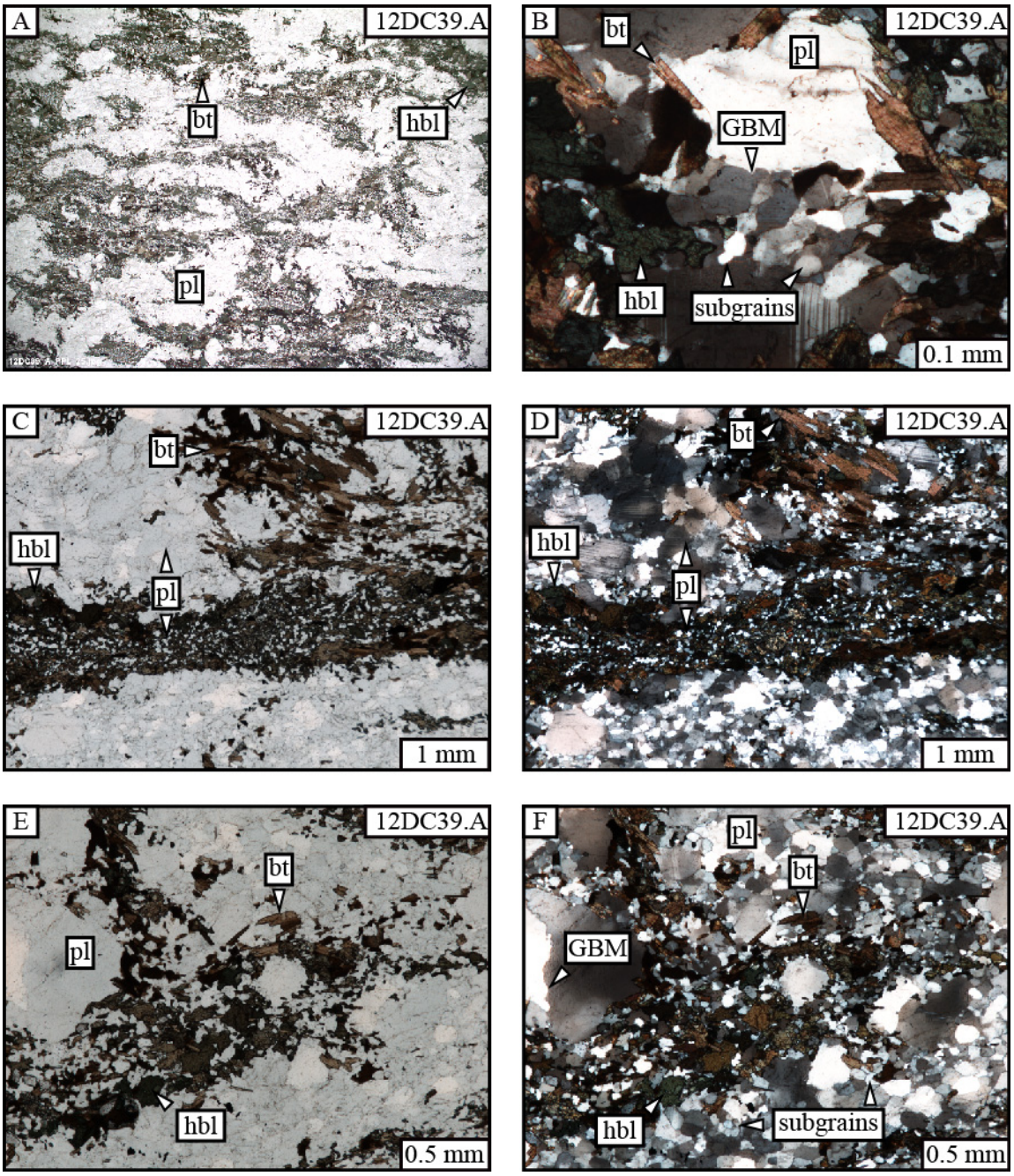
A
12DC39.A
bt
hbl
pl
B
12DC39.A
bt
pl
GBM
hbl
subgrains
0.1 mm
C
12DC39.A
bt
hbl
pl
1 mm
D
12DC39.A
bt
hbl
pl
1 mm
E
12DC39.A
bt
pl
hbl
0.5 mm
F
12DC39.A
pl
bt
GBM
hbl
subgrains
0.5 mm

Figure 25. All photomicrographs are from sample 12DC39.A and the rock is a metadiorite with D_2 deformation. These images show the heterogeneous compositoin of the folation and evidence of dislocation creep in plagioclase. A) An overview plane light photomicrograph showing clots of hornblende and biotite that are semiconnected yet set in the plagioclase matrix. B) A cross polarized photomicrograph showing grain boundary migration and subgrains in plagioclase, as well as biotite that has grown along plagioclase grain boundaries. C) A plane light photomicrograph of a hornblende, plagioclase and biotite layer that shows the fine inclusions of plagioclase. D) A cross polarized photomicrograph of "C". E) A plane light photomicrograph showing a large plagioclase grain on the left that is surrounded by a mixture of fine plagioclase, hornblende and biottie. F) A cross polarized photomicrograph of "E" that shows grain boundary migration and subgrains in plagioclase.

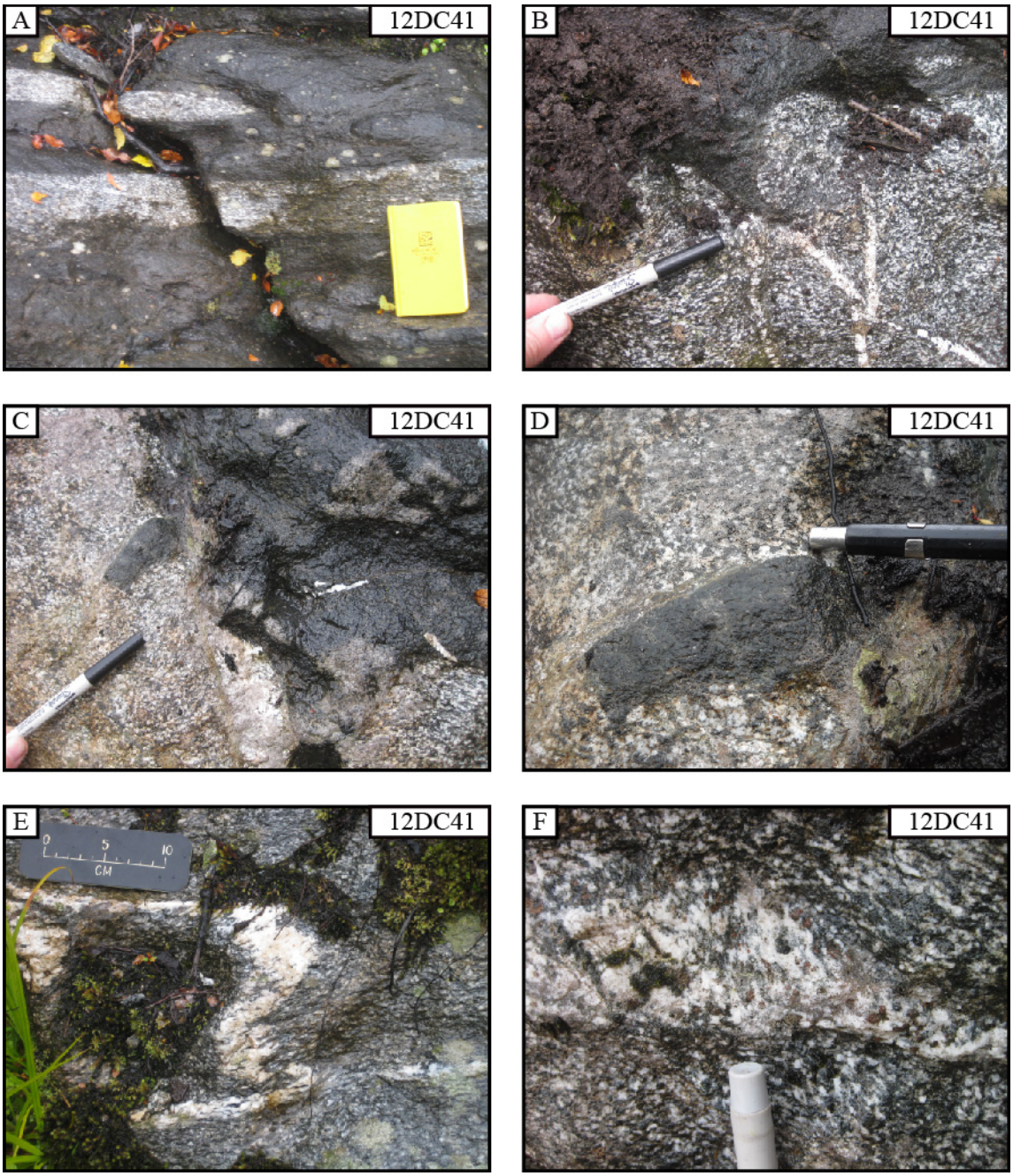

Figure 26. All photos are from site 12DC41. These images show the interaction of the dioritic orthogneiss with the hornblendites. A) A site photo showing bands of metadiorite that iintruded hornblendite. B) A photo showing the contact between the orthogneiss and hornblendite. C) A photo showing the orthogneiss and hornblendite. Just above the sharpie marker you can see a small enclave that is nearly dismembered from the mafic rock. D) A close up of the enclave from "C". E) A folded pegmatite dike that cross cuts the orthogneiss. F) A close up of the pegmatite dike from "E" showing a weak fabric and garnets.

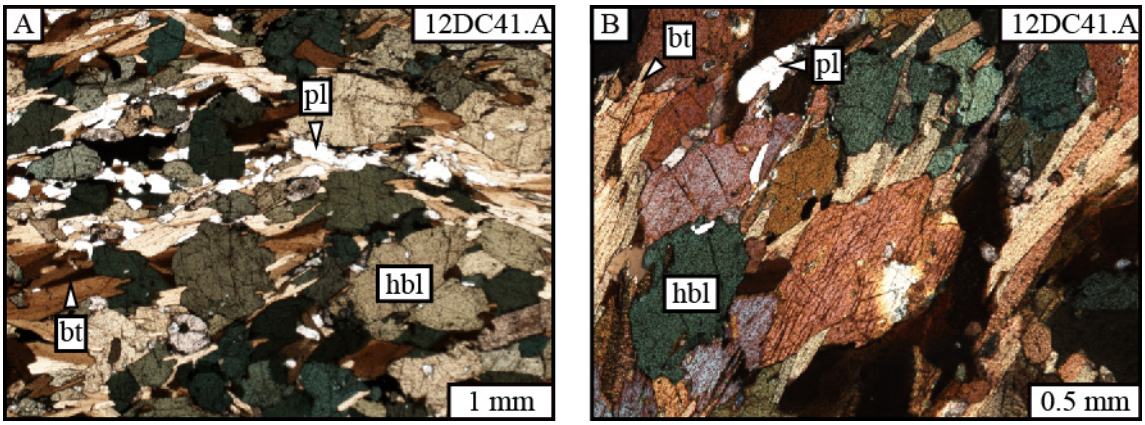

Figure 27. Both photomicrographs are cross polarized light and from sample 12DC41.A. The rock is a hornblendite that was in contact with a dioritic orthogneiss. A) An overview showing that the hornblendite is mainly composed of hornblende and biotite, but that it contains fine plagioclase along grain boundaries. B) This images shows the shape perferred orintation of hornblende. The foliation traces from the bottom left to the top right of the image.

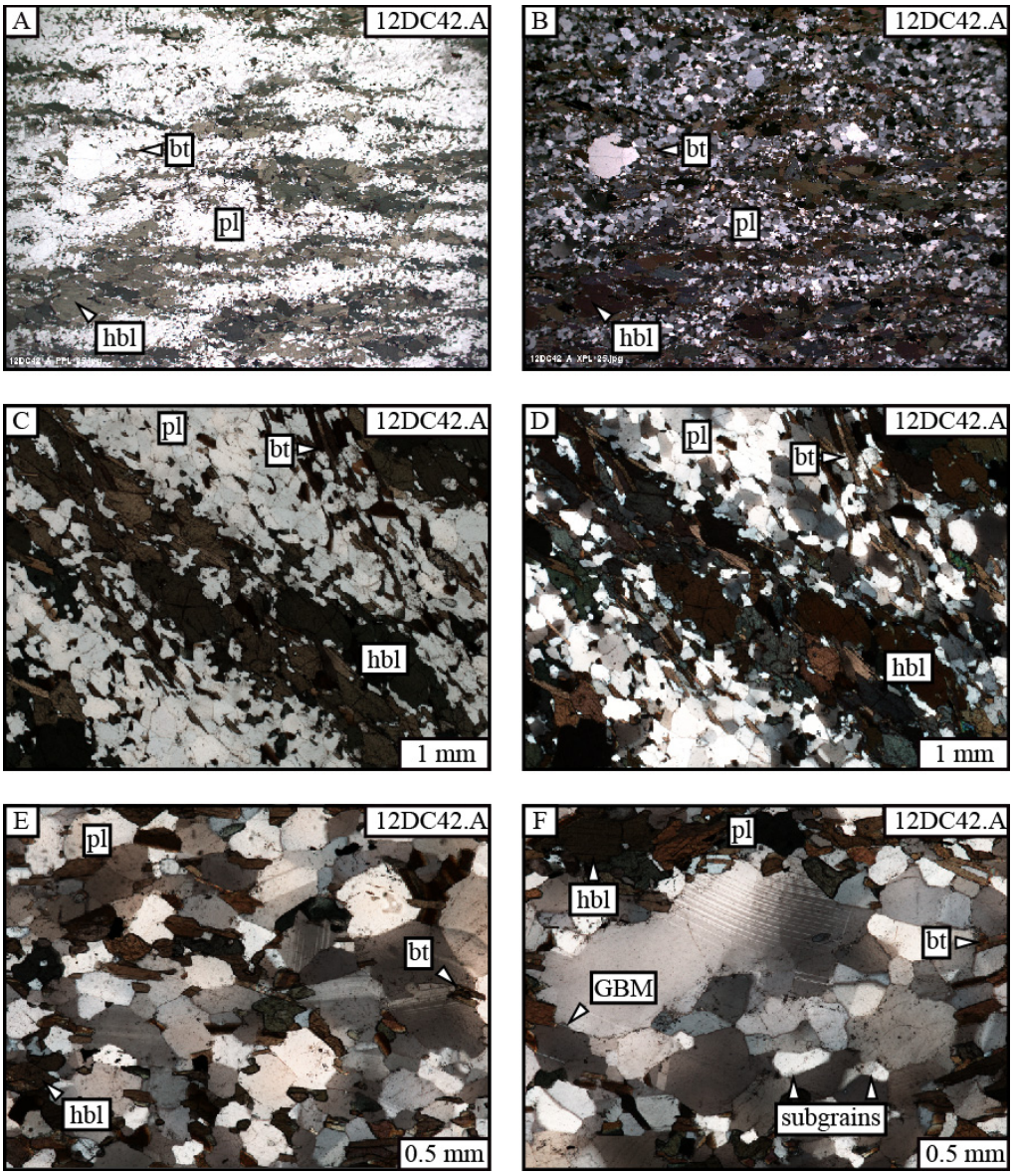

Figure 28. All photomicrographs are from sample 12DC42.A, a metadiorite that preserves D_2 deformation. The field of view for "A" and "B" is 12 mm. A) A plane light overview photomicrograph that shows aggregates of hornblende and a matrix of plagioclase with fine grained hornblende and biotite along the grain boundaries. B) A cross polarized photomicrograph of "A" that also shows a porphyroblastic plagioclase on the left of the image. C) A plane light photomicrograph of a hornblende aggregate showing subhedral to anhedral grain shapes and inclusions of plagioclase. D) A cross polarized photomicrograph of "C". E) A cross polarized photomicrograph of a plagioclase domain that shows fine hornblende and biotite along plagioclase grain boundaries. F) A cross polarized photomicrograph of a plagioclase domain showing grain boundary migration and subgrains.

Domain 2 (Crooked Arm)

Domain 2 of Crooked Arm exposes four rock types: 1) garnet granulite, 2) retrogressed granulite, 3) hornblendite 4) amphibolite. Garnet granulites and retrogressed granulites that have an $L_2>S_2$ fabric that formed during D_2 occur as large exposures and as lozenges. Both of these rock types generally have an E-W to NE-SW trending lineation. Mafic pods of hornblendite, usually found within the vicinity of granulites have a weak fabric and are prevalent along the west coast of Crooked Arm. Shear zones composed of amphibolites with an $S_3 \geq L_3$ fabric that formed during D_3 appear as thick sub-horizontal zones and as thinner, steeper splays. The shear zones cross cut the retrogressed granulites and generally have a NE-SW trending lineation. The following are descriptions of outcrops and microstructures for Domain 2.

Located in the "crook" of Crooked Arm, across from Turn Point, at site 12DC38 are outcrops of garnet granulite with a mostly $L_2>S_2$ fabric (Figure 29) and domains of $L_2 \geq S_2$ fabrics (Figure 30). Conspicuously neighboring the garnet granulite is a fine grained mafic pod of hornblende and biotite. The garnet granulite L_2 lineation of stretched pyroxene (opx + cpx) and plagioclase plunge down dip to the east. Aligned, elongate, and slightly flattened trains of pyroxene define a weak foliation.

The outcrop domains of $L_2>S_2$ garnet granulite fabrics at site 12DC38 are a high strain, stretching, top-down-to-the-southwest shear zone. Elongate grains of pyroxene set in a plagioclase matrix give the shear zone a streaky appearance. The shear zone transposes the relict $L_1 \geq S_1$ coarse grained garnet granulite.

Within the relict domains of S_1/L_1 plagioclase forms a leucosome matrix and pyroxene mostly occurs as tails on garnet. Mafic dikes are mostly intact in the relict domains (Figure 30.D) but become stretched and dismembered in the shear zone walls (Figure 30.E). Veins of leucosome are contained in the relict domain and the shear zone walls have peritectic garnets with tails of leucosome.

Microstructures from this site record evidence of metamorphism, anatexis, and deformation at temperatures greater than 750° C (Schwartz et al., 2016). Clinopyroxene grains are elongate with pinch and swell geometries. Orthopyroxene grains are often surrounded by double moats, the inner moat being clinopyroxene and the outer moat being potassium feldspar. The moats of potassium feldspar have a sharp boundary that roughly follows the geometry of the interior pyroxene grain. These moats, or films of potassium feldspar can also be found surrounding garnet (Figure 31). Shown in Figure 32 are orthopyroxene set in a plagioclase matrix with developed subgrains and a film of potassium feldspar is found around garnet with vermicular quartz inclusions. Figure 33 shows garnet coronas on elongate pyroxene grains and as aggregates with tails of pyroxene. The microstructures from site 12DC38 show that deformation outlasted anatexis and that both plagioclase and pyroxene accommodated crystal-plastic deformation.

Approximately 600 meters west of Turn Point, at site 12DC44, a large cliff face exposure of retrogressed granulites with a $L_2>S_2$ fabric that are cross cut by a network of amphibolite shear zones with a $L_3=S_3$ fabric. Photos of the site can be seen in Figure 34 and a schematic sketch can be seen in Figure 35. Centrally located and at the bottom of this exposure is a pod of retrogressed granulites cross cut by steep splays of amphibolite shear

zones. The retrogressed granulites are coarse grained with a northeast trending plagioclase and hornblende stretching lineation. A weak, northeast dipping foliation of aligned mafic minerals (S_2) is transposed by nearly 90 degrees into the amphibolite shear zone. When looking at the outcrop, the foliation is transposed on both the east and west sides of the pod, giving two opposing senses of shear. The east side of the pod gives a top-down-to-the-east sense of shear and the west side of the pod gives a top-down-to-the-west sense of shear. The alignment of hbl + bt and gneissic layering define the S_3 shear zone foliation that dips to the southeast on the east splay and dips to the east on the west splay. Aligned hornblende and biotite form a mineral lineation (L_3) that trends to the southwest on the east splay and trends to the northeast on the west splay. Both splays can be traced up the cliff face to a point where they merge into an apparently flat yet undulose horizon of foliated rocks that cap the exposure. Outside of the shear zones domains of granulite and retrogressed granulite rocks are identified by their massive appearance and transposition of S_2 foliation into the DSSZ.

A thin section from the retrogressed granulite pod shows masses of hornblende set in a plagioclase matrix (Figure 36). The masses of hornblende are rimmed by clots of radial biotite. Hornblende grains are not very distinct and they appear to be symplectite pseudomorphs of pyroxene and have a vermicular or blebby texture. Small, immature grains of plagioclase and biotite are often inter-grown and some aggregates of biotite have a radial fan shape. Within the matrix plagioclase grains are amoeboid with cuspate-lobate grain boundaries and show evidence of grain boundary migration and the formation of subgrains.

In contrast, a thin section from the amphibolite shear zone (Figure 37) shows a mostly continuous gneissic foliation (S_3). The mafic layers consist of well-developed hornblende, biotite, and fine grained plagioclase. Some of the larger porphyroblastic plagioclase are sigmoidal with tails of biotite. The plagioclase foliation layers are mostly monomineralic, and the grains are mostly annealed with the formation of triple junctions. Evidence of dislocation creep is preserved with grain boundary migration. Biotite has grown along some of the plagioclase grain boundaries and in some cases connect to form shear bands.

On the east coast of Crooked Arm, at site 12DC45, are coarse grained retrogressed granulites preserving D_2 deformation. Here S_2 is identified by aligned hornblende aggregates and dips to the north. Elongate plagioclase and hornblende aggregates form an east trending L_2 lineation. In thin section (Figure 38) plagioclase forms the matrix of the rock. Hornblende grains that collectively form hornblende aggregates are uniform in size and show a shape preferred orientation. Biotite shear bands cross cut the hornblende aggregates but do not penetrate the plagioclase matrix.

One kilometer north or site 12DC45, at site 13DC63 a lozenge of retrogressed granulites with an $L_2>S_2$ fabric is cross cut by an amphibolite shear zone with S_3/L_3 fabrics (Figure 39). The lozenge is approximately two meters tall and three meters long. A hornblende stretching lineation ($L_{2)}$ plunges to the northwest and the foliation (S_2) is transposed into the shear zones. On top of the lozenge is the thickest portion of the shear zone that is well foliated and has a northeast plunging mineral lineation.

A sample from the center of the lozenge (Figure 40) shows mafic aggregates with a heterogeneous composition set in a plagioclase matrix. The mafic aggregates have radial biotite, myrmekite and symplectites along the rims, whereas the cores of the aggregates have anhedral hornblende, symplectite, and fine grained vermicular plagioclase. The plagioclase in the matrix is mostly inclusion free and shows grain boundary migration. A sample from the capping shear zone (Figure 41) shows that the disjunctive S_3 foliation of aligned hornblende and biotite wrap aggregates of plagioclase. Porphyroblastic, rounded plagioclase are mantled with subgrains and have hornblende beards. Subgrain development and grain boundary migration in plagioclase is common. Hornblende grains are euhedral to subhedral and show simple twinning.

Across the fiord, on the west coast of Crooked Arm a landslide that occurred between 2012 and 2013 has exposed a large cliff face at site 13DC64. The landslide revealed the presence of a large hornblendite pod and a network of D_3 amphibolite shear zones (Figure 42). By using cross-cutting relationships the hornblendite pod was determined to be the oldest rock, followed by pods of coarse grained retrogressed granulites preserving S_2/L_2 that are then cut by the younger amphibolite shear zones (S_3/L_3). The hornblendite pod is shaped like a watermelon seed and pieces have been dismembered and incorporated into a steeply dipping shear zone. In the shadows of the retrogressed granulite pods the amphibolite shear zones are folded. Capping the exposure is a thick, sub-horizontal shear zone with northeast dipping shear bands (S_3). The steep shear zone splays eventually merge into this roof. A top-down-to-the-northeast sense of shear was derived

from the shear bands, asymmetric pods of older rock, and transposition of the S_2 foliation into the shear zones.

A sample taken form the amphibolite shear zone shows a semi-continuous S_3 foliation defined by the alignment of hornblende and plagioclase (Figure 43). The foliation wraps aggregates of plagioclase composed of millimeter scale grains. In plagioclase domains not enveloped by the foliation subgrains are found. Hornblende and biotite grains are large and euhedral.

At site 12DC46 a pod of retrogressed granulite that preserves the $L_2>S_2$ fabric is cross cut and wrapped by amphibolite shear zones that dip to the northwest (Figure 44). A sample from the margin of the shear zone (Figure 45) shows layers of hbl + bt + fine grained plagioclase compose the S_2 foliation. Thin layers of hornblende and biotite penetrate the plagioclase domains. Some hornblende grains retain inclusions of plagioclase. In the plagioclase domains evidence of dynamic recrystallization is seen by the development of subgrains through grain boundary migration.

Synthesis of domain 2

Domain 2 in Crooked Arm is the best location to observe the penetrative nature of the DSSZ, high strained garnet granulite deformation, and the retrogression from granulite to amphibolite. Outcrops here show that melting accompanied D_2, which produced $L_2>S_2$ fabrics. During D_2 both plagioclase and pyroxene deformed by dislocation creep. Retrogression and development of D_2 fabrics involved the heterogeneous replacement of pyroxene by hornblende symplectites, vermicular and fine grained plagioclase, as well as radial biotite. As retrogression progressed and D_3 fabrics

developed, shear bands begin to penetrate the plagioclase matrix until the new S_3 is formed. The preservation of each of these stages show that lithological and structural developments were dynamic in areas of fluid mobility and that dehydrated areas of garnet granulite were metastable during exhumation.

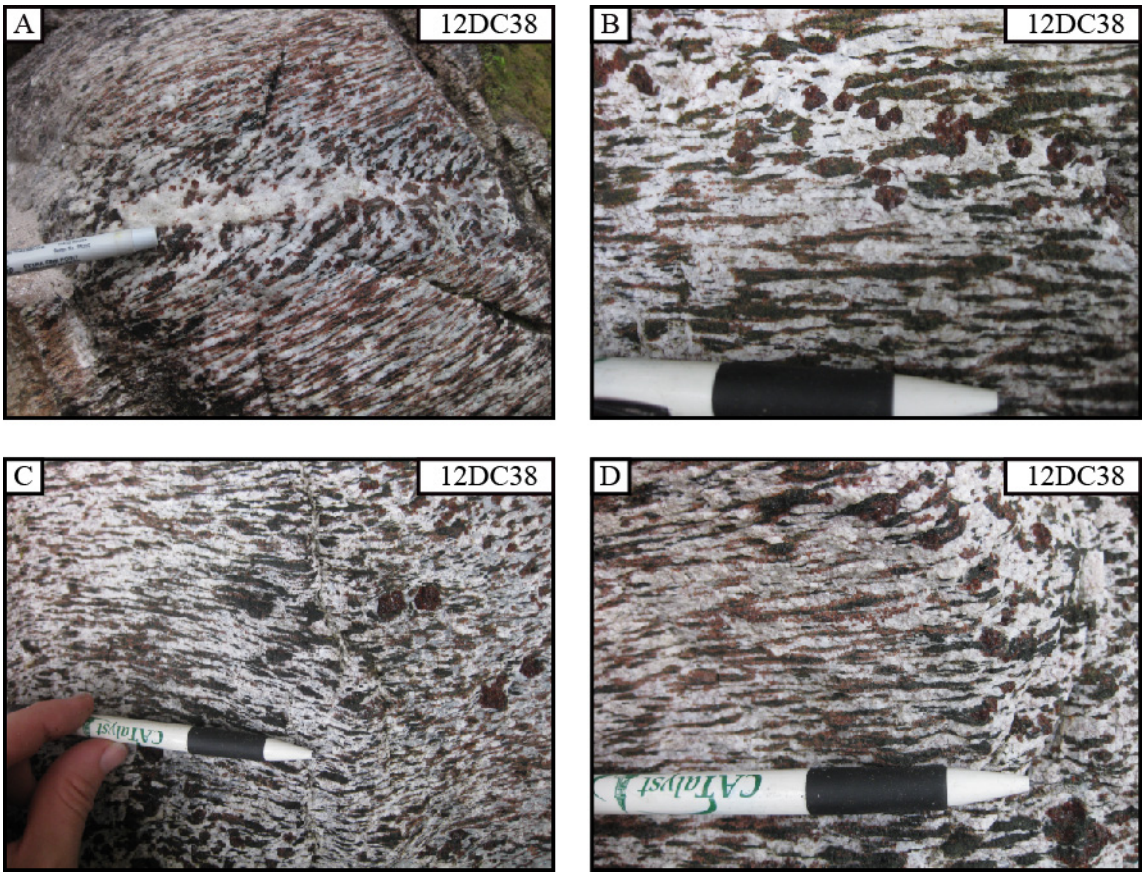

Figure 29. All photos are from site 12DC38 where garnet granulites with a S_2 and L_2 fabric are exposed. A) This image shows a relict domain of the $L_1 \geq S_1$ garnet granulite fabric with a leucosome vein that is transposed into a shearzone of the $L_2 > S_2$ garnet granulite rocks. B) A view of elongate pyroxene and plagioclase form an $L_2 > S_2$ domain of garnet granulite. Towards the top of the image is a train of peritectic garnets in a thin leucosome vein. C) $L_2 > S_2$ garnet granulites with peritectic garnet. D) $L_2 > S_2$ garnet granulites with pyroxenes rimmed by garnet.

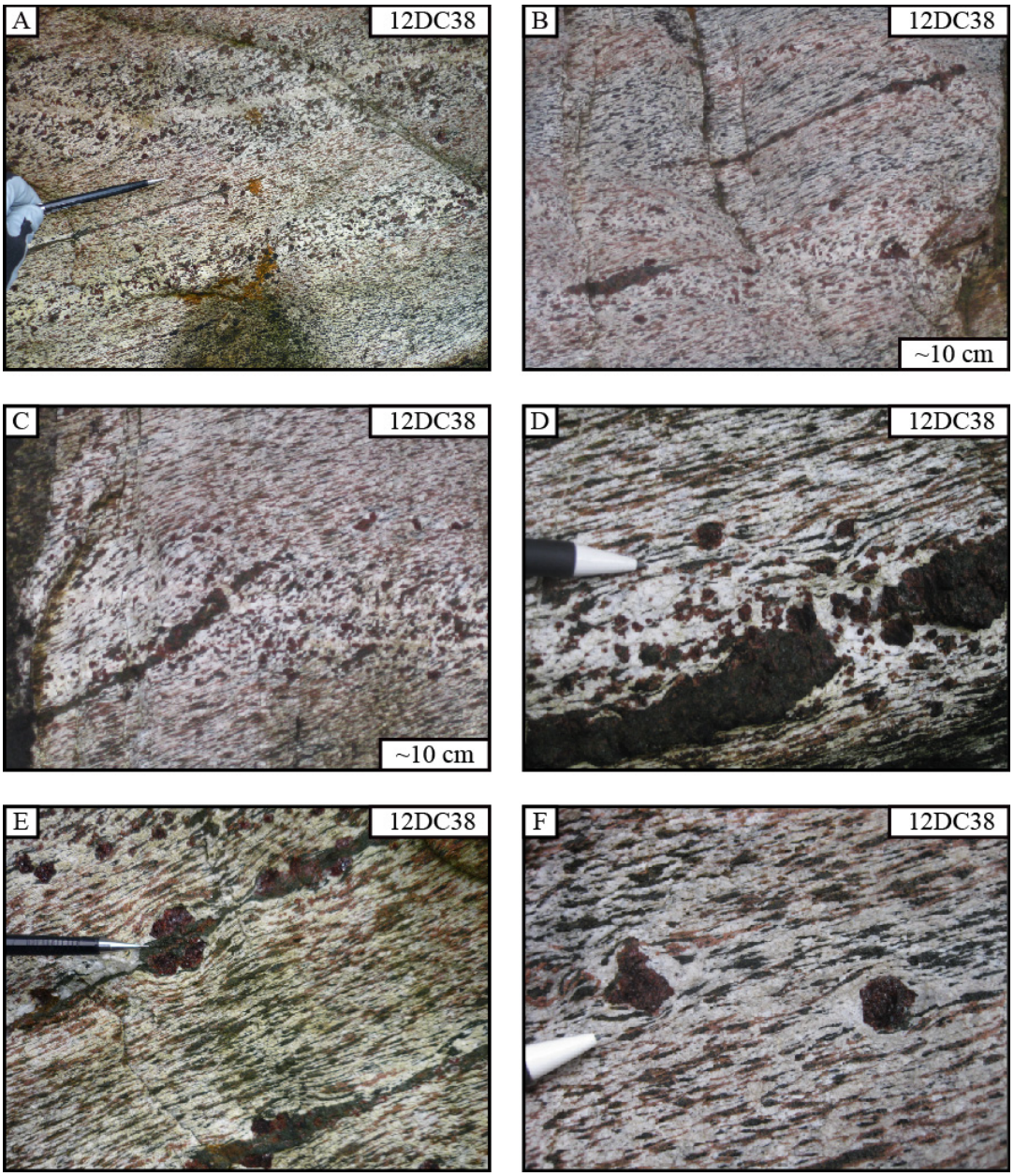

Figure 30. All photos are from site 12DC38 where garnet granulites with $L_2>S_2$ fabrics are exposed. A) An overview showing domains of $L_1 \geq S_1$ garnet granulite with leucosome veins and domains of $L_2>S_2$ garnet granulite. The $L_1 \geq S_1$ domains are identified by the coarser grained pyroxenes and the foliation being transposed into the streaky $L_2>S_2$. B) Mostly $L_2>S_2$ rocks with zones of garnet granulite. C) A relict domain of $L_1 \geq S_1$ garnet granulite in the center of the photo with the foliation being transposed into into the $L_2>S_2$ garnet granulites at the top and bottom. D) A boudinaged mafic dike surrounded by garnet granulite. E) The pencil points to a boudinaged mafic layer overprinted by garnet. F) Peritectic garnet surrounded by leucosome.

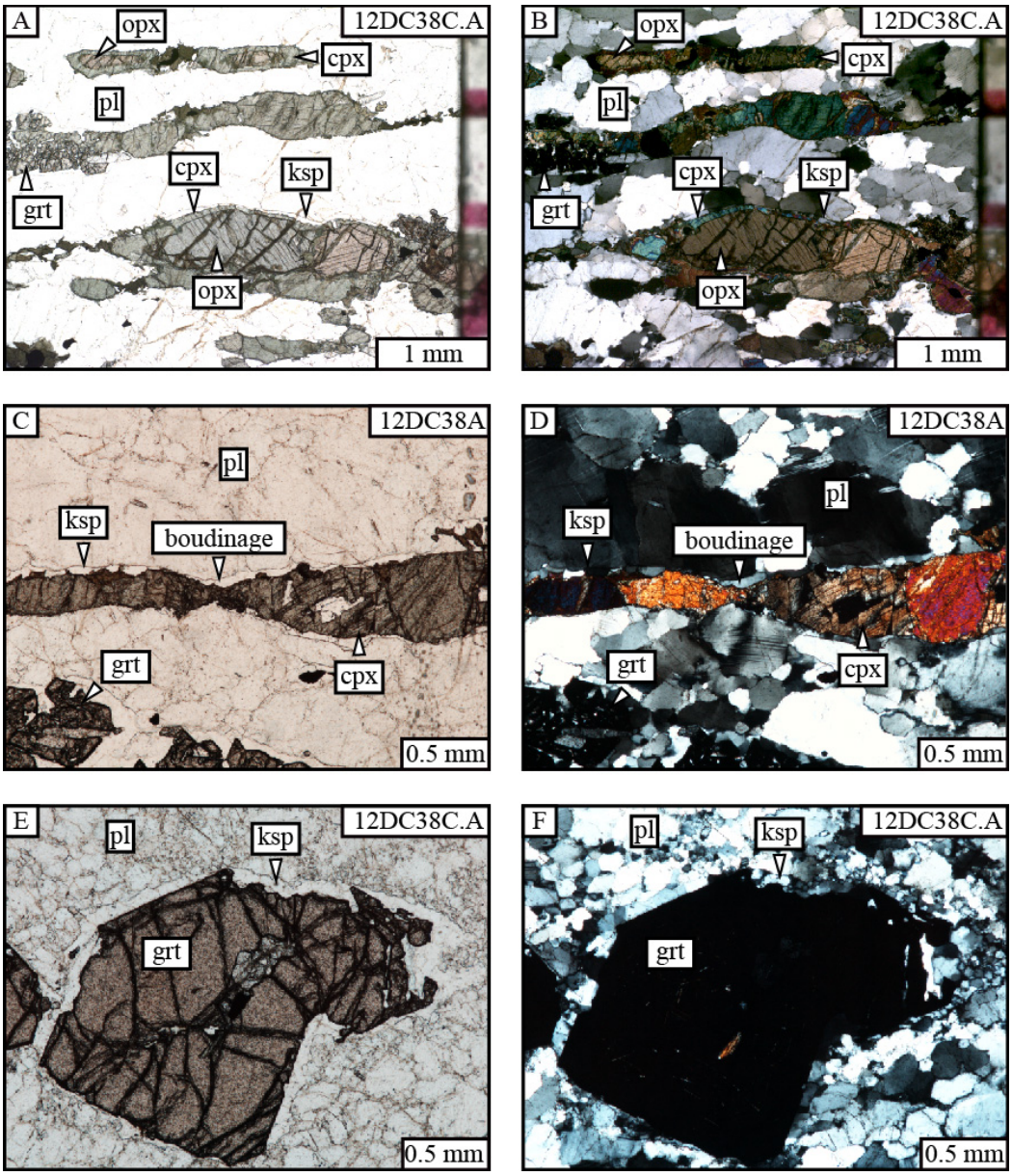

Figure 31. All photomicrographs are from site 12DC38. The sample is denoted in the top right corner. These images show evidence of anatexis and deformation at temperatures greater than 750° C (Schwartz et al., 2016) in garnet granulites that have a $L_2 > S_2$ fabric. A) A plane light photomicrograph showing clinopyroxene moats on orthphyroxene. The large grain of orthopyroxene towards the center of the image has a moat of clinopyroxene that is surrounded by a film/moat of potassium feldspar. B) A cross polarized photomicrograph of "A". C) A plane light photomicrograph of a garnet granulite showing a boudinaged aggregate of pyroxene with a moat of potassium feldspar. D) A cross polarized photomicrograph of "C". E) A plane light photomicrograph of a garnet surrounded by a film of potassium feldspar. F) A cross polarized photomicrograph of "F".

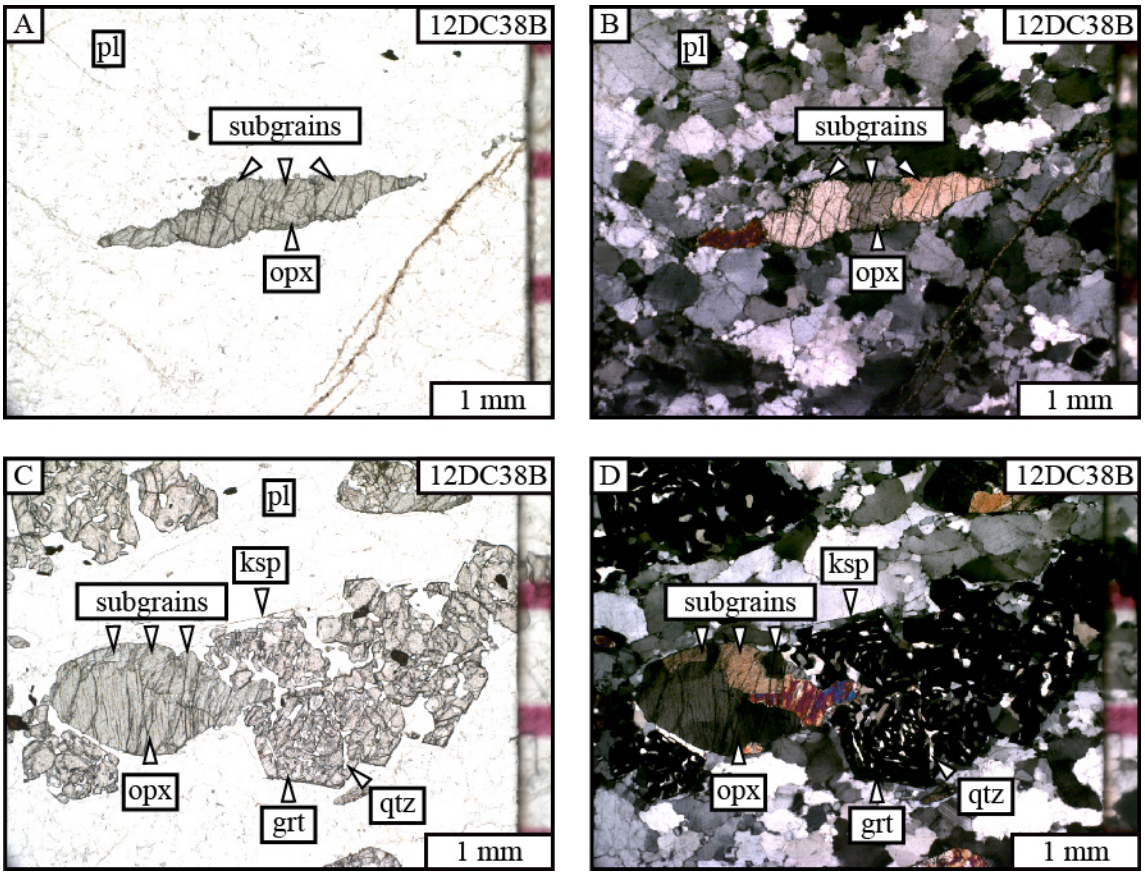

Figure 32. All photomicrographs are from sample 12DC38B which is a garnet granulite with L_2 and S_2 fabrics. These images show evidence of dislocation creep in orthopyroxene. A) A plane light photomicrograph of an asymmetric orthopyroxene aggregate with subgrains that is isolated in the plagioclase matrix. B) A cross polarized photomicrograph of "A". C) A plane light photomicrograph of a orthopyroxene grains with subgrains. Also shown are garnets with interstitial quarts and a film of potassium feldspar. D) A cross polarized photomicrograph of "C".

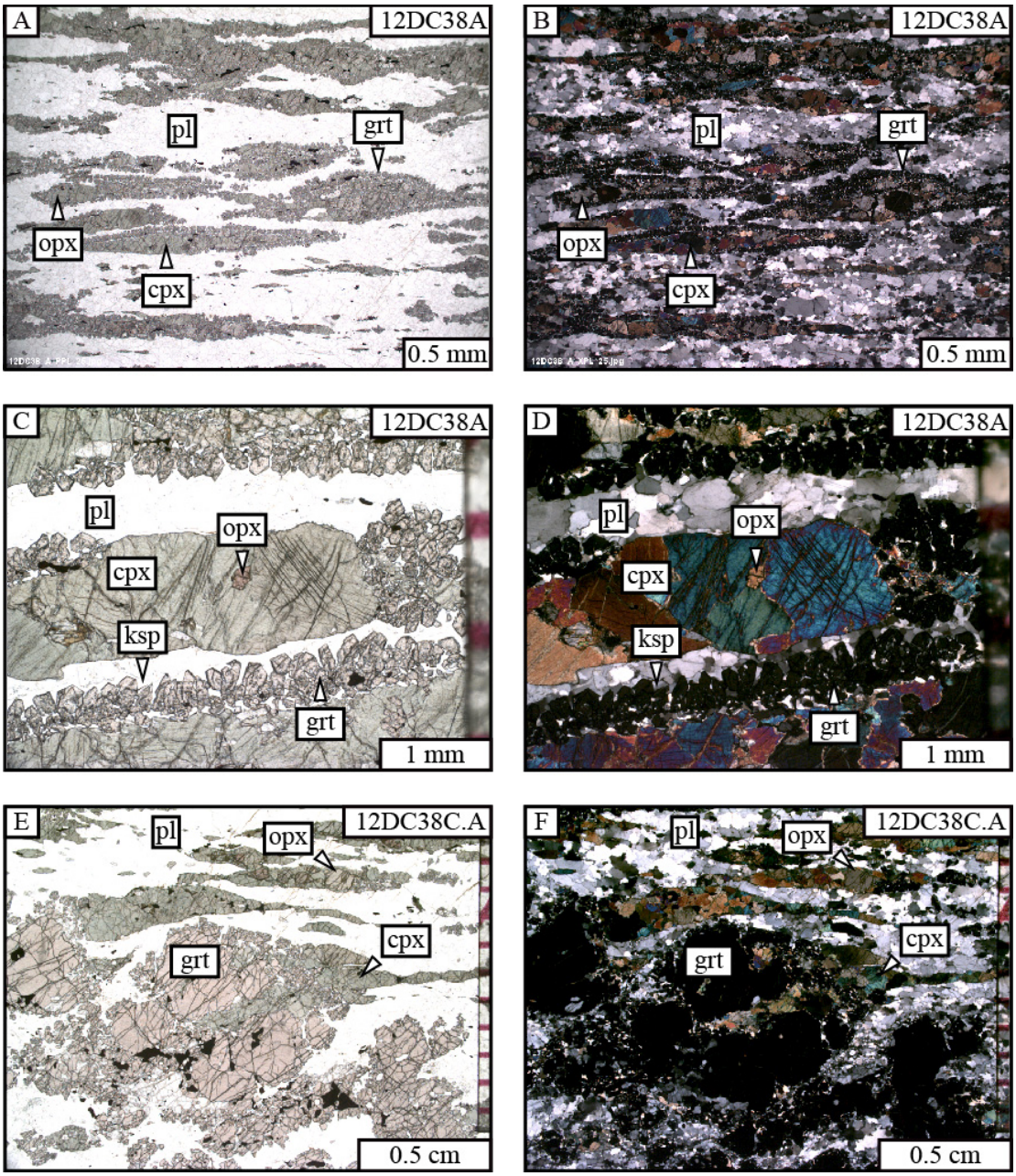

Figure 33. All photomicrographs are from site 12DC38. The samples are garnet granulites with L_2 and S_2 fabrics. The sample name is denoted in the upper right corner. These images show that garnet rims pyroxene grains and also occurs as large aggregates with tails of pyroxene. A) An overview plane light photomicrograph showing garnet rimming elongate pyroxene grains. B) A cross polarized photomicrograph of "B". C) A plane light photomicrograph showing rims of garnet on pyroxene. D) A cross polarized photomicrograph of "C". E) A plane light photomicrograph of a garnet aggregate with a tail of clinopyroxene. F) A cross polarized photomicrograph of "E".

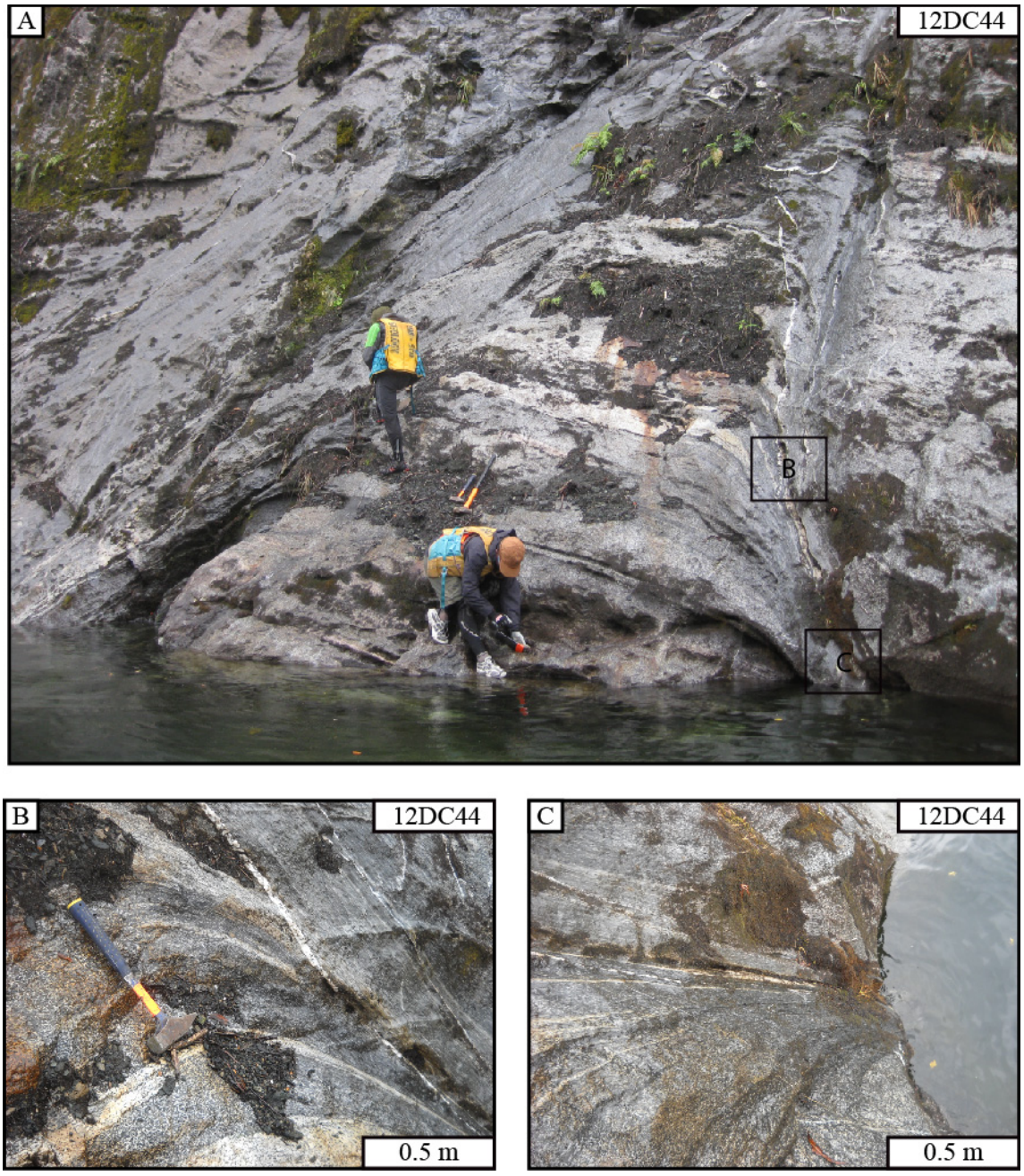

Figure 34. All images are from site 12DC44 and show an amphibolite shear zone (D_3) croscutting granulite fabrics (D_2). A) An overview of the site. The two persons are standing on the retrogressed granulite pod and the two boxes show the locations of images "B" and "C". B) This image shows the amphibolite shear zone in the top right quadrant transposing retrogressed granulites in the rest of the image. Note the transposition of the retrogressed granulite S_2 foliation into the shear zone just right of the hammer. C) An alternative view showing the shear zone in the center of the image and the transposition of the older fabric in the bottom of the image.

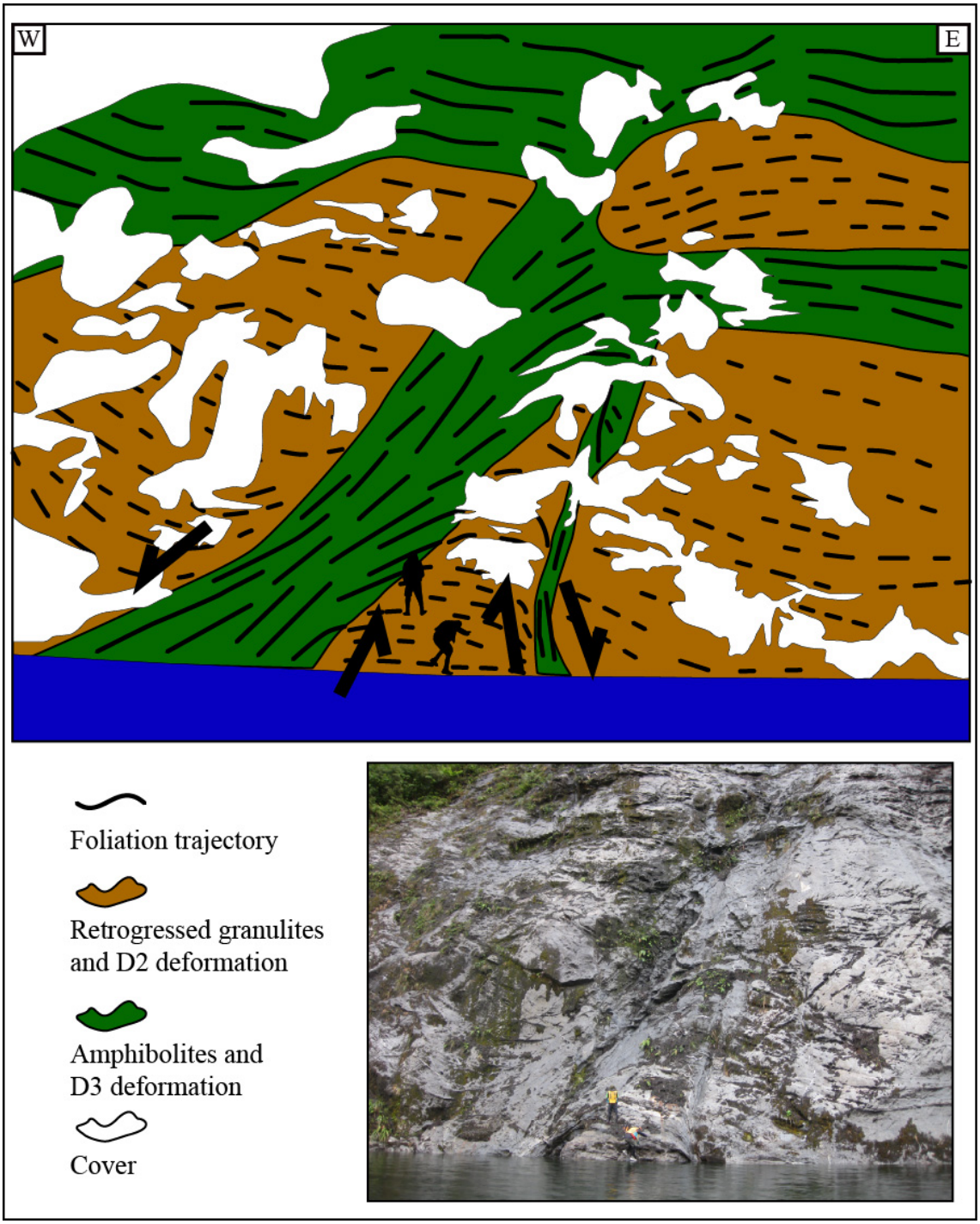

Figure 35. A outcrop sketch and photo of site 12DC44. This sketch shows domains of retrogressed granulites in orange (S_2/L_2) and amphibolite shear zones in green (S_3/L_3). The top of the exposure is a thick zone of foliated (S_3) amphibolites. Note the transposition of the retrogressed granulite fabrics into the shear zone and the two opposing senses of shear.

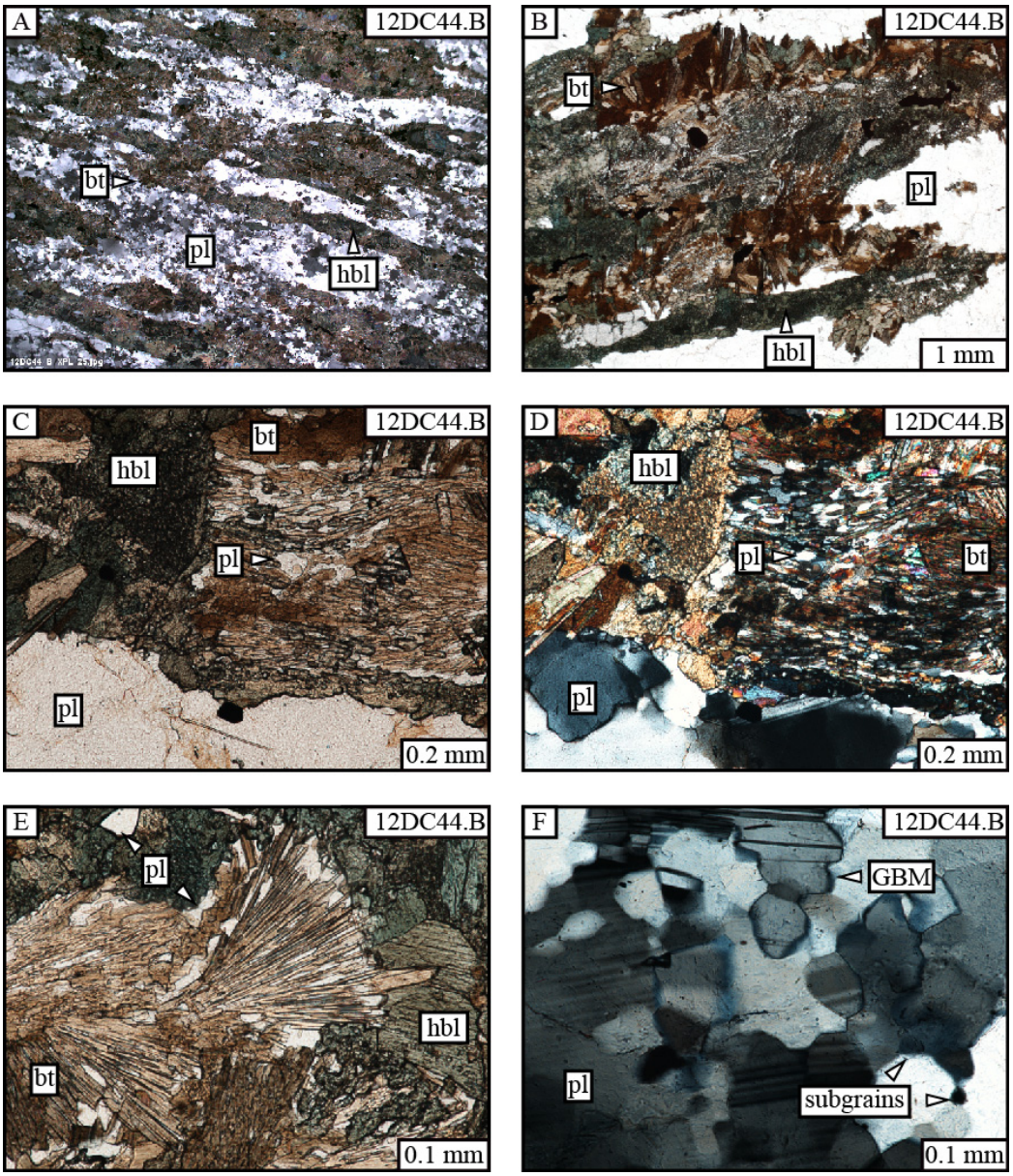

Figure 36. All photomicrograhs are from a pod of retrogressed granulite with a L_2>S_2 fabric at site 12DC44. These images show microstructures associated with D_2 deformation and the retrogression of granulites. Images A, B, C and E are plane polarized light and images D and E are cross polarized light. A) A overview photomicrograph showing elongate mafic aggregates and the plagioclase matrix. The field of view is 12 mm. B) This image shows radial clots of biotite growing along the margins of a mafic aggregate. C) This image shows the heterogeneous replacemnent of pyroxene by hornblende, plagioclase, and biotite. D) A cross polarized photomicrograph of "C". E) A fan of radial biotite. F) This image is from the plagioclase matrix and shows grain boundary migration and the formation of subgrains.

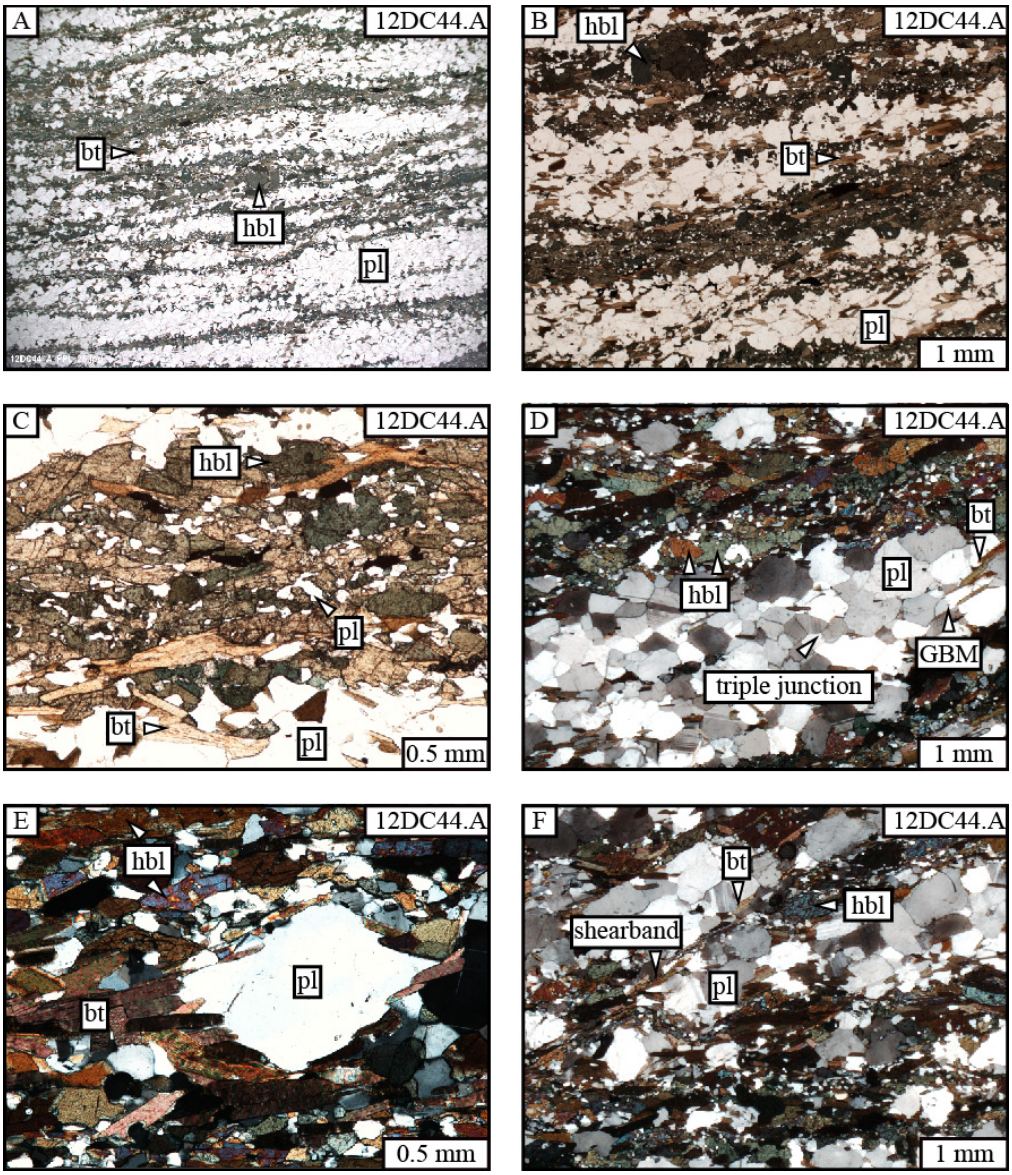

Figure 37. All images are photomicrographs taken from a amphibolite shear zone with L_3=S_3 fabrics that cross cuts retrogressed granulite rocks with L_2>S_2 fabrics. Images A, B, and C are plane light and images D, E and F are cross polarized light. These photomicrographs show the microstructures associated with D_3 deformation. A) An overview image that shows the gneissic layering. B) A cross polarized image of "A". C) This image is of a mafic foliation layer and shows subedral hornblende and biotite grains with the inclusions of fine grained plagioclase. D) A image of a plagioclase foliation layer that shows evidence of grain boudary migration and recovery via the formation of tripple junctions. E) An asymmetric porphyroblastic plagioclase grain with biotite beards. F) This image shows the biotite shear bands cross cutting plagioclase aggregates. The foliation is from left to right and the shear bands are from bottom left to upper right, giving a top-down to the northeast sense of shear.

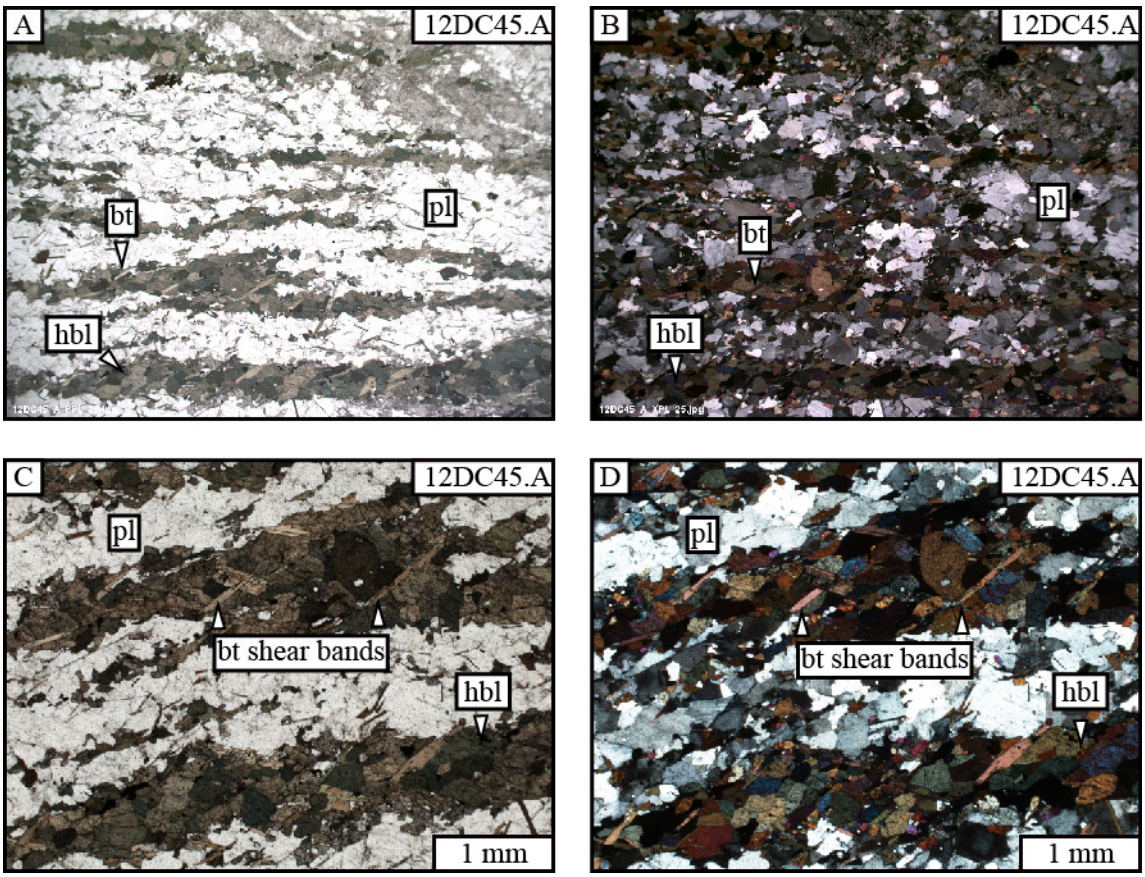

Figure 38. All photomicrographs are from sample 12DC45.A, a retrogressed granulite with a D_2 fabric that shows the early stages of S_3 overprinting S_2. The field of view for A and B is 12 mm. A) An overview plane light photomicrograph showing gneissic layering of hbl + bt layers and plagioclase layers. B) A cross polarized photomicrograph of "A". C) A plane light photomicrograph showing biotite shear bands cross cutting the hornblende aggregates. Foliation is from left to right and shear bands are from bottom left to upper right. D) A cross polarized photomicrograph of "C".

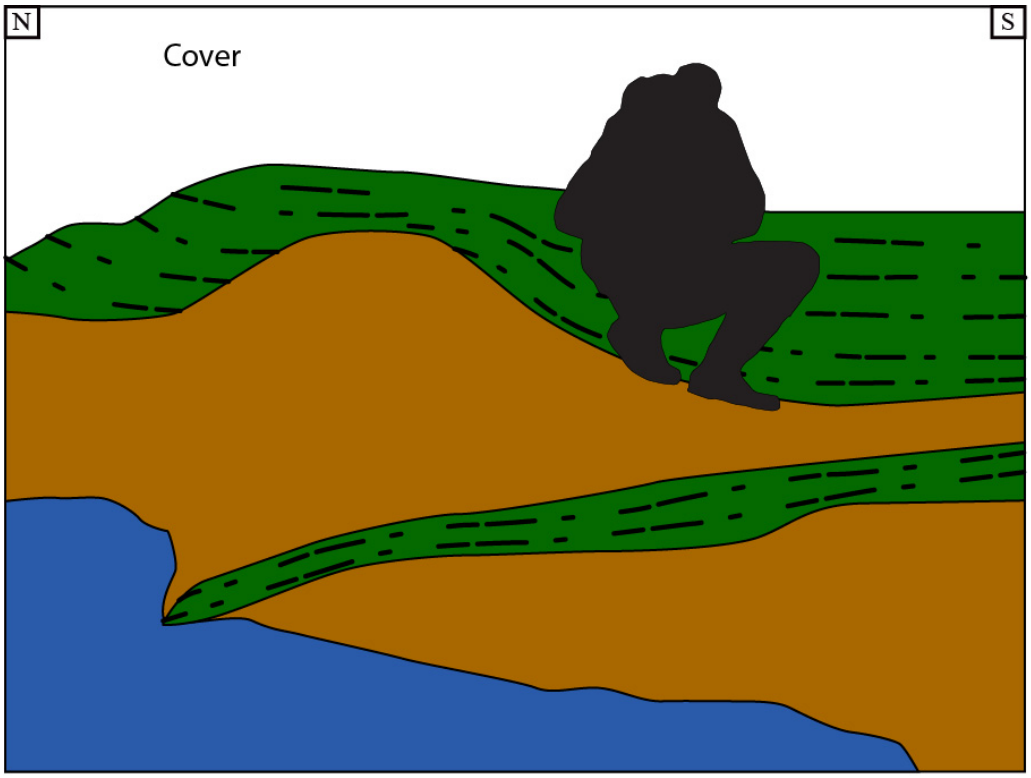

Figure 39. This is a outcrop sketch and photo of site 13DC63. The sketch shows amphibolite rocks penetrating retrogressed granulite which creates a lozenge of retrogressed granulite.

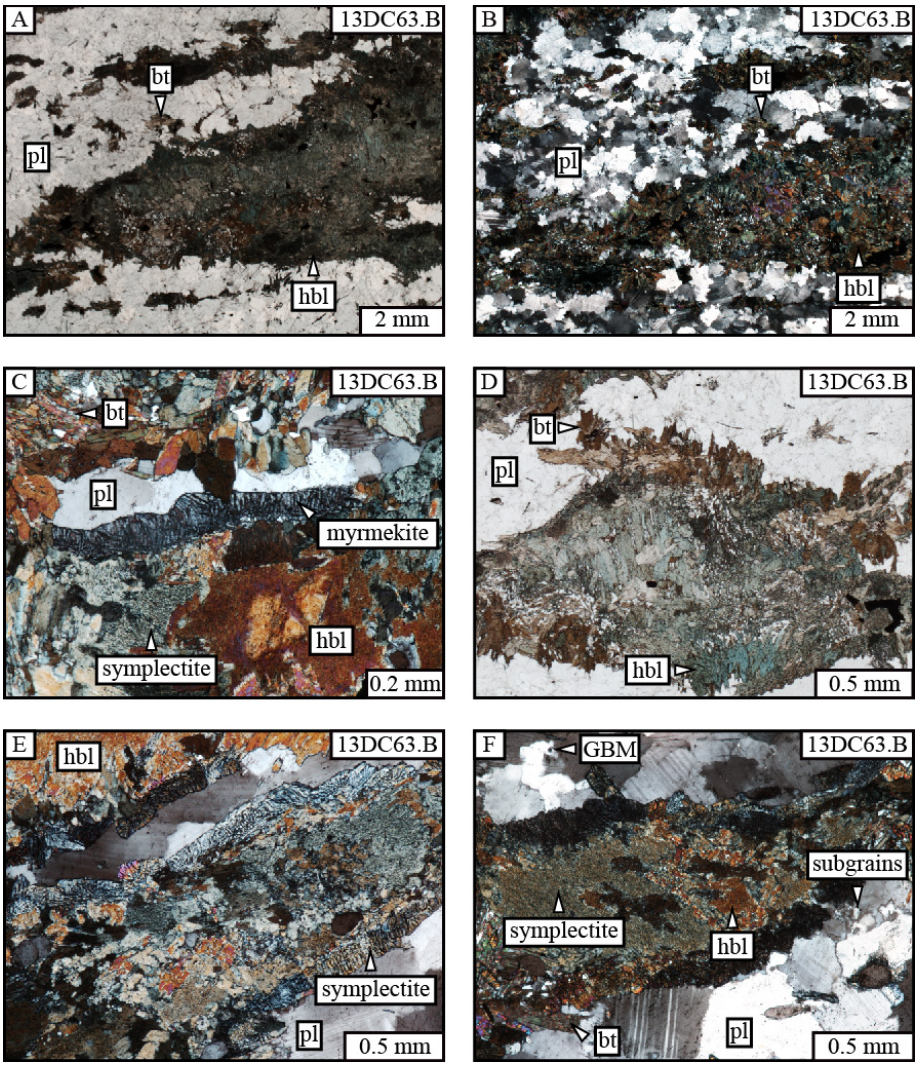

Figure 40. All images are from sample 13DC63.B, a retrogressed granulite from the center of a lozenge of D_2 deformation that is cross cut by a amphibolite shear zones (D_3). These images show the microstructures of plagioclase deformation during D_2 and the early stages of granulite retrogression. A) An overview plane light photomicrograph of a mafic aggregate. This image shows a mostly green core and brown rim of biotite on a aggregate of retrogressed pyroxene. B) A cross polarized phtomicrograph of "A" showing ameboid grain boudaries in the plagioclase matrix and heterogeneous phase mixture of the mafic aggregate. C) A cross polarized photomicrograph of a mafic aggregate that shows subhedral hornblende and symplectite in the core, with a rim of myrmekite. D) A plane light photomicrograph of a mafic aggregate show radial biotite on the rim of the aggregate and fine plagioclase inclusions in the core. E) A cross polarized photomicrograph of retrogressed mafic aggregate that has a heterogeneous core and a rim of symplectite. F) A cross polarized photomicrograph of a retrogressed mafic aggregate that shows a core of hornblende and symplectite, and grain boundary migration and subgrains in the plagioclase matrix.

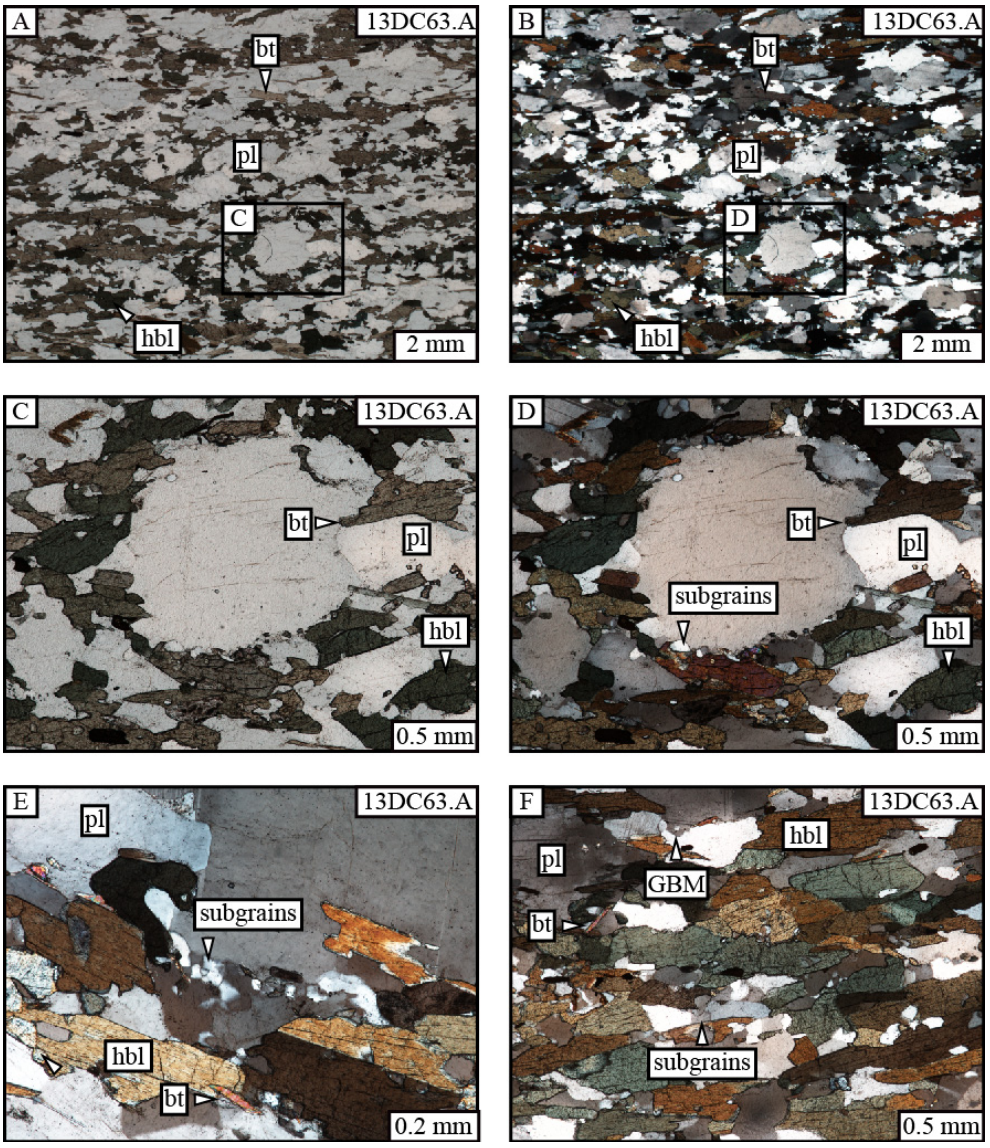

Figure 41. All photomicrographs are from sample 13DC63.A, an amphibolite from a D_3 shear zone that cross cuts retrogressed granulite rocks with D_2 deformation. A) A plane light overview photomicrograph showing the disjunctive and anastomosing S3 foliation from left to right. The box indicates the location of image "C". B) A cross polarized photomicrograph of "A". The box indicates the location of image "D". C) A plane light photomicrograph showing a rounded porphyroblastic plagioclase grain with a hornblende beard. D) A cross polarized photomicrograph of "C" that shows plagioclase subgrain mantles on the porphyroblast. E) A cross polarized photomicrograph that show subgrains in plagioclase and a simple twinned euhedral hornblende in the lower right. F) A cross polarized photomicrograph from a foliation domain. This image shows the shape preferred orientation of hornblende, plagioclase subgrains, and grain boundary migration in plagioclase.

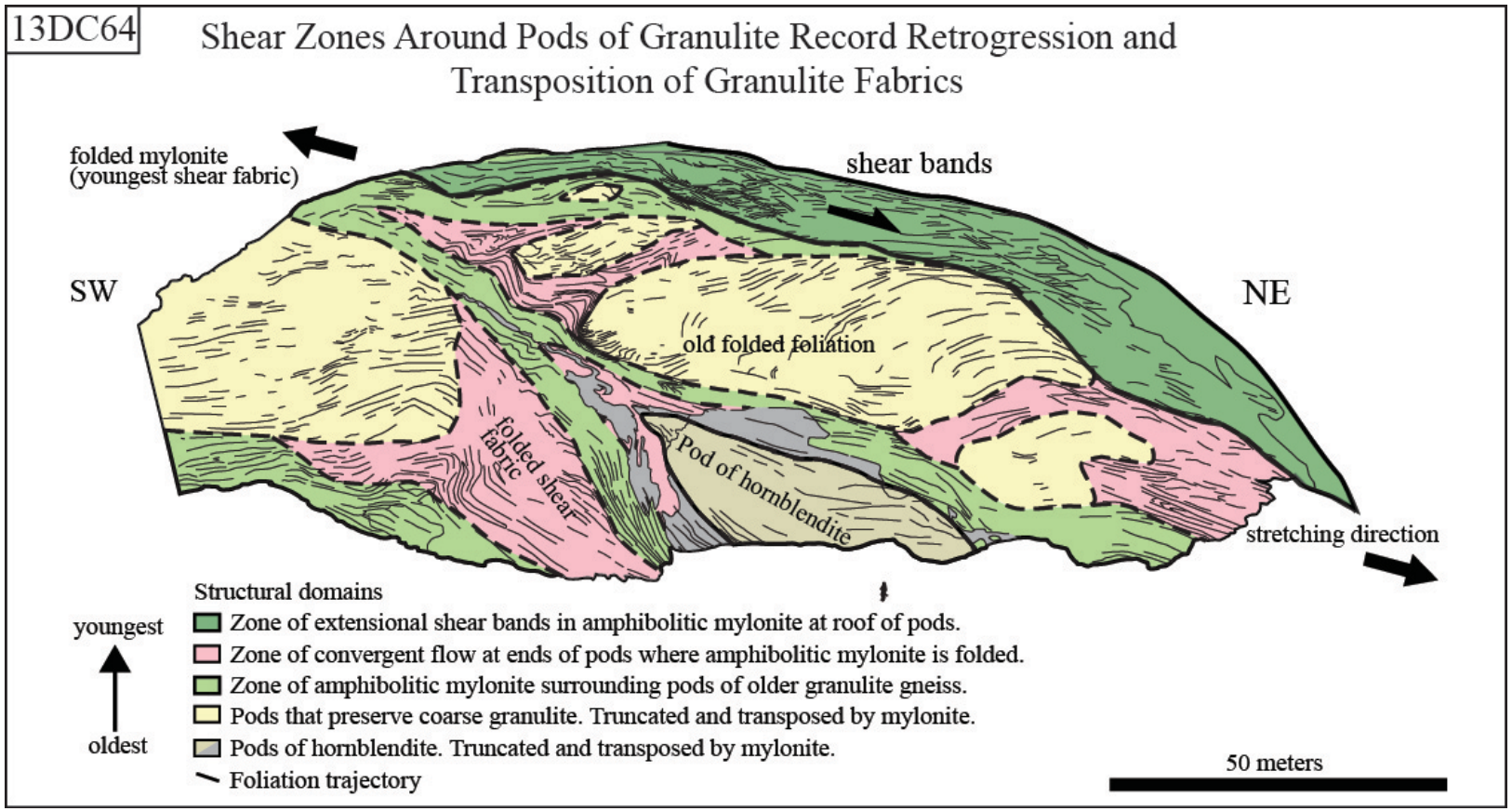

Figure 42. Diagram of a vertical face showing an outcrop sketch of site 13DC64 that exposes pods of hornblendite and coarse granulite that are cross cut by amphibolite shear zones. Domains in yellow preserve D_2 deformation and domains in green preserve D_3 deformation. The hornblendite pod in the bottom center of the image has dismembered pieces that have been included into the shear zones. In the shadows of the granulite pods the shear zone fabric is folded. Capping the outcrop is a horizon of extensional shear bands (S_3). Asymmetry of the pods and orientation of the shear bands give a top-down–to-the-northeast sense of shear.

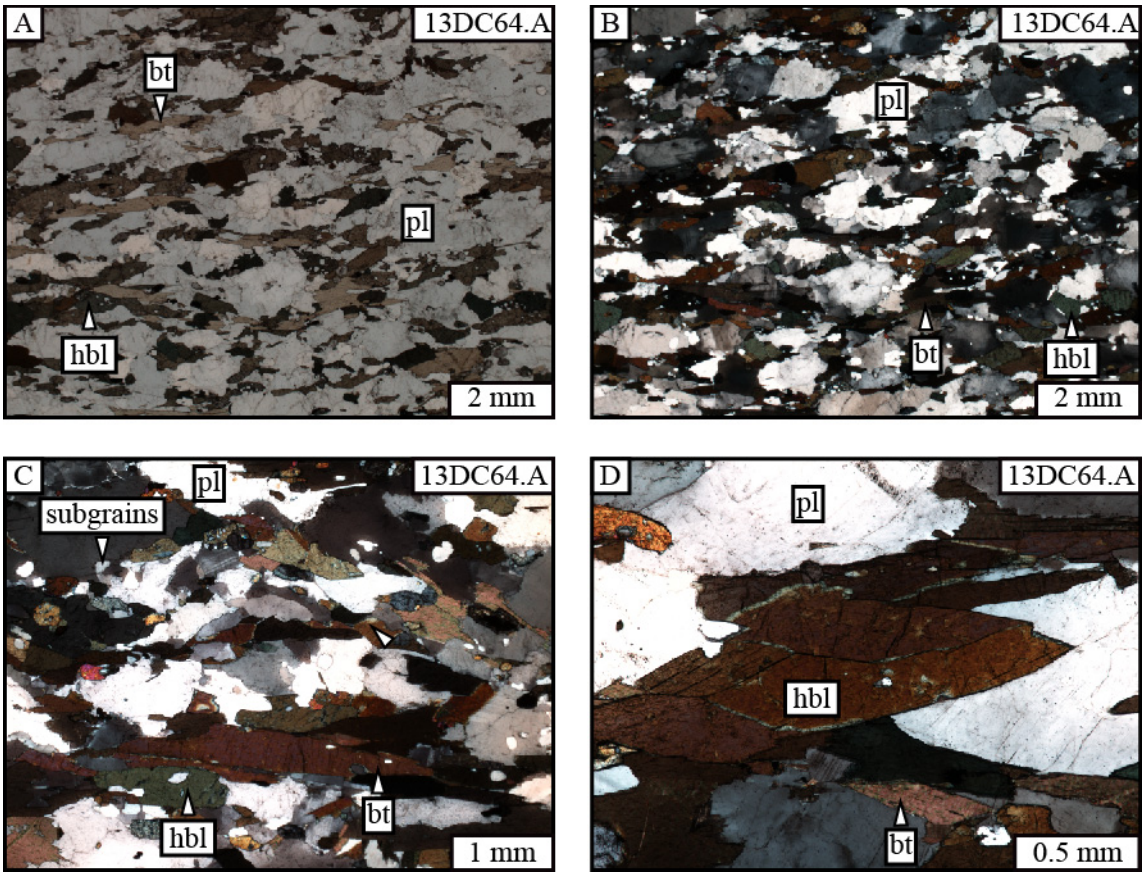

Figure 43. All photomicrographs are from sample 13DC64.A, a amphibolite rock from a D_3 shear zone that cross cuts retrogressed granulite rocks with D_2 deformation. These images show the microstructures associated with D_3 shearing. A) A plane light overview photomicrograph that shows the discontinuous and anastamosing foliation from left to right. B) A cross polarized photomicrograph of "A". C) A cross polarized photomicrograph that shows an isolated aggregate of plagioclase in the center of the image. The plagioclase aggregate is bound by hornblende and biotite and shows grain boundary migration. The development of subgrains is seen in the top left corner of the image. D) A cross polarized photomicrograph showing euhedral hornblende and laths of biotite.

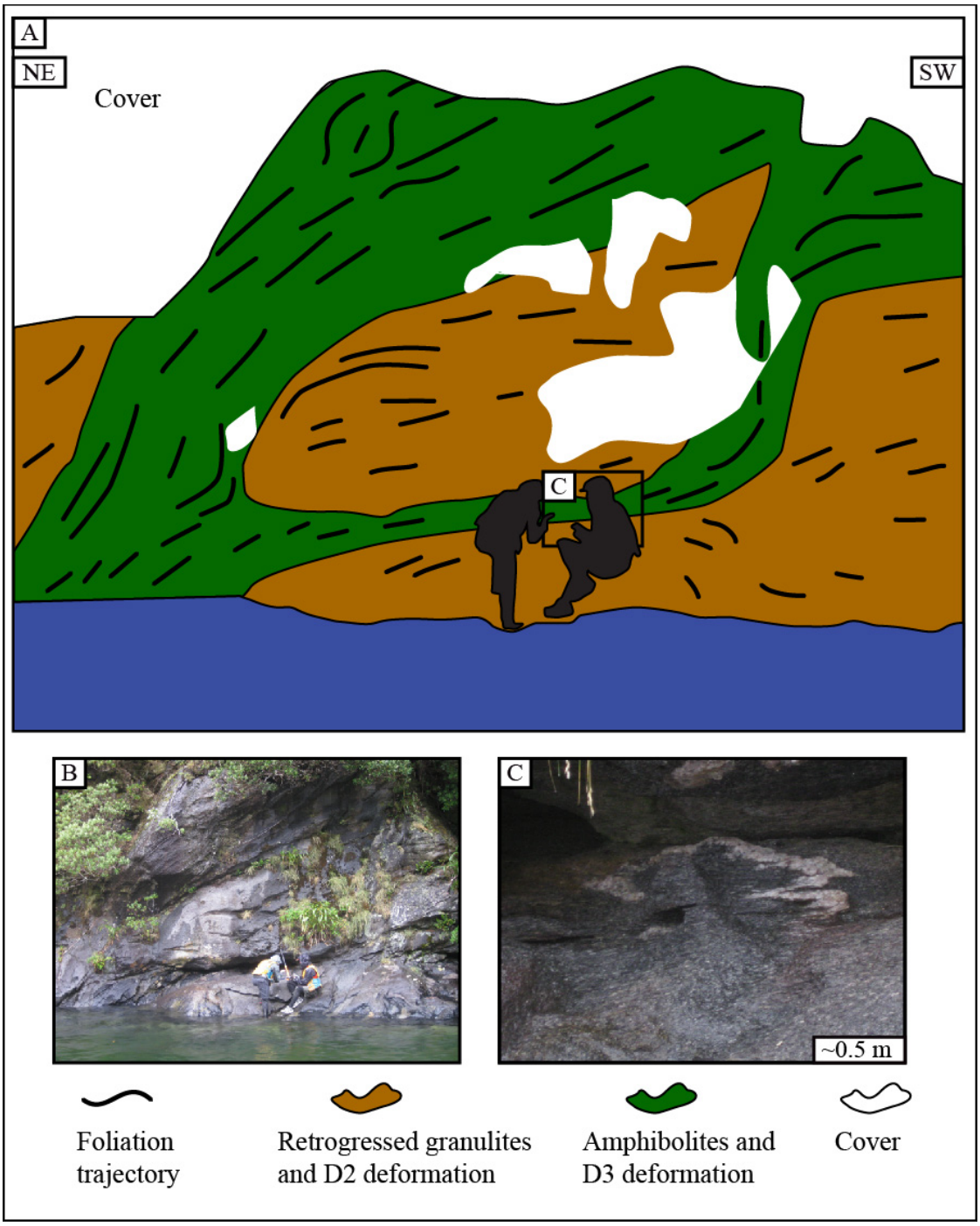

Figure 44. A) An outcrop sketch of site 12DC46. This outcrop exposes a lozenge of retrogressed granulites with D_2 deformation that is crosscut by D_3 shear zones of amphibolite rocks. Transposition of the older S_2 foliation gives a top-down-to-the-northeast sense of shear. The box in the lower left indicates where photo "C" was taken. B) An overview photo of the site. C) A photo of the D_3 amphibolite shear zone that shows a folded pegmatite dike and porphyroblastic plagioclase.

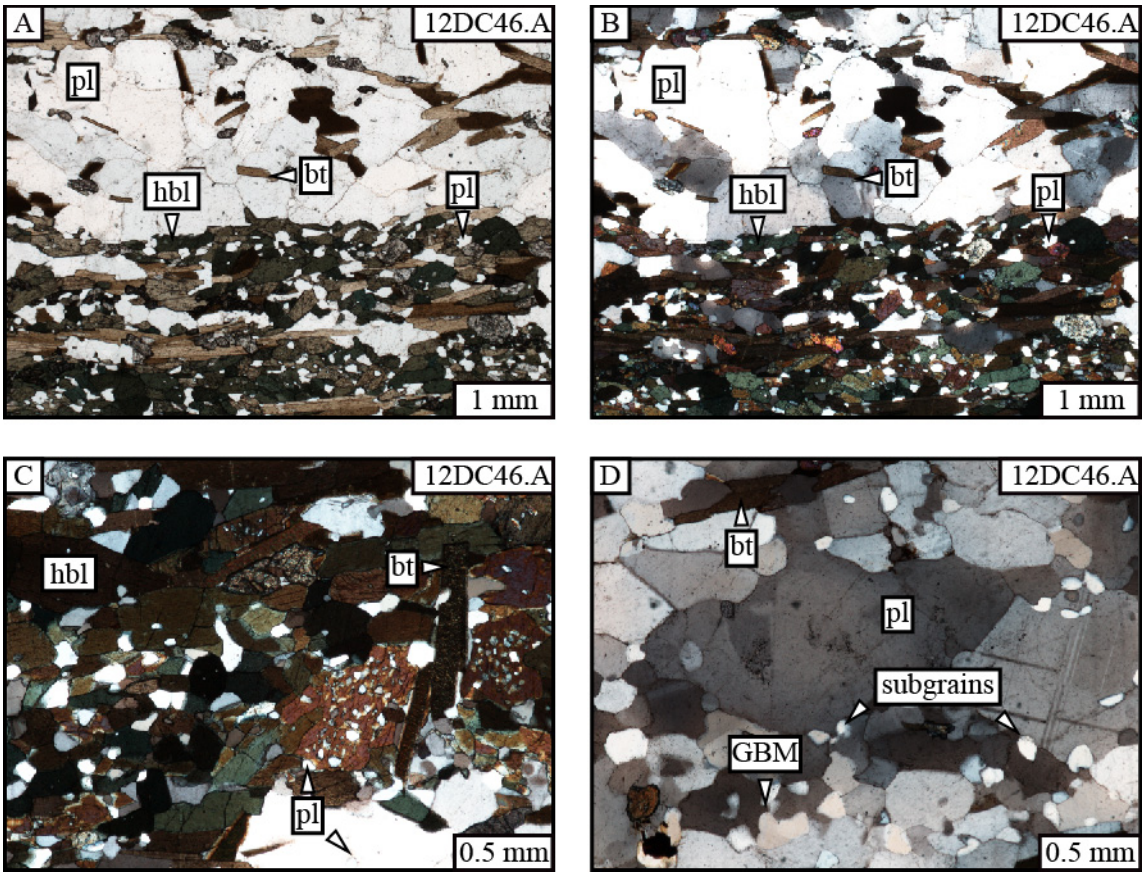

Figure 45. All photomicrographs are from a retrogressed granulite at site 12DC46 that preserves D_2 deformation. The sample was taken on the margin of a D_3 amphibolite shear zone. The lack of symplectites, lack of radial biotite, and the presence of lathe shaped biotite indicates a progression in the retrogression and transition from D_2 to D_3 fabrics. A) An overview plane light photomicrograph that shows heterogeneous foliation (from left to right) of hornblende, biotite, and fine grained plagioclase. Also shown are finer grained hornblende and biotite that are penetrating plagioclase domains. B) A cross polarized photomicrograph of "A". C) A cross polarized photomicrograph of a S_2 foliation layer that shows fine grained plagioclase inclusions in the foliation and hornblende grains. D) A cross polarized photomicrograph from a plagioclase domain that shows grain boundary migration and the development of subgrains.

3.5 Hall Arm

The structure of Hall Arm can be divided into three domains. Each of the domains exposes distinct fabrics that represent three stages of deformation. Outcrops of mostly metadiorite rock with S_1/L_1 are found in Domain 1, which is located on the on the northwest shore of Hall Arm and continues north along Doubtful Sound. Pods of similar metadiorite crop out towards the end and entrance of Hall Arm but are part of Domains 2 and 3. Domain 2 consists of granulite and weakly retrogressed granulite rock with S_2/L_2 fabrics, which are found at the end of Hall Arm on both the west and east shores. S_3/L_3 fabrics associated with the DSSZ are found in Domain 3, which is located along the eastern short and from the center of Hall Arm to the entrance. A site location map, structural map, and cross sections can be seen in Figure 46, Figure 47, and Figure 48, respectively.

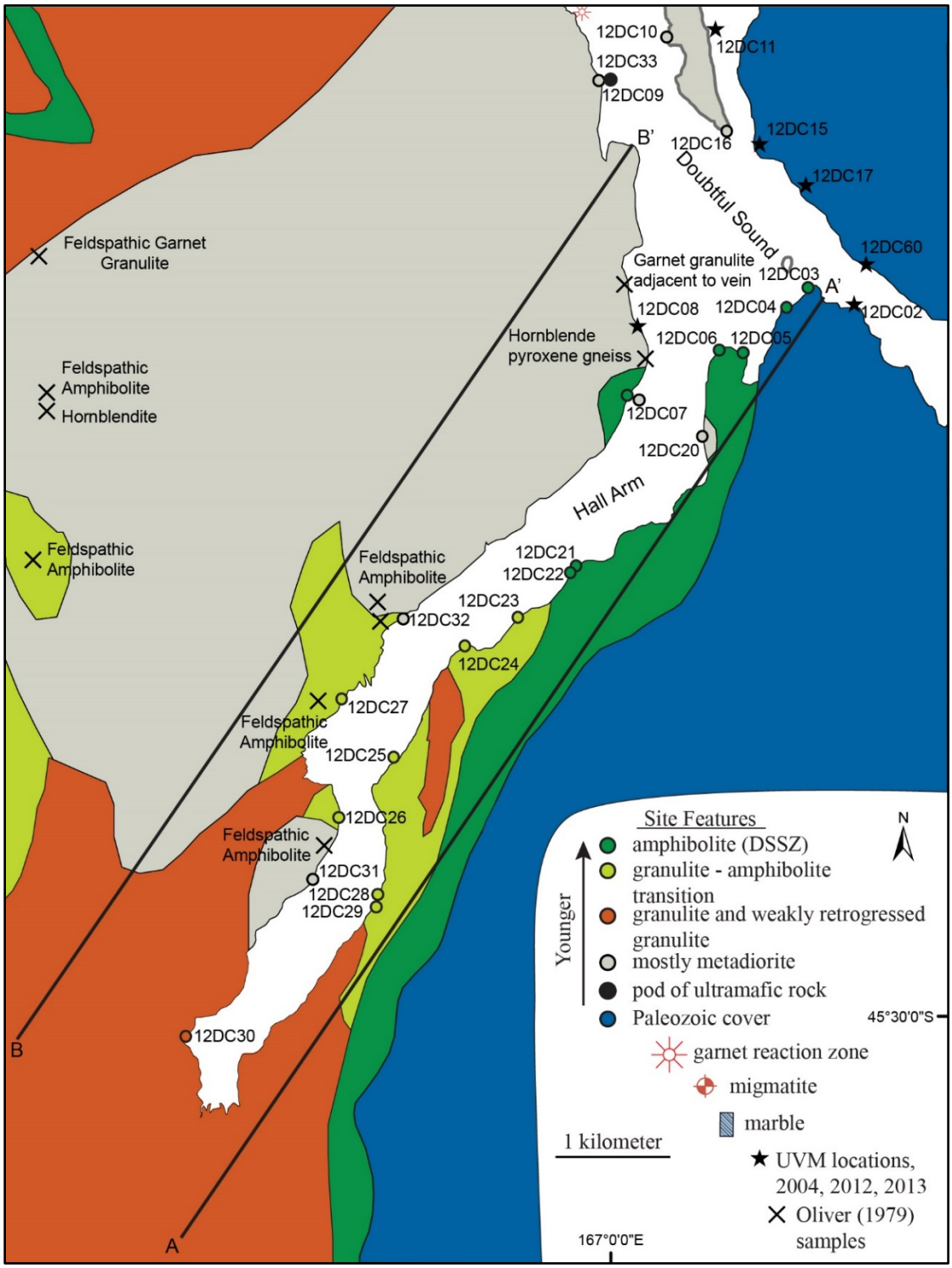

Figure 46. Geologic map of Hall Arm showing metadiorite rock along the northern shore, granulite rock at the end of Hall Arm and mostly granulite-amphibolite transitional and amphibolite rocks along the southern shore.

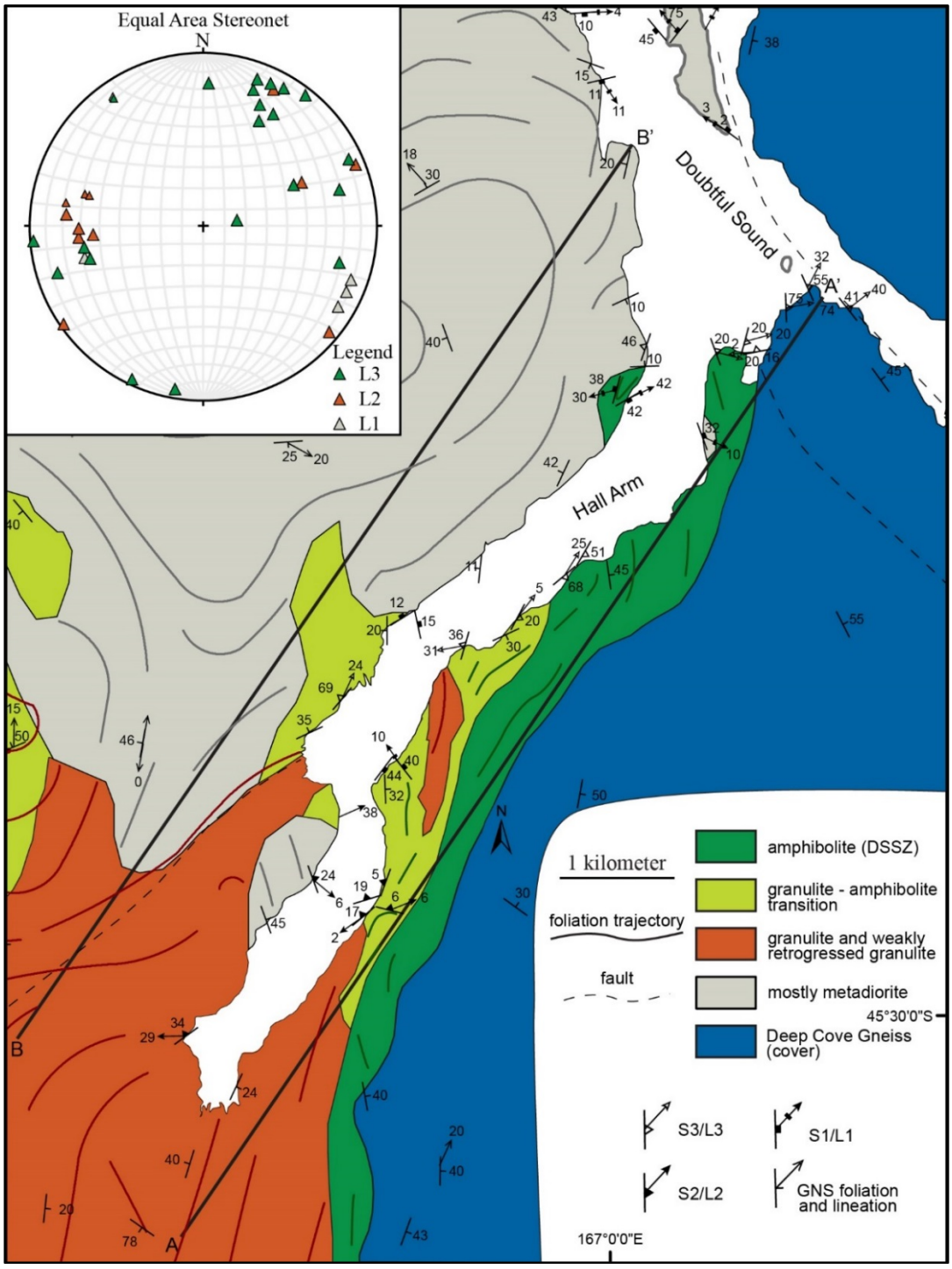

Figure 47. A structural map and equal area lower hemisphere stereographic projection showing SE trending lineations in the metadiorites (L_1), E-W trending lineations in the granulite (L_2), and NE-SW trending lineations in the amphibolite (L_3). Foliation trajectories show the metadiorite dome.

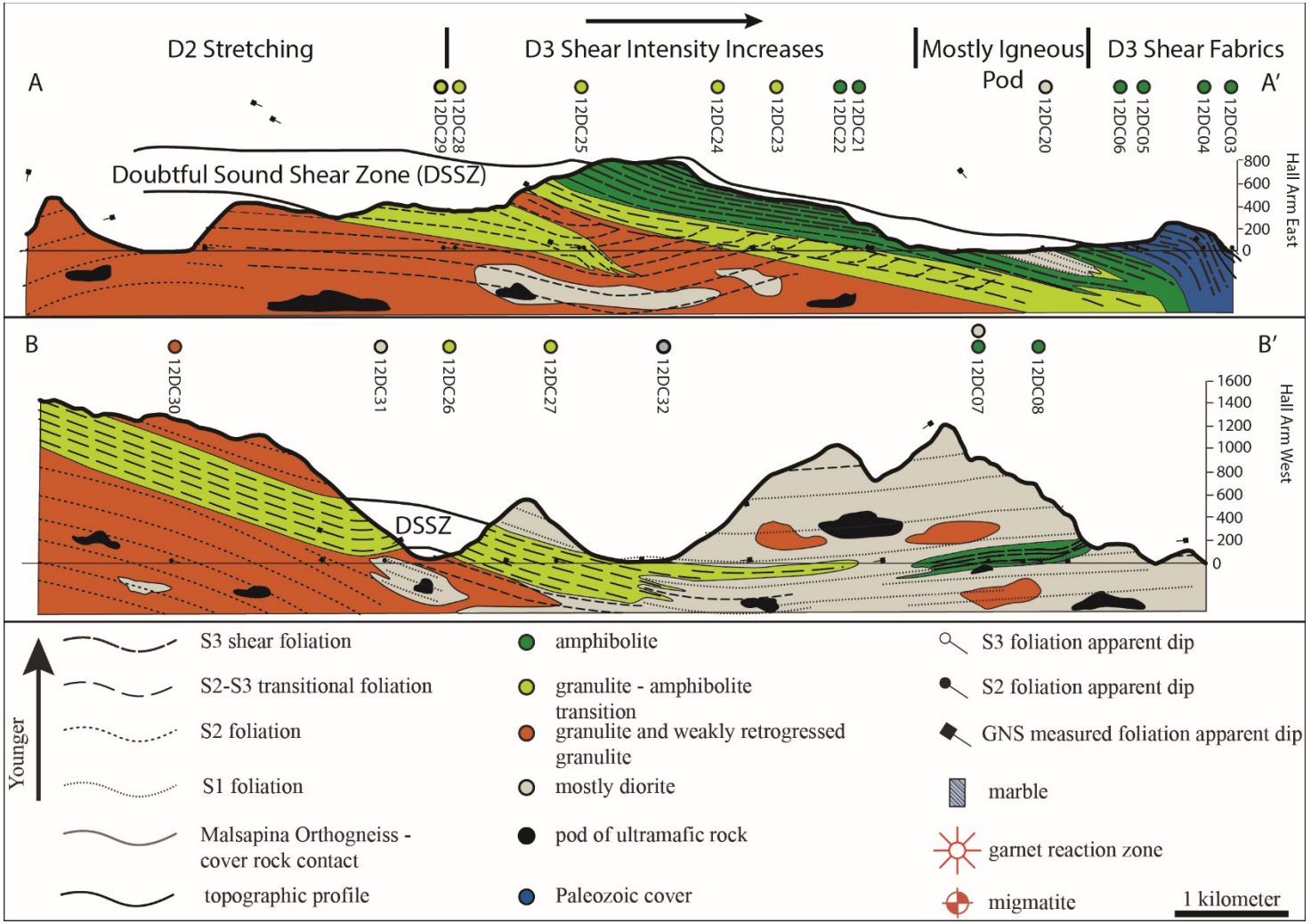

Figure 48. Cross sections of Hall Arm from Figure 46 showing a thick zone of the DSSZ along the east coast that has shear bands. Along the west coast are exposures of metadiorite with patchy granulite metamorphism and penetrative splays of amphibolite.

Domain 1 (Hall Arm)

Rocks within Domain 1 are mostly coarse grained metadiorites and granulites with local centimeter scale peritectic garnets. Hornblendite pods and intrusions are commonly observed. A weakly developed S_1 foliation defined by the alignment of hornblende and plagioclase is gently dipping and overprinted by ~100m scale folds that gently plunge to the northeast. Aligned hornblende and plagioclase mineral lineations plunge to the southeast and northwest.

Domain 2 (Hall Arm)

Domain 2 is characterized by strongly lineated to rodded, variably foliated retrogressed granulites and amphibolites with an $L_2 \geq S_2$ fabric. Plagioclase stretching lineations moderately plunge west at the southwest end of this domain. Here, aligned and elongate aggregates of hbl + pl ± cpx ± opx ± bt define a weak S_2 foliation. At site 12DC30 plagioclase mostly occurs as a monomineralic matrix which hosts aggregates of mafic minerals. The mafic aggregates have thick cores and tapered ends. Inside the mafic aggregates is a heterogeneous mixture of relict clinopyroxene, fractured orthopyroxene, a fine grain phase mixture of rounded hbl + pl, and radial masses of biotite (Figure 49).

In the center of Domain 2 at site 12DC29 plagioclase stretching lineations (L_2) gently plunge to the ENE-WSW. Mostly connected, anastomosing layers of subhedral hbl + bt + fine grained pl phase mixtures, ± euhedral epidote, define the S_2 foliation that wraps lenticular aggregates of plagioclase. Splays of biotite from the foliation layers begin to penetrate the plagioclase aggregates. The boundary between the foliation layers

and plagioclase aggregates often consists of fine grained plagioclase. Plagioclase shows deformation by grain boundary migration (Figure 50).

At the northern boundary of Domain 2 (site 12DC26) L_2 plagioclase stretching lineations plunge moderately to the ENE. A mostly continuous gneissic foliation of aligned, euhedral hbl + bt + fine grained plagioclase, bound plagioclase layers and branch around plagioclase aggregates. A fine film of incipient biotite also occurs around the hornblende grains. Blastic plagioclase have recrystallized tails of fine plagioclase, beards of biotite, and are mantled by fine plagioclase (Figure 51).

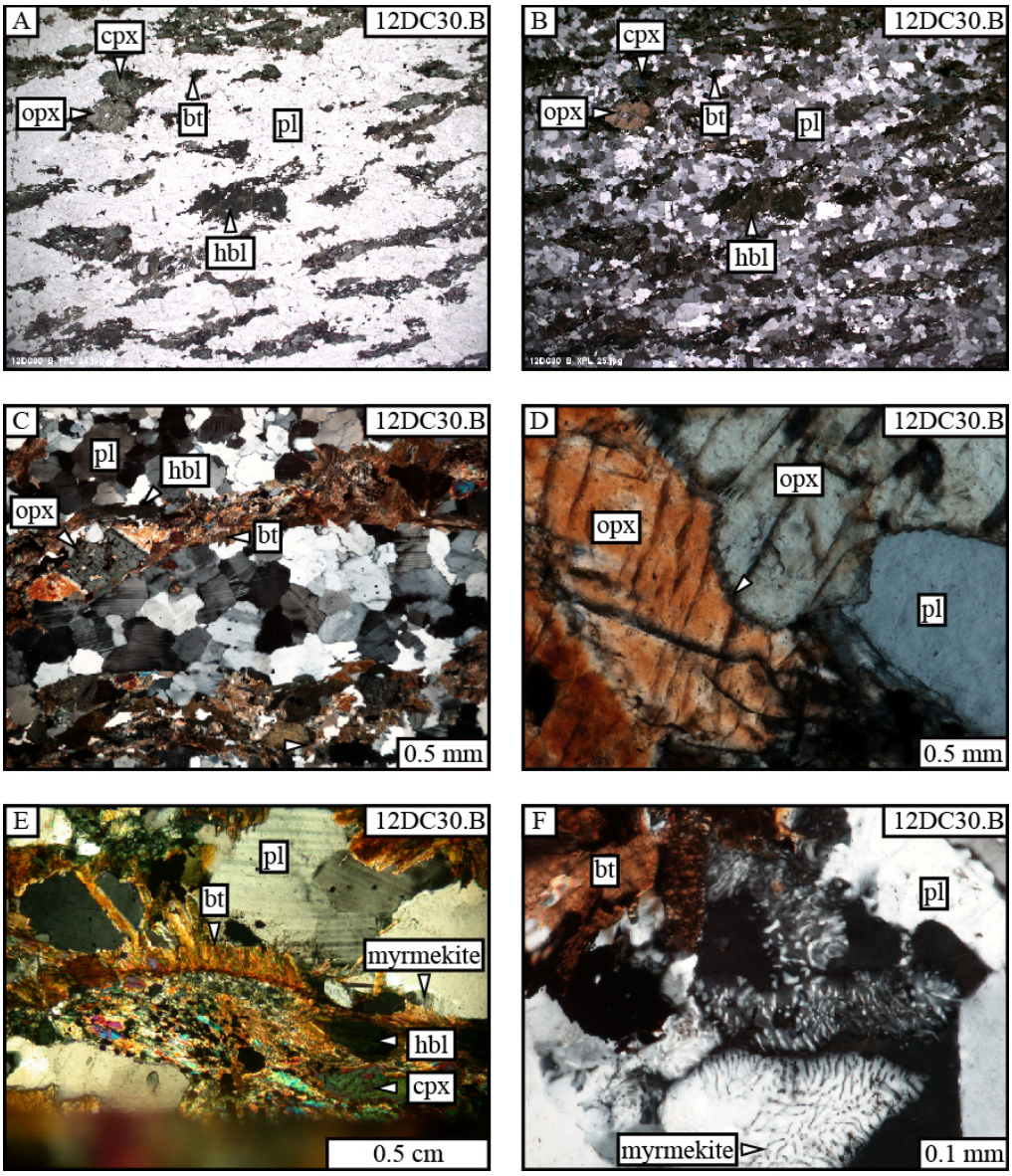

Figure 49. All photomicrographs are from sample 12DC30.B, a retrogressed granulite with a $L_2>S_2$ fabric from Domain 2 in Hall Arm that shows the plagioclase matrix and retrogression of pyroxene. A) An overview, plane polarized photomicrograph that shows a plagioclase matrix and aggregates of mafic minerals. B) A cross polarized photomicrograph of "A". C) A cross polarized photomicrograph that shows an orthopyroxene surrounded by hornblende and biotite. D) A cross polarized photomicrograph of two orthopyroxene grains. The arrow points to the grain boundary. E) A cross polarized photomicrograph of a retrogressed clinopyroxene aggregate. The center of the aggregate has a relict pyroxene surrounded by a heterogeneous mixture of plagioclase, hornblende, and opaque minerals. Rimming the aggregate is radial biotite. F) A cross polarized photomicrograph that shows myrmekite textures in plagioclase.

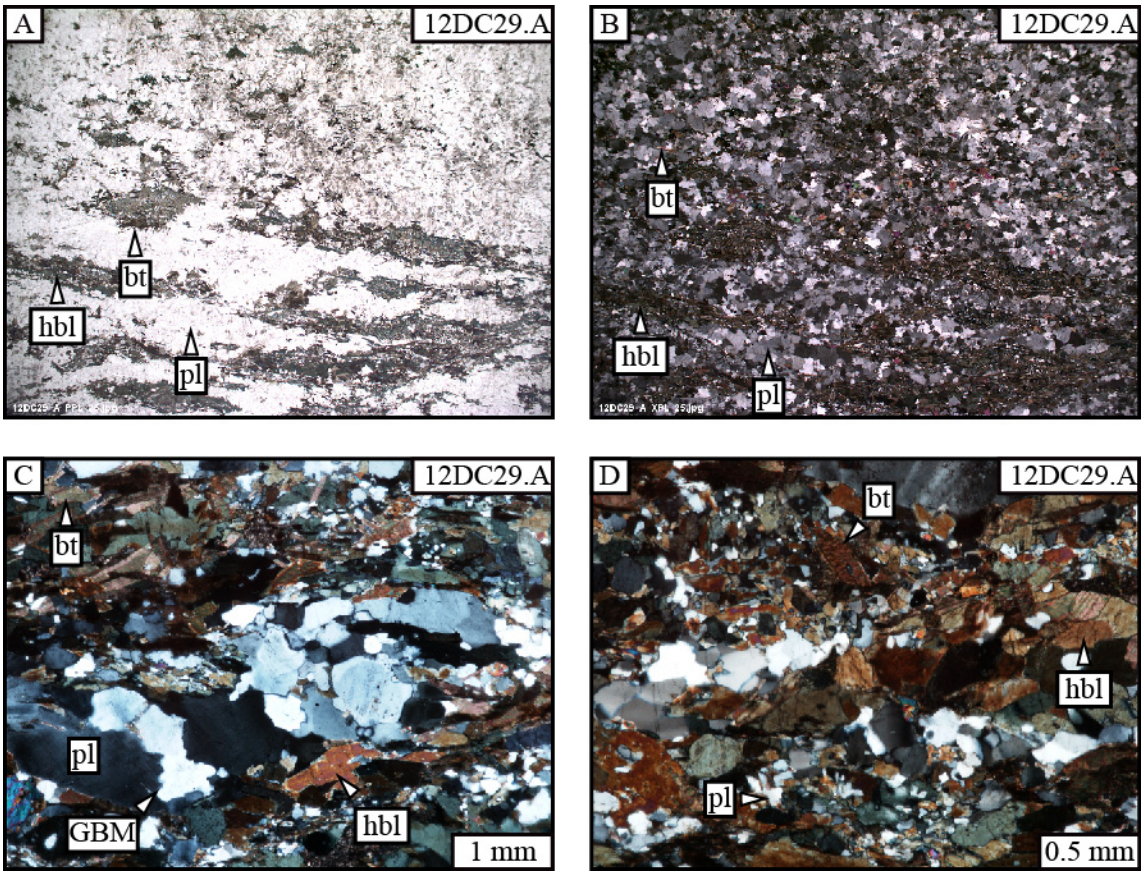

Figure 50. All photomicrographs are from sample 12DC29.A, a retrogressed granulite with a D_2 fabric from Domain 2 in Hall Arm. A) An overview, plane light photomicrograph that shows mafic aggregates set in a plagioclase matrix. B) A cross polarized photomicrograph of "A". C) A cross polarized photomicrograph of a plagioclase domain showing grain boundary migration. D) A cross polarized photomicrograph that shows the early stages of retrogression resulting in blebby plagioclase between anhedral grains of hornblende and biotite.

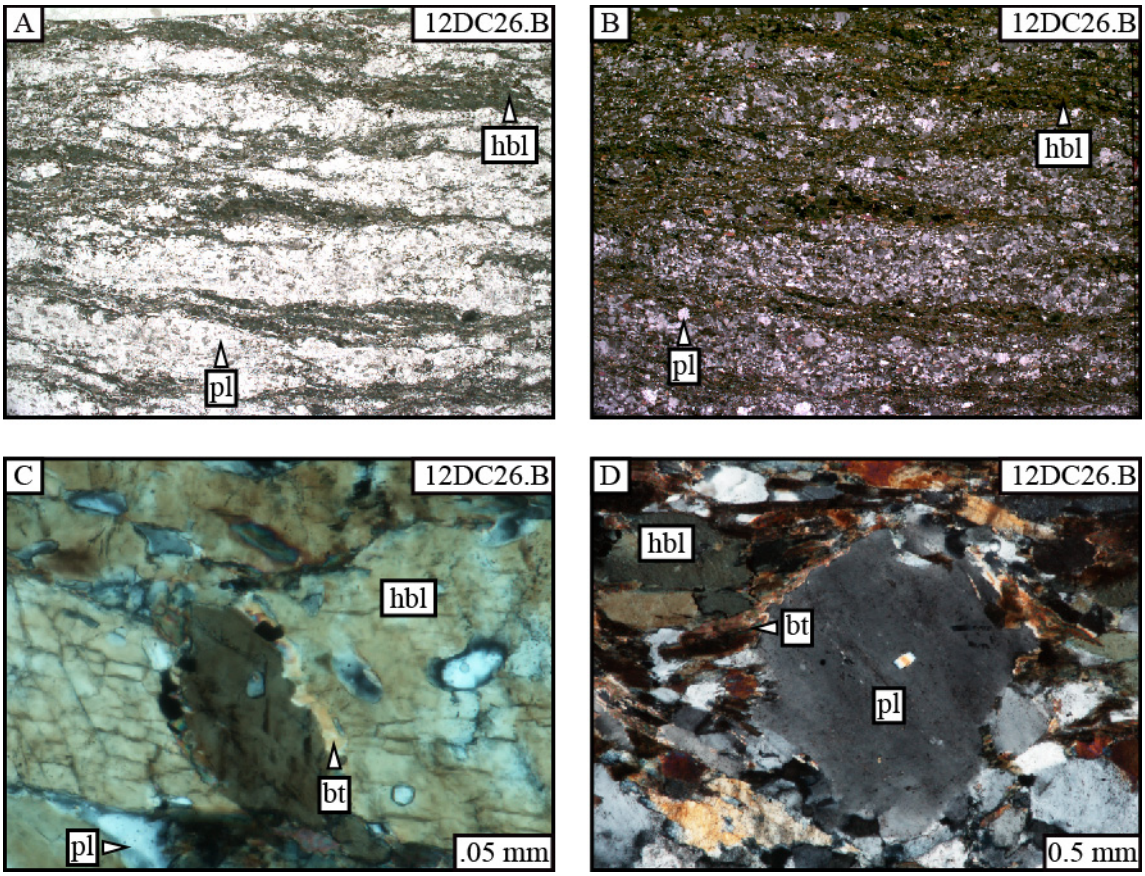

Figure 51. All photomicrographs are from sample 12DC26.B, a retrogressed granulite with a transitional fabric between D_2 and D_3 deformation. A) A plane light photomicrograph that shows the hbl + bt + pl foliation layers. B) A cross polarized photomicrograph of "A". C) A cross polarized photomicrograph of a broken hornblende grain that is in filled with biotite. D) A cross polarized photomicrograph of a porphyroblastic plagioclase grain that has recrystallized tails of plagioclase.

Domain 3 (Hall Arm)

Within Domain 3 the Malaspina orthogneiss is penetrated by the Doubtful Sound Shear Zone. Plagioclase lineations (L_3) are not as rodded as they are in Domain 2 and mostly plunge to the northeast. At site 12DC23, S_3, identified by trains of hornblende and biotite, are aligned in layers of near constant thickness. Plagioclase aggregates are bound by the S_3 layers. Hornblende-hornblende grain boundaries are often smooth and well defined. Brown hornblende is euhedral, whereas green hornblende is subhedral. Splays of finer grained hornblende and biotite branch from the foliation layers and partially penetrate the plagioclase aggregates. The plagioclase grain boundaries are often cuspate-lobate.

At site 12DC22 (Figure 52), the alignment of lath shaped, euhedral hornblende and biotite form an anastomosing S_3 foliation, which is partially developed in felsic dikes. Inside the foliation layers hornblende has serrated ends and the space between is in-filled with biotite. Biotite mostly occurs as subhedral laths, but also occurs as a fine grained incipient phase that forms a matrix around hornblende and epidote. Dynamically recrystallized tails occur on porphyroblastic plagioclase.

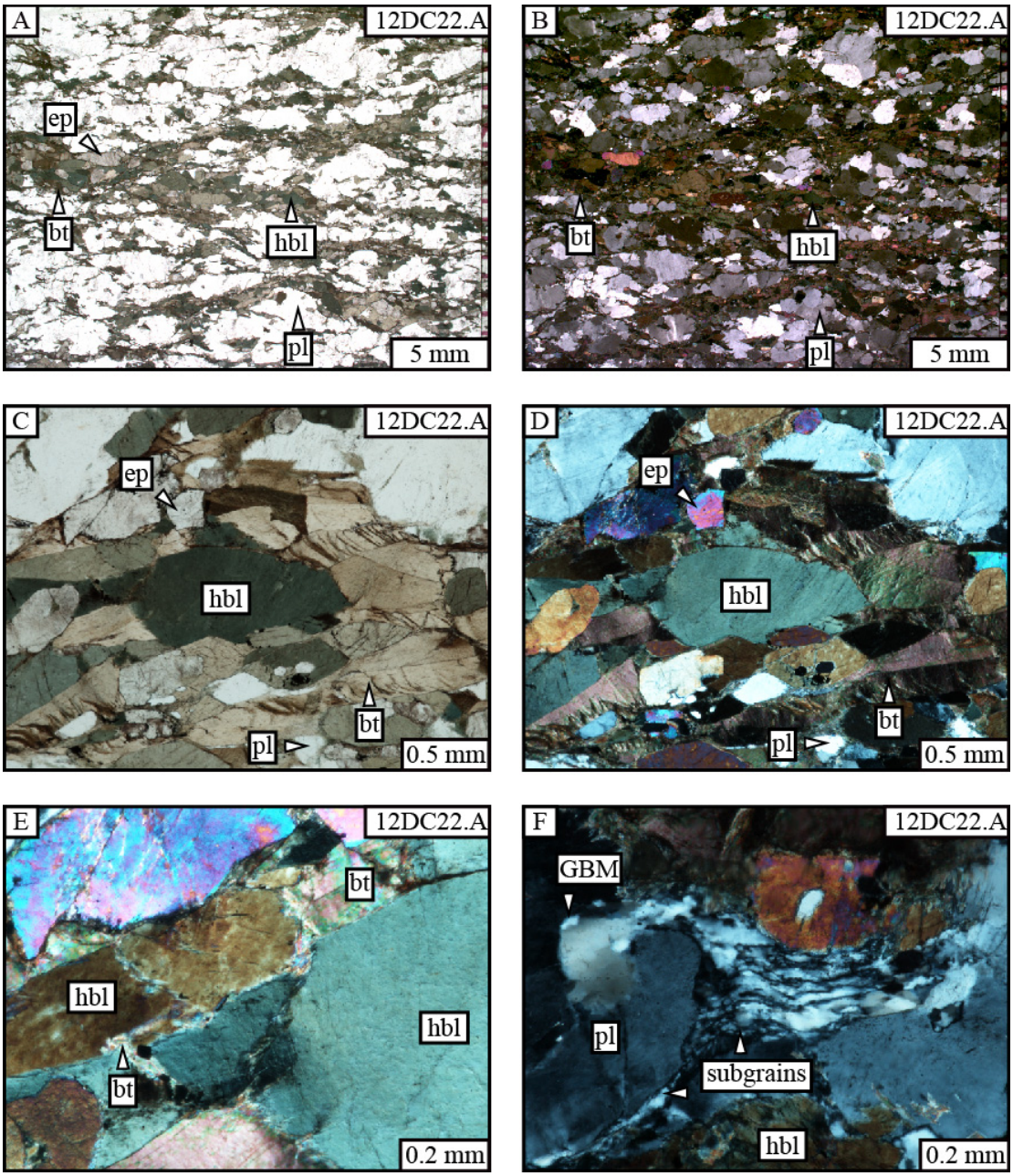

Figure 52. All photomicrographs are from sample 12DC22.A, an amphibolite rock with a D_3 fabric from domain 3 in Hall Arm. A) An overview, plane light photomicrograph that shows the anastomosing foliation layers of hornblende and biotite. B) A cross polarized photomicrograph of "A". C) A plane light photomicrograph of a foliation layer that shows euhedral hornblende and biotite. D) A cross polarized photomicrograph of "C". E) A cross polarized photomicrograph of fractured hornblende with incipient biotite. F) A cross polarized photomicrograph of a porphyroblastic plagioclase grain on the left with a recrystallized tail.

Synthesis of Hall Arm

Hall Arm records the delicate interplay of metamorphism and deformation across a ~5km stretch of fabric transformation during retrogression of granulites to amphibolites. At the end of Hall Arm (sites 12DC30 and 12DC29) retrogression of granulites to the amphibolite facies occurred. Relics of opx + cpx from sample 12DC30B suggest this region was once at the granulite facies. Early stages of retrogression are preserved by the heterogeneous phase mixture of fine hbl + pl + radial biotite. Sample 12DC30A shows the full retrogression of the relict granulites to hornblende granulites, and the initial stages of biotite growth in the plagioclase matrix. Just over a kilometer north, at site 12DC29, biotite has grown and aligned with the hbl + pl phase mixed foliation. By site 12DC26 hornblende forms porphyroblasts and biotite continues to grow along grain boundaries and in pressure shadows. In sites 12DC24, 12DC23, and 12DC22 biotite growth in interstitial space is abundant.

From the end of Hall Arm towards its entrance, porphyroblastic plagioclase and hornblende progressively penetrate the plagioclase matrix and align into S_3. The plagioclase matrix shows evidence of dislocation creep through grain boundary migration and sub grain rotation recrystallization. As the matrix progressively gets deformed by the hbl + bt S_3 foliation, and aggregates of plagioclase become isolated, ribbon plagioclase geometries form and sub grain rotation recrystallization is the dominant dislocation creep mechanism. Once plagioclase aggregates are completely isolated by the anastomosing foliation plagioclase develop undeformed cores and tails recrystallized through subgrain rotation and bulging.

Hornblende initially forms as severely anhedral blebs in a phase mix of hbl + pl + bt. In this scenario hornblende is too fine grained to determine how it is deforming. As the hornblende matures through solution mass transfer it aligns in clumps and then eventually aligns into anastomosing S_3 foliation layers that penetrate plagioclase aggregates. Biotite initially forms as radial masses in mafic aggregates, as "razor backs" along mafic aggregate boundaries, and along plagioclase grain boundaries. The masses of biotite progressively become aligned and merge with the biotite along plagioclase grain boundaries. Once the anastomosing S_3 foliation is constructed, thicker splays of biotite further penetrate plagioclase aggregates along grain boundaries. From sites 12DC26-12DC22 biotite forms a second interstitial phase of incipient biotite along hornblende grain boundaries. In sites 12DC24 and 12DC22 developed biotite grains kink and show a lamellae texture. I infer that biotite is also a result of solution mass transfer and is evidence of fluids along grain boundaries and in pressure shadows.

Estimated Temperatures of Deformation

The presence of myrmekite and subgrain rotation in the relict granulites at site 12DC30, and core-mantle structure at site 12DC22 suggests that deformation occurred at 850˚C > T > 600˚C across Hall Arm (Passchier and Trouw , 2005). The recrystallization of plagioclase from sites 12DC26 to site 12DC22 suggests that deformation in this region of Hall Arm occurred at T < 700˚C (Passchier and Trouw, 2005). Synthesizing these data I suggest that the end of Hall Arm (sites 12DC30 and 12DC29) deformed at 850˚C > T > 700˚C, and the middle of Hall Arm (sites 12DC26-12DC22) deformed at 700˚C > T > 600˚C.

Mechanisms of Deformation

All sites in Hall Arm record dislocation creep in plagioclase, however, this mechanism has results that are dependent on the mineralogy of the rock. During D_2 the rocks had a plagioclase matrix and through dislocation creep approximately equigranular subgrains of plagioclase form. When dislocation creep occurred during D_3, the plagioclase aggregates that are isolated by the hbl + bt foliation developed core mantle structures with recrystallized tails. Also during D_3, hornblende accommodated strain by alignment into foliation layers. At the suggested temperatures of deformation across Hall Arm, biotite is the weakest phase and flows via solution mass transfer into areas of low differential stress.

Chapter 4: FABRIC ANALYSIS

4.1 Introduction

A common goal in structural geology is to understand the three dimensional geometries of deformation and to correlate these to rock type, microstructural processes, and the metamorphic record. If this is achieved then a comprehensive story of the relative timing, style, and process involved during deformation can be told. To achieve this and to supplement my field and structural observations I performed fabric analysis on rock samples collected throughout my study area with the goals of determining the three dimension shape of deformed mineral aggregates and understanding how different minerals such as plagioclase, hornblende, and pyroxene, accommodated deformation. The analysis was conducted on a compilation of software that Webber (2012) streamlined. I used the results from this analysis to create a sequence of three dimensional deformation styles and then correlated these to rock type, field domains, microstructural deformation processes, and relative timing. The end result from this analysis is the four dimensional deformational history of the lower crust in Doubtful Sound that details how the different rock types accommodated strain during periods of pluton emplacement, granulite facies metamorphism, and extensional shearing.

Due to the destruction of overprinting structures and microlithons, larger scale of pervasive deformation, and recrystallization of minerals that once provided valuable information (Passchier and Coelho, 2006) I analyzed the deformation of mineral aggregates as opposed to individual grains. High grade rocks such as the Malaspina Orthogneiss preserve the shape preferred orientations (SPO) of mineral aggregates,

which are suitable for kinematic analysis (Passchier and Coelho, 2006). The geometries of SPO mineral aggregates are apparent at the hand sample scale, three-dimensional, and the shapes of these aggregates range from stretched to flattened. The end members of the stretching and flattening geometries are described as L-tectonites and S-tectonites (Figure 53). L-tectonites are prolate, or cigar shaped, have a strongly developed lineation, and a weakly developed foliation. S-tectonites are oblate, or pancake shaped, have a strongly developed foliation, and a weaker developed lineation. Collectively these shapes are referred to as tectonite fabrics.

My analysis has defined the tectonite fabrics and has determined their spatial relationship to the DSSZ. I made a qualitative assessment of the fabric types in the field and have supplemented these observations with oriented, three-dimensional fabric ellipsoids. The properties of the ellipsoids, such as axial lengths and orientation record the strain and rotation of mineral aggregates associated with the rocks (Lisle, 1985: Ramsay and Huber, 1983). I have used the ellipsoid data in conjunction with my field data to define strain gradients and strain facies in Doubtful Sound. This was accomplished by identifying changes in fabric type and orientations of structural data.

4.2 Methods

To create the fabric ellipsoids three mutually perpendicular cut faces of my hand samples were scanned into the computer so that mineral aggregates of plagioclase, hornblende, and pyroxene could be digitized. I chose to analyze plagioclase to determine how the weak minerals responded to deformation, and chose hornblende and pyroxene to determine how the stronger minerals responded to deformation in the lower crust.

Plagioclase aggregates occur in two primary styles in my samples. The first style is when the plagioclase forms the matrix of the rock, which is found in the garnet granulite, granulite, and weakly retrogressed granulite samples. The second style is when plagioclase occurs as porphyroblasts, which occurs in the retrogressed granulite and amphibolite samples. Hornblende and pyroxene also occurs in two scenarios. One being when the hornblende and pyroxene are set in a plagioclase matrix (granulite, garnet granulite, and weakly retrogressed granulite rocks), and the second is when hornblende is aligned into a foliation (retrogressed granulite and amphibolite rocks). By calculating the geometries of the aggregates in each of the scenarios I recorded how different minerals deformed at the hand sample scale and how they deformed with or without the support of a matrix.

Orienting cut faces

The first step in the fabric analysis was to cut the oriented samples along the three principle planes (xy, xz, yz) which yielded three perpendicular faces to select grains from. Once the samples were cut, the orientation of each cut face was calculated by using the field orientation of the sample and a stereonet. By cutting the faces along the principle planes and achieving three mutually perpendicular planes, calculating the orientations of the three faces was possible. The samples were placed into their field orientation with the use of clay, and then the strike and dip of one of the cut faces was taken with a compass. I called the first measured cut face “A”. The orientation of A and the pole to A was then plotted on a stereonet. Next, the rake from the strike line on A to an edge that is shared by A and one of the remaining cut faces, which I called B, was measured.

Plotting this rake along the greater circle of A calculated the trend and plunge of that shared edge, which I call line ab. Since faces A and B are perpendicular, B therefore contains the pole to A and line ab. The orientation of face B was then calculated by connecting the pole to A and line ab with a greater circle. To draw the strike and dip mark on face B, the rake from line ab was measured along the greater circle of face B, and this angle was then physically measured on the sample. Next, the rake from the strike line on B to the edge shared by the remaining face C was measured. This angle was then plotted on the greater circle of B to obtain the line bc. Since the remaining face C is mutually perpendicular to A and B, the orientation of C was calculated by connecting the poles to A and B with a greater circle. By default, the line bc falls on the greater circle of face C, therefore the rake of this line along the greater circle for C was used to draw the strike line on the sample for face C, as was done for face B.

Digitizing

The cut and oriented faces A, B, and C were scanned into the computer so that mineral aggregates of plagioclase, hornblende, and pyroxene could be digitized in the program Incscape©. This leads to further reasons why aggregates were chosen to analyze as opposed to single grains. Single grains were not detectable in the scanned images largely because of the deformational, metamorphic and recrystallization history of the rocks. For instance, much of the pyroxene is only partially retrogressed to hornblende and much of the plagioclase records subgrain development or dynamic recrystallization. These processes result in grain shapes specific to the reaction or microstructural process

occurring and are not representative of the larger scale deformation that is observable at the hand sample scale.

R_f/Φ technique

For each sample, three mutually perpendicular faces were analyzed individually with the R_f/Φ technique following assumptions by Webber (2015) and by assuming that deformation was homogenous at the hand sample scale. I applied the R_f/Φ technique by fitting a two-dimensional ellipse to the digitized shapes (Mulchrone et al., 2005). A single strain ellipse for each face of the rock samples that is representative of all the ellipses fit to the digitized aggregates was calculated using the R_f/Φ method (Dunnet, 1968; Lisle, 1977; Mulchrone and Meere, 2001; Ramsay 1976). The results are the average strain and ellipse orientation or the mineral aggregates.

To obtain three dimensional information on orientations and geometries of the deformed aggregates, the representative strain ellipses from each sample were combined into a three-dimensional ellipsoid with software from Launeau and Robin (2005). The ellipsoids represent the degree of flattening versus stretching in my hand samples. See Figure 54 through Figure 57 for examples of digitizing plagioclase, fitting ellipses, using the R_f/Φ technique, and creating the ellipsoids. I then plotted the axial data from the ellipsoids on a Nadai Plot so that the degree of strain, stretching and flattening could be compared among all of my samples. Samples that are higher on the Nadai plot record a greater amount of strain, samples to the left of the centerline are L>S tectonites (prolate), and samples to the right of the centerline are S>L tectonites (oblate).

Through this process information such as the orientations of the x, y and z axis, xy plane, and the incompatibility index for the fit of the ellipsoid to the three sectional ellipse were used to assess error. The x axis and xy plane orientations closely paralleled field measurements indicating error associated with the orientation of the ellipsoids was low. The incompatibility index numbers were also low (Appendix A), indicating a good 3D fit of the ellipsoids. In conjunction with these indicators of low error, the ellipsoid shapes closely matched field observations of deformation style (stretching vs. flattening), from all of which I conclude error associated with my fabric analysis was low

4.3 Fabric Results

My fabric analysis results shows that each rock type and deformation event records a range of strain intensity and deformation style. I plotted all of the results on a Nadai Plot (Figure 58) and then created clouds around each rock type (Figure 59) to help visualize the data by rock type. Individual R_f/Φ and Nadai Plots for each sample, as well as additional data from Breaksea Sound can be found in Appendix A. The Nadai Plots in Appendix A can also be used to compare the plagioclase and hornblende/pyroxene results for each sample.

Metadiorites and D_1

Five samples from the Misty Pluton that lack both a well-developed foliation and lineation were used to create baseline results to compare the Malaspina samples to. The five Misty Pluton samples that are undeformed show low strain and are L=S tectonites (Figure 60). Doubtful Sound was the main location where metadiorite samples were

found, and when comparing the metadiorite samples to the undeformed Misty Pluton samples, the metadiorites are only slightly higher in strain with an L=S fabric. They show a small range from prolate to oblate, and also show that pl and hbl/cpx accommodated nearly identical parts of the strain. Following Klepeis' (2016) conclusion that S_1/L_1 fabrics developed during the later stages of magmatism, I interpret these results to show that strain during D_1 was low, and that these samples can be used as the baseline to compare deformation during D_2 and D_3.

Granulites, weakly retrogressed granulites, and D_2

Granulite and weakly retrogressed granulite rocks have a plagioclase matrix, show the highest strain, are $L_2 \geq S_2$ tectonites and are the most prolate. The granulites along Doubtful Sound also show that plagioclase and pyroxene accommodated equal amounts of strain, where as in Crooked Arm and Hall Arm, many of the granulite samples show that plagioclase accommodated more of the strain. Areas of granulite and retrogressed granulite rock that record the highest strain, and are pure L>S tectonites outcrop from the end of Crooked Arm to the "crook", and at the end of Hall Arm. I interpret these findings to show that:

1) Granulites along Doubtful Sound record low strain during D_2 and the preferred orientation of minerals.
2) During peak metamorphism the competency of the plagioclase matrix was lowered by partial melting (Klepeis et al., 2016), and strain concentrated into pl + melt rich domains.
3) Temperatures from 850-900° C (Stowell et al., 2014) allow aggregates of pyroxene to stretch and accommodate crystal-plastic deformation.
4) During D_2 there were high strain zones in Crooked Arm and Hall Arm within domains where granulite facies metamorphism was achieved, which created a network of granulite facies shear zones on the margins of the crystallized metadiorite orthogneiss.

Granulite-amphibolite and D_2-D_3 transition

On a whole, the granulite-amphibolite transition samples throughout my study area record lower strain than the granulite rocks but also record similar shapes. In Crooked Arm and Hall Arm these rocks are L≥S tectonites and along Doubtful Sound they are L=S tectonites. Among these samples, Doubtful Sound has the lowest strained granulite-amphibolite rocks, whereas Crooked Arm and Hall Arm have the highest strained rocks. In Crooked Arm plagioclase records more strain than hornblende, along Doubtful Sound and Hall Arm plagioclase records equal strain to hornblende. In general, the range of strain recorded by hornblende is less than that of plagioclase. My interpretation of these results are:

1) Granulite-amphibolite rocks preserve S_2/L_2 and record the transformation of prolate S_2/L_2 fabrics into oblate S_3/L_3 fabrics.
2) In early stages of transformation from S_2/L_2 fabrics into S_3/L_3, plagioclase preserves the high D_2 strain, and in later stages of the transformation the fact that plagioclase and hornblende show approximate equal parts of strain attests to the development of the new D_3 fabric.
3) Similar fabric shapes for hornblende and plagioclase show that during the D_2-D_3 transition the porphyroblastic growth of plagioclase and solution mass transfer of hbl+bt occurred at similar rates.
4) Since the transitional rocks in Crooked Arm and Hall Arm show the highest strain in this group and are also more prolate than other outcrops of

transitional rock, the D_2 high strain zone boundaries can be extended to include the higher strained transitional outcrops.

Amphibolites and D_3

Results from the amphibolite samples, which are associated with the DSSZ, show low to moderate strain relative to the granulite-amphibolite transition rocks, and differ from all the rock types by being L=S tectonites. The results form a narrow girdle along the centerline of the Nadai Plot. I do not find there to be a geographical pattern of strain intensity for the amphibolites. I also find that plagioclase and hornblende accommodated approximately equal parts of the strain. These results show that:

1) During D_3 deformation was accommodated equally by stretching and flattening, producing oblate ellipsoids. In contrast, stretching was the dominant mechanism for deformation during D_2, producing prolate ellipsoids.
2) S_3/L_3 is a new fabric and the style and type of deformation was similar in each strand of the DSSZ.

Summary of results

To summarize the results of the fabric analysis and to show the relationship of fabric results to rock types and structures, I plotted lineations and the two dimensional XY ellipses on a geologic map of my study area (Figure 61). The XY ellipses were chosen because they represent the maximum stretching direction (X) and are the plane that lineations are observed on. These properties make the ellipses an indicator for strain intensity and flow direction. My map shows that the X axis of the ellipses closely parallel

lineations measured in the field, indicating that the results of the fabric analysis match the predictions made from field measurements.

The domain of mostly metadiorite rock between Hall Arm and Crooked Arm shows low strain and a northwest-southeast flow direction. L_2 from domains of granulite show that during D_2 flow was mostly east-west and perpendicular to the magmatic flow seen in the domain of metadiorite. The XY ellipses in domains of granulite show a gradient of increasing strain away from the domain of metadiorite, with the highest strain zones occurring in Crooked Arm and Hall Arm. This shows that during D_2, strain was partitioned to areas weakened by melt. Granulite-amphibolite transition rocks are located in close proximity to the amphibolite rocks and show intermediate strain with a flow direction the closely parallels the domains of granulite. Domains of amphibolite and L_3 record flow directions more northeasterly and oblique to the L_2 flow direction, as well as less stretching than the granulite domains. D_3 and the onset of extension focused strain to areas with fluid available for reaction softening.

4.4 Discussion

Recent studies (Klepeis et al., 2016; Sadorski, 2015) have concluded that the Malaspina Pluton was sourced from vertical feeder dikes that curved and flowed sub horizontally into the Doubtful Sound region from 118 Ma through 115 Ma (D_1). Coincident with emplacement of the Malaspina Pluton was an interval of high grade metamorphism and partial melting (Stowell et al., 2014), and in the final stages of emplacement dome structures formed between Crooked Arm and Hall Arm (Klepeis et al., 2016). The domes crystallized and preserved the S_1/L_1 fabrics as anataxis, granulite

facies metamorphism, and flow around the domes continued from 114 Ma through 106 Ma at 1.2-1.0 GPa (D_2), resulting in the high D_2 strain zones. Following D_2, the onset of extension and formation of the DSSZ (106 Ma to 98 Ma) occurred during decompression to 0.7-0.9 GPa and cooling to 550-650° C, marking the shift in deformation styles. I contribute to these findings by identifying the process of deformation and fabric development/transformation.

To determine how the high strain $L_2 \geq S_2$ fabric were reconstructed into high strain $L_3 = S_3$ fabrics I compared five samples from Crooked Arm that record the full range of D_2 and D_3 fabric types and mineral development during the retrograde metamorphism. From these five samples I chose to analyze the plagioclase fabric results because plagioclase is the only consistent mineral across all rock types and because during each stage of deformation it was one of the weakest phases, making plagioclase a good element and indicator for the degree of deformation. The results from this analysis is a five step fabric transformation process linked to microstructural process that shows how the onset of extension developed new fabrics that overprinted the high D_2 strain zones.

$L_2 > S_2$ granulites from site 12DC38 (Figure 62, step 0) are the highest strained and are among the most prolate rocks I analyzed. These samples represents the initial high strain fabric that was overprinted during D_3. The key characteristics of these rocks are the $L_2 > S_2$ fabric which consist of an inclusion free plagioclase matrix and elongate pyroxene rimmed with garnet. The key microstructural processes of deformation during D_2 are dislocation creep and grain boundary migration in plagioclase and pyroxene.

Step 1

Sample B from a granulite lozenge at site 12DC44 (Figure 62, step 1) shows that the L_2>S_2 granulites began retrogressing by the breakdown and replacement of pyroxene by hornblende. Biotite also begins to grow in radial clots on the margins of mafic aggregates. In this early stage of retrogression and transformation the plagioclase matrix remains inclusion free and the rocks still record the high strain L_2>S_2 fabric. Plagioclase continues to deform through the development of subgrains by grain boundary migration and the retrograde metamorphism continues until all of the pyroxene has been replaced by hornblende and biotite, which is observed at site 12DC45 (Figure 62, step 1). Microstructural deformation processes are not observable in the mafic minerals due to the intermediate phases of mineral development, however, I interpret the radial growth of biotite and vermicular symplectites of hornblende to indicate the onset of fluid mobility, solution mass transfer, and reaction softening.

Step 2

I documented the transition from L_2/S_2 to L_3/S_3 at site 12DC46 where porphyroblastic hornblende and biotite grow and begin to penetrate the plagioclase matrix (Figure 62, step 2). In this stage of transformation, aggregates of pyroxene have been completely replaced by hornblende and biotite and the relic D_2 fabric has degraded. Aggregates of hornblende and biotite that comprise the S_2 folia have irregular boundaries that begin to penetrate the elongate aggregates of plagioclase. Also occurring during step 2 is the growth of new hornblende and biotite along plagioclase grain boundaries in areas away from the foliation layers. Since the D_2 fabric has only been degraded and is still

present, the rocks remain classified as $L_2>S_2$ tectonites, but this stage in transformation marks a key process; the removal of the granulite plagioclase matrix and initial formation of isolated plagioclase aggregates. During this stage, grain size reduction of plagioclase continues through the development of subgrains by grain boundary migration. My observation of new hornblende and biotite growth suggests the continuation of solution mass transfer.

Step 3

Further into transformation to S_3/L_3 fabrics at site 13DC64, new plagioclase, hornblende, and biotite completely erase S_2/L_2 but have not formed a continuous S_3 foliation (Figure 63, step 3). The lack of a continuous foliation leaves the rock with a quasi-plagioclase matrix with lenticular plagioclase bound by hornblende and biotite. The amount of fine grained blebby plagioclase has reduced and plagioclase grains show deformation by grain boundary migration. Hornblende and biotite begin to show euhedral grain shapes which I interpret to represent equilibration with decompression. I interpret the lenticular shape of plagioclase and the quasi plagioclase matrix to create an apparent high strained D_3 fabric that records the resetting of the D_2 fabrics and growth of new minerals as opposed to a high strain D_3 rock with a well-developed foliation and lineation.

Step 4

At site 13DC63 (Figure 63, step 4) the amphibolites have porphyroblastic augen plagioclase with hbl+bt pressure shadows. Plagioclase begins to show asymmetry and the S_3 folia of hornblende and biotite is less disjunctive. Disjunctive biotite shear bands,

and hbl+bt pressure shadows on augen plagioclase further attest to solution mass transfer of the mafic minerals. Subgrains of plagioclase mantle strain free augen plagioclase indicating deformation by grain boundary migration. These amphibolites are the lowest strained L_3=S_3 tectonites and I interpret them to represent the starting point to developing the high strain D3 fabrics.

Step 5

An amphibolite shear zone at site 12DC44 records high strain L_3=S_3 tectonites. At this site the amphibolite rocks cross cut the weakly retrogressed and high strain D_2 rocks mentioned above, and the transformation from high strain L_2>S_2 tectonites to high strain L_3=S_3 tectonites is complete (Figure 63, step 5). S_3 is a continuous and gneissic folia of hbl+bt+ fine grained plagioclase. The final process that created the high strain L_3=S_3 shear fabric from site 13DC63 to 12DC44 was the connection of shear bands and development of the continuous, gneissic foliation seen at site 12DC44. The elongate aggregates of plagioclase are largely annealed but preserve evidence of grain boundary migration. Augen plagioclase have biotite beards which supports solution mass transfer during the final stages of D_3.

An annotated deformation path that shows the changes in P-T conditions accompanying deformation through time can be seen in Figure 64. This figure shows that during pluton emplacement and magmatic flow the Malaspina Orthogneiss did not develop a high strain fabric. During peak metamorphic temperatures and pressures (D_2) an upward trajectory in strain to L_2>S_2 tectonites were created by the suprasolidus flow of plagioclase. During the D_2-D_3 transition and initial transformation of the high strain L-tectonites (steps

2 and 3) an apparent decreasing strain path was produced, which I have shown to represent 1) retrograde metamorphism, 2) degradation of the D_2 fabrics, 3) early stages of D_3 fabric development, and 4) the onset to reaction softening.

While the transition rocks show an apparent decreasing strain path, the rocks record grain boundary migration in plagioclase and solution mass transfer of hornblende and biotite. I infer that strain was still high in areas that preserve D_2-D_3 transitional fabrics and that the Nadai Plot more closely represents changing minerology, mineral growth, and recrystallization than actual strain. As D_3 progress during cooling and decompression, an upward trajectory of strain in the amphibolite DSSZ samples is shown. The change in strain type and style, along with high strain fabrics in the DSSZ is compatible with the interpretation that the onset of D_3 marks the transition to extension, decompression, and exhumation along the margin of Gondwana.

Conclusion

By combining cross cutting relationships, microstructural and 3D fabric analysis with published P-T-t data I have shown the 4D structural history of the Malaspina Orthogneiss, and that each phase of deformation in the Malaspina produced unique fabrics. 3D fabric ellipsoids were used in conjunction with structural data to delineate domains of high and low strain, and I used microstructural analysis to determine the processes of deformation.

My research has shown that domes of metadiorite along Doubtful Sound record low strain, with L=S magmatic flow fabrics trending SE/NW, forming during pluton emplacement. Within these domes is the preservation of magmatic mingling, melting,

and localized granulite facies metamorphism. These regions can be identified by the presence of hornblendite dikes, coarse grained metadiorite rock, SE/NW mineral lineations, and gneissic foliation (S_1).

The high strain D_2 event focused an E/W, sub-horizontal flow of melt bearing garnet granulite around the crystallized domes of metadiorite. During D_2, deformation of plagioclase and pyroxene occurred in the presence of melt by grain boundary migration, resulting in $L_2>S_2$ fabrics. Deformation during D_2 was not uniform but was partitioned high strain to areas weakened by melt, which resulted in zones of low and high strain on the outcrop and regional scale. During this event thermally weakened plagioclase accommodated most of the strain. Strain partitioning to domains of high D_2 strain can readily be identified by a rodded appearance from the stretching lineation.

Transitioning from D_2 to D_3 involved the resetting of strain markers as retrograde metamorphism, decompression, and extension began, and a transition to hornblende and biotite accommodating more of the stain. Once the D_2 fabrics were erased from the rock record, the D_3 DSSZ shear zone fabrics developed by the solution mass transfer of hornblende and biotite, and grain boundary migration of plagioclase. This was a reaction softening event that decreased the structural competency of the rock and allowed for deformation at lower temperatures and pressures. The degree of D_3 shear zone fabric development is variable and occurs as both thick (100m) and thin (10m) splays that often wrap lozenges of high D_2 strain granulite. Resetting of the D_2 fabric makes some exposures of D_3 deformation appear unstrained, and unless they are observed to cross cut the older D_2 fabric, they can be mistaken for not being associated with the DSSZ. My

results illustrate the importance of melt/fluid mobility in controlling strain partitioning and the importance of coupling microstructural and fabric analysis when developing strain paths.

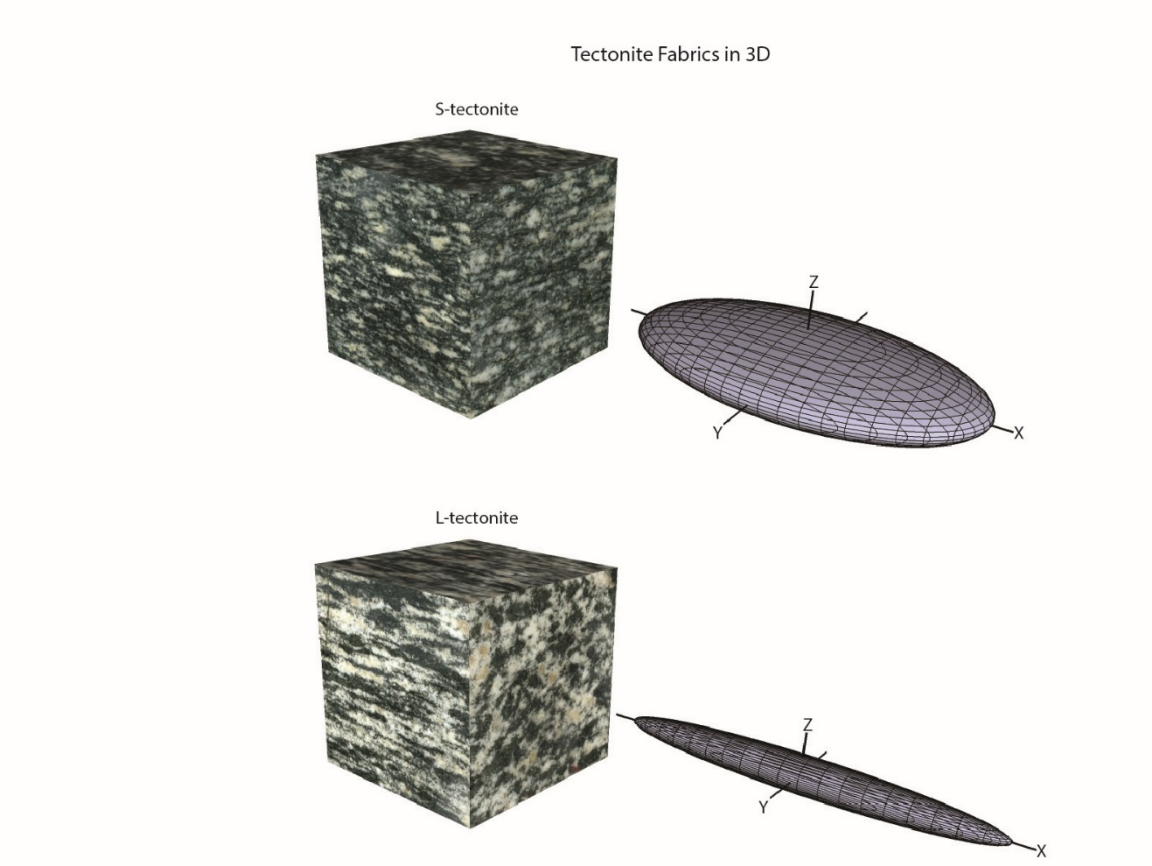

Figure 53. Examples of S-tectonites (top) and L-tectonites (bottom). Scanned images of cut rock sample faces were superimposed onto cubes to show the rock fabric. The three dimensional ellipsoids show how L-tectonites have a much more rodded shape than the more flattened S-tectonites. The ellipsoids are actual data from the fabric analysis with the X,Y, and Z axis showing the maximum stretching, intermediate, and maximum shortening directions, respectively.

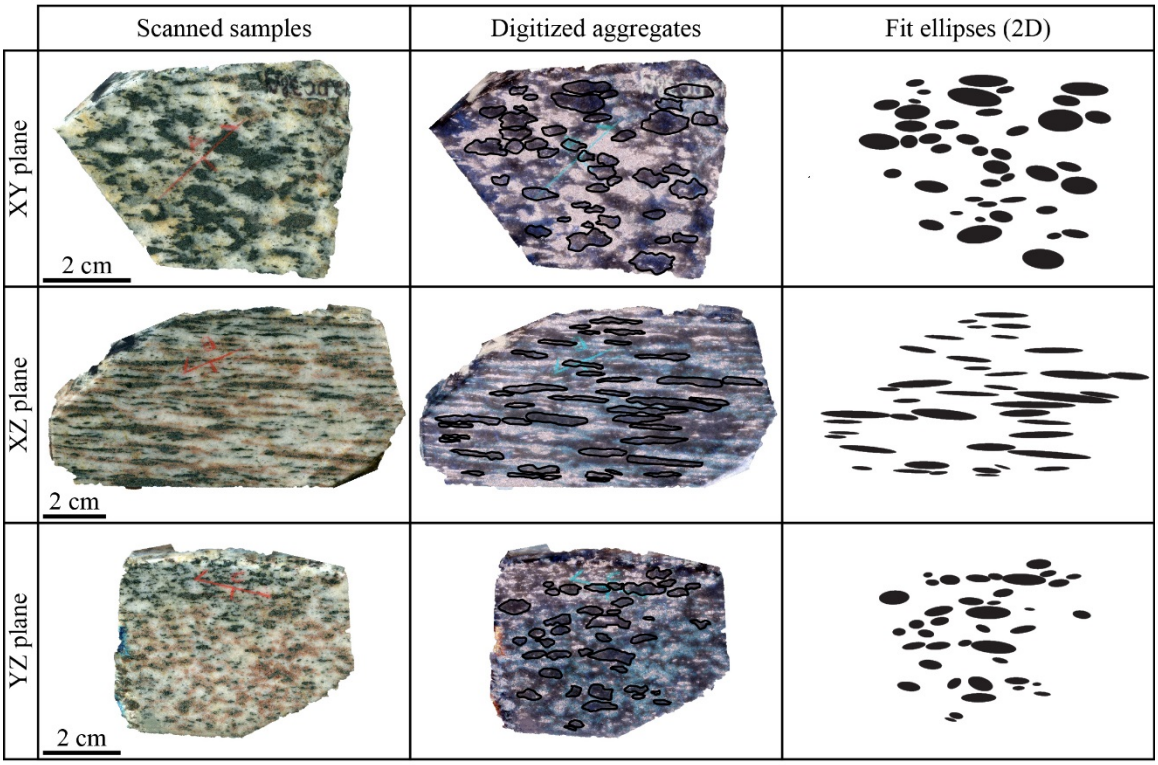

Figure 54. Scanned images and digitization of plagioclase on a high strain garnet granulite (D_2) sample.The left column shows the three faces that were cut for digitizing plagioclase aggregates. Digitizing is shown in the center column where the colors were inverted so that plagioclase appears black, which helped to identify boundaries. The right column shows the two dimensional ellipses that were fit to each digitized shape.

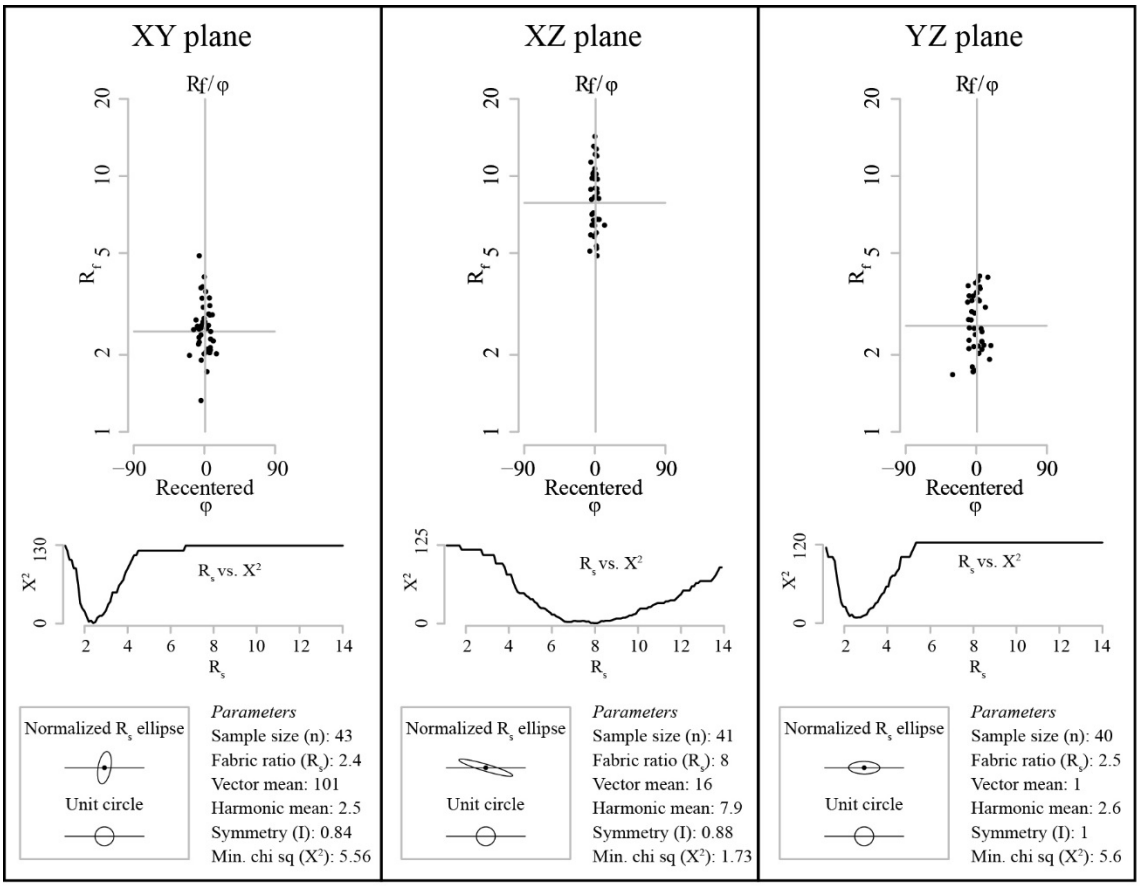

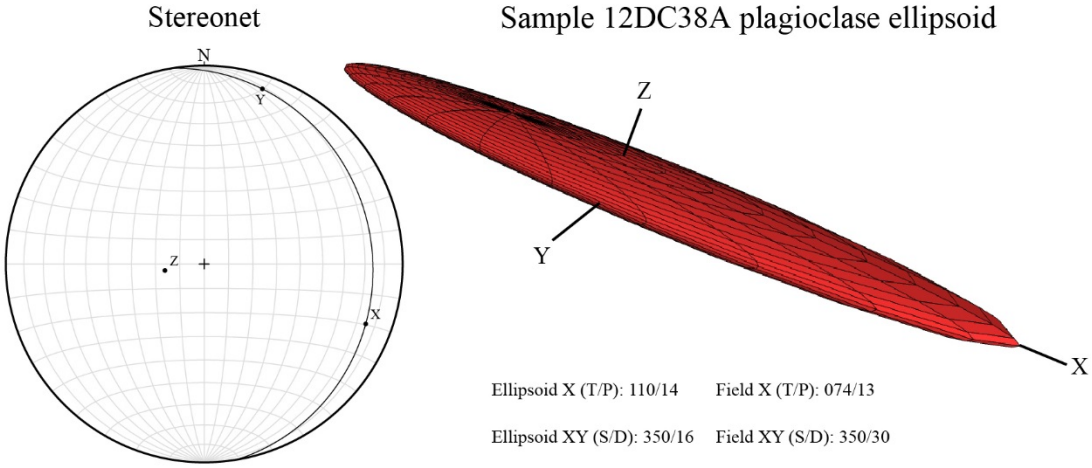

Figure 55. R_f/Φ plots (top of the figure) from the high strain garnet granulite (D_2) showing the calculation of strain for the three analyzed faces (XY, XZ, and YZ). A normalized ellipse is fit to each face which are then used to create the three dimensional ellipsoid (bottom right). Data generated from the ellipsoids include lineation trend and plunge (T/P), and the strike and dip of the foliation (S/D). These data were plotted on an equal-area lower

hemisphere stereographic projection (bottom left) and compared to actual field measurements. This comparison (shown below the ellipsoid) shows that the calculated lineations and foliations closely match the field measurements, indicating that the fabric results can be used for further analysis such as comparing flow directions with deformation style among different rock types.

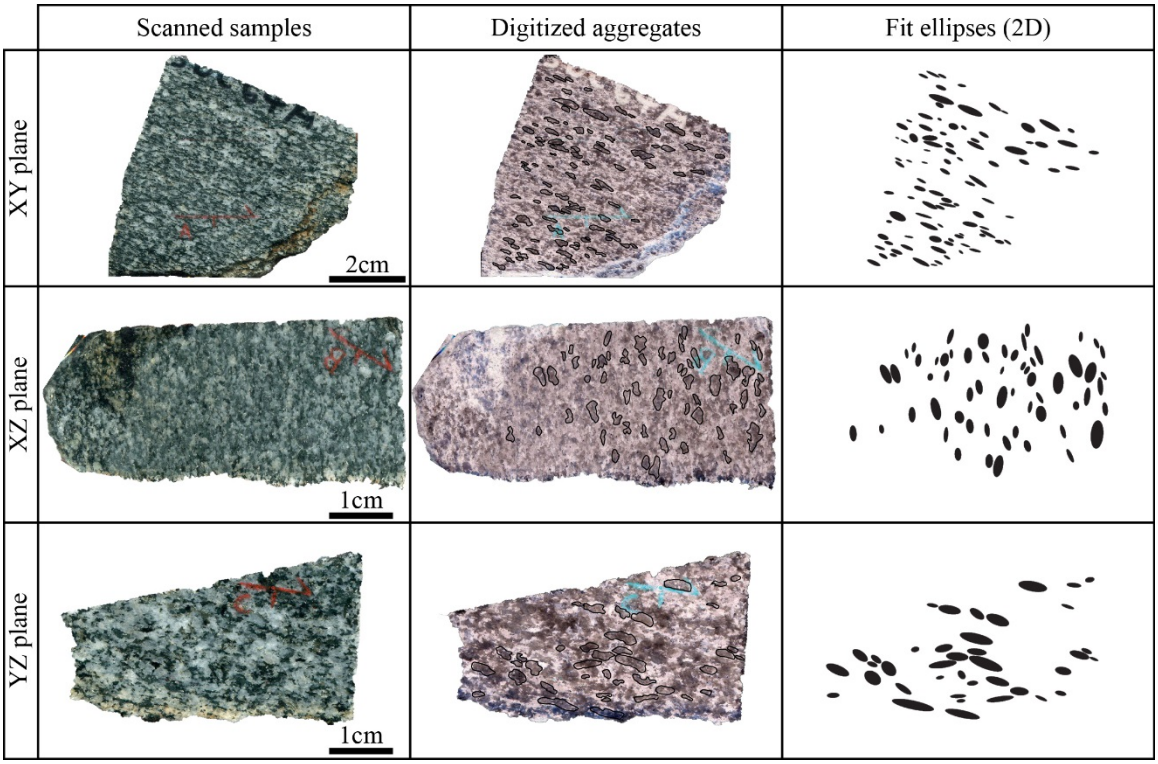

Figure 56. Scanned images and digitization of plagioclase on a low strain amphibolite sample (D_3).The left column shows the three faces that were cut for digitizing plagioclase aggregates. Digitizing is shown in the center column where the colors were inverted so that plagioclase appears black, which helped to identify boundaries. The right column shows the two dimensional ellipses that were fit to each digitized shape.

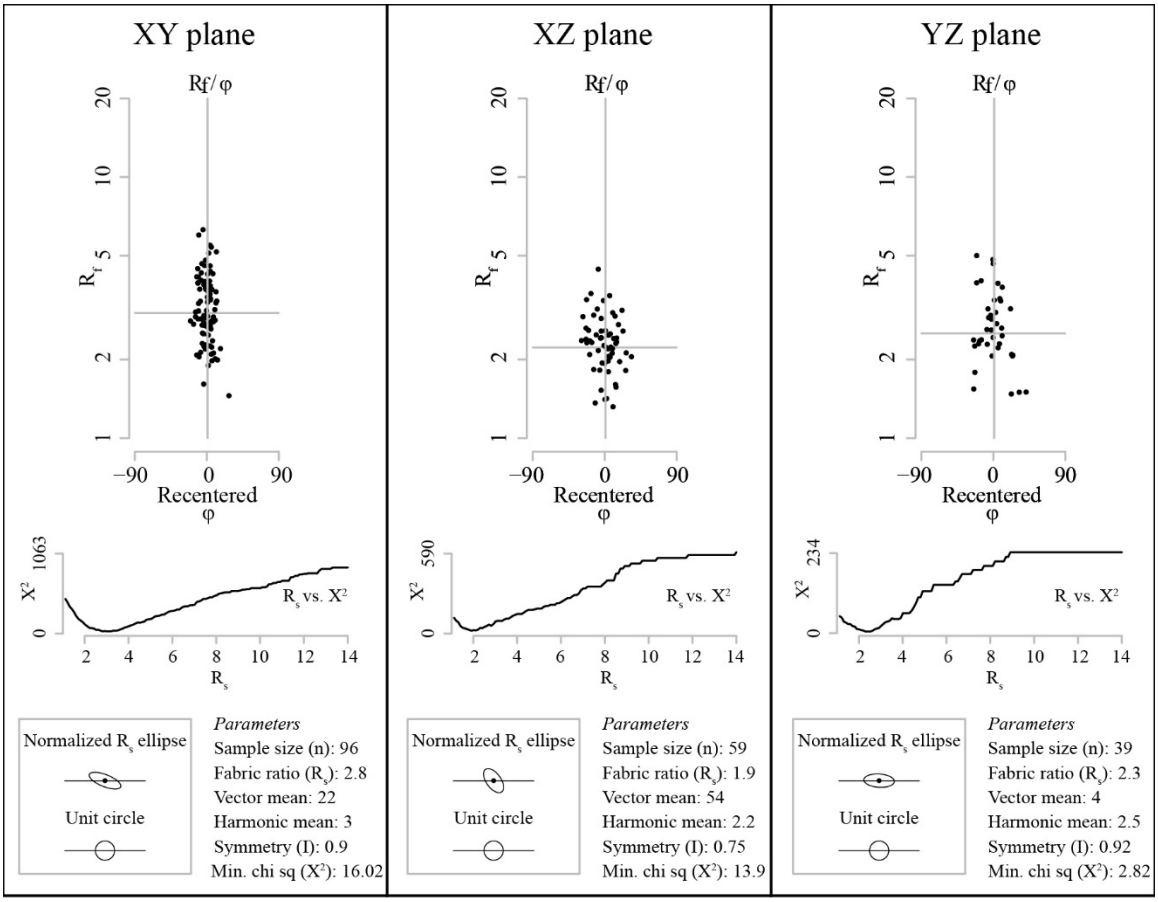

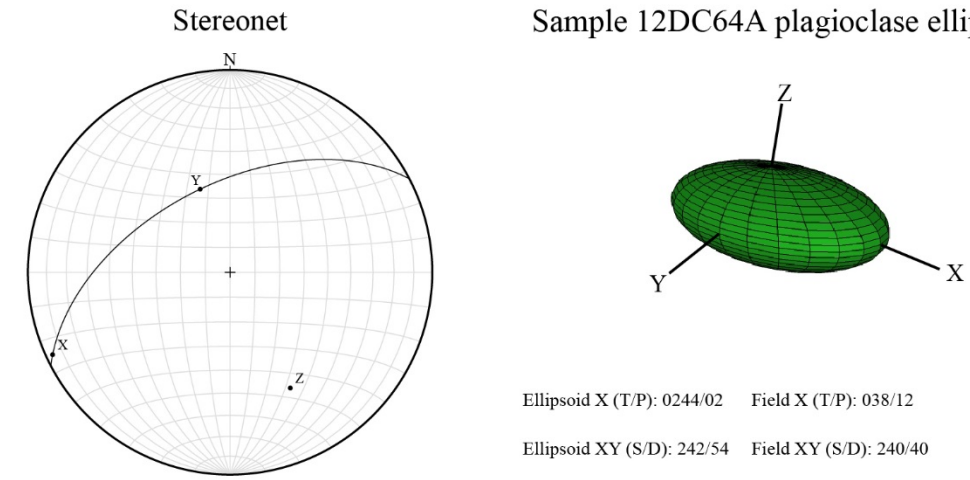

Figure 57. R_f/Φ plots (top of the figure) from the low strain amphibolite (D_3) showing the calculation of strain for the three analyzed faces (XY, XZ, and YZ). A normalized ellipse is fit to each face which are then used to create the three dimensional ellipsoid (bottom right). Data generated from the ellipsoids include lineation trend and plunge (T/P), and the strike and dip of the foliation (S/D). These data were plotted on an equal-area lower

hemisphere stereographic projection (bottom left) and compared to actual field measurements. This comparison (shown below the ellipsoid) shows that the calculated lineations and foliations closely match the field measurements, indicating that the fabric results can be used for further analysis such as comparing flow directions with deformation style among different rock types.

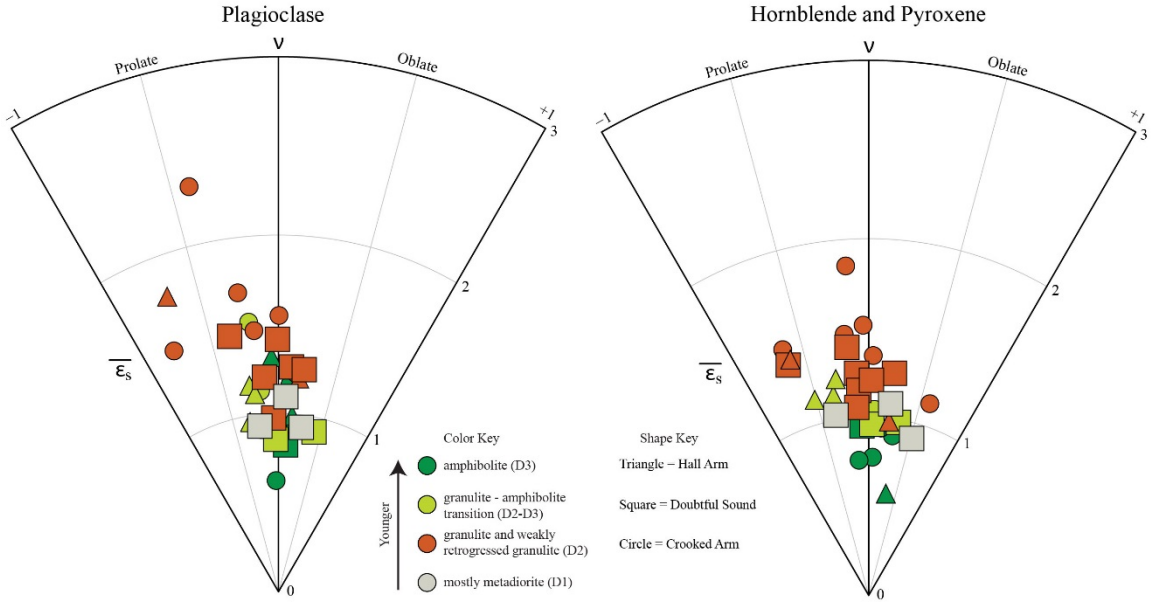

Figure 58. Nadai plots of plagioclase (left) and hornblende/pyroxene (right). Samples that plot in the upper part of the diagram are more strongly distorted (shape change) than those closer to the apex (bottom of diagram). The data show that the metadiorites are low strained, mostly an L=S fabric and that the garnet granulite samples were the highest strained and most prolate. The transitional and amphibolite rocks show a range in strain intensity but girdle the centerline indicating a mostly L=S fabric. Hornblende and pyroxene appear to accommodate less strain than plagioclase but when these minerals are compared for the same sample there is not a remarkable difference.

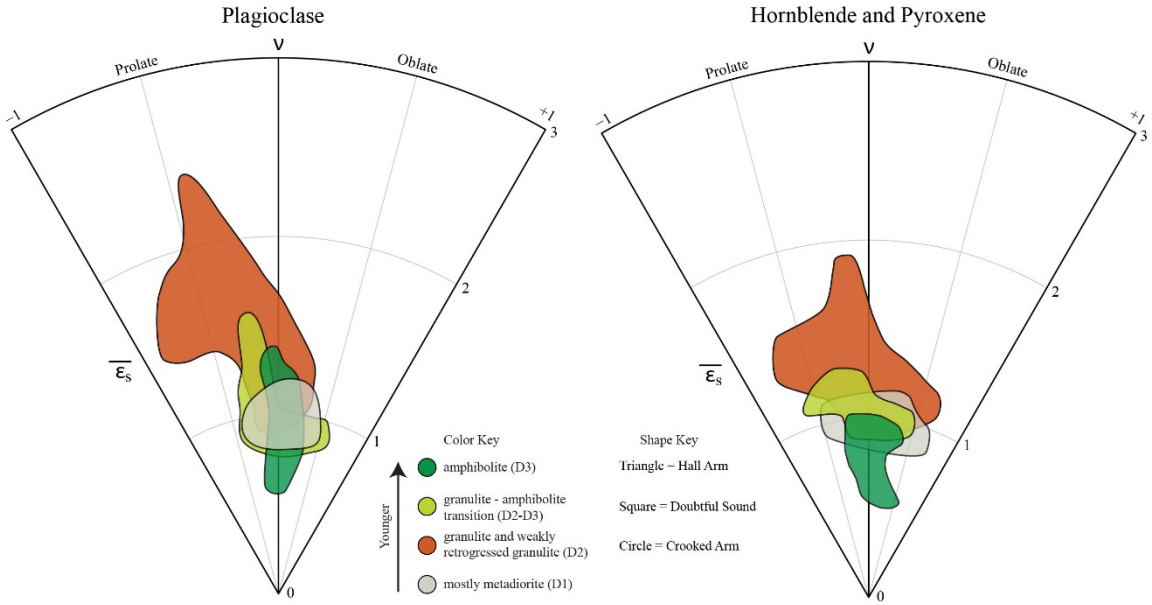

Figure 59. Clouds drawn around the point data (removed) from figure 58 to help visualize the range of fabrics for each rock type. The clouds are a means for assessing error and distinguishing deformation styles.

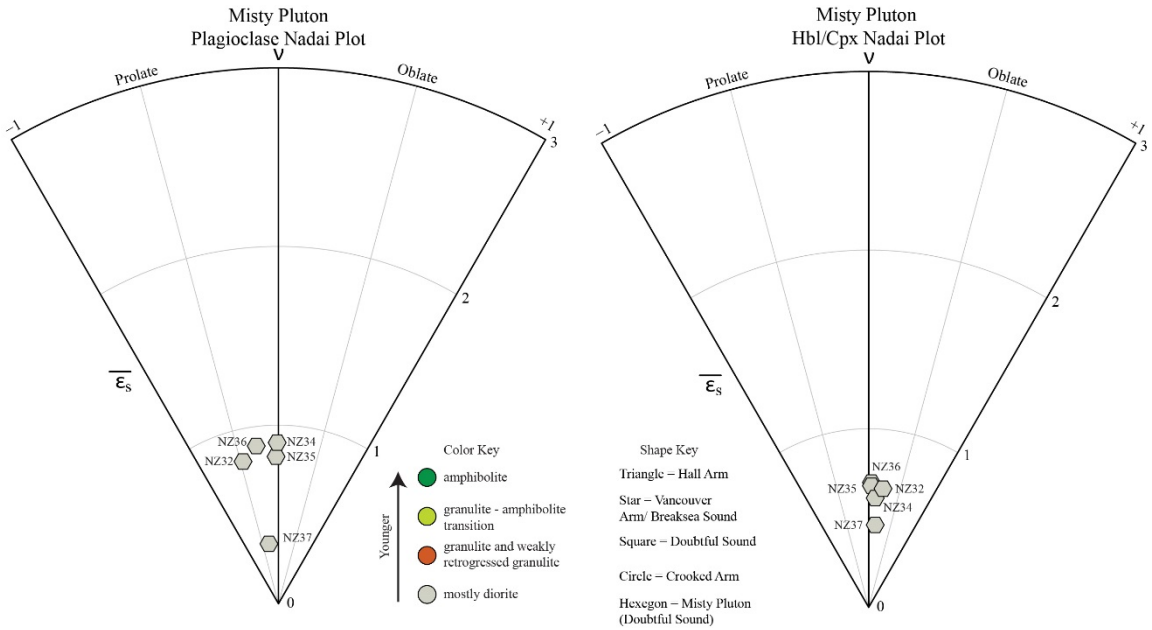

Figure 60. Fabric data from the undeformed Misty Pluton samples that were used as a baseline to compare the Malaspina Orthogneiss samples to. The Misty samples are dioritic without a foliation or lineation.

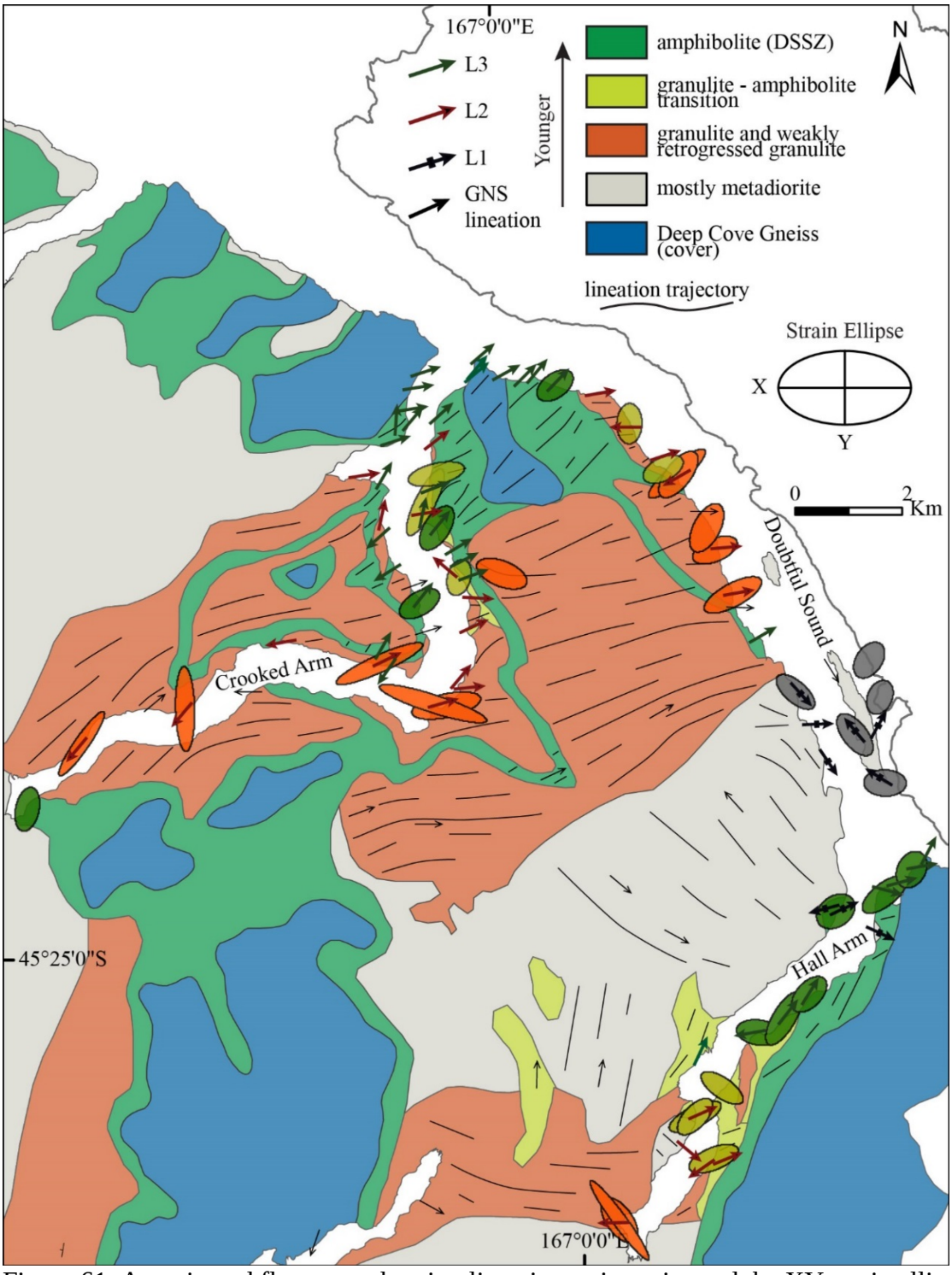

Figure 61. A strain and flow map showing lineation trajectories and the XY strain ellipses. This map shows the SE/NW flow in the domain of metadiorite, high strain and mostly E/W flow in domains of granulite and weakly retrogressed granulite, and low to moderate strain as well as NE/SW flow in domains of amphibolite.

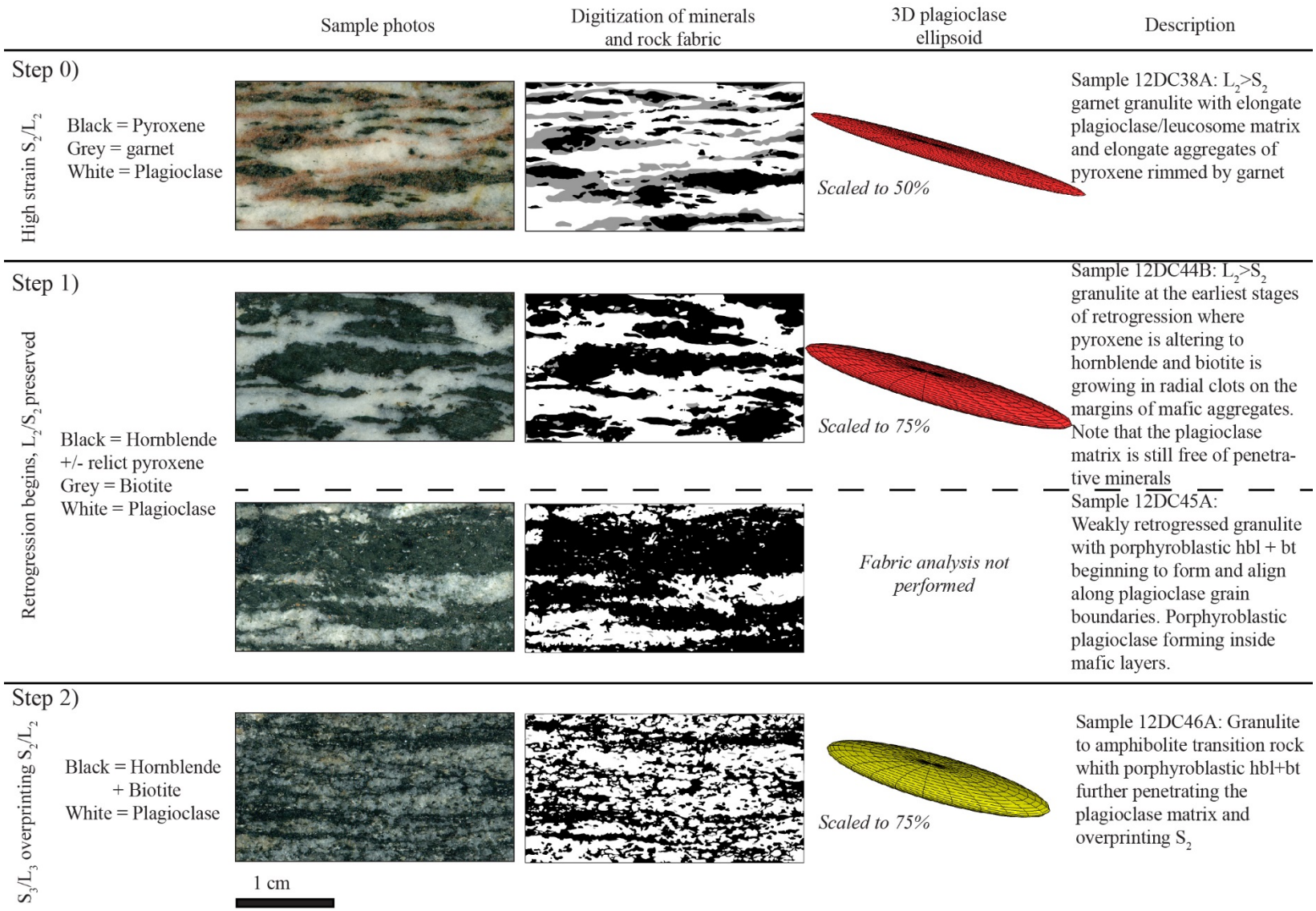
Sample photos
Digitization of minerals and rock fabric
3D plagioclase ellipsoid
Description
Step 0)
High strain S_2/L_2
Black = Pyroxene
Grey = garnet
White = Plagioclase
Scaled to 50%
Sample 12DC38A: $L_2>S_2$ garnet granulite with elongate plagioclase/leucosome matrix and elongate aggregates of pyroxene rimmed by garnet
Step 1)
Retrogression begins, L_2/S_2 preserved
Black = Hornblende
+/- relict pyroxene
Grey = Biotite
White = Plagioclase
Scaled to 75%
Sample 12DC44B: $L_2>S_2$ granulite at the earliest stages of retrogression where pyroxene is altering to hornblende and biotite is growing in radial clots on the margins of mafic aggregates. Note that the plagioclase matrix is still free of penetrative minerals
Fabric analysis not performed
Sample 12DC45A: Weakly retrogressed granulite with porphyroblastic hbl + bt beginning to form and align along plagioclase grain boundaries. Porphyroblastic plagioclase forming inside mafic layers.
Step 2)
S_3/L_3 overprinting S_2/L_2
Black = Hornblende
+ Biotite
White = Plagioclase
Scaled to 75%
Sample 12DC46A: Granulite to amphibolite transition rock whith porphyroblastic hbl+bt further penetrating the plagioclase matrix and overprinting S_2
1 cm

Figure 62. Steps 1 and 2 of fabric transformation from the high strain $L_2>S_2$ (step 0) garnet granulites to high strain $L_3=S_3$ amphibolites. Scanned faces of the XY plane were digitized to show how the inclusion free plagioclase matrix in the garnet granulites is eventually penetrated by porphyroblastic hornblende and biotite, which becomes apparent in step 2. The ellipoids show the three dimensional shape of plagioclase aggregates and how these shapes change from stretched to flattened (see figure 63 for steps 3 through 5).

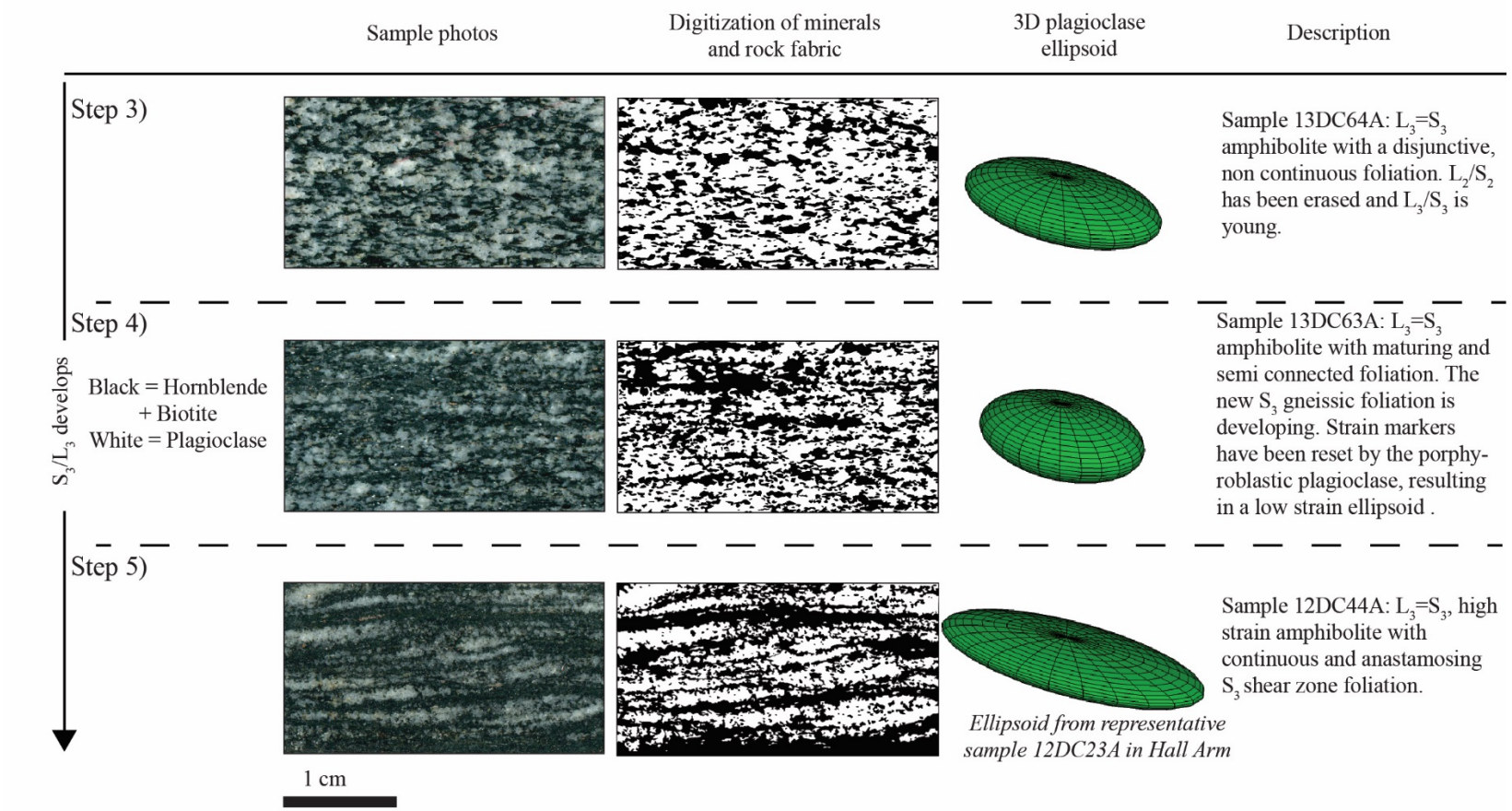

Figure 63. Steps 3 through 5 of reconstructing high strain L_2>S_2 garnet granulites (steps 1 and 2 in figure 62) to high strain L_3=S_3 amphibolites (step 5). Scanned faces of the XY plane were digitized to show the growth of new hornblende and biotite that eventually connects into a continuous S_3 foliation (step 5). The fabric ellipsoids show a resetting of the plagioclasee strain markers (step 4) as plagioclase becomes porphyroblastic.

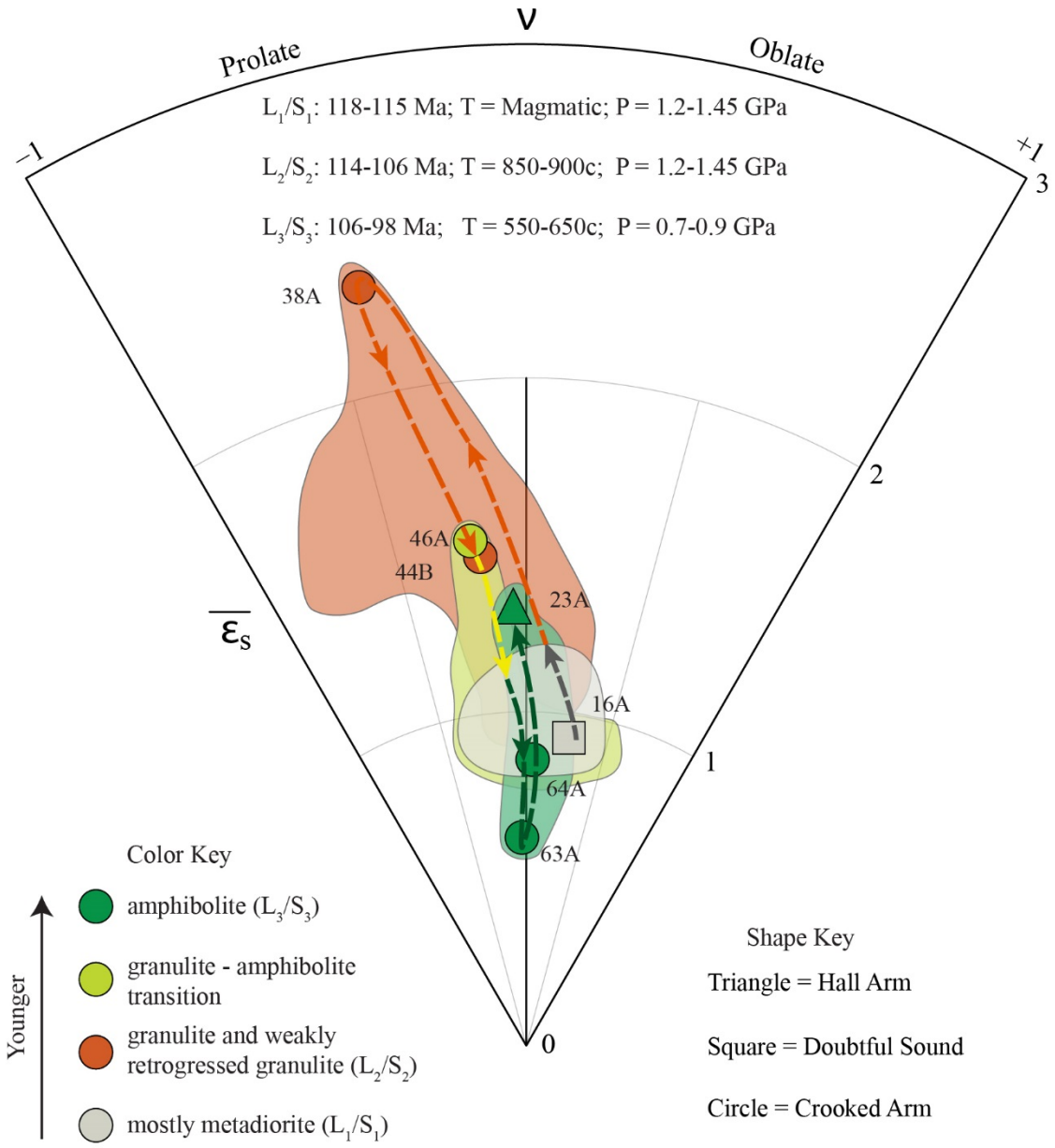

Figure 64. A Nadai Plot showing the strain path from D_1 (grey) to D_2 (orange) to D_3 (yellow and green). PTt data is included to show the conditions during each deformation event (Gibson and Ireland, 1995; Tulloch and Kimbrough, 2003; Hollis et al., 2004; Klepeis et al., 2007; King et al., 2008; Stowell et al., 2014; Klepeis et al., 2016; Schwartz et al., 2016).

BIBLIOGRAPHY

Afonso, J. C., & Ranalli, G. (2004). Crustal and mantle strengths in continental lithosphere: is the jelly sandwich model obsolete? Tectonophysics, 394(3–4), 221-232. doi:10.1016/j.tecto.2004.08.006

Allibone, A., Jongens, R., Scott, J., Tulloch, A., Turnbull, I., Cooper, A. Rattenbury, M. (2009). Plutonic rocks of the Median Batholith in eastern and central Fiordland, New Zealand: field relations, geochemistry, correlation, and nomenclature. New Zealand journal of geology and geophysics, 52(2), 101-148.

Allibone, A., Milan, L., Daczko, N., & Turnbull, I. (2009). Granulite facies thermal aureoles and metastable amphibolite facies assemblages adjacent to the Western Fiordland Orthogneiss in southwest Fiordland, New Zealand. Journal of Metamorphic Geology, 27(5), 349-369.

Alsleben, H., Wetmore, P., Schmidt, K., Paterson, S., & Melis, E. (2008). Complex deformation during arc-continent collision: Quantifying finite strain in the accreted Alisitos arc, Peninsular Ranges batholith, Baja California. Journal of Structural Geology, 30(2), 220-236.

Betka, P. M., & Klepeis, K. A. (2013). Three-stage evolution of lower crustal gneiss domes at Breaksea Entrance, Fiordland, New Zealand. Tectonics, 32(5), 1084-1106.

Bonamici, C. E., Tikoff, B., & Goodwin, L. B. (2011). Anatomy of a 10 km scale sheath fold, Mount Hay ridge, Arunta Region, central Australia: The structural record of deep crustal flow. Tectonics, 30(6).

Bradshaw, J. (1989). Origin and metamorphic history of an Early Cretaceous polybaric granulite terrain, Fiordland, southwest New Zealand. Contributions to mineralogy and petrology, 103(3), 346-360.

Brown, M., & Solar, G. (2000). Feedback relations between deformation and melt, the evolution from weakening to hardening in transpressive orogens. Journal of GEOsciences, 45(3-4), 215-210.

Bürgmann, R., & Dresen, G. (2008). Rheology of the lower crust and upper mantle: Evidence from rock mechanics, geodesy, and field observations. Annu. Rev. Earth Planet. Sci., 36, 531-567.

Bystricky, M., & Mackwell, S. (2001). Creep of dry clinopyroxene aggregates. J. Geophys. Res., 106(B7), 13443-13454. doi:10.1029/2001jb000333

Culshaw, N., Gerbi, C., Marsh, J., & Plug, L. (2011). Heterogeneous amphibolite facies deformation of a granulite facies layered protolith: Matches Island shear system, Parry Sound domain, Grenville Province, Ontario, Canada. Journal of Structural Geology, 33(5), 875-890. doi:10.1016/j.jsg.2011.03.005

Czeck, D. M., Fissler, D. A., Horsman, E., & Tikoff, B. (2009). Strain analysis and rheology contrasts in polymictic conglomerates: An example from the Seine metaconglomerates, Superior Province, Canada. Journal of Structural Geology, 31(11), 1365-1376. doi:10.1016/j.jsg.2009.08.004

Daczko, N. R., Klepeis, K. A., & Clarke, G. L. (2002). Thermomechanical evolution of the crust during convergence and deep crustal pluton emplacement in the Western Province of Fiordland, New Zealand. Tectonics, 21(4), 1022.

Dumond, G., Goncalves, P., Williams, M. L., & Jercinovic, M. J. (2010). Subhorizontal fabric in exhumed continental lower crust and implications for lower crustal flow: Athabasca granulite terrane, western Canadian Shield. Tectonics, 29(2).

Dunnet, D. (1969). A technique of finite strain analysis using elliptical particles. Tectonophysics, 7(2), 117-136.

Flowers, R., Bowring, S., Tulloch, A., & Klepeis, K. (2005). Tempo of burial and exhumation within the deep roots of a magmatic arc, Fiordland, New Zealand. Geology, 33(1), 17.

Gerbi, C., Culshaw, N., & Marsh, J. (2010). Magnitude of weakening during crustal-scale shear zone development. Journal of Structural Geology, 32(1), 107-117.

Gibson, G., & Ireland, T. (1995). Granulite formation during continental extension in Fiordland, New Zealand. Nature, 375(6531), 479-482.

Gibson, G., McDougall, I., & Ireland, T. (1988). Age constraints on metamorphism and the development of a metamorphic core complex in Fiordland, southern New Zealand. Geology, 16(5), 405.

Hollis, J., Clarke, G., Klepeis, K., Daczko, N., & Ireland, T. (2004). The regional significance of Cretaceous magmatism and metamorphism in Fiordland, New Zealand, from U–Pb zircon geochronology. Journal of Metamorphic Geology, 22(7), 607-627.

Ji, S., & Mainprice, D. (1990). Recrystallization and fabric development in plagioclase. The Journal of geology, 65-79.

King, D. S., Klepeis, K. A., Goldstein, A. G., Gehrels, G. E., & Clarke, G. L. (2008). The initiation and evolution of the transpressional Straight River shear zone, central Fiordland, New Zealand. Journal of Structural Geology, 30(4), 410-430.

Klepeis, K. A., King, D., De Paoli, M., Clarke, G. L., & Gehrels, G. (2007). Interaction of strong lower and weak middle crust during lithospheric extension in western New Zealand. Tectonics, 26(4), TC4017.

Klepeis, K. A., Schwartz, J., Stowell, H., & Tulloch, A. (2016). Gneiss domes, vertical and horizontal mass transfer, and the initiation of extension in the hot lower-crustal root of a continental arc, Fiordland, New Zealand. Lithosphere, 8(2), 116-140.

Kruse, R., & Stünitz, H. (1999). Deformation mechanisms and phase distribution in mafic high-temperature mylonites from the Jotun Nappe, southern Norway. Tectonophysics, 303(1), 223-249.

Labrousse, L., Prouteau, G., & Ganzhorn, A. C. (2011). Continental exhumation triggered by partial melting at ultrahigh pressure. Geology.

Launeau, P., & Robin, P.-Y. F. (2005). Determination of fabric and strain ellipsoids from measured sectional ellipses—implementation and applications. Journal of Structural Geology, 27(12), 2223-2233. doi:10.1016/j.jsg.2005.08.003

Lisle, R. J. (1977). Estimation of the tectonic strain ratio from the mean shape of deformed elliptical objects. Geologie en Mijnbouw, 56(2), 140-144.

Lisle, R. J. (1985). Geological Strain Analysis: A Manual for the RF/0 Method. Pergamon Press inc., Maxwell House, Fairview Park, Elmsford, New York, 10523, U.S.A: Pergamon press.

Mattinson, J., Kimbrough, D., & Bradshaw, J. (1986). Western Fiordland orthogneiss: Early Cretaceous arc magmatism and granulite facies metamorphism, New Zealand. Contributions to mineralogy and petrology, 92(3), 383-392.

McCulloch, M., Bradshaw, J., & Taylor, S. (1987). Sm-Nd and Rb-Sr isotopic and geochemical systematics in Phanerozoic granulites from Fiordland, southwest New Zealand. Contributions to mineralogy and petrology, 97(2), 183-195.

Mehl, L., & Hirth, G. (2008). Plagioclase preferred orientation in layered mylonites: Evaluation of flow laws for the lower crust. J. Geophys. Res., 113(B5), B05202. doi:10.1029/2007jb005075

Mortimer, N. (2008). Zealandia. ASEG Extended Abstracts, 2006(1), 1-4.

Mulchrone, K. F., & Meere, P. A. (2001). A Windows program for the analysis of tectonic strain using deformed elliptical markers. Computers & Geosciences, 27(10), 1251-1255.

Mulchrone, K. F., Meere, P. A., & Choudhury, K. R. (2005). SAPE: a program for semi-automatic parameter extraction for strain analysis. Journal of Structural Geology, 27(11), 2084-2098. doi:10.1016/j.jsg.2005.05.019

Oliver, G. (1980). Geology of the granulite and amphibolite facies gneisses of Doubtful Sound, Fiordland, New Zealand. New Zealand journal of geology and geophysics, 23(1), 27-41.

Oliver, G. (1990). An exposed cross-section of continental crust, Doubtful Sound Fiordland, New Zealand; Geophysical and Geological setting. Exposed Cross-Sections of the Continental Crust, 43-69.

Oliver, G. J. H. (1976). The high grade metamorphic rocks of Doubtful Sound, Fiordland, New Zealand: a study of the lower crust. University of Otago.

Passchier, C., & Coelho, S. (2006). An outline of shear-sense analysis in high-grade rocks. Gondwana Research, 10(1), 66-76.

Passchier, C. W., & Trouw, R. A. J. (2005). Microtectonics: Springer.

Ponce, C., Druguet, E., & Carreras, J. (2012). Development of shear zone-related lozenges in foliated rocks. Journal of Structural Geology (0). doi:10.1016/j.jsg.2012.04.001

Ramsay, J. (1967). Folding and fracturing of rocks (Vol. 56). New York New York: McGraw-Hill.

Ramsay, J. (1976). Displacement and strain. Philosophical Transactions of the Royal Society of London. Series A, Mathematical and Physical Sciences, 283(1312), 3-25.

Ramsay, J., & Huber, M. (1983). The techniques of modem structural geology. Vol. 1. Strain Analysis. London.

Reilly, W. I. (1965). Gravity map of New Zealand 1:4,000,000 (1 ed.). N.Z Department of Scientific and Industrial Research, Wellington.

Rosenberg, C. L., & Stünitz, H. (2003). Deformation and recrystallization of plagioclase along a temperature gradient: an example from the Bergell tonalite. Journal of Structural Geology, 25(3), 389-408.

Rybacki, E., & Dresen, G. (2004). Deformation mechanism maps for feldspar rocks. Tectonophysics, 382(3), 173-187.

Sadorski, J. (2015). Time scales of continental arc root construction and deep crustal magmatic flux rates: insights from U-Pb zircon geochronology of a Triassic-Cretaceous arc, Fiordland, New Zealand. California State University, Northridge.

Schwartz, J. J., Stowell, H.H, Klepeis, K.A., Zamora, C., Tulloch, A.J., Kylander-Clark, A.R.C., Hacker, B.R., and Coble, M. (2016). Thermochronology of extensional orogenic collapse in the deep crust, Fiordland, New Zealand. Geosphere, In Press.

Spell, T. L., McDougall, I., & Tulloch, A. J. (2000). Thermochronologic constraints on the breakup of the Pacific Gondwana margin: The Paparoa metamorphic core complex, South Island, New Zealand. Tectonics, 19(3), 433-451.

Stokes, M., Wintsch, R., & Southworth, C. (2012). Deformation of amphibolites via dissolution–precipitation creep in the middle and lower crust. Journal of Metamorphic Geology, 30(7), 723-737.

Stowell, H., Parker, K. O., Gatewood, M., Tulloch, A., & Koenig, A. (2014). Temporal links between pluton emplacement, garnet granulite metamorphism, partial melting and extensional collapse in the lower crust of a Cretaceous magmatic arc, Fiordland, New Zealand. Journal of Metamorphic Geology.

Tulloch, A. J., & Kimbrough, D. L. (2003). Paired plutonic belts in convergent margins and the development of high Sr/Y magmatism: Peninsular Ranges batholith of Baja-California and Median batholith of New Zealand. Special paper-Geological Society of America (374), 275-295.

Turner, F. (1939). Hornblende-gneisses, marbles and associated rocks from Doubtful Sound, Fiordland, New Zealand. 68, 570-598.

Waters-Tormey, C., & Tikoff, B. (2007). Characteristics of a kilometer-scale high strain zone in the lower continental crust: Mt. Hay block, central Australia. Journal of Structural Geology, 29(4), 562-582. doi:10.1016/j.jsg.2006.10.011

Webber, J. (2012). Advances in rock fabric quantification and the reconstruction of progressive dike emplacement in the Coastal Batholith of Central Chile. (Msc), University of Vermont.

Webber, J. R., Klepeis, K. A., Webb, L. E., Cembrano, J., Morata, D., Mora-Klepeis, G., & Arancibia, G. (2015). Deformation and magma transport in a crystallizing plutonic complex, Coastal Batholith, central Chile. Geosphere, 11(5), 1401-1426.

Whitney, D. L., & Evans, B. W. (2010). Abbreviations for names of rock-forming minerals. American Mineralogist, 95(1), 185.

Woodward, D. (1972). Gravity anomalies in Fiordland, south-west New Zealand. New Zealand journal of geology and geophysics, 15(1), 22-32.

Xypolias, P., Chatzaras, V., & Koukouvelas, I. (2007). Strain gradients in zones of ductile thrusting: Insights from the External Hellenides. Journal of Structural Geology, 29(9), 1522-1537.

APPENDIX A

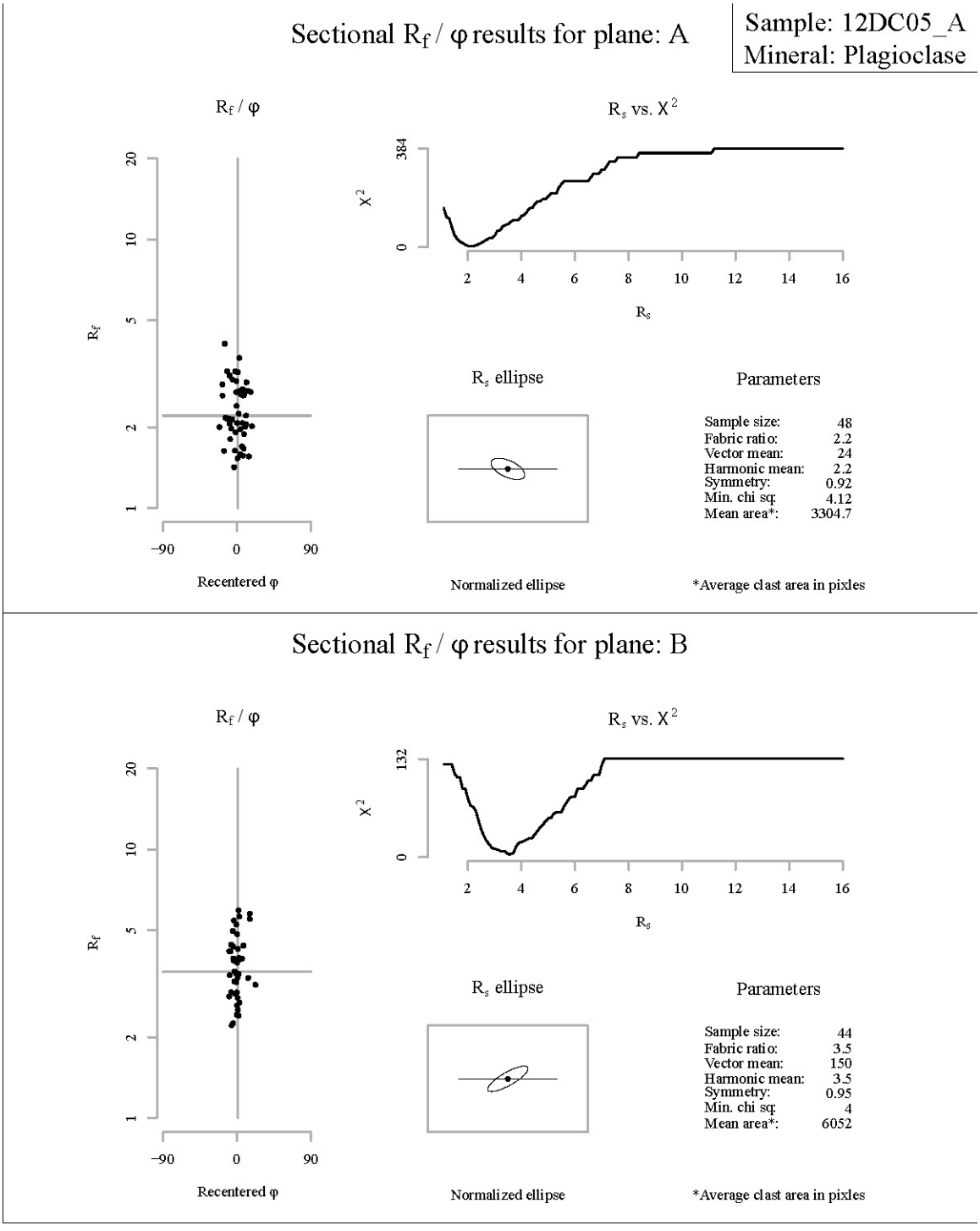
Sectional R_f / φ results for plane: A
Sample: 12DC05_A
Mineral: Plagioclase
R_f / φ
R_s vs. X^2
Recentered φ
R_s ellipse
Parameters
Sample size: 48
Fabric ratio: 2.2
Vector mean: 24
Harmonic mean: 2.2
Symmetry: 0.92
Min. chi sq: 4.12
Mean area*: 3304.7
Normalized ellipse
*Average clast area in pixles
Sectional R_f / φ results for plane: B
R_f / φ
R_s vs. X^2
Recentered φ
R_s ellipse
Parameters
Sample size: 44
Fabric ratio: 3.5
Vector mean: 150
Harmonic mean: 3.5
Symmetry: 0.95
Min. chi sq: 4
Mean area*: 6052
Normalized ellipse
*Average clast area in pixles

Sectional R_f / ϕ results for plane: C

Sample: 12DC05_A
Mineral: Plagioclase

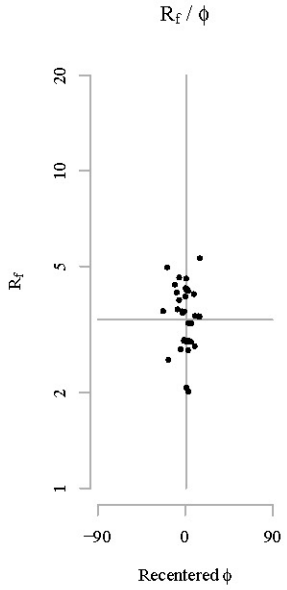

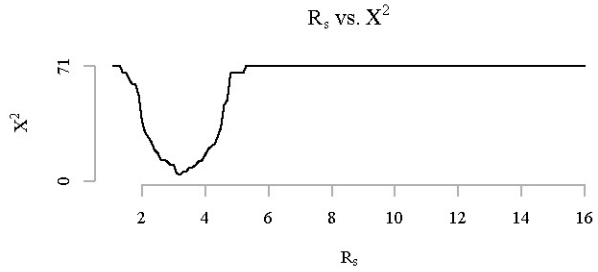

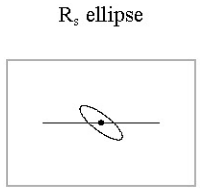

Normalized ellipse

Parameters

Sample size:	34
Fabric ratio:	3.2
Vector mean:	38
Harmonic mean:	3.4
Symmetry:	0.82
Min. chi sq:	3.76
Mean area*:	9660

*Average clast area in pixles

Stereonet

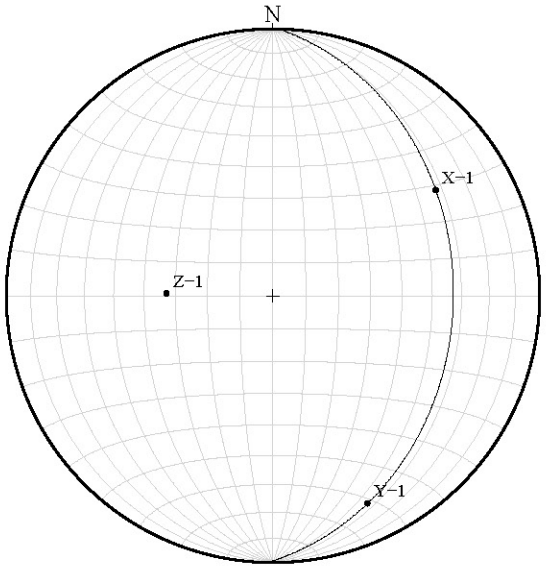

Nadai plot

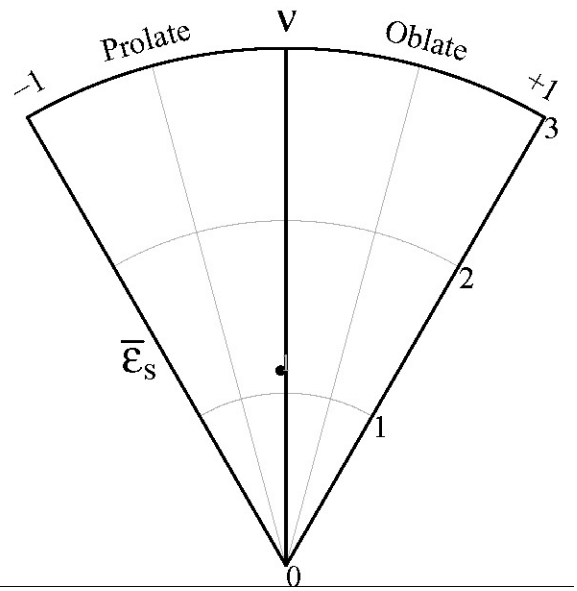

Sectional R_f / φ results for plane: A

Sample: 12DC07_A
Mineral: Plagioclase

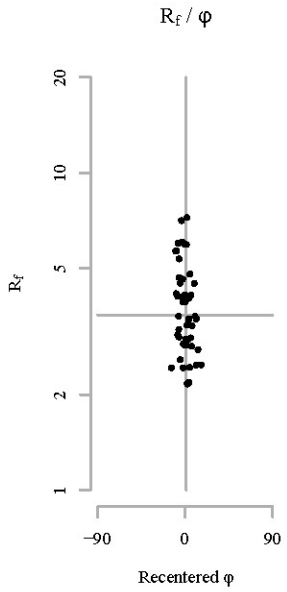

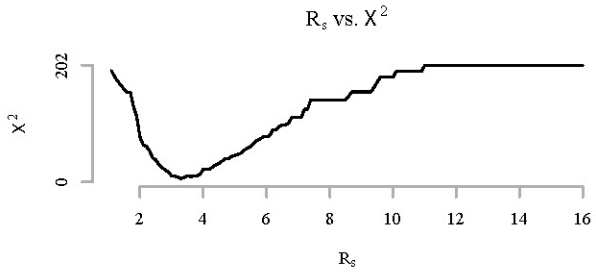

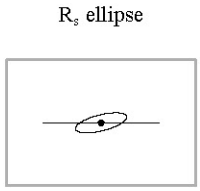

Normalized ellipse

Parameters

Sample size:	50
Fabric ratio:	3.3
Vector mean:	166
Harmonic mean:	3.6
Symmetry:	0.64
Min. chi sq:	5.6
Mean area*:	6014.4

*Average clast area in pixles

Sectional R_f / φ results for plane: B

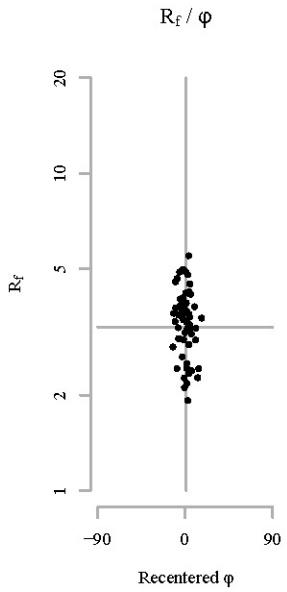

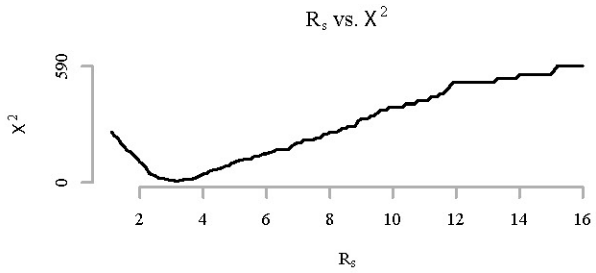

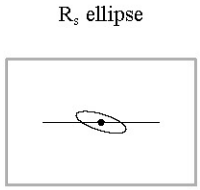

Normalized ellipse

Parameters

Sample size:	59
Fabric ratio:	3.2
Vector mean:	17
Harmonic mean:	3.3
Symmetry:	0.88
Min. chi sq:	6.44
Mean area*:	3115.4

*Average clast area in pixles

Sectional R_f / φ results for plane: C

Sample: 12DC07_A
Mineral: Plagioclase

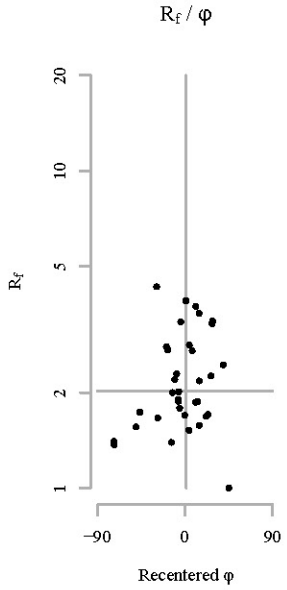

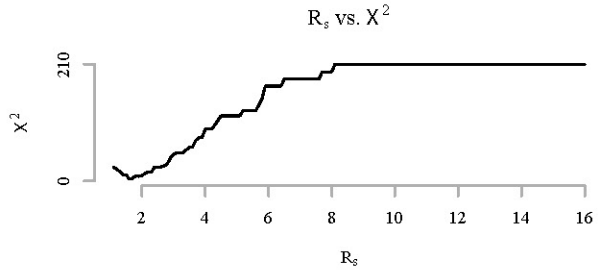

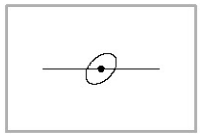

Normalized ellipse

Parameters

Sample size:	35
Fabric ratio:	1.6
Vector mean:	135
Harmonic mean:	2
Symmetry:	0.74
Min. chi sq:	3.2
Mean area*:	818718.7

*Average clast area in pixles

Stereonet

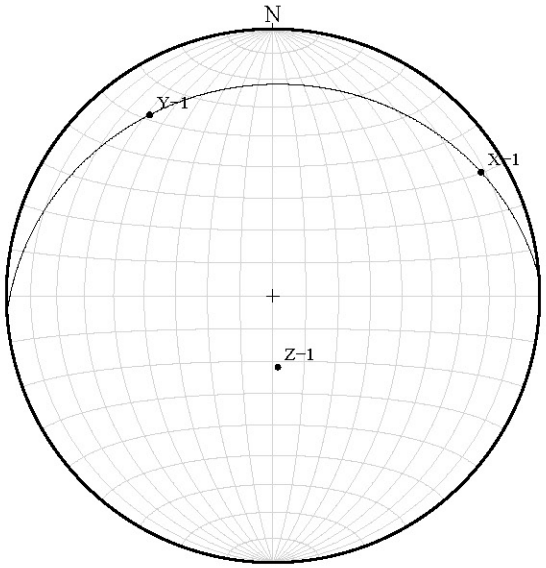

Nadai plot

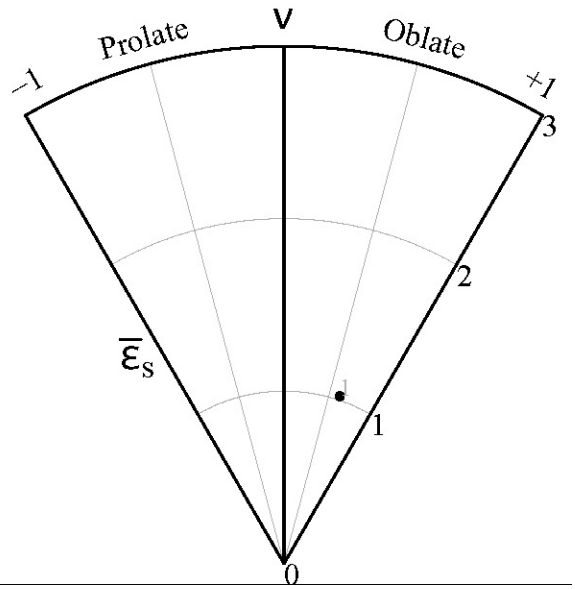

Sectional R_f / φ results for plane: A

Sample: 12DC10_A
Mineral: Hornblende

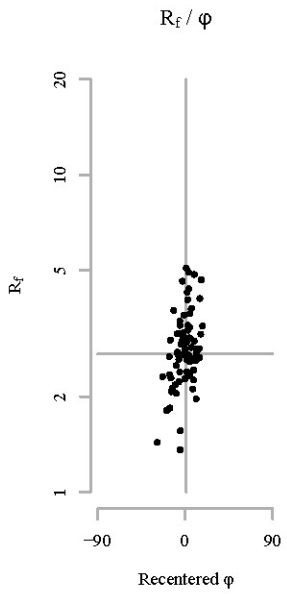

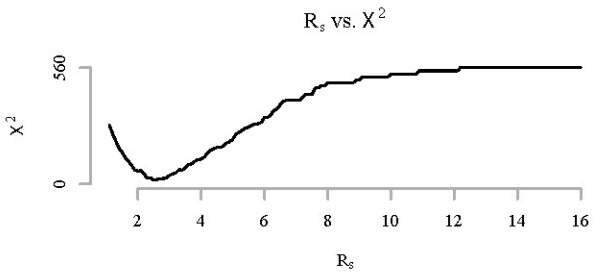

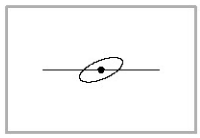

Normalized ellipse

Parameters

Sample size:	80
Fabric ratio:	2.5
Vector mean:	157
Harmonic mean:	2.7
Symmetry:	0.85
Min. chi sq:	18
Mean area*:	7013.6

*Average clast area in pixles

Sectional R_f / φ results for plane: B

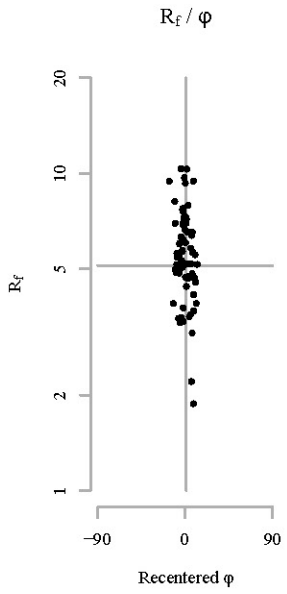

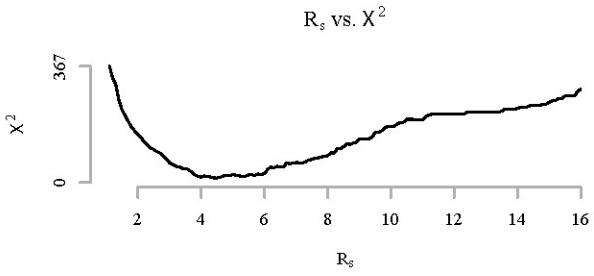

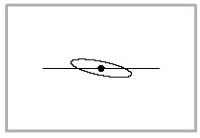

Normalized ellipse

Parameters

Sample size:	69
Fabric ratio:	4.5
Vector mean:	11
Harmonic mean:	5.1
Symmetry:	0.9
Min. chi sq:	13.71
Mean area*:	5426.1

*Average clast area in pixles

Sectional R_f / φ results for plane: C

Sample: 12DC10_A
Mineral: Hornblende

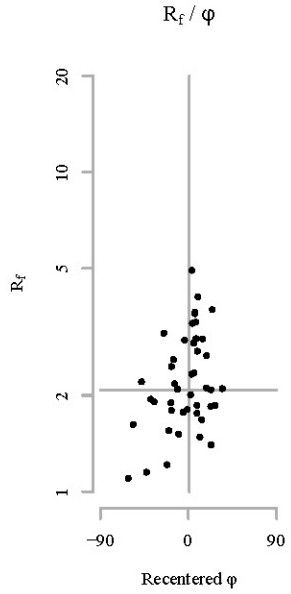

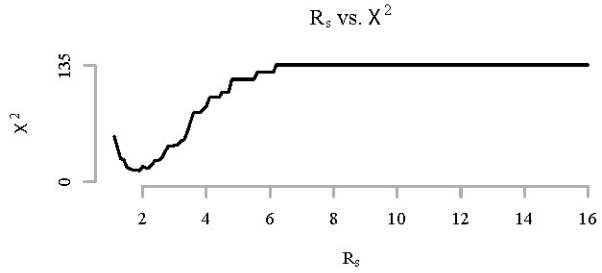

R_s ellipse

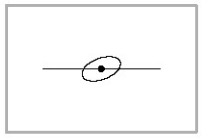

Normalized ellipse

Parameters

Sample size:	44
Fabric ratio:	1.9
Vector mean:	159
Harmonic mean:	2.1
Symmetry:	0.68
Min. chi sq:	12.36
Mean area*:	26643.3

*Average clast area in pixles

Stereonet

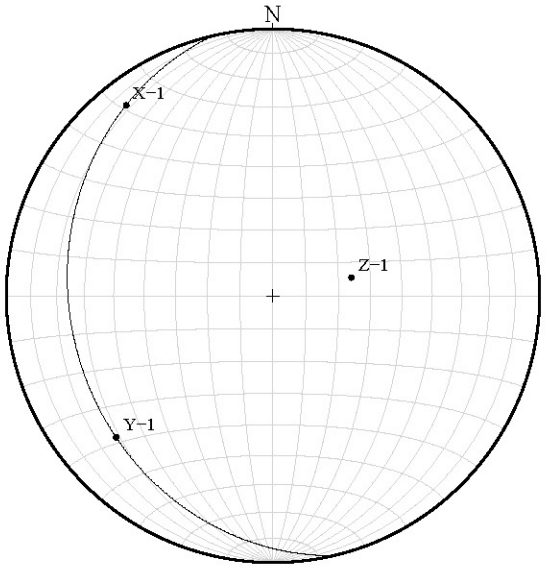

Nadai plot

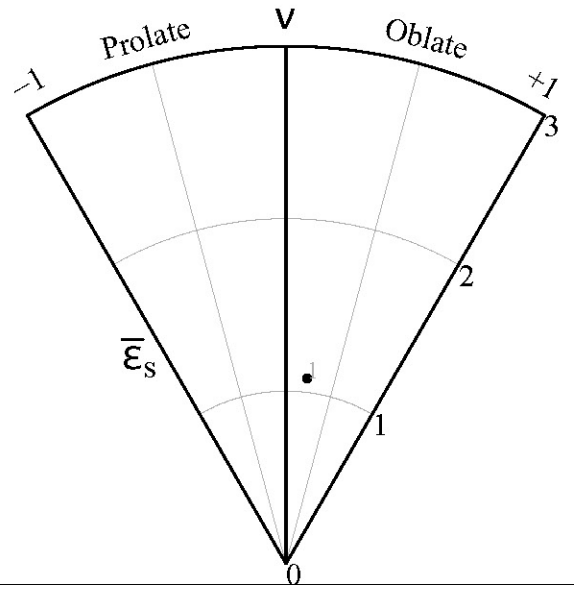

Sectional R_f / φ results for plane: A

Sample: 12DC10_A
Mineral: Plagioclase

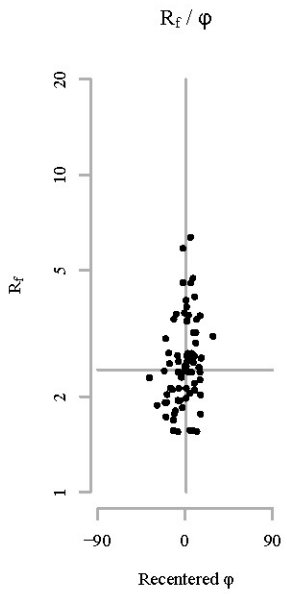

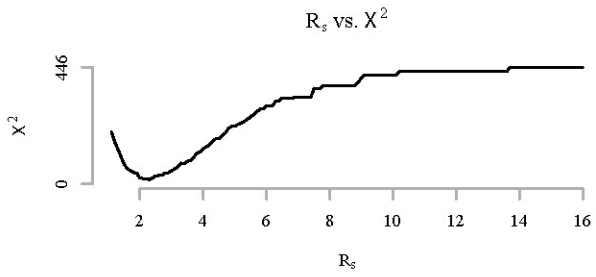

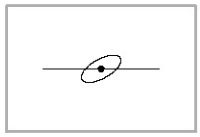

Normalized ellipse

Parameters

Sample size:	73
Fabric ratio:	2.3
Vector mean:	151
Harmonic mean:	2.4
Symmetry:	0.68
Min. chi sq:	16.56
Mean area*:	8888.1

*Average clast area in pixles

Sectional R_f / φ results for plane: B

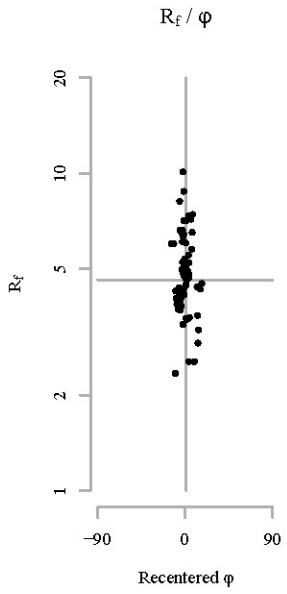

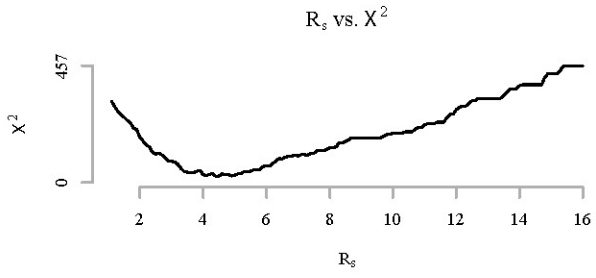

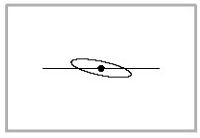

Normalized ellipse

Parameters

Sample size:	68
Fabric ratio:	4.4
Vector mean:	12
Harmonic mean:	4.6
Symmetry:	0.88
Min. chi sq:	23.38
Mean area*:	12847.7

*Average clast area in pixles

Sectional R_f / φ results for plane: C

Sample: 12DC10_A
Mineral: Plagioclase

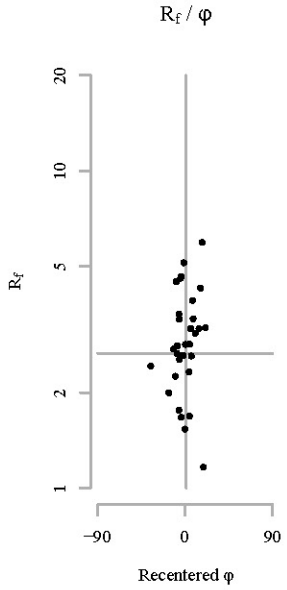

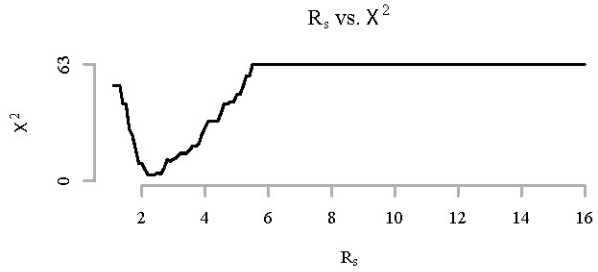

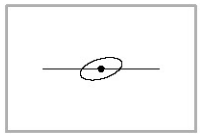

Parameters

Sample size:	31
Fabric ratio:	2.2
Vector mean:	163
Harmonic mean:	2.7
Symmetry:	0.84
Min. chi sq:	3.26
Mean area*:	32884.7

*Average clast area in pixles

Stereonet

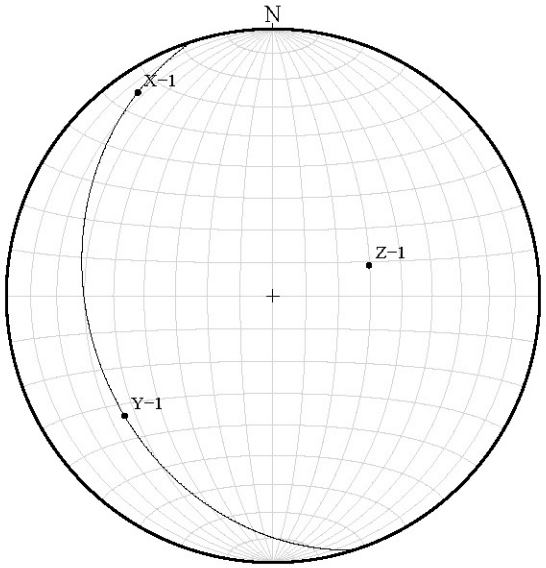

Nadai plot

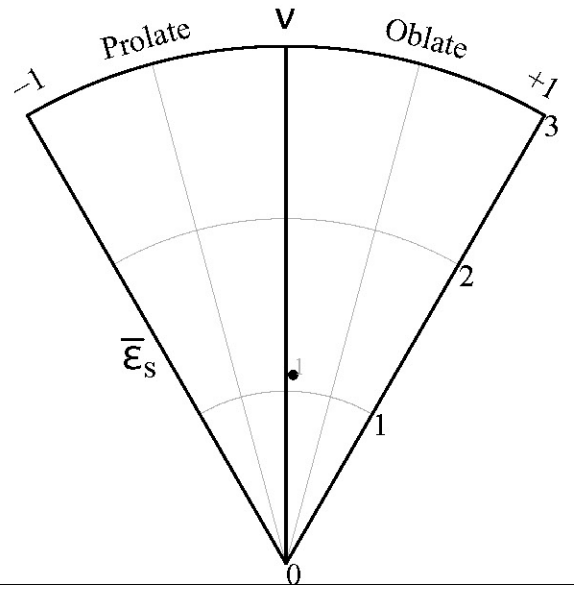

Sectional R_f / φ results for plane: A

Sample: 12DC12_A
Mineral: Hornblende

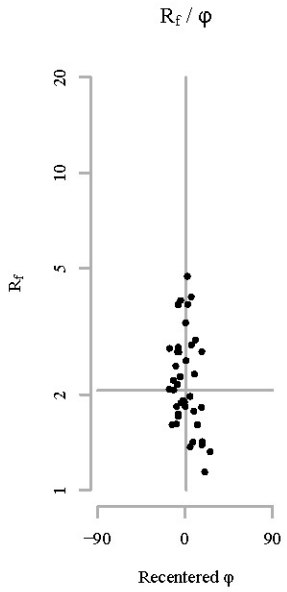

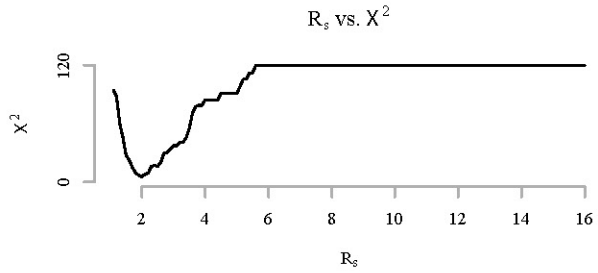

Rs ellipse

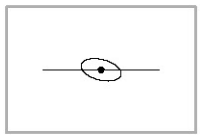

Normalized ellipse

Parameters

Sample size:	40
Fabric ratio:	2
Vector mean:	14
Harmonic mean:	2.1
Symmetry:	0.85
Min. chi sq:	5.2
Mean area*:	12844.2

*Average clast area in pixles

Sectional R_f / φ results for plane: B

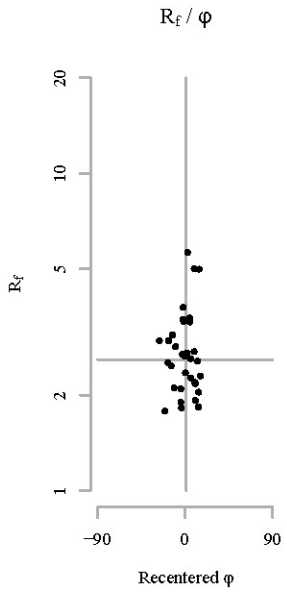

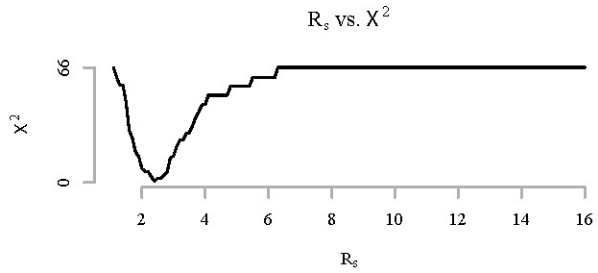

Rs ellipse

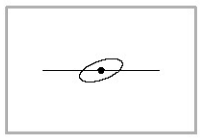

Normalized ellipse

Parameters

Sample size:	33
Fabric ratio:	2.4
Vector mean:	161
Harmonic mean:	2.6
Symmetry:	0.91
Min. chi sq:	0.64
Mean area*:	8204.5

*Average clast area in pixles

Sectional R_f / φ results for plane: C

Sample: 12DC12_A
Mineral: Hornblende

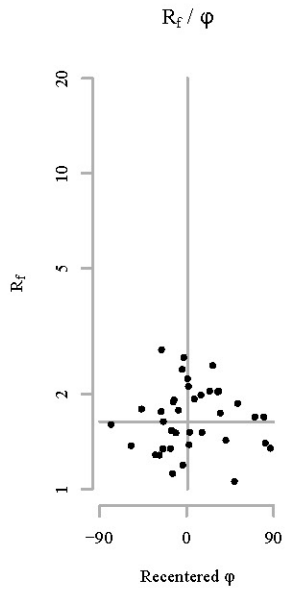

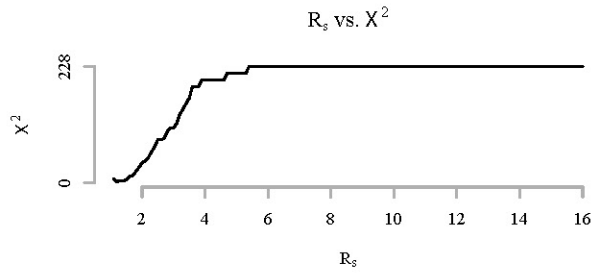

R_s ellipse

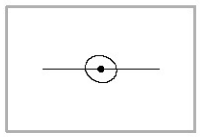

Normalized ellipse

Parameters

Sample size:	38
Fabric ratio:	1.2
Vector mean:	18
Harmonic mean:	1.6
Symmetry:	0.84
Min. chi sq:	1.42
Mean area*:	25675.4

*Average clast area in pixles

Stereonet

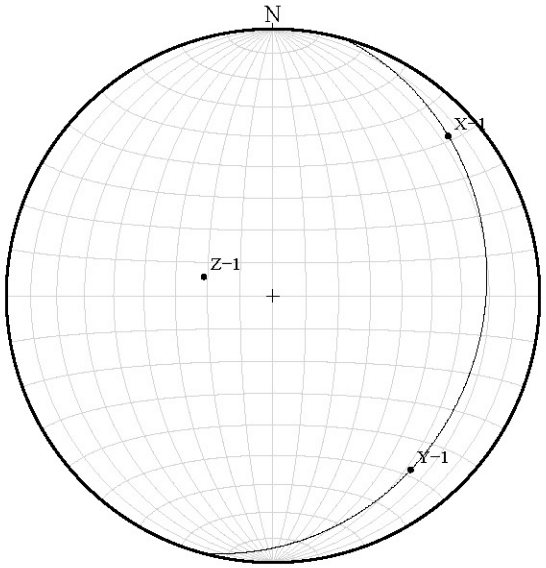

Nadai plot

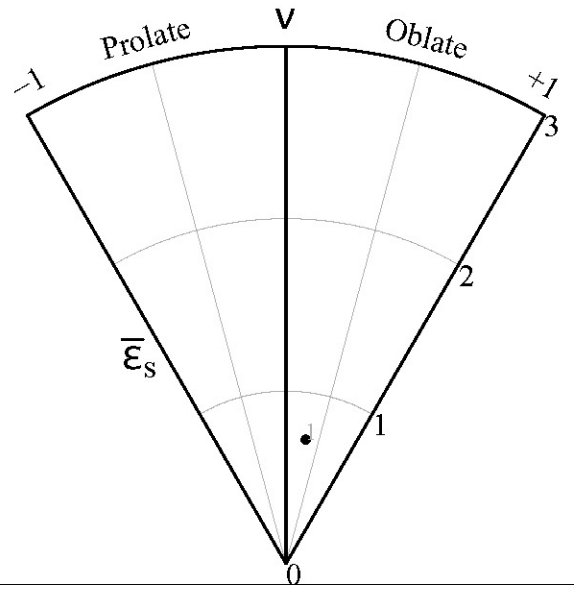

Sectional R_f / φ results for plane: A

Sample: 12DC12_A
Mineral: Plagioclase

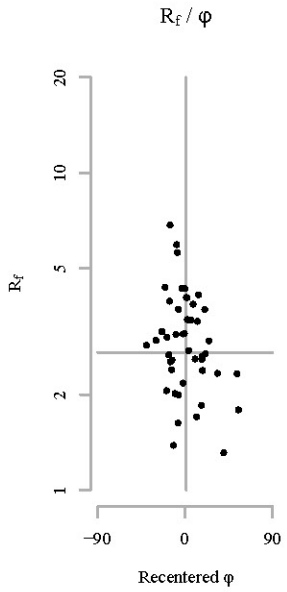

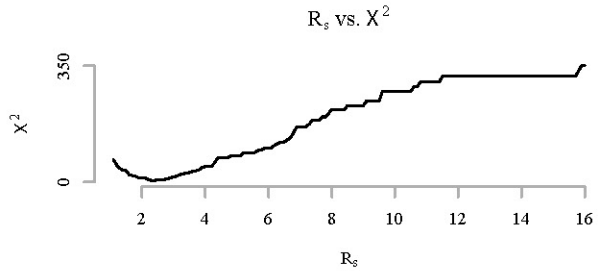

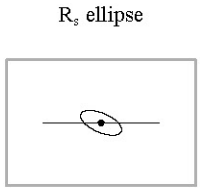

Normalized ellipse

Parameters

Sample size:	46
Fabric ratio:	2.3
Vector mean:	23
Harmonic mean:	2.7
Symmetry:	0.87
Min. chi sq:	4.09
Mean area*:	26042.7

*Average clast area in pixles

Sectional R_f / φ results for plane: B

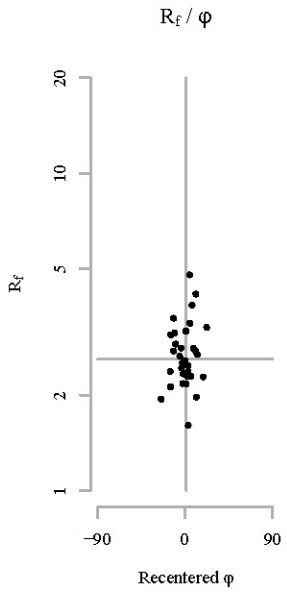

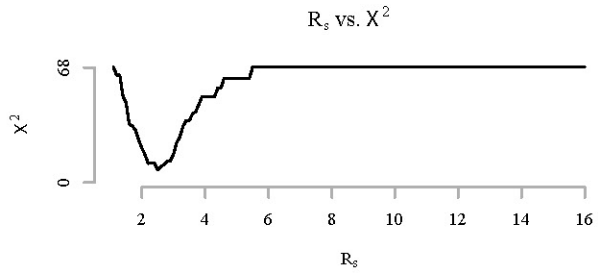

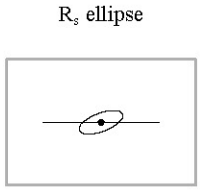

Normalized ellipse

Parameters

Sample size:	33
Fabric ratio:	2.5
Vector mean:	159
Harmonic mean:	2.6
Symmetry:	0.85
Min. chi sq:	7.55
Mean area*:	22584.3

*Average clast area in pixles

Sectional R_f / φ results for plane: C

Sample: 12DC12_A
Mineral: Plagioclase

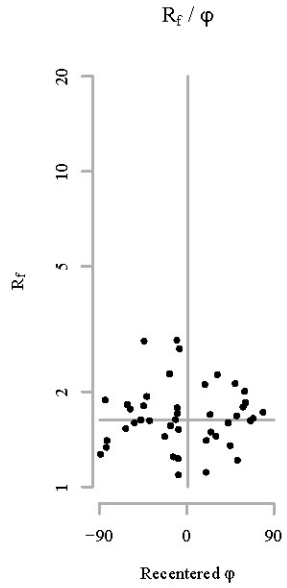

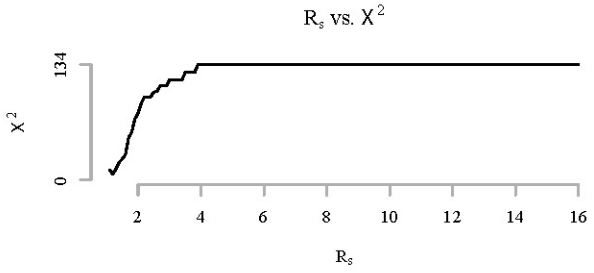

R_s ellipse

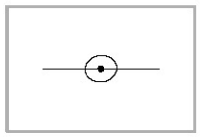

Normalized ellipse

Parameters

Sample size:	43
Fabric ratio:	1.2
Vector mean:	172
Harmonic mean:	1.6
Symmetry:	0.84
Min. chi sq:	7.05
Mean area*:	34966.8

*Average clast area in pixles

Stereonet

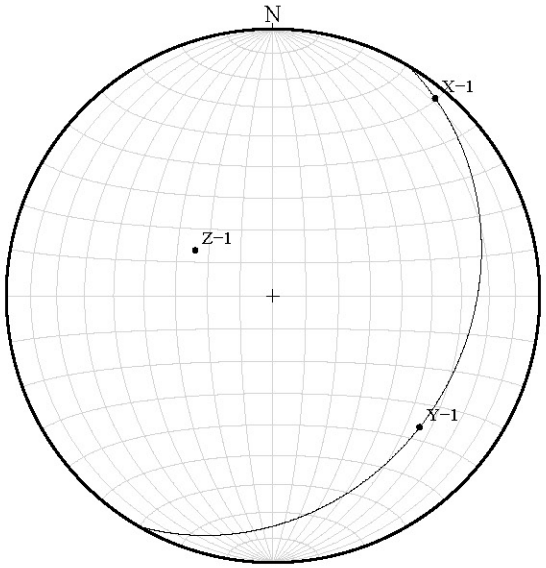

Nadai plot

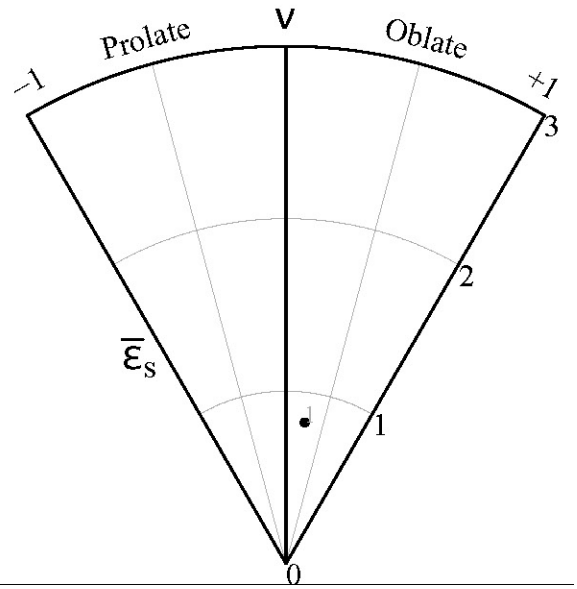

Sectional R_f / φ results for plane: A

Sample: 12DC13_A
Mineral: Hornblende

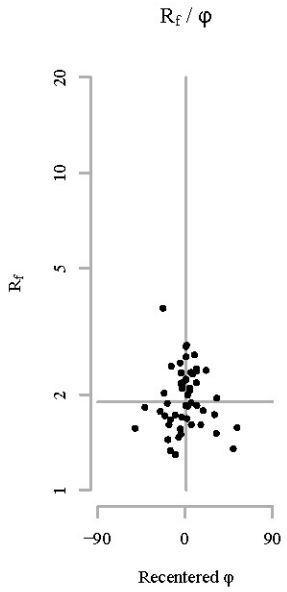

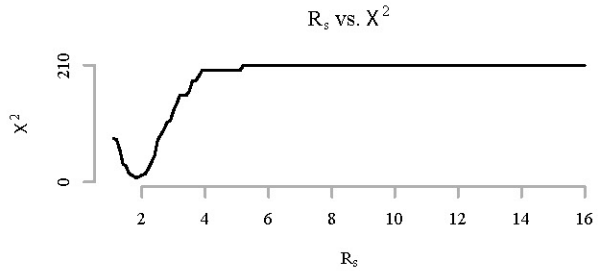

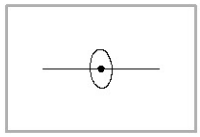

Normalized ellipse

Parameters

Sample size:	52
Fabric ratio:	1.8
Vector mean:	87
Harmonic mean:	1.9
Symmetry:	0.81
Min. chi sq:	7.62
Mean area*:	6545.4

*Average clast area in pixles

Sectional R_f / φ results for plane: B

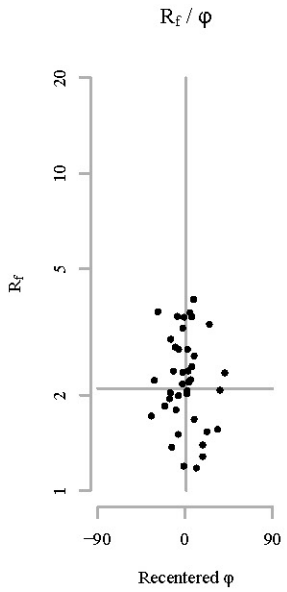

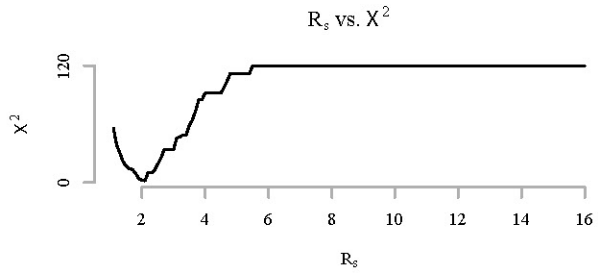

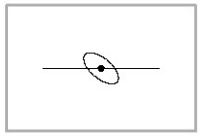

Normalized ellipse

Parameters

Sample size:	40
Fabric ratio:	2.1
Vector mean:	40
Harmonic mean:	2.1
Symmetry:	1
Min. chi sq:	1.6
Mean area*:	3137.4

*Average clast area in pixles

Sectional R_f / φ results for plane: C

Sample: 12DC13_A
Mineral: Hornblende

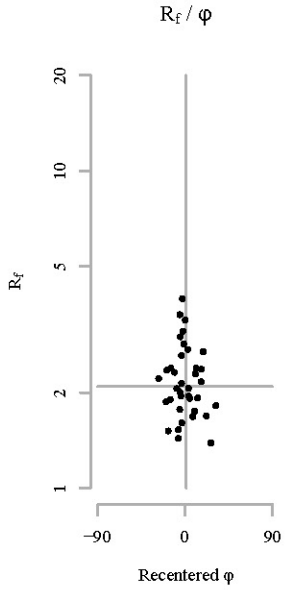

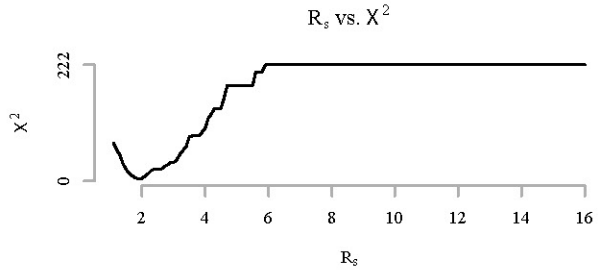

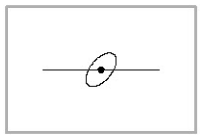

Parameters

Sample size:	37
Fabric ratio:	1.9
Vector mean:	129
Harmonic mean:	2.1
Symmetry:	0.86
Min. chi sq:	3.3
Mean area*:	3852

*Average clast area in pixles

Stereonet

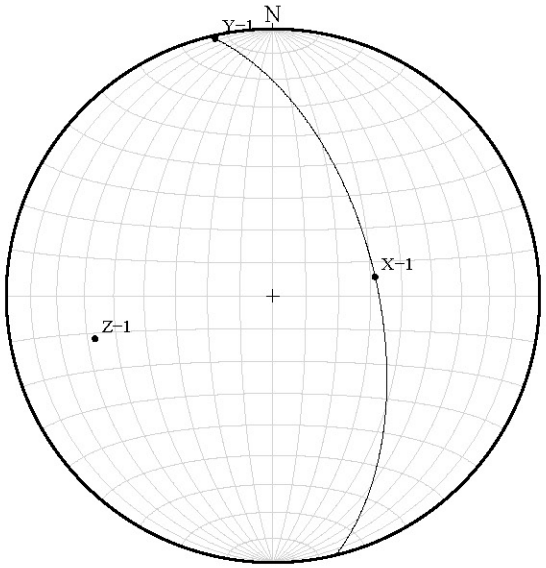

Nadai plot

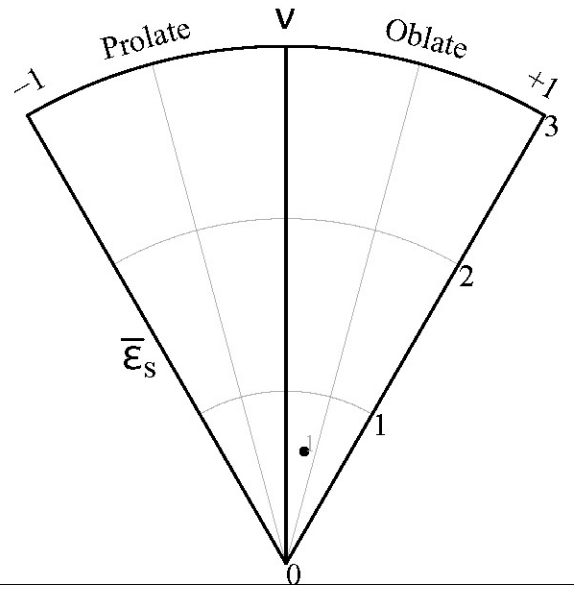

Sectional R_f / φ results for plane: A

Sample: 12DC13_A
Mineral: Plagioclase

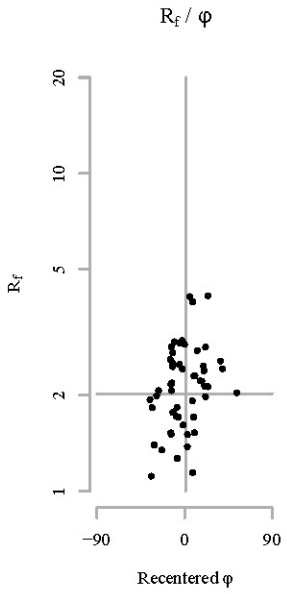

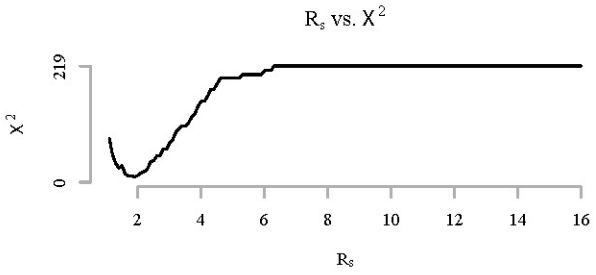

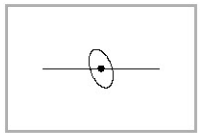

Normalized ellipse

Parameters

Sample size:	54
Fabric ratio:	1.9
Vector mean:	71
Harmonic mean:	2
Symmetry:	0.81
Min. chi sq:	10.07
Mean area*:	6612

*Average clast area in pixles

Sectional R_f / φ results for plane: B

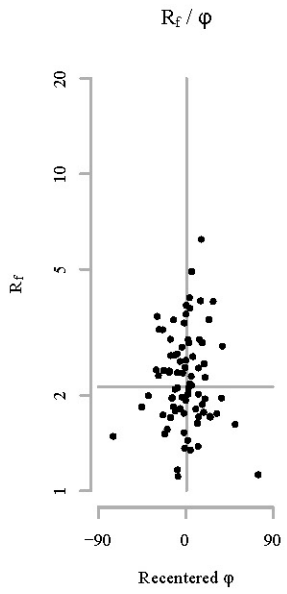

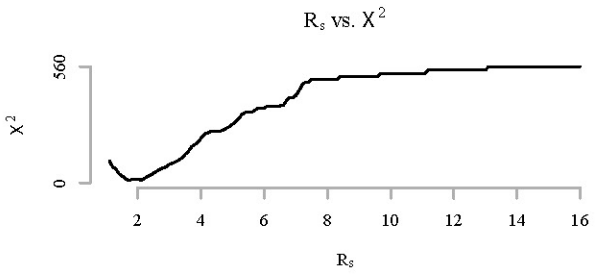

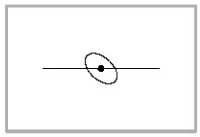

Normalized ellipse

Parameters

Sample size:	80
Fabric ratio:	1.7
Vector mean:	42
Harmonic mean:	2.1
Symmetry:	0.95
Min. chi sq:	12.8
Mean area*:	3856.1

*Average clast area in pixles

Sectional R_f / φ results for plane: C

Sample: 12DC13_A
Mineral: Plagioclase

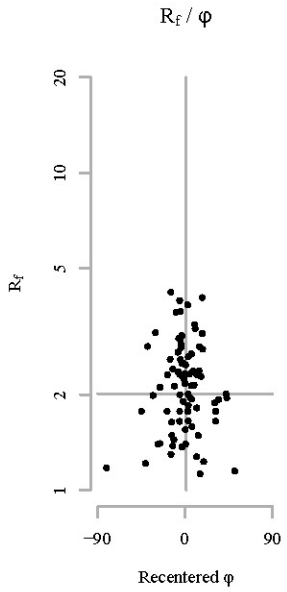

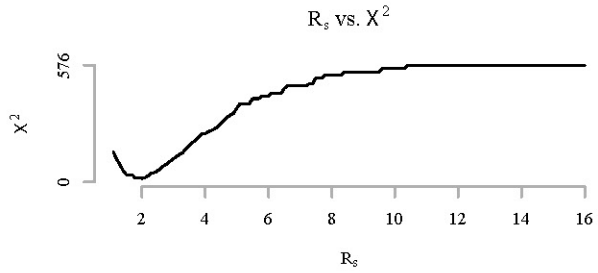

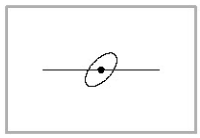

Parameters

Sample size:	82
Fabric ratio:	2
Vector mean:	132
Harmonic mean:	2
Symmetry:	0.88
Min. chi sq:	17.12
Mean area*:	4088.7

*Average clast area in pixles

Stereonet

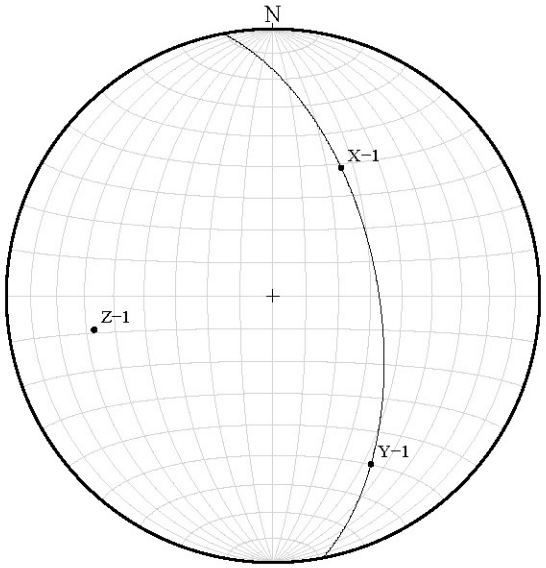

Nadai plot

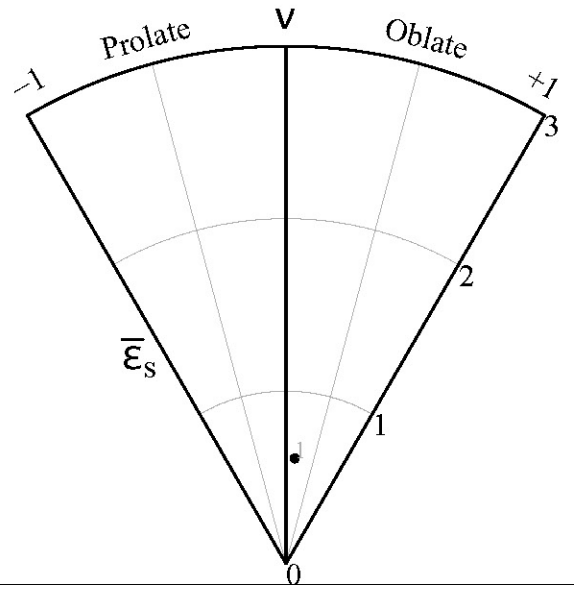

Sectional R_f / φ results for plane: A

Sample: 12DC16_A
Mineral: Hornblende

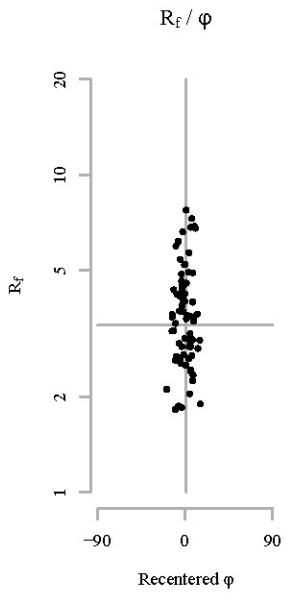

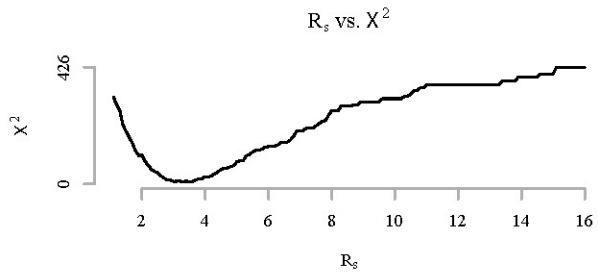

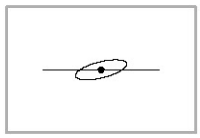

Normalized ellipse

Parameters

Sample size:	73
Fabric ratio:	3.3
Vector mean:	166
Harmonic mean:	3.4
Symmetry:	0.9
Min. chi sq:	7.74
Mean area*:	7333.1

*Average clast area in pixles

Sectional R_f / φ results for plane: B

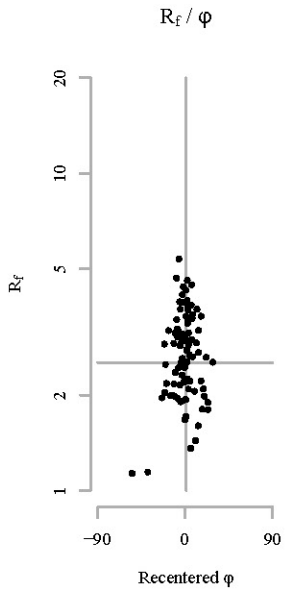

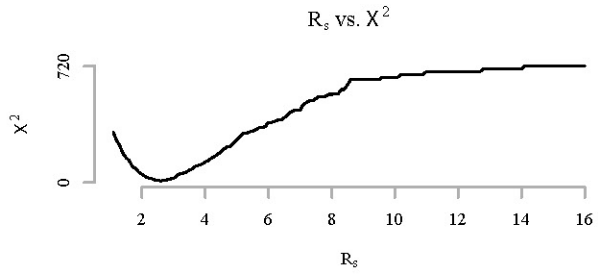

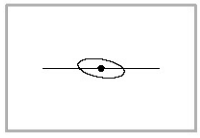

Normalized ellipse

Parameters

Sample size:	90
Fabric ratio:	2.6
Vector mean:	10
Harmonic mean:	2.5
Symmetry:	0.89
Min. chi sq:	8.4
Mean area*:	6282.5

*Average clast area in pixles

Sectional R_f / φ results for plane: C

Sample: 12DC16_A
Mineral: Hornblende

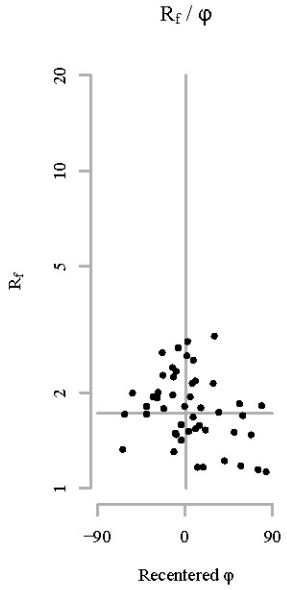

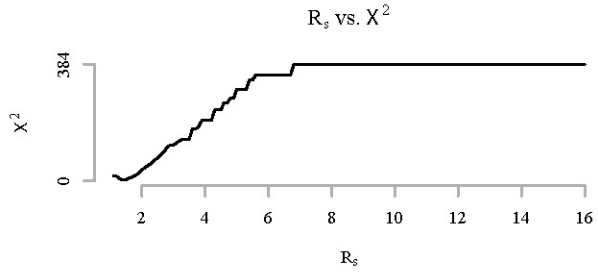

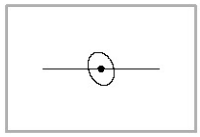

Parameters

Sample size:	48
Fabric ratio:	1.4
Vector mean:	68
Harmonic mean:	1.7
Symmetry:	0.83
Min. chi sq:	3
Mean area*:	22811.9

*Average clast area in pixles

Stereonet

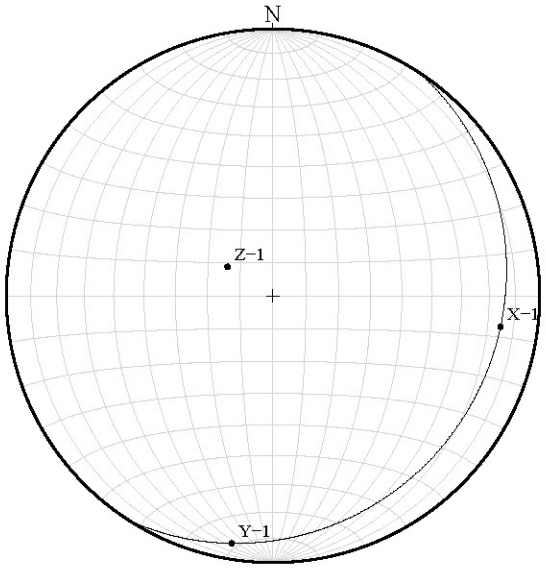

Nadai plot

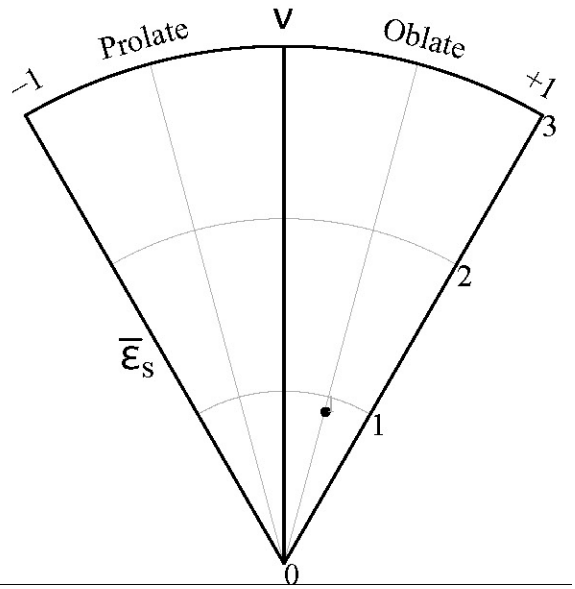

Sectional R_f / φ results for plane: A

Sample: 12DC16_A
Mineral: Plagioclase

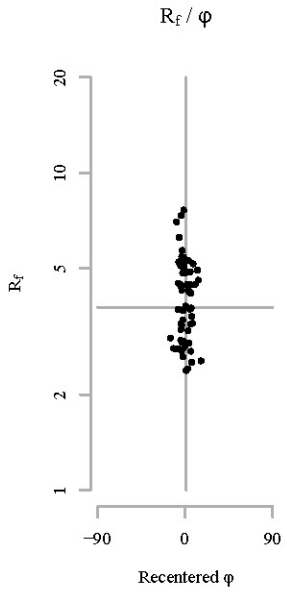

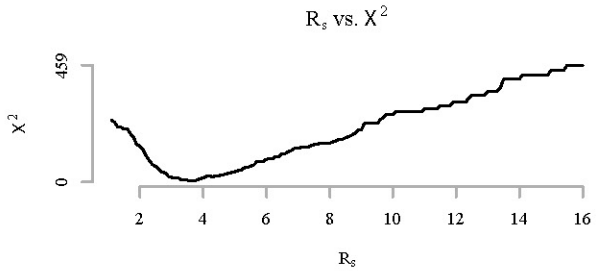

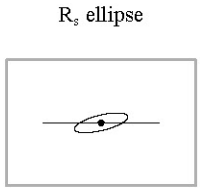

Normalized ellipse

Parameters

Sample size:	58
Fabric ratio:	3.6
Vector mean:	166
Harmonic mean:	3.8
Symmetry:	0.9
Min. chi sq:	3.45
Mean area*:	13675.7

*Average clast area in pixles

Sectional R_f / φ results for plane: B

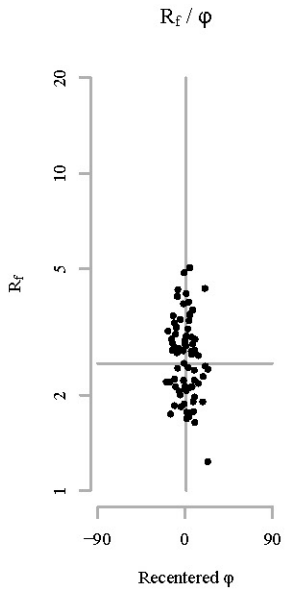

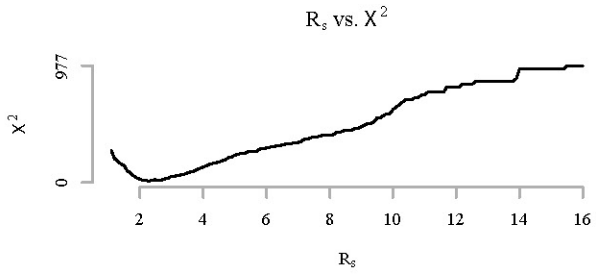

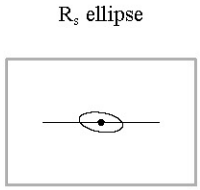

Normalized ellipse

Parameters

Sample size:	78
Fabric ratio:	2.3
Vector mean:	9
Harmonic mean:	2.5
Symmetry:	0.82
Min. chi sq:	10.46
Mean area*:	10738.3

*Average clast area in pixles

Sectional R_f / φ results for plane: C

Sample: 12DC16_A
Mineral: Plagioclase

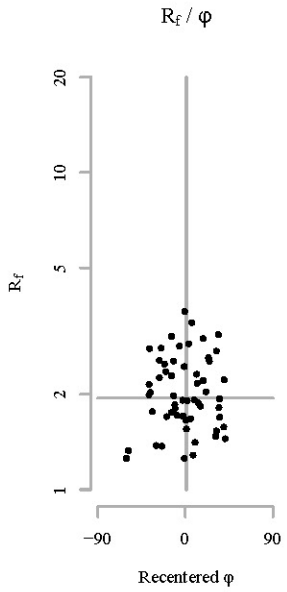

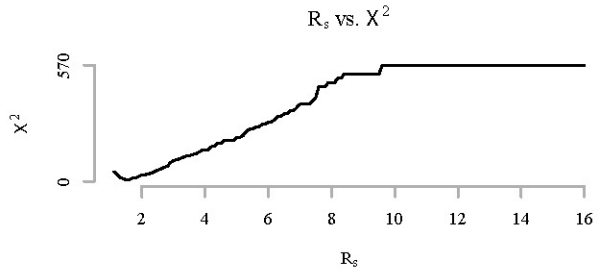

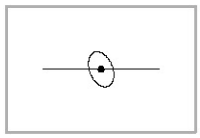

Parameters

Sample size:	57
Fabric ratio:	1.6
Vector mean:	68
Harmonic mean:	1.9
Symmetry:	0.88
Min. chi sq:	8.81
Mean area*:	34490.6

*Average clast area in pixles

Stereonet

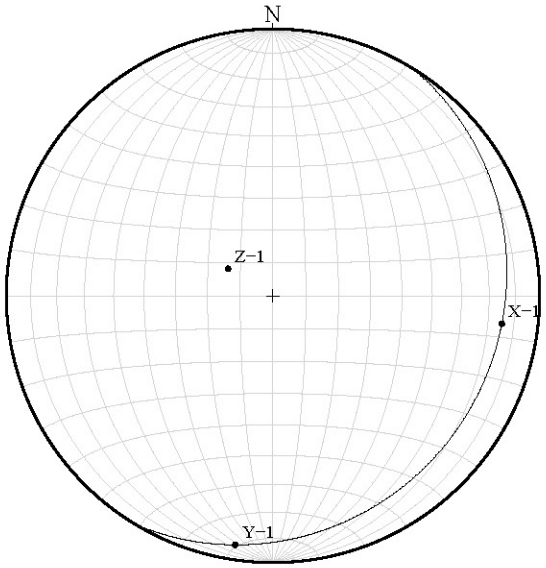

Nadai plot

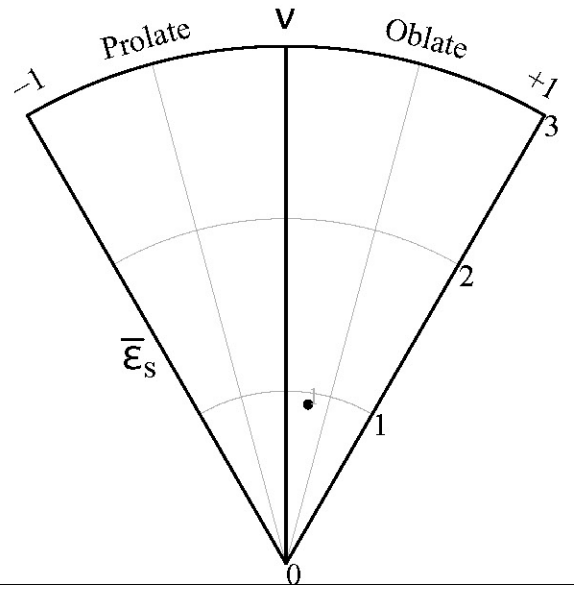

Sectional R_f / φ results for plane: A

Sample: 12DC22_A
Mineral: Hornblende

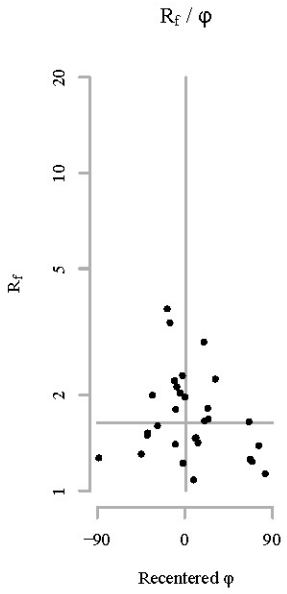

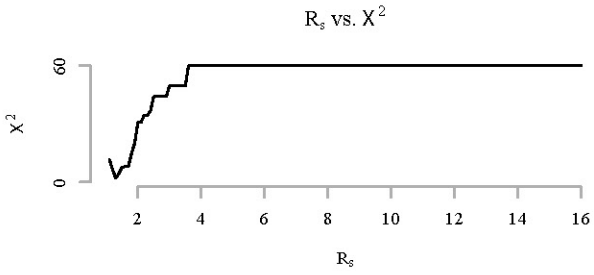

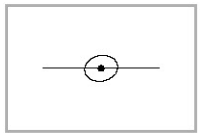

Normalized ellipse

Parameters

Sample size:	30
Fabric ratio:	1.3
Vector mean:	167
Harmonic mean:	1.6
Symmetry:	0.93
Min. chi sq:	2
Mean area*:	29150.2

*Average clast area in pixles

Sectional R_f / φ results for plane: B

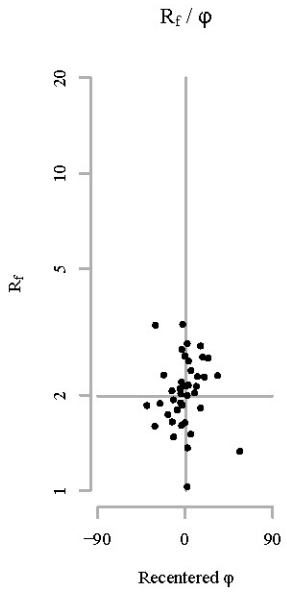

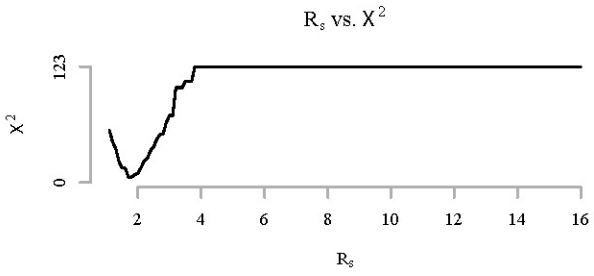

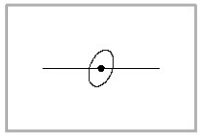

Normalized ellipse

Parameters

Sample size:	41
Fabric ratio:	1.7
Vector mean:	111
Harmonic mean:	2
Symmetry:	0.63
Min. chi sq:	5.63
Mean area*:	4625.1

*Average clast area in pixles

Sectional R_f / φ results for plane: C

Sample: 12DC22_A
Mineral: Hornblende

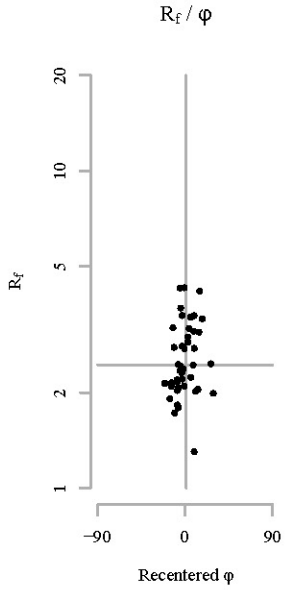

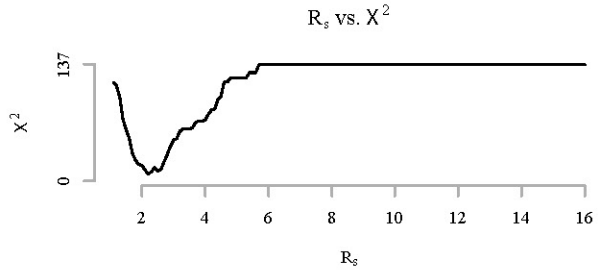

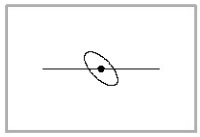

Parameters

Sample size:	43
Fabric ratio:	2.2
Vector mean:	46
Harmonic mean:	2.4
Symmetry:	0.7
Min. chi sq:	7.79
Mean area*:	5873.8

*Average clast area in pixles

Stereonet

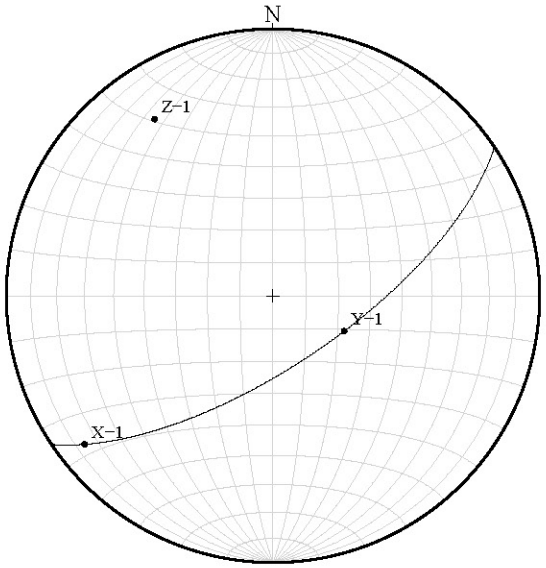

Nadai plot

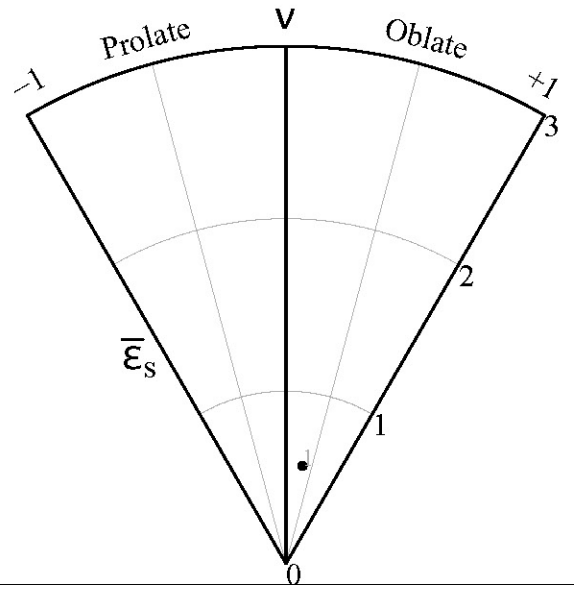

Sample: 12DC22_A
Mineral: Plagioclase

Sectional R_f / φ results for plane: A

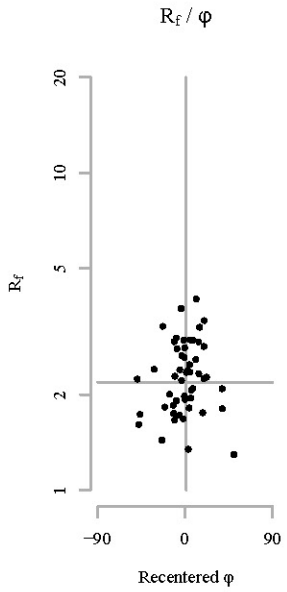

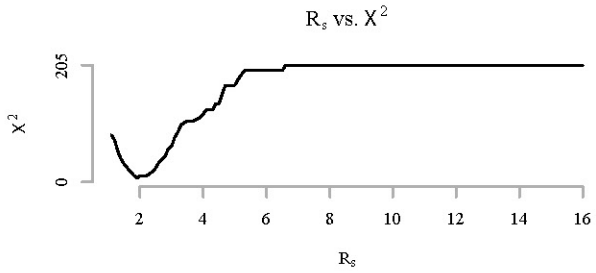

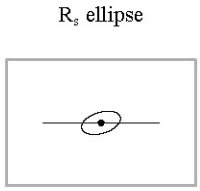

Parameters

Sample size:	51
Fabric ratio:	1.9
Vector mean:	163
Harmonic mean:	2.2
Symmetry:	0.9
Min. chi sq:	6.45
Mean area*:	16490.2

*Average clast area in pixles

Sectional R_f / φ results for plane: B

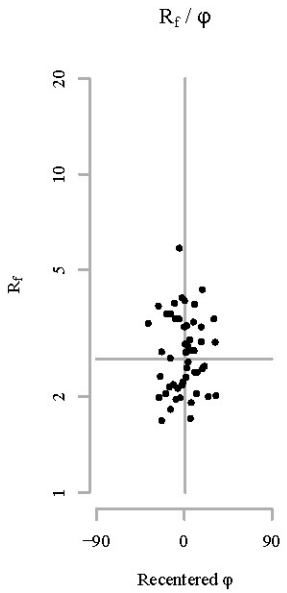

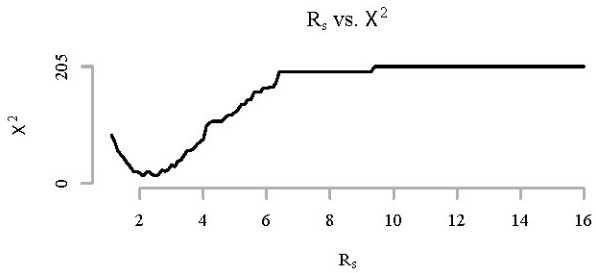

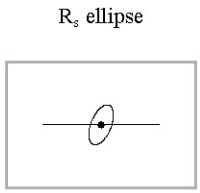

Parameters

Sample size:	51
Fabric ratio:	2.1
Vector mean:	112
Harmonic mean:	2.6
Symmetry:	0.94
Min. chi sq:	12.73
Mean area*:	4813.2

*Average clast area in pixles

Sectional R_f / φ results for plane: C

Sample: 12DC22_A
Mineral: Plagioclase

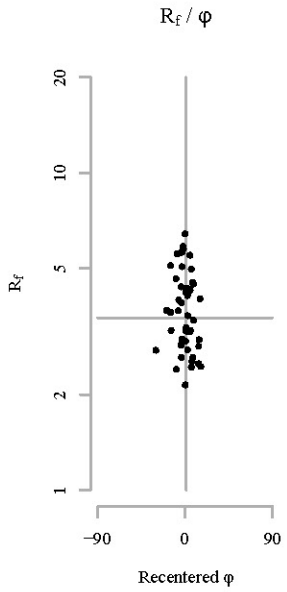

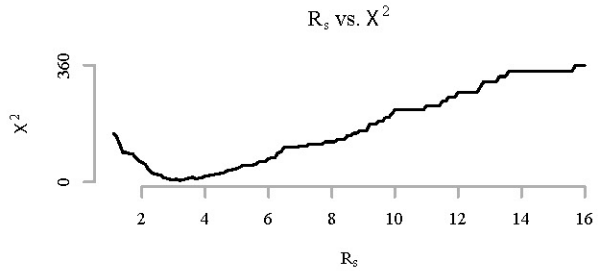

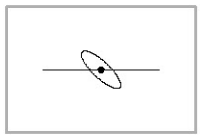

Parameters

Sample size:	45
Fabric ratio:	3.2
Vector mean:	44
Harmonic mean:	3.5
Symmetry:	0.76
Min. chi sq:	4.4
Mean area*:	10976.9

*Average clast area in pixles

Stereonet

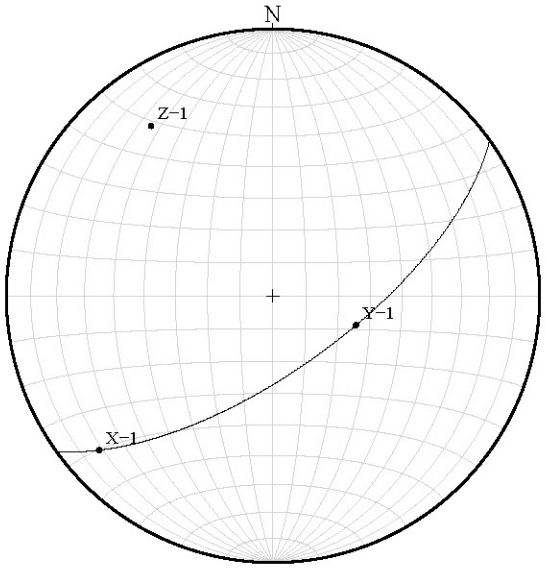

Nadai plot

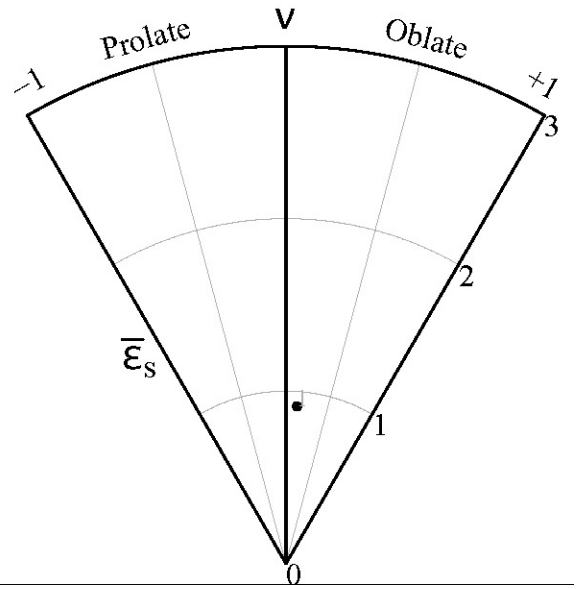

Sectional R_f / φ results for plane: A

Sample: 12DC23_A
Mineral: Plagioclase

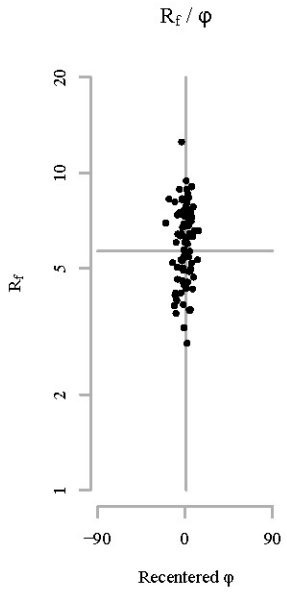

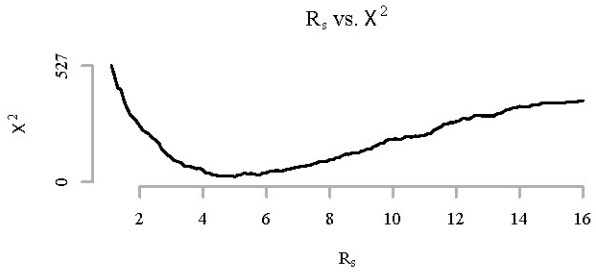

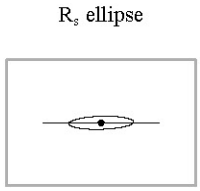

Normalized ellipse

Parameters

Sample size:	90
Fabric ratio:	5
Vector mean:	178
Harmonic mean:	5.7
Symmetry:	0.82
Min. chi sq:	22.8
Mean area*:	5550.2

*Average clast area in pixles

Sectional R_f / φ results for plane: B

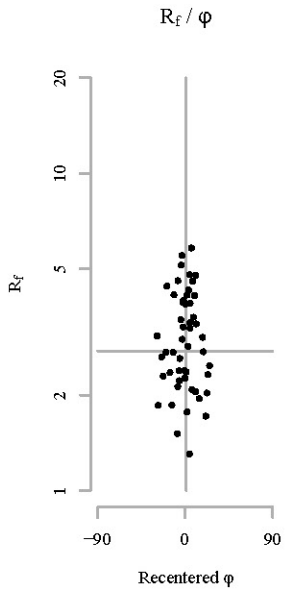

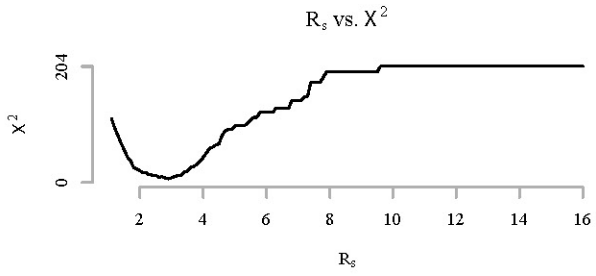

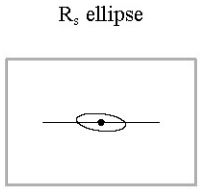

Normalized ellipse

Parameters

Sample size:	51
Fabric ratio:	2.9
Vector mean:	7
Harmonic mean:	2.8
Symmetry:	0.86
Min. chi sq:	6.06
Mean area*:	13582.2

*Average clast area in pixles

Sectional R_f / φ results for plane: C

Sample: 12DC23_A
Mineral: Plagioclase

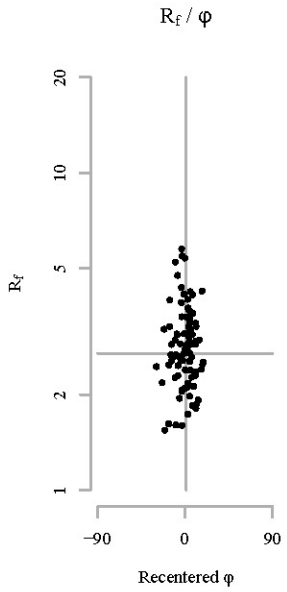

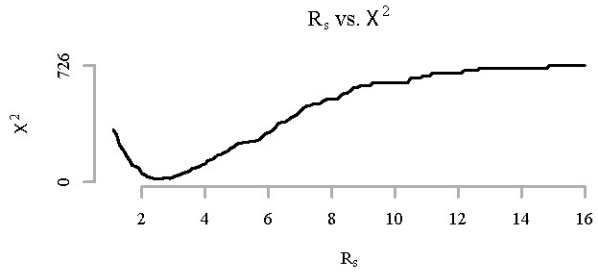

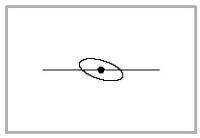

Parameters

Sample size:	90
Fabric ratio:	2.4
Vector mean:	17
Harmonic mean:	2.7
Symmetry:	0.89
Min. chi sq:	16.8
Mean area*:	2873.4

*Average clast area in pixles

Stereonet

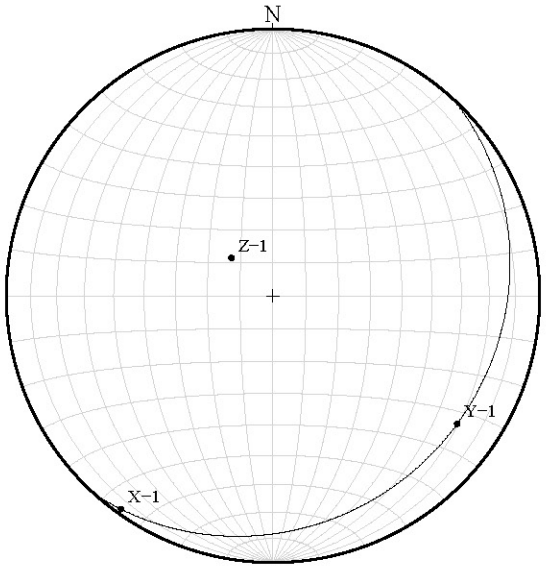

Nadai plot

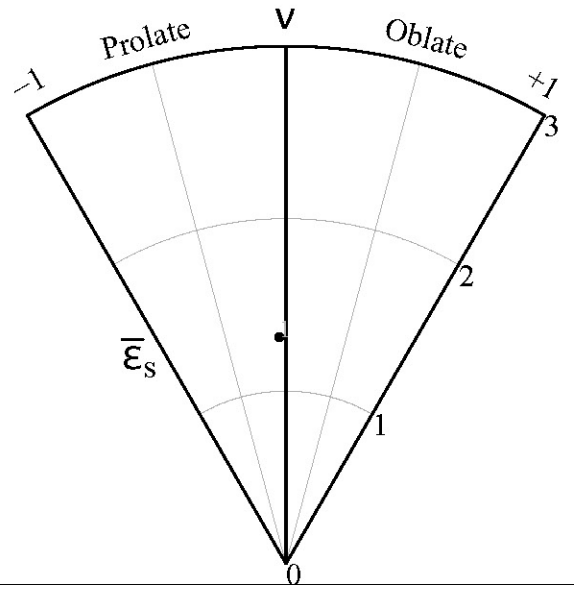

Sectional R_f / φ results for plane: A

Sample: 12DC24_A
Mineral: Plagioclase

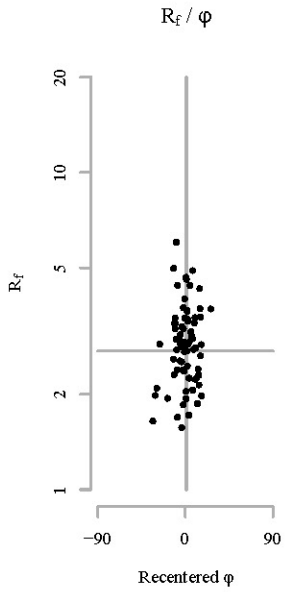

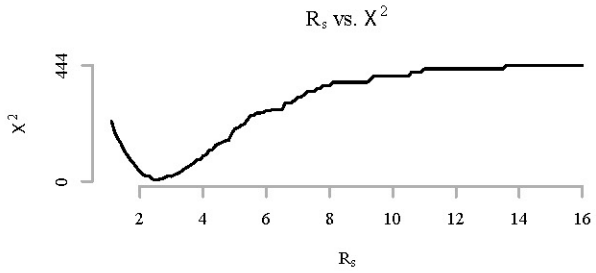

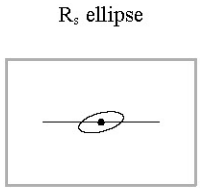

Normalized ellipse

Parameters

Sample size:	74
Fabric ratio:	2.5
Vector mean:	165
Harmonic mean:	2.7
Symmetry:	0.95
Min. chi sq:	6.97
Mean area*:	4023.9

*Average clast area in pixles

Sectional R_f / φ results for plane: B

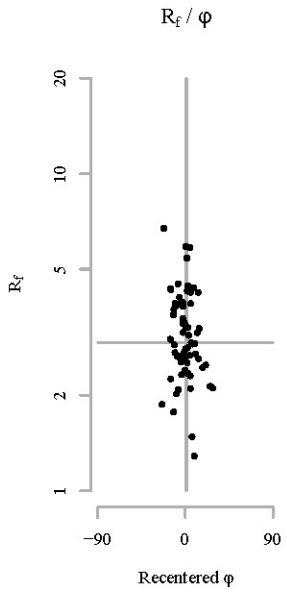

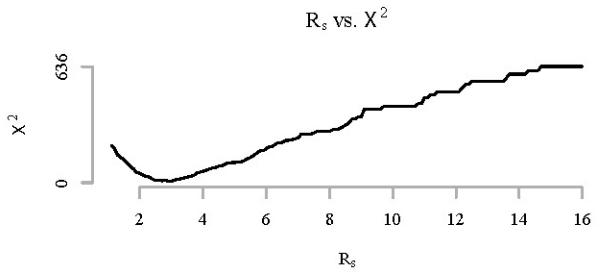

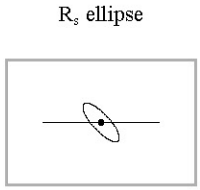

Normalized ellipse

Parameters

Sample size:	67
Fabric ratio:	3
Vector mean:	47
Harmonic mean:	2.9
Symmetry:	0.96
Min. chi sq:	8.09
Mean area*:	9469.6

*Average clast area in pixles

Sectional R_f / φ results for plane: C

Sample: 12DC24_A
Mineral: Plagioclase

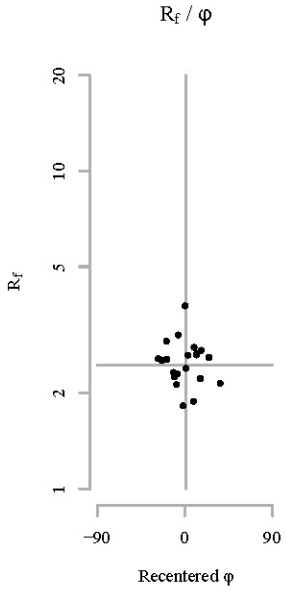

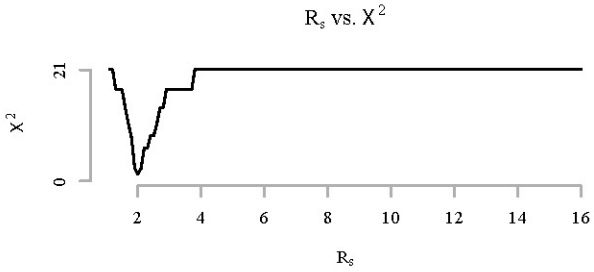

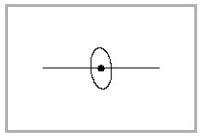

Parameters

Sample size:	21
Fabric ratio:	2
Vector mean:	84
Harmonic mean:	2.5
Symmetry:	0.86
Min. chi sq:	1.29
Mean area*:	35007.1

*Average clast area in pixles

Stereonet

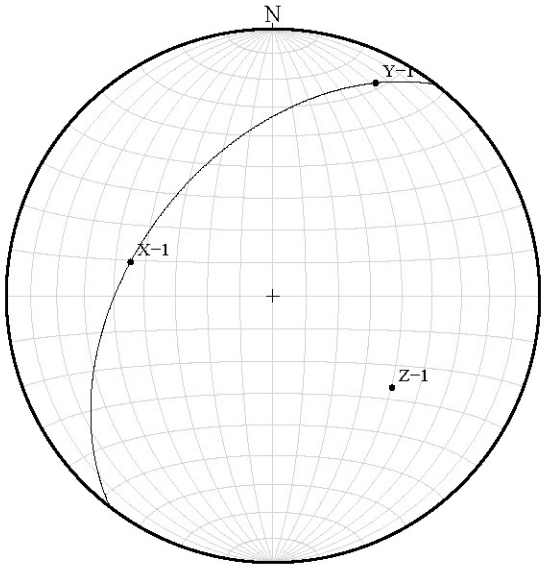

Nadai plot

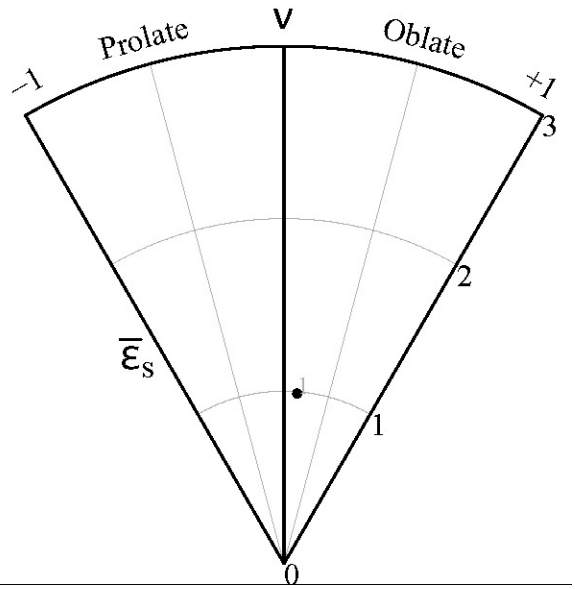

Sectional R_f / φ results for plane: A

Sample: 12DC25_A
Mineral: Hornblende

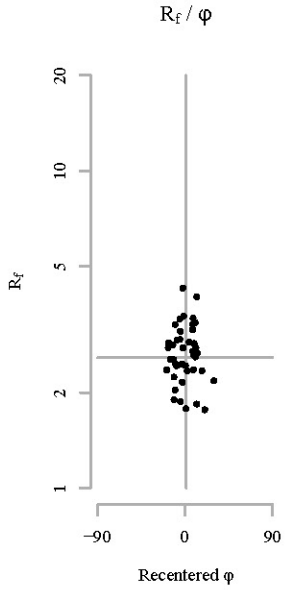

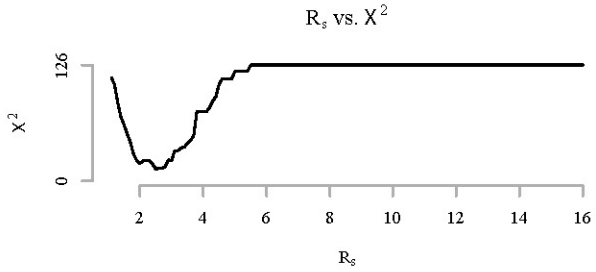

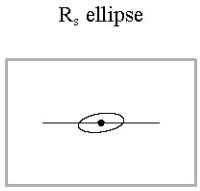

Parameters

Sample size:	42
Fabric ratio:	2.5
Vector mean:	172
Harmonic mean:	2.6
Symmetry:	0.9
Min. chi sq:	12.86
Mean area*:	10017.6

*Average clast area in pixles

Sectional R_f / φ results for plane: B

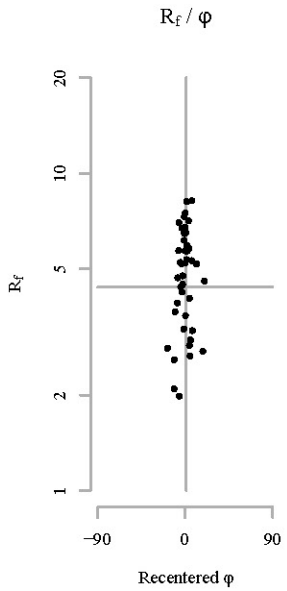

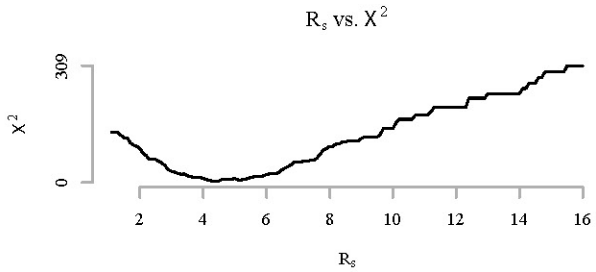

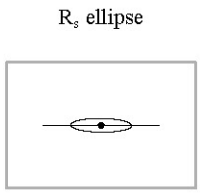

Parameters

Sample size:	45
Fabric ratio:	4.4
Vector mean:	1
Harmonic mean:	4.4
Symmetry:	0.93
Min. chi sq:	2.4
Mean area*:	7425.1

*Average clast area in pixles

Sectional R_f / φ results for plane: C

Sample: 12DC25_A
Mineral: Hornblende

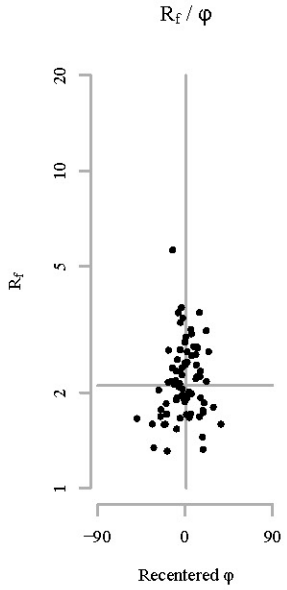

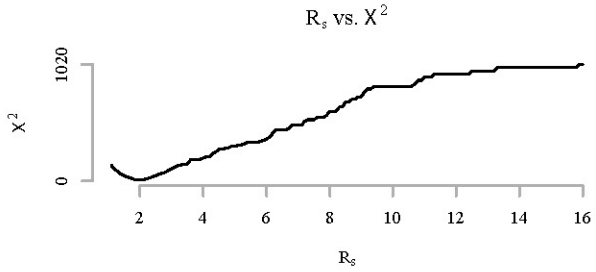

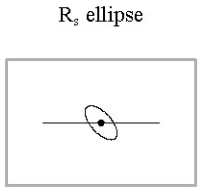

Parameters

Sample size:	75
Fabric ratio:	2.1
Vector mean:	48
Harmonic mean:	2.1
Symmetry:	0.88
Min. chi sq:	10.4
Mean area*:	3953.6

*Average clast area in pixles

Stereonet

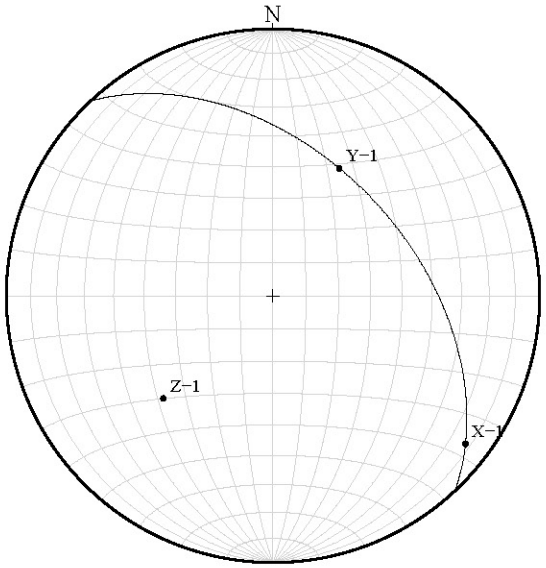

Nadai plot

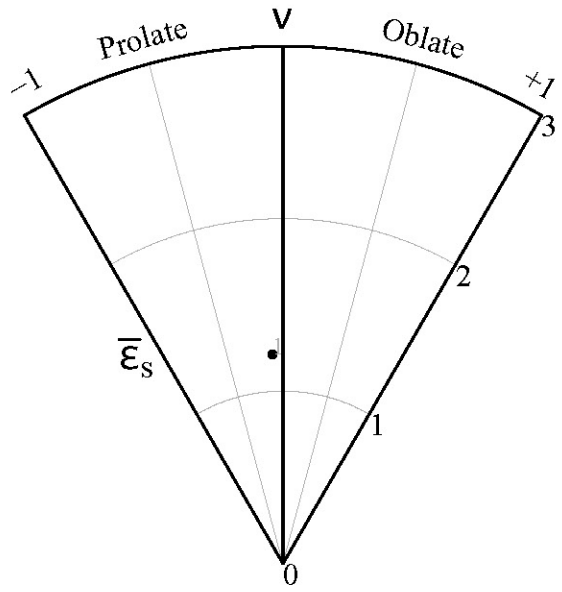

Sectional R_f / φ results for plane: A

Sample: 12DC25_A
Mineral: Plagioclase

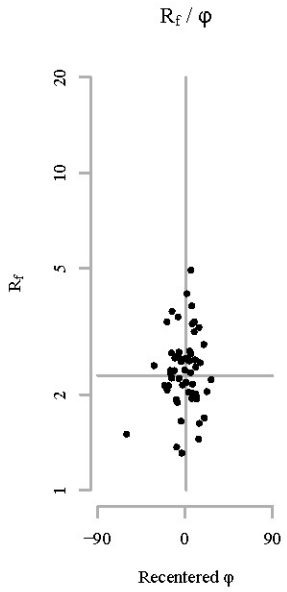

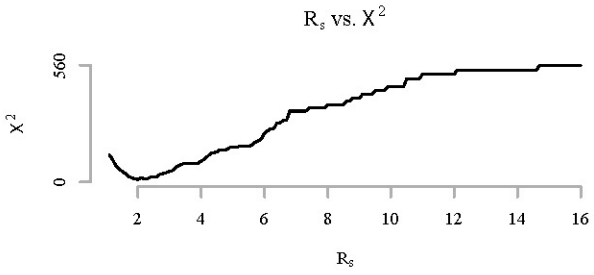

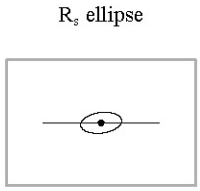

Parameters

Sample size:	56
Fabric ratio:	2
Vector mean:	172
Harmonic mean:	2.3
Symmetry:	0.93
Min. chi sq:	10.79
Mean area*:	11380.8

*Average clast area in pixles

Sectional R_f / φ results for plane: B

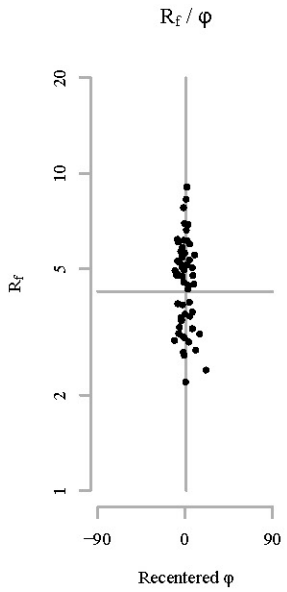

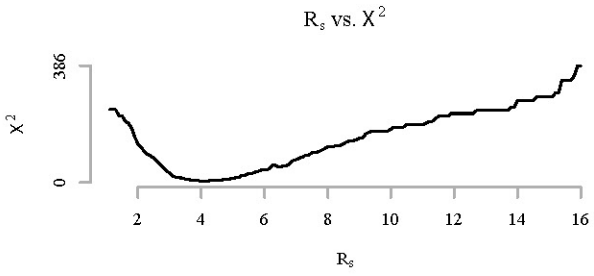

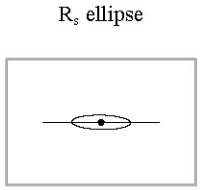

Parameters

Sample size:	56
Fabric ratio:	4.1
Vector mean:	1
Harmonic mean:	4.2
Symmetry:	0.86
Min. chi sq:	2.54
Mean area*:	13149.3

*Average clast area in pixles

Sectional R_f / φ results for plane: C

Sample: 12DC25_A
Mineral: Plagioclase

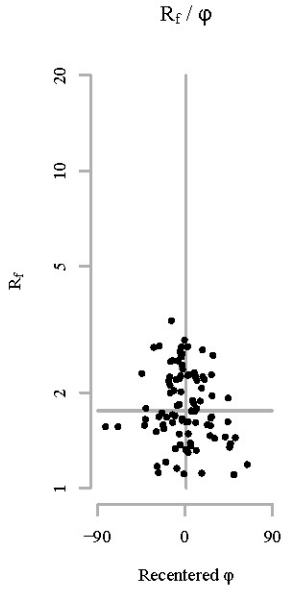

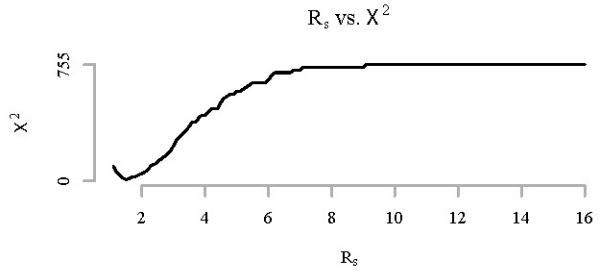

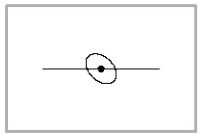

Parameters

Sample size:	94
Fabric ratio:	1.5
Vector mean:	43
Harmonic mean:	1.8
Symmetry:	0.89
Min. chi sq:	7.49
Mean area*:	5821.9

*Average clast area in pixles

Stereonet

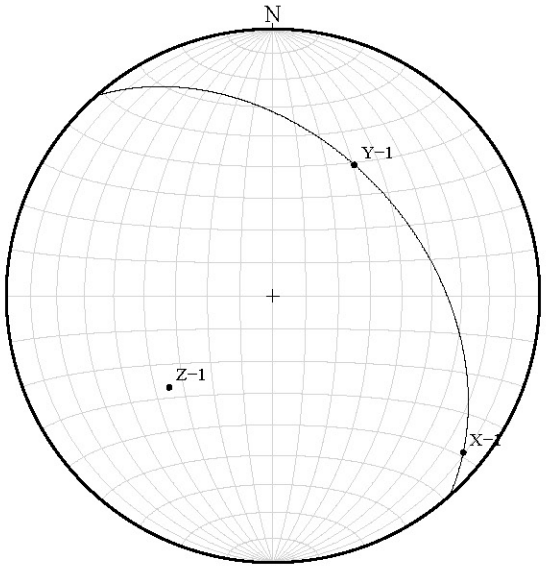

Nadai plot

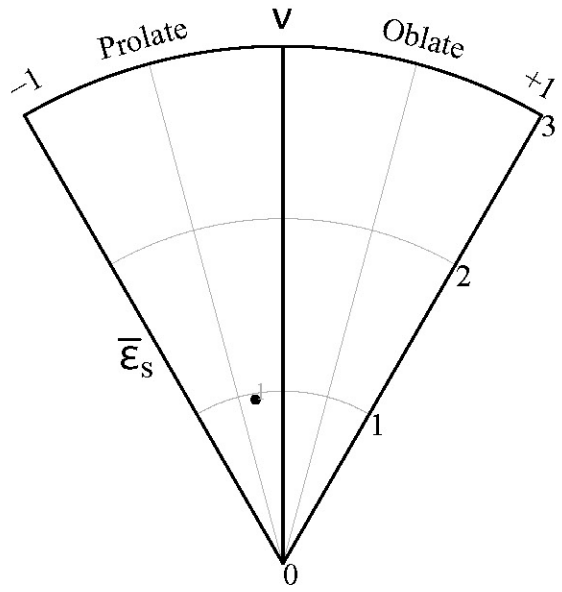

Sectional R_f / φ results for plane: A

Sample: 12DC26_A
Mineral: Hornblende

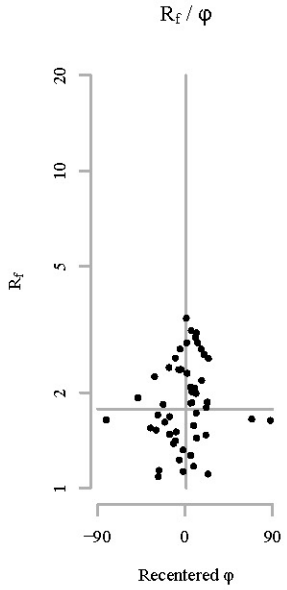

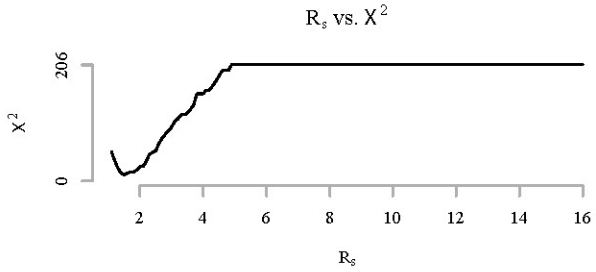

Rs ellipse

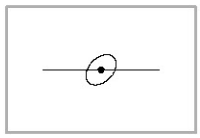

Normalized ellipse

Parameters

Sample size:	51
Fabric ratio:	1.5
Vector mean:	135
Harmonic mean:	1.8
Symmetry:	0.67
Min. chi sq:	10.76
Mean area*:	6458.1

*Average clast area in pixles

Sectional R_f / φ results for plane: B

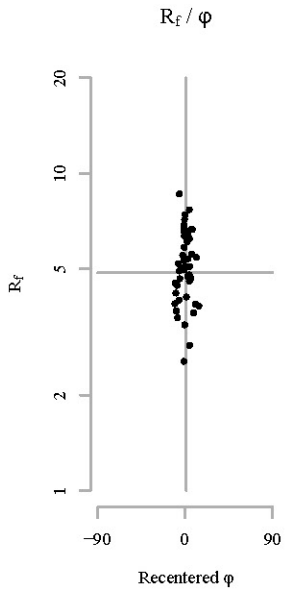

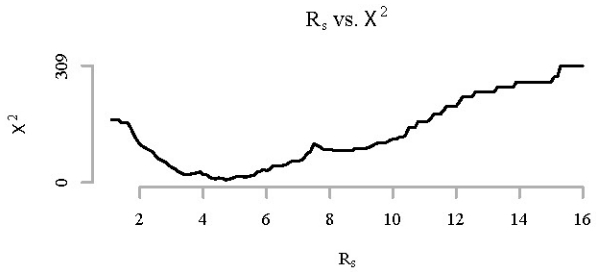

Rs ellipse

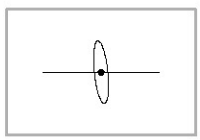

Normalized ellipse

Parameters

Sample size:	47
Fabric ratio:	4.7
Vector mean:	84
Harmonic mean:	4.9
Symmetry:	0.89
Min. chi sq:	6.04
Mean area*:	8359.1

*Average clast area in pixles

Sectional R_f / φ results for plane: C

Sample: 12DC26_A
Mineral: Hornblende

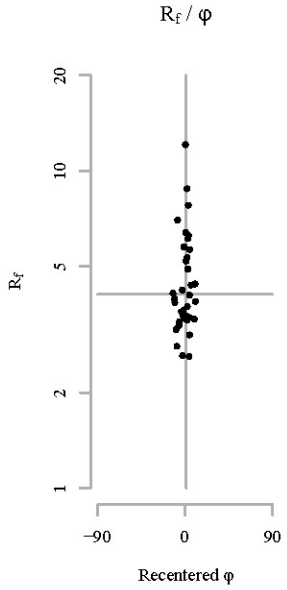

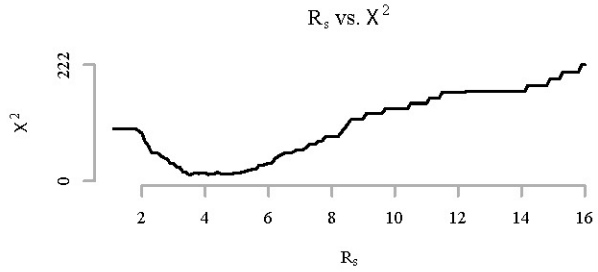

Rs ellipse

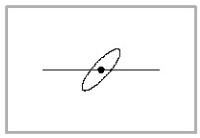

Normalized ellipse

Parameters

Sample size:	37
Fabric ratio:	3.5
Vector mean:	132
Harmonic mean:	4.1
Symmetry:	0.76
Min. chi sq:	11.24
Mean area*:	37742.9

*Average clast area in pixles

Stereonet

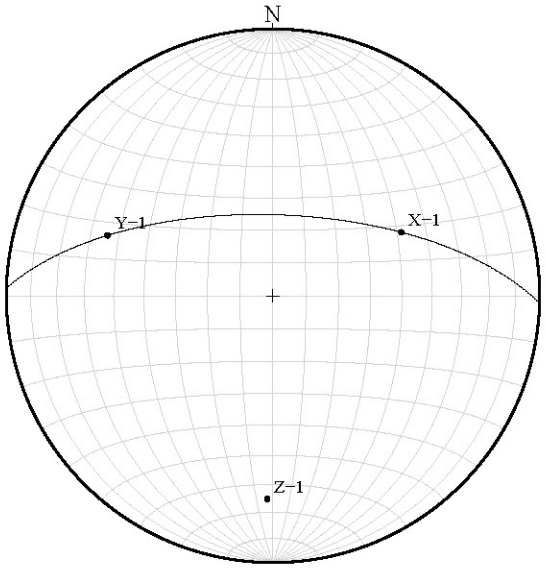

Nadai plot

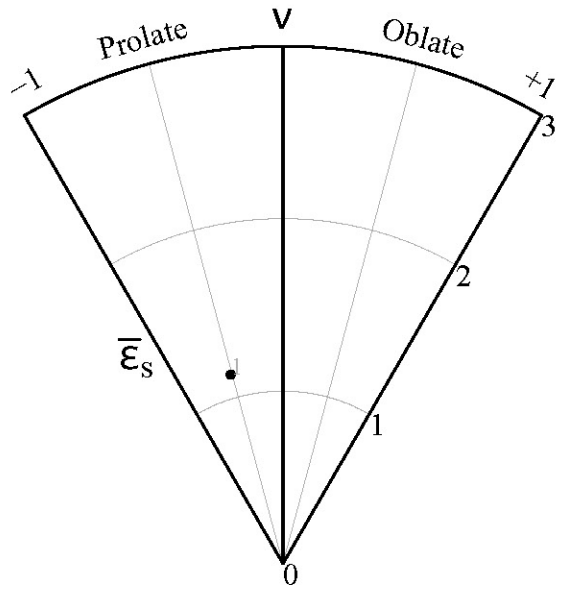

Sectional R_f / φ results for plane: A

Sample: 12DC26_A
Mineral: Plagioclase

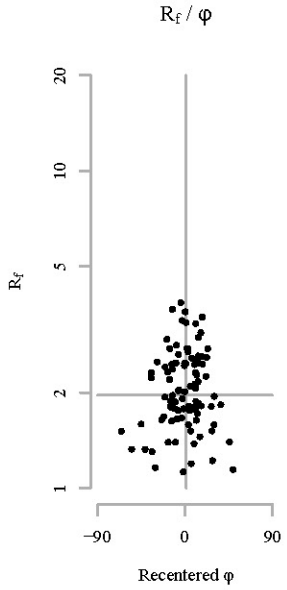

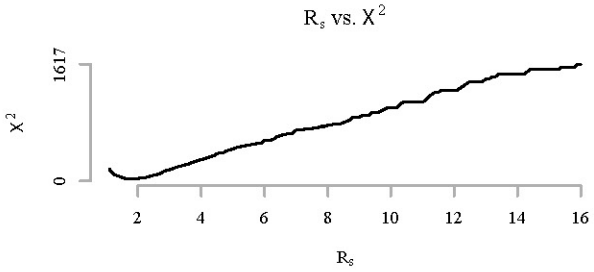

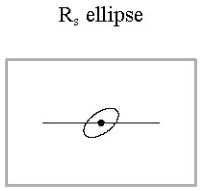

Normalized ellipse

Parameters

Sample size:	98
Fabric ratio:	1.9
Vector mean:	144
Harmonic mean:	2
Symmetry:	0.92
Min. chi sq:	22.98
Mean area*:	4593.6

*Average clast area in pixles

Sectional R_f / φ results for plane: B

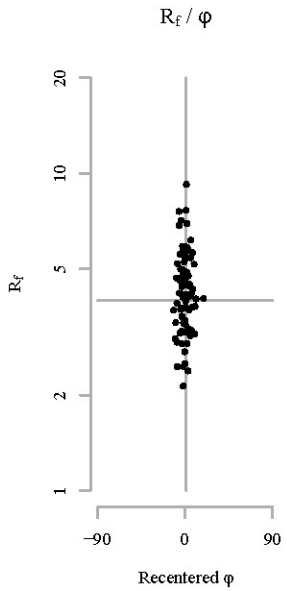

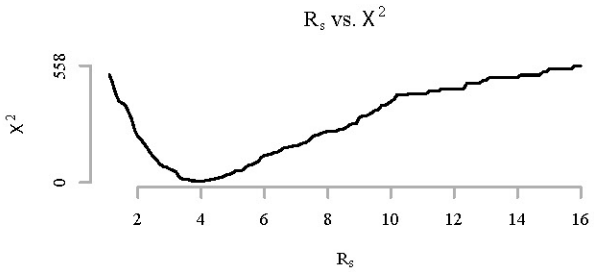

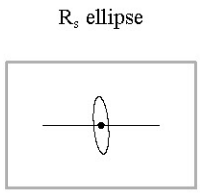

Normalized ellipse

Parameters

Sample size:	84
Fabric ratio:	3.9
Vector mean:	85
Harmonic mean:	4
Symmetry:	0.88
Min. chi sq:	4
Mean area*:	7629.2

*Average clast area in pixles

Sectional R_f / φ results for plane: C

Sample: 12DC26_A
Mineral: Plagioclase

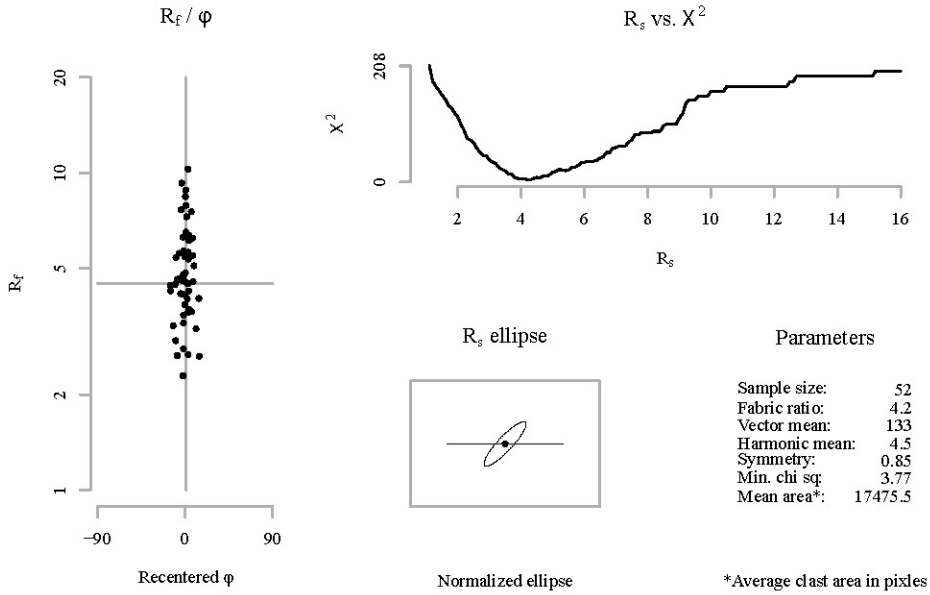

Stereonet

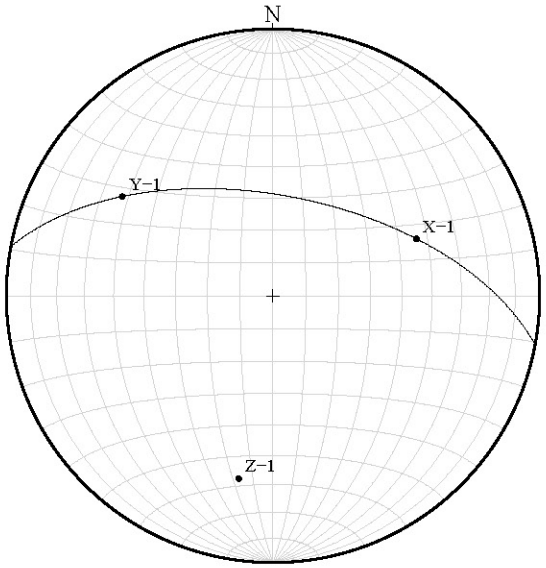

Nadai plot

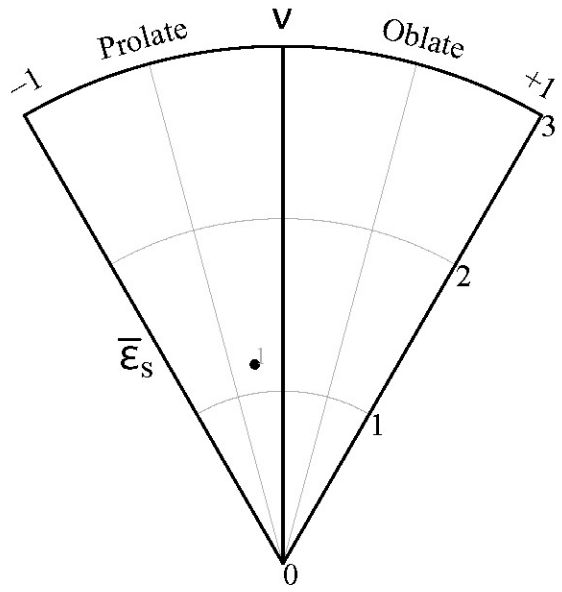

Sectional R_f / φ results for plane: A

Sample: 12DC26_B
Mineral: Hornblende

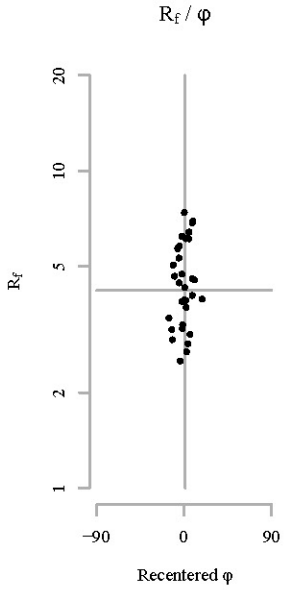

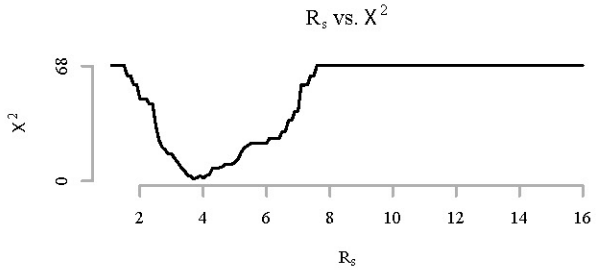

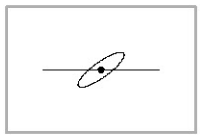

Normalized ellipse

Parameters

Sample size:	34
Fabric ratio:	3.7
Vector mean:	144
Harmonic mean:	4.2
Symmetry:	0.94
Min. chi sq:	1.29
Mean area*:	27968.4

*Average clast area in pixles

Sectional R_f / φ results for plane: B

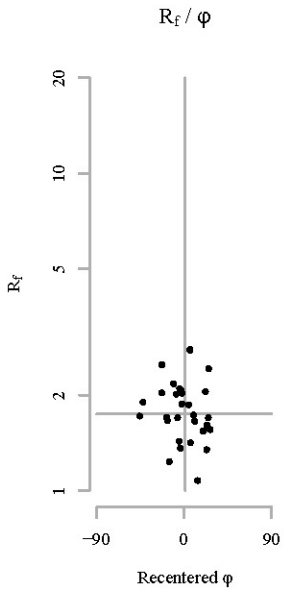

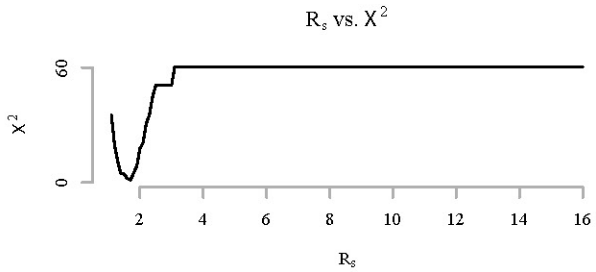

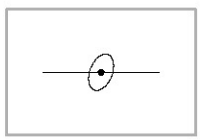

Normalized ellipse

Parameters

Sample size:	30
Fabric ratio:	1.7
Vector mean:	112
Harmonic mean:	1.7
Symmetry:	0.8
Min. chi sq:	1.2
Mean area*:	13208.1

*Average clast area in pixles

Sectional R_f / φ results for plane: C

Sample: 12DC26_B
Mineral: Hornblende

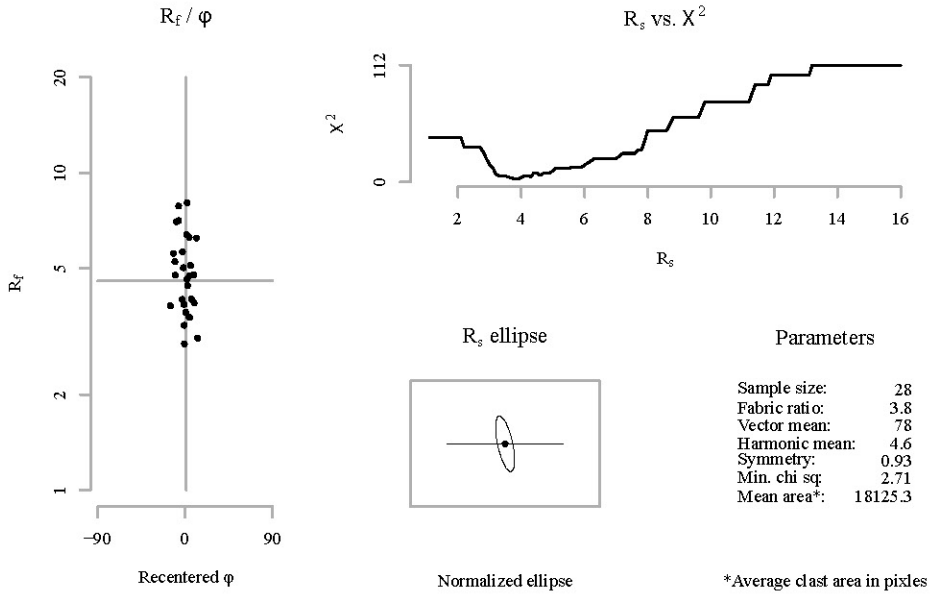

Stereonet

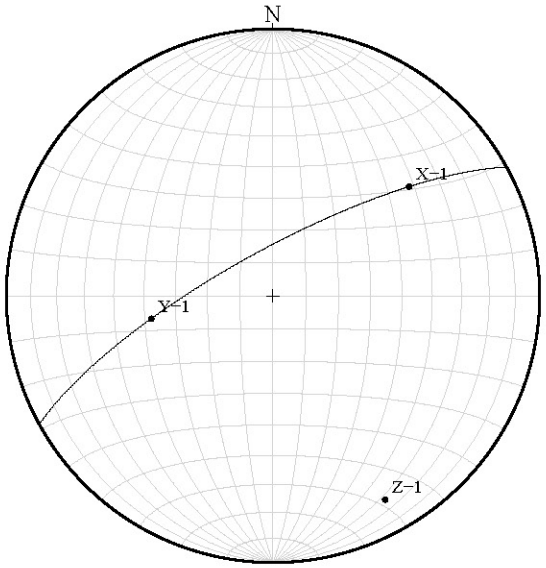

Nadai plot

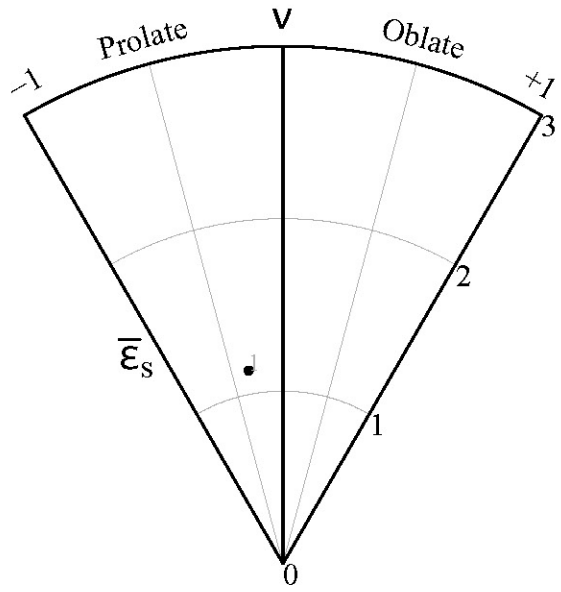

Sectional R_f / φ results for plane: A

Sample: 12DC26_B
Mineral: Plagioclase

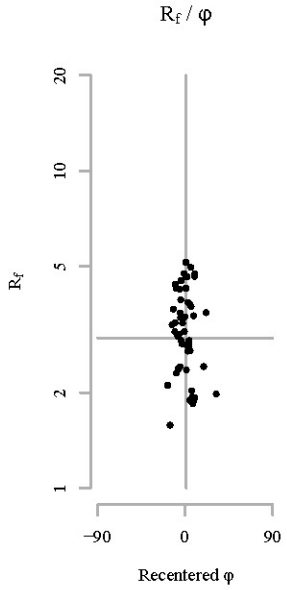

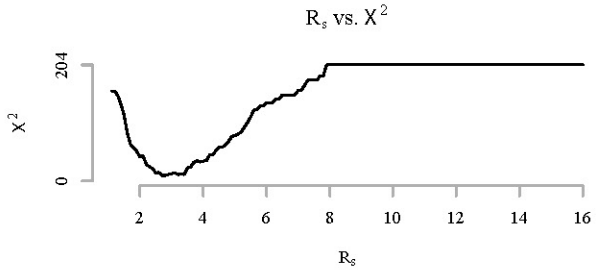

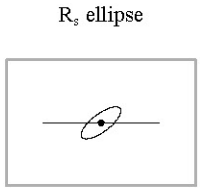

Parameters

Sample size:	51
Fabric ratio:	2.7
Vector mean:	143
Harmonic mean:	3
Symmetry:	0.75
Min. chi sq:	9.59
Mean area*:	15051.4

*Average clast area in pixles

Sectional R_f / φ results for plane: B

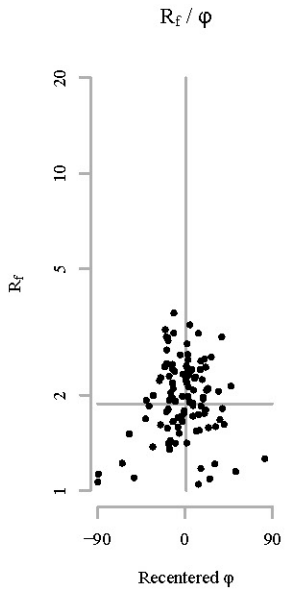

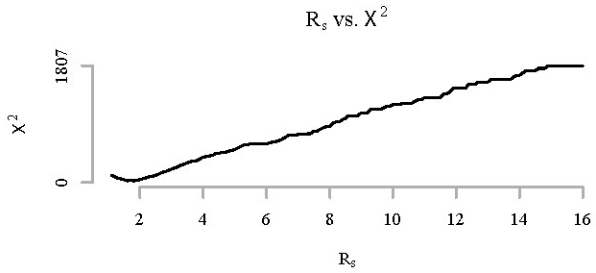

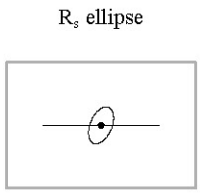

Parameters

Sample size:	106
Fabric ratio:	1.8
Vector mean:	113
Harmonic mean:	1.9
Symmetry:	0.89
Min. chi sq:	22.38
Mean area*:	2902.3

*Average clast area in pixles

Sectional R_f / φ results for plane: C

Sample: 12DC26_B
Mineral: Plagioclase

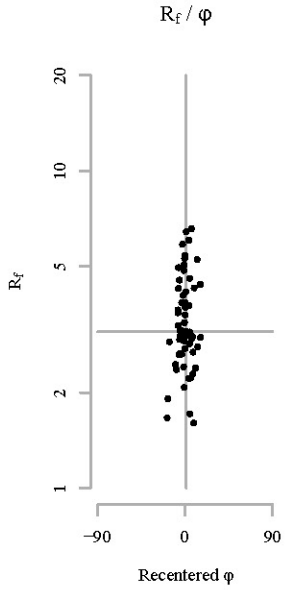

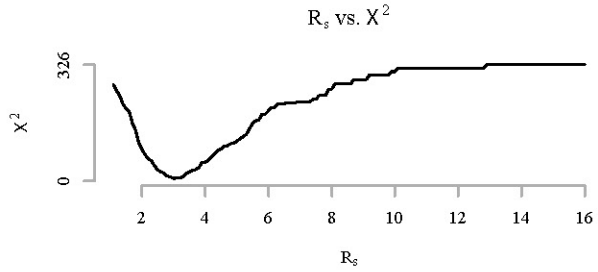

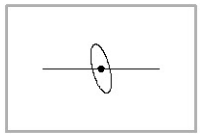

Parameters

Sample size:	64
Fabric ratio:	3
Vector mean:	76
Harmonic mean:	3.1
Symmetry:	0.88
Min. chi sq:	6.5
Mean area*:	4431

*Average clast area in pixles

Stereonet

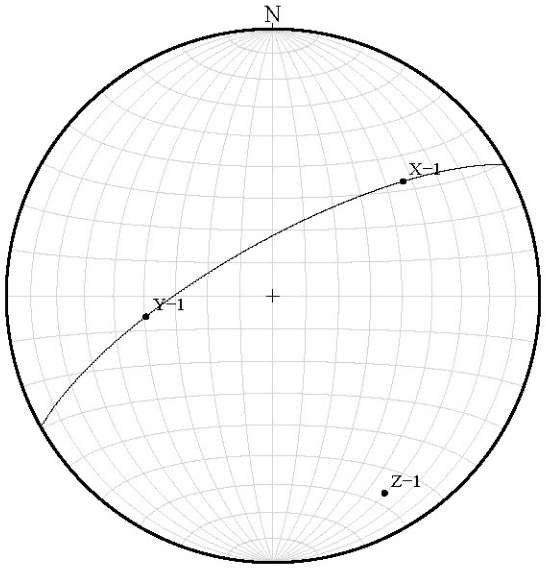

Nadai plot

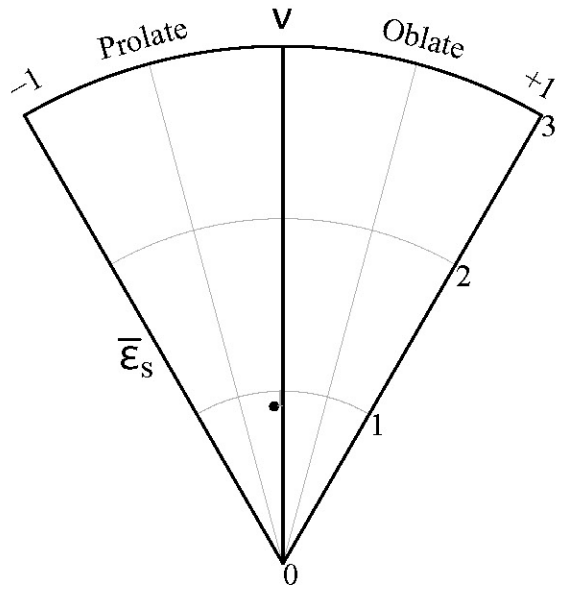

Sectional R_f / φ results for plane: A

Sample: 12DC29_A
Mineral: Hornblende

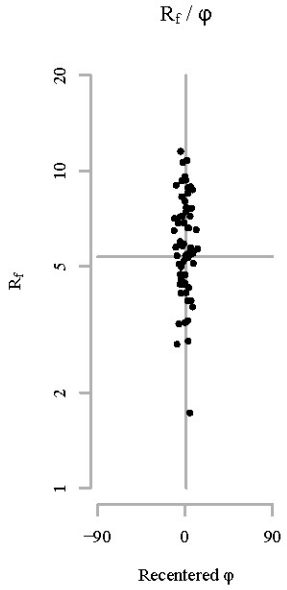

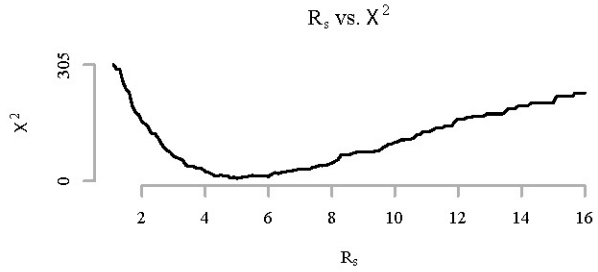

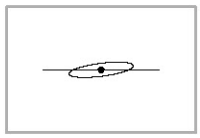

Normalized ellipse

Parameters

Sample size:	61
Fabric ratio:	5
Vector mean:	173
Harmonic mean:	5.4
Symmetry:	0.89
Min. chi sq:	6.48
Mean area*:	2370233.9

*Average clast area in pixles

Sectional R_f / φ results for plane: B

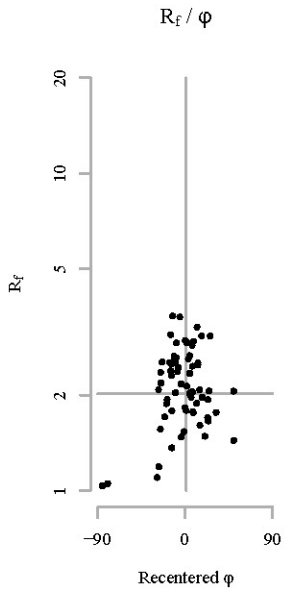

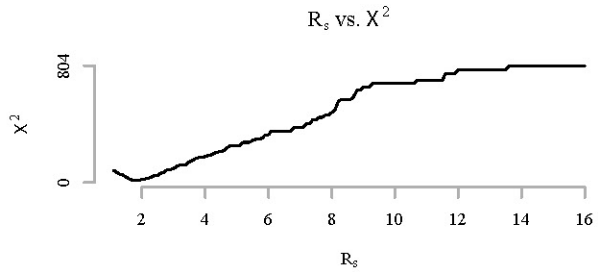

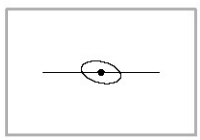

Normalized ellipse

Parameters

Sample size:	67
Fabric ratio:	1.9
Vector mean:	14
Harmonic mean:	2
Symmetry:	0.96
Min. chi sq:	11.97
Mean area*:	2244426.7

*Average clast area in pixles

Sectional R_f / φ results for plane: C

Sample: 12DC29_A
Mineral: Hornblende

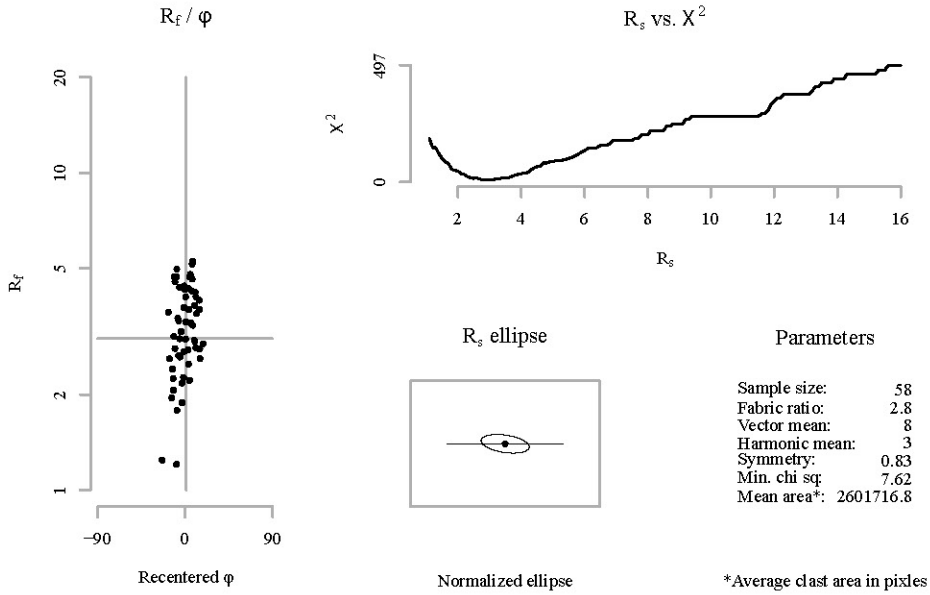

Stereonet

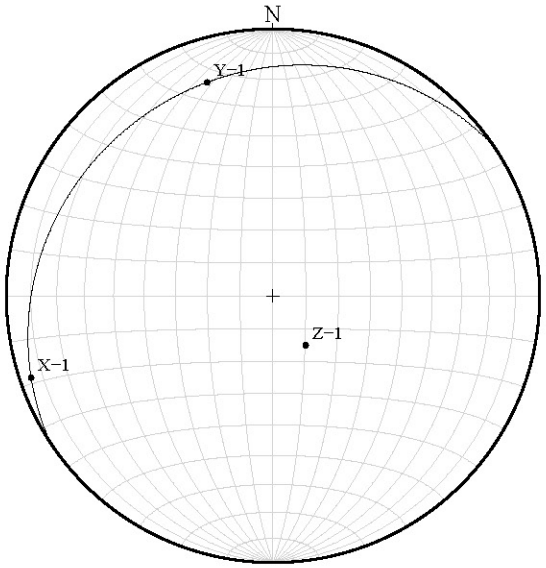

Nadai plot

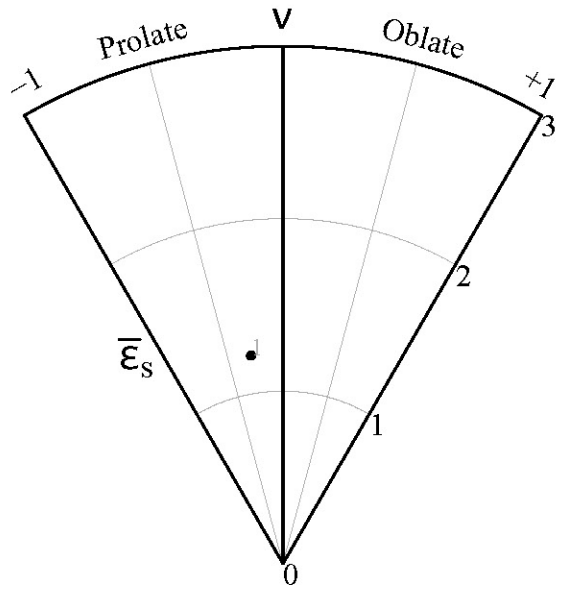

Sectional R_f / φ results for plane: A

Sample: 12DC29_A
Mineral: Plagioclase

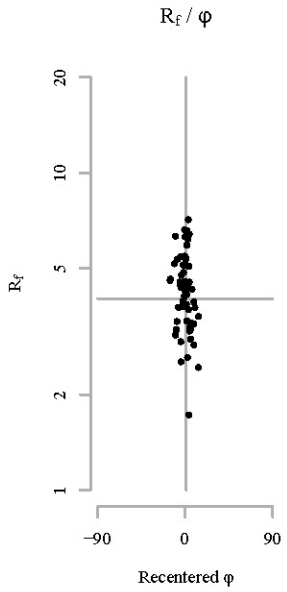

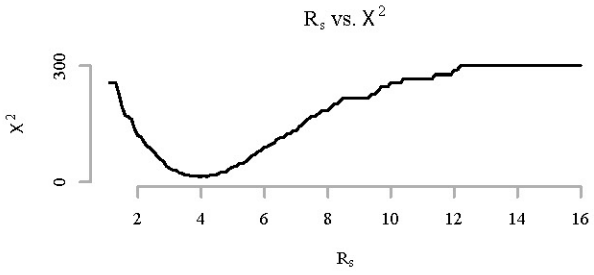

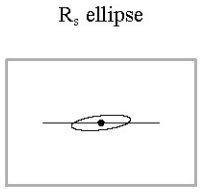

Parameters

Sample size:	60
Fabric ratio:	4.2
Vector mean:	174
Harmonic mean:	4
Symmetry:	0.83
Min. chi sq:	13.6
Mean area*:	2360587.8

*Average clast area in pixles

Sectional R_f / φ results for plane: B

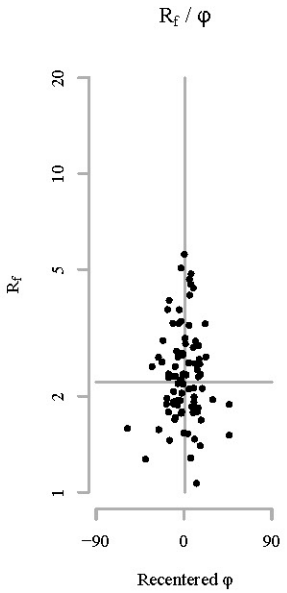

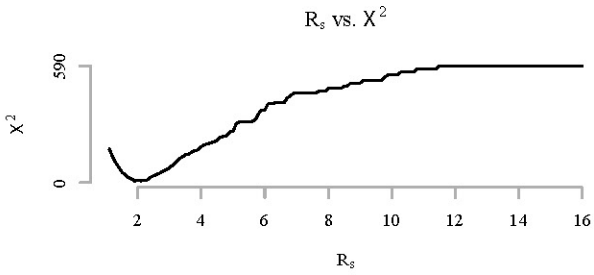

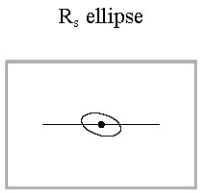

Parameters

Sample size:	84
Fabric ratio:	1.9
Vector mean:	16
Harmonic mean:	2.2
Symmetry:	0.95
Min. chi sq:	8.95
Mean area*:	1750141

*Average clast area in pixles

Sectional R_f / φ results for plane: C

Sample: 12DC29_A
Mineral: Plagioclase

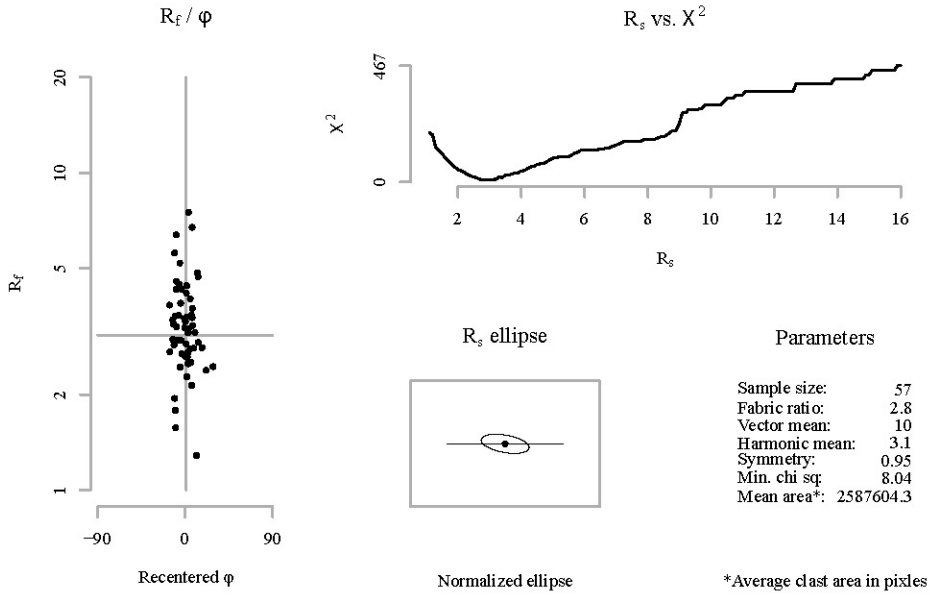

Stereonet

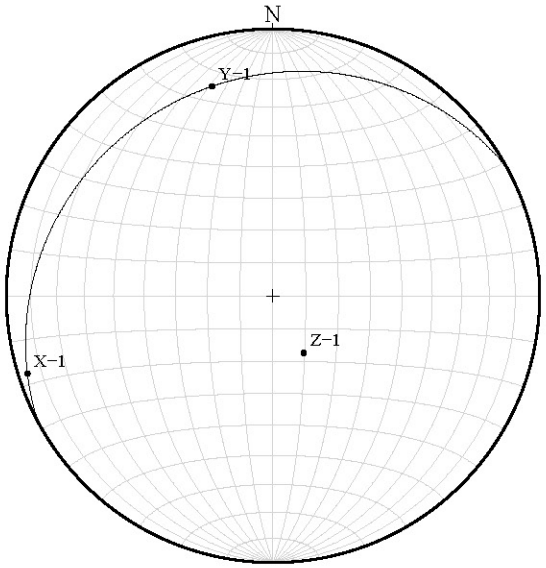

Nadai plot

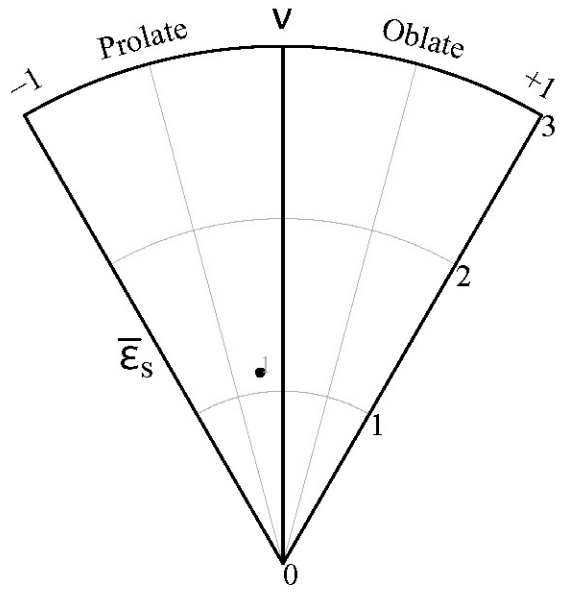

Sample: 12DC30_A
Mineral: Pyroxene / Hornblende

Sectional R_f / φ results for plane: A

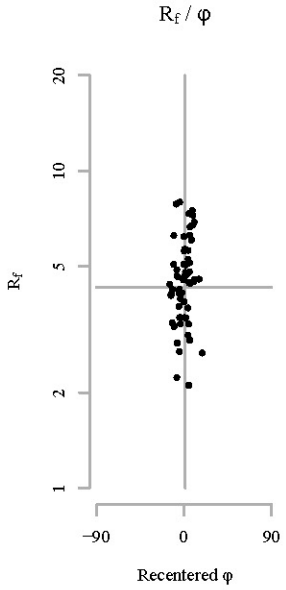

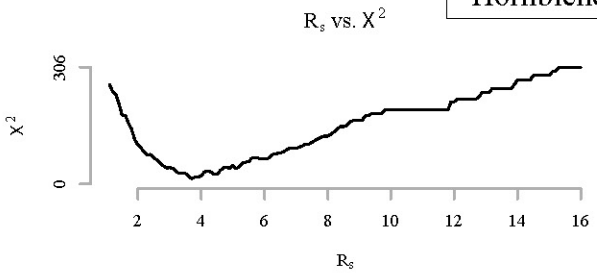

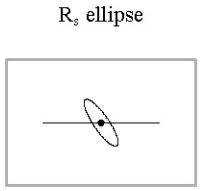

Normalized ellipse

Parameters

Sample size:	61
Fabric ratio:	3.7
Vector mean:	56
Harmonic mean:	4.3
Symmetry:	0.66
Min. chi sq:	13.95
Mean area*:	6208.2

*Average clast area in pixles

Sectional R_f / φ results for plane: B

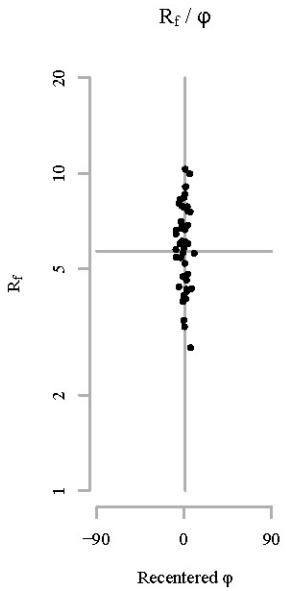

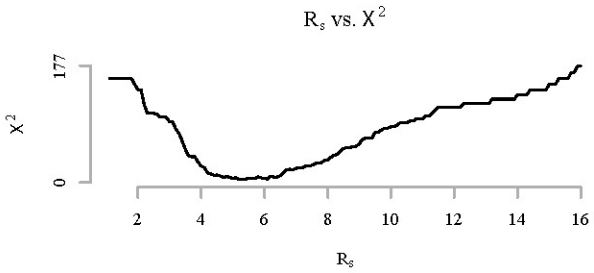

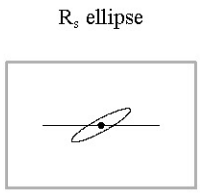

Normalized ellipse

Parameters

Sample size:	45
Fabric ratio:	5.2
Vector mean:	152
Harmonic mean:	5.7
Symmetry:	0.93
Min. chi sq:	4
Mean area*:	4817.5

*Average clast area in pixles

Sectional R_f / φ results for plane: C

Sample: 12DC30_A
Mineral: Pyroxene / Hornblende

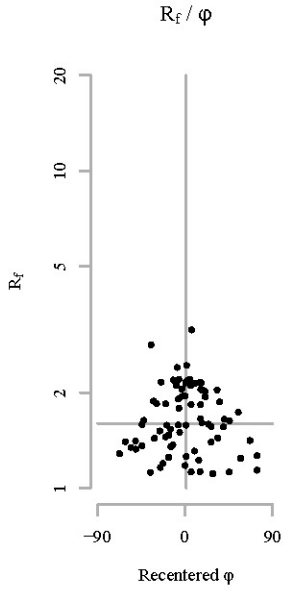

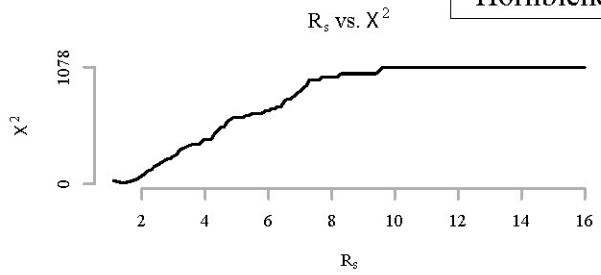

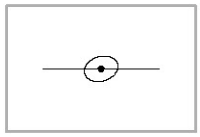

Normalized ellipse

Parameters

Sample size:	77
Fabric ratio:	1.4
Vector mean:	163
Harmonic mean:	1.6
Symmetry:	0.86
Min. chi sq:	10.86
Mean area*:	2568.5

*Average clast area in pixles

Stereonet

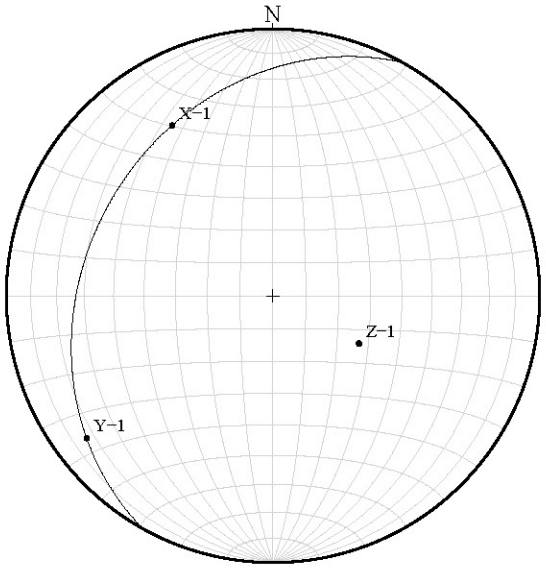

Nadai plot

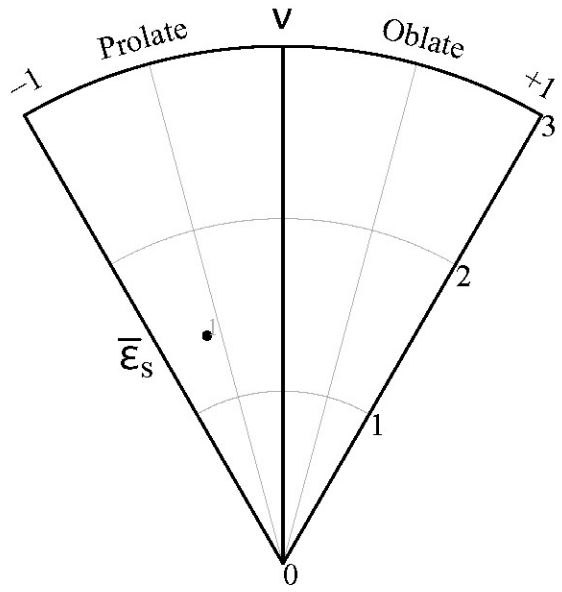

Sectional R_f / φ results for plane: A

Sample: 12DC30_A
Mineral: Plagioclase

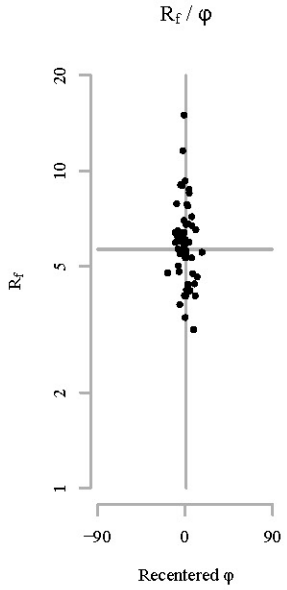

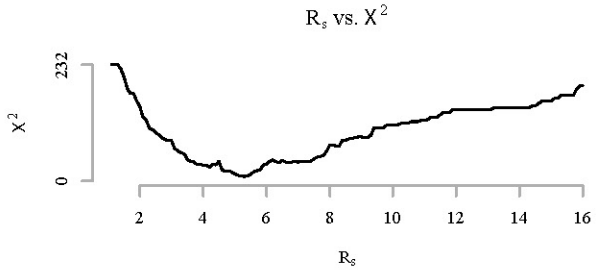

Rs ellipse

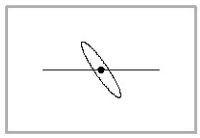

Normalized ellipse

Parameters

Sample size:	56
Fabric ratio:	5.3
Vector mean:	56
Harmonic mean:	5.7
Symmetry:	0.64
Min. chi sq:	8.82
Mean area*:	11483.7

*Average clast area in pixles

Sectional R_f / φ results for plane: B

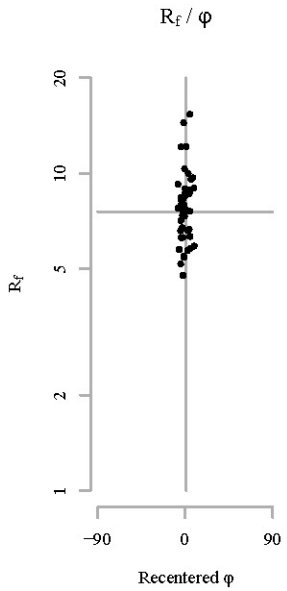

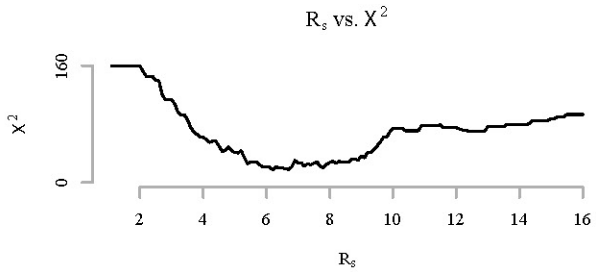

Rs ellipse

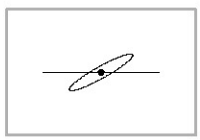

Normalized ellipse

Parameters

Sample size:	45
Fabric ratio:	6.2
Vector mean:	151
Harmonic mean:	7.6
Symmetry:	0.8
Min. chi sq:	17.2
Mean area*:	5750.9

*Average clast area in pixles

Sectional R_f / φ results for plane: C

Sample: 12DC30_A
Mineral: Plagioclase

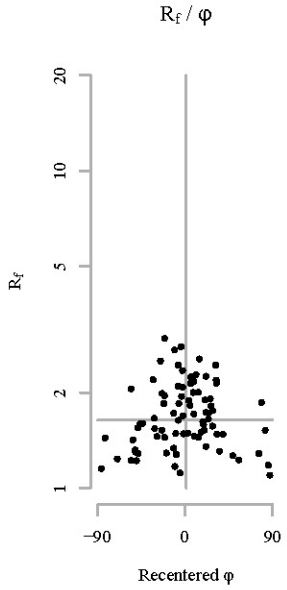

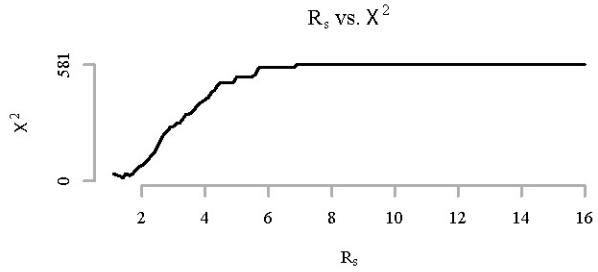

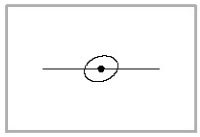

Normalized ellipse

Parameters

Sample size:	83
Fabric ratio:	1.4
Vector mean:	161
Harmonic mean:	1.6
Symmetry:	0.87
Min. chi sq:	14.73
Mean area*:	3228

*Average clast area in pixles

Stereonet

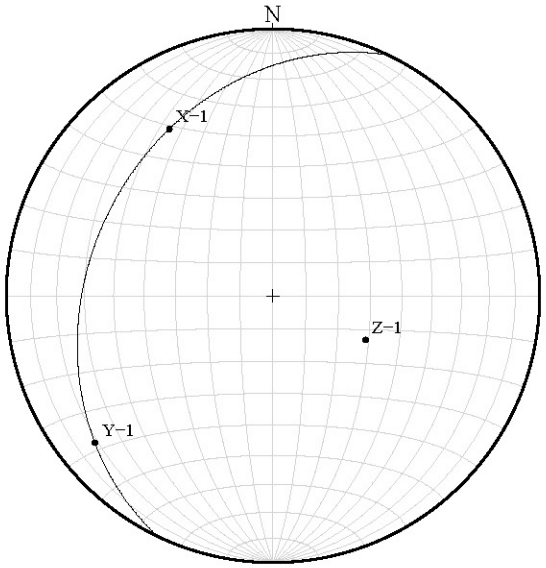

Nadai plot

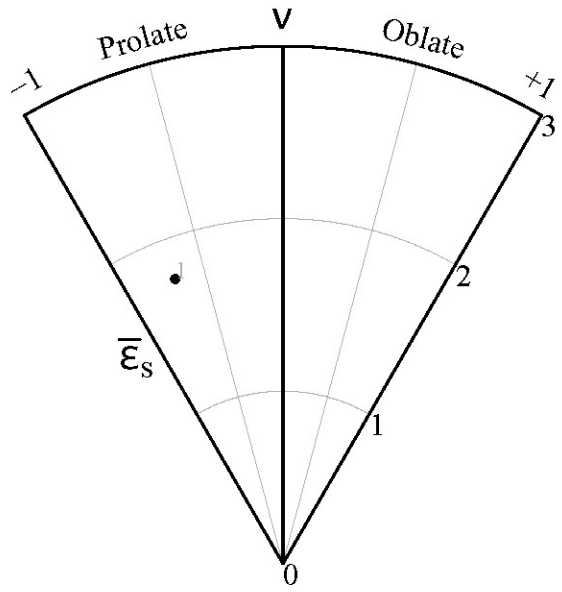

Sample: 12DC30_B
Mineral: Pyroxene / Hornblende

Sectional R_f / φ results for plane: A

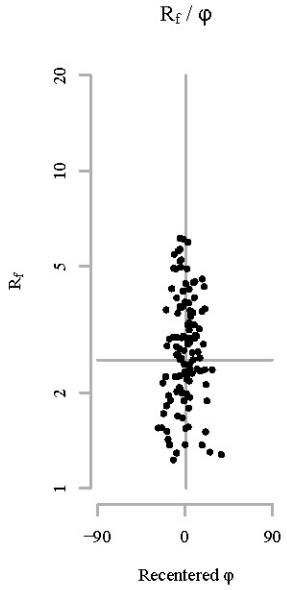

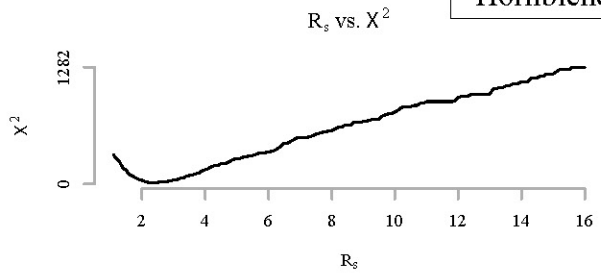

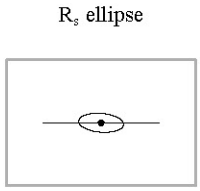

Parameters

Sample size:	116
Fabric ratio:	2.4
Vector mean:	5
Harmonic mean:	2.5
Symmetry:	0.97
Min. chi sq:	12.09
Mean area*:	12542.2

*Average clast area in pixles

Sectional R_f / φ results for plane: B

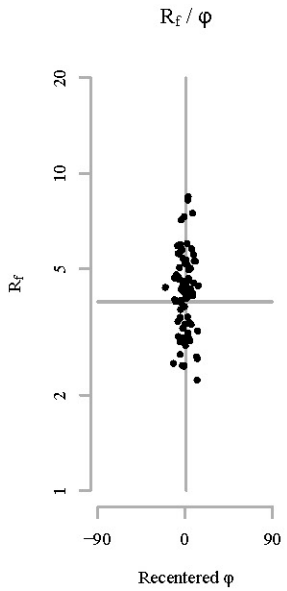

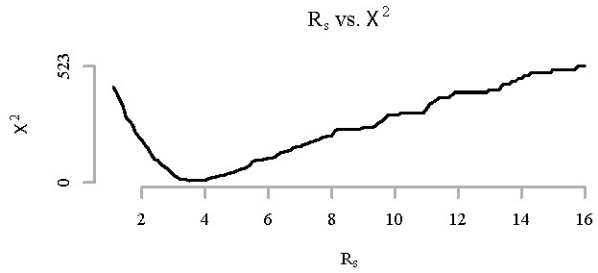

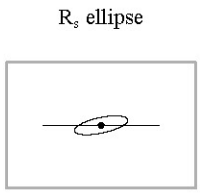

Parameters

Sample size:	81
Fabric ratio:	3.5
Vector mean:	168
Harmonic mean:	3.9
Symmetry:	0.96
Min. chi sq:	6.9
Mean area*:	12556.7

*Average clast area in pixles

Sectional R_f / φ results for plane: C

Sample: 12DC30_B
Mineral: Pyroxene / Hornblende

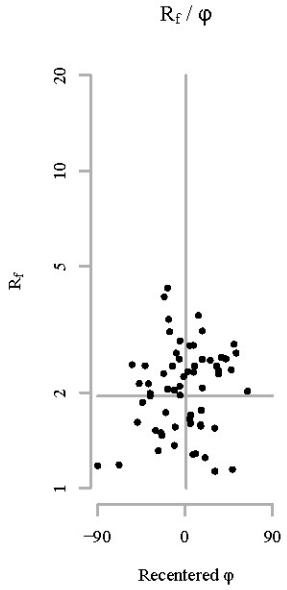

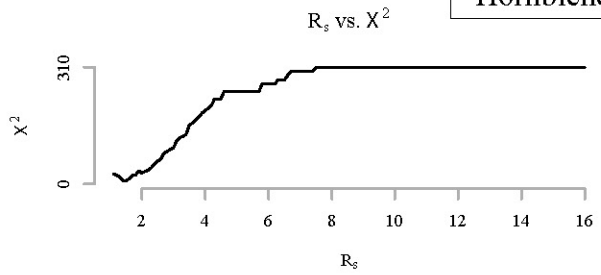

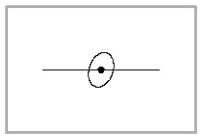

Normalized ellipse

Parameters

Sample size:	62
Fabric ratio:	1.5
Vector mean:	109
Harmonic mean:	1.9
Symmetry:	0.97
Min. chi sq:	8.06
Mean area*:	24464.6

*Average clast area in pixles

Stereonet

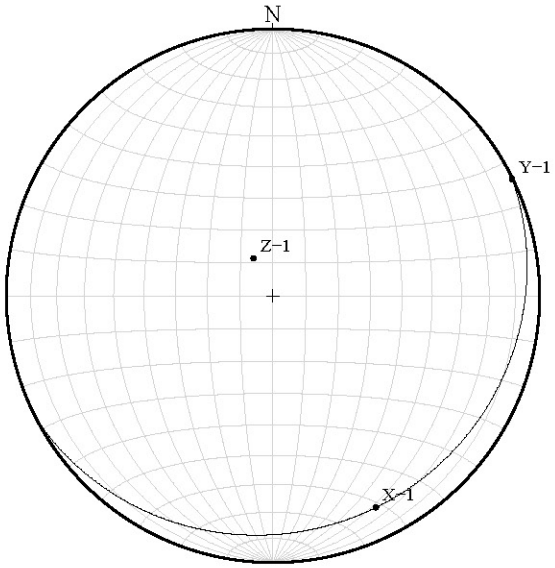

Nadai plot

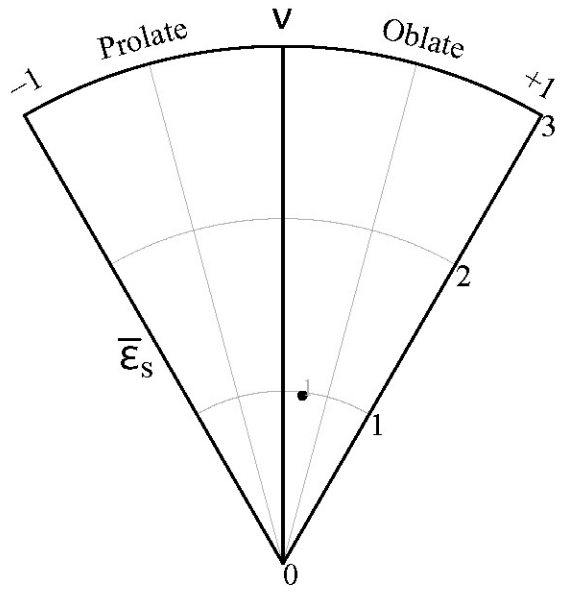

Sectional R_f / φ results for plane: A

Sample: 12DC30_B
Mineral: Plagioclase

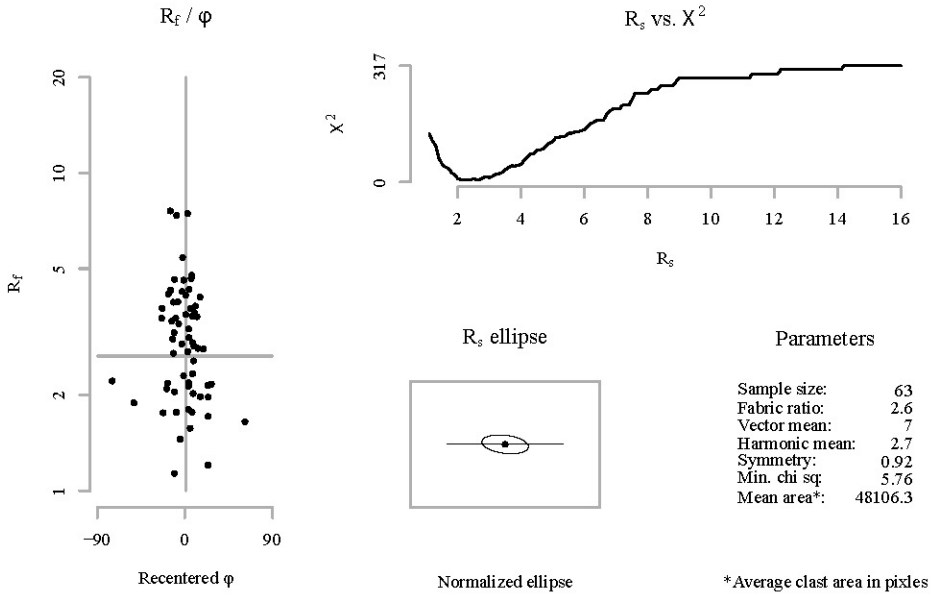

Sectional R_f / φ results for plane: B

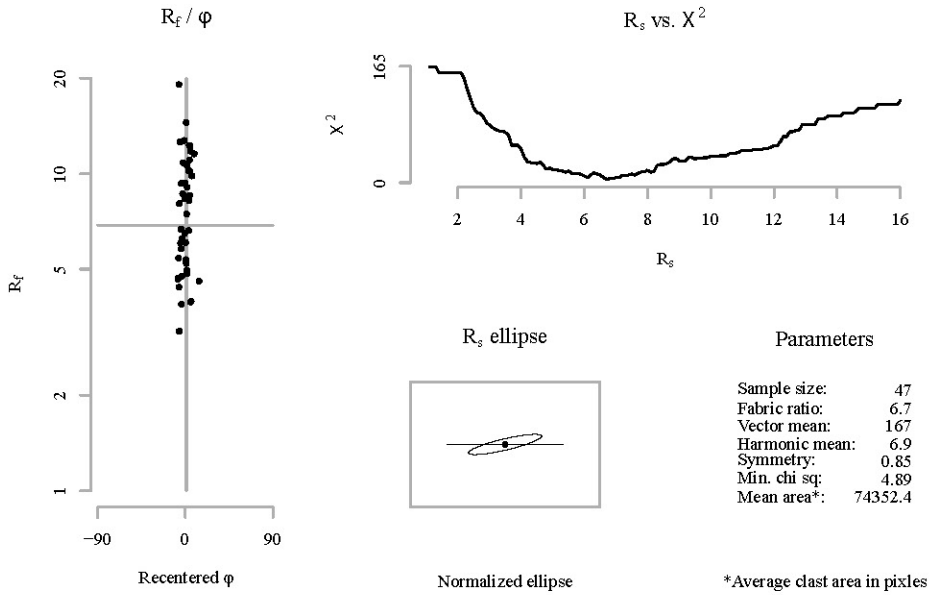

Sectional R_f / φ results for plane: C

Sample: 12DC30_B
Mineral: Plagioclase

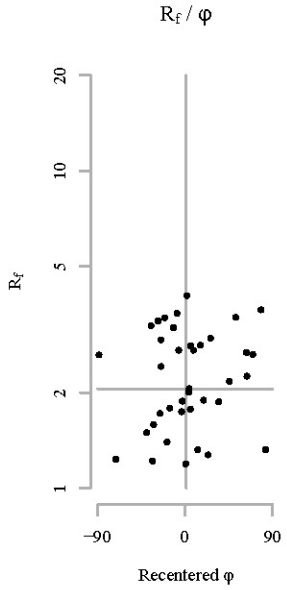

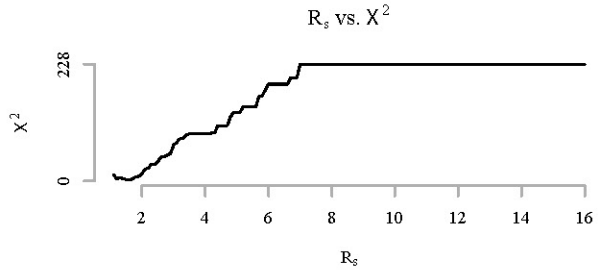

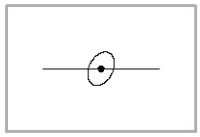

Parameters

Sample size:	38
Fabric ratio:	1.5
Vector mean:	117
Harmonic mean:	2.1
Symmetry:	0.89
Min. chi sq:	2.53
Mean area*:	122708.2

*Average clast area in pixles

Stereonet

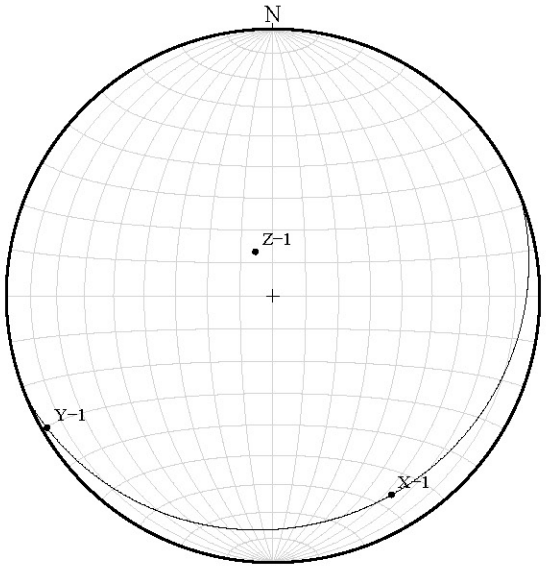

Nadai plot

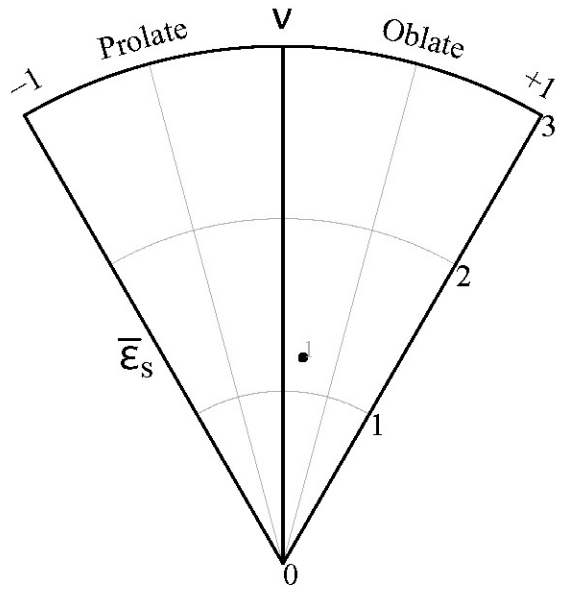

Sectional R_f / φ results for plane: C

Sample: 12DC30_B
Mineral: Plagioclase

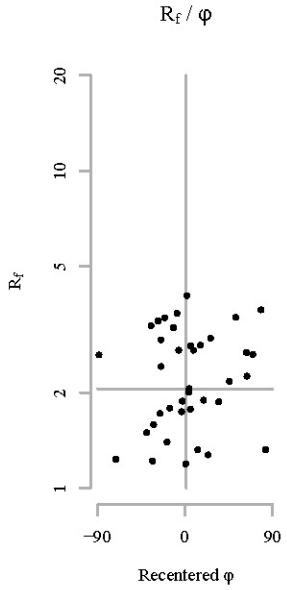

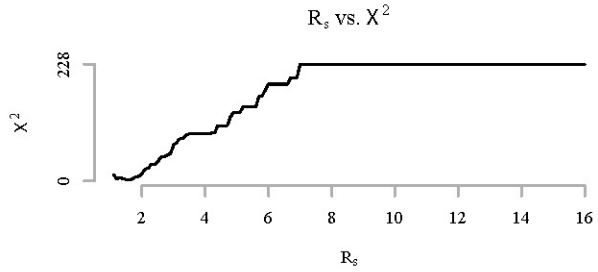

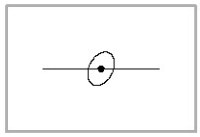

Normalized ellipse

Parameters

Sample size:	38
Fabric ratio:	1.5
Vector mean:	117
Harmonic mean:	2.1
Symmetry:	0.89
Min. chi sq:	2.53
Mean area*:	122708.2

*Average clast area in pixles

Stereonet

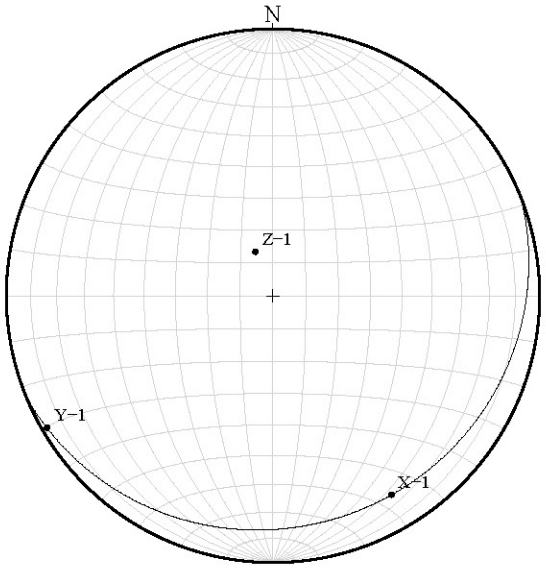

Nadai plot

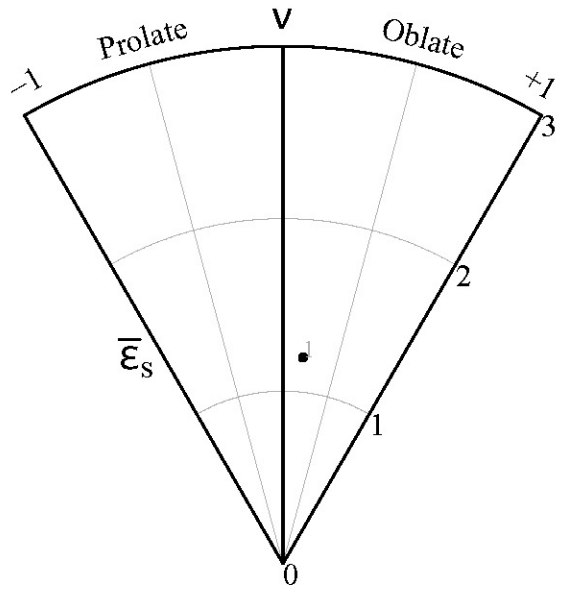

Sample: 12DC35_A
Mineral: Pyroxene / Hornblende

Sectional R_f / φ results for plane: A

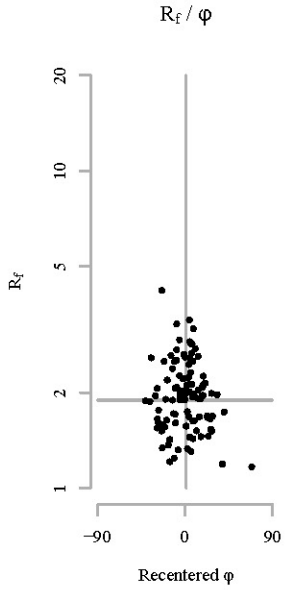

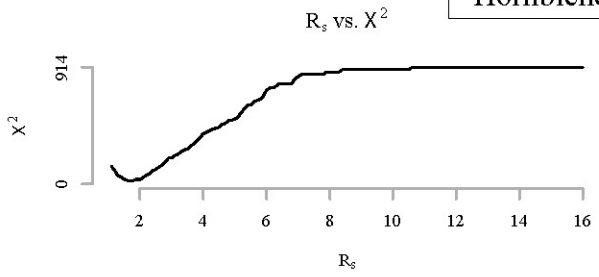

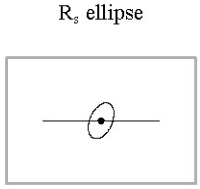

Parameters

Sample size:	101
Fabric ratio:	1.7
Vector mean:	114
Harmonic mean:	1.9
Symmetry:	0.93
Min. chi sq:	22.37
Mean area*:	5932.5

*Average clast area in pixles

Sectional R_f / φ results for plane: B

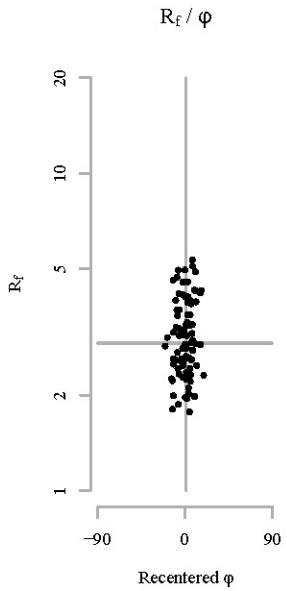

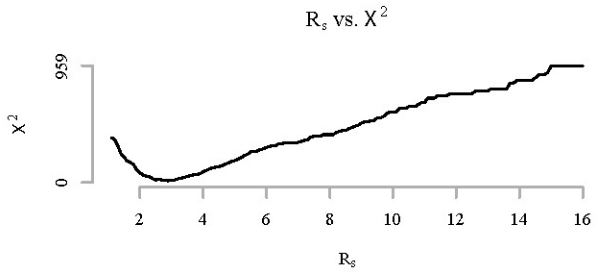

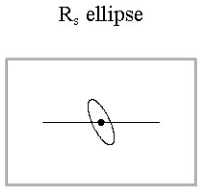

Parameters

Sample size:	86
Fabric ratio:	2.9
Vector mean:	65
Harmonic mean:	2.9
Symmetry:	0.88
Min. chi sq:	12.44
Mean area*:	6483.8

*Average clast area in pixles

Sectional R_f / φ results for plane: C

Sample: 12DC35_A
Mineral: Pyroxene / Hornblende

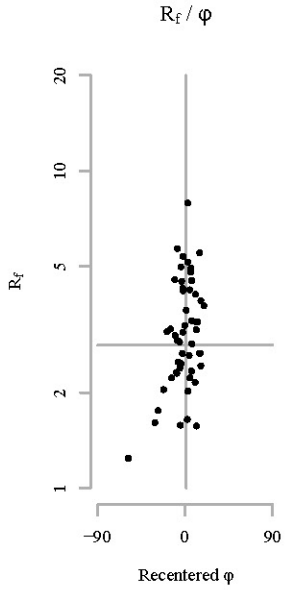

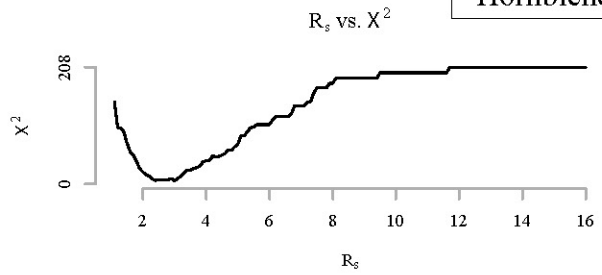

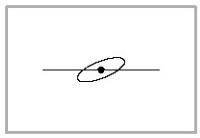

Parameters

Sample size:	52
Fabric ratio:	3
Vector mean:	158
Harmonic mean:	2.8
Symmetry:	0.92
Min. chi sq:	5.69
Mean area*:	17707.2

*Average clast area in pixles

Stereonet

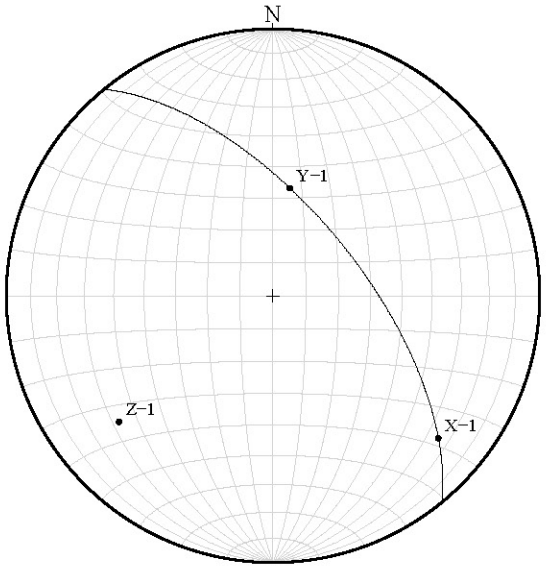

Nadai plot

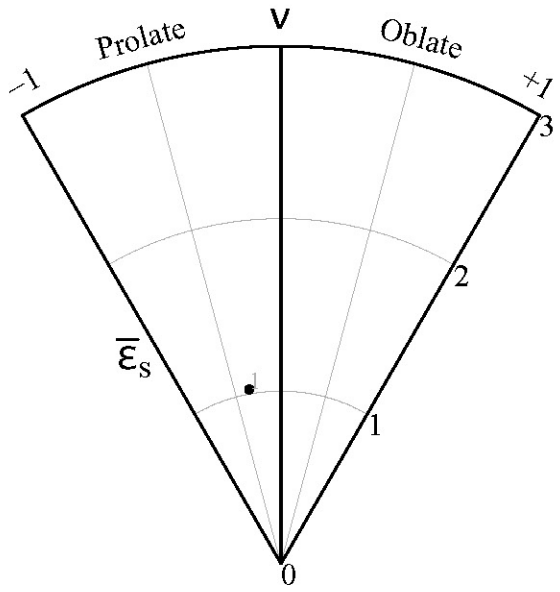

Sectional R_f / φ results for plane: A

Sample: 12DC35_A
Mineral: Plagioclase

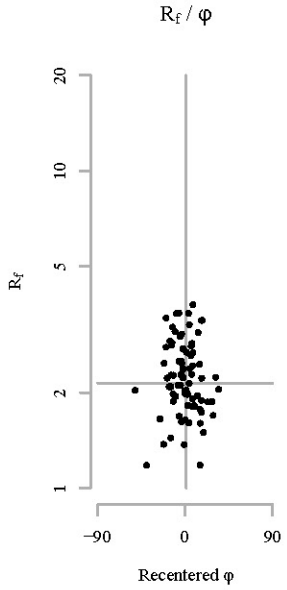

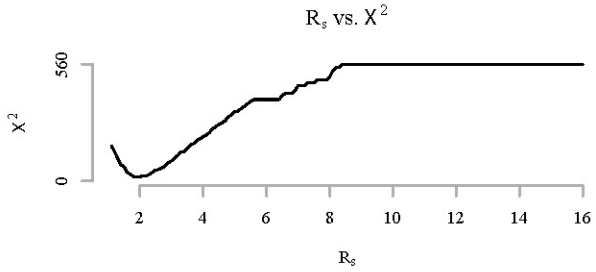

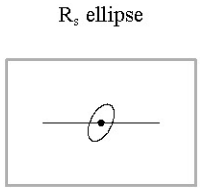

Parameters

Sample size:	80
Fabric ratio:	1.9
Vector mean:	116
Harmonic mean:	2.1
Symmetry:	0.82
Min. chi sq:	17.6
Mean area*:	15594

*Average clast area in pixles

Sectional R_f / φ results for plane: B

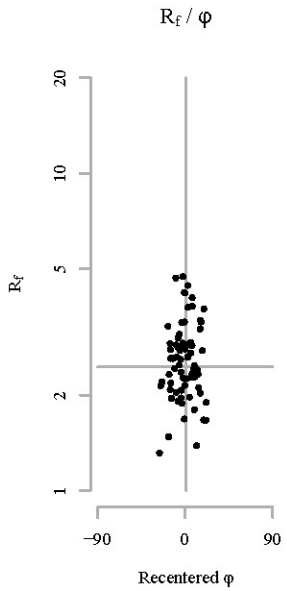

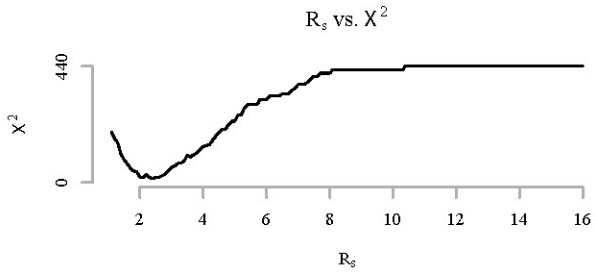

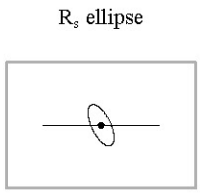

Parameters

Sample size:	73
Fabric ratio:	2.4
Vector mean:	64
Harmonic mean:	2.5
Symmetry:	0.93
Min. chi sq:	13.49
Mean area*:	15790.4

*Average clast area in pixles

Sectional R_f / φ results for plane: C

Sample: 12DC35_A
Mineral: Plagioclase

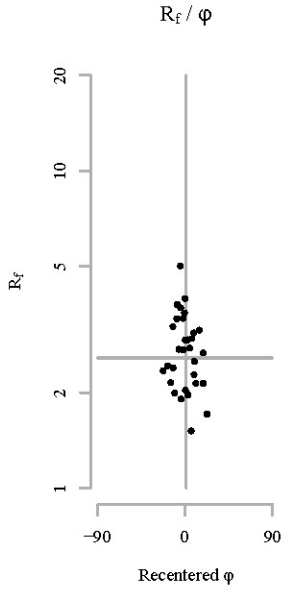

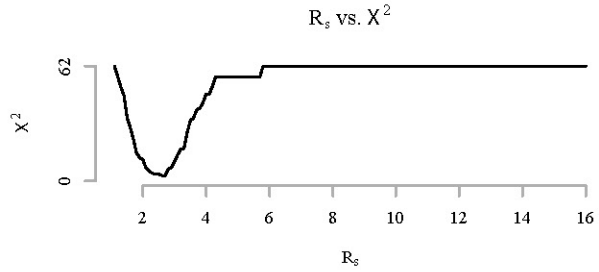

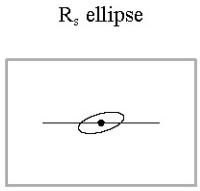

Parameters

Sample size:	31
Fabric ratio:	2.6
Vector mean:	165
Harmonic mean:	2.6
Symmetry:	0.84
Min. chi sq:	2.87
Mean area*:	51933.9

*Average clast area in pixles

Stereonet

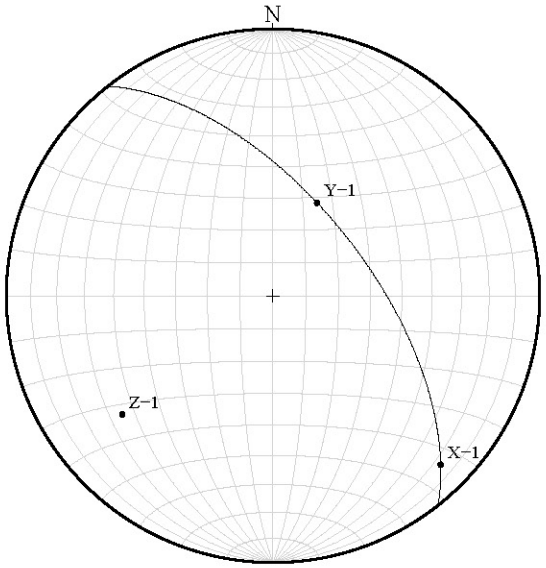

Nadai plot

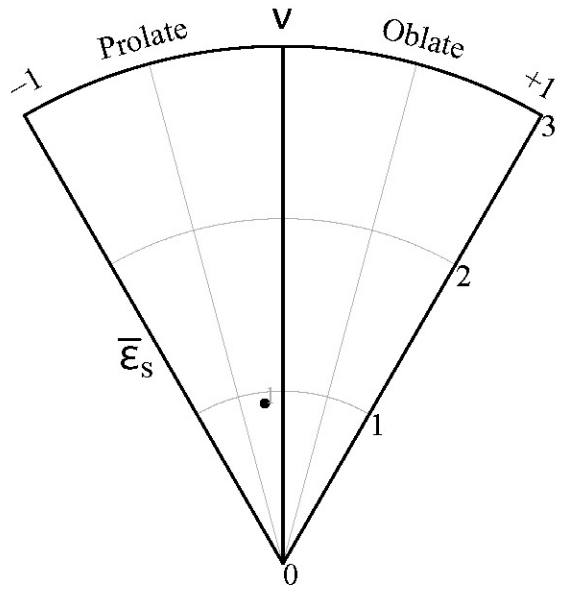

Sectional R_f / φ results for plane: A

Sample: 12DC35_B
Mineral: Pyroxene

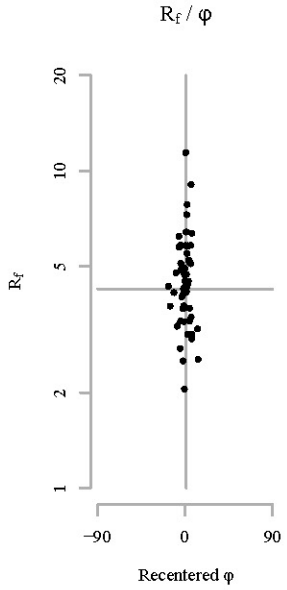

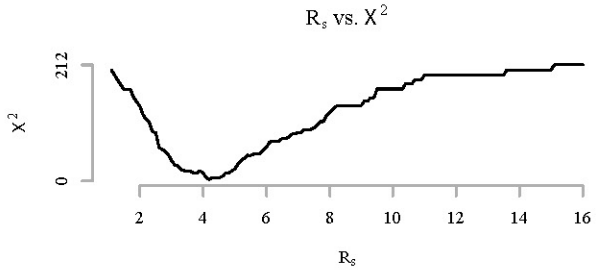

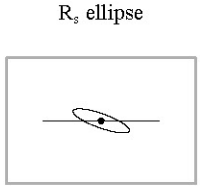

Normalized ellipse

Parameters

Sample size:	53
Fabric ratio:	4.2
Vector mean:	20
Harmonic mean:	4.2
Symmetry:	0.91
Min. chi sq:	2.66
Mean area*:	17102.7

*Average clast area in pixles

Sectional R_f / φ results for plane: B

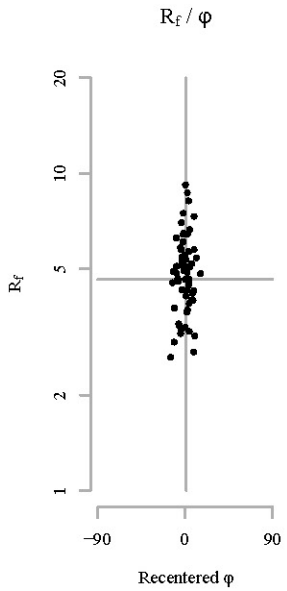

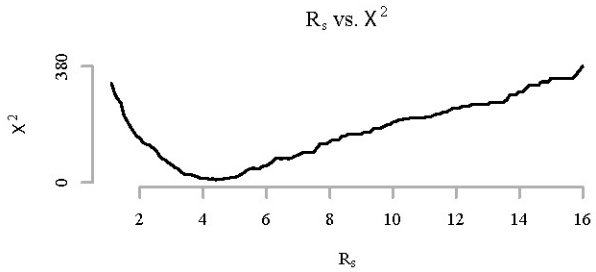

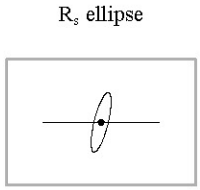

Normalized ellipse

Parameters

Sample size:	65
Fabric ratio:	4.4
Vector mean:	104
Harmonic mean:	4.6
Symmetry:	0.89
Min. chi sq:	8
Mean area*:	11121.3

*Average clast area in pixles

Sectional R_f / φ results for plane: C

Sample: 12DC35_B
Mineral: Pyroxene

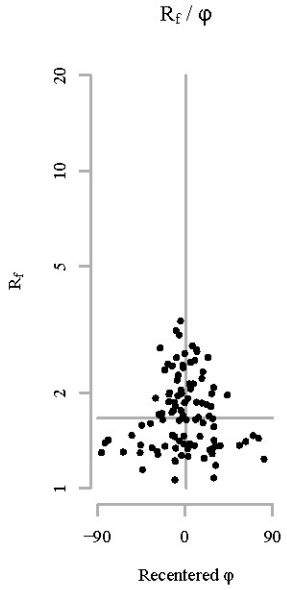

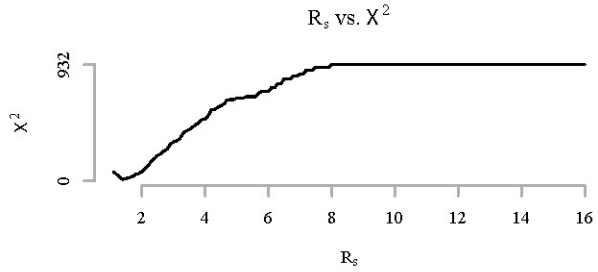

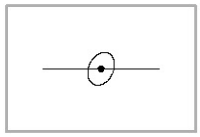

Parameters

Sample size:	102
Fabric ratio:	1.4
Vector mean:	115
Harmonic mean:	1.7
Symmetry:	0.88
Min. chi sq:	11.33
Mean area*:	8347.6

*Average clast area in pixles

Stereonet

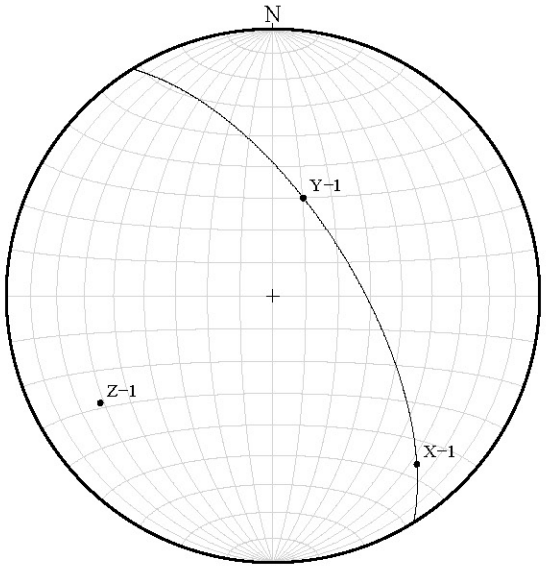

Nadai plot

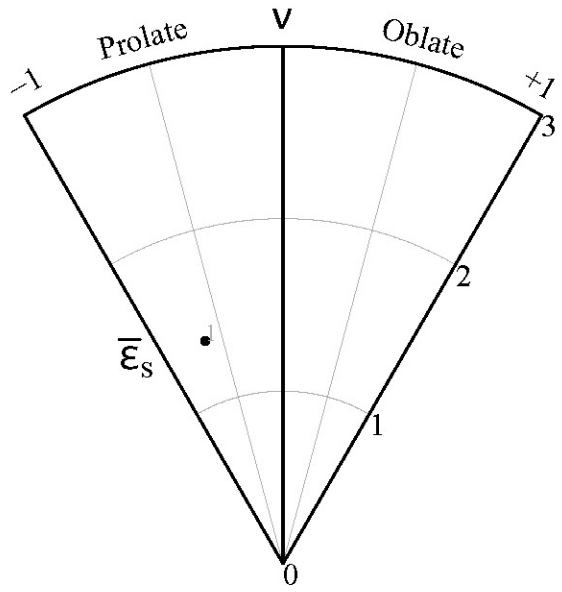

Sectional R_f / φ results for plane: A

Sample: 12DC38_A
Mineral: Pyroxene

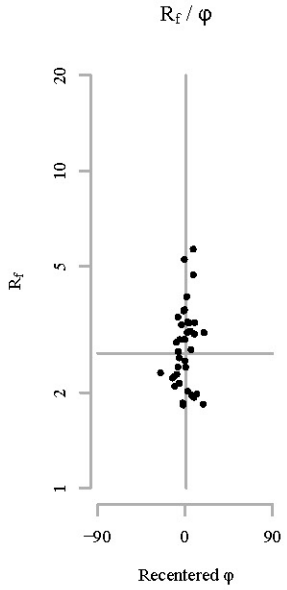

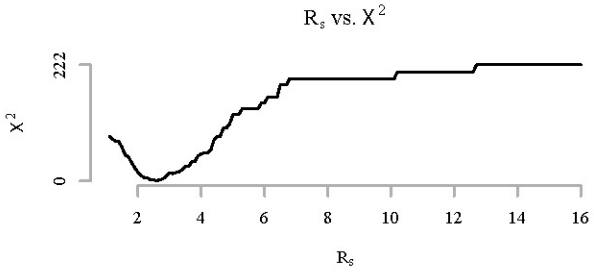

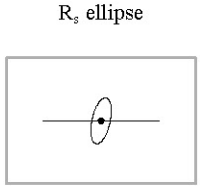

Normalized ellipse

Parameters

Sample size:	37
Fabric ratio:	2.6
Vector mean:	102
Harmonic mean:	2.7
Symmetry:	0.81
Min. chi sq:	0.65
Mean area*:	14950.9

*Average clast area in pixles

Sectional R_f / φ results for plane: B

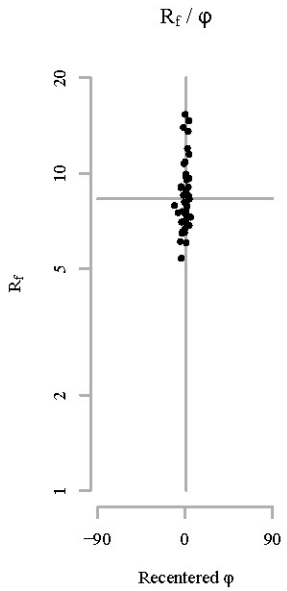

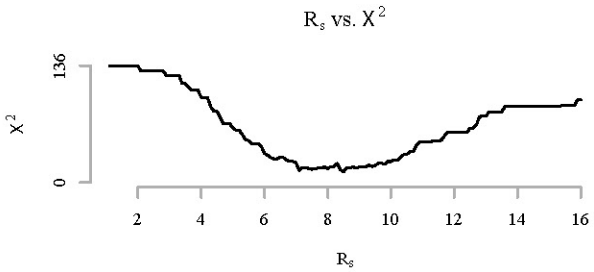

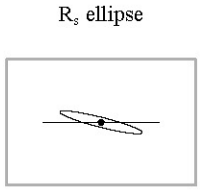

Normalized ellipse

Parameters

Sample size:	42
Fabric ratio:	8.5
Vector mean:	14
Harmonic mean:	8.3
Symmetry:	0.76
Min. chi sq:	12.1
Mean area*:	10529.6

*Average clast area in pixles

Sectional R_f / φ results for plane: C

Sample: 12DC38_A
Mineral: Pyroxene

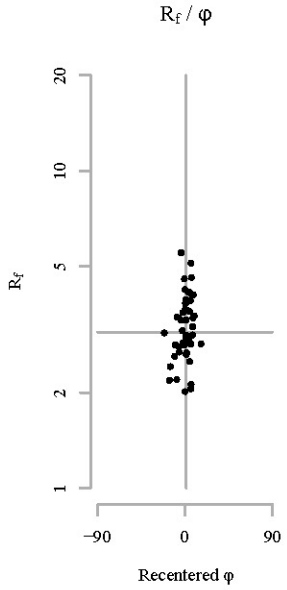

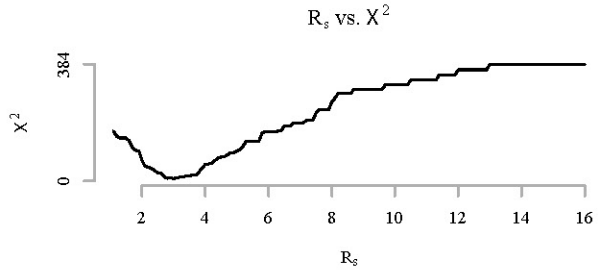

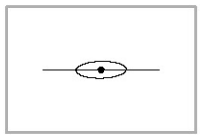

Parameters

Sample size:	48
Fabric ratio:	3
Vector mean:	179
Harmonic mean:	3.1
Symmetry:	0.79
Min. chi sq:	7.5
Mean area*:	3929.2

*Average clast area in pixles

Stereonet

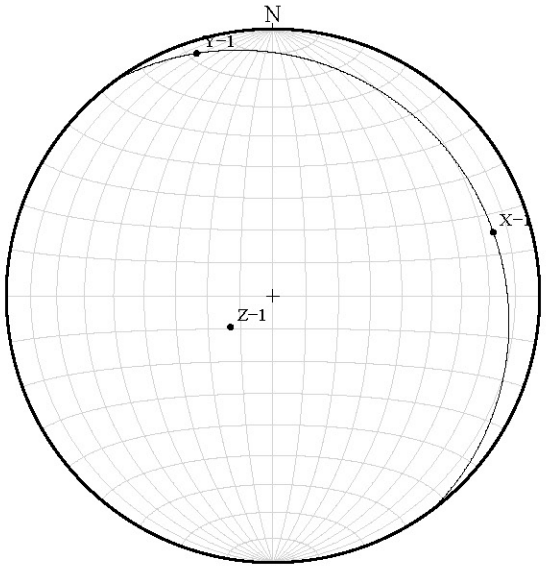

Nadai plot

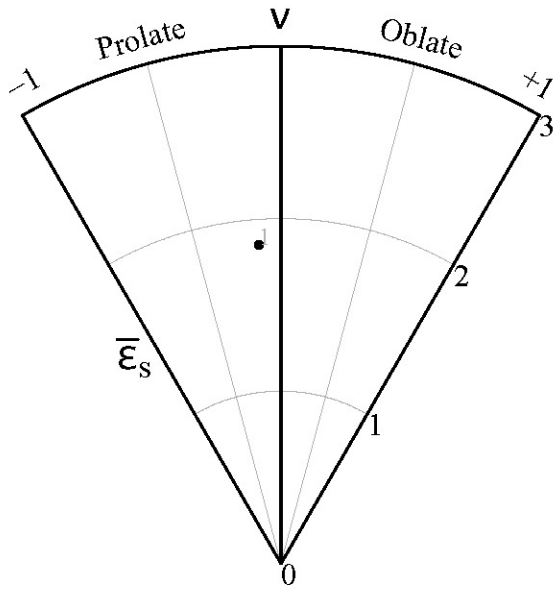

Sectional R_f / φ results for plane: A

Sample: 12DC38_A
Mineral: Plagioclase

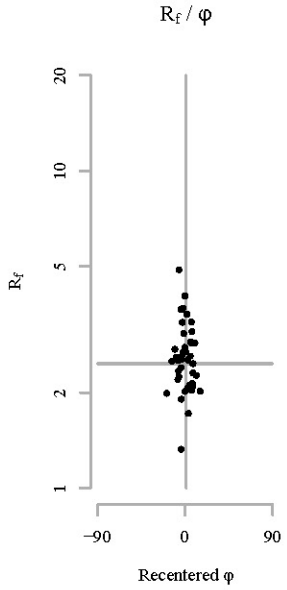

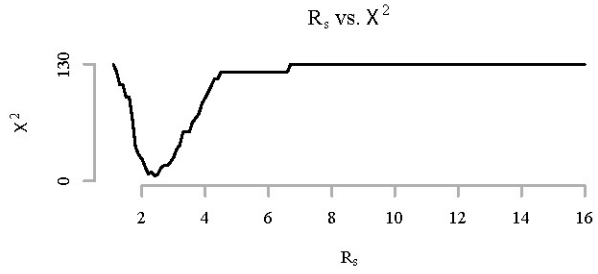

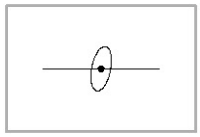

Normalized ellipse

Parameters

Sample size:	43
Fabric ratio:	2.4
Vector mean:	101
Harmonic mean:	2.5
Symmetry:	0.84
Min. chi sq:	5.56
Mean area*:	19641.5

*Average clast area in pixles

Sectional R_f / φ results for plane: B

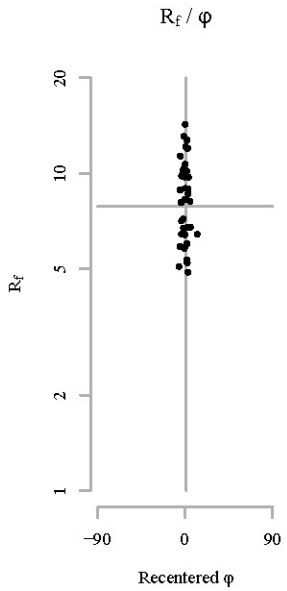

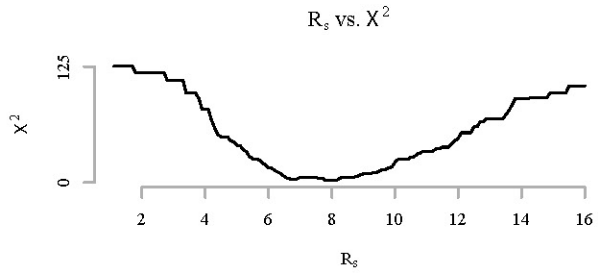

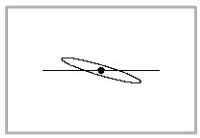

Normalized ellipse

Parameters

Sample size:	41
Fabric ratio:	8
Vector mean:	16
Harmonic mean:	7.9
Symmetry:	0.88
Min. chi sq:	1.73
Mean area*:	15718.2

*Average clast area in pixles

Sectional R_f / φ results for plane: C

Sample: 12DC38_A
Mineral: Plagioclase

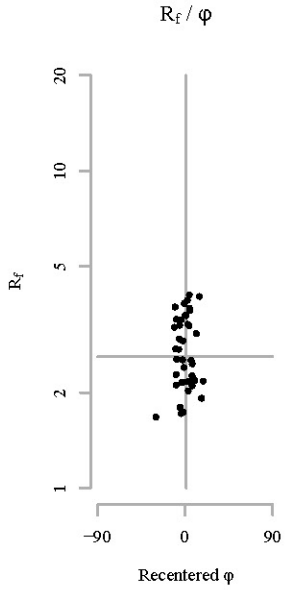

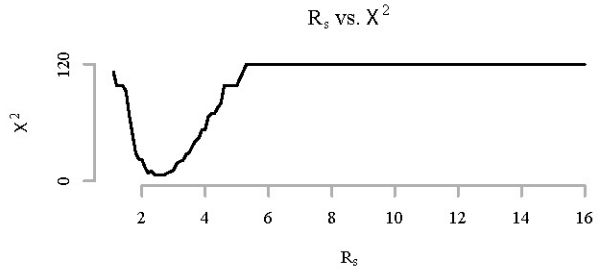

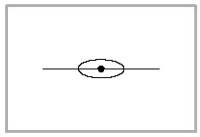

Parameters

Sample size:	40
Fabric ratio:	2.5
Vector mean:	1
Harmonic mean:	2.6
Symmetry:	1
Min. chi sq:	5.6
Mean area*:	11038

*Average clast area in pixles

Stereonet

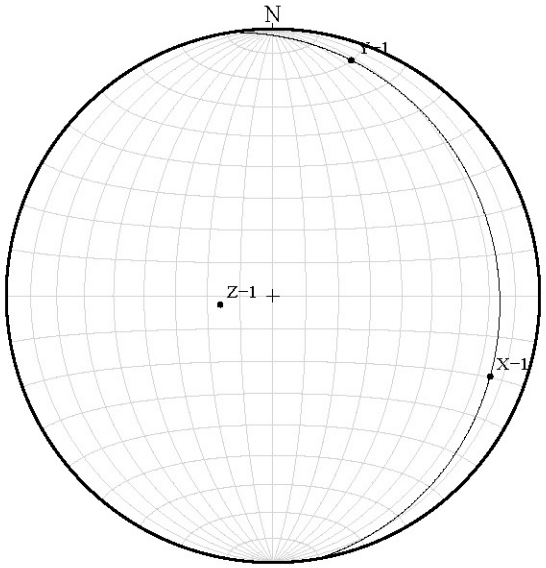

Nadai plot

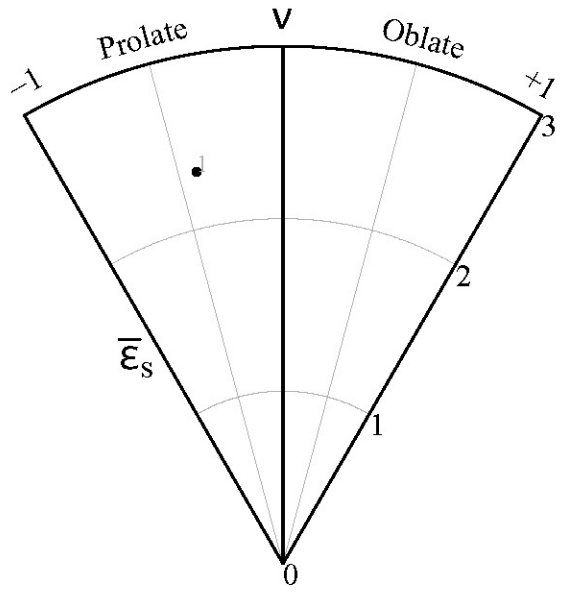

Sectional R_f / φ results for plane: A

Sample: 12DC38_C
Mineral: Pyroxene

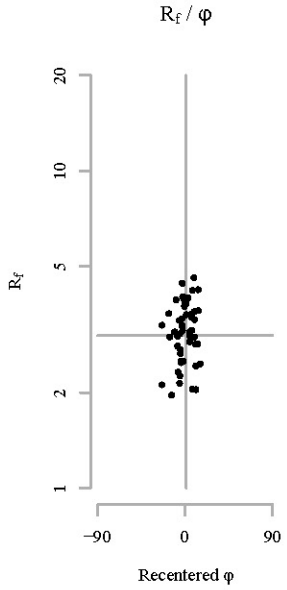

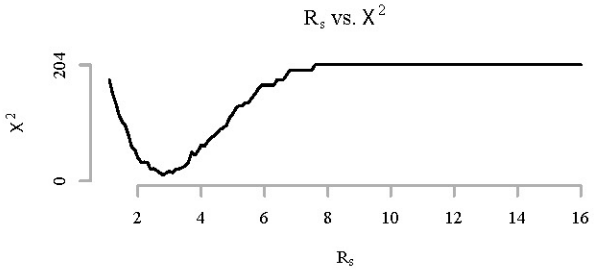

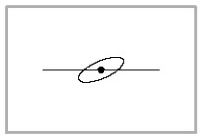

Normalized ellipse

Parameters

Sample size:	51
Fabric ratio:	2.8
Vector mean:	157
Harmonic mean:	3
Symmetry:	0.86
Min. chi sq:	9.59
Mean area*:	2994.4

*Average clast area in pixles

Sectional R_f / φ results for plane: B

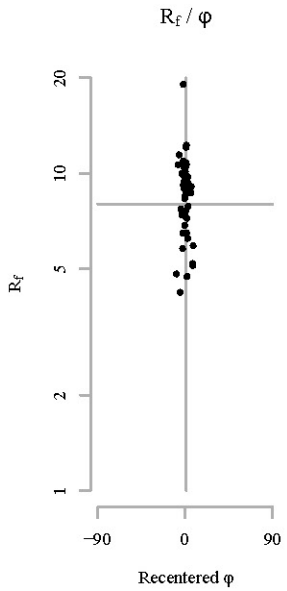

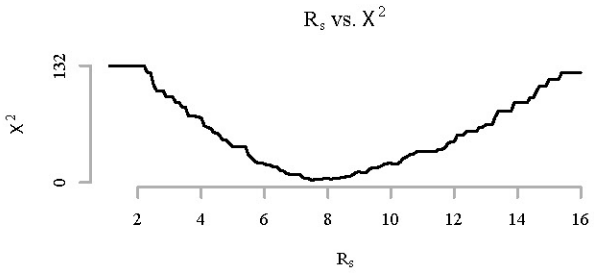

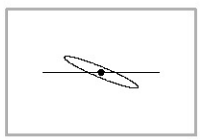

Normalized ellipse

Parameters

Sample size:	44
Fabric ratio:	7.5
Vector mean:	22
Harmonic mean:	8
Symmetry:	1
Min. chi sq:	2.18
Mean area*:	5732.8

*Average clast area in pixles

Sectional R_f / φ results for plane: C

Sample: 12DC38_C
Mineral: Pyroxene

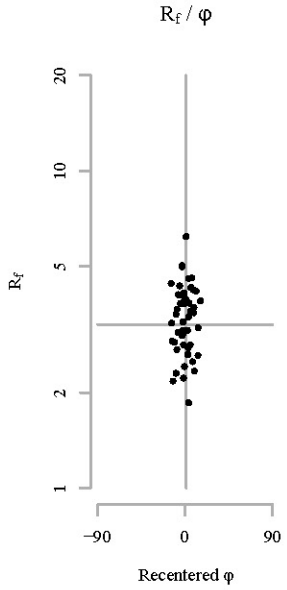

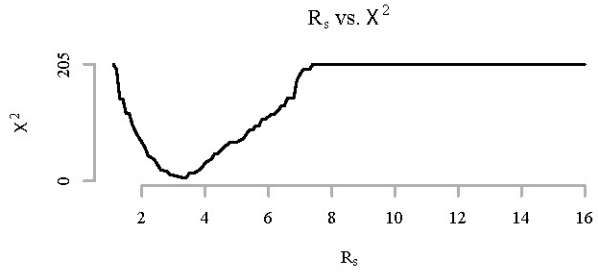

Rs ellipse

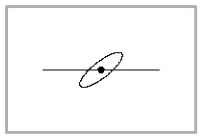

Normalized ellipse

Parameters

Sample size:	51
Fabric ratio:	3.3
Vector mean:	142
Harmonic mean:	3.3
Symmetry:	0.94
Min. chi sq:	4.88
Mean area*:	3263

*Average clast area in pixles

Stereonet

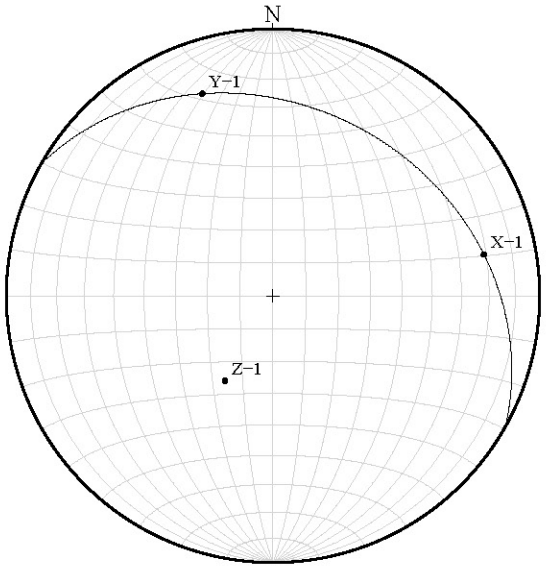

Nadai plot

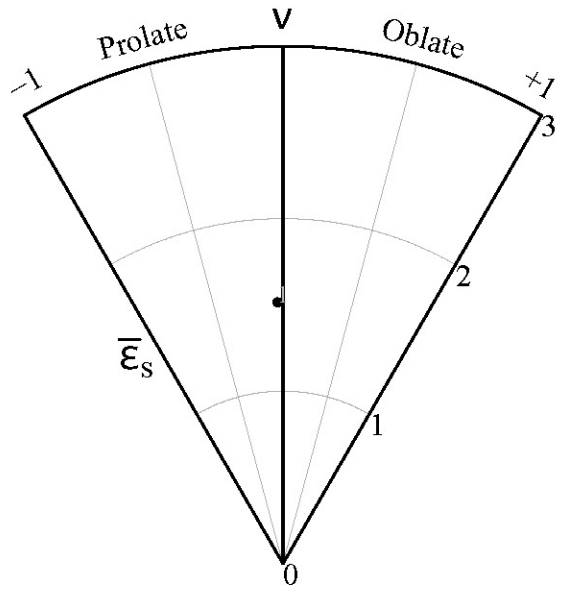

Sectional R_f / φ results for plane: A

Sample: 12DC38_C
Mineral: Plagioclase

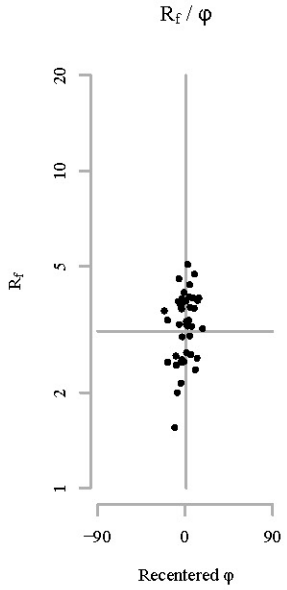

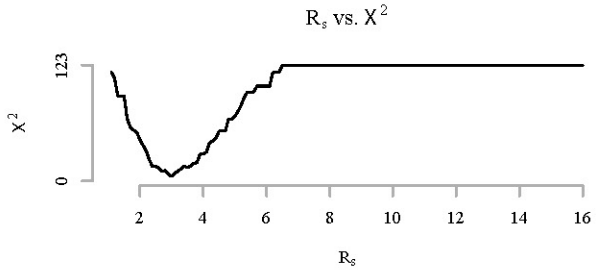

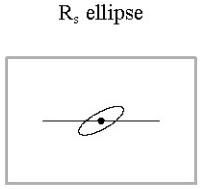

Normalized ellipse

Parameters

Sample size:	41
Fabric ratio:	3
Vector mean:	151
Harmonic mean:	3.1
Symmetry:	0.73
Min. chi sq:	4.85
Mean area*:	3648.5

*Average clast area in pixles

Sectional R_f / φ results for plane: B

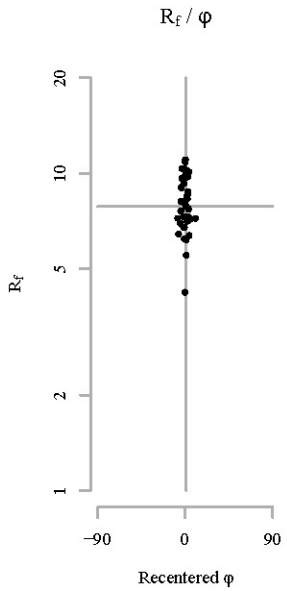

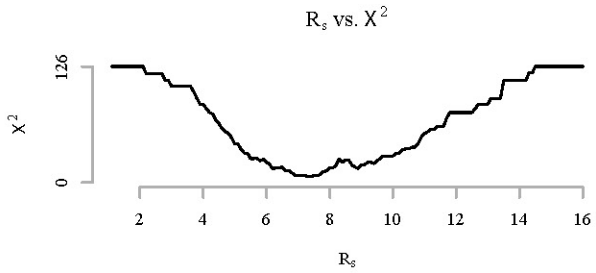

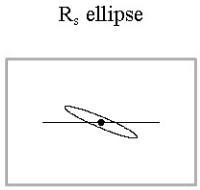

Normalized ellipse

Parameters

Sample size:	42
Fabric ratio:	7.3
Vector mean:	23
Harmonic mean:	7.9
Symmetry:	0.95
Min. chi sq:	6
Mean area*:	7531.9

*Average clast area in pixles

Sectional R_f / φ results for plane: C

Sample: 12DC38_C
Mineral: Plagioclase

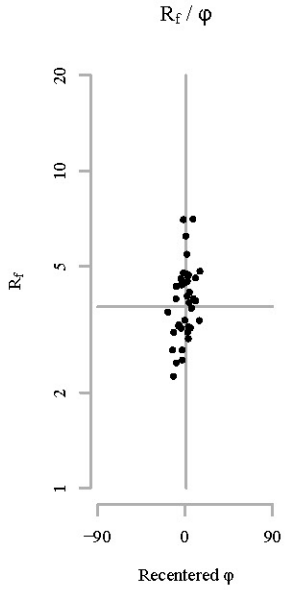

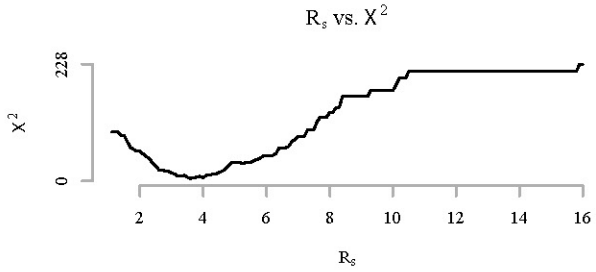

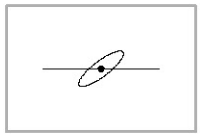

Parameters

Sample size:	38
Fabric ratio:	3.6
Vector mean:	143
Harmonic mean:	3.7
Symmetry:	0.68
Min. chi sq:	4.74
Mean area*:	3102.8

*Average clast area in pixles

Stereonet

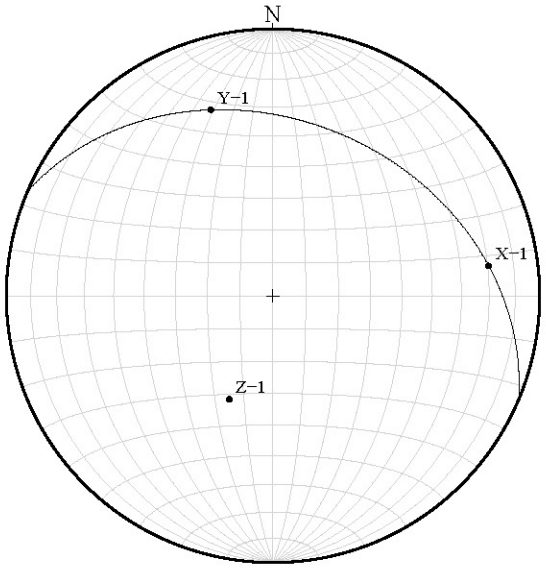

Nadai plot

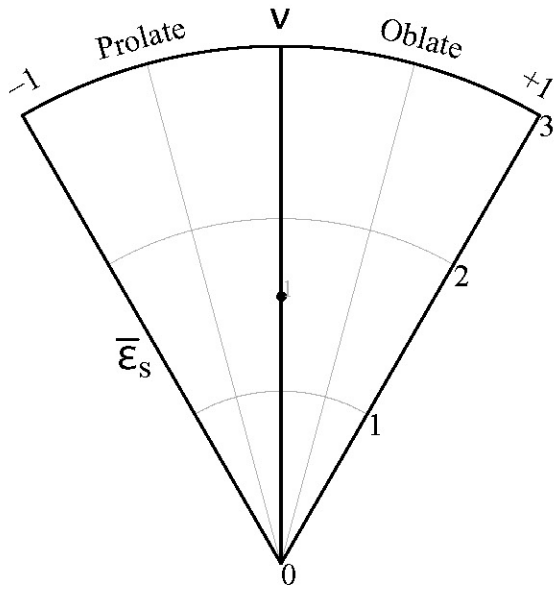

Sectional R_f / φ results for plane: A

Sample: 12DC39_A
Mineral: Hornblende

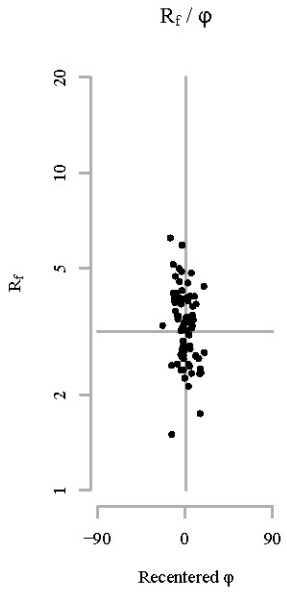

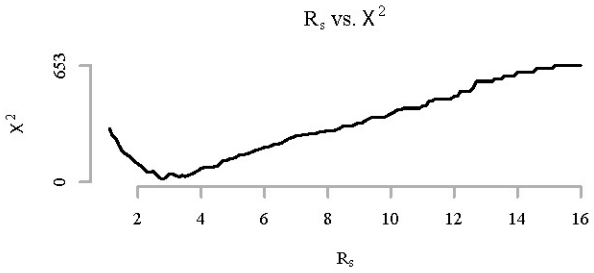

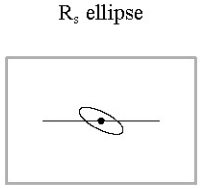

Normalized ellipse

Parameters

Sample size:	75
Fabric ratio:	2.8
Vector mean:	27
Harmonic mean:	3.2
Symmetry:	0.91
Min. chi sq:	15.6
Mean area*:	3279.6

*Average clast area in pixles

Sectional R_f / φ results for plane: B

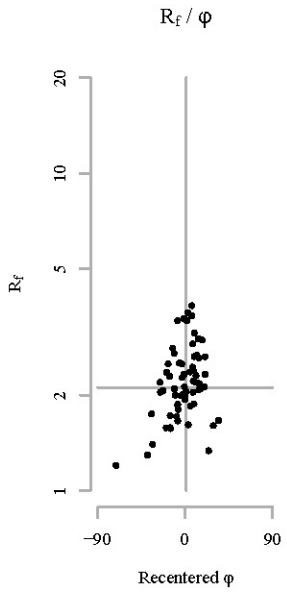

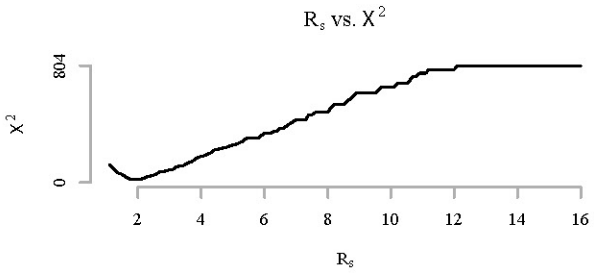

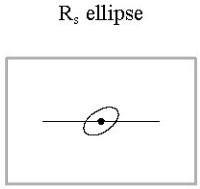

Normalized ellipse

Parameters

Sample size:	67
Fabric ratio:	1.8
Vector mean:	147
Harmonic mean:	2.1
Symmetry:	0.69
Min. chi sq:	20.12
Mean area*:	2229.2

*Average clast area in pixles

Sectional R_f / φ results for plane: C

Sample: 12DC39_A
Mineral: Hornblende

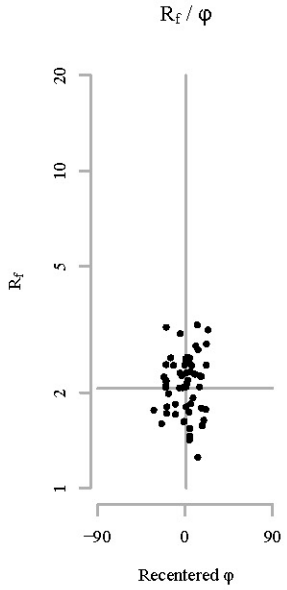

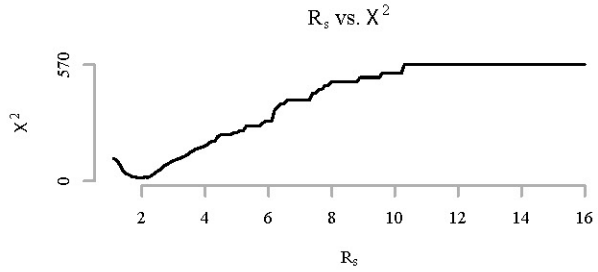

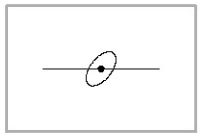

Parameters

Sample size:	57
Fabric ratio:	1.9
Vector mean:	128
Harmonic mean:	2.1
Symmetry:	0.84
Min. chi sq:	14.6
Mean area*:	4307.9

*Average clast area in pixles

Stereonet

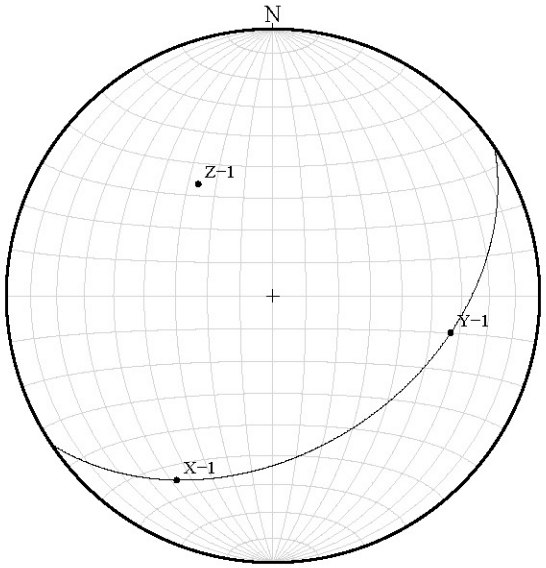

Nadai plot

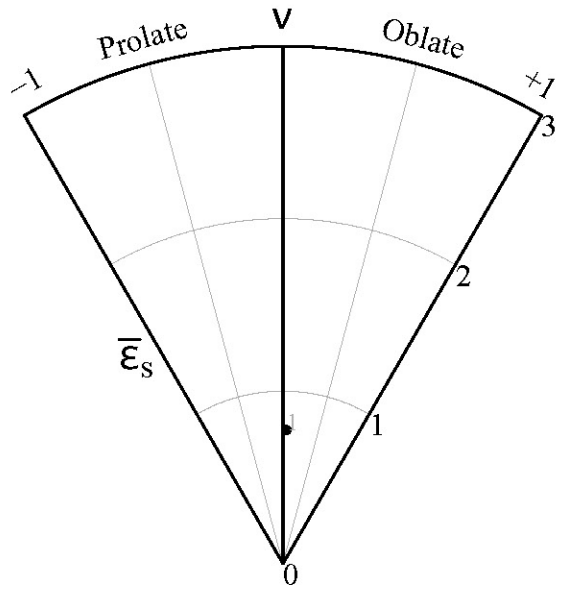

Sectional R_f / φ results for plane: A

Sample: 12DC39_A
Mineral: Plagioclase

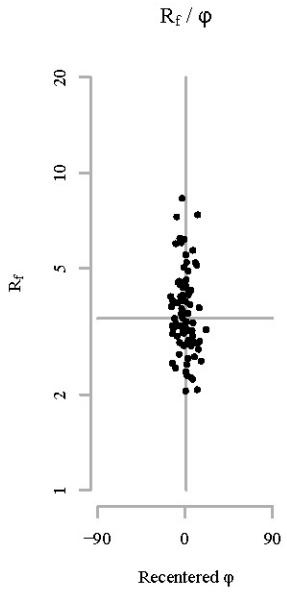

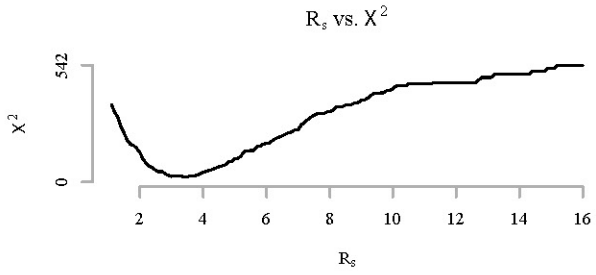

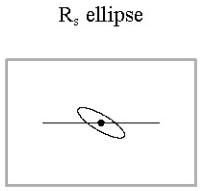

Parameters

Sample size:	84
Fabric ratio:	3.4
Vector mean:	30
Harmonic mean:	3.5
Symmetry:	0.81
Min. chi sq:	21.52
Mean area*:	4874

*Average clast area in pixles

Sectional R_f / φ results for plane: B

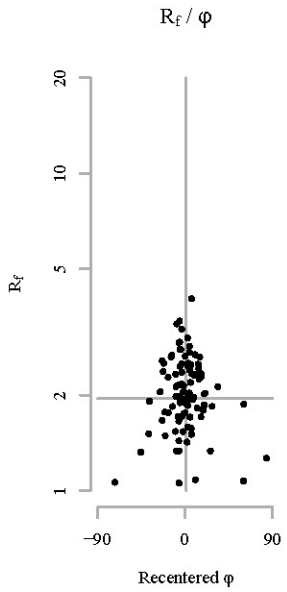

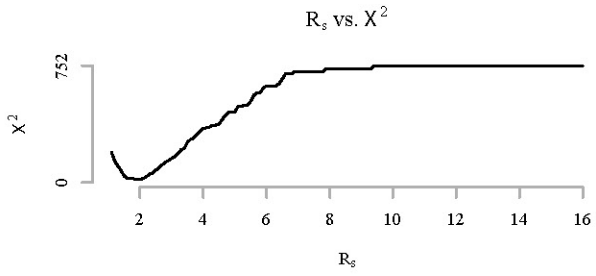

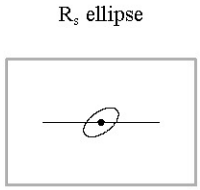

Parameters

Sample size:	94
Fabric ratio:	1.9
Vector mean:	144
Harmonic mean:	2
Symmetry:	0.94
Min. chi sq:	17.83
Mean area*:	3145.2

*Average clast area in pixles

Sectional R_f / φ results for plane: C

Sample: 12DC39_A
Mineral: Plagioclase

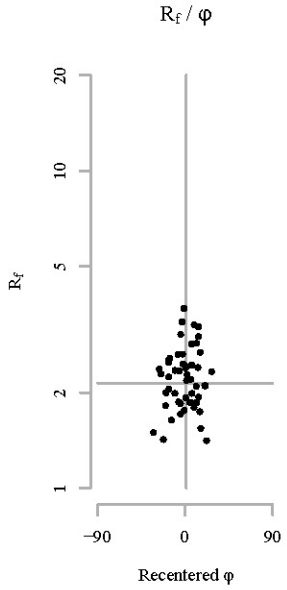

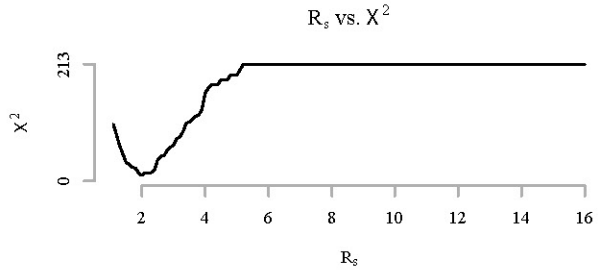

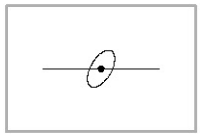

Parameters

Sample size:	53
Fabric ratio:	2
Vector mean:	120
Harmonic mean:	2.1
Symmetry:	0.94
Min. chi sq:	9.83
Mean area*:	5190.6

*Average clast area in pixles

Stereonet

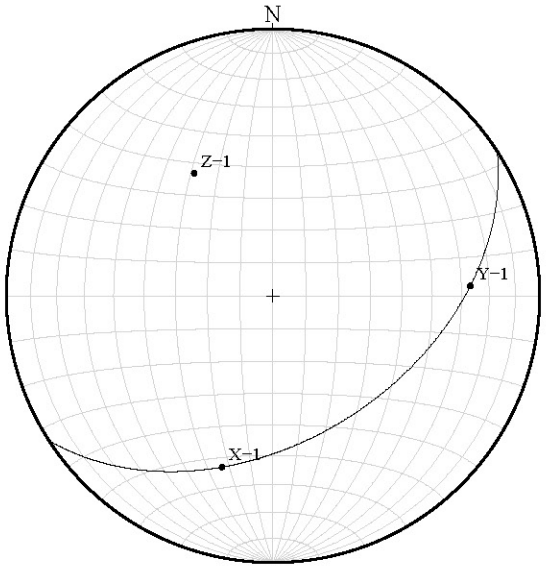

Nadai plot

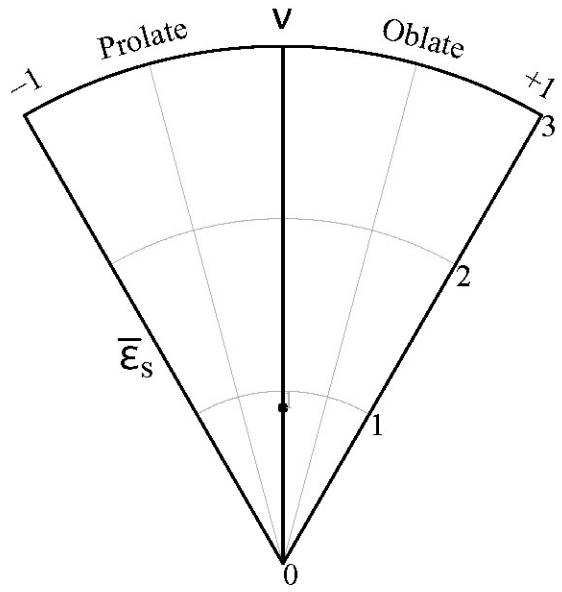

Sample: 12DC41_B
Mineral: Hornblende

Sectional R_f / φ results for plane: A

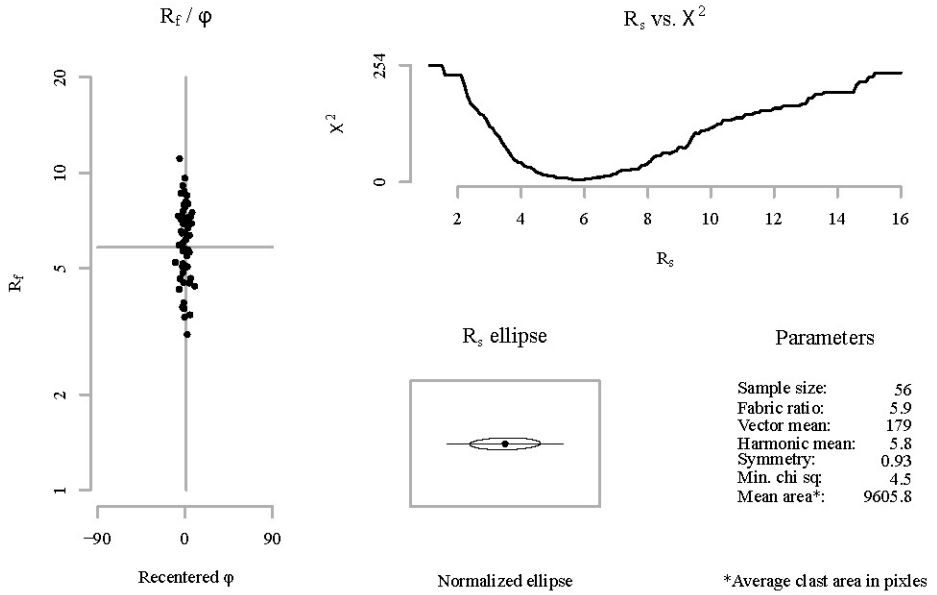

Sectional R_f / φ results for plane: B

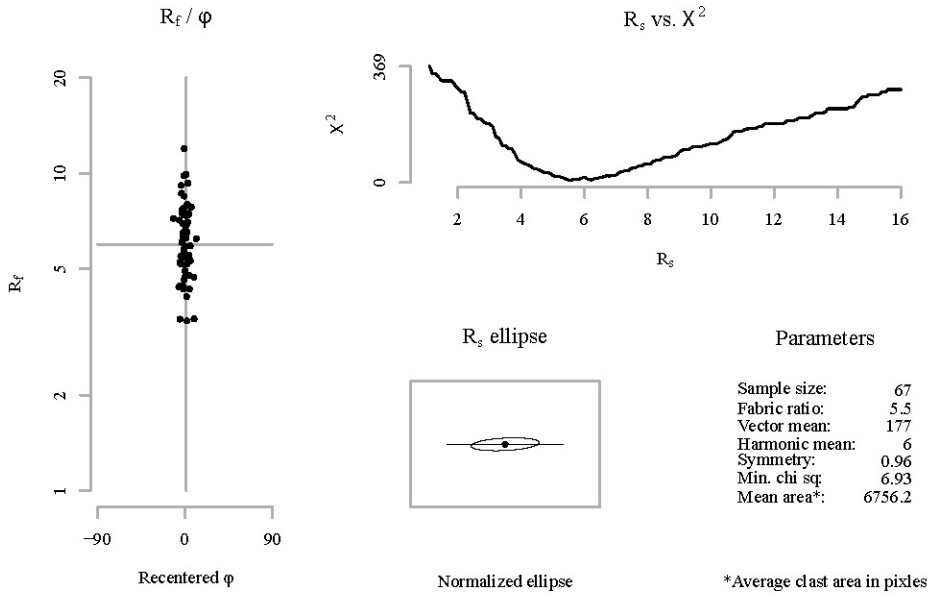

Sectional R_f / φ results for plane: C

Sample: 12DC41_B
Mineral: Hornblende

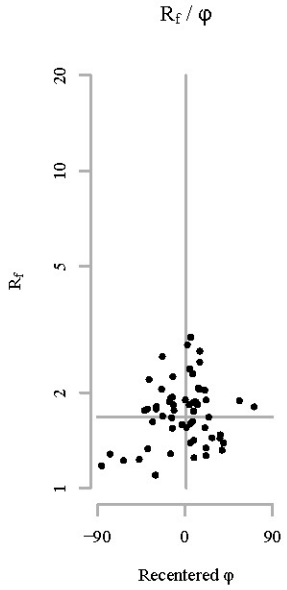

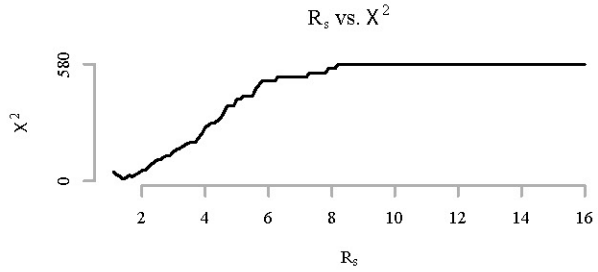

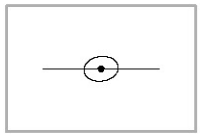

Parameters

Sample size:	58
Fabric ratio:	1.4
Vector mean:	172
Harmonic mean:	1.7
Symmetry:	0.86
Min. chi sq:	9.9
Mean area*:	3309.8

*Average clast area in pixles

Stereonet

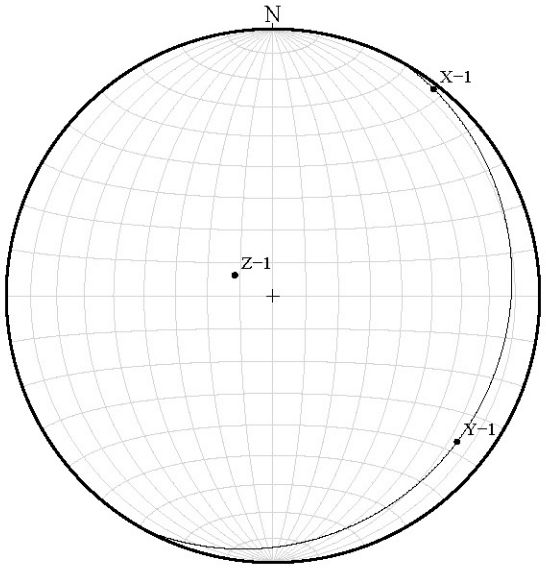

Nadai plot

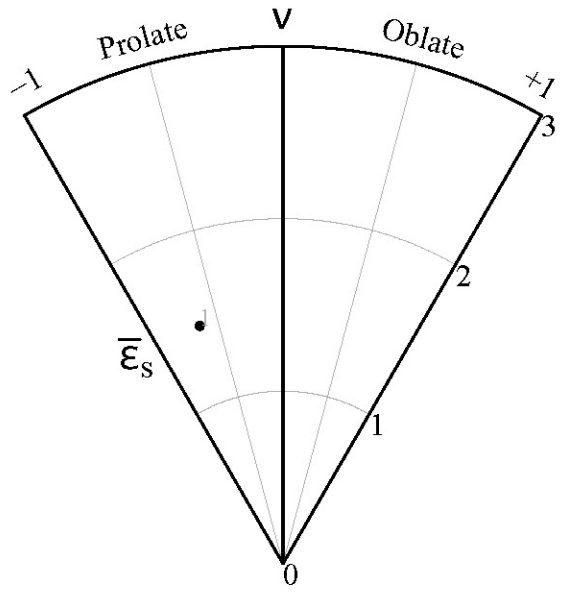

Sectional R_f / φ results for plane: A

Sample: 12DC41_B
Mineral: Plagioclase

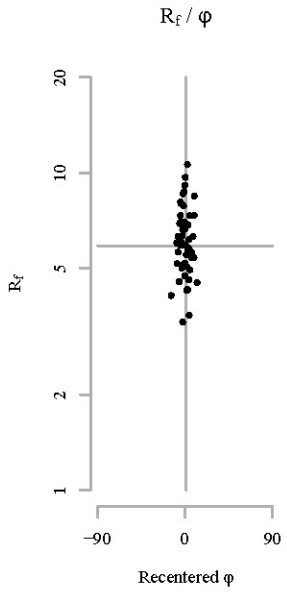

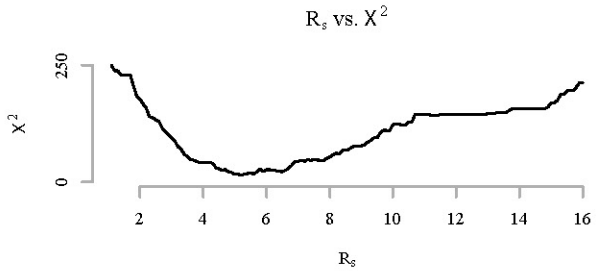

Rs ellipse

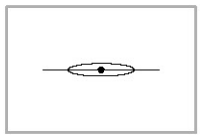

Normalized ellipse

Parameters

Sample size:	55
Fabric ratio:	5.2
Vector mean:	180
Harmonic mean:	5.9
Symmetry:	0.69
Min. chi sq:	14
Mean area*:	17428.5

*Average clast area in pixles

Sectional R_f / φ results for plane: B

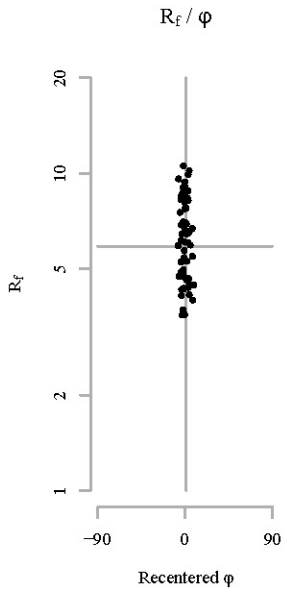

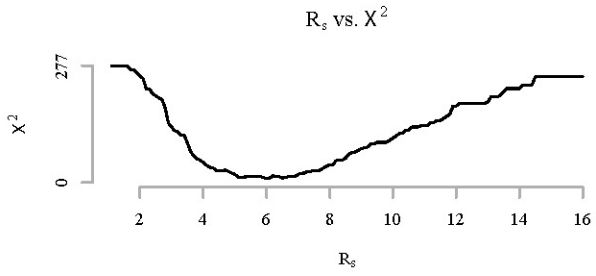

Rs ellipse

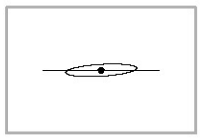

Normalized ellipse

Parameters

Sample size:	59
Fabric ratio:	6
Vector mean:	177
Harmonic mean:	5.9
Symmetry:	0.81
Min. chi sq:	9.42
Mean area*:	12128

*Average clast area in pixles

Sectional R_f / φ results for plane: C

Sample: 12DC41_B
Mineral: Plagioclase

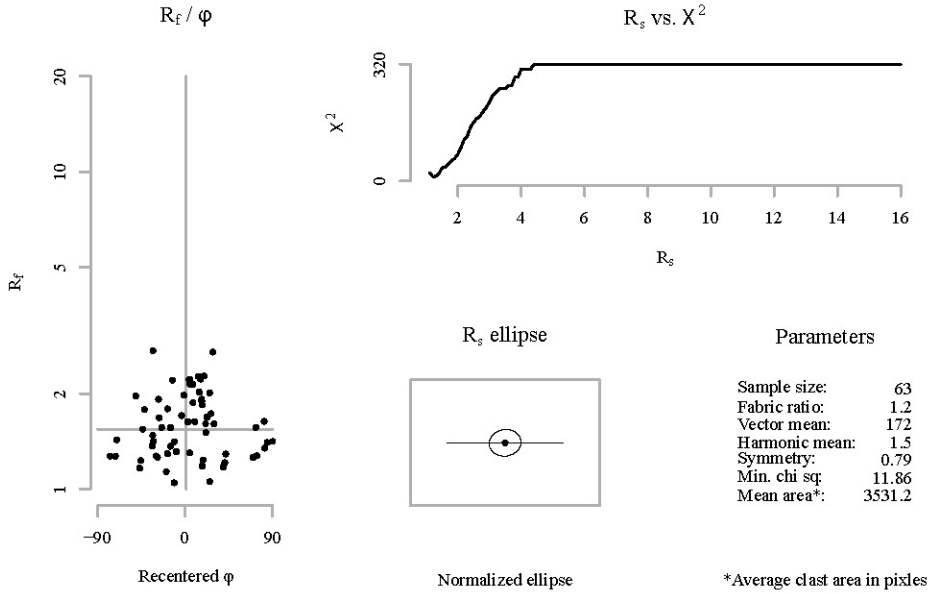

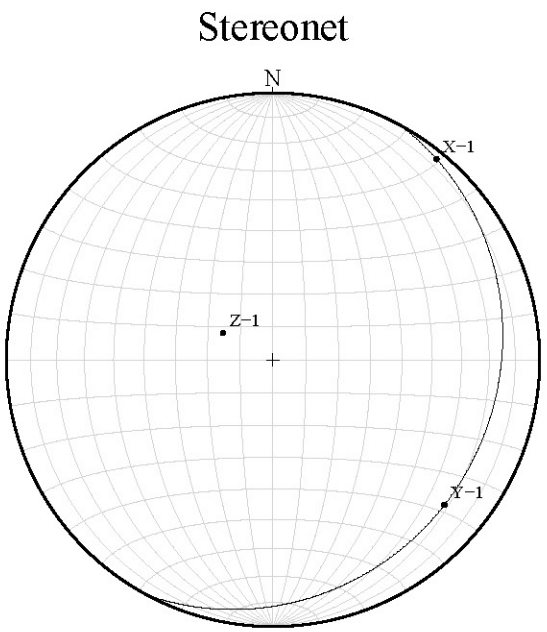

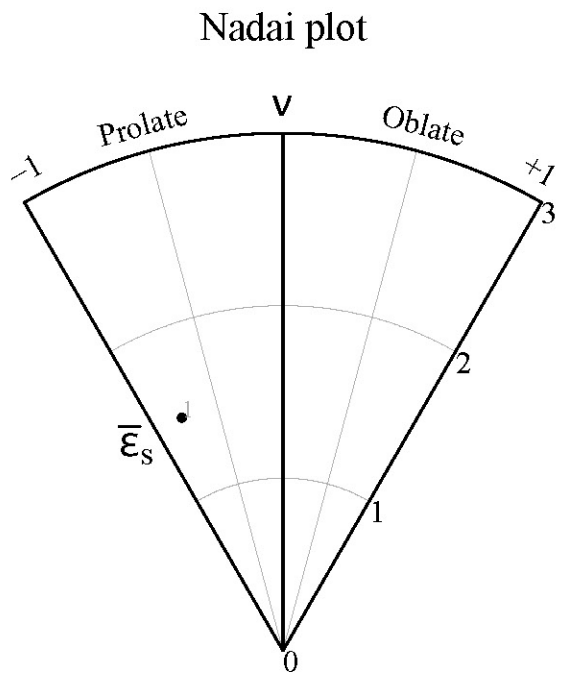

Sample: 12DC42_A
Mineral: Hornblende

Sectional R_f / φ results for plane: A

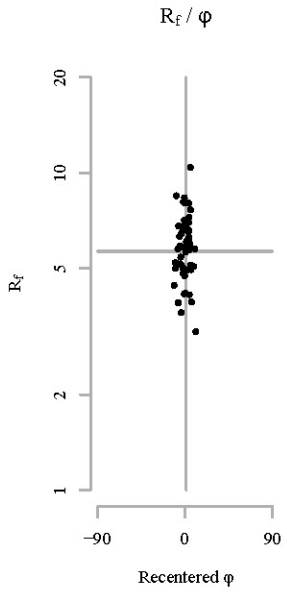

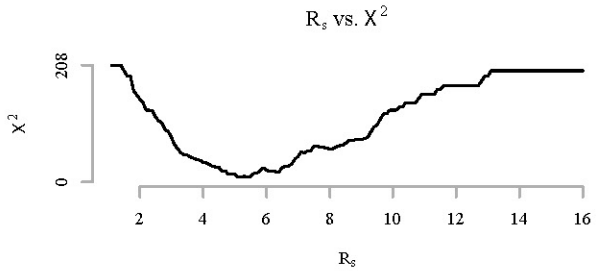

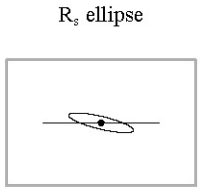

Normalized ellipse

Parameters

Sample size:	52
Fabric ratio:	5.2
Vector mean:	13
Harmonic mean:	5.7
Symmetry:	0.92
Min. chi sq:	8
Mean area*:	4605.5

*Average clast area in pixles

Sectional R_f / φ results for plane: B

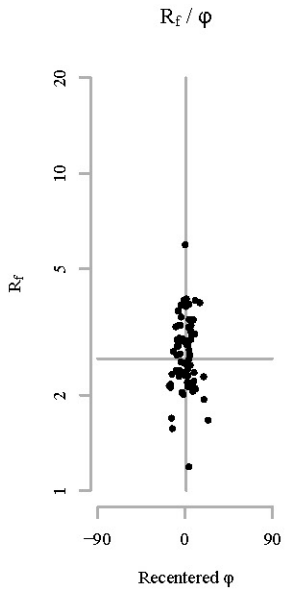

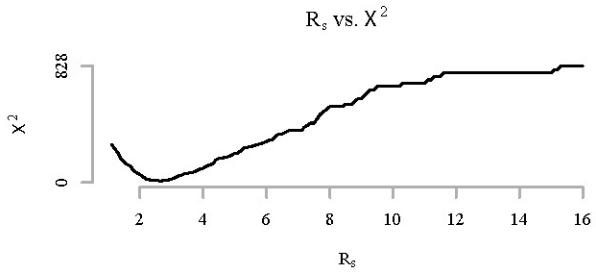

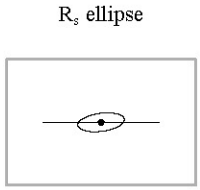

Normalized ellipse

Parameters

Sample size:	69
Fabric ratio:	2.6
Vector mean:	172
Harmonic mean:	2.6
Symmetry:	0.96
Min. chi sq:	10.7
Mean area*:	2508.1

*Average clast area in pixles

Sectional R_f / φ results for plane: C

Sample: 12DC42_A
Mineral: Hornblende

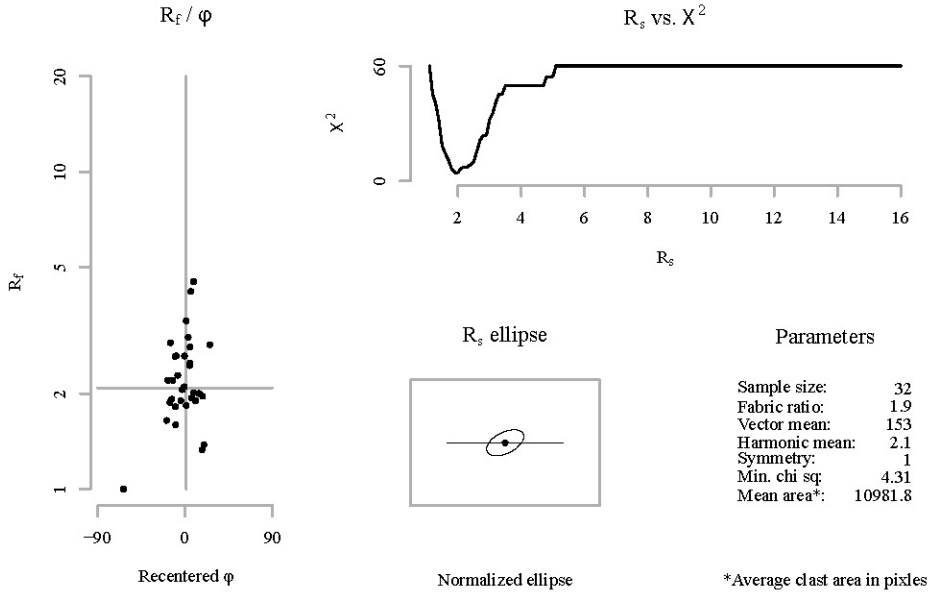

Stereonet

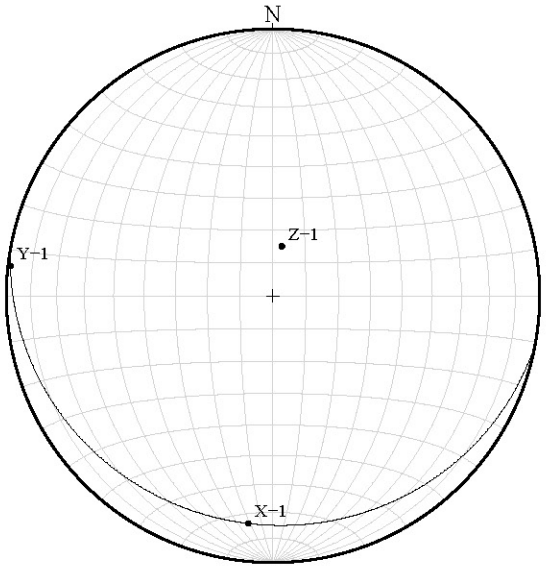

Nadai plot

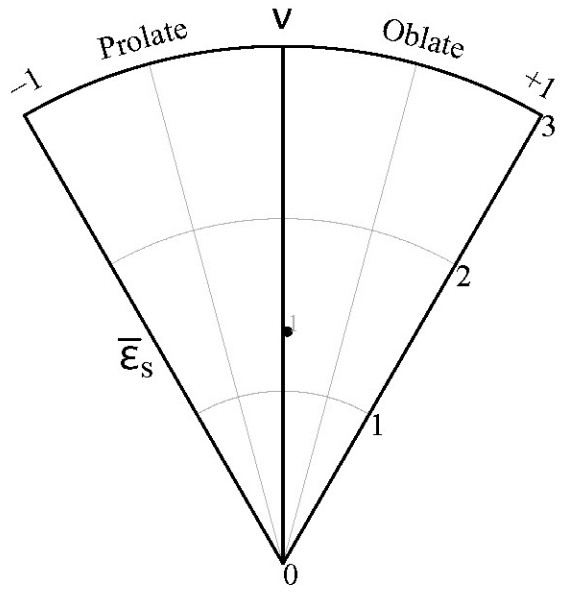

Sectional R_f / φ results for plane: A

Sample: 12DC42_A
Mineral: Plagioclase

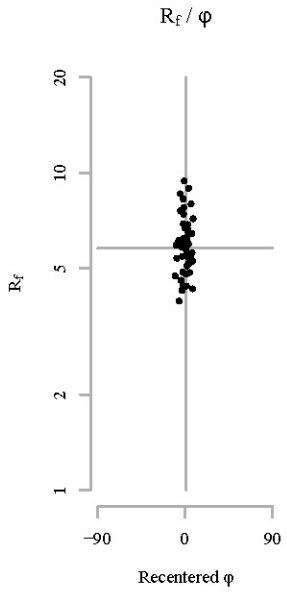

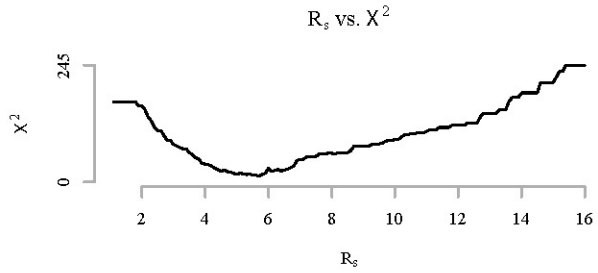

Rs ellipse

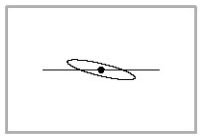

Normalized ellipse

Parameters

Sample size:	48
Fabric ratio:	5.7
Vector mean:	13
Harmonic mean:	5.8
Symmetry:	0.79
Min. chi sq:	12.38
Mean area*:	8012.7

*Average clast area in pixles

Sectional R_f / φ results for plane: B

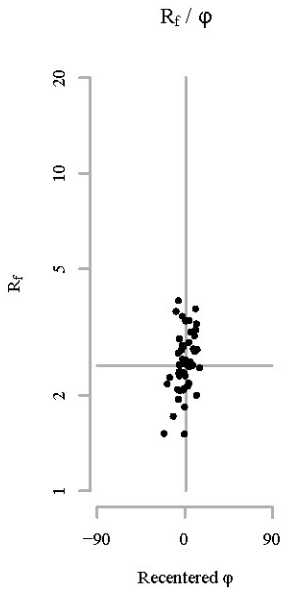

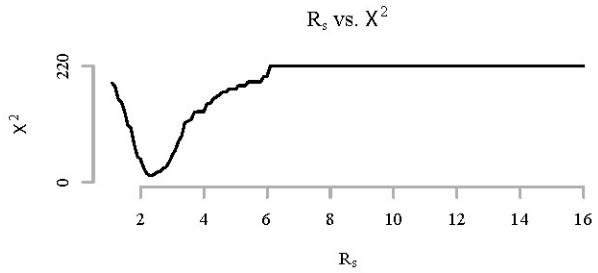

Rs ellipse

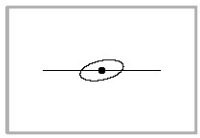

Normalized ellipse

Parameters

Sample size:	53
Fabric ratio:	2.3
Vector mean:	168
Harmonic mean:	2.5
Symmetry:	0.75
Min. chi sq:	12.85
Mean area*:	6423.7

*Average clast area in pixles

Sectional R_f / φ results for plane: C

Sample: 12DC42_A
Mineral: Plagioclase

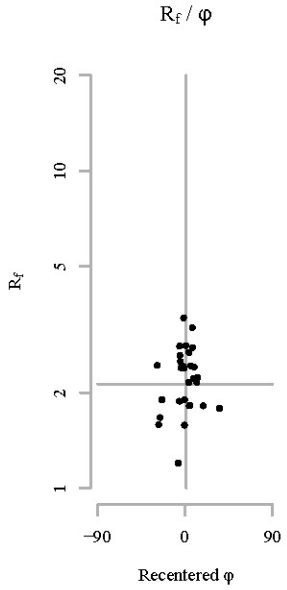

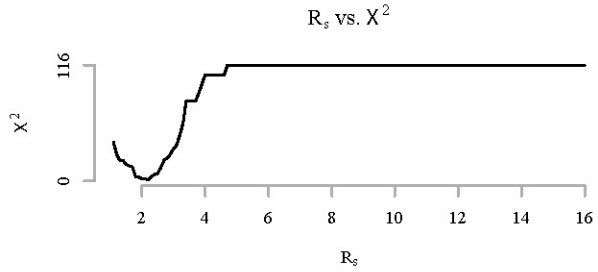

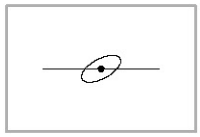

Normalized ellipse

Parameters

Sample size:	29
Fabric ratio:	2.2
Vector mean:	152
Harmonic mean:	2.1
Symmetry:	0.83
Min. chi sq:	1.17
Mean area*:	20001

*Average clast area in pixles

Stereonet

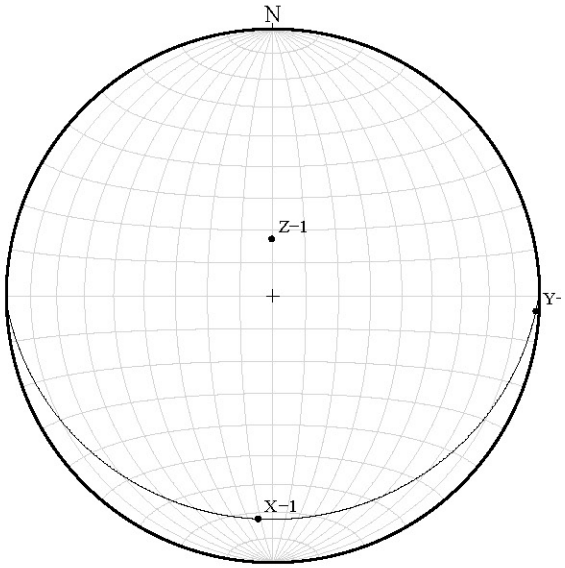

Nadai plot

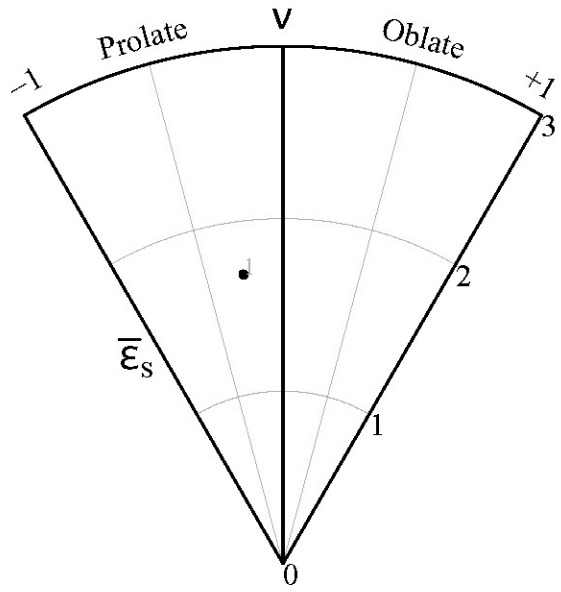

Sample: 12DC44_B
Mineral: Pyroxene / Hornblende

Sectional R_f / φ results for plane: A

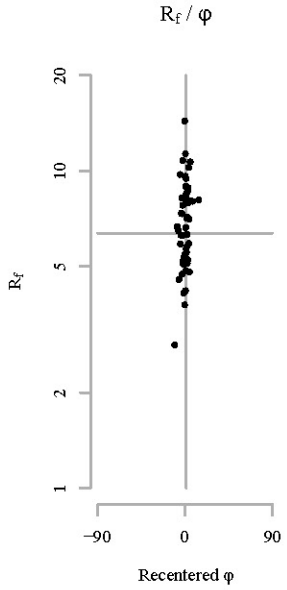

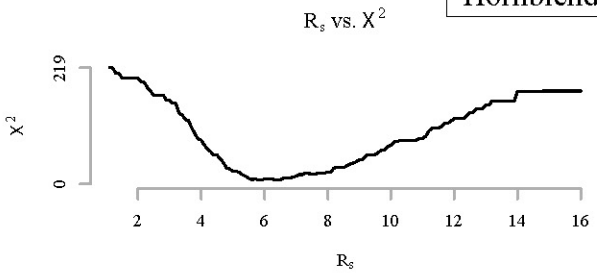

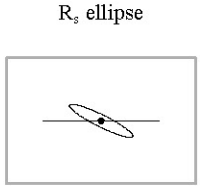

Parameters

Sample size:	54
Fabric ratio:	5.9
Vector mean:	26
Harmonic mean:	6.4
Symmetry:	0.78
Min. chi sq:	7.11
Mean area*:	9785.9

*Average clast area in pixles

Sectional R_f / φ results for plane: B

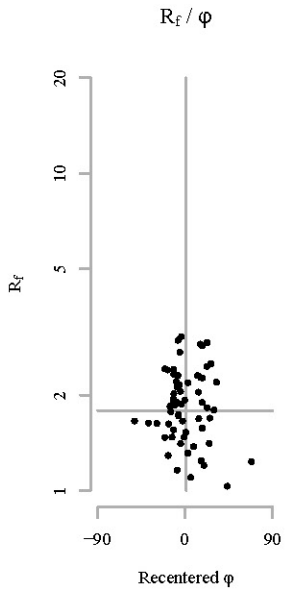

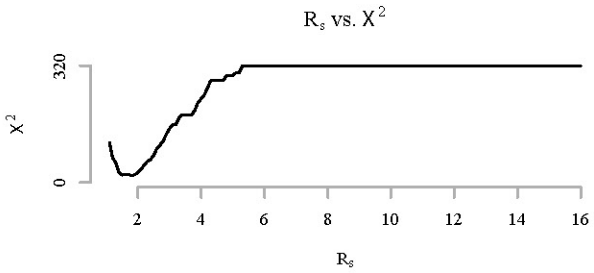

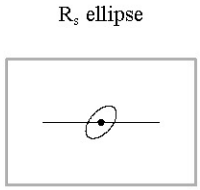

Parameters

Sample size:	62
Fabric ratio:	1.8
Vector mean:	132
Harmonic mean:	1.8
Symmetry:	0.84
Min. chi sq:	18.13
Mean area*:	13235.1

*Average clast area in pixles

Sectional R_f / φ results for plane: C

Sample: 12DC44_B
Mineral: Pyroxene / Hornblende

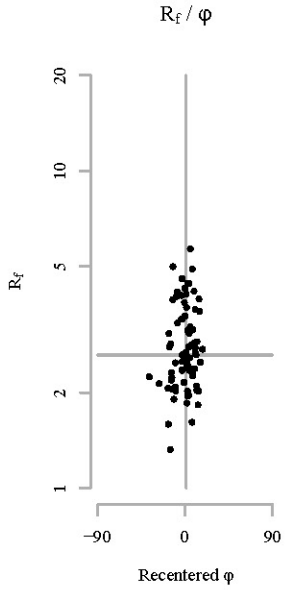

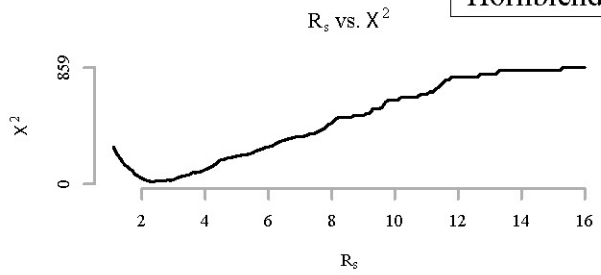

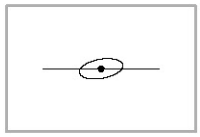

Parameters

Sample size:	79
Fabric ratio:	2.3
Vector mean:	170
Harmonic mean:	2.6
Symmetry:	0.86
Min. chi sq:	14.61
Mean area*:	13434.5

*Average clast area in pixles

Stereonet

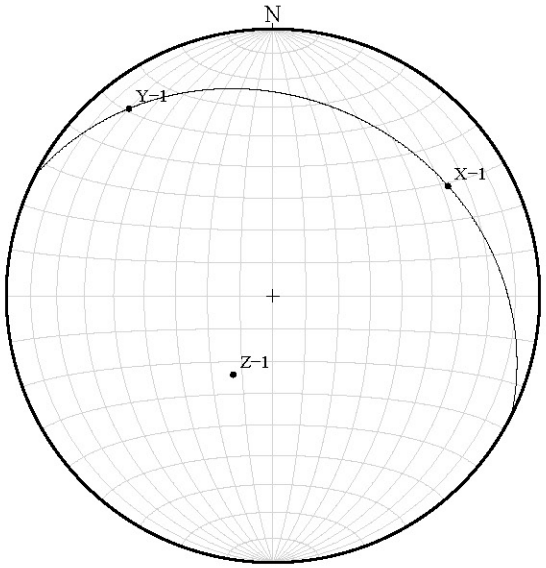

Nadai plot

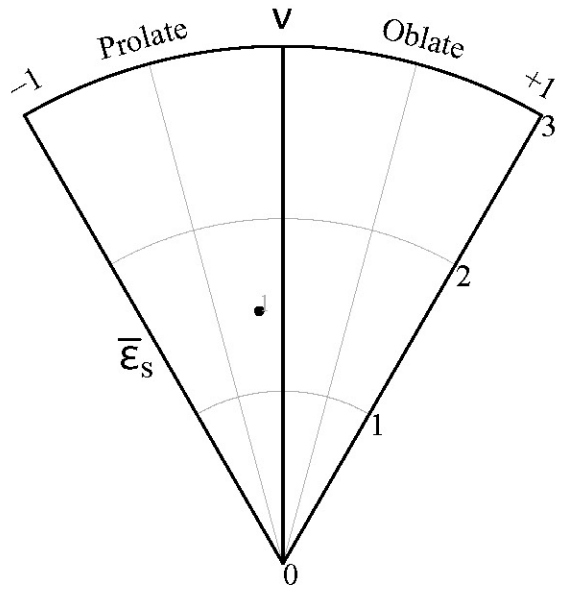

Sectional R_f / φ results for plane: A

Sample: 12DC44_B
Mineral: Plagioclase

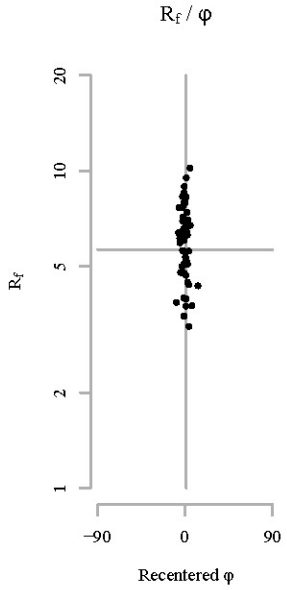

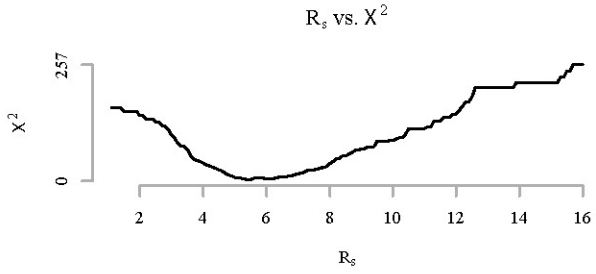

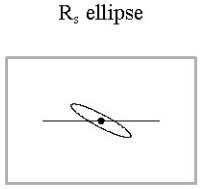

Normalized ellipse

Parameters

Sample size:	46
Fabric ratio:	5.4
Vector mean:	28
Harmonic mean:	5.6
Symmetry:	0.78
Min. chi sq:	2.13
Mean area*:	25975.1

*Average clast area in pixles

Sectional R_f / φ results for plane: B

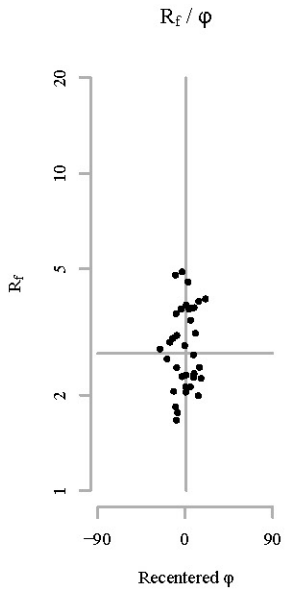

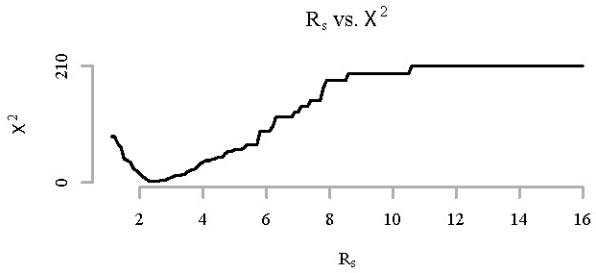

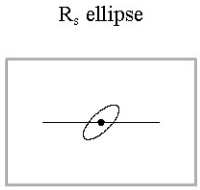

Normalized ellipse

Parameters

Sample size:	35
Fabric ratio:	2.5
Vector mean:	136
Harmonic mean:	2.7
Symmetry:	0.91
Min. chi sq:	1.2
Mean area*:	54722.5

*Average clast area in pixles

Sectional R_f / φ results for plane: C

Sample: 12DC44_B
Mineral: Plagioclase

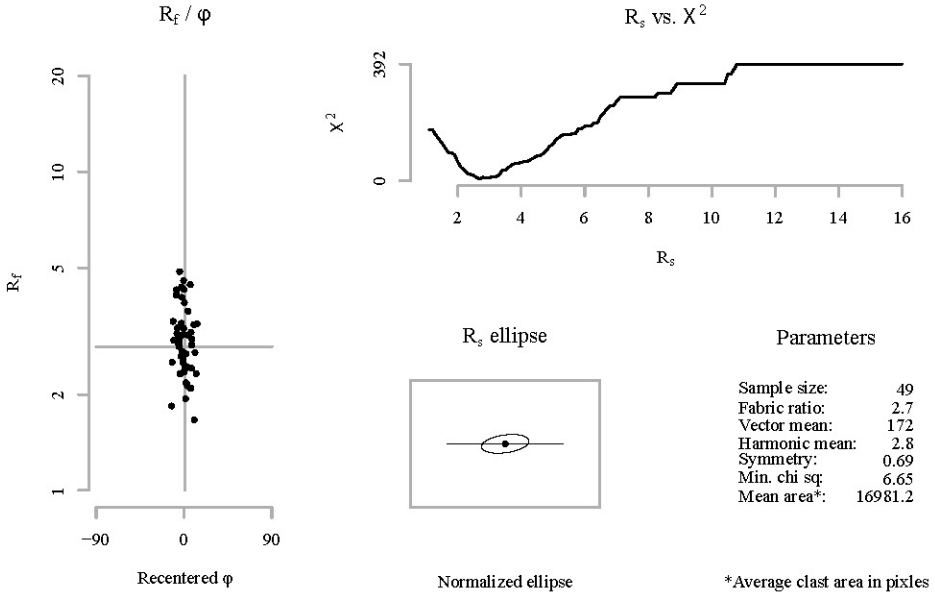

Stereonet

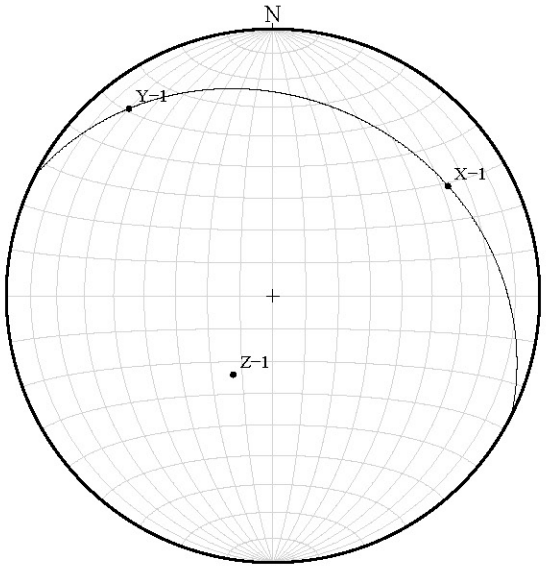

Nadai plot

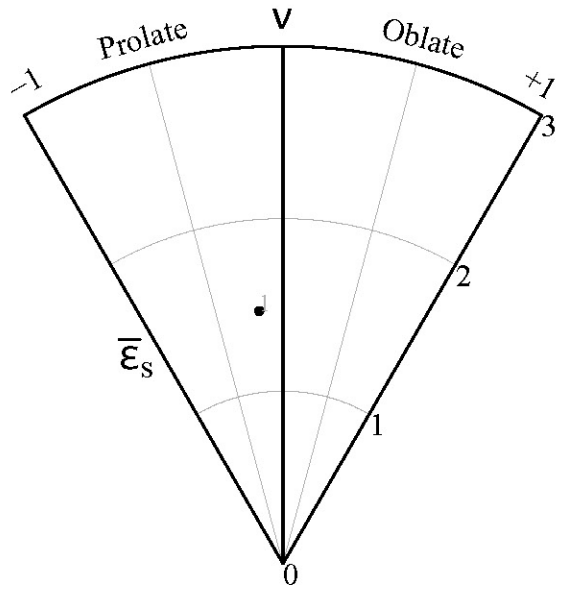

Sectional R_f / φ results for plane: A

Sample: 12DC46_A
Mineral: Plagioclase

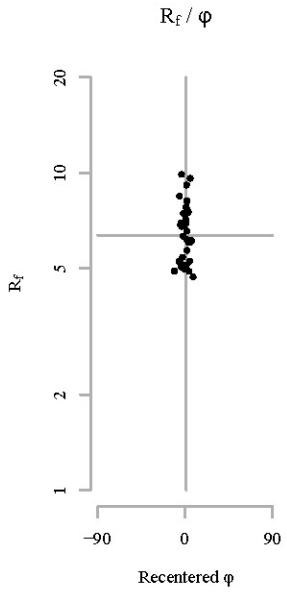

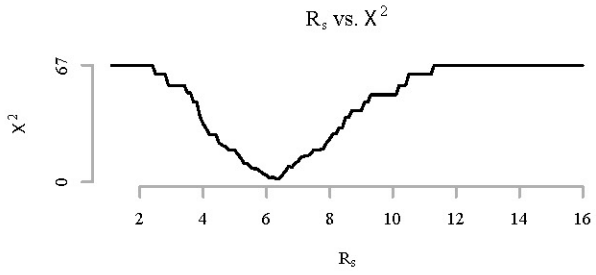

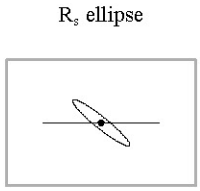

Normalized ellipse

Parameters

Sample size:	33
Fabric ratio:	6.3
Vector mean:	39
Harmonic mean:	6.3
Symmetry:	0.91
Min. chi sq:	1.73
Mean area*:	19239.3

*Average clast area in pixles

Sectional R_f / φ results for plane: B

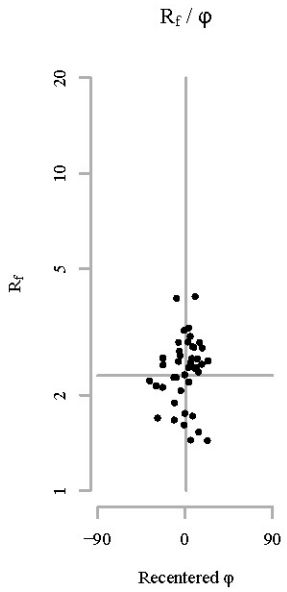

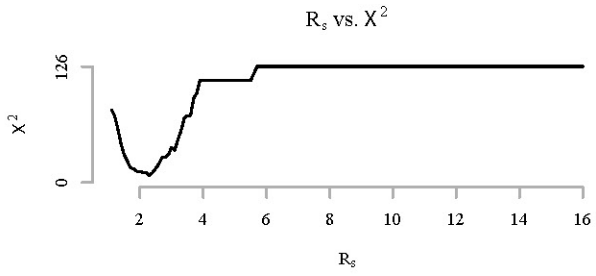

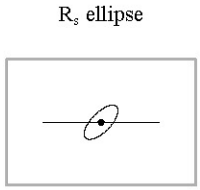

Normalized ellipse

Parameters

Sample size:	42
Fabric ratio:	2.3
Vector mean:	134
Harmonic mean:	2.3
Symmetry:	0.67
Min. chi sq:	7.52
Mean area*:	13218.6

*Average clast area in pixles

Sectional R_f / φ results for plane: C

Sample: 12DC46_A
Mineral: Plagioclase

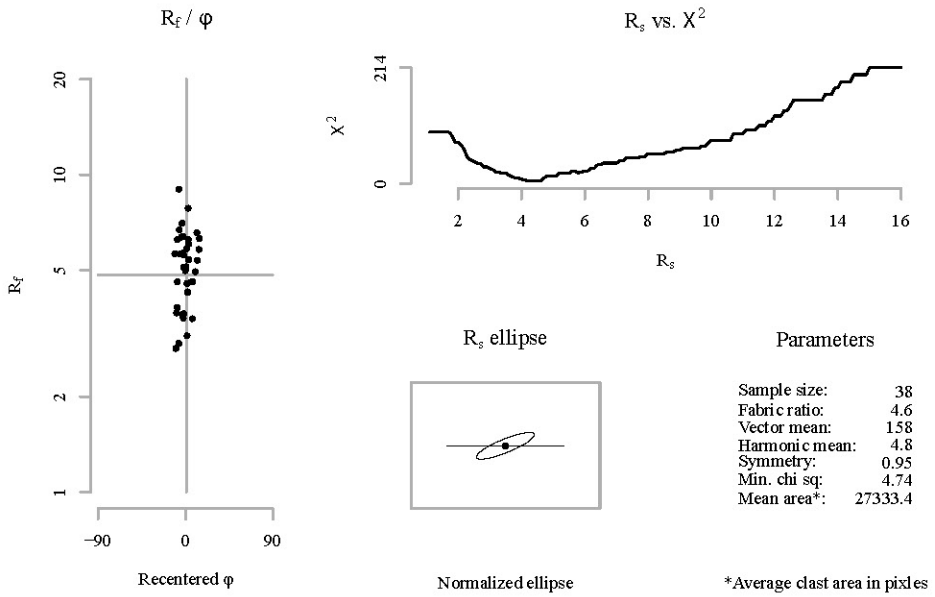

Stereonet

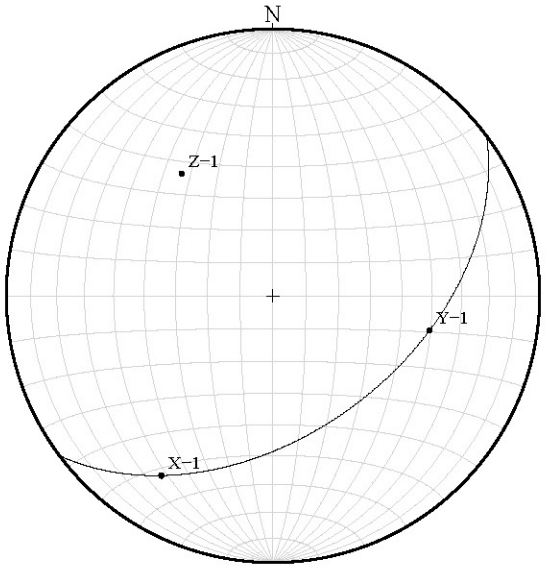

Nadai plot

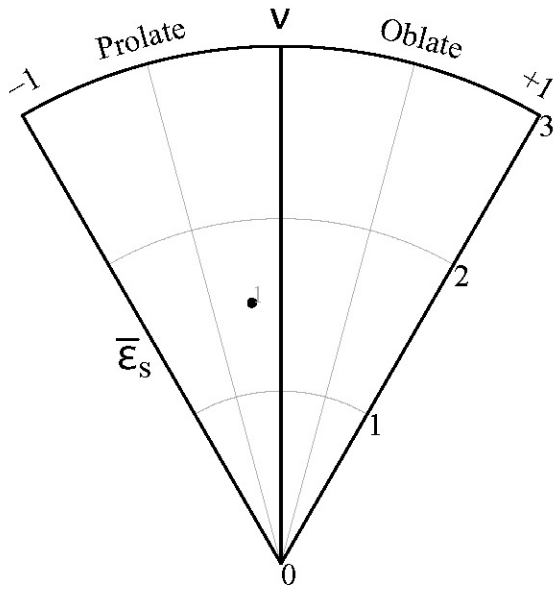

Sample: 12DC50_A
Mineral: Hornblende

Sectional R_f / φ results for plane: A

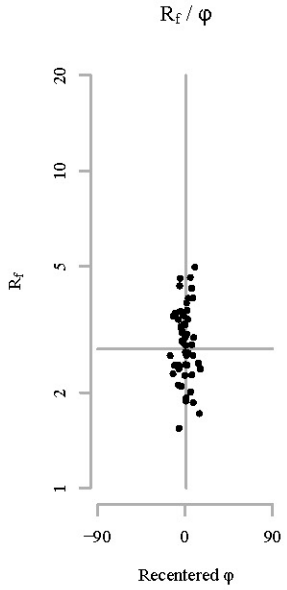

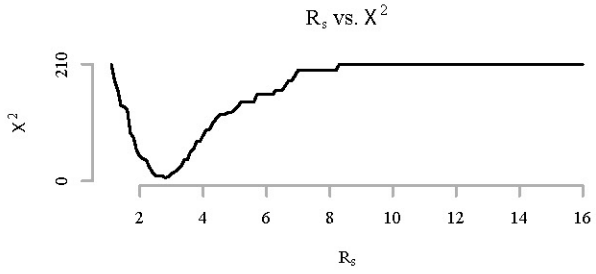

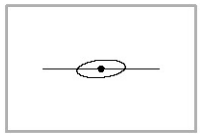

Parameters

Sample size:	52
Fabric ratio:	2.8
Vector mean:	175
Harmonic mean:	2.7
Symmetry:	0.92
Min. chi sq:	5.69
Mean area*:	6232.8

*Average clast area in pixles

Sectional R_f / φ results for plane: B

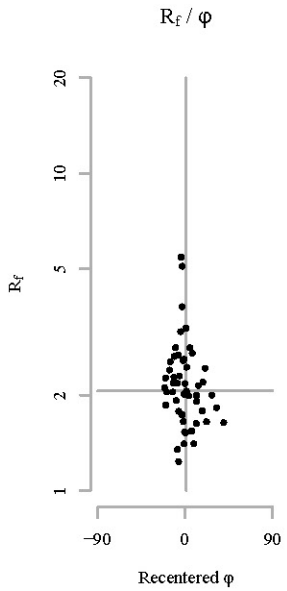

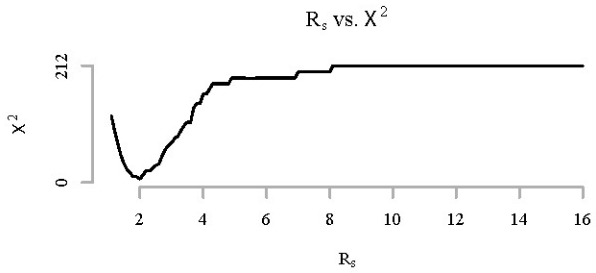

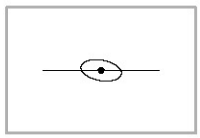

Parameters

Sample size:	51
Fabric ratio:	2
Vector mean:	10
Harmonic mean:	2.1
Symmetry:	0.75
Min. chi sq:	6.06
Mean area*:	7145.7

*Average clast area in pixles

Sectional R_f / φ results for plane: C

Sample: 12DC50_A
Mineral: Hornblende

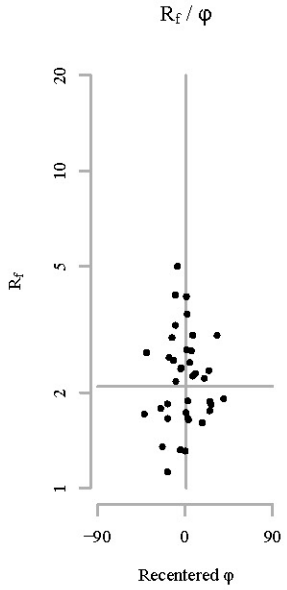

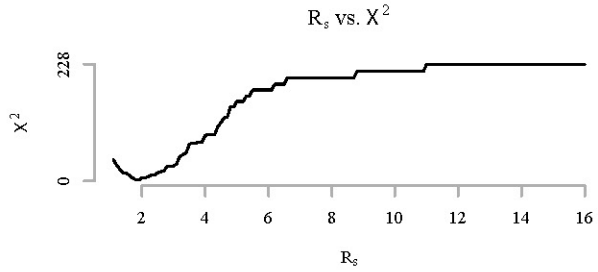

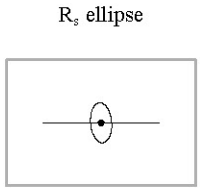

Parameters

Sample size:	38
Fabric ratio:	1.9
Vector mean:	85
Harmonic mean:	2.1
Symmetry:	0.89
Min. chi sq:	1.79
Mean area*:	26163.3

*Average clast area in pixles

Stereonet

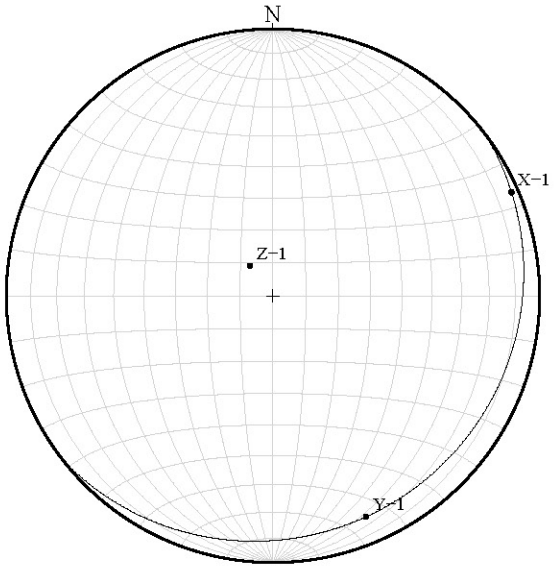

Nadai plot

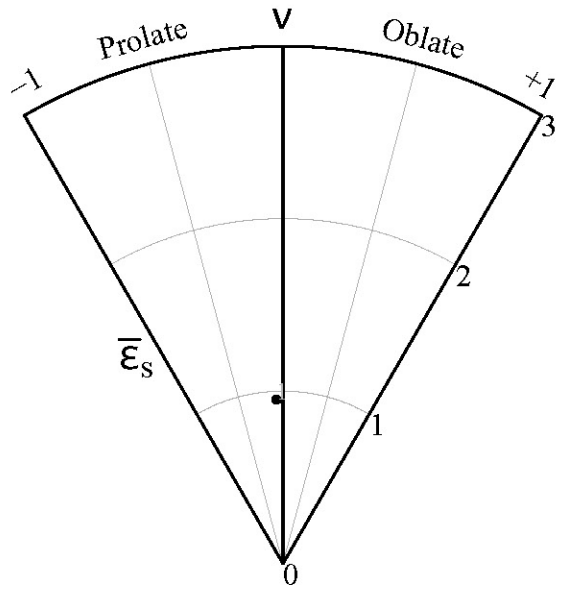

Sectional R_f / φ results for plane: A

Sample: 12DC50_A
Mineral: Plagioclase

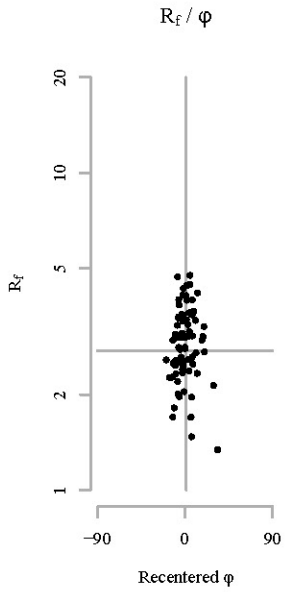

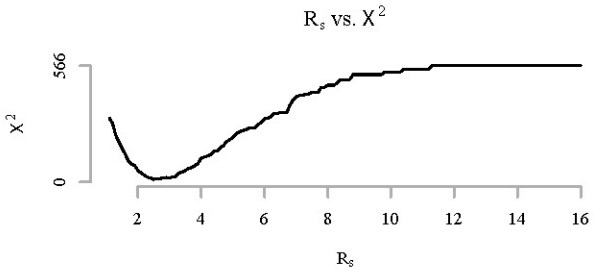

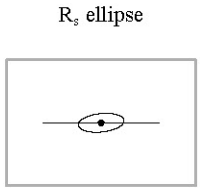

Parameters

Sample size:	80
Fabric ratio:	2.5
Vector mean:	174
Harmonic mean:	2.7
Symmetry:	0.9
Min. chi sq:	12
Mean area*:	8550

*Average clast area in pixles

Sectional R_f / φ results for plane: B

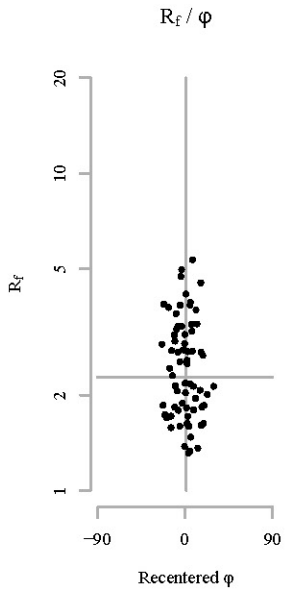

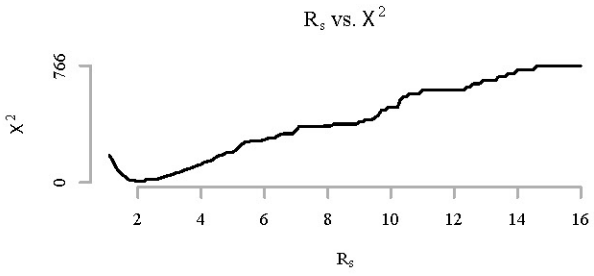

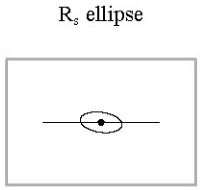

Parameters

Sample size:	68
Fabric ratio:	2.1
Vector mean:	8
Harmonic mean:	2.3
Symmetry:	0.82
Min. chi sq:	4.26
Mean area*:	11467.9

*Average clast area in pixles

Sectional R_f / φ results for plane: C

Sample: 12DC50_A
Mineral: Plagioclase

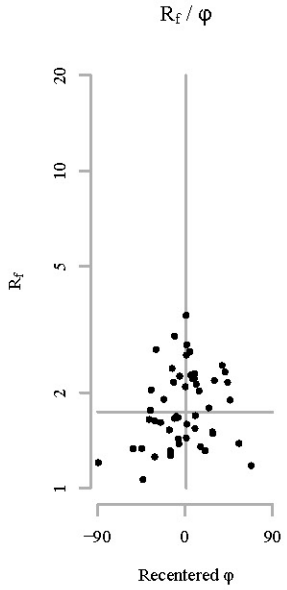

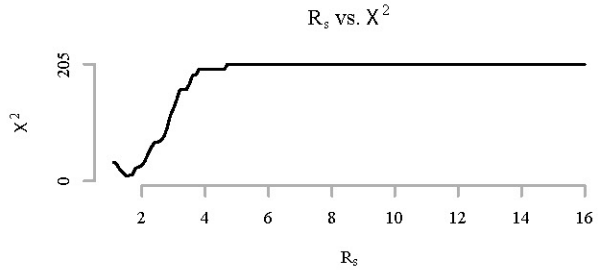

Rs ellipse

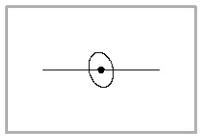

Normalized ellipse

Parameters

Sample size:	51
Fabric ratio:	1.5
Vector mean:	76
Harmonic mean:	1.7
Symmetry:	0.71
Min. chi sq:	8.8
Mean area*:	23973.6

*Average clast area in pixles

Stereonet

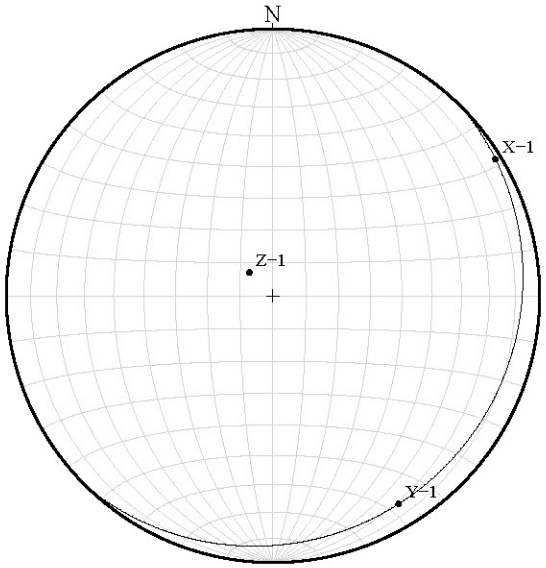

Nadai plot

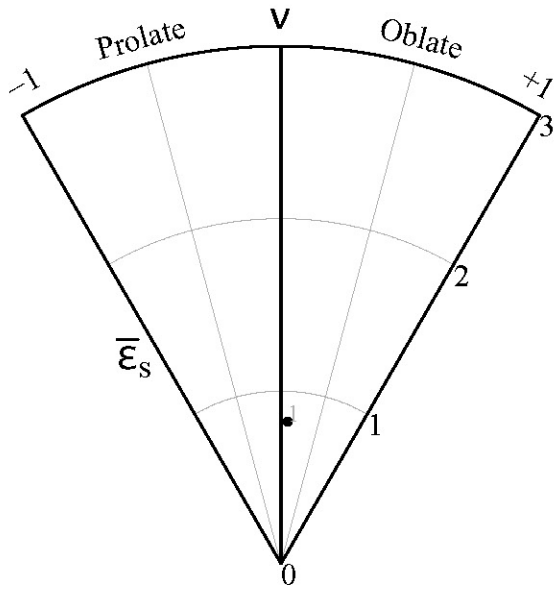

Sample: 12DC53_A
Mineral: Hornblende

Sectional R_f / φ results for plane: A

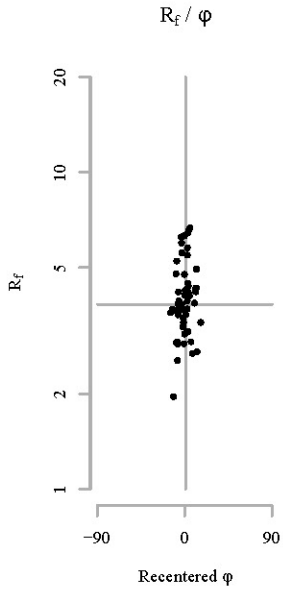

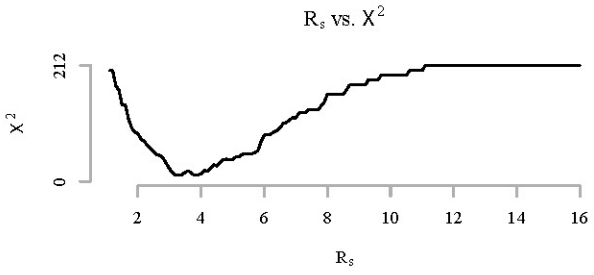

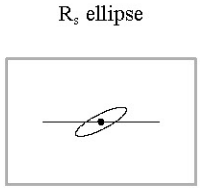

Normalized ellipse

Parameters

Sample size:	53
Fabric ratio:	3.8
Vector mean:	153
Harmonic mean:	3.8
Symmetry:	0.75
Min. chi sq:	10.96
Mean area*:	5805.6

*Average clast area in pixles

Sectional R_f / φ results for plane: B

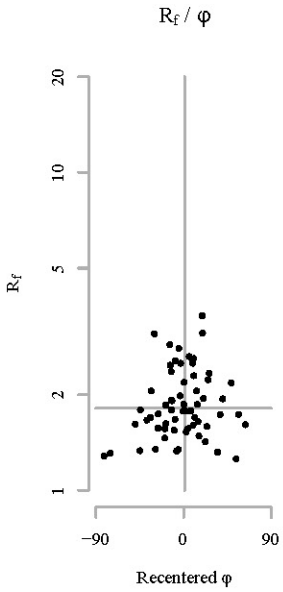

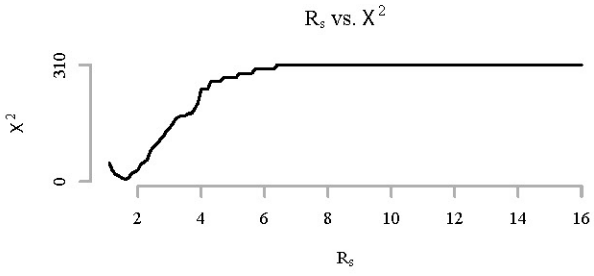

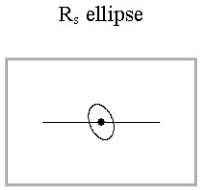

Normalized ellipse

Parameters

Sample size:	62
Fabric ratio:	1.6
Vector mean:	68
Harmonic mean:	1.8
Symmetry:	0.87
Min. chi sq:	6.13
Mean area*:	11546.3

*Average clast area in pixles

Sectional R_f / φ results for plane: C

Sample: 12DC53_A
Mineral: Hornblende

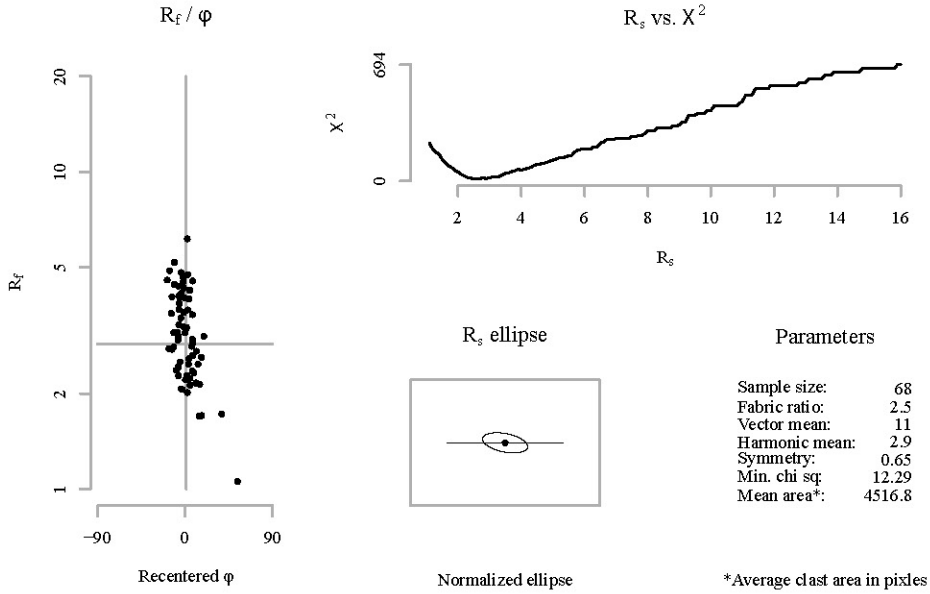

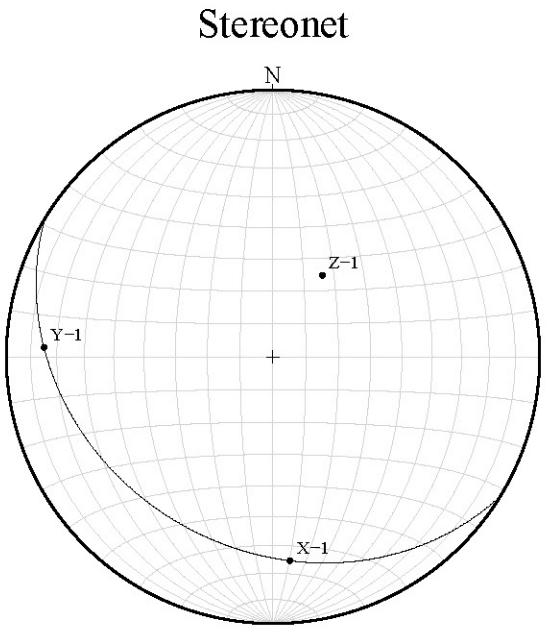

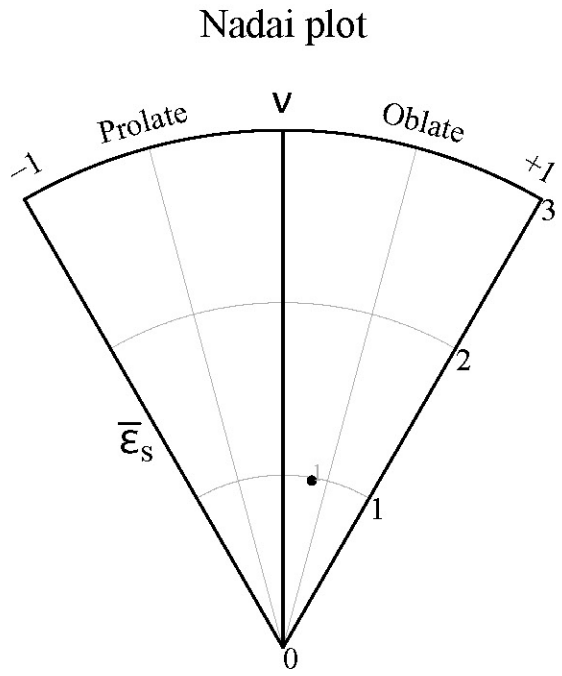

Sectional R_f / φ results for plane: A

Sample: 12DC53_A
Mineral: Plagioclase

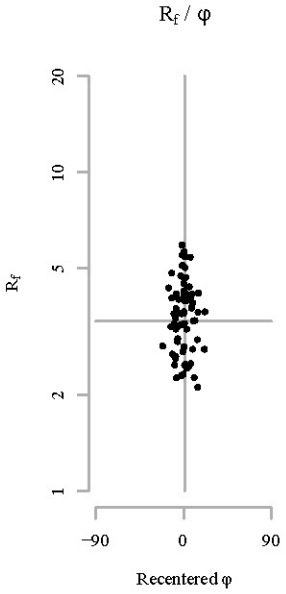

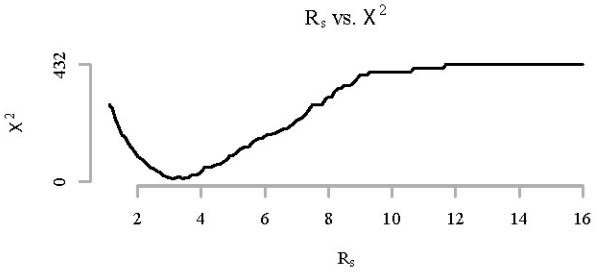

Rs ellipse

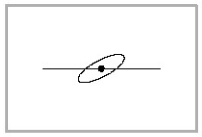

Normalized ellipse

Parameters

Sample size:	72
Fabric ratio:	3.1
Vector mean:	152
Harmonic mean:	3.4
Symmetry:	0.92
Min. chi sq:	10.06
Mean area*:	4962.1

*Average clast area in pixles

Sectional R_f / φ results for plane: B

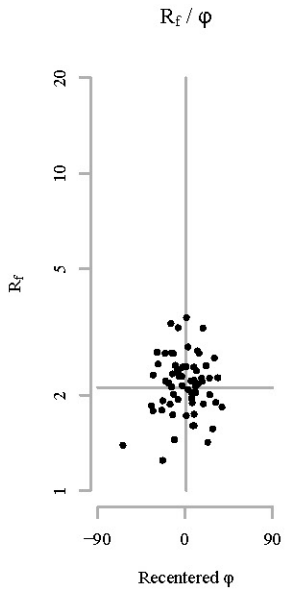

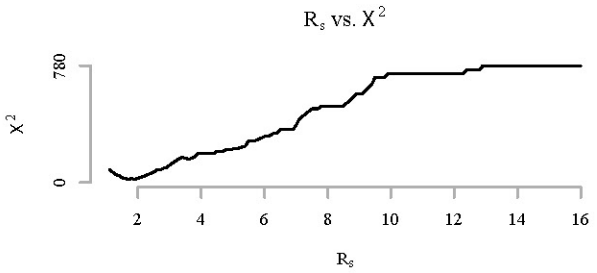

Rs ellipse

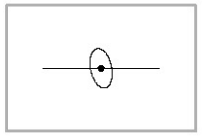

Normalized ellipse

Parameters

Sample size:	65
Fabric ratio:	1.9
Vector mean:	78
Harmonic mean:	2.1
Symmetry:	0.89
Min. chi sq:	20
Mean area*:	8739.4

*Average clast area in pixles

Sectional R_f / φ results for plane: C

Sample: 12DC53_A
Mineral: Plagioclase

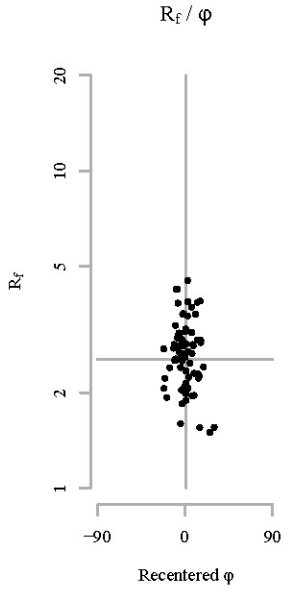

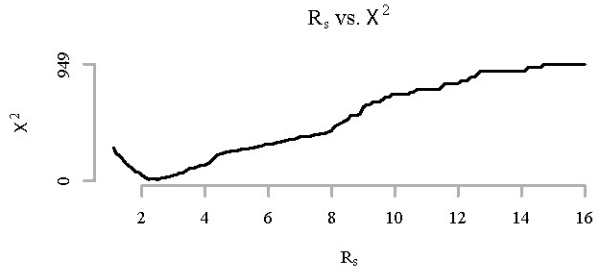

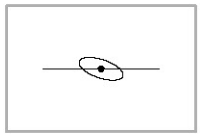

Parameters

Sample size:	76
Fabric ratio:	2.5
Vector mean:	18
Harmonic mean:	2.5
Symmetry:	0.87
Min. chi sq:	10.05
Mean area*:	4531.3

*Average clast area in pixles

Stereonet

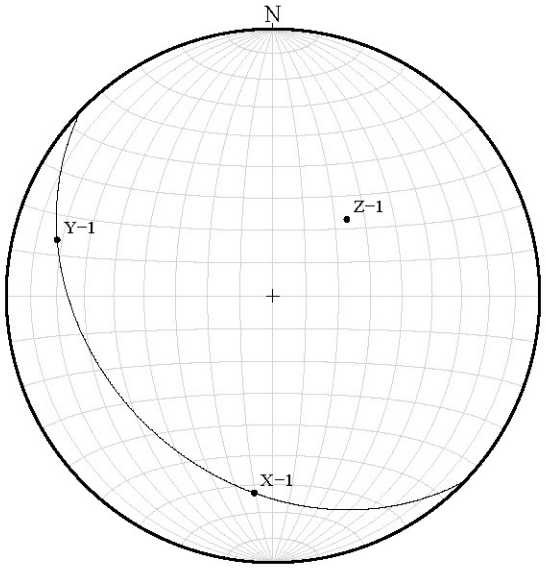

Nadai plot

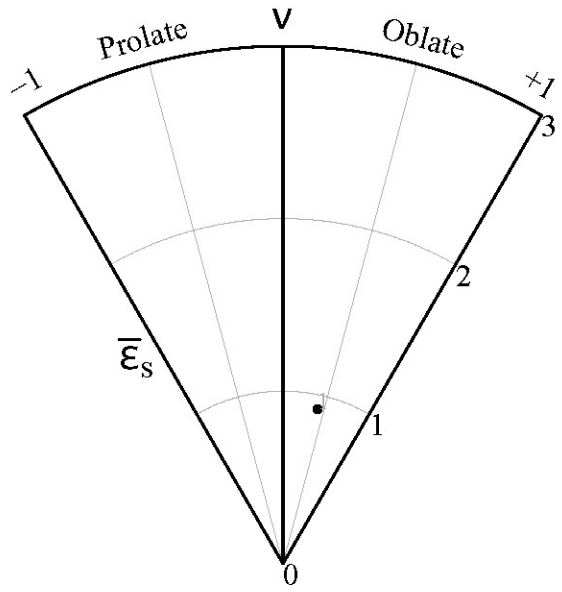

Sample: 12DC54_B
Mineral: Hornblende

Sectional R_f / φ results for plane: A

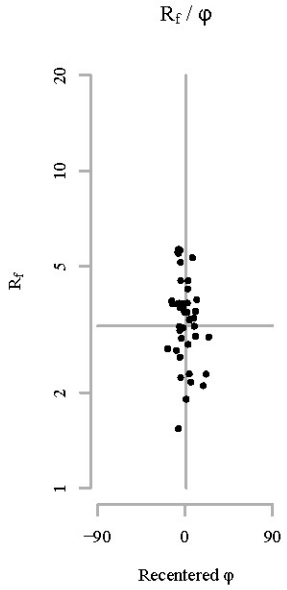

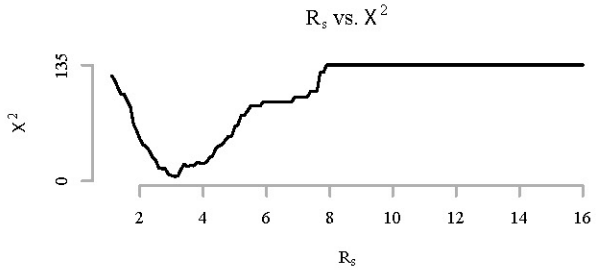

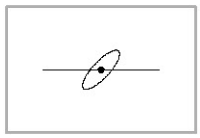

Parameters

Sample size:	44
Fabric ratio:	3.1
Vector mean:	133
Harmonic mean:	3.2
Symmetry:	0.86
Min. chi sq:	5.09
Mean area*:	4846.8

*Average clast area in pixles

Sectional R_f / φ results for plane: B

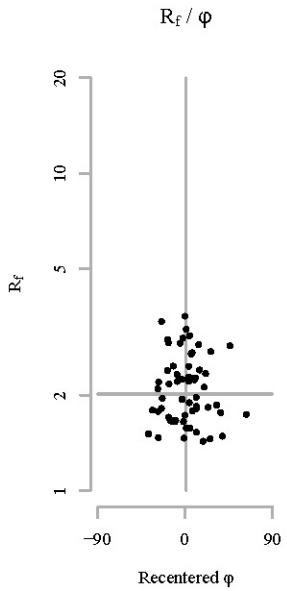

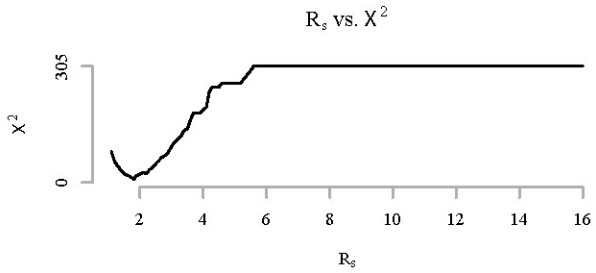

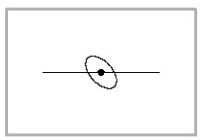

Parameters

Sample size:	61
Fabric ratio:	1.8
Vector mean:	47
Harmonic mean:	2
Symmetry:	0.95
Min. chi sq:	8.05
Mean area*:	4316.6

*Average clast area in pixles

Sectional R_f / φ results for plane: C

Sample: 12DC54_B
Mineral: Hornblende

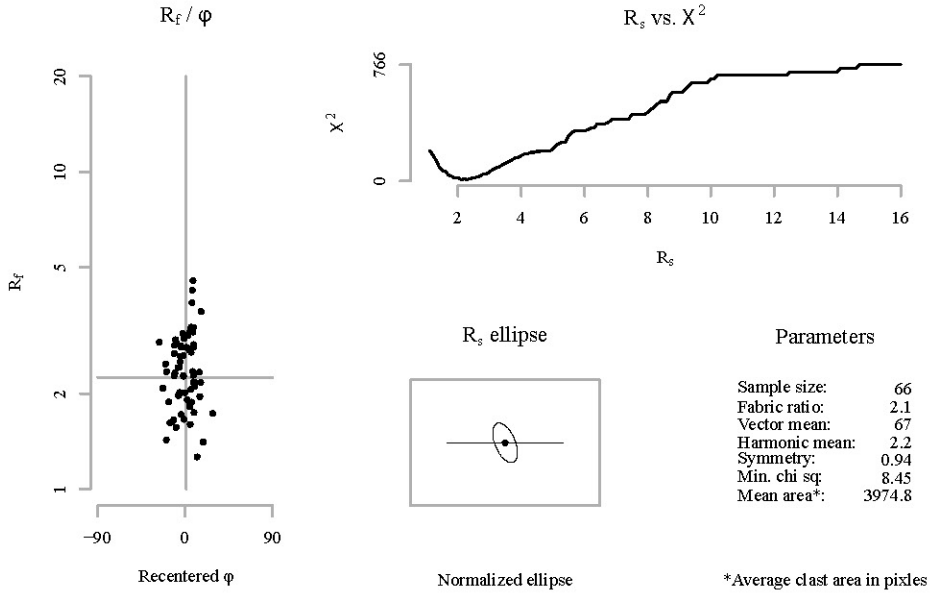

Stereonet

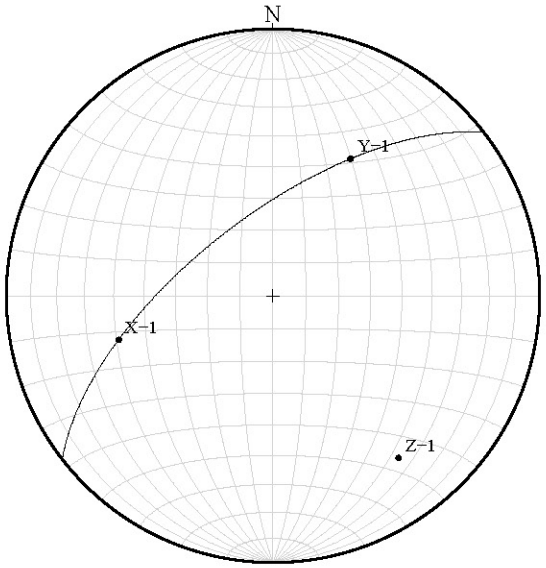

Nadai plot

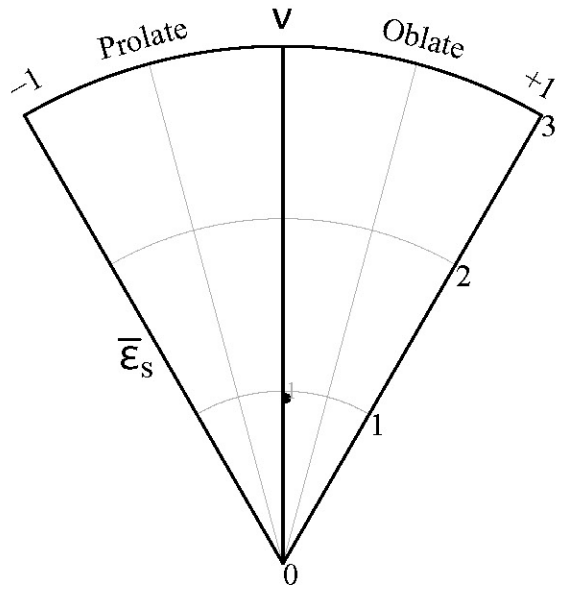

Sample: 12DC54_B
Mineral: Plagioclase

Sectional R_f / φ results for plane: A

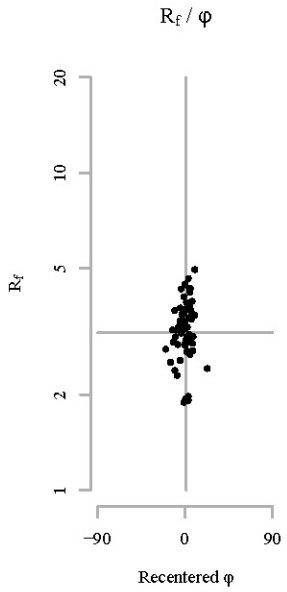

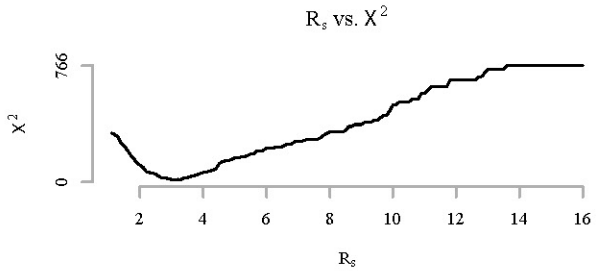

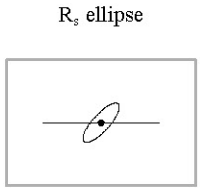

Parameters

Sample size:	66
Fabric ratio:	3.1
Vector mean:	132
Harmonic mean:	3.1
Symmetry:	0.85
Min. chi sq:	12
Mean area*:	3128

*Average clast area in pixles

Sectional R_f / φ results for plane: B

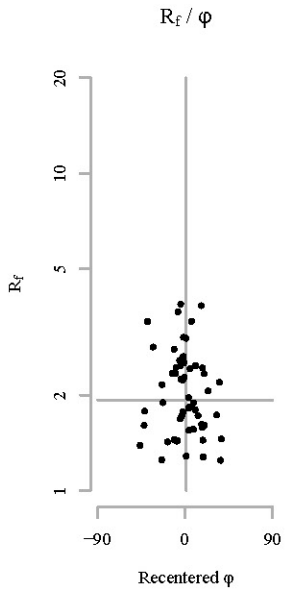

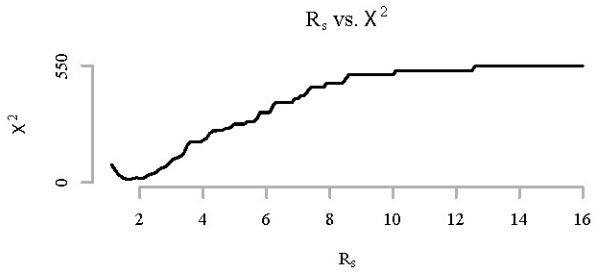

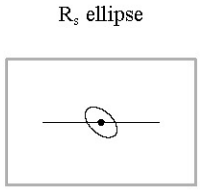

Parameters

Sample size:	55
Fabric ratio:	1.7
Vector mean:	42
Harmonic mean:	1.9
Symmetry:	0.8
Min. chi sq:	14.4
Mean area*:	13631.3

*Average clast area in pixles

Sectional R_f / φ results for plane: C

Sample: 12DC54_B
Mineral: Plagioclase

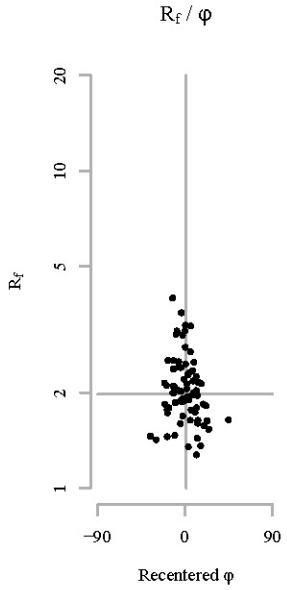

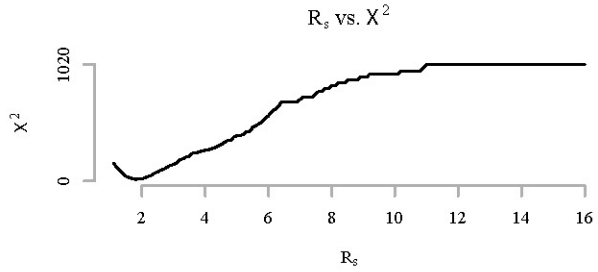

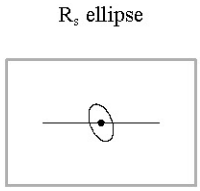

Parameters

Sample size:	75
Fabric ratio:	1.8
Vector mean:	68
Harmonic mean:	2
Symmetry:	0.88
Min. chi sq:	12.8
Mean area*:	2534.2

*Average clast area in pixles

Stereonet

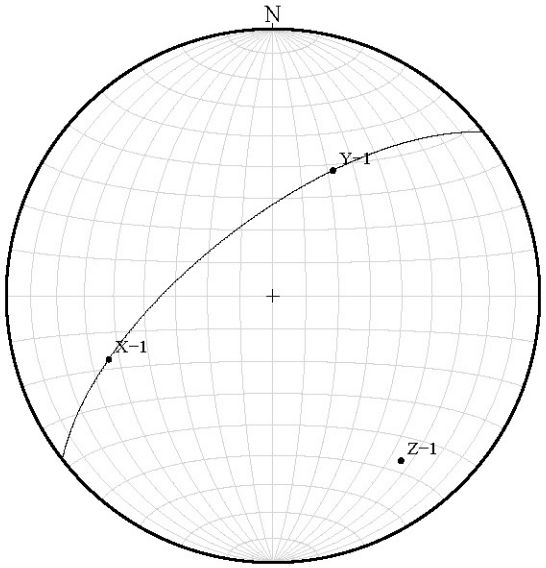

Nadai plot

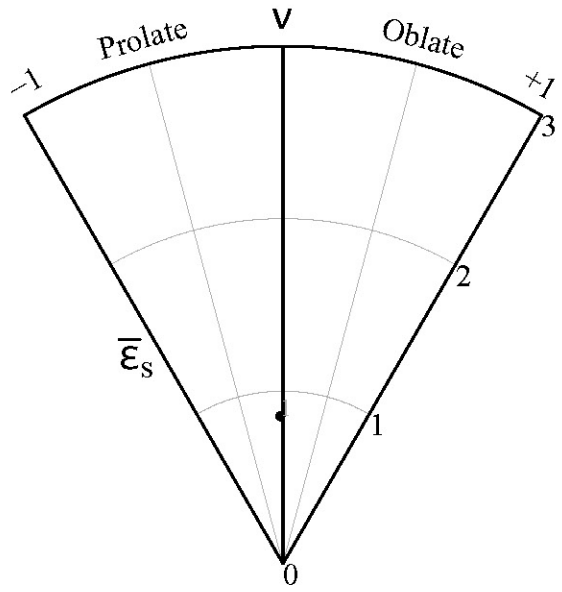

Sample: 12DC55_A
Mineral: Pyroxene

Sectional R_f / φ results for plane: A

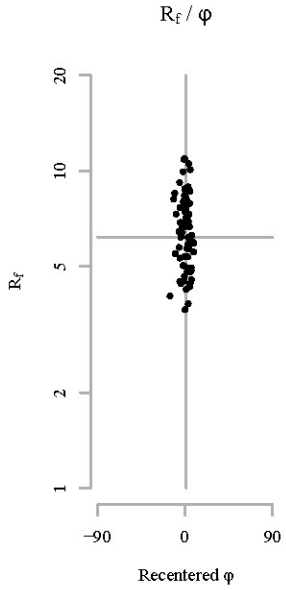

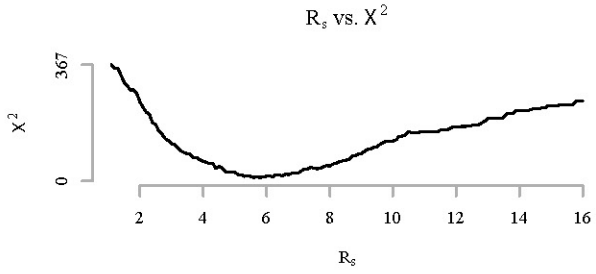

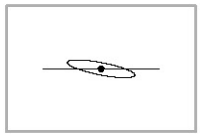

Normalized ellipse

Parameters

Sample size:	69
Fabric ratio:	5.6
Vector mean:	11
Harmonic mean:	6.2
Symmetry:	0.87
Min. chi sq:	10.7
Mean area*:	5915.4

*Average clast area in pixles

Sectional R_f / φ results for plane: B

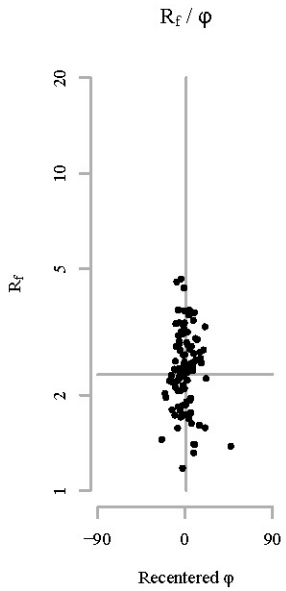

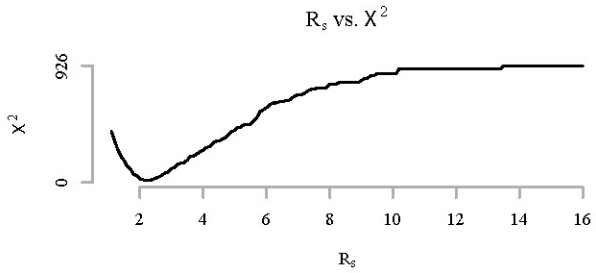

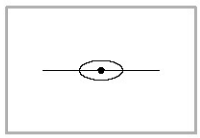

Normalized ellipse

Parameters

Sample size:	101
Fabric ratio:	2.2
Vector mean:	180
Harmonic mean:	2.3
Symmetry:	0.87
Min. chi sq:	12.86
Mean area*:	2823.8

*Average clast area in pixles

Sectional R_f / φ results for plane: C

Sample: 12DC55_A
Mineral: Pyroxene

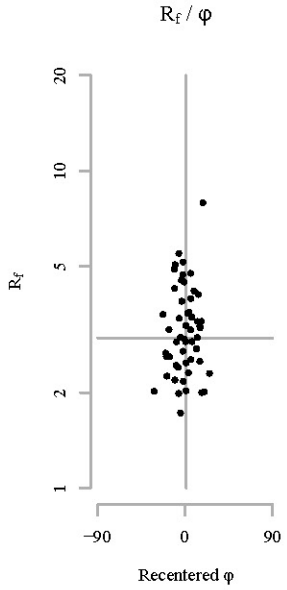

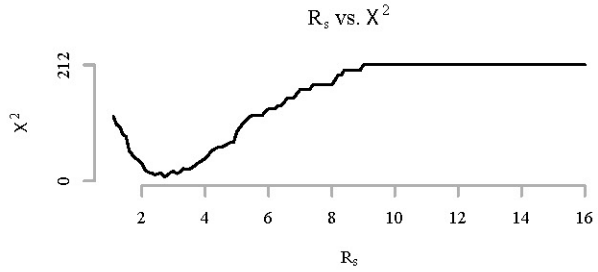

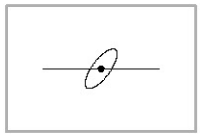

Parameters

Sample size:	53
Fabric ratio:	2.7
Vector mean:	127
Harmonic mean:	3
Symmetry:	0.91
Min. chi sq:	7.57
Mean area*:	10318.6

*Average clast area in pixles

Stereonet

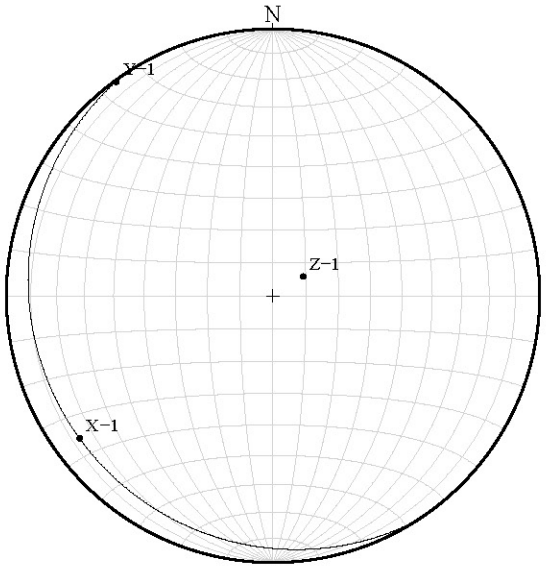

Nadai plot

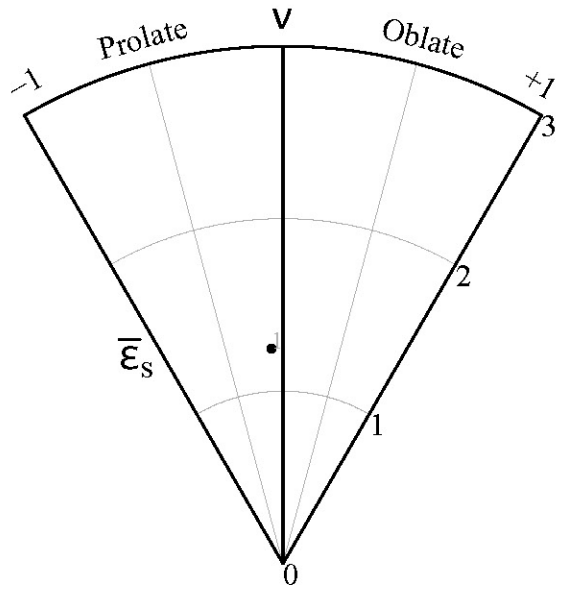

Sectional R_f / φ results for plane: A

Sample: 12DC55_A
Mineral: Plagioclase

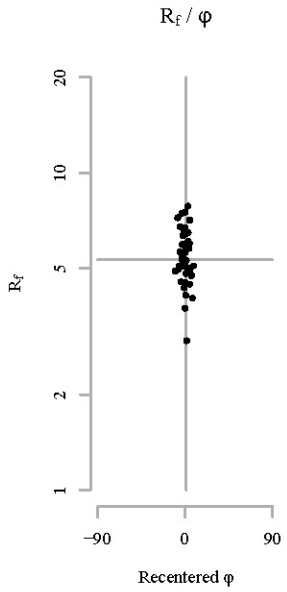

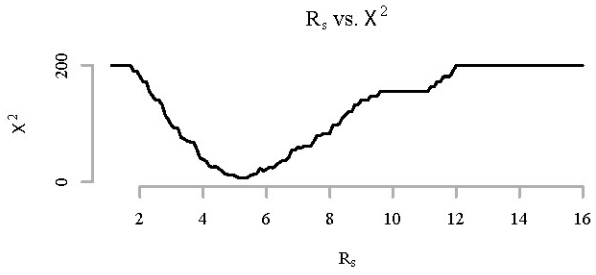

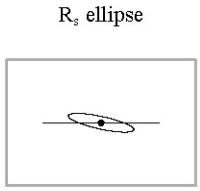

Normalized ellipse

Parameters

Sample size:	50
Fabric ratio:	5.3
Vector mean:	12
Harmonic mean:	5.3
Symmetry:	0.76
Min. chi sq:	6.4
Mean area*:	7376.9

*Average clast area in pixles

Sectional R_f / φ results for plane: B

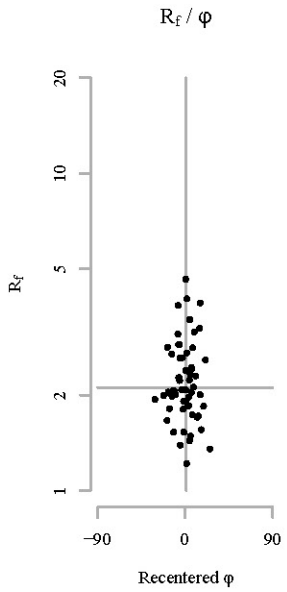

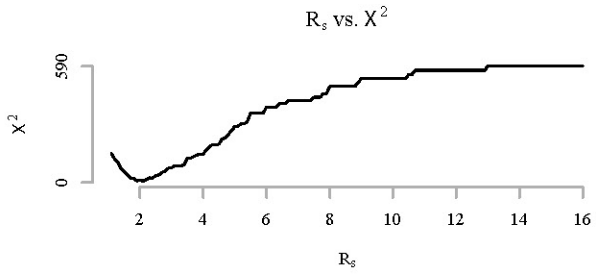

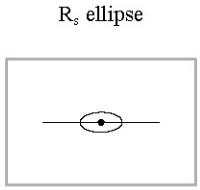

Normalized ellipse

Parameters

Sample size:	59
Fabric ratio:	2.1
Vector mean:	179
Harmonic mean:	2.1
Symmetry:	0.88
Min. chi sq:	6.44
Mean area*:	6148.3

*Average clast area in pixles

Sectional R_f / φ results for plane: C

Sample: 12DC55_A
Mineral: Plagioclase

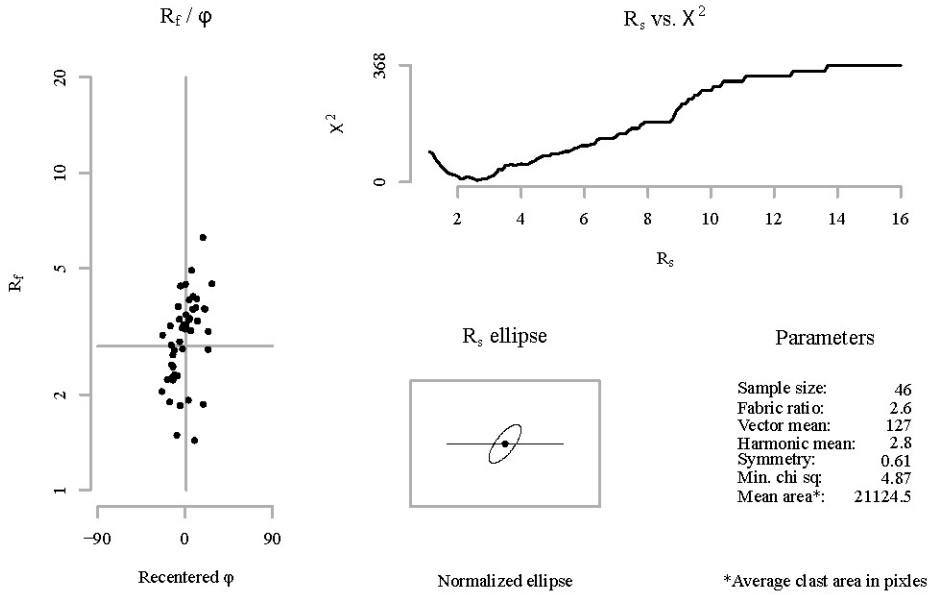

Stereonet

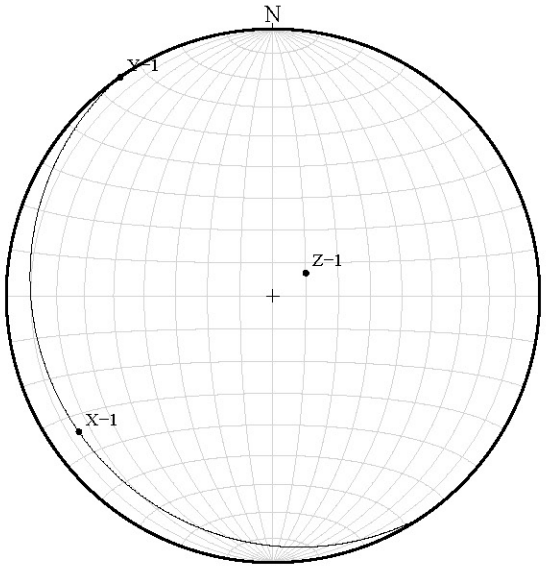

Nadai plot

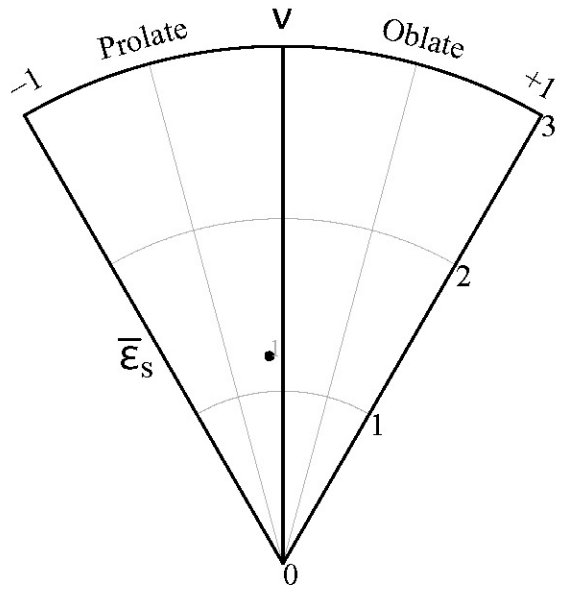

Sample: 12DC55_B
Mineral: Pyroxene

Sectional R_f / φ results for plane: A

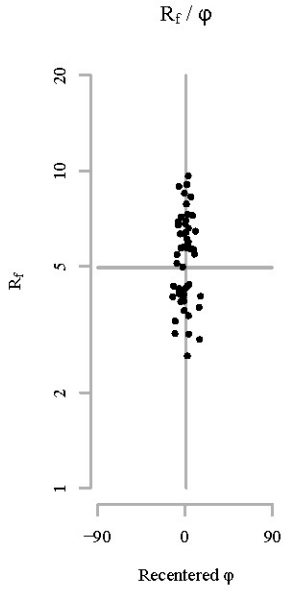

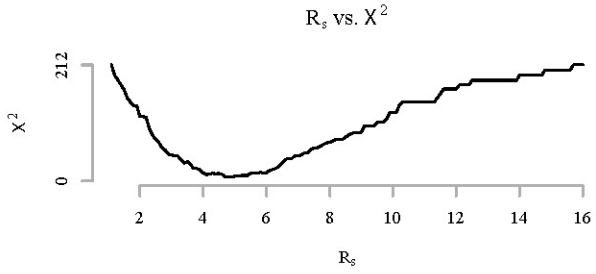

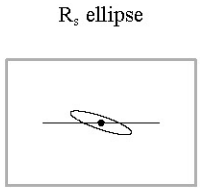

Normalized ellipse

Parameters

Sample size:	53
Fabric ratio:	4.9
Vector mean:	18
Harmonic mean:	5
Symmetry:	0.75
Min. chi sq:	6.81
Mean area*:	5761.1

*Average clast area in pixles

Sectional R_f / φ results for plane: B

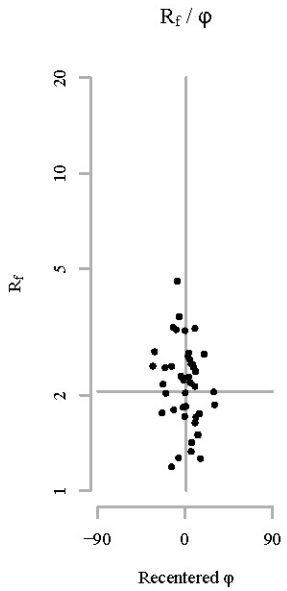

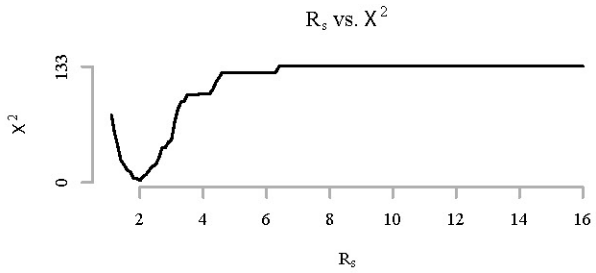

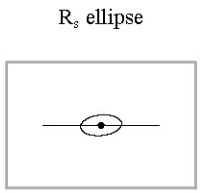

Normalized ellipse

Parameters

Sample size:	44
Fabric ratio:	2
Vector mean:	174
Harmonic mean:	2.1
Symmetry:	0.86
Min. chi sq:	1.82
Mean area*:	4622.2

*Average clast area in pixles

Sectional R_f / φ results for plane: C

Sample: 12DC55_B
Mineral: Pyroxene

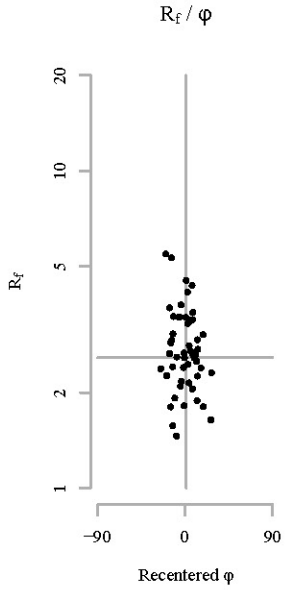

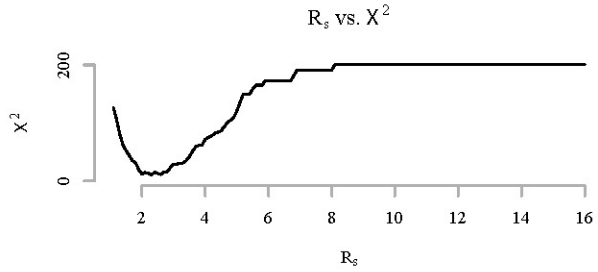

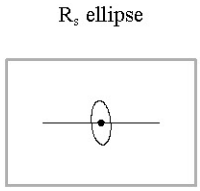

Parameters

Sample size:	50
Fabric ratio:	2.3
Vector mean:	85
Harmonic mean:	2.6
Symmetry:	0.96
Min. chi sq:	10
Mean area*:	9067.6

*Average clast area in pixles

Stereonet

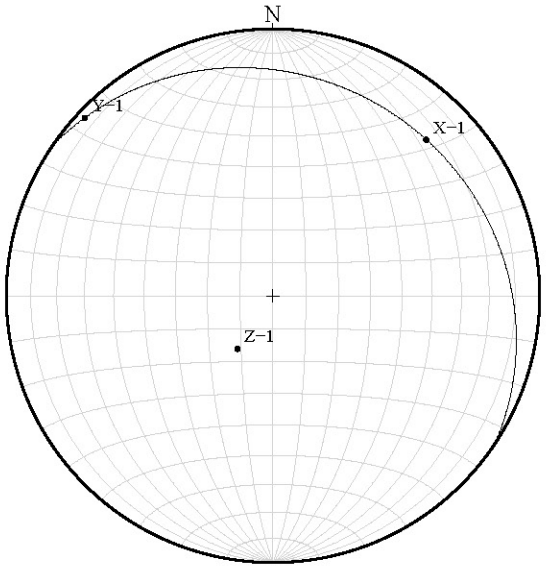

Nadai plot

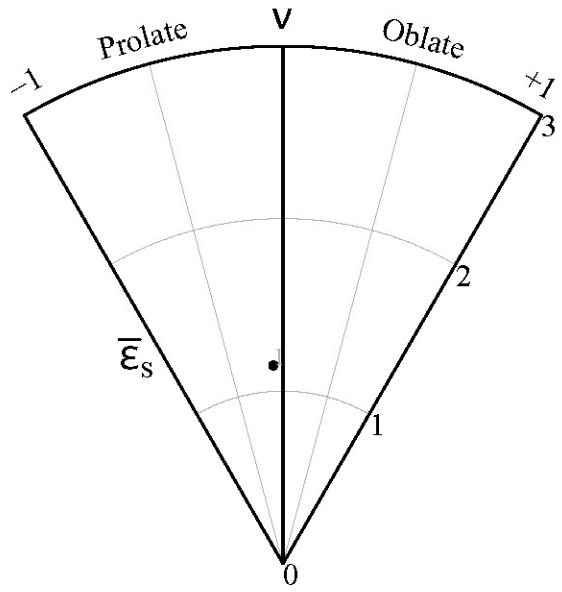

Sample: 12DC55_B
Mineral: Plagioclase

Sectional R_f / φ results for plane: A

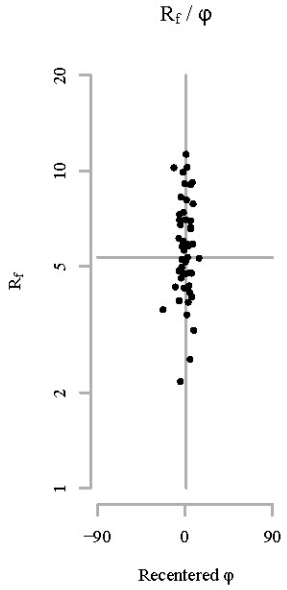

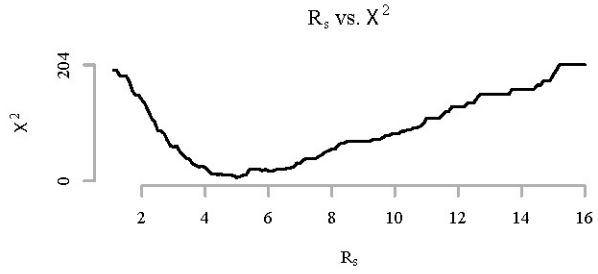

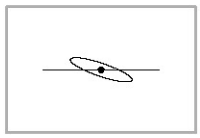

Normalized ellipse

Parameters

Sample size:	51
Fabric ratio:	5
Vector mean:	19
Harmonic mean:	5.3
Symmetry:	0.98
Min. chi sq:	5.67
Mean area*:	14631.9

*Average clast area in pixles

Sectional R_f / φ results for plane: B

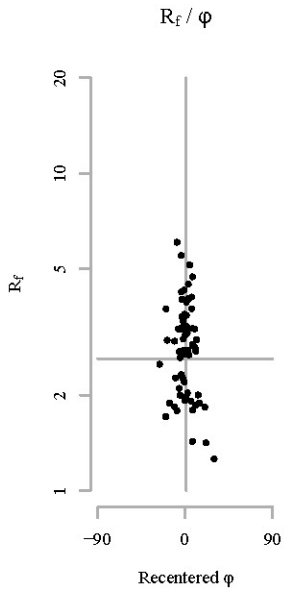

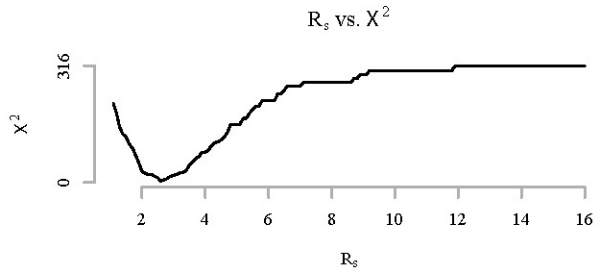

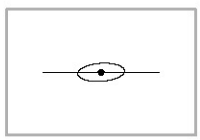

Normalized ellipse

Parameters

Sample size:	63
Fabric ratio:	2.6
Vector mean:	176
Harmonic mean:	2.6
Symmetry:	0.95
Min. chi sq:	3.48
Mean area*:	10260.3

*Average clast area in pixles

Sectional R_f / φ results for plane: C

Sample: 12DC55_B
Mineral: Plagioclase

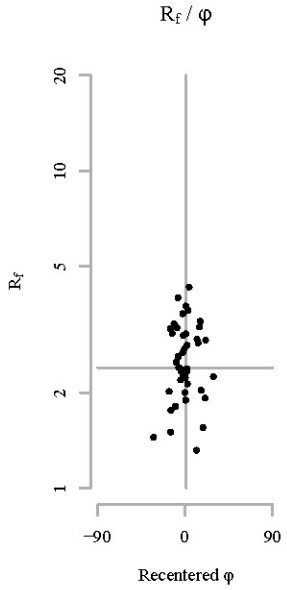

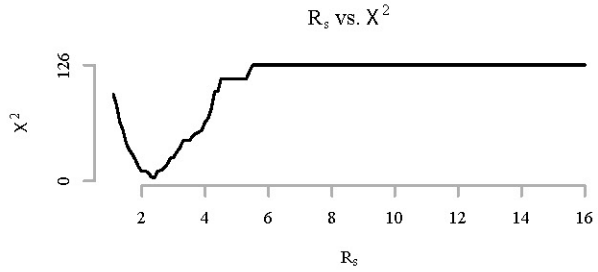

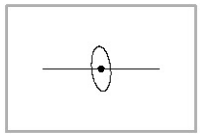

Parameters

Sample size:	42
Fabric ratio:	2.4
Vector mean:	84
Harmonic mean:	2.4
Symmetry:	0.95
Min. chi sq:	3.33
Mean area*:	24378.1

*Average clast area in pixles

Stereonet

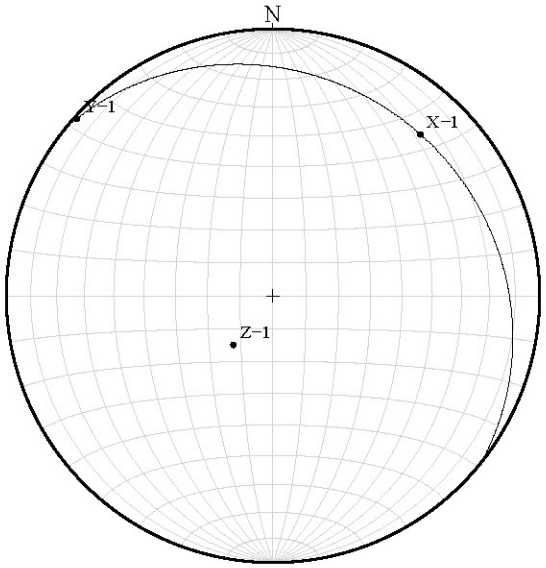

Nadai plot

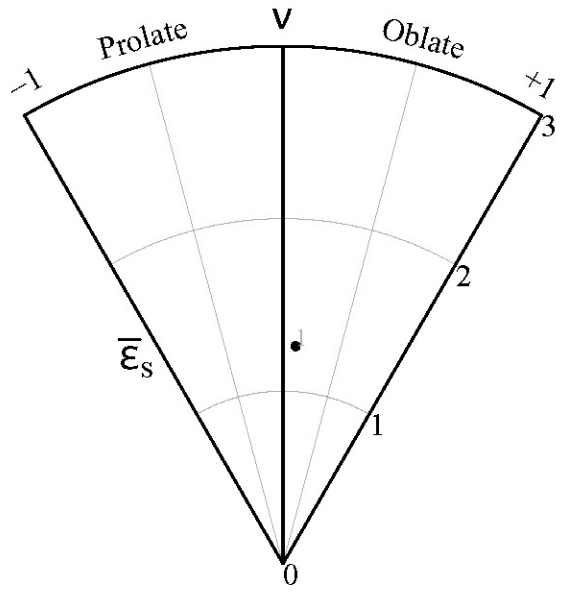

Sectional R_f / φ results for plane: A

Sample: 12DC55_C
Mineral: Pyroxene

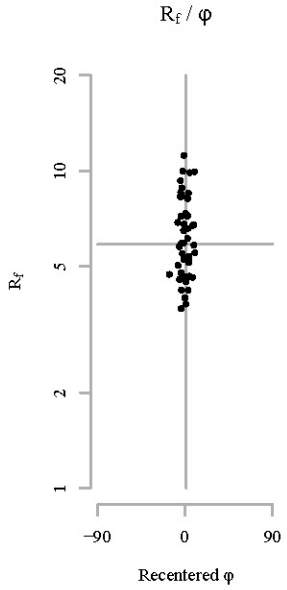

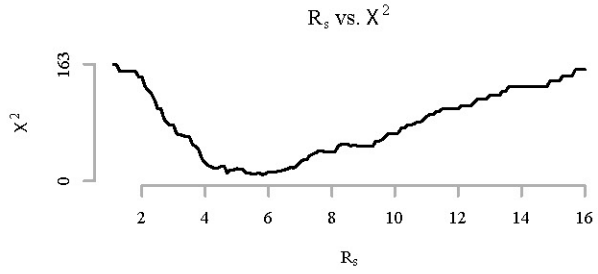

Rs ellipse

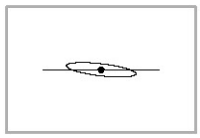

Normalized ellipse

Parameters

Sample size:	46
Fabric ratio:	5.8
Vector mean:	7
Harmonic mean:	5.9
Symmetry:	0.91
Min. chi sq:	8.39
Mean area*:	8257.2

*Average clast area in pixles

Sectional R_f / φ results for plane: B

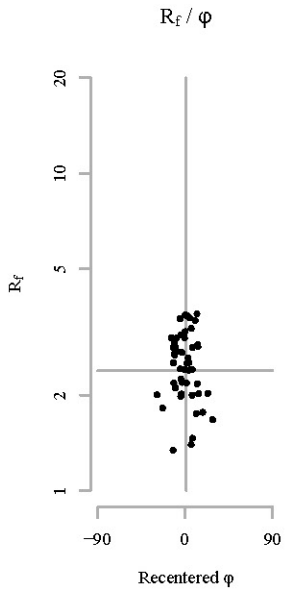

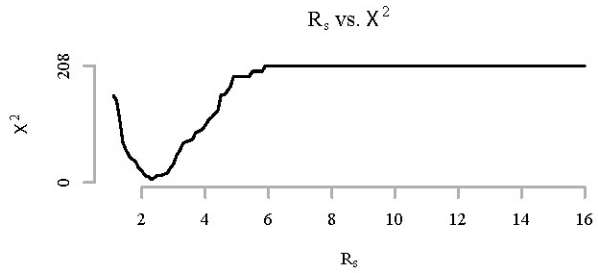

Rs ellipse

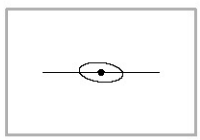

Normalized ellipse

Parameters

Sample size:	52
Fabric ratio:	2.3
Vector mean:	6
Harmonic mean:	2.4
Symmetry:	0.96
Min. chi sq:	5.31
Mean area*:	6553.8

*Average clast area in pixles

Sectional R_f / φ results for plane: C

Sample: 12DC55_C
Mineral: Pyroxene

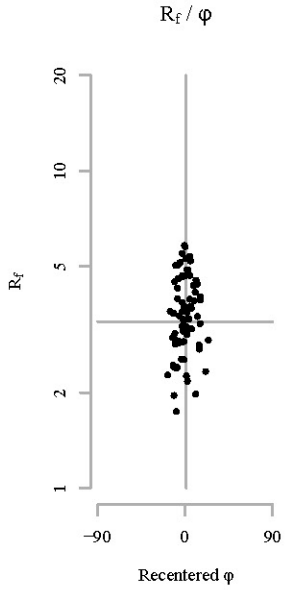

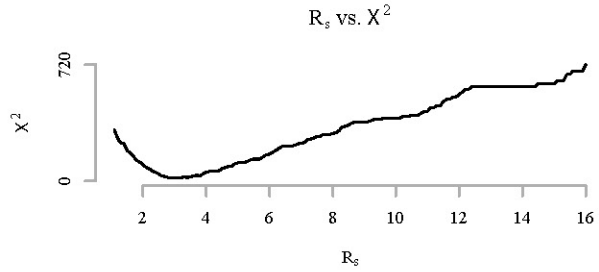

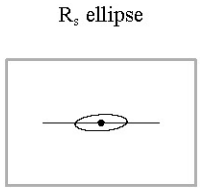

Parameters

Sample size:	79
Fabric ratio:	3.2
Vector mean:	177
Harmonic mean:	3.3
Symmetry:	0.89
Min. chi sq:	16.89
Mean area*:	7639

*Average clast area in pixles

Stereonet

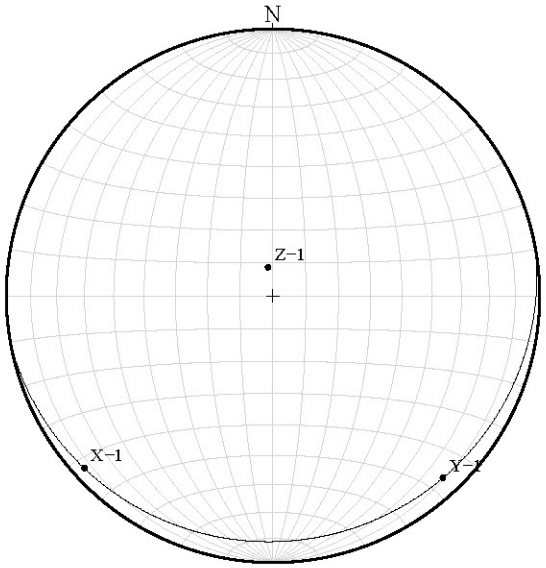

Nadai plot

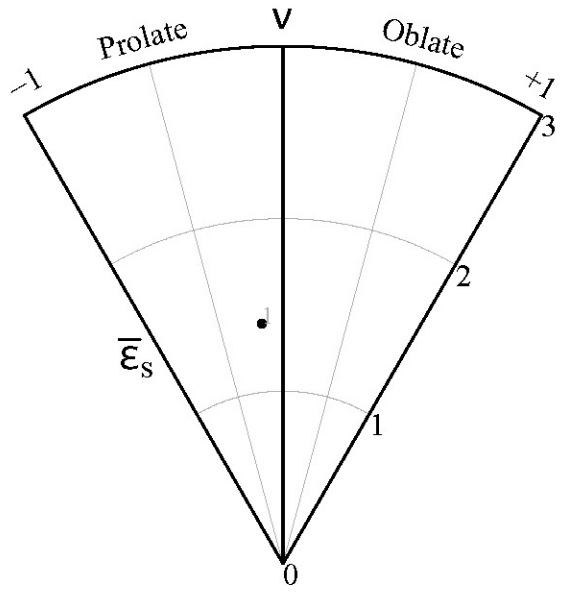

Sectional R_f / φ results for plane: A

Sample: 12DC55_C
Mineral: Plagioclase

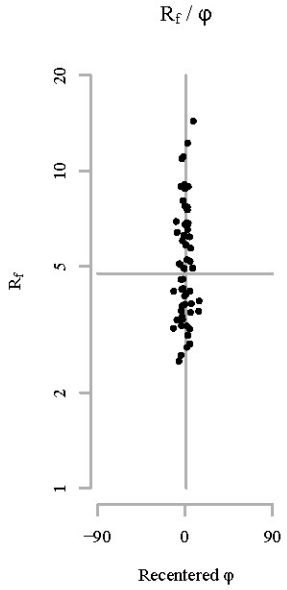

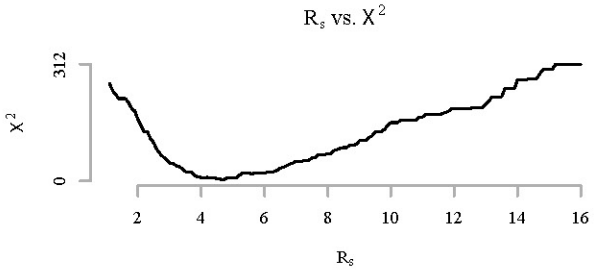

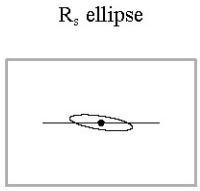

Parameters

Sample size:	58
Fabric ratio:	4.7
Vector mean:	8
Harmonic mean:	4.7
Symmetry:	0.86
Min. chi sq:	2.69
Mean area*:	10515.2

*Average clast area in pixles

Sectional R_f / φ results for plane: B

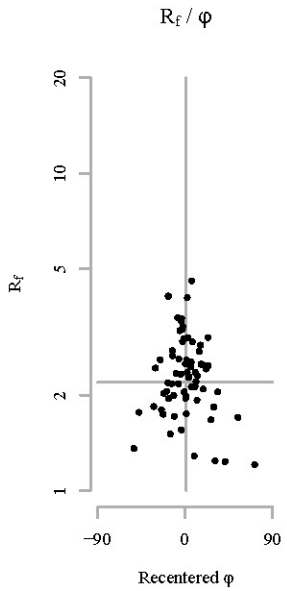

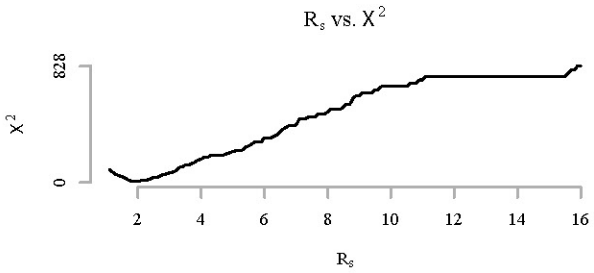

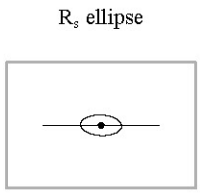

Parameters

Sample size:	69
Fabric ratio:	2
Vector mean:	3
Harmonic mean:	2.2
Symmetry:	0.93
Min. chi sq:	5.42
Mean area*:	4919.8

*Average clast area in pixles

Sectional R_f / φ results for plane: C

Sample: 12DC55_C
Mineral: Plagioclase

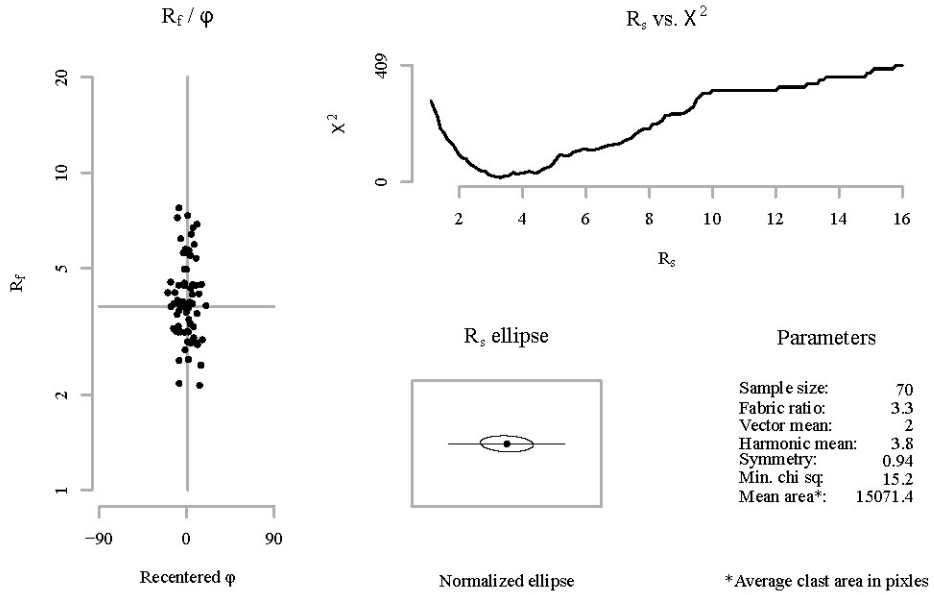

Stereonet

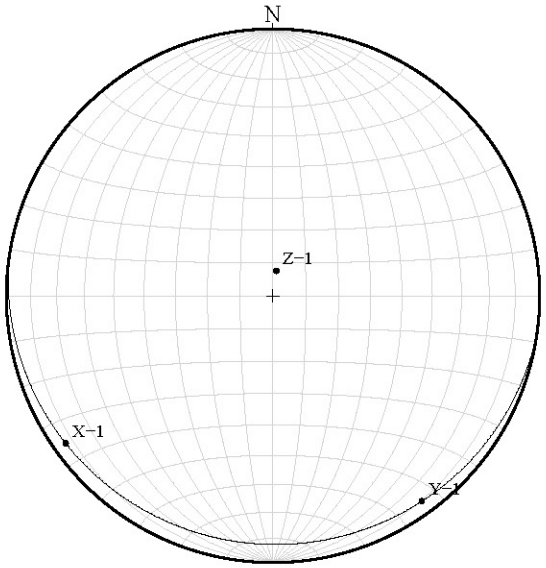

Nadai plot

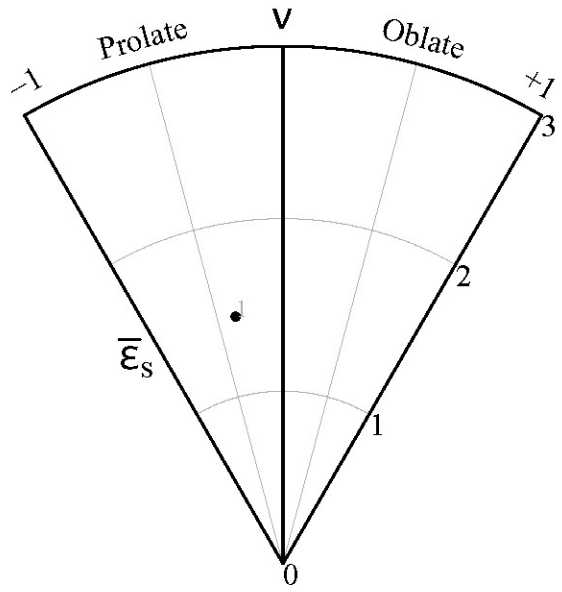

Sample: 12DC57_A
Mineral: Pyroxene

Sectional R_f / φ results for plane: A

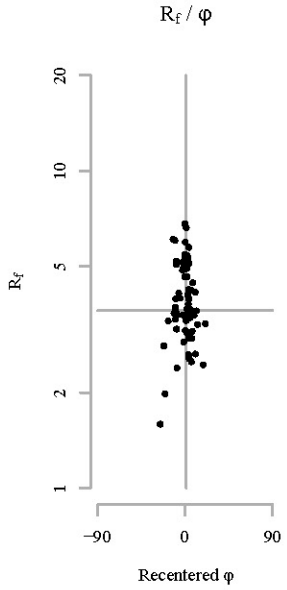

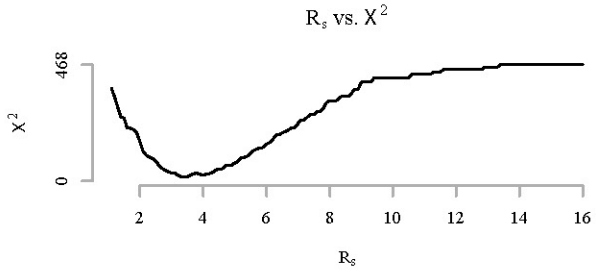

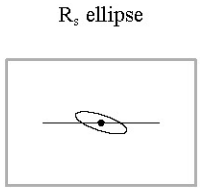

Parameters

Sample size:	74
Fabric ratio:	3.4
Vector mean:	18
Harmonic mean:	3.6
Symmetry:	0.78
Min. chi sq:	15.68
Mean area*:	6690.2

*Average clast area in pixles

Sectional R_f / φ results for plane: B

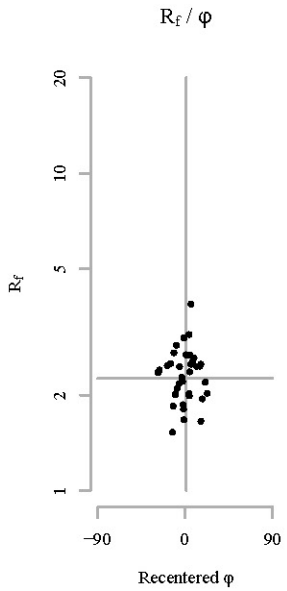

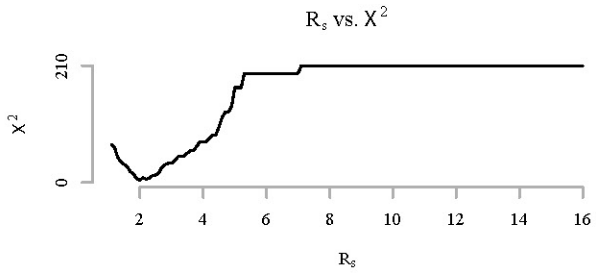

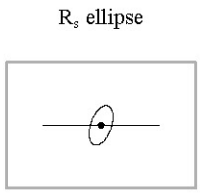

Parameters

Sample size:	35
Fabric ratio:	2
Vector mean:	109
Harmonic mean:	2.3
Symmetry:	0.86
Min. chi sq:	4
Mean area*:	5396.5

*Average clast area in pixles

Sectional R_f / φ results for plane: C

Sample: 12DC57_A
Mineral: Pyroxene

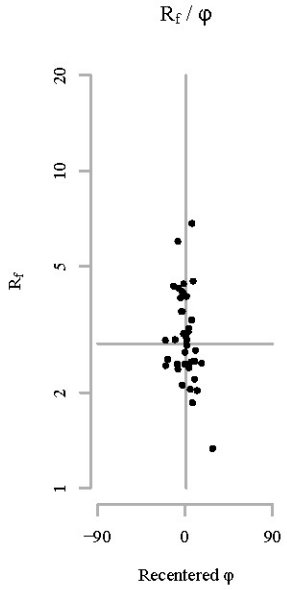

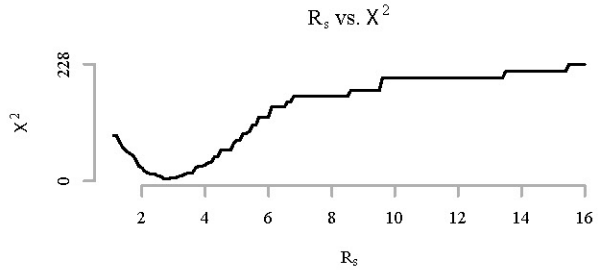

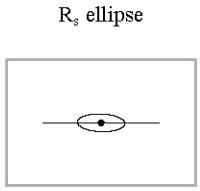

Parameters

Sample size:	38
Fabric ratio:	2.7
Vector mean:	2
Harmonic mean:	2.9
Symmetry:	0.79
Min. chi sq:	4
Mean area*:	11436.8

*Average clast area in pixles

Stereonet

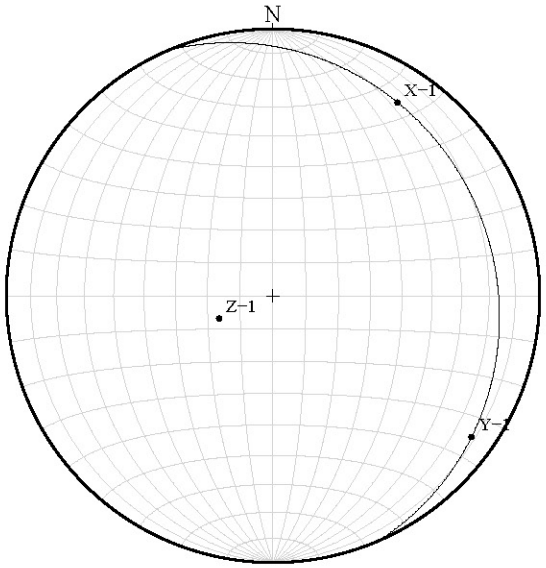

Nadai plot

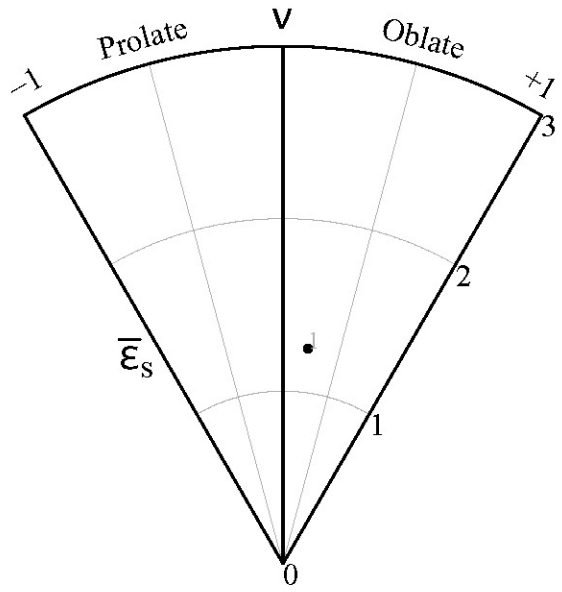

Sectional R_f / φ results for plane: A

Sample: 12DC57_A
Mineral: Plagioclase

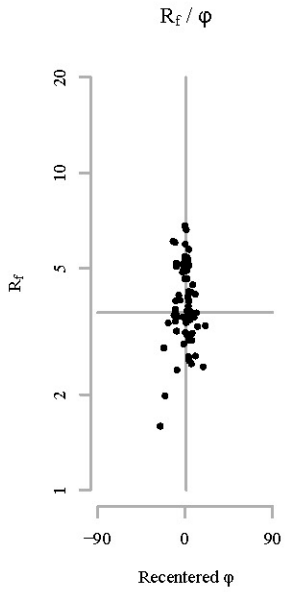

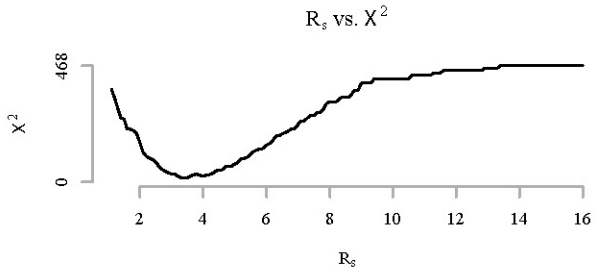

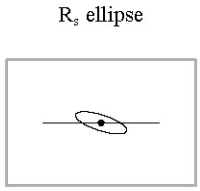

Normalized ellipse

Parameters

Sample size:	74
Fabric ratio:	3.4
Vector mean:	18
Harmonic mean:	3.6
Symmetry:	0.78
Min. chi sq:	15.68
Mean area*:	6690.2

*Average clast area in pixles

Sectional R_f / φ results for plane: B

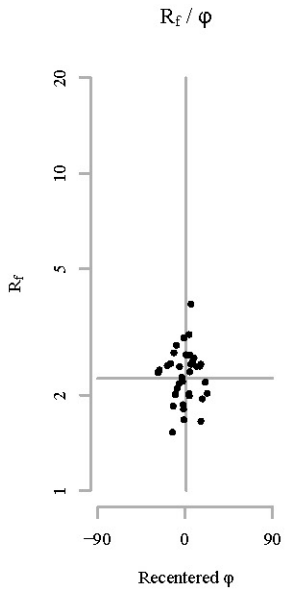

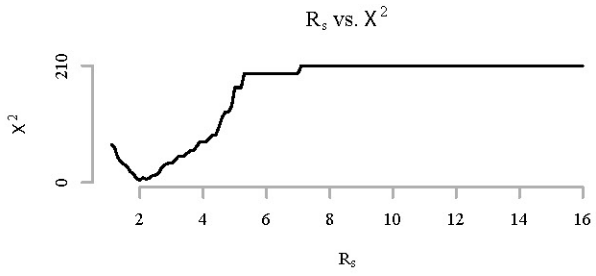

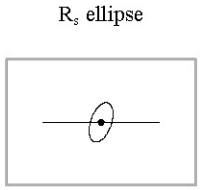

Normalized ellipse

Parameters

Sample size:	35
Fabric ratio:	2
Vector mean:	109
Harmonic mean:	2.3
Symmetry:	0.86
Min. chi sq:	4
Mean area*:	5396.5

*Average clast area in pixles

Sectional R_f / φ results for plane: C

Sample: 12DC57_A
Mineral: Plagioclase

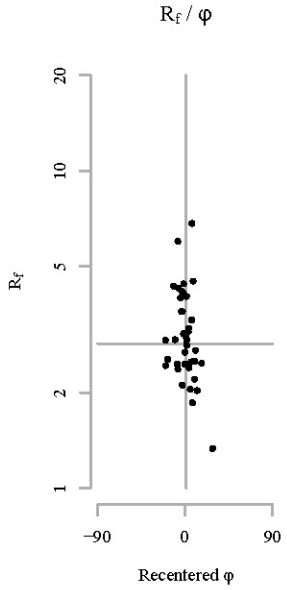

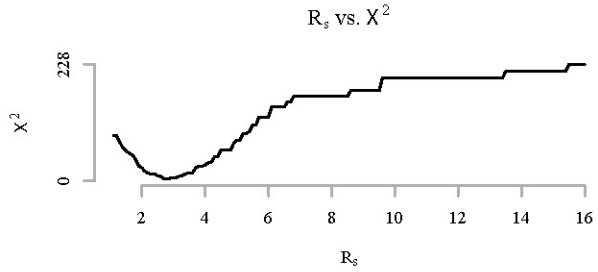

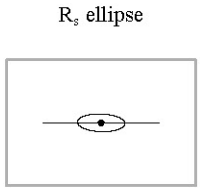

Parameters

Sample size:	38
Fabric ratio:	2.7
Vector mean:	2
Harmonic mean:	2.9
Symmetry:	0.79
Min. chi sq:	4
Mean area*:	11436.8

*Average clast area in pixles

Stereonet

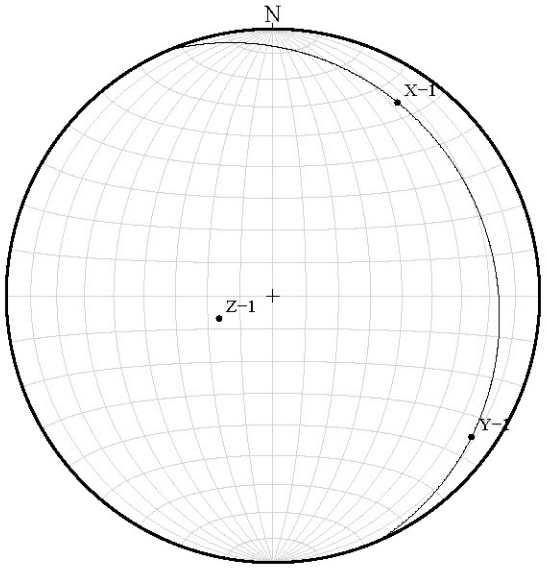

Nadai plot

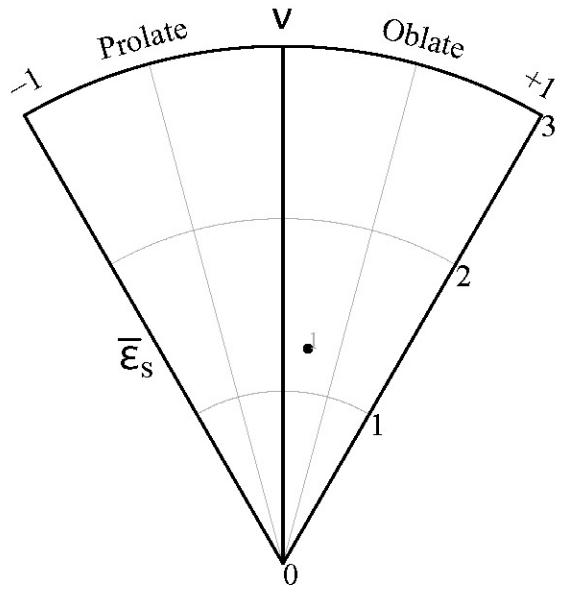

Sample: 12DC58_A
Mineral: Pyroxene

Sectional R_f / φ results for plane: A

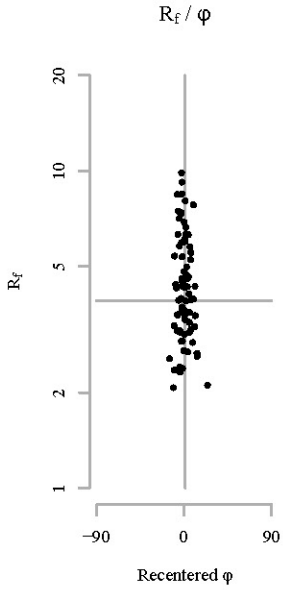

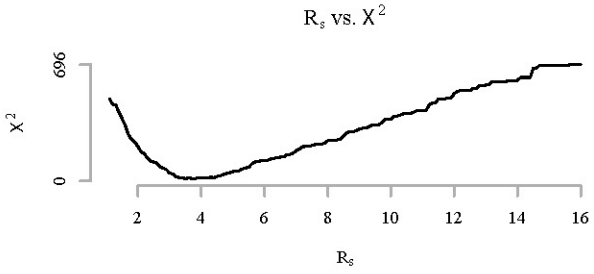

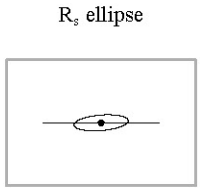

Parameters

Sample size:	88
Fabric ratio:	3.5
Vector mean:	175
Harmonic mean:	3.9
Symmetry:	0.91
Min. chi sq:	13.61
Mean area*:	4875.2

*Average clast area in pixles

Sectional R_f / φ results for plane: B

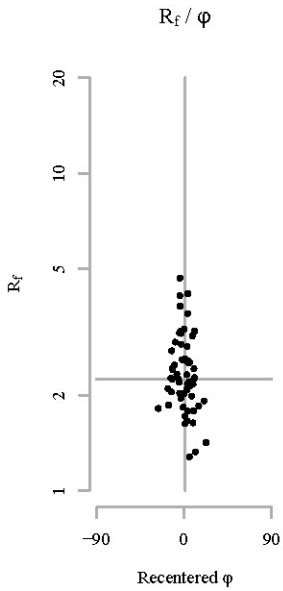

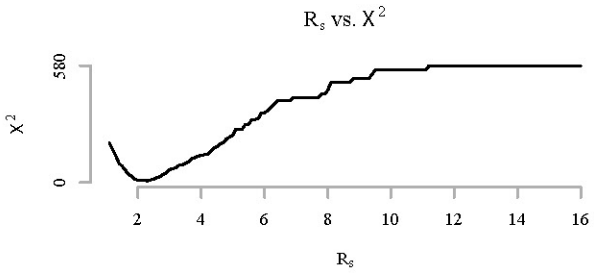

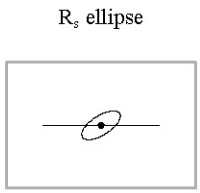

Parameters

Sample size:	58
Fabric ratio:	2.3
Vector mean:	147
Harmonic mean:	2.2
Symmetry:	0.83
Min. chi sq:	6.86
Mean area*:	5114.2

*Average clast area in pixles

Sectional R_f / φ results for plane: C

Sample: 12DC58_A
Mineral: Pyroxene

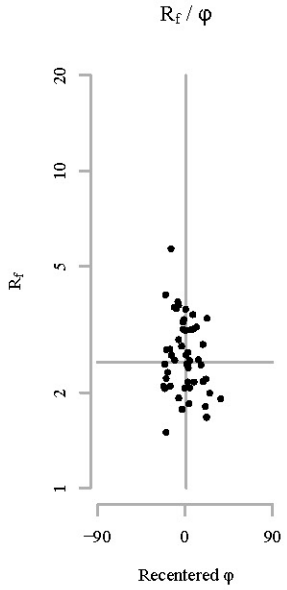

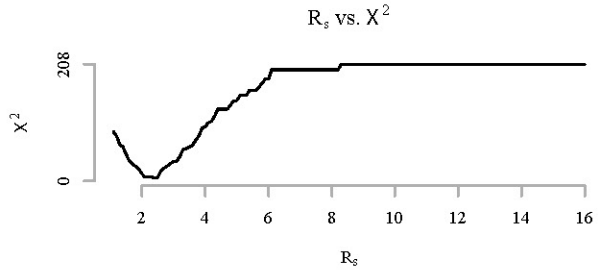

R_s ellipse

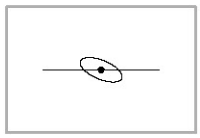

Normalized ellipse

Parameters

Sample size:	52
Fabric ratio:	2.4
Vector mean:	23
Harmonic mean:	2.5
Symmetry:	0.81
Min. chi sq:	4.54
Mean area*:	4648.8

*Average clast area in pixles

Stereonet

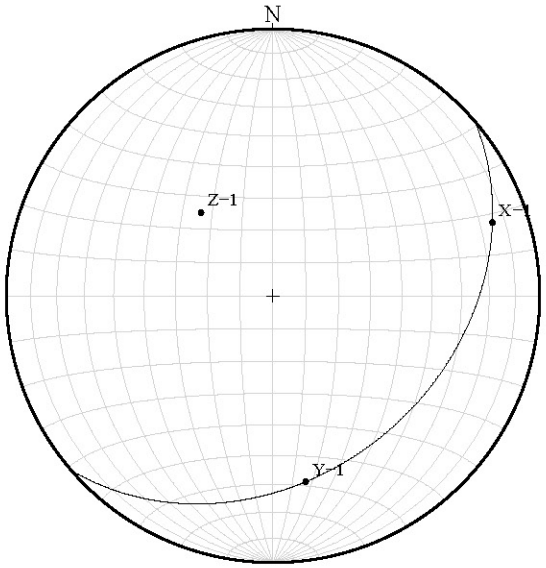

Nadai plot

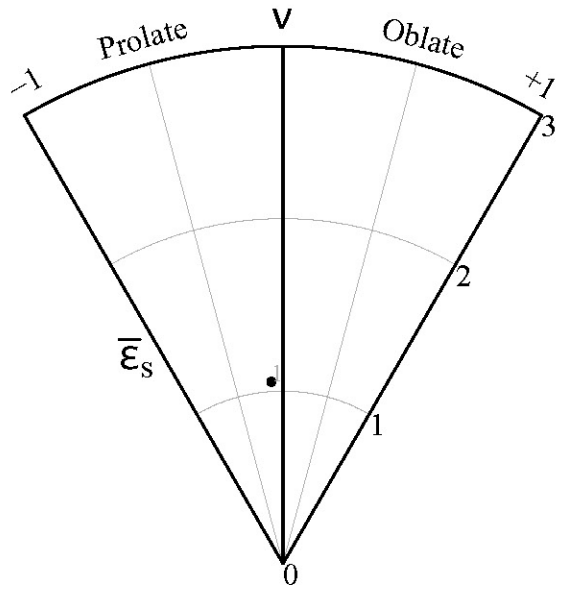

Sectional R_f / φ results for plane: A

Sample: 12DC58_A
Mineral: Plagioclase

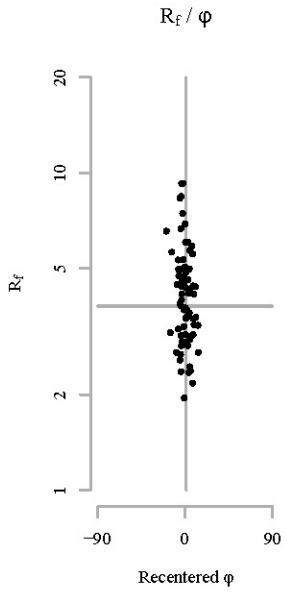

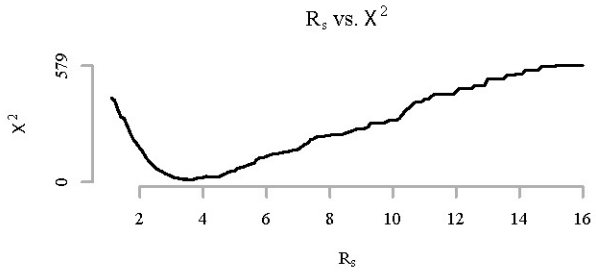

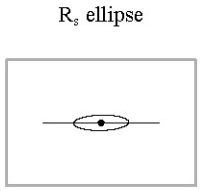

Normalized ellipse

Parameters

Sample size:	77
Fabric ratio:	3.6
Vector mean:	179
Harmonic mean:	3.8
Symmetry:	0.78
Min. chi sq:	10.08
Mean area*:	9193.7

*Average clast area in pixles

Sectional R_f / φ results for plane: B

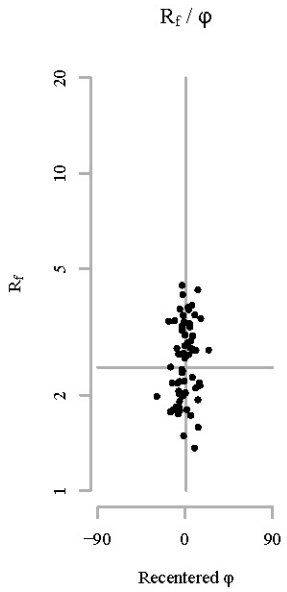

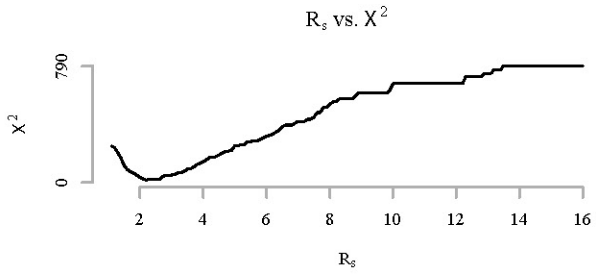

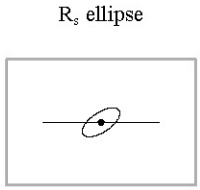

Normalized ellipse

Parameters

Sample size:	68
Fabric ratio:	2.2
Vector mean:	146
Harmonic mean:	2.4
Symmetry:	0.82
Min. chi sq:	14.21
Mean area*:	12224.2

*Average clast area in pixles

Sectional R_f / φ results for plane: C

Sample: 12DC58_A
Mineral: Plagioclase

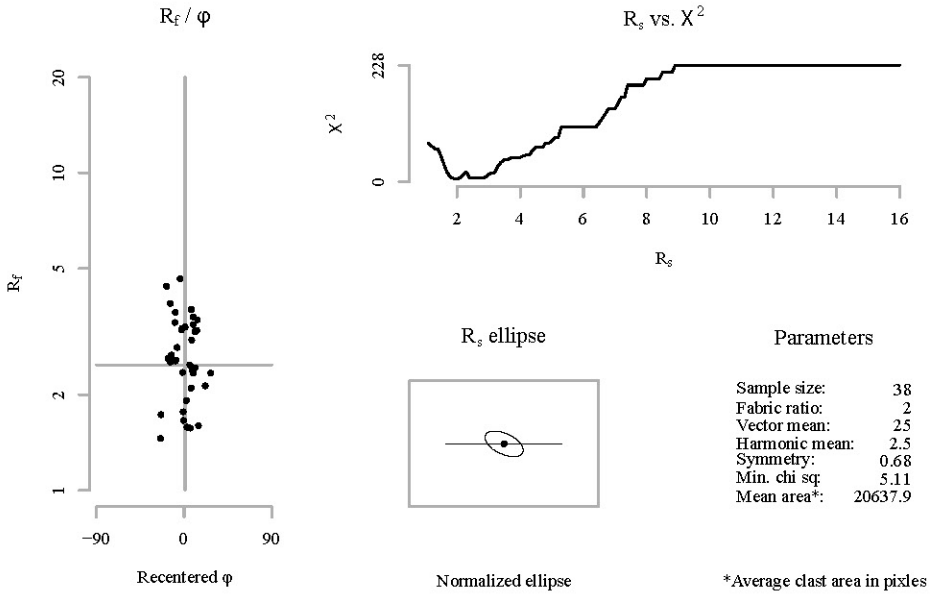

Stereonet

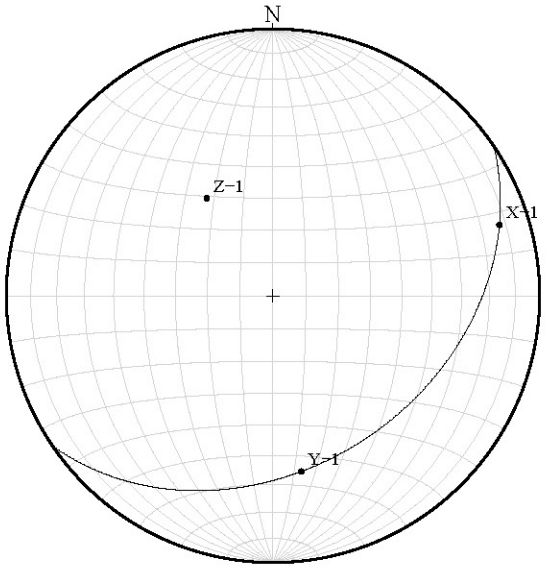

Nadai plot

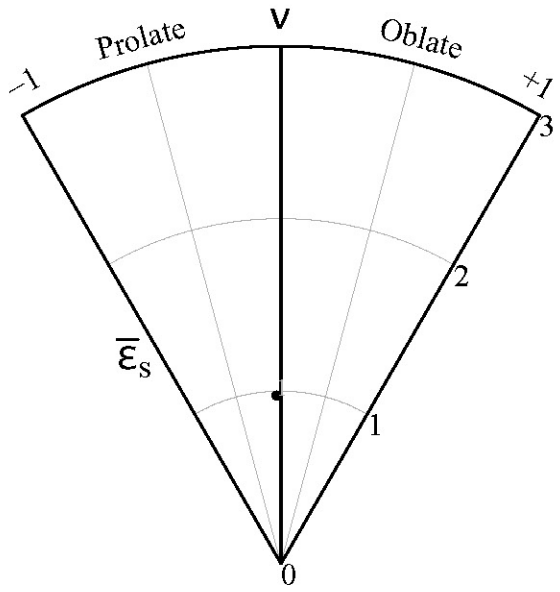

Sample: 12DC59_A
Mineral: Pyroxene

Sectional R_f / φ results for plane: A

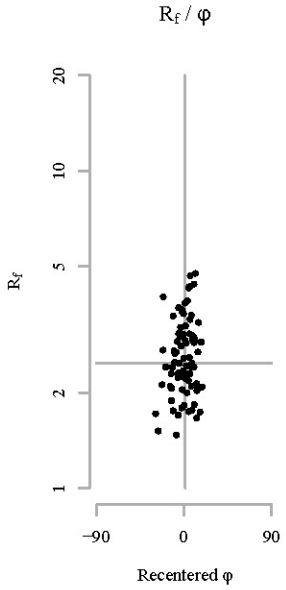

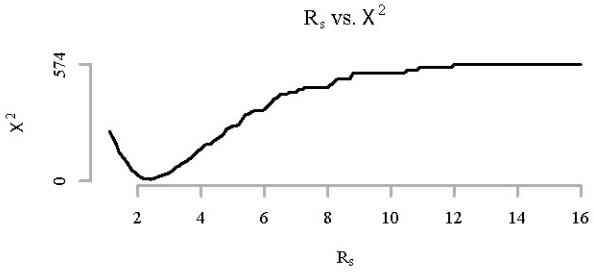

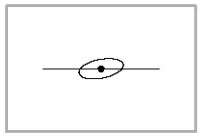

Parameters

Sample size:	82
Fabric ratio:	2.4
Vector mean:	169
Harmonic mean:	2.5
Symmetry:	0.9
Min. chi sq:	7.76
Mean area*:	2859.8

*Average clast area in pixles

Sectional R_f / φ results for plane: B

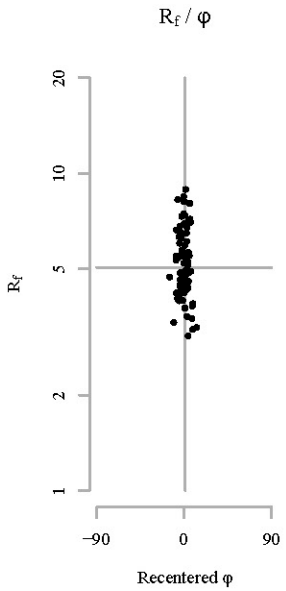

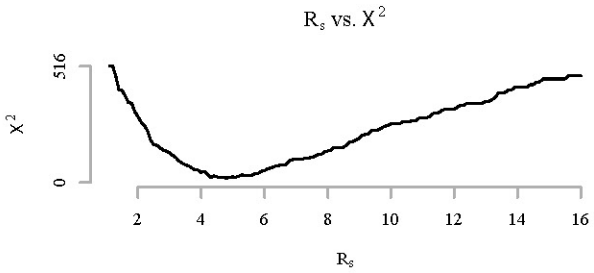

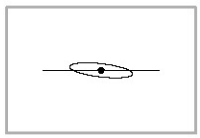

Parameters

Sample size:	80
Fabric ratio:	4.8
Vector mean:	7
Harmonic mean:	5
Symmetry:	0.88
Min. chi sq:	18.8
Mean area*:	3795.1

*Average clast area in pixles

Sectional R_f / φ results for plane: C

Sample: 12DC59_A
Mineral: Pyroxene

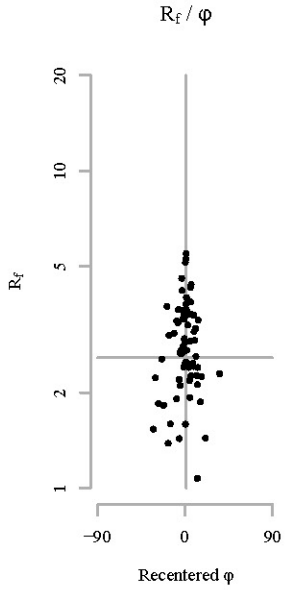

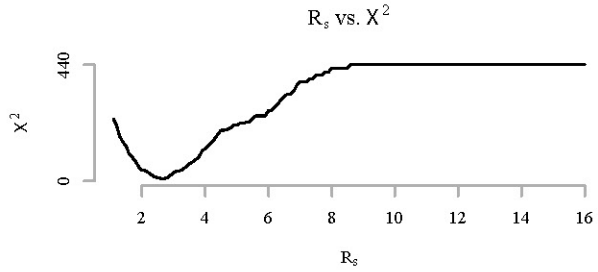

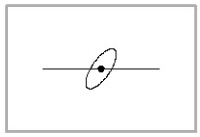

Normalized ellipse

Parameters

Sample size:	73
Fabric ratio:	2.6
Vector mean:	124
Harmonic mean:	2.6
Symmetry:	0.93
Min. chi sq:	8.89
Mean area*:	7502

*Average clast area in pixles

Stereonet

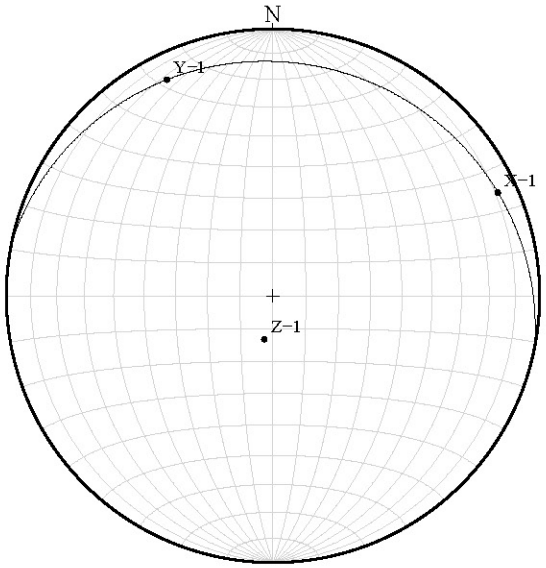

Nadai plot

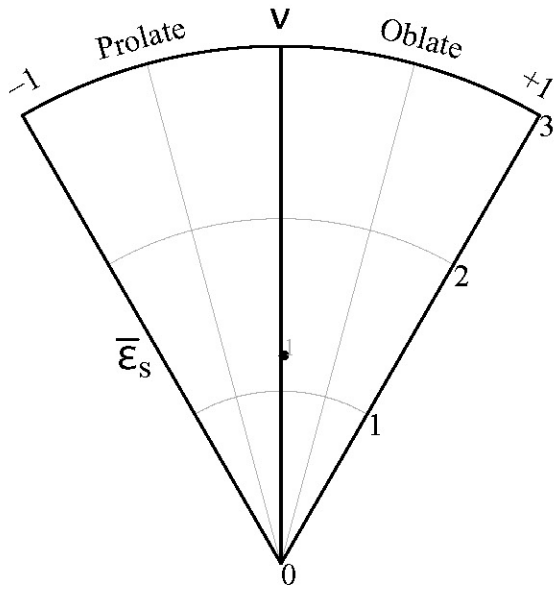

Sectional R_f / φ results for plane: A

Sample: 12DC59_A
Mineral: Plagioclase

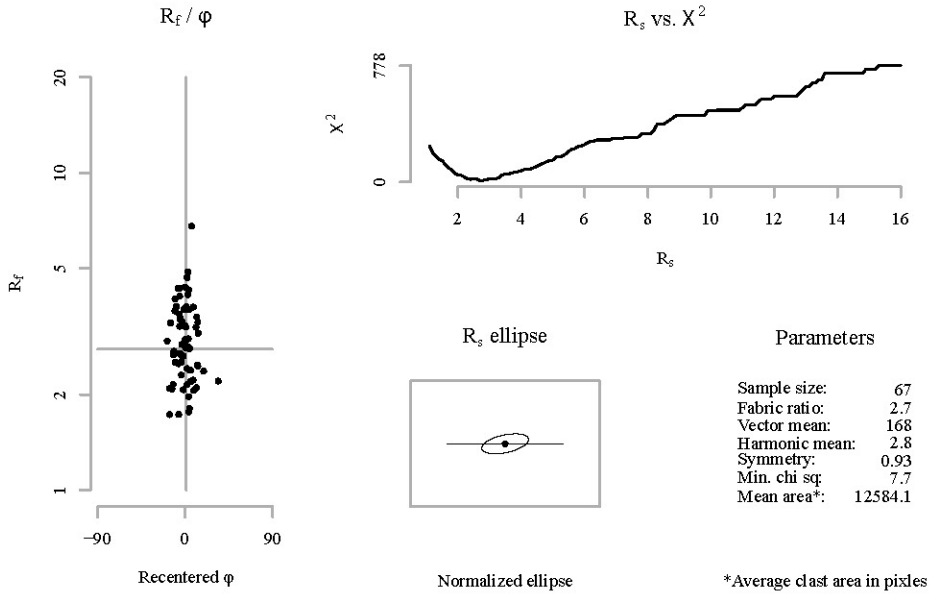

Sectional R_f / φ results for plane: B

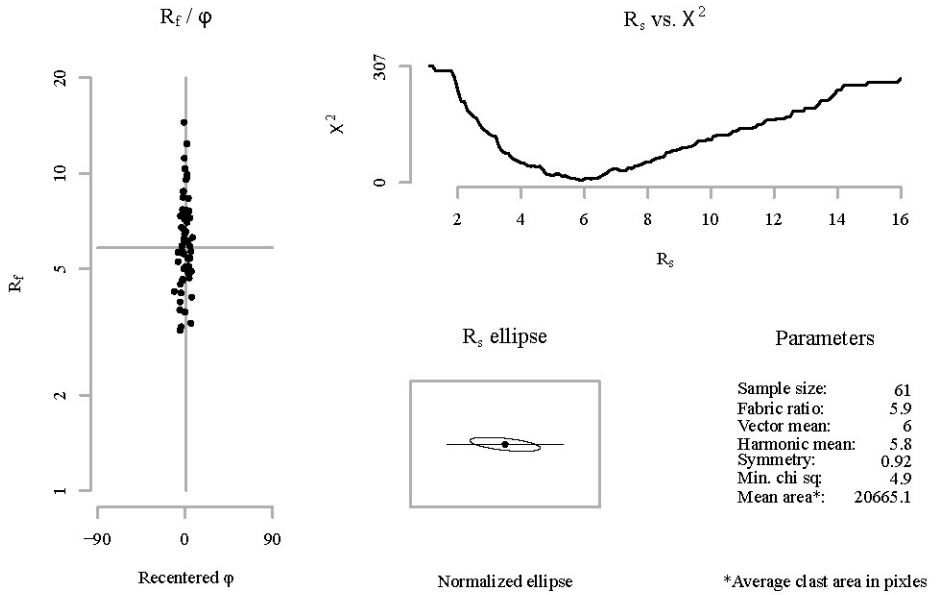

Sectional R_f / φ results for plane: C

Sample: 12DC59_A
Mineral: Plagioclase

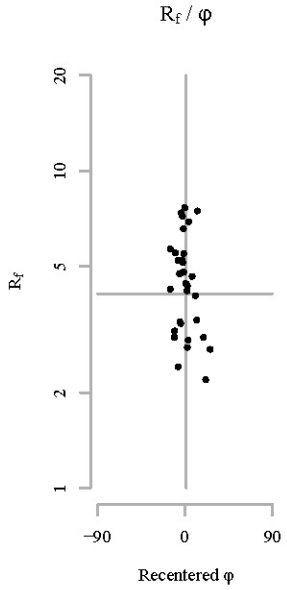

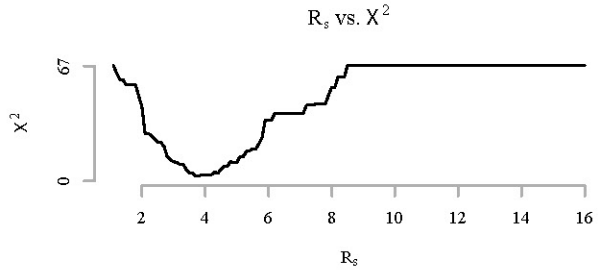

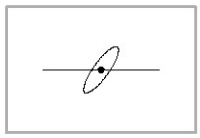

Normalized ellipse

Parameters

Sample size:	32
Fabric ratio:	3.7
Vector mean:	126
Harmonic mean:	4.1
Symmetry:	0.69
Min. chi sq:	2.88
Mean area*:	25293.1

*Average clast area in pixles

Stereonet

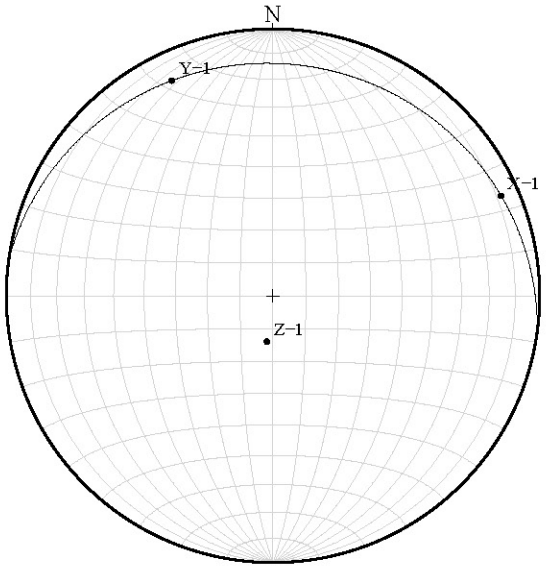

Nadai plot

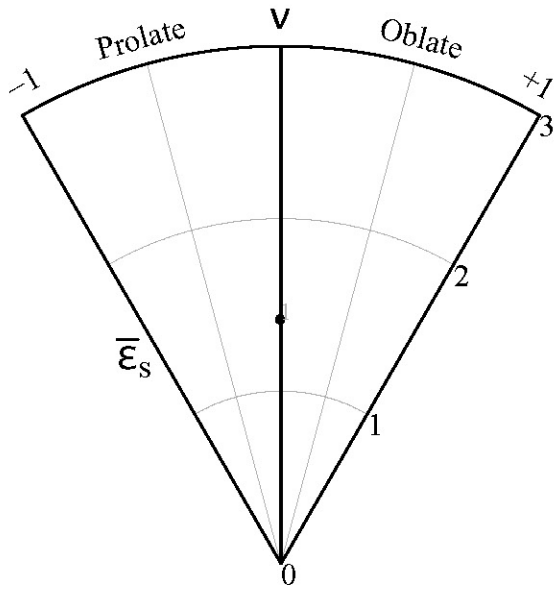

Sectional R_f / φ results for plane: A

Sample: 13DC63_A
Mineral: Hornblende

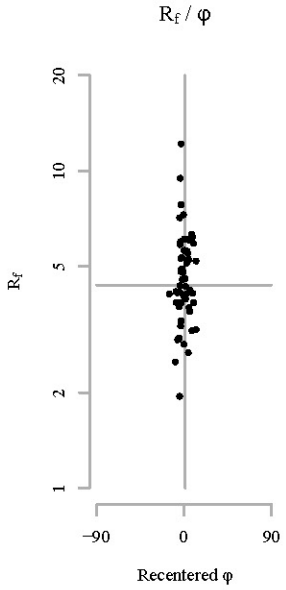

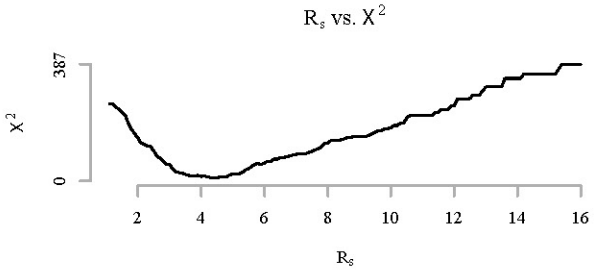

Rs ellipse

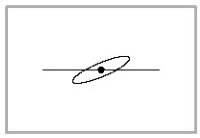

Normalized ellipse

Parameters

Sample size:	58
Fabric ratio:	4.5
Vector mean:	157
Harmonic mean:	4.4
Symmetry:	0.86
Min. chi sq:	9.14
Mean area*:	4687.8

*Average clast area in pixles

Sectional R_f / φ results for plane: B

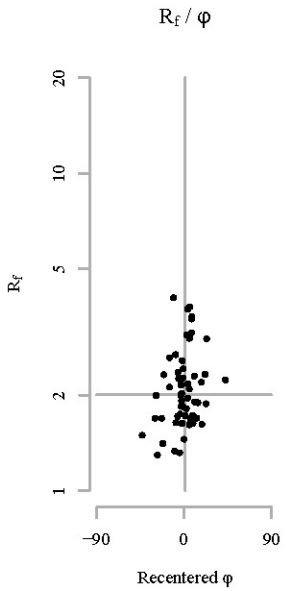

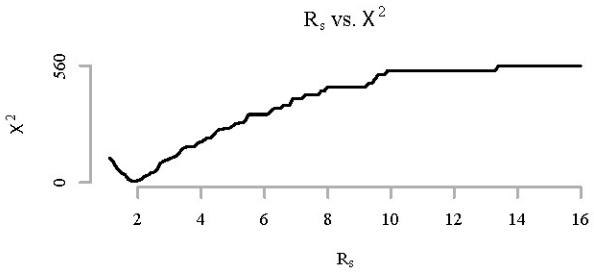

Rs ellipse

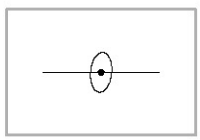

Normalized ellipse

Parameters

Sample size:	56
Fabric ratio:	1.9
Vector mean:	95
Harmonic mean:	2
Symmetry:	0.89
Min. chi sq:	5.29
Mean area*:	4886.6

*Average clast area in pixles

Sectional R_f / φ results for plane: C

Sample: 13DC63_A
Mineral: Hornblende

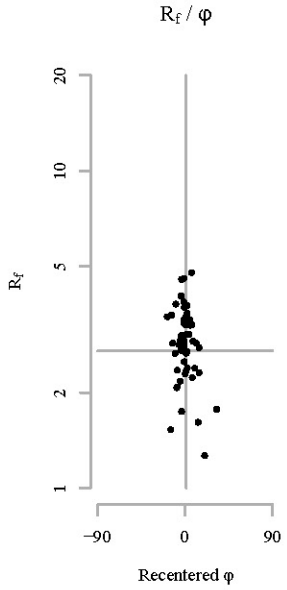

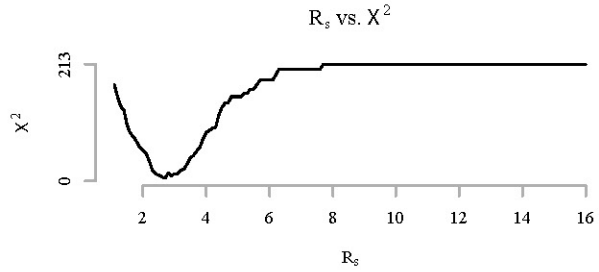

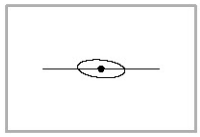

Parameters

Sample size:	53
Fabric ratio:	2.7
Vector mean:	5
Harmonic mean:	2.7
Symmetry:	0.83
Min. chi sq:	4.55
Mean area*:	4369.4

*Average clast area in pixles

Stereonet

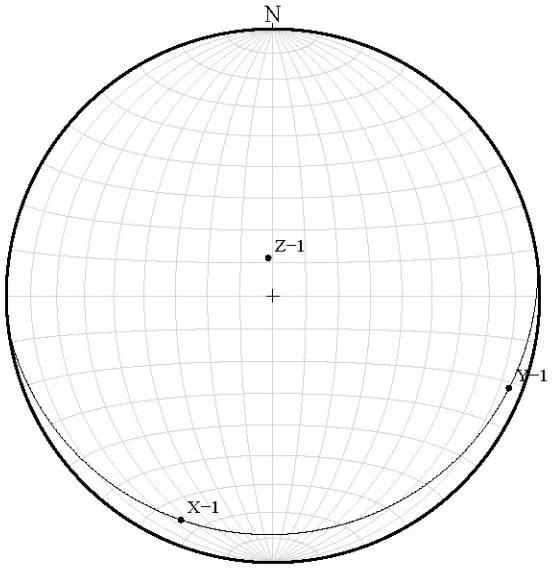

Nadai plot

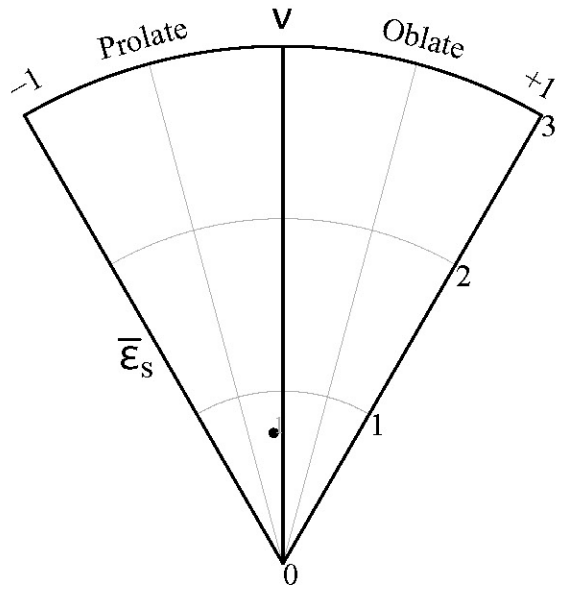

Sectional R_f / φ results for plane: A

Sample: 13DC63_A
Mineral: Plagioclase

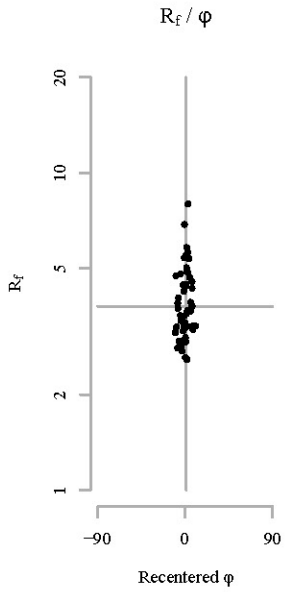

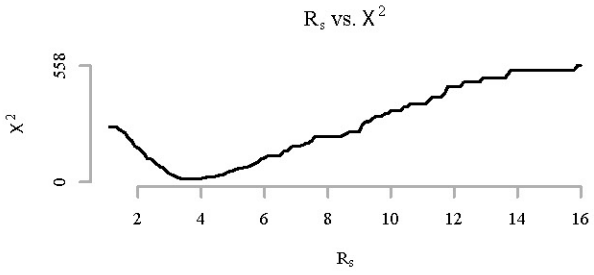

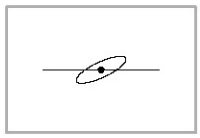

Normalized ellipse

Parameters

Sample size:	58
Fabric ratio:	3.5
Vector mean:	155
Harmonic mean:	3.8
Symmetry:	0.79
Min. chi sq:	14.83
Mean area*:	5294.6

*Average clast area in pixles

Sectional R_f / φ results for plane: B

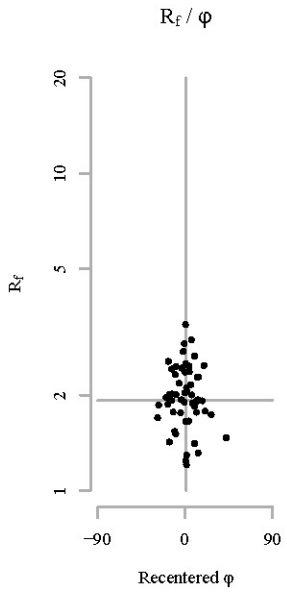

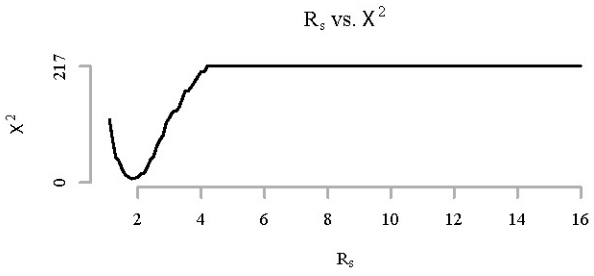

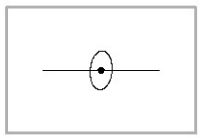

Normalized ellipse

Parameters

Sample size:	54
Fabric ratio:	1.8
Vector mean:	95
Harmonic mean:	1.9
Symmetry:	0.89
Min. chi sq:	6.37
Mean area*:	4654.2

*Average clast area in pixles

Sectional R_f / φ results for plane: C

Sample: 13DC63_A
Mineral: Plagioclase

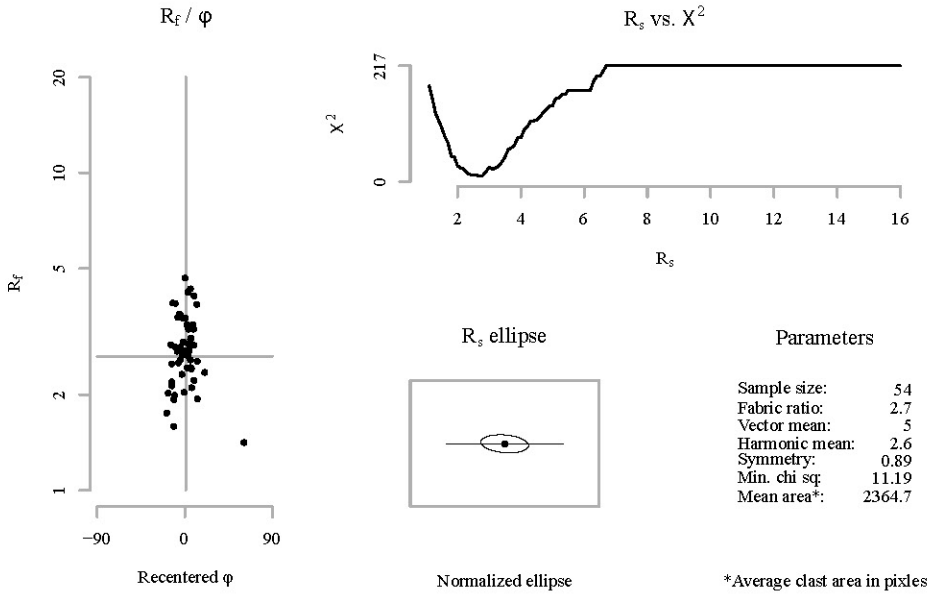

Stereonet

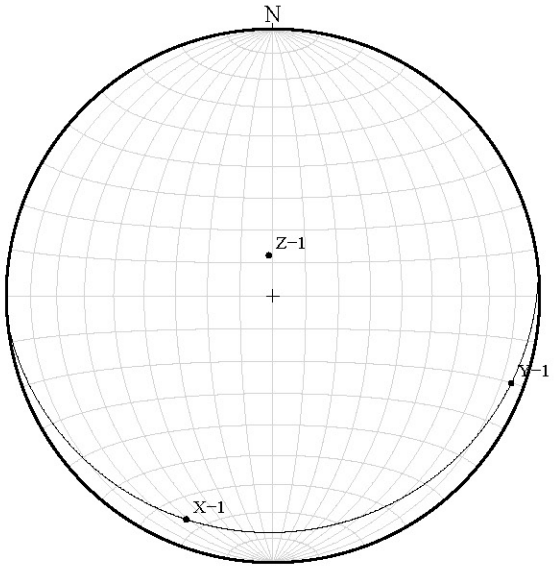

Nadai plot

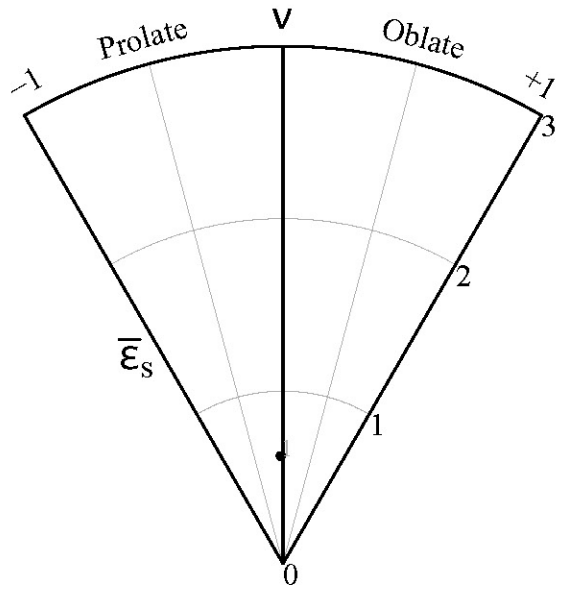

Sample: 13DC63_B
Mineral: Pyroxene / Hornblende

Sectional R_f / φ results for plane: A

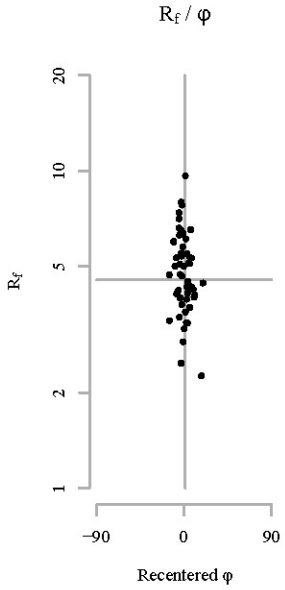

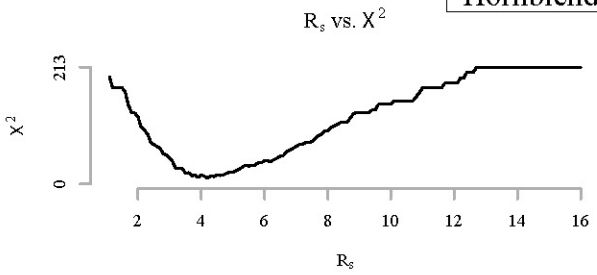

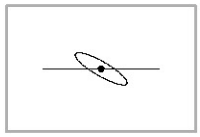

Normalized ellipse

Parameters

Sample size:	53
Fabric ratio:	4.2
Vector mean:	30
Harmonic mean:	4.5
Symmetry:	0.6
Min. chi sq:	10.58
Mean area*:	8065.7

*Average clast area in pixles

Sectional R_f / φ results for plane: B

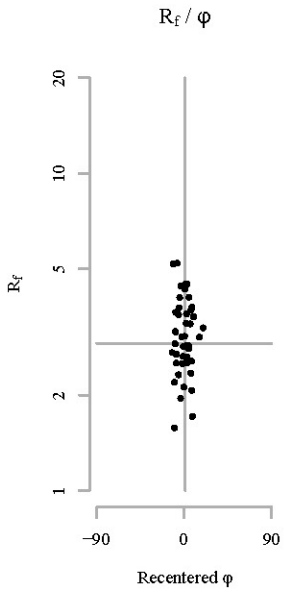

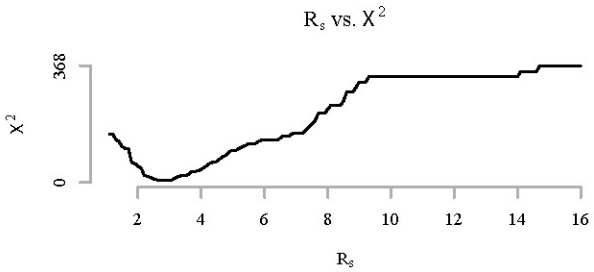

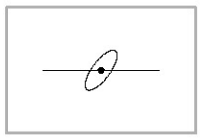

Normalized ellipse

Parameters

Sample size:	46
Fabric ratio:	2.7
Vector mean:	127
Harmonic mean:	2.9
Symmetry:	0.91
Min. chi sq:	5.65
Mean area*:	8931.7

*Average clast area in pixles

Sectional R_f / φ results for plane: C

Sample: 13DC63_B
Mineral: Pyroxene / Hornblende

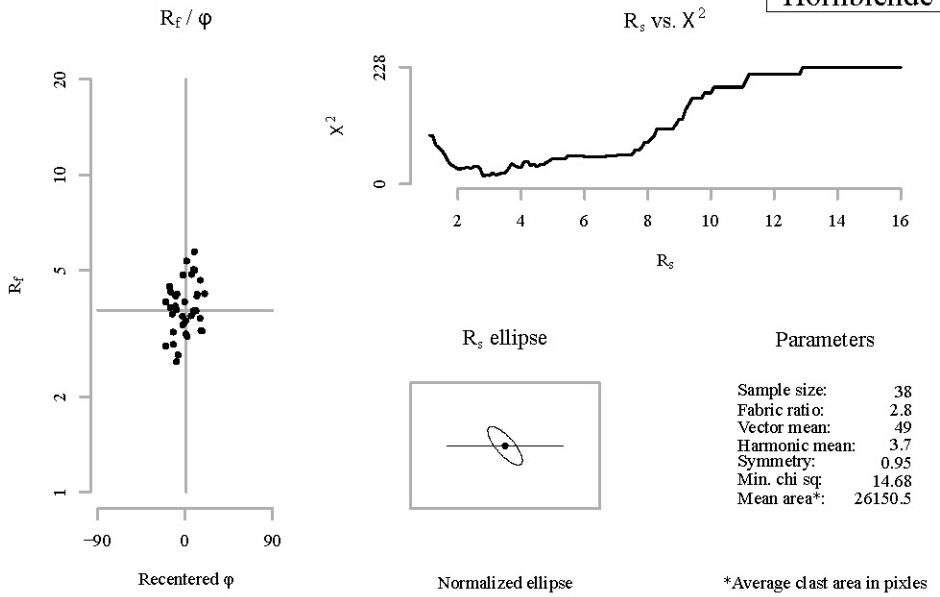

Stereonet

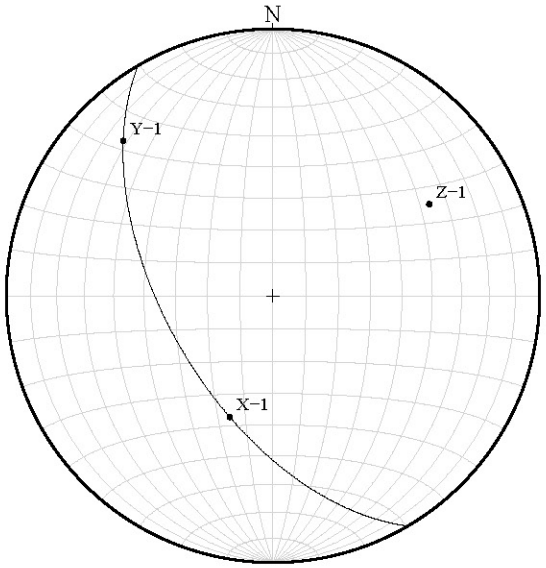

Nadai plot

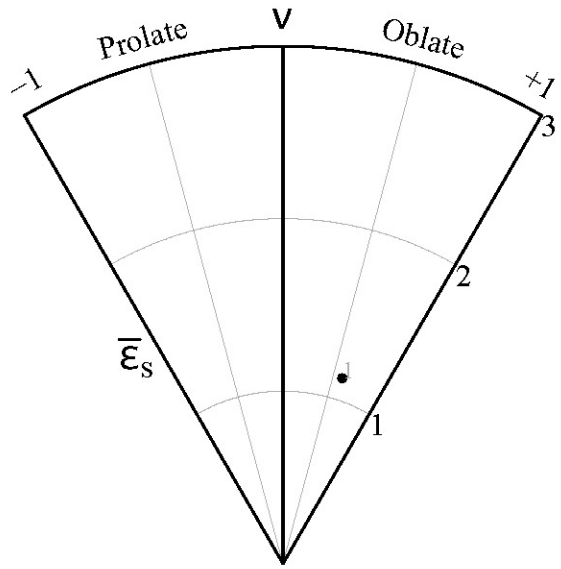

Sectional R_f / φ results for plane: A

Sample: 13DC63_B
Mineral: Plagioclase

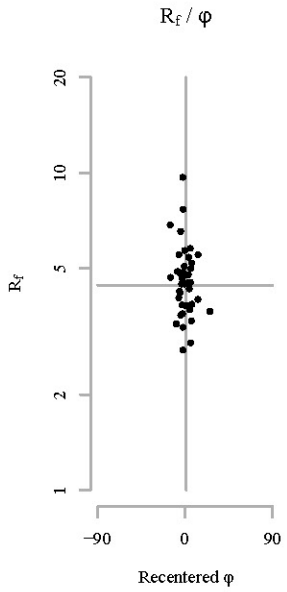

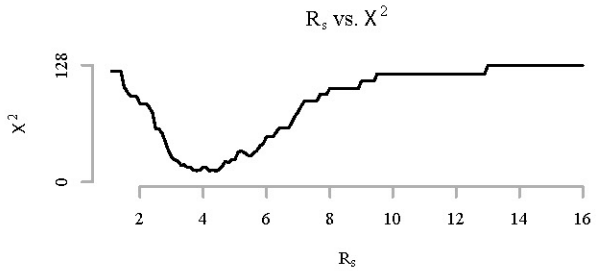

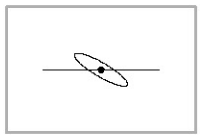

Normalized ellipse

Parameters

Sample size:	41
Fabric ratio:	4.4
Vector mean:	30
Harmonic mean:	4.4
Symmetry:	0.83
Min. chi sq:	11.88
Mean area*:	18659

*Average clast area in pixles

Sectional R_f / φ results for plane: B

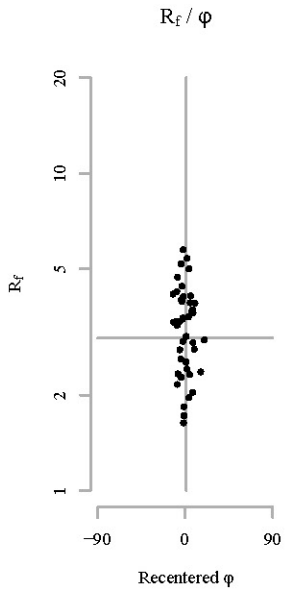

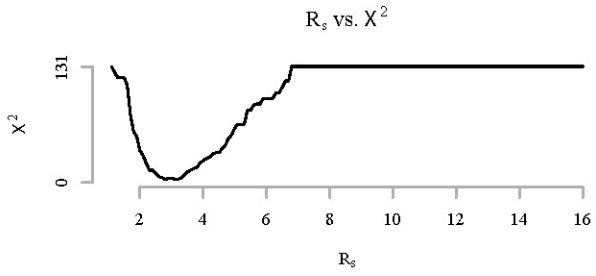

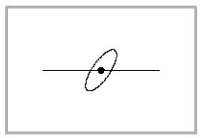

Normalized ellipse

Parameters

Sample size:	43
Fabric ratio:	2.8
Vector mean:	125
Harmonic mean:	3
Symmetry:	0.88
Min. chi sq:	2.95
Mean area*:	12899.7

*Average clast area in pixles

Sectional R_f / φ results for plane: C

Sample: 13DC63_B
Mineral: Plagioclase

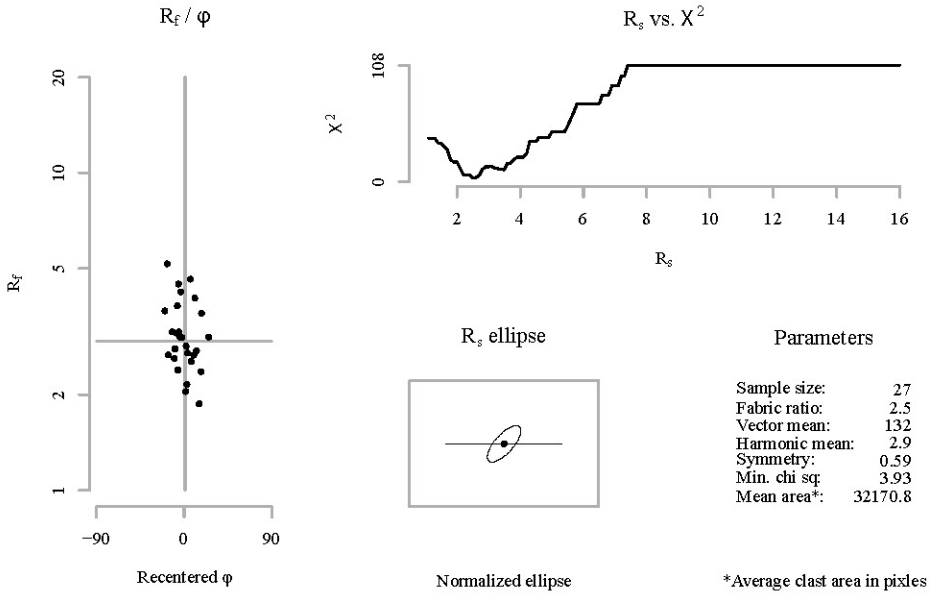

Stereonet

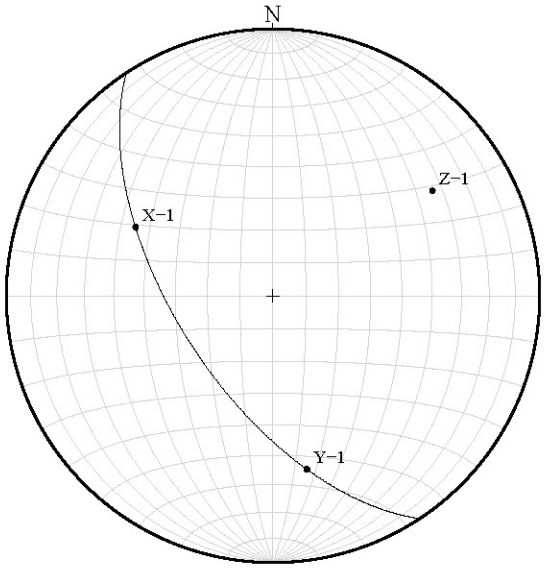

Nadai plot

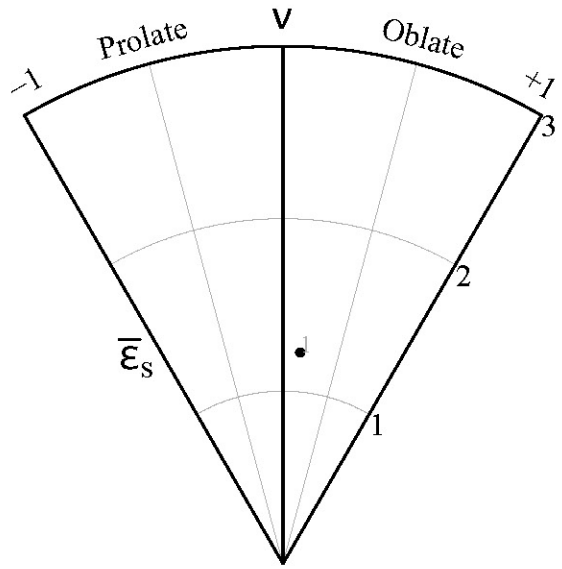

Sectional R_f / φ results for plane: A

Sample: 13DC64_A
Mineral: Hornblende

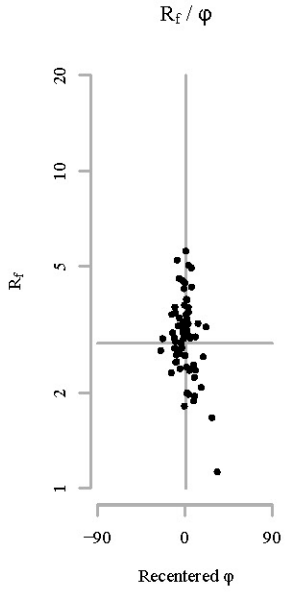

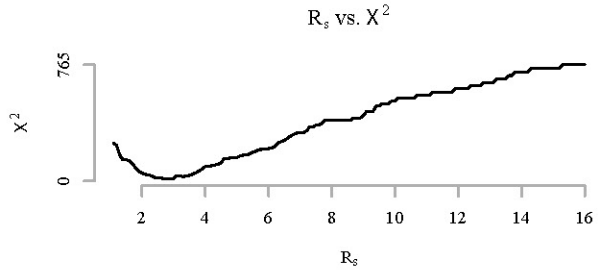

Rs ellipse

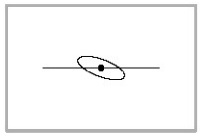

Normalized ellipse

Parameters

Sample size:	68
Fabric ratio:	2.9
Vector mean:	20
Harmonic mean:	2.9
Symmetry:	0.91
Min. chi sq:	11.15
Mean area*:	2482.5

*Average clast area in pixles

Sectional R_f / φ results for plane: B

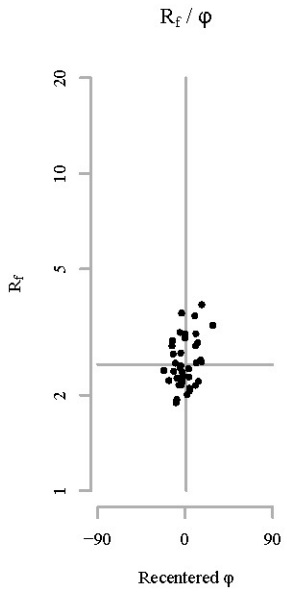

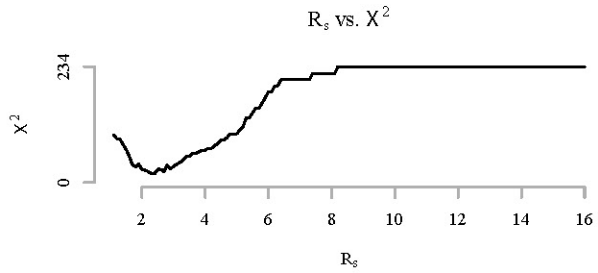

Rs ellipse

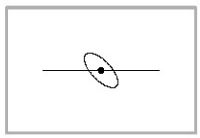

Normalized ellipse

Parameters

Sample size:	39
Fabric ratio:	2.3
Vector mean:	46
Harmonic mean:	2.5
Symmetry:	0.82
Min. chi sq:	17.54
Mean area*:	3346.6

*Average clast area in pixles

Sectional R_f / φ results for plane: C

Sample: 13DC64_A
Mineral: Hornblende

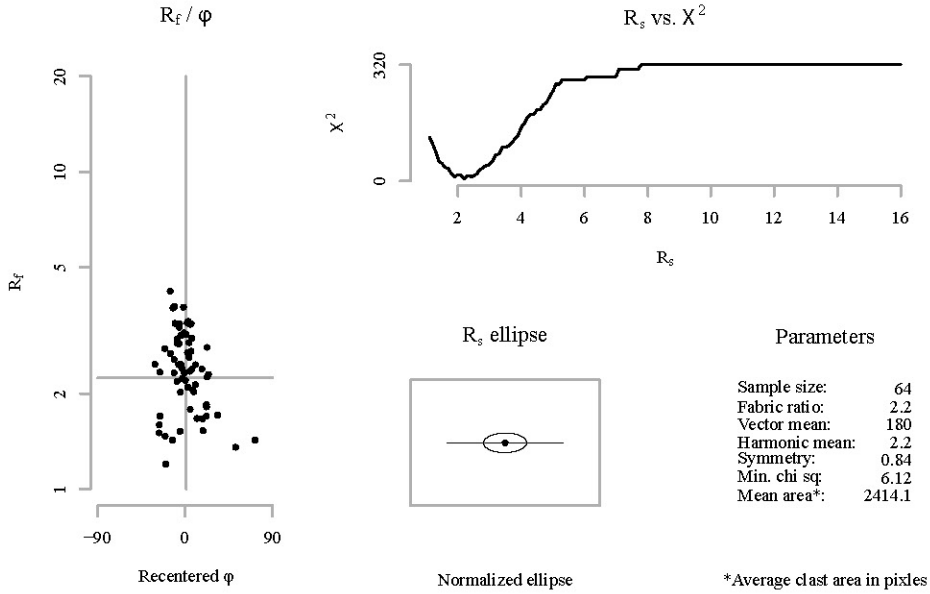

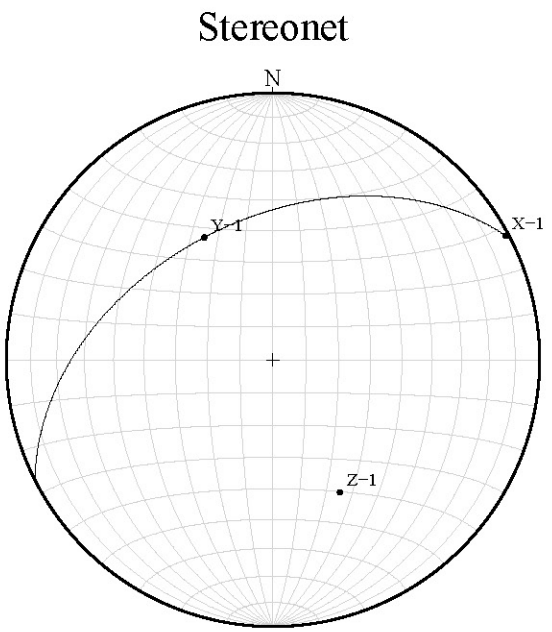

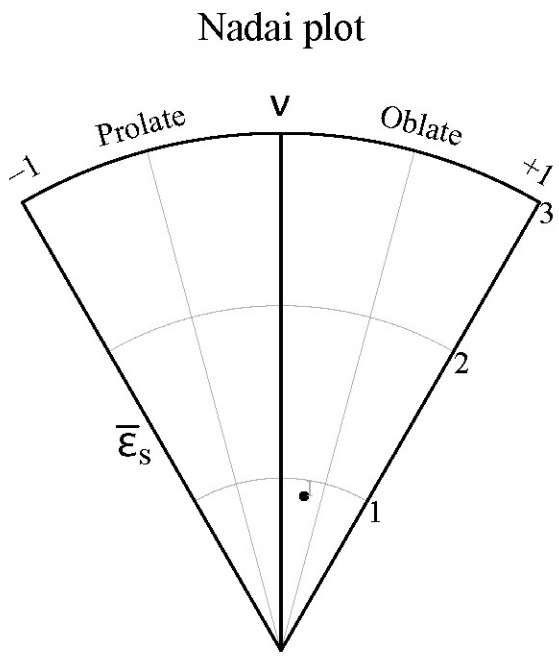

Sectional R_f / φ results for plane: A

Sample: 13DC64_A
Mineral: Plagioclase

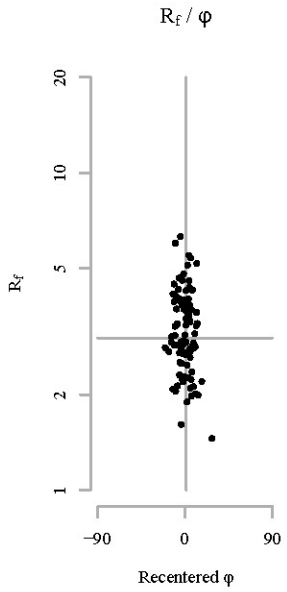

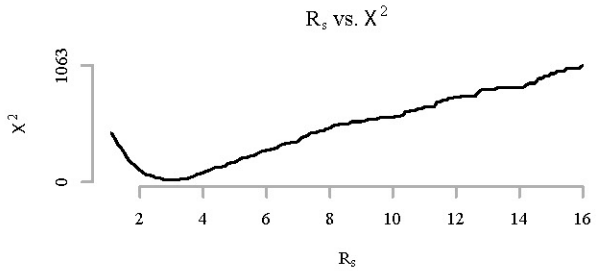

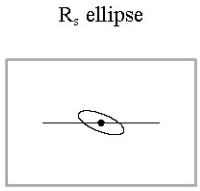

Parameters

Sample size:	96
Fabric ratio:	2.8
Vector mean:	22
Harmonic mean:	3
Symmetry:	0.9
Min. chi sq:	16.02
Mean area*:	6302.3

*Average clast area in pixles

Sectional R_f / φ results for plane: B

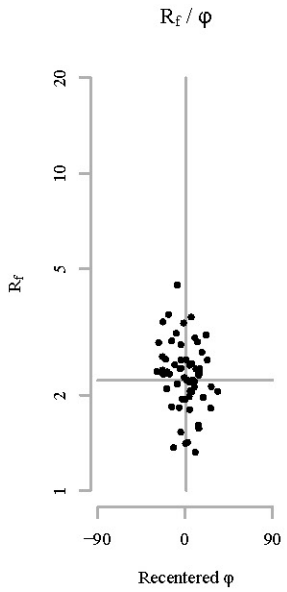

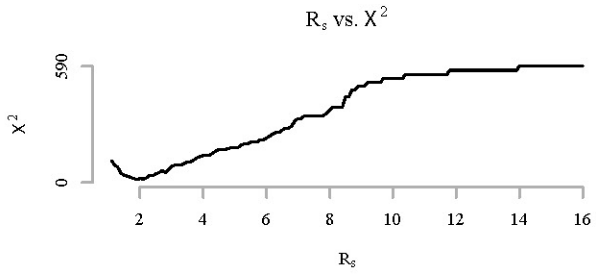

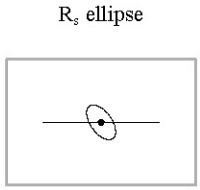

Parameters

Sample size:	59
Fabric ratio:	1.9
Vector mean:	54
Harmonic mean:	2.2
Symmetry:	0.75
Min. chi sq:	13.9
Mean area*:	5603.6

*Average clast area in pixles

Sectional R_f / φ results for plane: A

Sample: 13DC66_A
Mineral: Hornblende

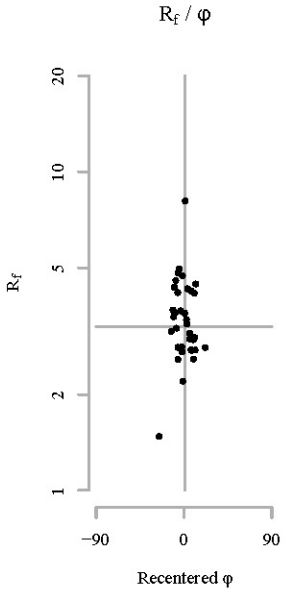

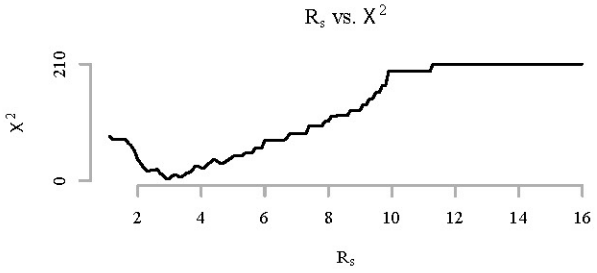

Rs ellipse

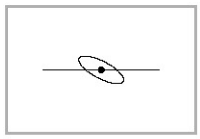

Normalized ellipse

Parameters

Sample size:	35
Fabric ratio:	2.9
Vector mean:	28
Harmonic mean:	3.3
Symmetry:	0.91
Min. chi sq:	3.2
Mean area*:	1079.5

*Average clast area in pixles

Sectional R_f / φ results for plane: B

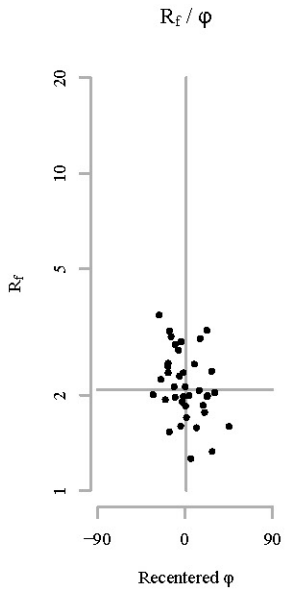

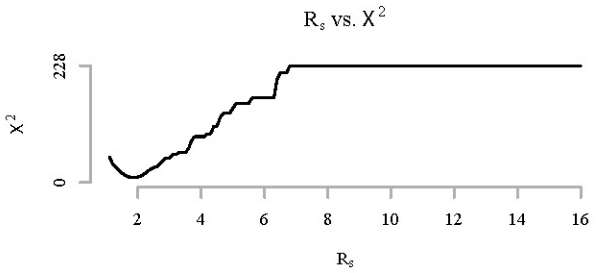

Rs ellipse

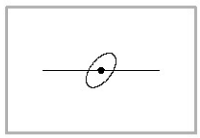

Normalized ellipse

Parameters

Sample size:	38
Fabric ratio:	1.9
Vector mean:	128
Harmonic mean:	2.1
Symmetry:	0.63
Min. chi sq:	9.16
Mean area*:	2732.3

*Average clast area in pixles

Sectional R_f / φ results for plane: C

Sample: 13DC66_A
Mineral: Hornblende

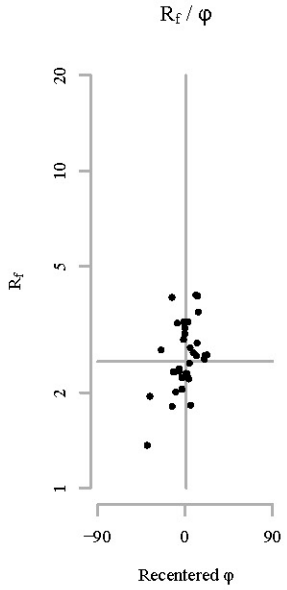

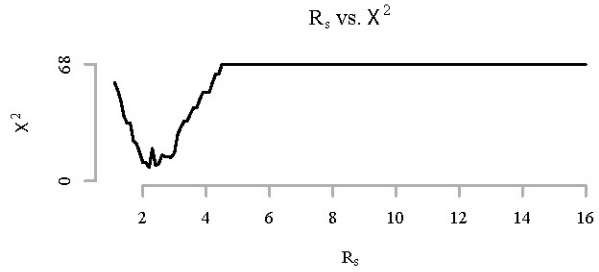

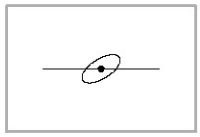

Parameters

Sample size:	34
Fabric ratio:	2.2
Vector mean:	148
Harmonic mean:	2.5
Symmetry:	0.76
Min. chi sq:	7.65
Mean area*:	1745.2

*Average clast area in pixles

Stereonet

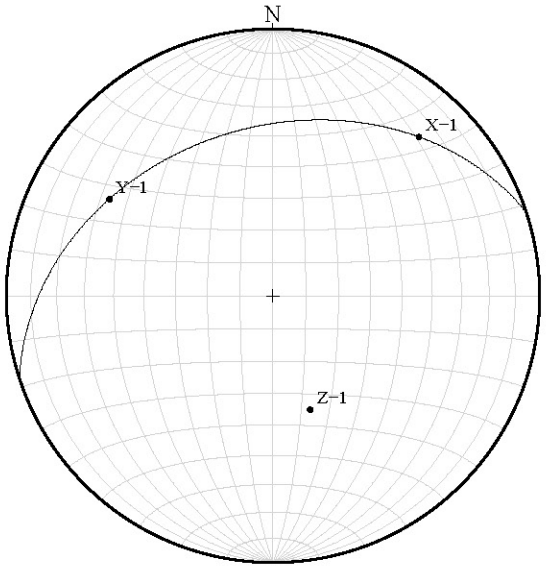

Nadai plot

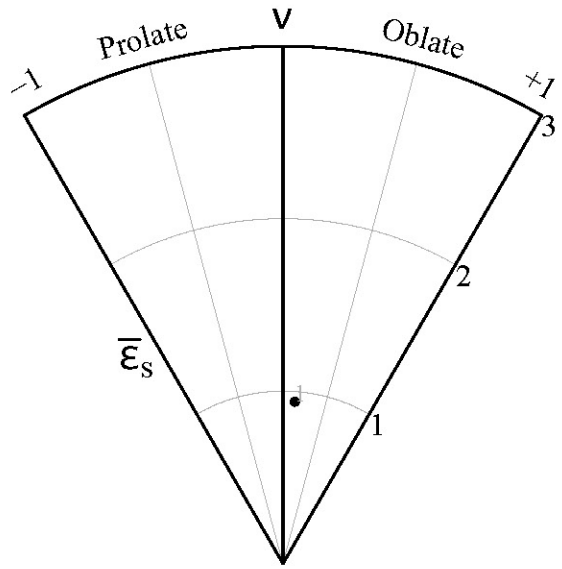

Sectional R_f / φ results for plane: A

Sample: 13DC66_A
Mineral: Plagioclase

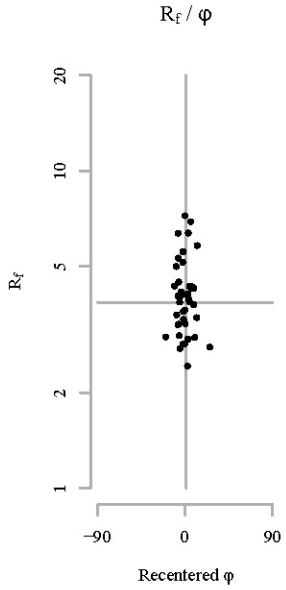

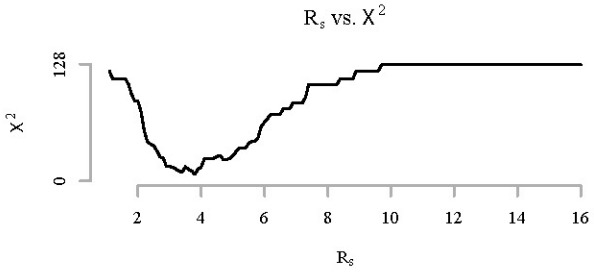

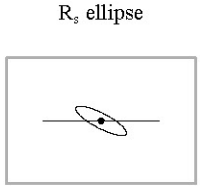

Parameters

Sample size:	42
Fabric ratio:	3.8
Vector mean:	27
Harmonic mean:	3.8
Symmetry:	0.9
Min. chi sq:	7.14
Mean area*:	2424.6

*Average clast area in pixles

Sectional R_f / φ results for plane: B

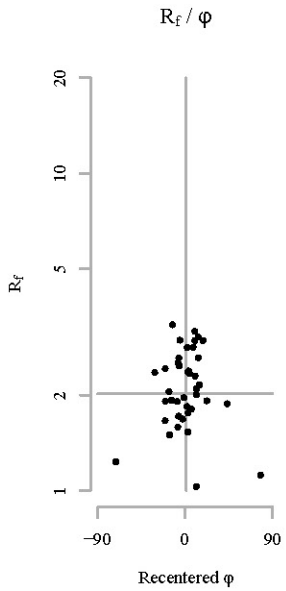

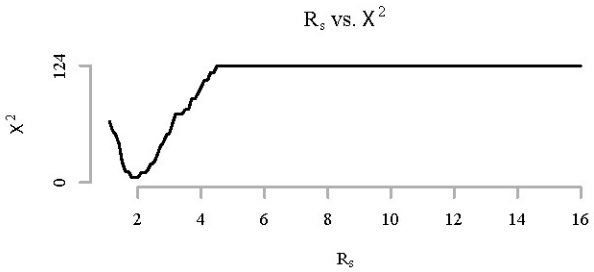

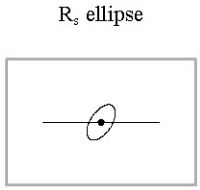

Parameters

Sample size:	41
Fabric ratio:	1.9
Vector mean:	123
Harmonic mean:	2
Symmetry:	0.88
Min. chi sq:	4.85
Mean area*:	3002.2

*Average clast area in pixles

Sectional R_f / φ results for plane: C

Sample: 13DC66_A
Mineral: Plagioclase

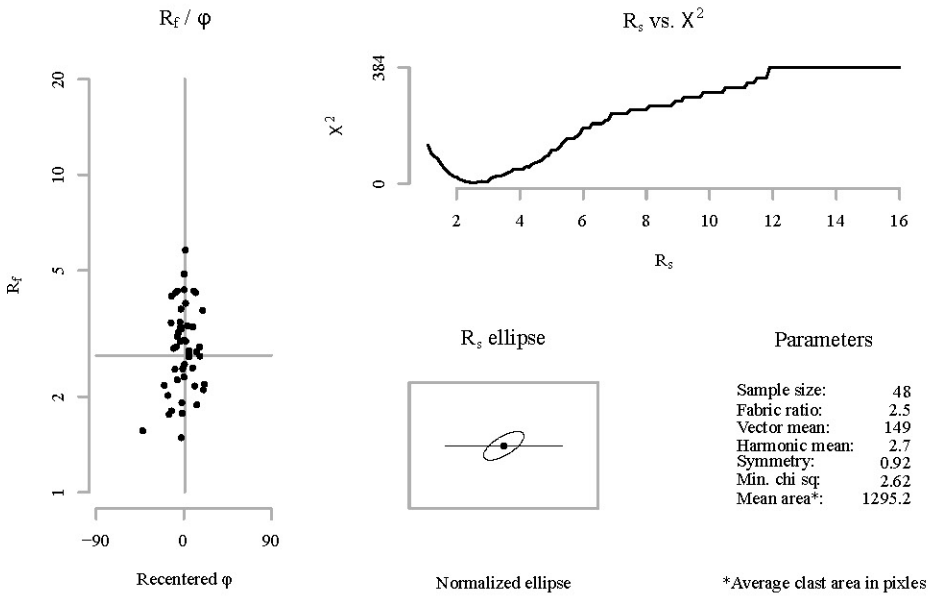

Stereonet

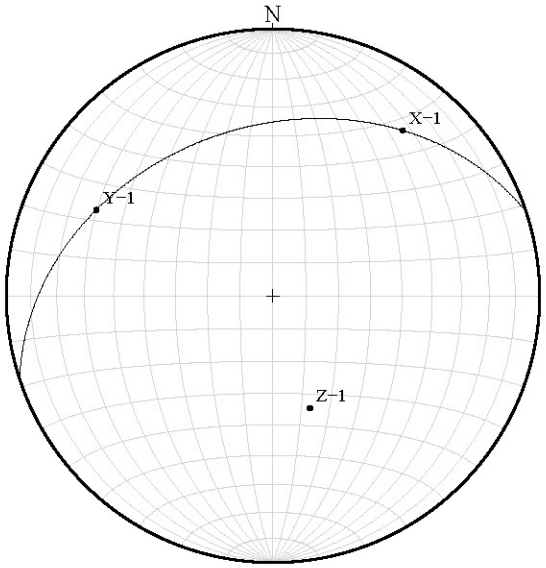

Nadai plot

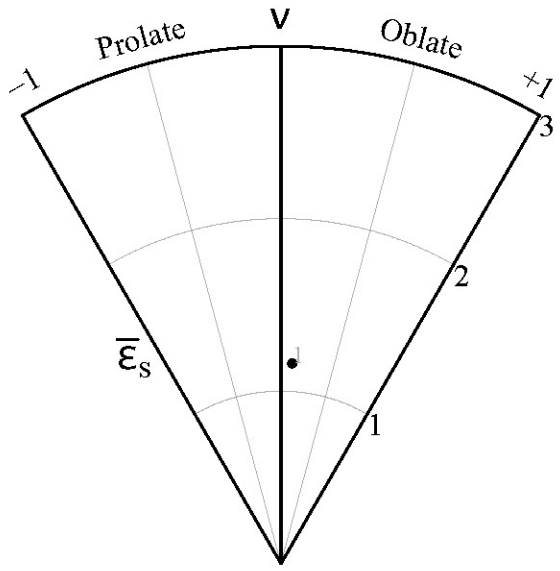

Sectional R_f / φ results for plane: A

Sample: 13DC68_A
Mineral: Hornblende

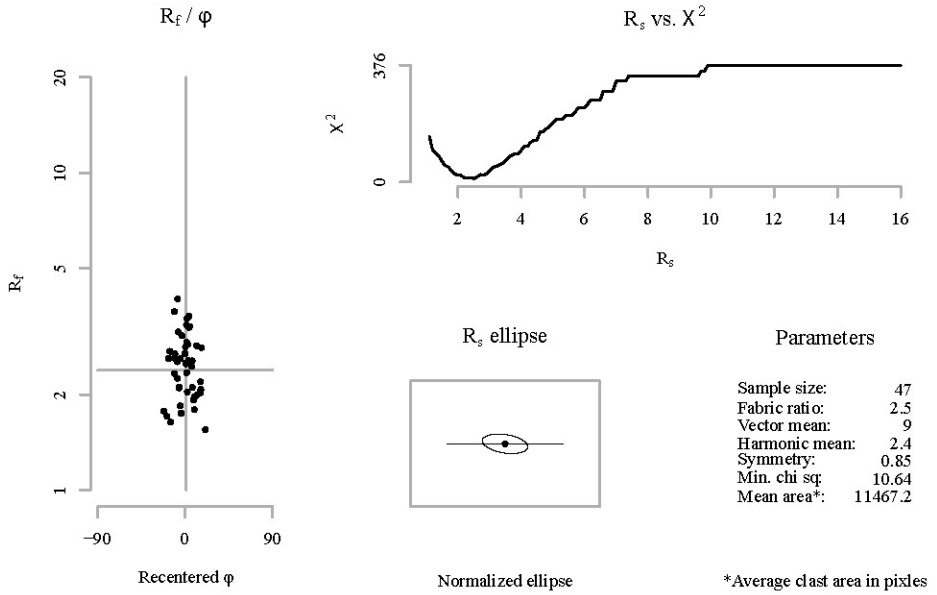

Sectional R_f / φ results for plane: B

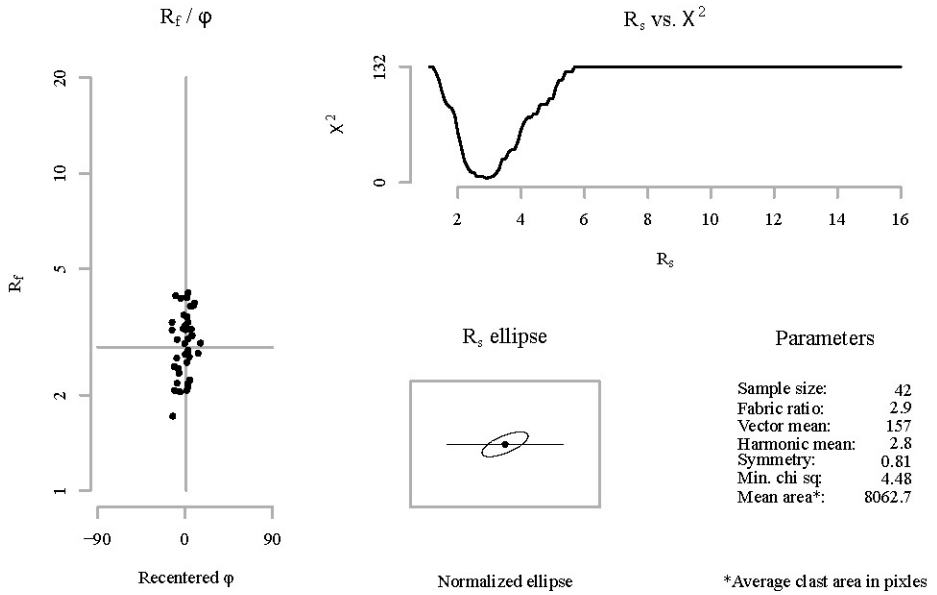

Sectional R_f / φ results for plane: C

Sample: 13DC68_A
Mineral: Hornblende

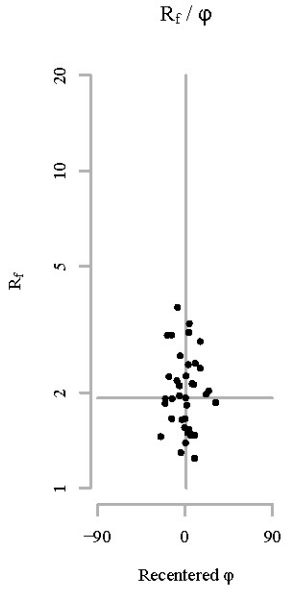

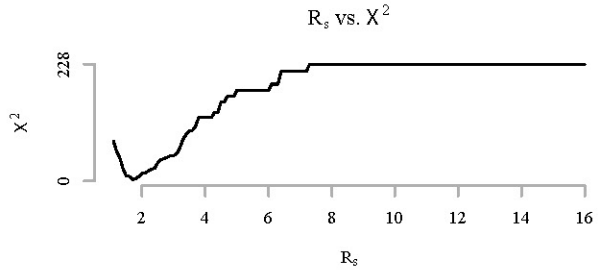

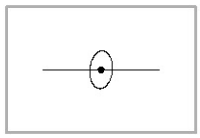

Parameters

Sample size:	38
Fabric ratio:	1.7
Vector mean:	95
Harmonic mean:	1.9
Symmetry:	0.84
Min. chi sq:	2.53
Mean area*:	9916

*Average clast area in pixles

Stereonet

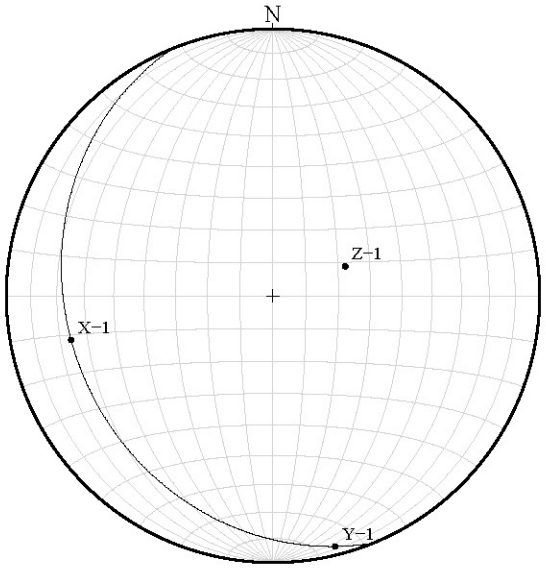

Nadai plot

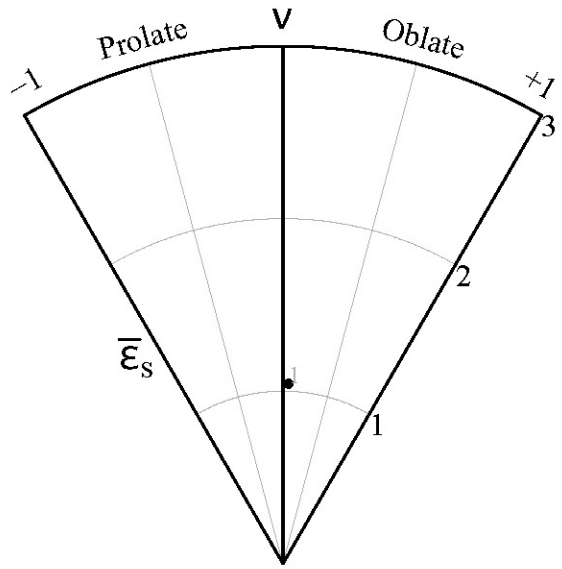

Sectional R_f / φ results for plane: A

Sample: 13DC68_A
Mineral: Plagioclase

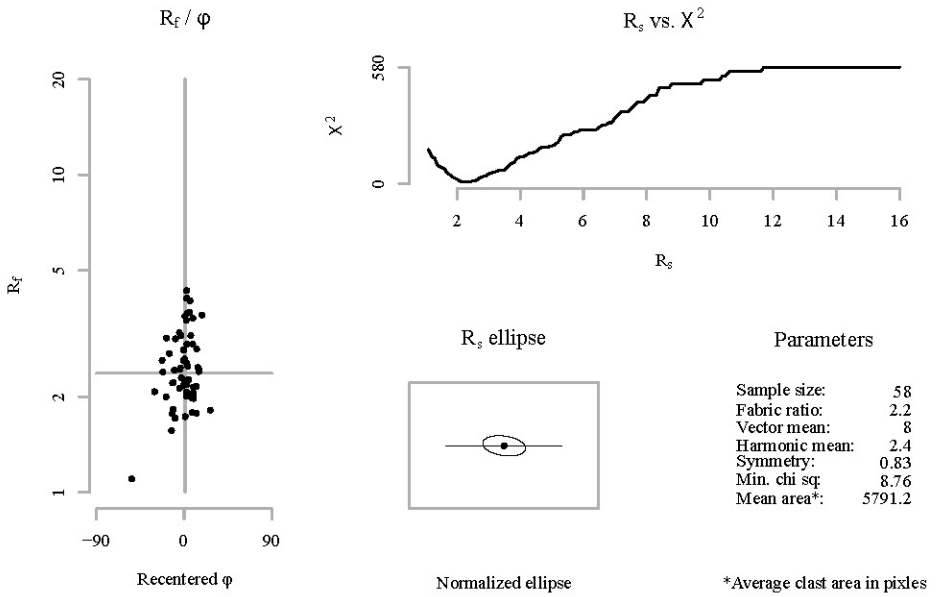

Sectional R_f / φ results for plane: B

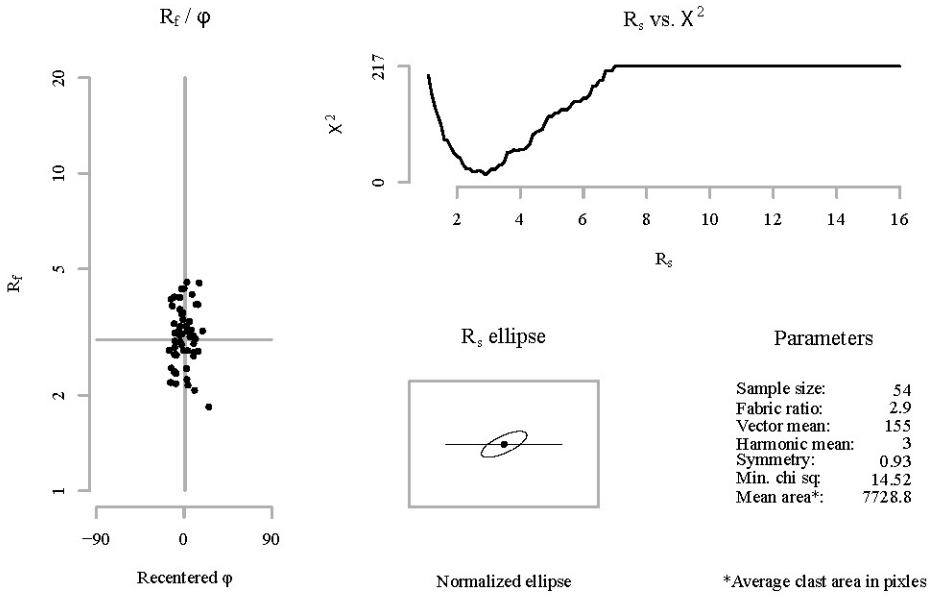

Sectional R_f / φ results for plane: C

Sample: 13DC68_A
Mineral: Plagioclase

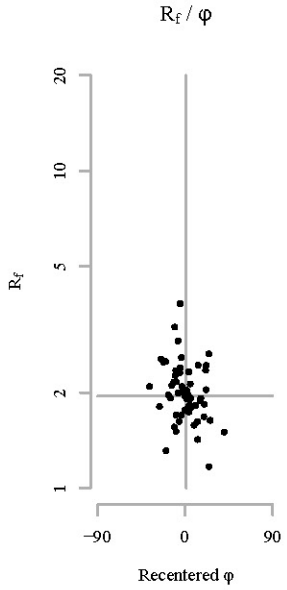

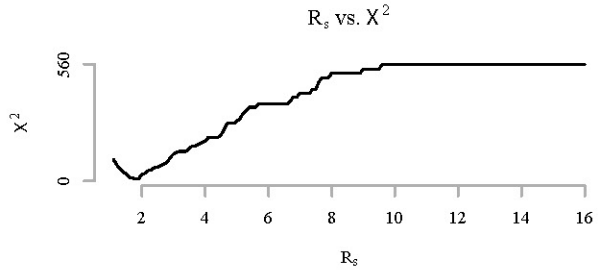

R_s ellipse

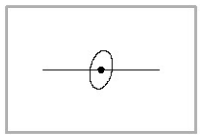

Normalized ellipse

Parameters

Sample size:	56
Fabric ratio:	1.8
Vector mean:	102
Harmonic mean:	2
Symmetry:	0.64
Min. chi sq:	10.79
Mean area*:	9510

*Average clast area in pixles

Stereonet

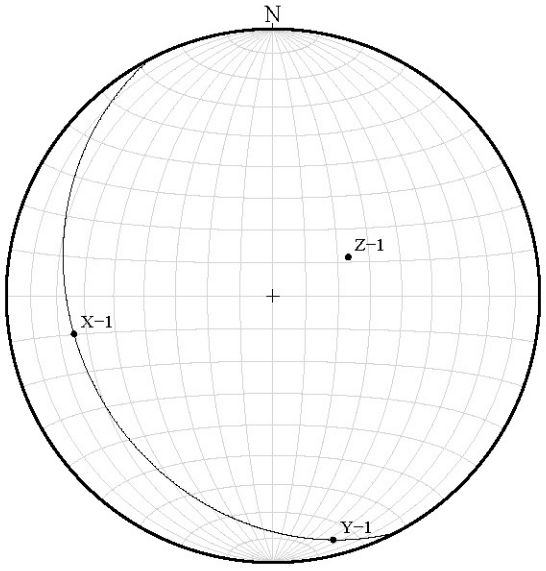

Nadai plot

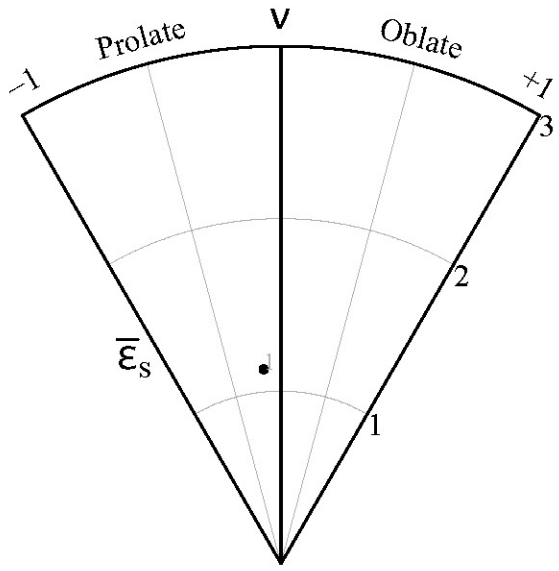

Sectional R_f / φ results for plane: A

Sample: 13DC165_A
Mineral: Plagioclase

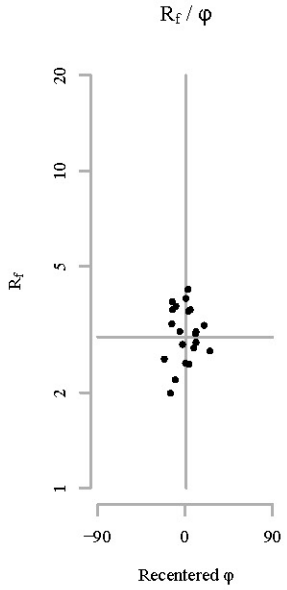

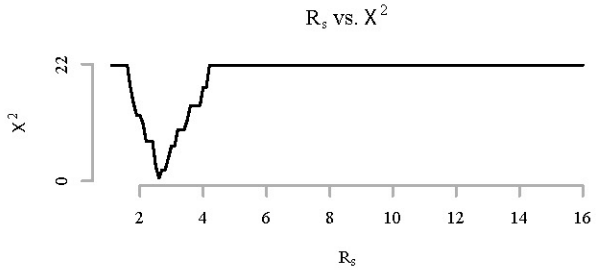

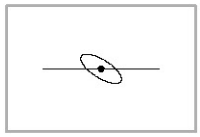

Normalized ellipse

Parameters

Sample size:	21
Fabric ratio:	2.6
Vector mean:	32
Harmonic mean:	3
Symmetry:	0.86
Min. chi sq:	0.52
Mean area*:	17246.5

*Average clast area in pixles

Sectional R_f / φ results for plane: B

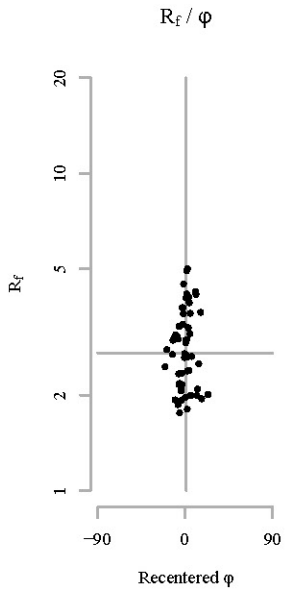

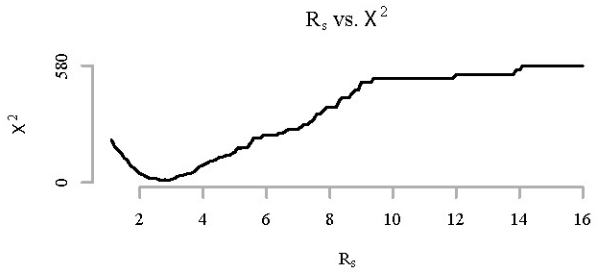

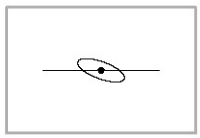

Normalized ellipse

Parameters

Sample size:	58
Fabric ratio:	2.9
Vector mean:	20
Harmonic mean:	2.7
Symmetry:	0.83
Min. chi sq:	9.52
Mean area*:	3446.1

*Average clast area in pixles

Sectional R_f / φ results for plane: C

Sample: 13DC165_A
Mineral: Plagioclase

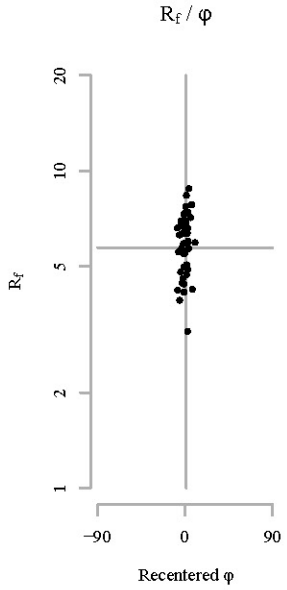

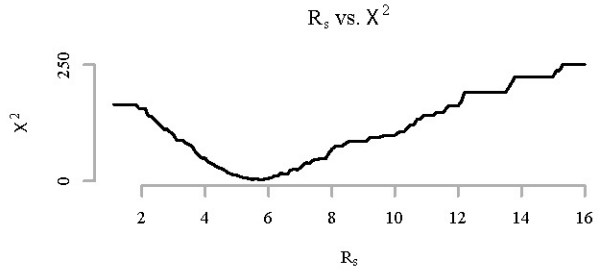

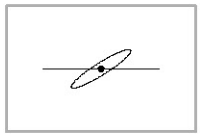

Parameters

Sample size:	47
Fabric ratio:	5.8
Vector mean:	148
Harmonic mean:	5.7
Symmetry:	0.81
Min. chi sq:	2.6
Mean area*:	4980.7

*Average clast area in pixles

Stereonet

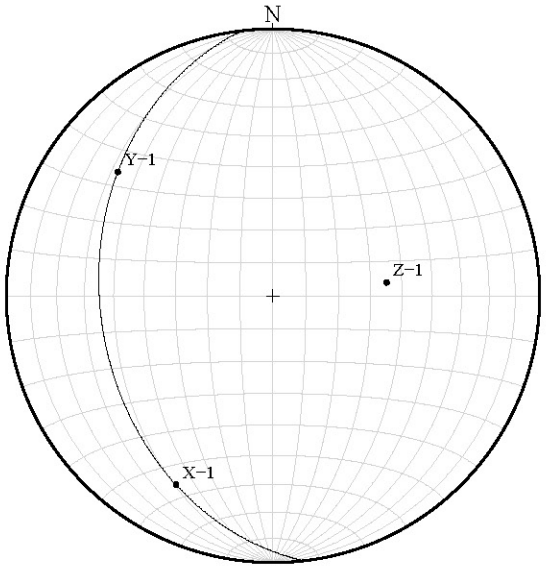

Nadai plot

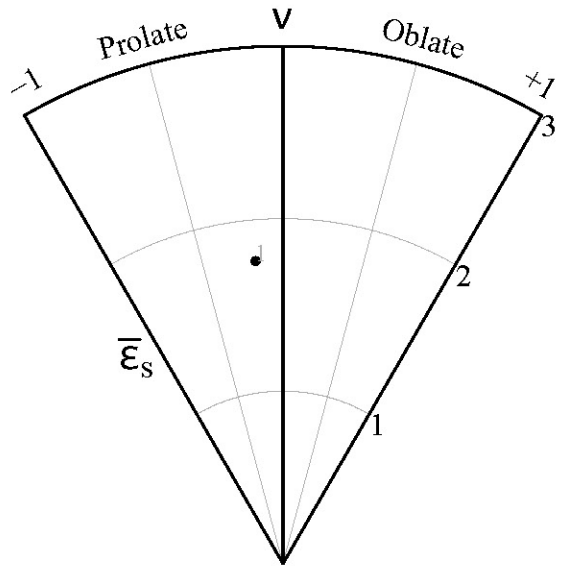

Sectional R_f / φ results for plane: A

Sample: 13VA166_BCD
Mineral: Pyroxene / Hornblende

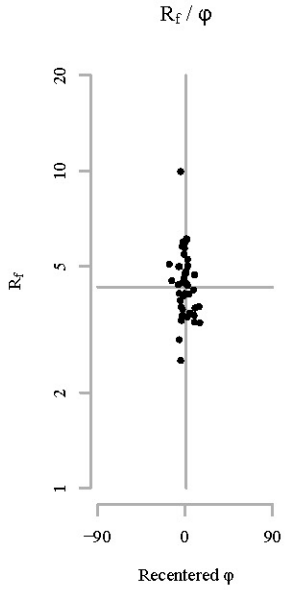

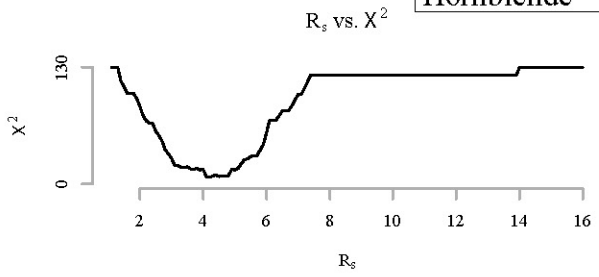

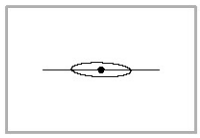

Normalized ellipse

Parameters

Sample size:	43
Fabric ratio:	4.2
Vector mean:	2
Harmonic mean:	4.3
Symmetry:	0.93
Min. chi sq:	7.42
Mean area*:	33605.6

*Average clast area in pixles

Sectional R_f / φ results for plane: B

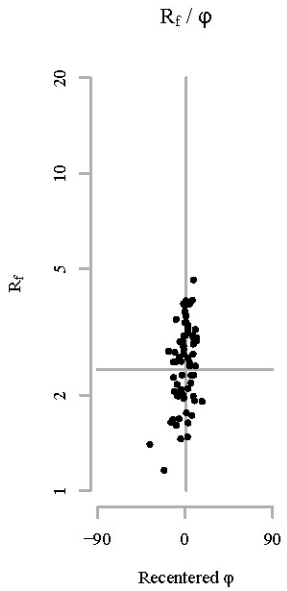

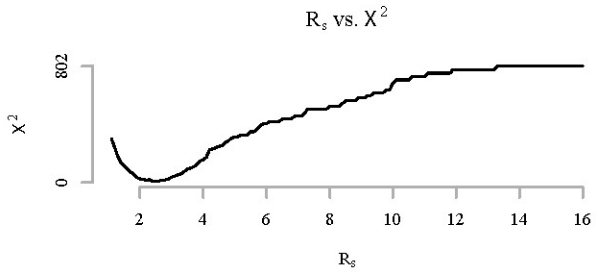

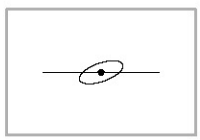

Normalized ellipse

Parameters

Sample size:	69
Fabric ratio:	2.5
Vector mean:	161
Harmonic mean:	2.4
Symmetry:	0.84
Min. chi sq:	7.3
Mean area*:	6826.6

*Average clast area in pixles

Sectional R_f / φ results for plane: C

Sample: 13VA166_BCD
Mineral: Pyroxene / Hornblende

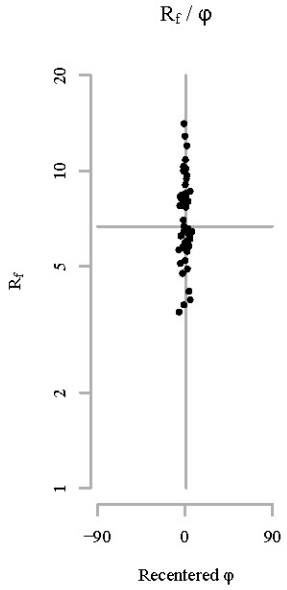

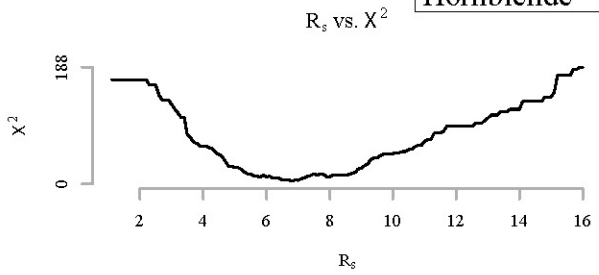

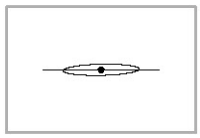

Parameters

Sample size:	48
Fabric ratio:	6.8
Vector mean:	179
Harmonic mean:	6.7
Symmetry:	0.96
Min. chi sq:	4.12
Mean area*:	11422.9

*Average clast area in pixles

Stereonet

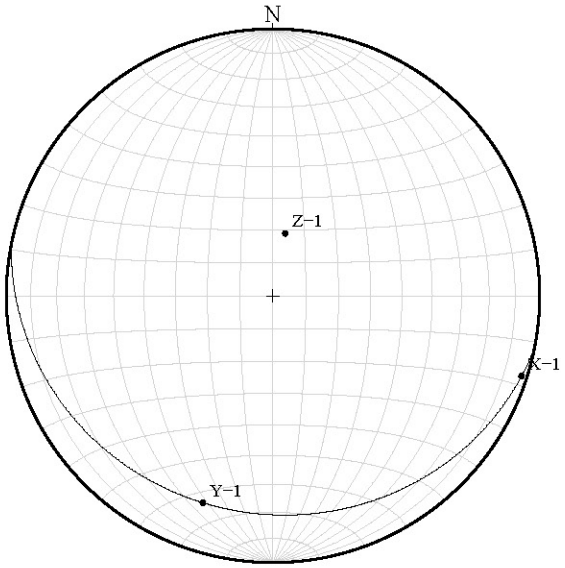

Nadai plot

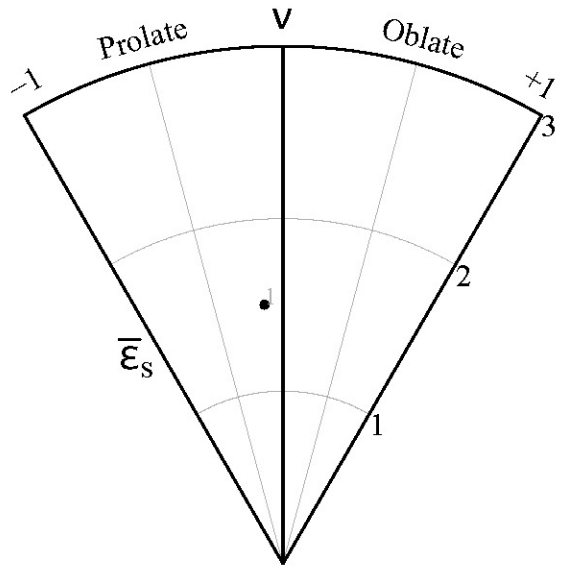

Sectional R_f / φ results for plane: A

Sample: 13DC166_BCD
Mineral: Plagioclase

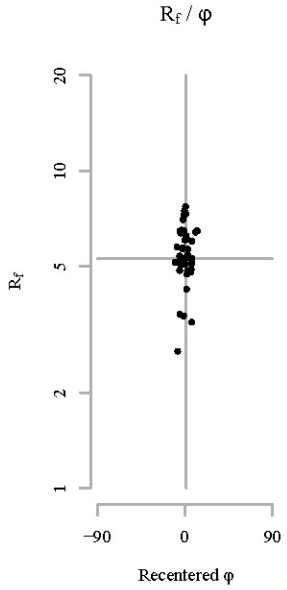

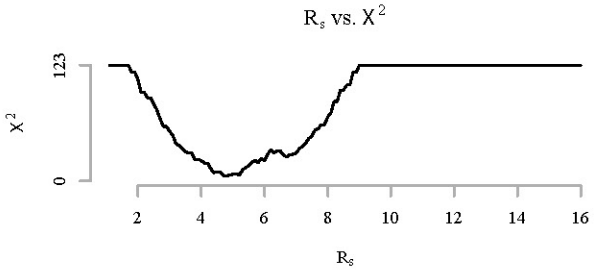

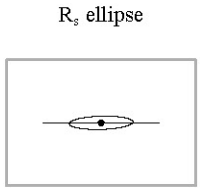

Parameters

Sample size:	41
Fabric ratio:	4.8
Vector mean:	178
Harmonic mean:	5.3
Symmetry:	0.98
Min. chi sq:	4.85
Mean area*:	43003.9

*Average clast area in pixles

Sectional R_f / φ results for plane: B

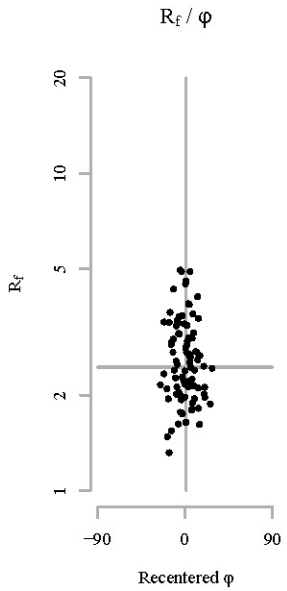

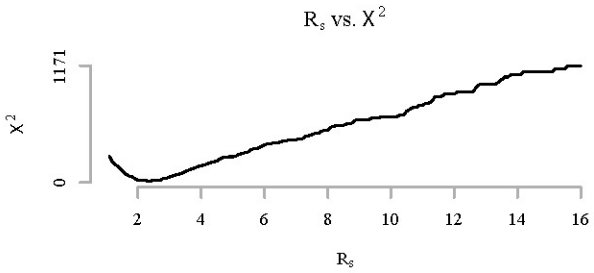

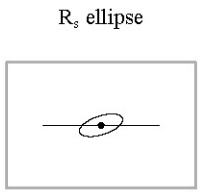

Parameters

Sample size:	89
Fabric ratio:	2.4
Vector mean:	162
Harmonic mean:	2.5
Symmetry:	0.92
Min. chi sq:	12.43
Mean area*:	4305.9

*Average clast area in pixles

Sectional R_f / φ results for plane: C

Sample: 13DC166_BCD
Mineral: Plagioclase

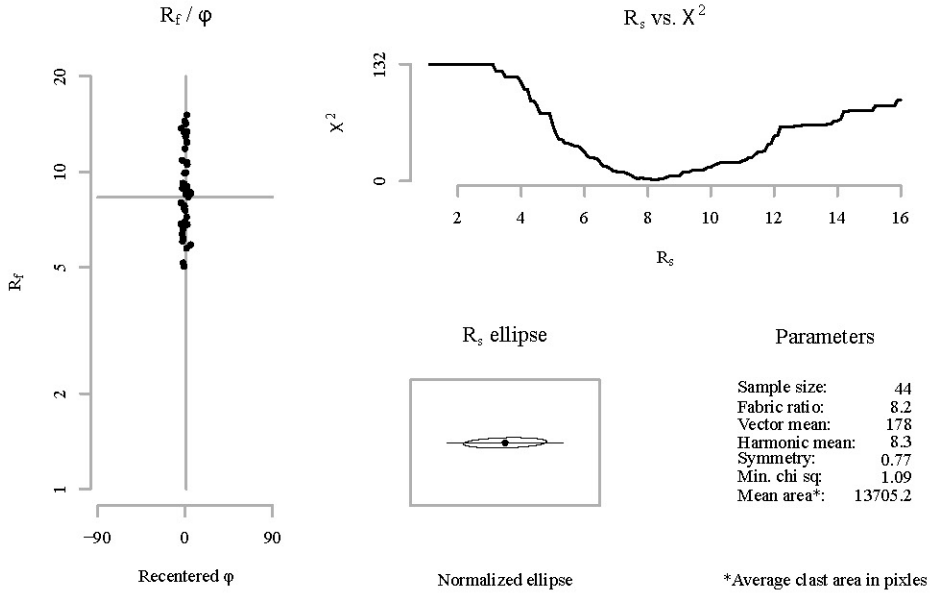

Stereonet

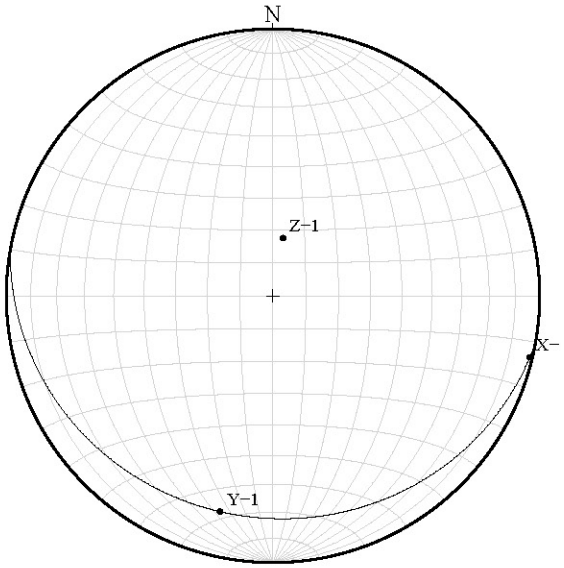

Nadai plot

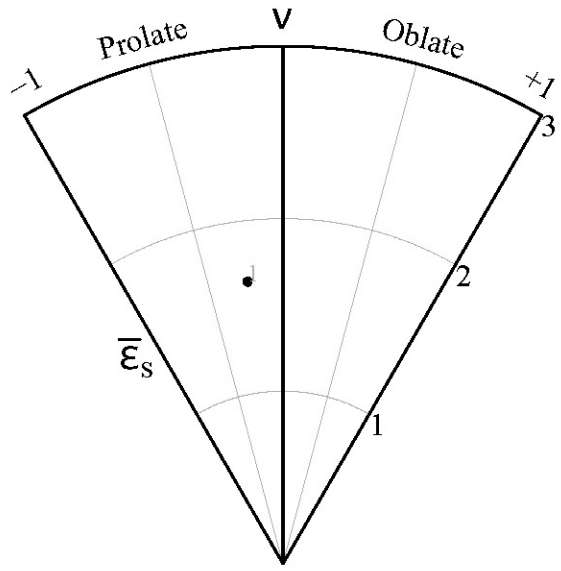

Sectional R_f / φ results for plane: A

Sample: 13DC167_A
Mineral: Plagioclase

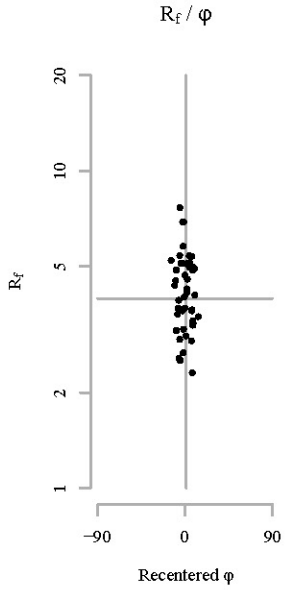

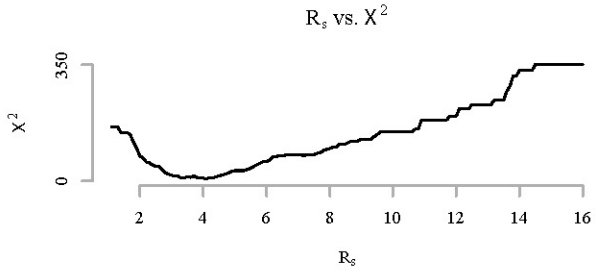

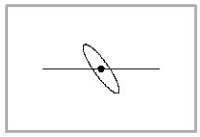

Normalized ellipse

Parameters

Sample size:	46
Fabric ratio:	4.1
Vector mean:	55
Harmonic mean:	4
Symmetry:	0.91
Min. chi sq:	6.43
Mean area*:	5988.7

*Average clast area in pixles

Sectional R_f / φ results for plane: B

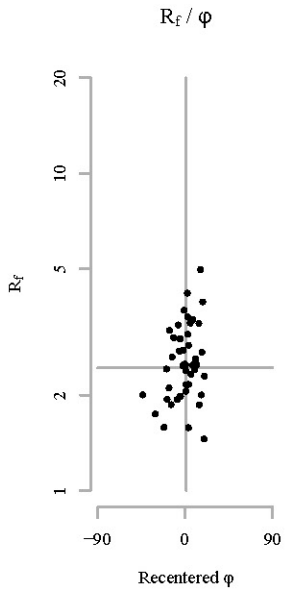

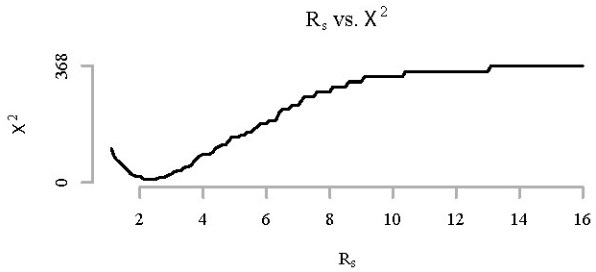

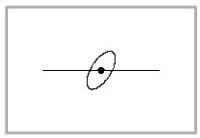

Normalized ellipse

Parameters

Sample size:	46
Fabric ratio:	2.2
Vector mean:	122
Harmonic mean:	2.4
Symmetry:	0.87
Min. chi sq:	8.39
Mean area*:	4578.5

*Average clast area in pixles

Sectional R_f / φ results for plane: C

Sample: 13DC167_A
Mineral: Plagioclase

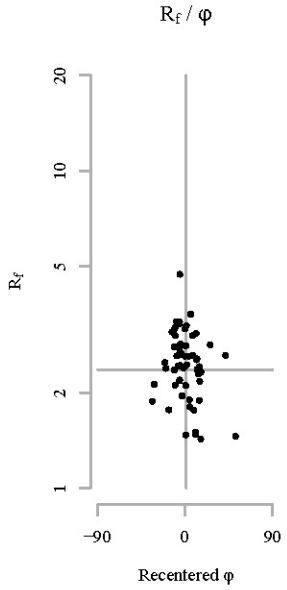

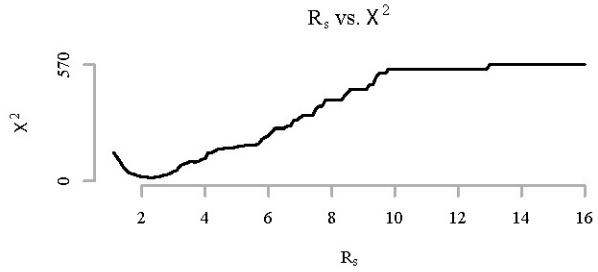

R_s ellipse

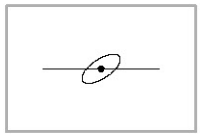

Normalized ellipse

Parameters

Sample size:	57
Fabric ratio:	2.3
Vector mean:	147
Harmonic mean:	2.4
Symmetry:	0.84
Min. chi sq:	13.82
Mean area*:	2884.1

*Average clast area in pixles

Stereonet

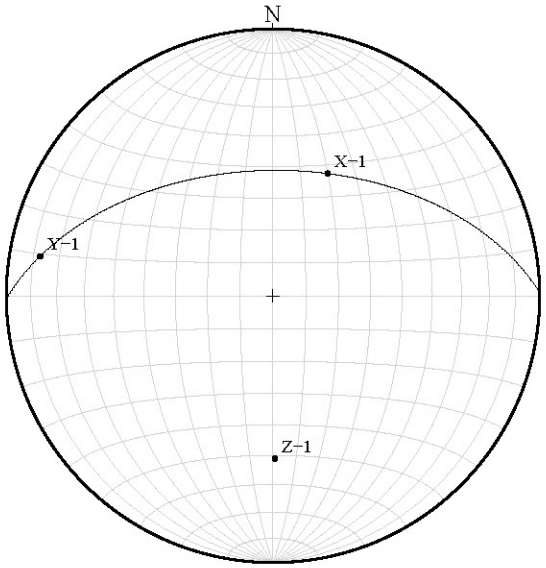

Nadai plot

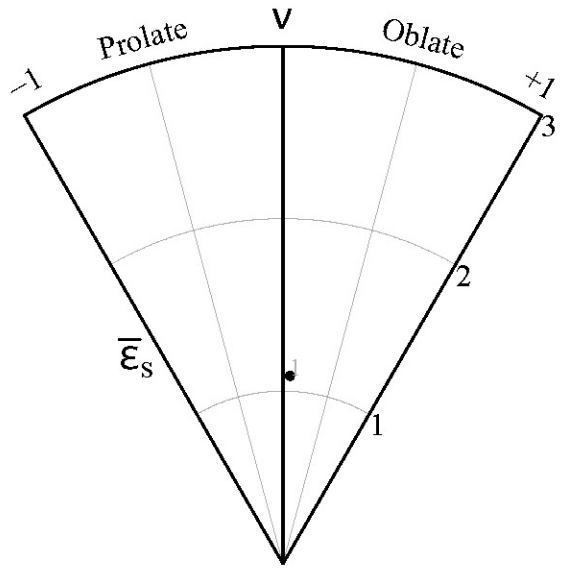

Sectional R_f / φ results for plane: C

Sample: 13DC174_B
Mineral: Plagioclase

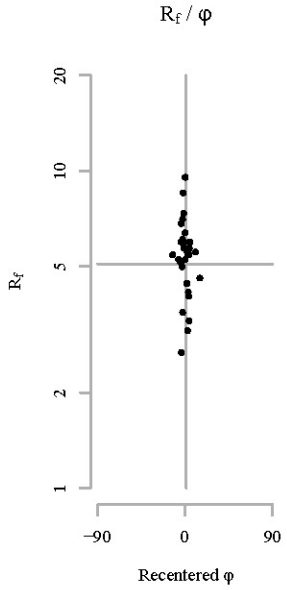

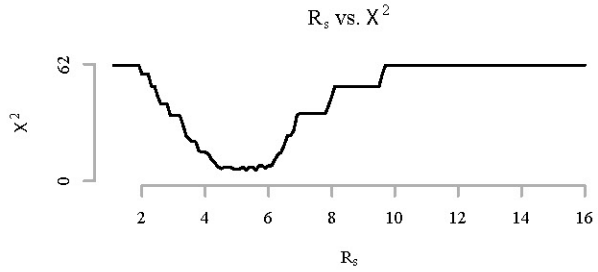

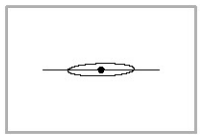

Parameters

Sample size:	30
Fabric ratio:	5.3
Vector mean:	179
Harmonic mean:	5.1
Symmetry:	0.67
Min. chi sq:	5.6
Mean area*:	8663.9

*Average clast area in pixles

Stereonet

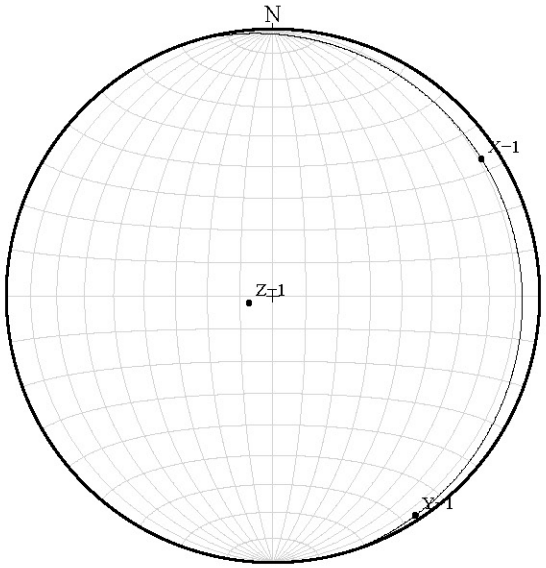

Nadai plot

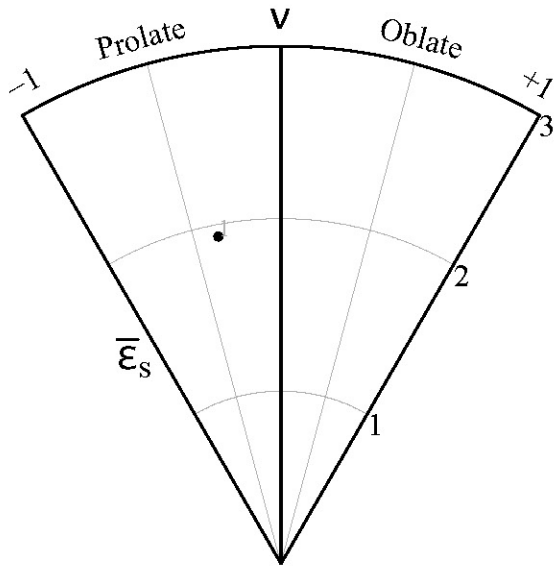

Sample	Def. Event	Min	Face	Sample Size	Fabric Ratio	Vector Mean	Harmonic Mean	Symmetry	Min. Chi Squared	Mean Area	Incompatibility Index	Es octss	v lodes	XY Att	XY Incl	X Att	X Incl	Y Att	Y Incl	Z Att	Z Incl	X Mag	Y Mag	Z Mag
12DC04.A	3	Plag	A	48	2.1	95	2.6	0.88	7.12	16014.8	5.1%	0.86	0.47	12.9	81.8	33.4	67.7	189.8	20.6	282.9	8.2	1.64	1.20	0.51
			B	30	1.4	76	1.7	0.87	2	16369														
			C	61	2.4	140	2.7	0.82	4.51	6494														
12DC04.A	3	Hbl	A																					
			B																					
			C																					
12DC05.A	3	Plag	A	48	2.2	24	2.2	0.92	4.12	3304.7	2.0%	1.13	-0.05	1.2	32.8	57.0	28.1	155.6	15.6	271.2	57.2	2.26	0.97	0.46
			B	44	3.5	150	2.5	0.95	4	6052														
			C	34	3.2	38	3.4	0.82	3.76	9660														
12DC05.A	3	Hbl	A																					
			B																					
			C																					
12DC07.A	3	Plag	A	50	3.3	166	3.6	0.64	5.6	6014.4	4.3%	1.04	0.56	266.1	21.9	59.1	10.3	325.5	19.1	176.1	68.1	1.77	1.30	0.43
			B	59	3.2	17	3.3	0.88	6.44	3115.4														
			C	34	1.8	135	2.1	0.71	4.82	20405.2														
12DC07.A	3	Hbl	A																					
			B																					
			C																					
12DC10.A	1	Plag	A	73	2.3	151	2.4	0.68	16.56	8888.1	0.9%	1.09	0.07	162.4	31.0	326.4	9.4	231.1	29.2	72.4	59.0	2.13	1.04	0.45
			B	68	4.4	12	4.6	0.88	23.38	12847.7														
			C	31	2.2	163	2.7	0.84	3.26	32884.7														
12DC10.A	1	Hbl	A	80	2.5	157	2.7	0.85	18	7013.6	0.1%	1.08	0.22	167.0	24.7	322.4	10.8	228.0	21.9	77.0	65.3	2.02	1.12	0.44
			B	69	4.5	11	5.1	0.9	13.71	5426.1														
			C	44	1.9	159	2.1	0.68	12.36	26643.3														
12DC12.A	1	Plag	A	46	2.3	23	2.7	0.87	4.09	26042.7	0.1%	0.82	0.25	30.2	27.6	39.4	4.8	131.9	27.1	300.2	62.4	1.70	1.10	0.53
			B	33	2.5	159	2.6	0.85	7.55	22584.3														
			C	43	1.3	172	1.6	0.84	7.05	34966.8														
12DC12.A	1	Hbl	A	40	2	14	2.1	0.85	5.2	12844.2	2.5%	0.73	0.30	15.4	21.9	47.7	12.1	141.6	18.0	285.4	68.1	1.58	1.11	0.57
			B	33	2.4	161	2.6	0.91	0.64	8204.5														
			C	38	1.2	18	1.6	0.84	1.42	25675.4														

Sample	Def. Event	Min	Face	Sample Size	Fabric Ratio	Vector Mean	Harmonic Mean	Symmetry	Min. Chi Squared	Mean Area	Incompatibility Index	Es octss	v lodes	XY Att	XY Incl	X Att	X Incl	Y Att	Y Incl	Z Att	Z Incl	X Mag	Y Mag	Z Mag
12DC13.A	1	Plag	A	54	1.9	71	2	0.81	10.07	6612	8.6%	0.61	0.16	349.2	57.8	28.1	44.8	149.8	27.8	259.2	32.2	1.50	1.05	0.64
			B	80	1.7	42	2.1	0.95	12.8	3856.1														
			C	82	2	132	2	0.88	17.12	4088.7														
12DC13.A	1	Hbl	A	52	1.8	87	1.9	0.81	7.62	6545.4	10.0%	0.66	0.31	346.4	58.1	79.6	58.0	347.3	1.4	256.4	31.9	1.51	1.10	0.60
			B	40	2.1	40	2.1	1	1.6	3137.4														
			C	37	1.9	129	2.1	0.86	3.3	3852														
12DC16.A	1	Plag	A	58	3.6	166	3.8	0.9	3.45	13675.7	0.1%	0.93	0.26	31.0	16.0	97.0	14.7	188.6	6.2	301.0	74.0	1.81	1.12	0.49
			B	78	2.3	9	2.5	0.82	10.46	10738.3														
			C	57	1.6	68	1.9	0.88	8.81	34490.6														
12DC16.A	1	Hbl	A	73	3.3	166	3.4	0.9	7.74	7333.1	1.0%	0.91	0.51	32.6	16.4	97.7	15.0	189.5	6.6	302.6	73.6	1.67	1.23	0.48
			B	90	2.6	10	2.5	0.89	8.4	6282.5														
			C	48	1.4	68	1.7	0.83	3	22811.9														
12DC22.A	3	Plag	A	51	1.9	163	2.2	0.9	6.45	16490.2	2.9%	0.91	0.13	54.3	67.3	228.4	13.9	109.5	63.0	324.3	22.7	1.85	1.06	0.51
			B	51	2.1	112	2.6	0.94	12.73	4813.2														
			C	45	3.2	44	3.5	0.76	4.4	10976.9														
12DC22.A	3	Hbl	A	30	1.3	167	1.6	0.93	2	29150.2	0.0%	0.57	0.32	56.1	68.6	231.8	11.0	116.3	65.7	326.1	21.4	1.43	1.09	0.64
			B	41	1.7	111	2	0.63	5.63	4625.1														
			C	43	2.2	46	2.4	0.7	7.79	5873.8														
12DC23.A	3	Plag	A	90	5	178	5.7	0.82	22.8	5550.2	1.2%	1.31	-0.06	42.3	17.2	215.5	2.1	124.8	17.0	312.3	72.8	2.57	0.97	0.40
			B	51	2.9	7	2.8	0.86	6.06	13582.2														
			C	90	2.4	17	2.7	0.89	16.8	2873.4														
12DC23.A	3	Hbl	A																					
			B																					
			C																					
12DC24.A	3	Plag	A	74	2.5	165	2.7	0.95	6.97	4023.9	1.2%	0.99	0.15	217.6	47.0	283.3	44.4	25.8	12.4	127.6	43.0	1.94	1.07	0.48
			B	67	3	47	2.9	0.96	8.09	9469.6														
			C	21	2	84	2.5	0.86	1.29	35007.1														
12DC24.A	3	Hbl	A																					
			B																					
			C																					

Sample	Def. Event	Min	Face	Sample Size	Fabric Ratio	Vector Mean	Harmonic Mean	Symmetry	Min. Chi Squared	Mean Area	Incompatibility Index	Es octss	v lodes	XY Att	XY Incl	X Att	X Incl	Y Att	Y Incl	Z Att	Z Incl	X Mag	Y Mag	Z Mag
12DC25.A	2-3	Plag	A	56	2	172	2.3	0.93	10.79	11380.8	2.9%	0.96	-0.32	318.6	43.0	129.5	8.4	31.9	41.8	228.6	47.0	2.10	0.87	0.55
			B	56	4.1	1	4.2	0.86	2.54	13139.3														
			C	94	1.5	43	1.8	0.89	7.49	5821.9														
12DC25.A	2-3	Hbl	A	42	2.5	172	2.6	0.9	12.86	10017.6	1.4%	1.21	-0.10	316.9	46.9	127.6	9.8	27.5	45.3	226.9	43.1	2.42	0.95	0.44
			B	45	4.4	1	4.4	0.93	2.4	7425.1														
			C	75	2.1	48	2.1	0.88	10.4	3953.6														
12DC26.A	2-3	Plag	A	98	1.9	144	2	0.92	22.98	4593.6	0.8%	1.17	-0.27	280.6	59.1	68.3	41.7	303.3	32.8	190.6	30.9	2.43	0.86	0.48
			B	84	3.9	85	4	0.88	4	7629.2														
			C	52	4.2	133	4.5	0.85	3.77	17475.4														
12DC26.A	2-3	Hbl	A	51	1.5	135	1.8	0.67	10.76	6458.1	0.9%	1.14	-0.51	271.6	65.2	63.7	45.4	290.0	34.3	181.6	24.8	2.47	0.77	0.53
			B	47	4.7	84	4.9	0.89	6.04	8359.1														
			C	37	3.5	132	4.1	0.76	11.24	37742.9														
12DC26.B	2-3	Plag	A	51	2.7	143	3	0.75	9.59	15051.4	4.5%	0.91	-0.11	240.5	73.9	48.7	35.4	260.7	50.1	150.5	16.1	1.95	0.95	0.54
			B	106	1.8	113	1.9	0.89	22.38	2902.3														
			C	64	3	76	3.3	0.88	6.5	4431														
12DC26.B	2-3	Hbl	A	34	3.7	144	4.2	0.94	1.29	27968.4	3.2%	1.14	-0.34	241.2	76.2	51.3	34.9	259.3	51.7	151.2	13.8	2.40	0.84	0.50
			B	30	1.7	112	1.7	0.8	1.2	13208.1														
			C	28	3.8	78	4.6	0.93	2.71	18125.3														
12DC29.A	2-3	Plag	A	59	3.9	174	4.1	0.88	7.19	8195	1.8%	1.11	-0.10	241.9	19.7	252.3	3.7	343.5	19.3	151.9	70.3	2.24	0.95	0.47
			B	83	2.1	16	2.2	0.96	8.57	7766.7														
			C	56	2.9	10	3.1	0.93	8.82	20111.3														
12DC29.A	2-3	Hbl	A	60	5.1	173	5.6	0.97	6	57208.4	0.8%	1.24	-0.36	236.6	18.6	251.4	4.9	343.0	17.9	146.6	71.4	2.61	0.82	0.47
			B	66	1.8	14	2	0.94	11.21	60748.2														
			C	57	2.9	9	3	0.84	7.26	79515.2														
12DC30.A	2	Plag	A	56	5.3	56	5.7	0.64	8.82	11483.7	1.4%	1.76	-0.69	205.5	31.5	328.2	27.3	230.5	14.5	115.5	58.5	4.16	0.59	0.41
			B	45	6.2	151	7.6	0.8	17.2	5750.9														
			C	83	1.4	161	1.6	0.87	14.73	3228														
12DC30.A	2	Hbl	A	61	3.7	56	4.3	0.66	13.95	6208.2	0.7%	1.39	-0.61	209.0	30.3	329.4	26.7	232.6	13.1	119.0	59.7	3.06	0.68	0.48
			B	45	5.2	152	5.7	0.93	4	4817.5														
			C	77	1.4	163	1.6	0.86	10.86	2568.5														

Sample	Def. Event	Min	Face	Sample Size	Fabric Ratio	Vector Mean	Harmonic Mean	Symmetry	Min. Chi Squared	Mean Area	Incompatibility Index	Es octss	v lodes	XY Att	XY Incl	X Att	X Incl	Y Att	Y Incl	Z Att	Z Incl	X Mag	Y Mag	Z Mag
12DC30.B	2	Plag	A	63	2.6	7	2.7	0.92	5.76	48106.3	4.1%	1.20	0.18	68.2	14.4	149.2	14.3	239.7	2.2	338.2	75.6	2.21	1.11	0.41
			B	47	6.7	167	6.9	0.85	4.89	74352.4														
			C	38	1.7	117	2.1	0.89	2.53	122708.2														
12DC30.B	2	Hbl	A	116	2.4	5	2.5	0.97	12.09	12542.2	0.4%	0.98	0.22	62.7	12.8	154.1	12.8	64.0	0.3	332.7	77.2	1.89	1.11	0.48
			B	81	2.5	168	3.9	0.96	6.9	12556.7														
			C	62	1.5	109	1.9	0.97	8.06	24464.6														
12DC35.A	1	Plag	A	80	1.9	116	2.1	0.82	17.6	15594	3.6%	0.93	-0.21	321.8	61.1	135.2	11.8	25.4	58.4	231.8	28.9	2.02	0.91	0.54
			B	73	2.4	64	2.5	0.93	13.49	15790.4														
			C	31	2.6	165	2.6	0.84	2.87	51933.9														
12DC35.A	1	Hbl	A	101	1.7	114	1.9	0.93	22.37	5932.5	2.1%	1.03	-0.34	320.7	63.7	130.7	19.3	8.9	56.4	230.7	26.3	2.21	0.85	0.53
			B	86	2.9	65	2.9	0.88	12.44	6483.8														
			C	52	3	158	2.8	0.92	5.69	17707.2														
12DC38.A	2	Plag	A	43	2.4	101	2.5	0.84	5.56	19641.5	3.8%	2.33	-0.42	350.6	16.3	110.4	14.2	18.4	7.8	260.6	73.7	6.18	0.64	0.25
			B	41	8	16	7.9	0.88	1.73	15718.2														
			C	40	2.5	1	2.6	1	5.6	11038														
12DC38.A	2	Cpx	A	78	2.5	103	2.7	0.67	11.23	8524.3	2.9%	2.05	-0.28	351.9	15.3	112.9	13.2	21.1	7.6	261.9	74.7	4.79	0.76	0.27
			B	94	6.8	15	6.8	0.89	9.79	5015.5														
			C	94	2.8	0	2.9	0.83	15.15	2872.7														
12DC38.C	2	Plag	A	41	3	151	3.1	0.73	4.85	3648.5	0.8%	1.55	0.00	292.9	34.6	82.1	19.5	341.5	27.4	202.9	55.4	2.99	1.00	0.33
			B	42	7.3	23	7.9	0.95	6	7531.9														
			C	38	3.6	143	3.7	0.68	4.74	3102.8														
12DC38.C	2	Cpx	A	51	2.8	157	3	0.86	9.59	2994.4	0.5%	1.52	-0.04	299.4	30.0	78.9	20.5	340.7	20.9	209.4	60.0	2.96	0.97	0.35
			B	44	7.5	22	8	1	2.18	5732.8														
			C	51	3.3	142	3.3	0.94	4.88	3263														
12DC39.A	3	Plag	A	83	3.4	30	3.5	0.84	21.29	4914.1	0.1%	0.90	0.00	57.1	45.4	196.6	33.3	87.1	26.9	327.1	44.6	1.89	1.00	0.53
			B	94	1.9	144	2	0.94	17.83	3145.2														
			C	53	2	120	2	0.94	9.83	5190.6														
12DC39.A	3	Hbl	A	75	2.8	27	3.2	0.91	15.6	3279.6	1.9%	0.78	0.05	56.2	41.7	207.6	23.1	101.8	32.5	326.2	48.3	1.71	1.02	0.57
			B	67	1.8	147	2.1	0.69	20.12	2229.2														
			C	57	1.9	128	2.1	0.84	14.6	4307.9														

Sample	Def. Event	Min	Face	Sample Size	Fabric Ratio	Vector Mean	Harmonic Mean	Symmetry	Min. Chi Squared	Mean Area	Incompatibility Index	Es octss	v lodes	XY Att	XY Incl	X Att	X Incl	Y Att	Y Incl	Z Att	Z Incl	X Mag	Y Mag	Z Mag
12DC41.B	2	Plag	A	55	5.2	180	5.9	0.69	14	17428.5	0.5%	1.47	-0.78	28.2	17.3	39.2	3.4	130.2	16.9	298.2	72.7	3.31	0.61	0.50
			B	59	6	177	5.9	0.81	9.42	12128														
			C	63	1.2	172	1.5	0.79	11.86	3531.2														
12DC41.B	2	Hbl	A	56	5.9	176	5.8	0.93	4.5	9605.8	1.4%	1.46	-0.64	28.4	13.2	37.9	2.2	128.4	13.0	298.4	76.8	3.24	0.66	0.47
			B	67	5.5	177	6	0.96	6.93	6756.2														
			C	58	1.4	172	1.7	0.86	9.9	3309.8														
12DC42.A	2	Plag	A	48	5.7	13	5.8	0.79	12.38	8012.7	10.4%	1.69	-0.26	88.7	17.3	183.8	17.3	93.4	1.5	358.7	72.7	3.62	0.81	0.34
			B	53	2.3	168	2.5	0.75	12.85	6423.7														
			C	29	2.2	152	2.1	0.83	1.17	20001														
12DC42.A	2	Hbl	A	52	5.2	13	5.7	0.92	8	4605.5	6.1%	1.34	0.04	100.3	15.3	186.2	15.3	276.5	1.0	10.3	74.7	2.56	1.02	0.38
			B	69	2.6	172	2.6	0.96	10.7	2508.1														
			C	32	1.9	153	2.1	1	4.31	10981.8														
12DC44.B	2	Plag	A	41	4.6	26	4.8	0.93	7.2	12882.7	3.9%	1.79	-0.37	304.7	24.8	70.4	20.5	335.4	13.2	214.7	65.2	4.03	0.74	0.34
			B	35	2.5	136	2.7	0.91	1.2	54722.6														
			C	95	2.3	175	2.3	0.8	16.4	8392.2														
12DC44.B	2	Hbl	A	54	5.9	26	6.4	0.78	7.11	9785.9	1.9%	1.47	-0.18	296.7	27.1	58.0	23.6	322.4	12.5	206.7	62.9	2.99	0.88	0.38
			B	62	1.8	132	1.8	0.84	18.13	13235.1														
			C	79	23	170	2.6	0.86	14.61	13434.5														
12DC46.A	2-3	Plag	A	33	6.3	39	6.3	0.91	1.73	19239.3	0.8%	1.52	-0.21	53.2	47.6	211.8	21.8	102.5	39.7	323.2	42.4	3.13	0.86	0.37
			B	32	2.3	134	2.3	0.67	7.52	13218.6														
			C	38	4.6	158	4.8	0.95	4.74	27333.4														
12DC46.A	2-3	Hbl	A																					
			B																					
			C																					
12DC50.A	3	Plag	A	80	2.5	174	2.7	0.9	12	8550	3.1%	0.82	0.09	44.5	10.1	58.5	2.5	148.9	9.8	314.5	79.9	1.76	1.04	0.55
			B	68	2.1	8	2.3	0.82	4.26	11467.9														
			C	51	1.5	76	1.7	0.71	8.8	23973.6														
12DC50.A	3	Hbl	A	52	2.8	175	2.7	0.92	5.69	6232.8	4.7%	0.95	-0.08	52.3	11.5	66.6	2.9	157.2	11.1	322.3	78.5	1.99	0.97	0.52
			B	51	2	10	2.1	0.75	6.06	7145.7														
			C	38	1.9	85	2.1	0.89	1.79	26163.3														

Sample	Def. Event	Min	Face	Sample Size	Fabric Ratio	Vector Mean	Harmonic Mean	Symmetry	Min. Chi Squared	Mean Area	Incompatibility Index	Es octss	v lodes	XY Att	XY Incl	X Att	X Incl	Y Att	Y Incl	Z Att	Z Incl	X Mag	Y Mag	Z Mag
12DC53.A	2-3	Plag	A	91	3	152	3.1	0.92	13.24	4321.8	1.6%	0.83	0.18	129.6	31.5	186.3	27.2	284.1	14.8	39.6	58.5	1.73	1.07	0.54
			B	84	1.8	78	2.1	0.9	23.81	7486.4														
			C	116	2	16	2.1	0.97	21.21	3278.3														
12DC53.A	2-3	Hbl	A	75	3.4	153	3.3	0.99	8.4	5095.6	0.3%	0.91	0.29	118.2	28.7	175.5	24.8	272.0	13.6	28.2	61.3	1.77	1.13	0.50
			B	63	1.6	69	1.8	0.92	4.24	11353.8														
			C	103	2.3	10	2.4	0.97	20.69	3334.4														
12DC54.B	2-3	Plag	A	66	3.1	132	3.1	0.85	12	3128	0.5%	0.85	-0.03	232.2	67.2	248.8	34.3	25.6	46.8	142.2	22.8	1.84	0.99	0.55
			B	55	1.7	42	1.9	0.8	14.4	13631.3														
			C	75	1.8	68	2	0.88	12.8	2534.2														
12DC54.B	2-3	Hbl	A	44	3.1	133	3.2	0.86	5.09	4846.8	2.6%	0.96	0.03	232.2	65.8	254.1	39.7	29.5	40.7	142.2	24.2	1.95	1.02	0.50
			B	61	1.8	47	2	0.95	8.05	4316.6														
			C	66	2.1	67	2.2	0.94	8.45	3974.8														
12DC55.A	2	Plag	A	50	5.3	12	5.3	0.76	6.4	7376.9	0.1%	1.21	-0.12	145.4	12.2	235.0	12.2	325.0	0.1	55.4	77.8	2.42	0.93	0.44
			B	59	2.1	179	2.1	0.88	6.44	6148.3														
			C	56	2.6	127	2.8	0.61	4.87	21124.5														
12DC55.A	2	Cpx	A	69	5.6	11	6.2	0.87	10.7	5915.4	0.1%	1.25	-0.10	147.5	10.9	233.6	10.9	323.8	0.7	57.5	79.1	2.49	0.94	0.43
			B	101	2.2	180	2.3	0.87	12.86	2823.8														
			C	53	2.7	127	3	0.91	7.57	10318.6														
12DC55.B	2	Plag	A	51	5	19	5.3	0.98	5.67	14631.9	1.0%	1.26	0.11	308.9	19.3	42.4	19.2	312.1	1.1	218.9	70.7	2.36	1.07	0.40
			B	63	2.6	176	2.6	0.95	3.48	10260.3														
			C	42	2.4	84	2.4	0.95	3.33	24378.1														
12DC55.B	2	Cpx	A	53	4.9	18	5	0.75	6.81	5761.1	0.4%	1.15	-0.09	303.9	19.5	44.5	19.2	313.3	3.3	213.9	70.5	2.31	0.95	0.46
			B	44	2	174	2.1	0.86	1.82	4622.2														
			C	50	2.3	85	2.6	0.96	10	9067.6														
12DC55.C	2	Plag	A	58	4.7	8	4.7	0.86	2.69	10515.2	0.8%	1.46	-0.36	97.7	7.6	234.6	5.2	144.1	5.5	7.7	82.4	3.10	0.78	0.41
			B	69	2	3	2.2	0.93	5.42	4919.8														
			C	70	3.3	2	3.8	0.94	15.2	15071.4														
12DC55.C	2	Cpx	A	46	5.8	7	5.9	0.91	8.39	8257.2	0.5%	1.40	-0.17	79.9	79.9	227.6	4.7	137.0	7.4	349.9	81.2	2.82	0.90	0.40
			B	52	2.3	6	2.4	0.96	5.31	6553.8														
			C	79	3.2	177	3.3	0.89	16.89	7639														

Sample	Def. Event	Min	Face	Sample Size	Fabric Ratio	Vector Mean	Harmonic Mean	Symmetry	Min. Chi Squared	Mean Area	Incompatibility Index	Es octss	v lodes	XY Att	XY Incl	X Att	X Incl	Y Att	Y Incl	Z Att	Z Incl	X Mag	Y Mag	Z Mag
12DC57.A	2	Plag	A	74	3.4	18	3.6	0.78	15.68	6690.2	4.1%	1.25	0.22	337.0	17.9	32.8	14.9	125.4	9.6	247.0	72.1	2.26	1.14	0.39
			B	35	2	109	2.3	0.86	4	5396.5														
			C	38	2.7	2	2.9	0.79	4	11436.8														
12DC57.A	2	Cpx	A	51	3.4	19	3.4	0.94	1.75	1724.2	3.8%	1.11	0.15	336.7	19.0	47.4	18.0	139.3	5.9	246.7	71.0	2.10	1.08	0.44
			B	59	2.4	111	2.5	0.85	12.03	4336.5														
			C	46	2	2	2.1	0.91	0.96	872.3														
12DC58.A	2	Plag	A	77	3.6	179	3.8	0.78	10.08	9193.7	1.2%	0.97	-0.05	55.8	36.4	72.6	12.0	170.8	33.7	325.8	53.6	2.02	0.98	0.51
			B	68	2.2	146	2.4	0.82	14.21	12224.2														
			C	38	2	25	2.5	0.68	5.11	20637.9														
12DC58.A	2	Cpx	A	88	3.5	175	3.9	0.91	13.61	4875.2	1.1%	1.06	-0.12	49.2	33.9	71.5	14.3	170.0	30.0	319.2	56.1	2.17	0.94	0.49
			B	58	2.3	147	2.2	0.83	6.86	5114.2														
			C	52	2.4	23	2.5	0.81	4.54	4648.8														
12DC59.A	2	Plag	A	67	2.7	168	2.8	0.93	7.7	12584.1	1.2%	1.42	-0.01	277.5	14.1	66.4	7.4	334.8	11.9	187.5	75.9	2.73	1.00	0.37
			B	61	5.9	6	5.8	0.92	4.9	20665.1														
			C	32	3.7	126	4.1	0.69	2.88	25293.1														
12DC59.A	2	Cpx	A	82	2.4	169	2.5	0.9	7.76	2859.8	1.1%	1.21	0.02	281.4	13.5	65.4	8.0	333.8	10.7	191.4	76.5	2.33	1.01	0.42
			B	80	4.8	7	5	0.88	18.8	3795.1														
			C	73	2.6	124	2.6	0.93	8.89	7502														
13DC63.A	3	Plag	A	58	3.5	155	3.8	0.83	14.83	5294.8	54.2%	0.62	-0.04	83.6	12.5	201.7	11.1	110.6	5.7	353.6	77.5	1.56	0.99	0.65
			B	56	1.8	95	1.9	0.93	2.93	4386.7														
			C	54	2.7	5	2.6	0.89	11.19	2364.7														
13DC63.A	3	Hbl	A	59	4.5	157	4.4	0.88	7.93	4596.8	51.6%	0.76	-0.14	81.9	11.6	201.6	10.1	110.6	5.6	351.9	78.4	1.75	0.95	0.60
			B	56	1.9	95	2	0.89	5.29	4886.6														
			C	53	2.7	5	2.7	0.83	4.55	4369.4														
13DC63.B	2	Plag	A	41	4.4	30	4.4	0.83	11.88	18658.7	0.1%	1.23	0.16	147.1	60.2	296.7	41.5	169.9	34.2	57.1	29.8	2.27	1.10	0.40
			B	44	2.8	125	3.1	0.86	2.55	12560.5														
			C	27	2.5	132	2.9	0.59	3.93	32170.3														
13DC63.B	2	Hbl	A	81	4	31	4.3	0.69	23.49	7887.8	17.0%	0.99	0.59	152.6	57.5	223.0	56.0	326.7	9.1	62.6	32.5	1.70	1.30	0.45
			B	86	2.5	127	2.5	0.88	8.09	6525.1														
			C	44	2.8	49	3.6	0.95	16	28837.2														

Sample	Def. Event	Min	Face	Sample Size	Fabric Ratio	Vector Mean	Harmonic Mean	Symmetry	Min. Chi Squared	Mean Area	Incompatibility Index	Es octss	v lodes	XY Att	XY Incl	X Att	X Incl	Y Att	Y Incl	Z Att	Z Incl	X Mag	Y Mag	Z Mag
13DC64.A	3	Plag	A	97	2.8	21	3	0.89	14.85	6224.8	0.0%	0.90	0.01	242.6	54.1	244.2	2.2	337.3	54.0	152.6	35.9	1.89	1.00	0.53
			B	59	1.9	54	2.2	0.75	13.9	5603.6														
			C	40	2.3	4	2.5	0.95	4.4	7401.4														
13DC64.A	3	Hbl	A	99	3.7	32	3.9	0.91	14.81	6350.2	4.3%	0.88	0.32	242.4	46.4	243.0	0.6	333.6	46.4	152.4	43.6	1.73	1.14	0.51
			B	106	2.4	128	2.4	0.92	13.26	5676.8														
			C	51	2.5	51	3.1	0.94	9.98	27155.5														
13DC66.A	3	Plag	A	47	3.5	27	4	0.94	14.85	2079.5	6.2%	1.13	0.17	251.9	36.0	37.4	22.4	295.5	26.6	161.9	54.0	2.12	1.10	0.43
			B	44	2	123	2.1	0.82	8	2684.9														
			C	50	2.6	149	2.8	0.92	6	1217														
13DC66.A	3	Hbl	A	38	2.9	28	3.4	0.84	6.58	965.6	6.0%	0.92	0.17	252.2	37.3	42.9	20.5	300.6	29.6	162.2	52.7	1.84	1.08	0.50
			B	41	1.8	128	2.1	0.78	7.98	2463														
			C	34	2.2	148	2.5	0.76	7.65	1745.2														
13DC68.A	2-3	Plag	A	60	2.4	9	2.4	0.87	7.6	5516.5	3.2%	1.21	-0.17	155.6	26.1	261.4	25.3	168.5	6.2	65.6	63.9	2.45	0.91	0.45
			B	54	2.9	155	3	0.93	14.52	7728.9														
			C	56	1.8	102	2	0.64	10.79	9509.9														
13DC68.A	2-3	Hbl	A	48	2.3	10	2.4	0.83	9	11175.9	3.1%	1.02	-0.01	159.2	24.2	256.2	24.0	165.0	2.6	69.2	65.8	2.07	1.00	0.49
			B	42	2.9	157	2.8	0.81	4.48	8062.7														
			C	38	1.7	95	1.9	0.84	2.53	9916														
13VA105.A	2	Plag	A	61	2.7	38	2.8	0.85	9.62	14237.6	0.4%	1.46	-0.05	347.4	38.9	9.9	17.1	111.8	33.7	257.4	51.1	2.86	0.96	0.36
			B	49	5.2	15	5.4	0.94	2.24	20621.9														
			C	49	5.6	146	5.8	0.65	9.22	12908.7														
13VA105.A	2	Hbl	A	71	2	36	2.3	0.87	18.32	2162.1	0.5%	1.27	-0.23	351.6	346.1	37.3	14.5	105.8	33.5	256.1	52.7	2.61	0.87	0.44
			B	58	4.5	14	5	0.79	6.86	10969.9														
			C	52	4.6	146	4.9	0.96	8.38	6077.4														
13VA144.A	1	Plag	A	39	1.7	150	1.9	0.92	5.69	11268.4	0.8%	0.80	-0.06	198.1	32.6	357.0	13.0	259.5	29.3	108.1	57.4	1.77	0.98	0.58
			B	44	1.8	163	1.8	0.73	8.73	24451.4														
			C	45	3	14	2.9	0.93	4.8	13788.7														
13VA144.A	1	Hbl	A	56	1.9	158	2	0.61	10.39	3008	1.3%	0.89	0.02	195.3	23.8	358.3	7.4	265.3	22.5	105.3	66.2	1.86	1.01	0.53
			B	56	2	167	2	0.86	5.68	4668.8														
			C	63	3.3	10	3.2	0.97	6.5	3831.2														

Sample	Def. Event	Min	Face	Sample Size	Fabric Ratio	Vector Mean	Harmonic Mean	Symmetry	Min. Chi Squared	Mean Area	Incompatibility Index	Es octss	v lodes	XY Att	XY Incl	X Att	X Incl	Y Att	Y Incl	Z Att	Z Incl	X Mag	Y Mag	Z Mag
13VA165.A	2	Plag	A	33	2.3	44	2.8	0.73	4.64	12779.6	1.7%	1.45	0.04	172.7	35.3	217.2	26.4	318.6	21.7	82.7	54.7	2.75	1.02	0.35
			B	59	2.9	20	2.8	0.85	7.93	3364.5														
			C	47	5.8	148	5.7	0.81	2.6	4980.7														
13VA165.A	2	Hbl	A																					
			B																					
			C																					
13VA166.BCD	2	Plag	A	46	5.1	179	5.4	0.96	15.43	38403.5	0.7%	1.65	-0.24	101.0	17.8	104.3	1.1	194.6	17.8	11.0	72.2	3.47	0.83	0.35
			B	89	2.4	162	2.5	0.92	12.43	4305.9														
			C	56	8.1	179	8.2	0.71	4.5	11634.1														
13VA166.BCD	2	Hbl	A	43	4.2	2	4.3	0.93	7.42	33605.6	1.1%	1.47	-0.12	101.3	19.4	108.0	2.4	198.8	19.2	11.3	70.6	2.94	0.92	0.37
			B	69	2.5	161	2.4	0.84	7.3	6826.6														
			C	65	6.4	179	6.5	0.95	4.4	10335.9														
13VA167.A	3	Plag	A	63	3.3	54	3.3	0.92	6.14	4845.7	1.5%	0.95	0.16	270.4	50.6	26.8	47.4	281.7	13.4	180.4	39.4	1.89	1.07	0.49
			B	55	2.1	124	2.3	0.84	6	4496.7														
			C	60	2.2	148	2.4	0.93	8.8	2682.9														
13VA167.A	3	Hbl	A	67	2.9	52	3.1	0.93	10.03	2385.9	3.7%	0.90	0.29	267.3	49.6	24.5	46.3	279.5	13.9	177.3	40.4	1.77	1.13	0.50
			B	60	2	127	2.2	0.8	23.6	2017.6														
			C	48	2.3	146	2.3	0.88	10.88	2945.3														
13VA170.A	2-3	Plag	A	77	3.1	168	3.1	0.94	9.69	4643.1	4.7%	0.99	0.07	210.3	81.4	29.1	7.8	257.3	78.3	120.3	8.6	1.98	1.04	0.49
			B	77	2.2	81	2.4	0.91	14.75	2626.5														
			C	72	2.2	6	2.2	0.89	4.22	3438.3														
13VA170.A	2-3	Hbl	A	82	2.9	171	2.8	0.88	14	1951.4	3.8%	0.95	-0.03	211.5	77.9	29.6	8.7	264.9	75.0	121.5	12.1	1.97	0.99	0.51
			B	76	2	78	2.4	0.76	14	1630														
			C	78	2.1	7	2.2	0.9	13.54	2317														
13VA173.A	2-3	Plag	A	191	1.8	97	1.9	0.88	27.25	4076.4	4.0%	0.98	-0.16	331.4	83.5	148.2	26.4	344.2	62.7	241.4	6.5	2.07	0.93	0.52
			B	46	3.5	25	3.2	0.7	9.57	11754.7														
			C	76	3.1	122	3	0.82	15.97	6427.1														
13VA173.A	2-3	Hbl	A																					
			B																					
			C																					

Sample	Def. Event	Min	Face	Sample Size	Fabric Ratio	Vector Mean	Harmonic Mean	Symmetry	Min. Chi Squared	Mean Area	Incompatibility Index	Es octss	v lodes	XY Att	XY Incl	X Att	X Incl	Y Att	Y Incl	Z Att	Z Incl	X Mag	Y Mag	Z Mag
13VA174.A	2	Plag	A	75	2.2	10	2.3	0.88	18.8	4509.3	1.2%	1.24	-0.10	203.6	17.2	259.8	14.5	352.1	9.2	113.6	72.8	2.46	0.94	0.43
			B	43	3.1	51	3.4	0.88	5.93	17977.2														
			C	59	5	166	5.2	0.88	5.32	5316														
13VA174.A	2	Cpx	A	100	2.2	10	2.2	0.94	20.4	4929	1.1%	1.27	-0.12	202.9	18.4	259.9	15.6	352.6	9.5	112.9	71.6	2.53	0.93	0.42
			B	40	3.2	52	3.5	0.9	4	8097.5														
			C	45	5.2	165	4.9	0.93	6	3539.2														
13VA174.B	2	Plag	A	75	2.2	10	2.3	0.88	18.8	4509.3	1.2%	1.82	-0.32	349.1	6.6	54.3	6.0	144.6	2.7	259.1	83.4	4.05	0.76	0.32
			B	43	3.1	51	3.4	0.88	5.93	17977.2														
			C	59	5	166	5.2	0.88	5.32	53.16														
13VA174.B	2	Hbl	A	79	2.5	1	2.6	0.91	5.11	4150	2.1%	1.61	-0.21	326.9	5.6	56.0	146.0	146.0	0.1	236.9	84.4	3.34	0.86	0.35
			B	52	2.9	31	3	0.77	8	8721.6														
			C	48	4.6	180	4.9	0.92	1.5	3588.9														
13VA179.A	1	Plag	A	70	2.6	149	2.9	0.66	14	6755	3.0%	1.17	0.05	102.7	31.1	120.4	10.4	216.2	28.9	12.7	58.9	2.25	1.03	0.43
			B	42	2.5	7	2.6	0.86	3.33	14731.9														
			C	73	3.5	2	3.6	0.82	6.21	5528.6														
13VA179.A	1	Hbl	A	85	2.8	149	2.7	0.82	17.2	4893.2	3.8%	1.07	0.20	109.7	31.4	126.5	10.0	222.1	29.4	19.7	58.6	2.01	1.10	0.45
			B	55	2.3	10	2.4	0.8	9.6	16538.4														
			C	71	3.1	6	3.6	0.93	10.44	5730.7														
13VA190.A	1	Plag	A	51	1.6	92	1.7	0.75	6.84	19245.8	6.5%	0.49	0.30	342.0	80.9	135.6	70.1	344.9	17.5	252.0	9.1	1.36	1.07	0.69
			B	54	1.8	76	1.9	0.89	5.63	14175.9														
			C	50	1.4	107	1.6	0.96	6	21526.3														
13VA190.A	1	Hbl	A	64	1.2	133	1.6	0.91	9.12	6147.5	12.0%	0.32	-0.04	15.2	66.9	160.5	53.1	27.8	27.0	285.2	23.1	1.25	0.99	0.80
			B	60	1.7	80	1.9	0.93	7.2	9178.3														
			C	54	1.2	136	1.7	0.89	8.59	13479.4														
13VA206.A	1	Plag	A	53	1.7	43	2	0.94	3.79	12404.4	1.8%	0.56	0.20	231.0	43.1	258.6	23.5	5.5	33.7	141.0	46.9	1.45	1.05	0.66
			B	59	1.8	166	1.9	0.95	6.44	14093.4														
			C	53	1.6	19	1.8	0.98	2.28	14922.3														
13VA206.A	1	Hbl	A	58	1.4	38	1.7	0.59	4.21	7715.6	5.4%	0.55	-0.20	225.9	36.8	249.8	16.8	350.5	31.6	135.9	53.2	1.51	0.95	0.70
			B	58	1.7	165	2.1	0.79	5.72	8660.9														
			C	55	2	16	2	0.91	2	14985.8														

Sample	Def. Event	Min	Face	Sample Size	Fabric Ratio	Vector Mean	Harmonic Mean	Symmetry	Min. Chi Squared	Mean Area	Incompatibility Index	Es octss	v lodes	XY Att	XY Incl	X Att	X Incl	Y Att	Y Incl	Z Att	Z Incl	X Mag	Y Mag	Z Mag
13VA210.A	1	Plag	A	60	2	176	2.3	0.8	14.4	34984.5	1.8%	0.60	0.08	286.6	11.9	98.4	1.7	8.0	11.8	196.6	78.1	1.51	1.02	0.65
			B	43	1.5	152	1.6	0.88	3.33	36693.3														
			C	40	1.7	169	2	0.85	8.8	17760.7														
13VA210.A	1	Hbl	A	131	2.1	1	2.3	0.95	28.77	8209.6	4.3%	0.61	0.60	317.6	8.3	115.7	3.1	25.3	7.7	227.6	81.7	1.39	1.18	0.61
			B	49	1.3	171	1.7	0.86	3.71	30549.8														
			C	53	2	172	2.3	0.91	4.92	8474.1														
13VA214.A	1	Plag	A	67	1.9	38	2	0.93	5.76	15979.9	3.6%	0.52	0.18	20.2	47.5	149.1	40.3	40.5	20.7	290.2	42.5	1.41	1.04	0.68
			B	53	1.6	139	2.1	0.83	17.75	15465														
			C	51	1.4	120	1.7	0.86	12.73	21178														
13VA214.A	1	Hbl	A	59	2.3	43	2.4	0.95	8.31	9806	2.9%	0.67	0.16	27.3	49.3	153.5	43.2	44.6	19.0	297.3	40.7	1.56	1.05	0.61
			B	74	1.8	141	2	0.92	10.76	5957.1														
			C	61	1.6	121	1.7	0.95	5.69	11362.1														
001-010	2	Plag	XY		1.93							1.65	-0.58			277.0	5.0	7.0	12.0	164.0	77.0	3.73	0.65	0.41
			XZ		1.97																			
			YZ		1.69																			
001-026	3?	Plag	XY		1.46							0.41	0.31			24.0	6.0	293.0	4.0	171.0	83.0	1.29	1.06	0.73
			XZ		1.36																			
			YZ		1.31																			
001-028		Plag	XY																					
			XZ																					
			YZ																					

Sample	Def. Event	Min	Face	Sample Size	Fabric Ratio	Vector Mean	Harmonic Mean	Symmetry	Min. Chi Squared	Mean Area	Incompatibility Index	Es octss	v lodes	XY Att	XY Incl	X Att	X Incl	Y Att	Y Incl	Z Att	Z Incl	X Mag	Y Mag	Z Mag
001-044	3?	Plag	XY		1.46							0.45	0.00			254.0	5.0	347.0	25.0	153.0	65.0	1.37	1.00	0.73
			XZ		1.76																			
			YZ		1.29																			
001-056		Plag	XY																					
			XZ																					
			YZ																					
12NZ32	1	Plag	A	32	1.9	23	1.89	0.94	0.254		2.5%	0.82	-0.47	160.0	11.0	291.0	9.0	200.0	7.0	70.0	79.0	1.91	0.84	0.62
			B	40	2.45	14	2.61	0.85	1.035															
			C	47	1.45	179	1.58	0.94	0.777															
12NZ32	1	Hbl	A	42	1.55	177	1.74	0.95	0.333		5.0%	0.67	0.23	182.0	12.0	275.0	12.0	185.0	1.0	92.0	78.0	1.54	1.08	0.6
			B	34	2.25	14	2.27	0.76	2.733															
			C	31	1.8	179	1.93	0.71	1.844															
12NZ34	1	Plag	A	23	2.6	26	2.27	0.52	1.5		6.2%	0.90	-0.02	224.0	12.0	266.0	8.0	358.0	9.0	134.0	78.0	1.89	0.99	0.53
			B	26	2.05	11	2.48	0.77	1.4															
			C	48	2.5	177	2.71	0.88	0.336															
12NZ34	1	Hbl	A	28	1.55	21	2.01	0.86	1.867		0.3%	0.62	0.12	213.0	11.0	255.0	7.0	346.0	8.0	123.0	79.0	1.52	1.04	0.64
			B	29	1.65	9	2.13	0.48	2.421															
			C	41	2.25	174	2.43	0.98	0.293															
12NZ35	1	Plag	A	17	2	15	2.4	0.71	0.733		4.4%	0.82	-0.03	337.0	24.0	135.0	9.0	41.0	22.0	247.0	66.0	1.8	0.99	0.56
			B	29	1.8	14	1.99	0.9	0.611															
			C	26	2.55	16	2.66	0.92	0.5															
12NZ35	1	Hbl	A	47	1.6	13	1.83	0.64	2.077		2.3%	0.68	0.04	340.0	21.0	132.0	10.0	38.0	18.0	250.0	69.0	1.6	1.01	0.62
			B	48	1.65	12	1.96	0.88	0.554															
			C	43	2.35	15	2.6	0.6	3.232															

Sample	Def. Event	Min	Face	Sample Size	Fabric Ratio	Vector Mean	Harmonic Mean	Symmetry	Min. Chi Squared	Mean Area	Incompatibility Index	Es octss	v lodes	XY Att	XY Incl	X Att	X Incl	Y Att	Y Incl	Z Att	Z Incl	X Mag	Y Mag	Z Mag
12NZ36.A	1	Plag	A	28	1.55	96	1.74	1	0		0.7%	0.90	-0.27	35.0	3.0	91.0	3.0	181.0	2.0	305.0	87.0	1.98	0.89	0.57
			B	41	1.95	3	2.11	0.93	0.293															
			C	43	2.4	2	2.42	0.88	1.616															
12NZ36.A	1	Hbl	A	30	1.45	112	1.77	0.93	0.286		0.6%	0.70	0.03	141.0	6.0	287.0	3.0	196.0	5.0	51.0	84.0	1.63	1	0.61
			B	32	1.75	175	2.04	0.75	0.254															
			C	38	2.5	177	2.53	0.84	1.333															
12NZ37.B	1	Plag	A	34	1.2	10	1.41	0.94	0.4		21.1%	0.34	-0.30	288.0	65.0	296.0	15.0	54.0	60.0	198.0	25.0	1.3	0.95	0.81
			B	19	1.3	54	1.57	0.84	0.667															
			C	27	1.85	16	2.04	0.67	1.217															
12NZ37.B	1	Hbl	A	34	1.4	169	1.62	0.76	0.4		20.8%	0.47	0.15	271.0	57.0	292.0	30.0	55.0	43.0	181.0	33.0	1.37	1.03	0.7
			B	25	1.7	54	1.94	0.64	0.7															
			C	41	1.85	12	2.25	0.73	5.771															